Motion Control and Energy Management of Electric Vehicles

Ricardo Jorge Pinto de Castro

A thesis submitted for the degree of
Doctor of Philosophy

Department of Electrical and Computer Engineering
Faculdade de Engenharia da Universidade do Porto
Porto, Portugal

September, 2013

Abstract

From an engineering perspective, the recent emergence of electric vehicles (EV) is demanding a redesign of the powertrain control in order to better accommodate a new actuator: the electric motor (EM). Besides the advantages offered by regenerative braking, the high energy and power densities of the EM enables the development of multi-motor configurations, where each vehicle wheel is driven by independent EM, e.g., with in-wheel motors (IWM). This configuration represents a very attractive prospect, mainly due to the torque vectoring capabilities, independent wheel torque control, and the elimination of some mechanical components. However, this distributed propulsion also poses some practical challenges, owing to the constraints arising from motor installation in a confined space, to the increased unsprung mass weight and to the integration of the electric motor with the friction brakes. This last issue represents the starting point for this work which in particular focuses on the integration of the IWM within the EV safety and motion control systems.

Since the majority of today's driving aid systems, such as the anti-lock braking system (ABS), are designed around a frictional brake actuator, the simplest approach is to disable the IWM whenever these systems become active, and employ only the mechanical brake actuator during emergency situations. However, this approach does not exploit the full potential of the two braking devices and ignores, for example, the benefits of the high bandwidth of IWM, a useful property to quickly stabilize the wheel slip in limit adhesion conditions. Motivated by this problem, a new braking control system for EVs propelled by IWMs was developed. Firstly, as this is a redundant control problem, we elected a control allocation technique to determine the optimal split between electric and friction brake torque, taking into account the energy performance metrics, actuator constraints and different bandwidths. Secondly, to maximize the generation of the longitudinal force of the tyre, the EV braking system is endowed with a wheel-slip-based ABS. In order to deal with the model uncertainty, e.g., tyre-road friction, that affects the wheel slip regulation, two control approaches are derived: *i*) the first assumes that the tyre-road friction can be approximated with a linear parameterization, and deals with this uncertainty via adaptive methods; *ii*) the second uses sliding mode control to deal with parametric and nonparametric uncertainties, and features a chattering-free operation thanks to a conditional integrator technique. Finally, a peak friction estimator is also incorporated in the braking system, which enables the generation of the slip setpoint for the wheel slip controllers. With the intent to facilitate the real-time identification of the peak friction, the nonlinear Burckhardt model is approximated by a linear parameterization and estimated through the constrained recursive least squares method. The effectiveness of all the aforementioned algorithms was demonstrated through tests carried out in the high-fidelity

CarSim simulator, while the friction estimator and the sliding-mode (wheel-slip) controller were successfully evaluated in an experimental EV prototype.

On the actuation level, a control strategy to regulate the braking force generated by a brake-by-wire (BBW) actuator was developed. Given that this system is governed by a complex structure, involving electrical, mechanical and hydraulic domains, the first step was the construction of a control-oriented model for the actuator, capable of capturing its fundamental dynamics. Based on this reduced model, an adaptive-robust controller to regulate the hydraulic pressure in the actuator was then designed. The proposed control strategy relies on an adaptive term to cope with parameter uncertainties, particularly in the friction model, while the robust term, based on continuous sliding mode, attenuates the disturbances due to modelling approximation errors and other factors. The stability and robustness of the controller were demonstrated with the help of the Lyapunov method, and confirmed through experimental tests carried out in a dedicated BBW test bench.

On top of the above layers, we addressed the motion control of highly redundant EVs, composed of four IWMs and four-wheel steer, with particular focus on the path-following problem. The main goal is to find the values of the wheels' torques and steer such that the vehicle follows a pre-specified path: in *i*) in minimum time; *ii*) with minimum energy; or, *iii*) a trade-off between the travel time and energy consumption. It will be shown that, by bringing together different control and optimisation tools, such as time-to-space transformations, convex optimisation, robust control methods, and control allocation techniques, this complex system can be effectively tackled.

The second major theme of the work is related to the energy management of EVs with multiple sources. Due to well-known technological constraints in the energy storage systems (batteries, supercapacitors and fuel cells), there has been a growing interest in combining various types of energy sources with complementary features. Among the many possible combinations, our interest here lies on the battery and supercapacitors (SC) hybridization, with an active parallel arrangement, i.e., the sources are connected to the DC bus through two bidirectional DC/DC (step-up) converters. We start by investigating the sizing problem of the above-mentioned hybrid storage unit, targeting the minimisation of the installation and running costs of the EV, and subject to performance requirements and technical constraints of the sources. To tackle this problem, an optimisation-based approach was adopted. The obtained results revealed that, as long as the range requirements of the EV are not very high (i.e., below 50km for the particular configuration addressed in this work), the SCs can reduce the hybrid storage unit cost by 20%. After completing the sizing task, our attention focused on developing a robust controller for the DC-Link control layer, i.e., regulating the output voltage of the (parallel) converters and tracking the SC current, in spite of model uncertainties, such as the load current and the SC voltage. This controller is posed as a robust linear-quadratic regulator problem and numerically solved within a linear matrix inequalities framework; a gain-scheduling mechanism on the SC voltage is also incorporated. Experimental validation of the control architecture is carried out in a reduced-scale setup and its advantages, against non-robust and non-gain-scheduled controllers, investigated.

Resumo

Nas sociedades contemporâneas, existe uma grande esperança depositada nos veículos elétricos (VEs) para que estes possam atenuar os problemas de poluição e de baixa eficiência energética associados ao atual modelo de transportes, assentes em combustíveis fósseis. Do ponto de vista prático, este processo de eletrificação exige uma reformulação profunda na cadeia propulsão do veículo, a fim de acomodar um novo sistema de armazenamento de energia e um novo actuador, i.e., o motor elétrico (ME). Para além das vantagens oferecidas pela travagem regenerativa, as elevadas densidades de energia e potência do ME abrem a porta ao desenvolvimento de propulsões elétricas multimotor, em que o binário produzido por cada roda pode ser controlado individualmente, e.g., através de *in-wheel motors* (IWMs). Esta configuração representa uma perspetiva muito atraente para o controlo de movimento do VE, pois possibilita, através da aplicação de estratégias inteligentes de distribuição ativa de binário, uma maior manobrabilidade, desempenho e agradabilidade de condução do veículo. Contudo, este tipo de propulsão também coloca vários entraves práticos, relacionados com a instalação do IWM num espaço com fortes restrições volumétricas, com a interação IWM-suspensão e a com a integração entre o IWM e os travões friccionais. Esta última questão representa o ponto de partida deste trabalho, o qual irá incidir principalmente no estabelecimento de métodos de controlo de movimento para VEs propulsionado por vários IWMs.

Uma vez que a maioria dos sistemas atuais de ajudas de condução, e.g., mecanismos de travagem antibloqueio, são concebidos em torno de um actuador de travagem mecânico, tecnologicamente maduro, a abordagem mais simples passa por desabilitar os IWMs sempre que estes sistemas são ativos, e empregar apenas o actuador mecânico durante situações de condução limite. No entanto, é importante salientar que esta abordagem não explora todo o potencial oferecido pelos dois dispositivos de travagem existentes no VE, e ignora, até, várias das vantagens do IWM, e.g., rápida resposta e elevada eficiência energética. Motivado por este problema, neste trabalho desenvolveu-se novas abordagens de controlo para os sistemas de travagem dos VEs propulsionados por IWMs. Perante a redundância de atuação existente neste sistema, começou-se por desenvolver um método inovador de alocação de binário, visando a determinação do valor ótimo de binário elétrico e binário mecânico, tendo em consideração a eficiência energética de cada actuador, as suas restrições e respetivas larguras de banda. Em segundo lugar, para maximizar a geração de força longitudinal do pneu, o sistema de travagem do EV irá ser dotado de um controlador de deslizamento do pneu. Dado que este controlador necessita de garantir uma operação robusta perante variações paramétricas, e.g., relacionados com o desconhecimento das condições de aderência pneu-estrada, duas abordagens de controlo serão investigadas. A primeira assume que o modelo do atrito pneu-estrada pode ser

aproximado por uma parametrização linear (i.e., um modelo (possivelmente) não-linear, mas cujos parâmetros incertos têm um efeito linear), e adota métodos adaptativos para lidar com a incerteza paramétrica. A segunda, recorre a métodos de controlo puramente robustos, baseados na técnica de controlo por modo de deslizamento incorporando integradores condicionais. Por último, o algoritmo proposto também incorpora um estimador do coeficiente de fricção entre o pneu e a estrada, o qual permite gerar uma referência ótima que o controlador de deslizamento deve impor ao pneu. Nesse sentido, e com o intuito de facilitar a identificação em tempo real do coeficiente de atrito, o modelo Burckhardt é aproximado por uma parametrização linear e os seus parâmetros estimados através de métodos iterativos, sujeitos a restrições (paramétricas). A eficácia de todos os algoritmos acima mencionados demonstrou-se através de ensaios realizados no simulador CarSim, enquanto que o estimador do coeficiente de atrito e o controlador de deslizamento do pneu avaliou-se experimentalmente num protótipo de VE.

No plano dos actuadores, desenvolveu-se também métodos de controlo para a regulação da força de travagem gerada por um actuador do tipo *brake-by-wire* (BBW). Dado que este sistema é composto por uma estrutura complexa, envolvendo domínios elétricos, mecânicos e hidráulicos, a primeira etapa passou por construir um modelo simplificado do actuador, capaz de caracterizar a sua dinâmica fundamental. Com base neste modelo de ordem reduzida, desenvolveu-se, posteriormente, um controlador adaptativo-robusto para regular a pressão hidráulica do actuador BBW. Para atenuar as incertezas paramétricas, particularmente na componente do modelo de fricção, o controlador proposto dotou-se de métodos adaptativos, enquanto que a robustez a perturbações e erros resultantes de simplificações de modelos é garantida através de controlo por modos deslizantes contínuos. A estabilidade, assim como a robustez do controlador perante incertezas, será demonstrada com a ajuda do método de Lyapunov, e corroborada através de vários testes experimentais realizados num banco de ensaio.

Para além do desenvolvimento do sistema de travagem, ao longo deste trabalho concebeu-se metodologias de controlo de movimento para VEs altamente redundantes, com particular enfoque na problemática associada ao seguimento de trajetórias. O objetivo principal consistiu em encontrar o valor de binário e o ângulo de direção das rodas de forma a que o VE percorra uma dada trajetória: *i*) em tempo mínimo, *ii*) com energia mínima; ou *iii*) um valor de compromisso entre os dois objetivos anteriores. Demonstrou-se que, através da exploração de diferentes técnicas de controlo e otimização, tais como a transformação espaço-tempo, otimização convexa, e métodos de controlo robusto, este sistema complexo e de ordem elevada pode ser controlado de uma forma prática e eficaz.

Na segunda parte da tese a problemática associada à gestão de energia em VEs com múltiplas fontes será abordada. Entre as várias combinações possíveis, o estudo incidiu na hibridização bateria-supercondensadores (SC), com uma topologia do tipo paralelo-ativo, isto é, as fontes são conectadas ao barramento DC através de dois conversores (elevadores) bidirecionais. Como ponto de partida, começou-se por investigar o problema de dimensionamento do sistema de armazenamento híbrido, visando a minimização dos custos de instalação e de funcionado do VE. Os resultados, obtidos através de métodos de otimização não-linear, revelam que, desde que os requisitos de autonomia do VE não sejam muito elevados (isto é, abaixo de 50 km neste trabalho), a utilização dos SCs contribui para uma redução do custo do sistema armazenamento híbrido até 20%. Após conclusão da tarefa de dimensionamento, a nossa atenção foi redirecionada para o desenvolvimento de um controlador robusto para o barramento DC do VE, tendo como objetivo regular, simultaneamente, a tensão de saída dos conversores e corrente dos SCs. Uma das principais

dificuldades na construção deste controlador consistiu em garantir uma operação robusta perante perturbações (tais como variações na corrente de carga do barramento DC) e variações paramétricas do modelo, e.g., tensão dos SCs. Para endereçar estes desafios, explorou-se variantes robustas do regulador linear quadrático e métodos de escalonar os ganhos de realimentação do controlador com base no valor de tensão dos SCs. A validação experimental do controlador realizou-se com recurso a um banco de ensaio de escala reduzida, o qual permitiu avaliar as vantagens do algoritmo proposto face a outras estratégias de controlo, nomeadamente controladores lineares com ganhos de realimentação fixos (i.e., não-escalonados).

Acknowledgements

Special thanks to my advisor, Professor Rui Araújo, for providing me with the guidance, support and motivation throughout the PhD journey, which are also extended to my co-advisor, Professor Diamantino Freitas.

I am grateful to Professors Mara Tanelli, Sergio Savaresi, and Matteo Corno, as well as Fabio Todeschini, from Politecnico di Milano, for their help during the development of the hybrid ABS and the brake-by-wire control algorithms, and for their hospitality during my visits to Milano. I also appreciate the valuable discussion with Dr. Jochen Rauh, from Daimler AG, during the IAVSD11 congress, which has helped to extend the functionalities of the torque blending strategy.

I would like to thank Professors João Tasso, Lobo Pereira and Jaime Cardoso, from FEUP, with whom I had the privilege to write joint publications resulting from work carried out at the PDEEC courses. I also must thank Cláudio Pinto and Pedro Pacheco, former undergraduate students at FEUP, João Trovão and Professor Paulo Pereirinha, from ISEC, for our joint efforts on the energy management of EVs with multiple sources.

I owe a great debt of gratitude to Hugo Oliveira, Nuno Cerqueira and Rui Araújo (Jr.) for their help in the experimental tests with the uCar; this is extended to the MCA & Associados Lda., and the WeMoveU team, who developed the electronics control system of the uCar, and upon which the experimental results of this document rely. I also acknowledge the efforts carried out by Nelson Costa and Jorge Ferreira, former undergraduate students at FEUP, in the development of the hardware and software for the uCar datalogging system. Thanks are also due to my PhD colleagues Pedro Melo, Alexandre Silveira and Antonio Salazar for their valuable discussion, which have helped to improve the quality of many of my publications. I would like to express my gratitude to Bruno Bispo, a friend who accompanied me throughout the journey in the PhD studies.

I would like to acknowledge the financial support provided by the FCT (Fundação para a Ciência e a Tecnologia), through the scholarship SFRH/BD/47882/2008, which was fundamental to carrying out this research. Finally, thanks are due to my family, in particular my mother and brother, for their invaluable support.

Contents

List of Abbreviations

1WD	One wheel drive vehicle
2WD	Two wheel drive vehicle
4WD	Four wheel drive vehicle
4WS	Four wheel steer
8WD	Eight wheel drive vehicle
ABS	Anti-lock braking system
BBW	Brake-by-wire
CA	Control allocation
CGI	Cascading generalized inverse
CI	Conditional integrators
CoG	Centre of gravity
CRLS	Constrained recursive least squares
CSMC	Continuous sliding mode control
EHB	Electro-hydraulic braking
EM	Electric motor
EMB	Electro-mechanical braking
EMS	Energy management system
ESP	Electronic stability program
ESS	Energy storage systems
EV	Electric vehicle
FCV	Fuel-Cells vehicles
HEV	Hybrid electric vehicles

ICE Internal combustion engine

IWM In-wheel motor

LMI Linear matrix inequality

LP Linear-programming problem

LQR Linear-quadratic regulator

MIMO Multiple input, multiple output

PHEV Plug-in hybrid electric vehicles

PI Proportional+Integral controller

QCM quarter-car model

QP Quadratic-programming problem

RLS Recursive least squares

SC Supercapacitor

SISO Single input, single output

SMC Sliding mode control

SoC State of charge

TC Traction control

VEM Vehicle energy management

List of Figures

List of Tables

Chapter 1

Introduction

1.1 Research Motivation

The mobility of people represents an essential factor in the activities of contemporary societies. Of the various transport modes (air, sea, rail and road), the road option has been the most popular, in particular the automobile based on the internal combustion engine (ICE). Recent surveys indicate that, at the end of 2009, there were more than 244 million passenger vehicles circulating in Europe, which represents, on average, 472 cars per 1 000 inhabitants [1]. The mass usage of this transportation mode has spurred industry and academia to the development of several technological improvements, in aspects such as: energy efficiency, safety (active and passive), comfort, reliability, electronics, performance (acceleration, braking and handling), pollutant emissions and costs. The list of improvements is almost endless, but the interested reader is referred to the two-volume work of Genta and Morello [2, 3] for an historical account of the technical progress made to the automobile in recent decades.

Despite these advances, the majority of today's vehicles still relies on the ICE, which, due to its mass-usage and oil dependence, raises a host of sustainability and environmental concerns. For example, according to the indicators provided by the Eurostat [4], the transport sector was responsible in 2010 for 20% of greenhouse gas emissions in the European Union (EU-27), contributing to a further aggravation of the global warming problem. In addition, with the exception of Denmark, all the EU-27 countries are oil dependent and imported 553 million tons of crude oil in 2010, of which 32% are used in transportation [4]. Given that the reserves of fossil fuels available on the planet Earth are finite (e.g., reference [5] estimates that, at the 2011 production levels, the proved oil reserves will last 46.2 years), this dependence is a clear menace to the sustainability of the transportation based on ICE. Driven by these concerns, Legislators around the world are putting strict limits on the pollution emission and oil consumption of future vehicle fleets. As an example, the regulation 2009/443/EC defines that, until 2020, the average emissions on all new vehicles sold in the EU-27 should be less than 95 gCO2/km. Taking into consideration the average emission of 136 gCO2/km registered in 2011 [6], there is a clear need to develop reduced-pollution vehicles in order to reach the 2020 goal.

In this context, alternative forms of propulsion, like electric vehicles (EVs), hybrid electric vehicles (HEVs), plug-in hybrid electric vehicles (PHEV) and Fuel-Cells vehicles (FCV) [8] are being recognized as an indispensable means to meet the environmental, sustainability and legislation requirements. As discussed in [9, 10], HEVs and PHEVs

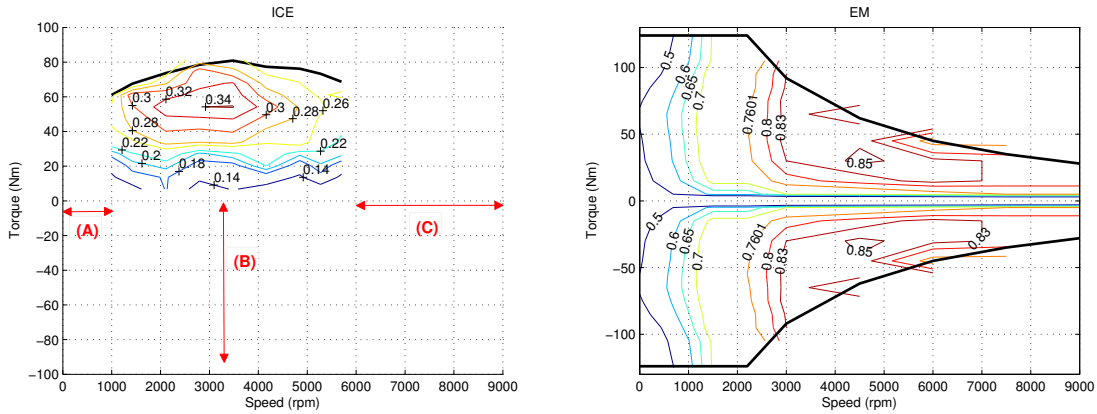

(a) ICE (b) EM

Figure 1.1: Comparison of the operation envelope and energy efficiency of an ICE (41kW) and an induction EM (30kW), retrieved from ADVISOR simulator [7]. The ICE is unable to operate at low speeds (A), or regenerate power (B); in addition, the EM offers a wide speed range (C) and higher energy efficiency.

significantly reduce tailpipe emissions, whereas the EVs and FCVs have zero local emissions. Further, EVs, when integrated with renewable energy sources, e.g., through smart grid concepts [11], allow a truly sustainable mobility solution, free from the dependence on fossil fuels. Nonetheless, the advantages of the electric propulsion do not end with the environmental benefits. Besides the obvious change in the energy source, the electric propulsion will also introduce a major modification in the vehicle powertrain: the electric motor (EM).

The replacement of the ICE, present in today's vehicles, by EMs [1] brings several technical advantages, worthy of discussion:

1. energy efficiency: even taking into account the motor inverter losses, the EM is generally much more efficient than ICE. For instance, the typical efficiency level curves shown in Figure 1.1 clearly illustrate this fact;

2. regenerative braking: unlike the ICE, the EM is able to operate as a generator and recuperate part of the kinetic energy of the vehicle when braking (see zone B in Figure 1.1). Together with the previous point, this feature represents another key element to improving the energy efficiency, particularly in urban driving cycles with frequent stop-and-go operations [12];

3. extended operation envelope: the superiority of the EM speed range over the ICE can be summarized in three zones; firstly, whereas the EM is able to electronically invert the motor speed, the ICE needs a special reverse gear; secondly, the ICE is unable to operate at zero motor speeds, while the EMs do not suffer from such limitations (see zone A); and thirdly, the EM offers a wider speed range ($3-4$ times the base speed [13]) than the ICE, which is illustrated in zone C of Figure 1.1. Owing to this extended operation envelope, the EM-based powertrain can be designed around a gearbox with a single ratio, dismissing the clutch and reducing the transmission

[1] the replacement of the ICE by the EM is complete in EVs and FCVs, while for HEVs and PHEVs both EM and ICE may coexist in the vehicle

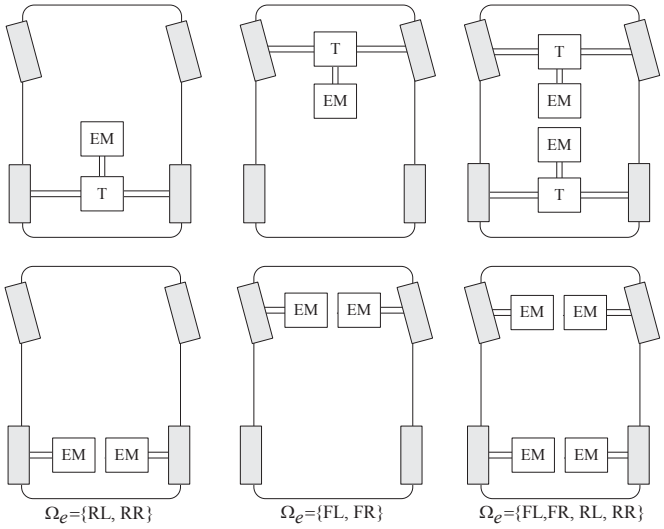

Figure 1.2: Most common powertrain configurations available with the electric propulsion. The top configurations employ a generic transmission (composed of a mechanical differential and a gearbox), while the bottom configurations employ in-wheel (or, alternatively, "close to the wheel") electric motor. The elements in the set Ω_e, FL=front left, FR=front right, RL=rear left, RR=rear right, refer to the driven wheels in each configuration.

complexity. As an added bonus, the driving is also easier since no gear shifting is required [9].

4. torque response: despite the recent advances in the control of ICEs, the torque response of such engines is still relatively slow (typically a few tenths of a second [14]). On the other hand, the EM offers a significantly faster response (a few milliseconds [15]) and precise torque control. Although being of little value to the vehicle driver, this feature can be explored to improve the effectiveness of the vehicle safety systems, like the traction control [16];

5. the high specific power (kW/kg) and torque (N.m/kg) of the EM represents another key feature that is enabling the development of new powertrain configurations. In particular, multi-motor configurations in which several EMs are allocated to each driven wheel of the vehicle (see Figure 1.2), represent an attractive configuration for EVs, due to the independent wheel torque control and the elimination of some mechanical systems, like the differential.

In view of these new features offered by the EM, it is clear that the traditional powertrain design, centered today on ICE, should be reviewed. Besides the regenerative features and extended speed range of the EM, the distributed propulsion with multiple motors is the most disruptive feature for the powertrain design. In contrast to the ICE-based powertrains, which typically rely on a single motor complemented by a mechanical transmission, the EM opens the door to a wider range of configurations (see Figure 1.2). For instance, the most simple and (possibly) cost-effective approach to building the EV powertrain is to maintain the traditional transmission and drive it with one electric motor [10], or, as an alternative, use two electric motors to separately drive the front and rear axles [33, 34]. From the EV motion-control perspective, however, the most appealing configurations are those in which the electric torque transmitted to each driven wheel can be independently

Table 1.1: Some research projects and concept cars that employ IWMs or, alternatively, motors "close to the wheel".

Type[*]	**Group**	**Name**	**IWM** (Ω_e) [**]	**Steer** (Π)[***]
1	FEUP	uCar [17]	FL, FR	-
1	MIRA	H4V [18]	RL, RR	-
1	Hori Lab.	COMS3 [16]	RL, RR	-
1		UOT March II [15]	4WD	-
1	Sungkyunkwan Univ.	- [19]	4WD	-
1	Metropolia	ERA [20]	4WD	-
1	Ohio State Univ.	EGV [21]	4WD	-
1	Keio University	Eliica [22]	8WD (A)	-
1	Fujimoto Lab.	FPEV2-Kanon [23]	RL, RR	F,R
1	DLR	ROMO [24]	4WD	F,R
2	Mitsubishi	Colt EV [25]	RL, RR	-
2	Toyota	Fine X and N [14]	4WD	-
2	Michelin	Concept [26]	4WD	-
2	Audi	e-Tron [27]	4WD	-
2	Mercedes-Benz	SLS E-CELL [28]	4WD	-
2	Venturi	Volage [29]	4WD	-
3	Univ. of Zagreb	- [30]	1WD (B)	-
3	Univ. of Kaiserslautern	meCarScale [31]	4WD	F,R
3	Univ. of São Paulo	HELVIS [32]	RL, RR	F

[*] 1 = research prototypes, 2 = concept cars, 3 = reduced scale prototypes
[**] 4WD = vehicle with four wheel drive, i.e., $\Omega_e = \{FR, FL, RR, RR\}$
[***] Active Steer, F= Front, R=Rear
(A) vehicle with eight driven wheels (8WD)
(B) vehicle with a single driven wheel

regulated, e.g., with in-wheel motors (IWM)[2]. The reason for this interest lies in the possibility of actively modifying the vehicle handling and yaw response [18, 25, 28, 35], which is very useful when the vehicle is operating close to its limits. In addition, for the configurations in which IWMs are present in both front and rear axles, the amount of energy that is recuperated during braking can be maximized and, by carefully integrating the EM within the anti-lock braking system (ABS), the stopping distances decreased. For example, according to the experimental tests reported in [14], by using IWMs in emergency braking the average stopping distance decreased by 7%, while the acceleration times (0 to 100 m) improved 3%. Moreover, as the IWM eliminates the need for a mechanical differential and clutch, the energy losses in the mechanical transmission are reduced, leading to higher energy efficiency. Despite these advantages, the implementation of the traction structure based on IWMs still faces many practical challenges. The main drawback is the higher number of components in the powertrain (e.g., several motors and respective power electronics), which increases the complexity, building costs and maintenance requirements. For these reasons, the IWM usage has been restricted to special classes of vehicles, such as sports [26, 36], military [37], off-road [38], concept cars and research prototypes (see

[2]Throughout the document we will refer to IWM, not only for motors inside the wheel hub, but also for configuration where the motors are "close to the wheel". This "notation abuse" simplifies the discussion.

Table 1.1). Another common concern in the IWM's application is related to the negative effect of the unsprung mass increase on vehicle handling, like ride comfort, but recent studies indicate that such issues have a relatively small impact on the vehicle and can be effectively attenuated [39].

1.1.1 IWM and Motion Control of EVs

The first part of this work intends to investigate the potential impact of the IWM in the motion control of EVs and its active safety systems. The contributions made by systems like ABS and electronic stability program (ESP) to vehicle safety are widely recognized by drivers, the automobile industry and governmental authorities [40]. These systems are, in general, designed around a technologically mature and reliable actuator, the friction brakes, having a good track record in crash avoidance [41]. Consequently, when we consider EVs endowed with IWM, the wisest approach is to retain the current versions of ABS and ESP algorithms, based on friction brakes, and disable the IWM whenever these systems become active [42]. However, this is not the most effective option because, besides ignoring the greater energy efficiency of the electric motor, it also denies one of IWM's main advantages: the quick and precise torque response. As pointed out in [28], the IWM inclusion will not require the re-invention of the control algorithms associated with the vehicle dynamics systems, but it is now clear that, in order to take full advantage of the potential offered by the distributed electric propulsion, the above-mentioned safety systems will have to be reformulated. The key issue in this redesign is to find a suitable strategy to split the braking torque between the IWM and the friction brakes. On one hand, this sharing strategy should use, as much as possible, the IWM, to maximize the energy efficiency, and take advantage of its fast torque response to improve the bandwidth and effectiveness of the safety control system. On the other hand, compared with the friction brakes, the electric motor has a smaller torque range and there are periods of time (e.g., when the energy source is fully charged) where regenerative braking is impossible, introducing important constraints that must be taken into account in the controller design. Up to now, the majority of studies about the electric/friction torque splitting have focused on "normal" braking manoeuvres, i.e., with negligible tyre slips, in mono- or bi-motor topologies (see top part of Figure 1.2 and [12, 43]). However, these studies do not address the powertrain configurations with IWM or the braking allocation suitable for emergency operation, when the ABS (and also ESP) is enabled. To the best of the author's knowledge, with the exception of the reference [14], in the specialized literature very little can be found on this subject. One of the main goals of the present study is to address this lacuna.

The inclusion of IWM in the powertrain should also be analysed along with the growing number of vehicle actuators and safety-related systems that have emerged in recent years (see Figure 1.3). Besides the friction brakes, active front/rear steer and suspensions are receiving increasing attention due to the extension of the lateral operation envelope of the vehicle [44] and the ride-quality improvement [28], respectively. In conjunction with the advances on the drive-by-wire technology [45], such as brake-by-wire (BBW) and steer-by-wire (SBW), the simultaneous use of all these actuators has instigated the development of smart wheel concepts, targeting the integration of electric motor, friction brakes, steering and dampers inside the wheel (or in its vicinity). Several research and industrial projects, such as the ROMO [24], Siemens VDO eCorner [46] and the Michelin Active Wheel [47], are currently being conducted in that direction. The inclusion of smart wheels in the vehicle also poses a multitude of additional objectives to the chassis control (see Figure 1.3). More specifically, in addition to the design of longitudinal controllers, like the ABS and traction

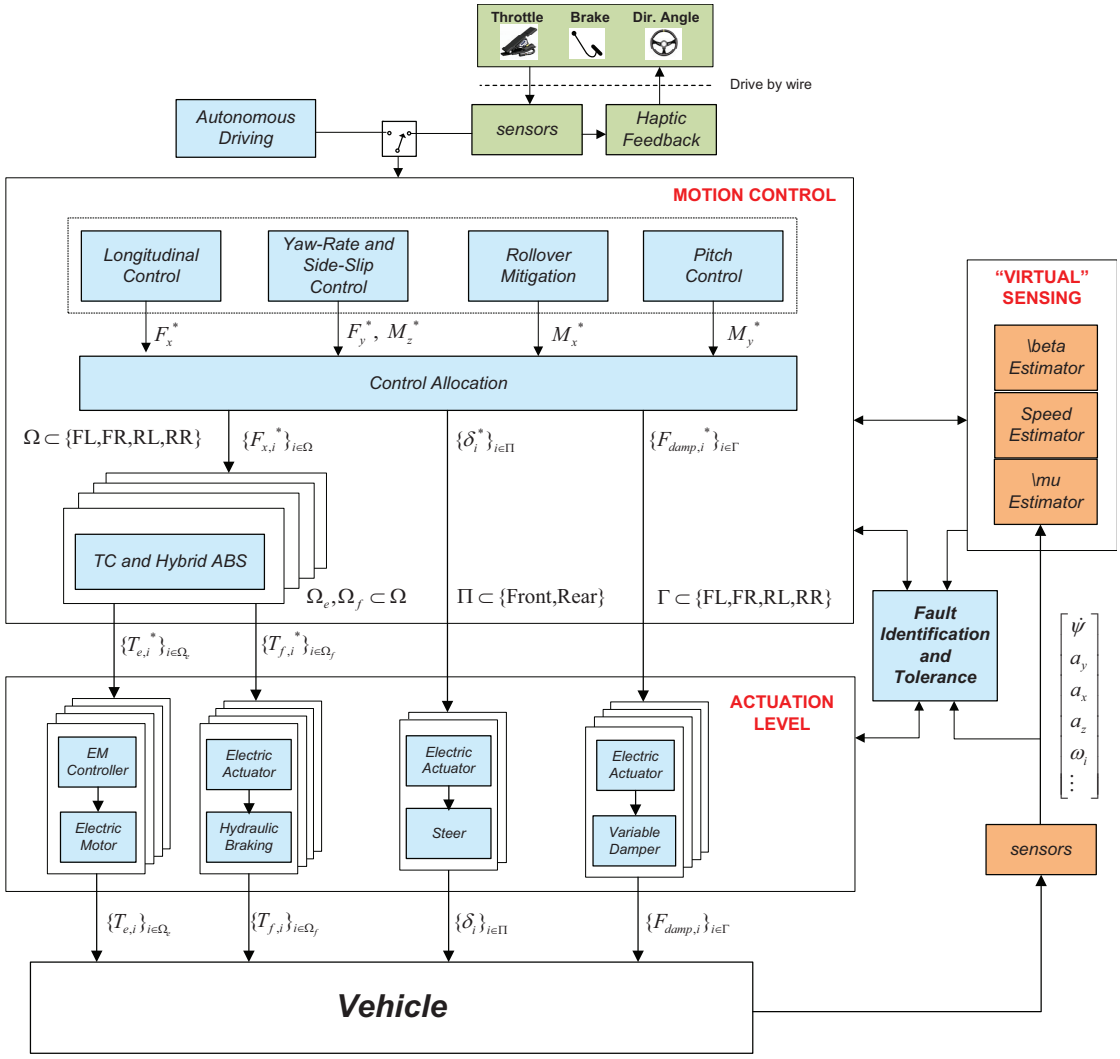

Figure 1.3: Global overview of advanced motion control systems for road EVs. The set Ω_e represents the wheels driven by electric motors, Ω_f the friction brakes, Π the axles with active steer and Γ the active suspension actuators.

control, and the yaw-rate stabilizers, e.g., the ESP [40], other objectives associated with the roll and pitch control [48, 49, 50] need to be considered. Although we could design separated controllers to handle each one of these objectives, in practice, there is interaction between the loops, which may deteriorate the global performance of the system. This issue has motivated a recent trend toward the development of centralized motion control systems [50, 51, 52, 53], complemented with control allocation techniques. The basic idea behind this approach is to use an integrated controller to generate the desired amount of longitudinal force (F_x), lateral force (F_y), yaw (M_z), roll (M_x) and pitching (M_y) moments that should be applied to the vehicle's centre-of-gravity, in order to meet all the control objectives mentioned above. Given the overactuation provided by the smart wheels, the forces and moments required by the motion controller can be generated with different combinations of actuators. To explore this actuation redundancy, and to also cope with the different characteristics (e.g., energy efficiency) and constraints (amplitude and

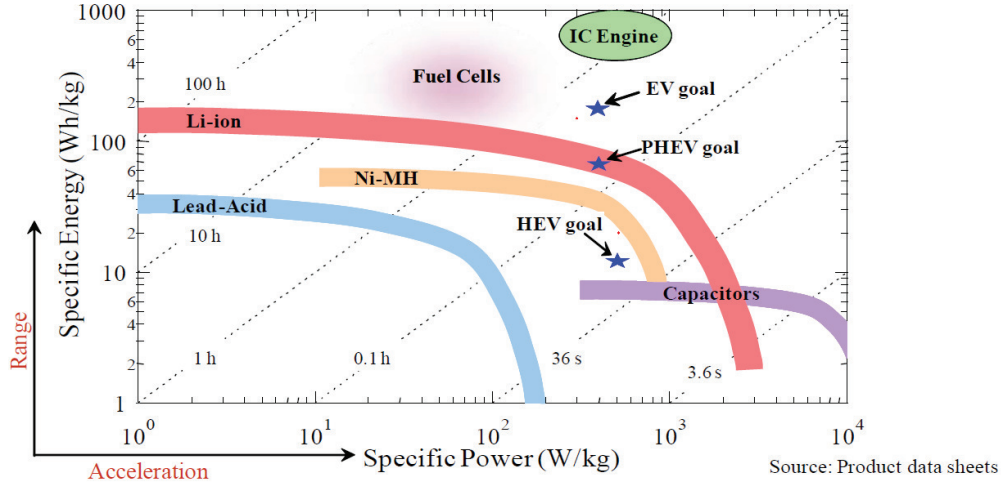

Figure 1.4: Ragone plot for several electrochemical energy storage and conversion devices (retrieved from [55]).

dynamic response), the actuators' setpoints are, in general, obtained through optimization-based techniques [51]. In the literature this task is known as the control allocation (see Figure 1.3), and represents a fundamental building block of the EV's motion controllers that will be developed in later chapters.

The effectiveness of the vehicle's motion controller is dependent upon the access of some critical variables, like vehicle speed, side-slip (β) and tyre-road friction (μ). Some of these variables are not easy to measure and normally require costly sensors that are only available in special prototypes [54]. As cost is a critical factor in automotive applications, there is a practical interest for the development of observers, also denominated of virtual sensors, to extract the value of the above-mentioned variables, using only standard vehicle sensors, such as accelerometers, gyroscopes and wheel encoders (see Figure 1.3). In this work, we will focus mainly on one particular estimation problem: the real-time identification of the μ. The μ information is intrinsically related to the maximum amount of longitudinal and lateral forces that the tyres can generate. As a matter of fact, it depends on several time-varying factors, like road surfaces, precipitation, among many others. Consequently, access to this information is of paramount importance to adapt the safety systems algorithms, like the wheel slip control (ABS and TC) and the motion controller of the vehicle, to the grip levels available on the road [54] and, possibly, alert the driver to dangerous situations [15].

1.1.2 EV Energy Management

In spite of the environmental benefits provided by EVs and the IWM flexibility, the main obstacle to the affirmation of electric propulsion lies in the energy storage systems (ESS). The widespread use of this new transportation option will only be achieved if the ESS offers sound features, like long life-cycle, reasonable cost, fast charge times and high power and energy densities [56]. However, given the current state of technology, these features are difficult to combine into a single class of storage, and remain distant from the energy capacity offered by ICE based vehicles (see Figure 1.4). For instance, batteries, even taking into account the most recent Li-ion chemistries, are generally bulky, relatively expensive

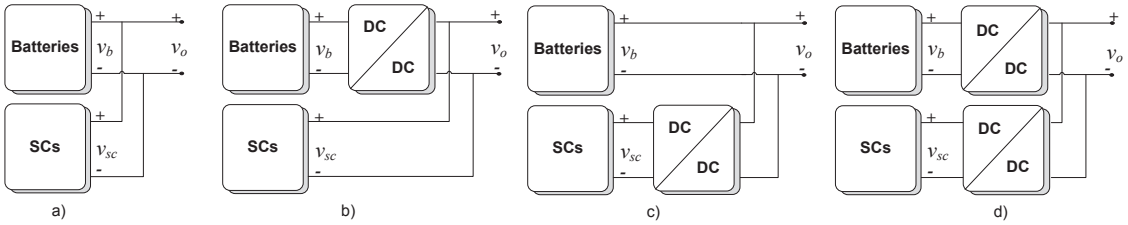

Figure 1.5: Most common configurations employed in batteries-SCs hybridization: a) direct connection; b) and c) represent single converter topologies, and d) a two parallel converters approach.

and withstand a limited number of charges/discharges [57]. Although they remain the most popular choice for the ESS, the typical range is still insufficient to meet the goals of pure EVs [55] (see Figure 1.4). On the other hand, supercapacitors (SCs)[3] support a much larger number of charge/discharge cycles and have a good ability to cope with high current peaks, thanks to their reduced energy losses, but the low specific energy hampers their cause [58]. Consequently, using SCs as the sole energy source of the vehicle leads to a very low autonomy and, for this reason, the SCs are generally more useful in hybrid ESS. Fuel Cells (FC) are another attractive energy source, but suffer from the limited ability to satisfy power peaks and are still at an early stage of commercial development, facing many practical challenges associated with hydrogen storage and refuelling [8].

In the absence of the "ideal" power source, several ESS hybridization strategies have been proposed in the literature [58, 59, 60, 61, 62, 63, 64], driven by the idea of combining sources with complementary features. As pointed out by [58] and [57], in the majority of these hybridizations there is a main energy storage with high energy density (and slow response), which is aided by a secondary source having high power density (and fast response). For example, to compensate for the slow dynamics of the FC, several studies investigated the possibility of complementing FCs with SCs [59], batteries [63], or both [64]. Similarly, the battery-SC combination is also a promising approach to stress reduction in the battery, and improving both the energy efficiency and lifetime [57, 58].

The second part of the present work aims at developing an Energy Management System (EMS) for an EV, based on the batteries-SC hybridization. There are several possibilities to interconnect these two sources: (*i*) direct connection, (*ii*) employ one power converter or (*iii*) use two power converters (see Figure 1.5). In the first option, also known as a passive connection, the power sharing among the sources is dictated only by their impedance, which generally is not suitable for maximizing the hybridization potential [65]. From the cost point of view, using a single converter is the most advantageous solution, e.g., fixing the DC-Link voltage with the battery and employing a converter to regulate the SC power [60, 61, 63, 66]. From a practical perspective, however, this configuration is not always possible, since the battery pack voltage may not match the motor inverter ratings. Because of this, there has been increasing interest in the development of an active parallel arrangement [67, 68, 69, 70], which was the configuration adopted in this work (see Figure 1.5d).

Besides the selection of the appropriate power electronics structure, there are three other fundamental issues that must be addressed in the design of the hybrid ESS. The first consists of finding the number of batteries and SCs cells (i.e., the sizing task) so that the ESS is capable of providing enough power and energy to fulfil the vehicle's specifications, like the range, maximum speed and acceleration, climbing capabilities, etc.

[3] also known as Ultracapacitors [58] and Electrochemical double-layer capacitors (EDLC) [57]

Secondly, it is necessary to determine the power split between the battery and the SCs, having in mind the minimization of the energy losses along the EV mission. Although this goal can be formulated with an optimization problem, and numerically solved [71], in practice the optimum power allocation requires prior knowledge on the driving cycle, an information rarely available during real-time operation. Thus, to overcome these hindrances, sub-optimal, but causal, techniques, like stochastic optimization [72], machine learning[73] and several types of heuristics [66, 74] are receiving increasing attention in the recent literature. After determining the desired power among the batteries and SCs, we need to devise a suitable control strategy for the DC/DC power converters in order to: *i*) impose the required power setpoints in the energy sources and *ii*) ensure an adequate level for the converter's output voltage (v_o in Figure 1.5). As we will see in later chapters, the DC-DC boost converters have nonlinear dynamics and are subject to time-varying exogenous inputs (e.g., the batteries and SCs voltages and the load current), which further complicates the controller design. The design of this controller, named as DC-Link controller, represents an additional goal of the present study.

1.2 Research Goals

In light of the above discussion, it is clear that the inclusion of the IWM within the EV will require a substantial reformulation of the powertrain, not only at the mechanical level, but also at the control systems level. The present study is primarily concerned with the last point, in particular the application of new control and estimation techniques to the EV motion control problem, capable of extracting the full potential offered by the IWMs.

First, we will propose a new design for the braking system of EVs, in order to ensure an appropriate torque distribution between IWMs and frictional brakes. This system must comply with several constraints (e.g., torque range and rate change) and maximize, as far as possible, the vehicle's energy efficiency. In addition to the torque allocator, the braking system should also be equipped with two additional mechanisms: the wheel-slip controller and the μ estimator. The former subsystem is responsible for preventing excessive wheel slip during emergency braking, in spite of modelling errors and measurement noise. It is further expected that the IWM presence, with a higher bandwidth than the frictional brake actuator, will improve the transient response of the slip controller. The later subsystem is used prior to the activation of the slip controller and aims at the identification of the peak friction point, providing not only information about the maximum μ, but also the ideal wheel slip set-point. After establishing a proper split between electric and friction torque it is necessary to send this information to the actuation level, i.e., the electric drives of the IWMs and BBWs actuators; within this level, it is our intention to develop high-performance and robust control strategies for regulating the braking torque produced by the BBW actuator. On top of the above layers, we also aim to develop a motion controller for highly redundant EVs, composed of four IWMs and four-wheel steer. The ultimate goal of the motion controller is to find the wheels' torques and steers, such that the EV is capable of following a pre-defined path, taking into account the road adhesion limits, as well as the performance (i.e., journey time) and energy consumption requirements specified for the vehicle.

In the second place, the problem of energy management in EVs powered by batteries and SCs will be addressed. Assuming that each source has a bidirectional power converter, connected in parallel, we intend to apply robust control techniques to regulate both the

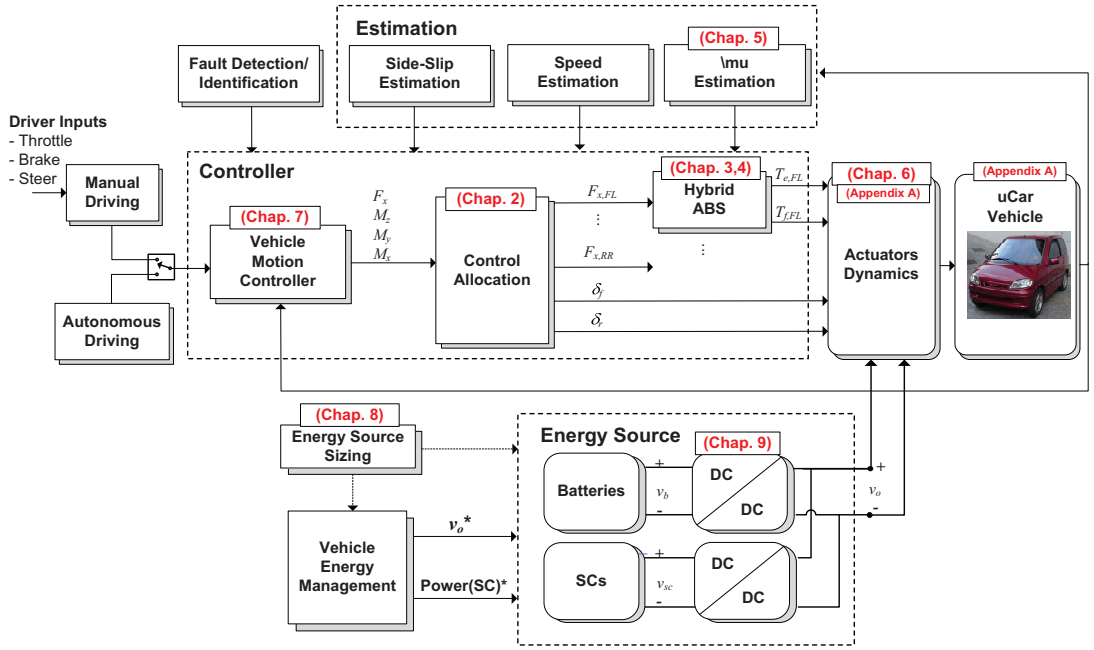

Figure 1.6: Block diagram illustrating the areas covered by each chapter of this work.

output (DC bus) voltage and the power supplied by the auxiliary source, the SCs. Validation in a reduced scale experimental setup is also required. We will also address the sizing task of the hybrid storage unit, aiming at finding a suitable number of batteries and SCs cells, so that *i*) the installation cost of cells is minimised; *ii*) the energy efficiency is maximised, or *iii*) a trade-off between the previous two goals.

1.3 Outline and Contributions

The focus of the present work is spread among many areas of electric propulsion, in particular: *i*) motion control and active safety of EVs driven by IWMs; *ii*) design and implementation of the control systems for the vehicle's actuators; and *iii*) energy management with multiple sources. To help the reader navigate through the document, Figure 1.6 identifies the research areas addressed in each one of the subsequent chapters. The organization and contributions of the work are as follows:

Chapter 2, Review of Control Allocation Methods, introduces the basic principles behind the Control Allocation (CA) technique and lays the foundations for the control of redundant/overactuated systems, developed in later sections. The added value of this chapter consists of a detailed survey of the CA methods available in the recent literature.

Chapter 3, Hybrid ABS, discusses the design of a braking system for EVs equipped with IWMs and friction brakes. The main contribution of this chapter is twofold: first, an adaptive wheel slip controller, gain-scheduled on the vehicle velocity, and capable of dealing with significant uncertainties in grip conditions is proposed; and second, the problem of splitting the electric/friction braking torque is solved with a CA based method, which, besides handling the actuators' constraints, also explores the different bandwidths in the

braking actuators to improve the transient response of the slip controller. The findings of this chapter were disseminated in the following publications:

[I] de Castro, R., Araújo, R.E., Tanelli, M., Savaresi, S., Freitas, D., (2012) Torque Blending and Wheel Slip Control in EVs with In-Wheel Motors, *Vehicle System Dynamics*, vol. 50:sup1, pp. 71-94.

[II] de Castro, R., Araújo, R.E., Freitas, D. (2011) Hybrid ABS with Electric Motor and Friction Brakes. *22nd International Symposium on Dynamics of Vehicles on Roads and Tracks* (IAVSD11), Manchester, UK

Chapter 4, Wheel Slip Control based on Sliding Modes and Conditional Integrator, is concerned with the design of a wheel slip controller based on the sliding mode framework. The main achievement of this chapter consists of the application of an anti-chattering technique, relying on conditional integrators, to the sliding mode wheel slip control and its experimental evaluation in the uCar prototype. Related publications:

[III] de Castro, R., Araújo, R.E., Freitas, D., (2013) Wheel Slip Control of EVs based on Sliding Mode Technique with Conditional Integrators, *IEEE Transactions on Industrial Electronics*, vol. 60, no. 8, pp. 3256 – 3271 .

[IV] de Castro, R., Araújo, R.E., Freitas, D. (2010) A Single Motion Chip For Multi-Motor EV Control. *10th International Symposium on Advanced Vehicle Control* (AVEC10), Loughborough, UK

Chapter 5, Optimal Linear Parameterization for Friction Peak Estimation, presents a new linear parameterization (LP) to represent the friction between the tyre and the road. Compared with other LPs proposed in the literature, the optimal LP offers a reduction in fitting errors and less complexity. Furthermore, a modified version of the recursive least squares, subject to a set of equality constraints on parameters, is employed to identify the LP in real time. The inclusion of these constraints, arising from the parametric relationships present when the tyre is in free-rolling, reduces the variance of the parametric estimation and improves the convergence of the identification algorithm, particularly in situations with low tyre slips. Simulation and experimental results demonstrate the effectiveness of the proposed LP and the robustness of the friction peak estimation method, particularly in low grip situations. This chapter formed the basis for the following publications:

[V] de Castro, R., Araújo, R.E., Freitas, D., (2012) Real-time Estimation of Tire-Road Friction Peak with Optimal Linear Parameterization, *IET Control Theory and Applications*, vol. 6, no.20, pp. 2257-2268.

[VI] de Castro, R., Araújo, R.E., Freitas, D. (2011) Optimal Linear Parameterization for On-Line Estimation of Tire-Road Friction *18th World Congress of the International Federation of Automatic Control* (IFAC11), Milano, Italy

Chapter 6, Adaptive-Robust Friction Compensation in a Hybrid Brake-by-Wire Actuator, reports the development of a pressure-loop controller for BBW systems composed by a hydraulic link and an electro-mechanical actuator. This structure represents an emerging technology within the BBW field, and in the literature there are very few studies that have addressed the modelling and control of such systems. To address this lacuna, we will start by proposing a practical control-oriented model for the actuator. More specifically, it will be shown that under some reasonable assumptions, the actuator can be approximated by an uncertain second-order model, affected by two types of disturbances: parametric and non-parametric. The first, resulting from the friction uncertainties, will be handled by the controller through adaptation mechanisms (switch-σ), while the latter, resulting from modelling approximations, is attenuated with a continuous sliding mode term. The stability and ultimate boundedness of the proposed controller are established analytically through the Lyapunov method, and confirmed with experimental tests carried out in a dedicated BBW testbench. Related papers:

[VII] de Castro, R., Todeschini, F., Araújo, R.E., Savaresi, S. M., Corno, M., Freitas, D. (2013) Adaptive-Robust Friction Compensation in a Hybrid Brake-by-Wire Actuator, *Proceedings of the Institution of Mechanical Engineers, Part I: Journal of Systems and Control Engineering*, in press

[VIII] de Castro, R., Araújo, R.E., Freitas, D. (2012) Adaptive Compensation of the Stribeck Friction in Brake-by-Wire Actuators, *The 13th Mechatronics Forum International Conference*, Linz, Austria.

Chapter 7, Minimum-time Path Following in Highly Redundant Vehicles, represents the culmination of our research on the motion-control topic. The main contributions of this chapter are twofold. First, we propose a convex formulation for the minimum-time optimal problem of EVs endowed with four IWMs and four-wheel steer. Besides being capable of coping with the nonlinearities of the vehicle model, together with the obvious numerical advantages associated with the convex setting, this formulation also contains mechanisms that allow the designer to trade-off journey time and energy consumption of the EV. Secondly, two control allocation algorithms, tailored for the force-splitting problem in highly redundant EVs, are also developed and evaluated in the chapter. The first allocation algorithm extends the cascading generalised inverse method for the force splitting problem. It is shown that, despite being a computationally efficient approach, this method exhibits difficulties in coping with unfeasible forces. To mitigate this issue, a second allocation algorithm, based on the linearizing the friction circle constraints, is proposed. The effectiveness of these algorithms is demonstrated through several tests carried out in the high-fidelity CarSim simulator.

Chapter 8, Combined Sizing and Energy Management in EVs with Batteries and SCs, contains an introductory study on hybridization of storage units, with particular focus on the sizing task. The main contribution of this chapter is the combination of the (optimal) energy management algorithm with the sizing task, which is carried out within a nonlinear optimization setting. The most striking feature of the proposed methodology is the possibility to pursue trade-offs between installation costs and the energy efficiency of the hybrid storage unit. The study also revealed that the SC usage is most useful

when the range requirements are not very high (below 50 km), and may even contribute to a decrease in the installation cost of the hybrid storage unit (when compared with the "battery-only" solution). This research was explored in the following publications:

[IX] Araújo, R.E., de Castro, R., Pinto, C., Melo, P., Freitas, D., (2013) Combined Sizing and Energy Management in EVs with Batteries and SCs, submitted for possible journal publication

[X] de Castro, R., Pinto, C., Araújo, R.E., Melo, P., Freitas, D., (2012) Optimal Sizing and Energy Management of Hybrid Storage Systems. *IEEE Vehicle Power and Propulsion Conference* (VPPC12), Seoul, South Korea

[XI] de Castro, R., Melo, P., Pacheco, P., Araújo, R.E., Freitas, D. (2011) A Control Allocation Approach to Manage Multiple Energy Sources in EVs. *IEEE Vehicle Power and Propulsion Conference* (VPPC11), Chicago, USA

Chapter 9, Robust DC-Link Control in EVs with Multiple Energy Sources, deals with the problem of stabilizing the DC-bus voltage and track the SC current in a hybrid ESS. To cope with the uncertainties in the system, a robust Linear-quadratic Regulator (LQR) is proposed and then numerically solved within a Linear Matrix Inequalities (LMIs) framework. Albeit the LQR+LMI has been previously applied to the control of boost converter (with single-input single-output structure), this technique is extended in this work for the configuration with multiple DC/DC step-up converters, typical of hybrid ESS applications. A second novelty of the proposed controller is the gain-scheduling of the energy source voltages, which is particularly helpful for handling the large voltage variations in the SCs. Experimental validation of the control architecture is carried out in a reduced-scale hybrid ESS, and its advantages over non-robust and non-gain-scheduled controllers, investigated. This study was published in:

[XII] de Castro, R., Araújo, R.E., Trovão, J.P., Pereirinha, P.G., Melo, P., Freitas, D., (2012) Robust DC-Link Control in EVs with Multiple Energy Sources, *IEEE Transactions on Vehicular Technology*, vol.61, no.8, pp.3553-3565.

Chapter 10, reports the final remarks and establishes plans for future work.

Appendix A, Description of the uCar Prototype, contains a brief overview of the EV prototype employed in experimental validation of this work. The main features of the uCar are: *i*) a distributed powertrain architecture, composed of two electric motors coupled to the front wheels of the vehicle, and *ii*) a reconfigurable control system, based on Field Programmable Gate Array (FPGA) technology, and able to simultaneously control the various electric motors in the EV powertrain. Related Publications:

[XIII] de Castro, R., Araújo, R.E., Freitas, D. (2011) FPGA Based Powertrain Control for Electric Vehicles. *Electric Vehicles - Modelling and Simulations*, Seref Soylu (Ed.), ISBN: 978-953-307-477-1, InTech

[XIV] de Castro, R., Araújo, R.E., Freitas, D. (2010) Reusable IP Cores Library for EV Propulsion Systems. *IEEE International Symposium on Industrial Electronics* (ISIE10), Bari, Italy

[XV] de Castro, R., Araújo, R.E. and Oliveira, H. (2009) Design, Development and Characterisation of a FPGA Platform for Multi-Motor Electric Vehicle Control. *5th IEEE Vehicle Power and Propulsion Conference* (VPPC09), Dearborn, MI, USA

[XVI] de Castro, R., Araújo, R.E. and Oliveira, H. (2009) Control in Multi-Motor Electric Vehicle with a FPGA Platform. *4th IEEE Symposium on Industrial Embedded Systems* (SIES09), Lausanne, Switzerland

Within the scope of the present research, the following additional articles were published:

[XVII] de Castro, R., Trovão, J.P., Pacheco, P., Melo, P., Pereirinha, P.G., Araújo, R.E.(2011) DC Link Control for Multiple Energy Sources in Electric Vehicles. *IEEE Vehicle Power and Propulsion Conference* (VPPC11), Chicago, USA

[XVIII] de Castro, R., Araújo, R.E., Cardoso, J.S., Freitas, D. (2010) A New Linear Parametrization for Peak Friction Coefficient Estimation in Real Time. *IEEE Vehicle Power and Propulsion Conference* (VPPC10), Lille, France

[XIX] de Castro, R., Sousa, J., Araújo, R.E., Pereira, F.L., Freitas, D. (2010) Hybrid Modeling, Control and Estimation in ABS Applications based on In-Wheel Electric Motors. *19th International Symposium on Mathematical Theory of Networks and Systems* (MTNS10), Budapest, Hungary

Part I

EV Safety and Motion Control

Chapter 2

Review of Control Allocation Methods

Abstract: *The main objective of this chapter is to provide a revision of the main Control Allocation (CA) techniques found in the recent literature. CA arises in the context of overactuated systems, with more actuators than degrees of freedom; the resulting control law can be easily reconfigurable to handle actuators' failures, and can further explore the redundancy to minimise a performance metric associated with the actuator use. The CA field has strong ties with numeric optimisation methods, real-time and nonlinear control systems. This connection arises since the CA is normally posed as a constrained optimisation problem that must be executed in a real-time system, with limited processing capabilities, and integrated in nonlinear control systems. A systematic classification of the CA methods is also developed in this chapter, presenting a unified vision of this field. The main motivation for studying this problem is based on the dynamic control of a (overactuated) multi-motor electric vehicle, but other applications in avionics, marine and automotive domains are frequently found.*

2.1 Introduction

In recent years, the automotive industry witnessed a progressive increase in the number of actuators available to the vehicle dynamics controller. There are several reasons for this trend; the first one is related to the deployment of hydraulic actuated brakes, used by the Anti-lock Braking System (ABS) to maximise the traction force. The usefulness of these actuators was rapidly extended to address more effective vehicle safety and manoeuvrability systems, like the yaw-rate and side-slip control, representing a cornerstone for the current Electronic Stability Systems (ESP) [40]. A second factor that contributed to the growth of vehicle overactuation was the steady improvements made in reliability, performance and cost of the electronic control (and actuation) systems, which allowed the introduction of drive-by-wire units [45] in the vehicle. This development paved the way to the integration of the active front/rear steer in the ESP, and methods to take full advantage of this new actuator are still under research [53, 75]. More recently, stimulated by environmental and economic reasons, hybrid and electric powertrains began to spur interest in academia and the automotive industry. A particular attractive configuration, from the vehicle dynamics point of view, is the inclusion of in-wheel motors. With this configuration, four electric motors can be distributed by the vehicle wheels and further

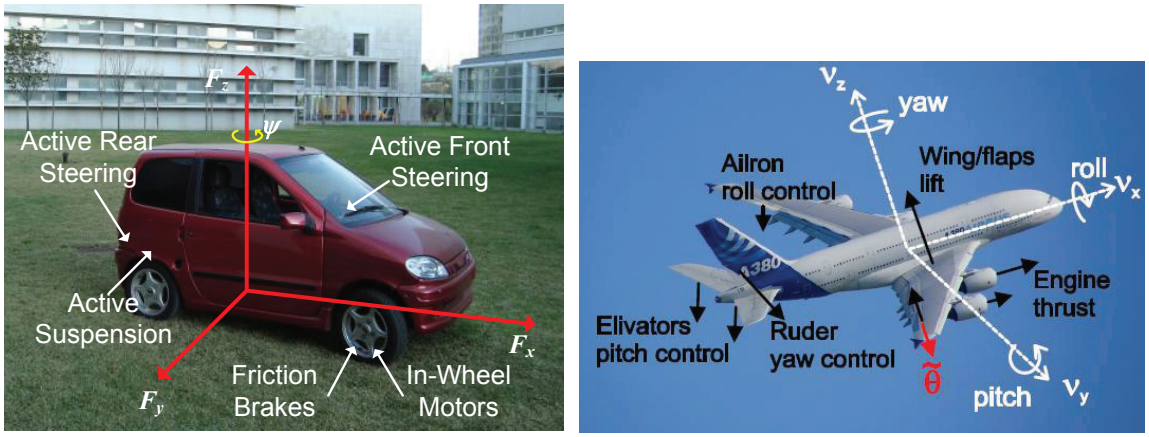

(a) Ground Vehicle (b) Air Vehicle (from [80])

Figure 2.1: Some control allocation applications.

improvements on the traction and ESP systems can be obtained [15]. Finally, active suspensions are also receiving considerable attention due to their notorious impact on ride quality, vehicle handling [76] and (potentential) energy regeneration [77].

In the framework of vehicle dynamics, this growth in the vehicle actuation triggered the development of new control objectives, like roll [78] and pitch control [49], which must be integrated with the traditional yaw-rate, side-slip and longitudinal controls. Therefore, in future automobiles it will not be uncommon to design vehicle dynamic controllers with 14 (friction brakes, in-wheel electric motor, front and rear steering and active suspensions) or more actuators. In fact, the full impact of these actuators in the vehicle dynamics remains an on-going research topic (see [52]). Naturally, the inclusion of all these actuators in the automobile may be economically unfeasible (at least by today's standards). Notwithstanding, this integration is technically viable [79] and, from the research point of view, perfectly acceptable to explore new vehicle limits.

A well-known design tool to address overactuated systems (see Figure 2.1) is the Control Allocation (CA) method. The benefits of this approach will be discussed in the next sections; but, in a nutshell, the capability to reconfigure itself in the event of actuator failure and the vehicular controller simplification are the most attractive factors. Although the before-mentioned automotive application provided the main motivation for studying CA, the remainder of the chapter is completely devoted to the CA methodology, since this area is one of the most complex and challenging modules in the vehicular controller design [53].

Control Allocation has been a research topic in flight control systems for a long time [81], and application-oriented surveys can be found for avionics [82, 83, 84], underwater [85] and ground [86] vehicles. However, most of these references focus on a single application domain and do not give an integrated perspective of the CA field. Therefore, one of the main contributions of this chapter is to present a global and unified overview of the CA field, providing simultaneously a comprehensive review of the main methods proposed in the open literature in the last 20 years. This journey starts with the discussion of the first practical CA method, named non-optimal CA, which is based on the well-known pseudo-inverse inversions techniques [87] and iterative derivations. Though simple, this approach does not take full advantage of the overactuation present in the system. More effective methods, based on constraint optimisation theory, have been explored in the last

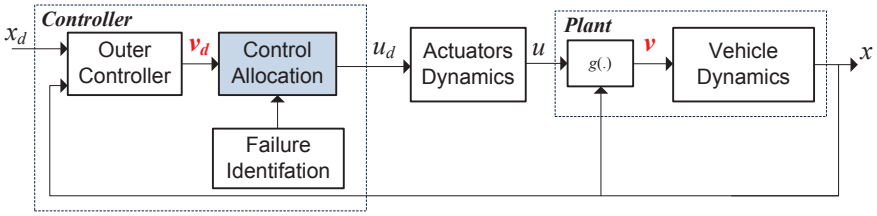

(a) Controlled System

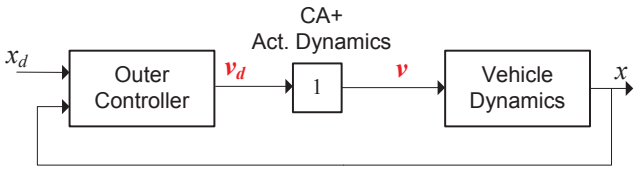

(b) Concept view for the outer loop controller

Figure 2.2: The CA method advocates a two-layer separation: outer control loop, which manipulates a virtual variable v to regulate the plant; and an inner control loop (the Control Allocation), responsible for selecting the actuators to be used. With the CA, the design of the outer layer is simplified (b) and becomes completely insulated from the actuator selection task.

few years [82, 88] to take advantage of the redundancy and to pursue more appealing objectives, such as energy minimisation. This approach has been proven to be an effective means to solve linear CA problems, but may present excessive computational burden for realtime applications. More recently, adaptive laws [80] have been derived to address these issues.

The remainder of this chapter is organised as follows. Section 2.2 discusses the Control Allocation principles of operation and integration with other control methods. Thereafter, details of the main CA categories are given, following a chronological path: non-optimal methods are discussed first in Section 2.3, followed by the optimal approaches in Section 2.4 and adaptive laws in Section 2.5. Finally, some conclusions and topics regarding future work are presented in Section 2.6.

2.2 CA Principles of Operation

In this section a brief introduction to the CA methodology is presented, focusing on the integration between the CA and the system controller. Although the CA can be applied to any type of redundant system, this chapter privileges the use of CA in the motion control of ground, water and air vehicles. To this aim, consider a typical dynamic system represented in state space as:

$$\dot{\mathbf{x}} \;=\; f(\mathbf{x}) + g(\mathbf{x}, \mathbf{u}) \tag{2.1}$$

where $\mathbf{x} \in \mathbb{R}^n$ is the state, $\mathbf{u} \in \mathbb{R}^m$ is the actuator input, $f : \mathbb{R}^n \to \mathbb{R}^n$ and $g : \mathbb{R}^n \times \mathbb{R}^m \to \mathbb{R}^n$ are functions which define the vector field[1]. Although the formulation (2.1) does not cover every type of nonlinear system, it is a sufficient means to represent the main dynamic phenomena of ground [75], water [85] and air [82] vehicles. Obviously, each type

[1] f and g may also depend on time, but to simplify the notation, this dependence was omitted in this chapter

of vehicle model has its own peculiarities; for instance, ground vehicles are very sensitive to the friction conditions in the tyre-road interface, while aerodynamics and fluid dynamics are more relevant to air and underwater vehicles, respectively. Albeit important, these modelling issues are not the main point of the present chapter. In any case, most of the vehicle models can be cast in a state space setting like (2.1), where the state vector $\mathbf{x}$ includes position, orientation and/or speeds (translation and rotation) of the vehicle, and the function $g(.)$ can be viewed as a control effectiveness term, which maps the actuators' values to external forces/moments applied to the vehicle. Another important property that is assumed for $g(.)$ is the actuator redundancy, i.e., $m > n$.

From the vehicle motion control point of view, it is much more useful to directly manipulate the external forces/moments applied to the vehicle than the individual values of the actuators. The reason for this claim is related with a possible nonlinear, time-varying, state-dependent and redundant mapping between the actuators' values and the external forces/moments. Moreover, in the before-mentioned applications the control authority of the actuators is normally constrained, overactuated, and, in conjunction with the nonlinearities of $g(.)$, can significantly increase the complexity of the system controller design.

In order to overcome some of these issues, the CA advocates a separation between the regulation layer, i.e., tracking the state vector $\mathbf{x}$, and selection of the actuators. To illustrate this idea, consider, for a moment, that a direct action on the external forces/moments can be exercised. In this case, the system dynamics can be simplified as:

$$\dot{\mathbf{x}} \quad = \quad f(\mathbf{x}) + \mathbf{v} \tag{2.2}$$

where $\mathbf{v} \in \mathbb{R}^n$ is referred to as virtual control, i.e., the external forces/moments. Under these assumptions, we can build an outer controller (see Figure 2.2b) that manipulates the virtual control, which is much easier to design, since the overactuation and/or nonlinearities in the mapping $g(.)$ are eliminated. For instance, in a paradigmatic aeronautic application [82], by employing the concept of virtual control, the outer controller just needs to manipulate $n = 3$ (virtual) controls, instead of the $m = 16$ original actuators (see [82] for the C-17 aircraft case study). Similar examples can be found on automotive and underwater vehicles [75, 89, 90]. However, this design simplicity comes with a price: the burden in selecting the actuators and handling some nonlinearities is transferred to an inner control loop, the Control Allocation (CA). It is the responsibility of the CA layer to ensure that the virtual control demands are effectively generated. To do so, the CA selects the control intensity $\mathbf{u}$ to meet the virtual control $\mathbf{v}$ requests:

$$\mathbf{v} \quad = \quad g(\mathbf{x}, \mathbf{u}) \tag{2.3}$$

and respect some additional constraints, e.g., position and rate limit bounds, which will be discussed shortly.

The main benefits from the CA approach can be synthesised as follows: 1) the CA can explore the actuation redundancy to easily reconfigure itself when actuator failures occur [53, 91]; naturally, to take full advantage of this property, fault identification techniques must be in place [92]; 2) the CA can handle, to some extent, actuator saturation; for instance, when one actuator saturates, another redundant control can be activated to compensate this nonlinearity [91]; 3) the actuator redundancy can be exploited to optimize a performance index (like minimisation of actuation energy, maintenance costs, etc.); 4) the CA transforms a redundant control problem in a non-redundant system [93]; based on this separation, the outer loop may focus solely on system regulation, possible with a

simpler and more robust controller, being completely insulated from actuators' selection; 5) the CA can be sensitive to the frequency content of the virtual control signal; e.g., by exploiting actuators' bandwidth, slow actuators can respond to low frequencies and fast actuators to high-frequency signals [94].

On the other hand, CA also has some disadvantages. The most notorious drawback is the assumption of very fast actuator dynamics; the CA method assumes that the plant dynamics are much slower than the actuator, and, as a result, the actuator dynamics are usually neglected. Nevertheless, this is not always the case, and in some situations additional compensation must be introduced [95], which is simple for first-order actuators (modelled with a dominant time-constant), but much more complicated for second and higher actuators models. Therefore, the CA is most adequate to systems where a clear bandwidth separation exists between the actuator and the plant. Another important issue is related with non-controlled states (i.e., the zero-dynamics [96]). If the outer controller does not control all the system states, then the CA layer may introduce undesirable dynamics on those states, which may lead to system instability [97].

2.2.1 Mathematical Formulation

As stated before, the primary objective of the CA is to find the inversion mapping of (2.3) and explore the actuator redundancy to pursue secondary objectives, like energy minimisation. The solution to this problem depends on the mapping $g(.)$, which, most of the time, is assumed linear:

$$\mathbf{v} \;=\; \mathbf{B}\mathbf{u} \quad , \qquad \mathbf{B} \in \mathbb{R}^{n \times m} \tag{2.4}$$

as a result of model simplifications, model linearization [75, 91] or a change of variable [85]. Furthermore, the control effectiveness matrix $\mathbf{B}$ has more columns than rows ($n < m$), as a consequence of the actuator redundancy, and there isn't a unique relation between $\mathbf{v}$ and $\mathbf{u}$, i.e., for each $\mathbf{v}$ there are many possible vectors $\mathbf{u}$. Due to physical constraints, the vehicle actuators have limitations in operating range:

$$\mathbf{u}_{min} \leq \mathbf{u} \leq \mathbf{u}_{max} \tag{2.5}$$

where $\mathbf{u}_{min}$ and $\mathbf{u}_{max}$ represent the minimum and maximum range and the operator $\leq$ is applied component wise. Moreover, some actuators, particularly hydraulic based, may have rate limits:

$$\dot{\mathbf{u}}_{min} \leq \dot{\mathbf{u}} \leq \dot{\mathbf{u}}_{max} \tag{2.6}$$

Since the CA methods are normally executed in discrete systems, a common trick to merge the constraints (2.5) and (2.6) is to approximate the derivative by $\dot{\mathbf{u}} = (\mathbf{u}(t) - \mathbf{u}(t-T))/T$, where T is the sampling time. Hence, the rate limit can be posed as a position constraint:

$$\mathbf{u}(t-T) + T\dot{\mathbf{u}}_{min} \leq \mathbf{u} \leq \mathbf{u}(t-T) + T\dot{\mathbf{u}}_{max} \tag{2.7}$$

and, in conjunction with (2.5), generate a single position constraint [91, 98]:

$$\mathcal{U} = \{\, \mathbf{u} \in \mathbb{R}^m \mid \underline{\mathbf{u}} \leq \mathbf{u} \leq \overline{\mathbf{u}} \,\} \tag{2.8a}$$

$$\underline{\mathbf{u}} = \max\{\mathbf{u}_{min}, \mathbf{u}(t-T) + T\dot{\mathbf{u}}_{max}\} \tag{2.8b}$$

$$\overline{\mathbf{u}} = \min\{\mathbf{u}_{max}, \mathbf{u}(t-T) + T\dot{\mathbf{u}}_{min}\} \tag{2.8c}$$

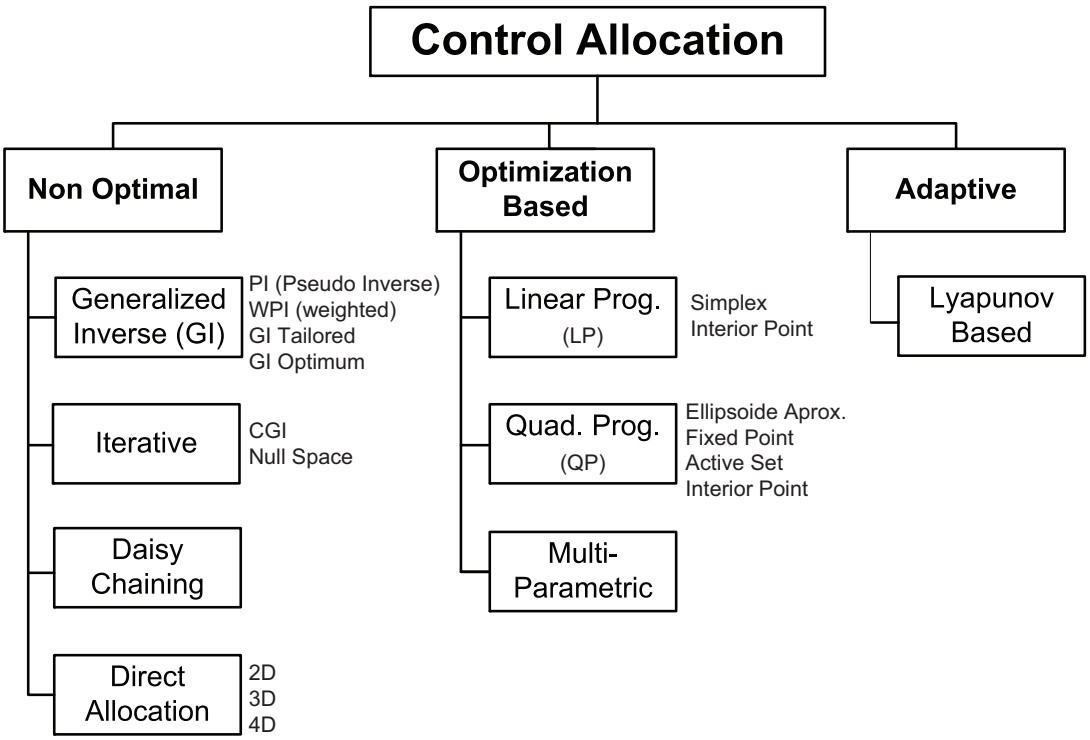

Figure 2.3: Methods for solving the Control Allocation (CA) problem.

In addition to the constraints (2.4) and (2.8), the CA problem normally includes a performance metric $J(\mathbf{u})$, which measures the cost of the actuators' use. Thus, the generic CA method can be posed as an optimisation problem with linear equality and inequalities constraints:

$$\begin{aligned} \min_{\mathbf{u}} \quad & J(\mathbf{u}) \\ s.t. \quad & \mathbf{B}\mathbf{u} = \mathbf{v}_d \\ & \underline{\mathbf{u}} \leq \mathbf{u} \leq \overline{\mathbf{u}} \end{aligned} \tag{2.9}$$

where $\mathbf{v}_d \in \mathbb{R}^n$ is the desired virtual control, generated by the outer controller (see Figure 2.2). In this context, one of the objectives of this chapter it to review the major contributions presented in the literature to solve (2.9), suitable for real-time applications. Before proceeding with the description of the CA methods it is useful to introduce some additional nomenclature. For the simplest CA methods, the solution to (2.9) can be found using a close-form expression, like $\mathbf{u} = \rho(\mathbf{v}_d)$. The CA method can generate solutions that violate the constraints $\mathcal{U}$. In this case, it is necessary to apply a saturation function to ensure the limits $\underline{\mathbf{u}}$ and $\overline{\mathbf{u}}$:

$$\text{sat}(.) = \begin{bmatrix} \text{sat}_1(.) & \dots & \text{sat}_m(.) \end{bmatrix}^T : \mathbb{R}^m \longmapsto \mathcal{U} \tag{2.10}$$

Moreover, the problem (2.9) may not have any feasible solution, so it is useful to define the set of admissible virtual controls:

$$\mathcal{V} \quad = \quad \{ \, \mathbf{v} \in \mathbb{R}^n \mid \mathbf{v} = \mathbf{B}\mathbf{u}, \mathbf{u} \in \mathcal{U} \, \} \tag{2.11}$$

2.2.2 CA Methods

Although the CA problem (cf. (2.9)) appears, at first sight, to be easily solvable with modern computers, there are some practical difficulties. Firstly, the CA is normally executed in real-time systems, with limited processing capabilities and short response times, making it very difficult to calculate the optimal solution in the timeframe available to the CA process. For example, typical control rates in the aeronautics and automotive fields can easily exceed 100Hz; thus, the constrained optimisation problem must be solved in less than 10ms. Secondly, the cost function $J(\mathbf{u})$ can be formulated in different settings, such as linear, quadratic, nonlinear, etc., producing optimisation problems that can be obtained with a wide variety of solvers (like simplex [82], interior point [88], and active sets [91], among others), most of them based on iterative searches, which may not be well suited to real-time implementation. Because of all these factors, the evolution of the CA methods have a strong tie with the development of real-time controllers and their processing capabilities, as will be seen in the next sections.

During the bibliography review, it was possible to catalogue the CA methods in three main approaches (see Figure 2.3): *i*) non-optimal, *ii*) optimal and *iii*) adaptive. The first, non-optimal-based approach, was developed mainly during the '80s and '90s, when the computational resources for the vehicle motion controllers were very limited. As a result, this approach only presents approximate solutions for the problem (2.9), ignoring, most of time, the secondary objective of the CA [98]. Subsequently, with the computational resources gains made in the last decade to the real-time controllers, an increased interest in CA optimisation based techniques has been observed [82, 88, 89], producing successful solutions for the linear CA problem. Despite these promising results, the nonlinear CA problem (which can appear if $J(\mathbf{u})$ or $g(.)$ are formulated as nonlinear functions) remains a challenging problem to be efficiently solved by the embedded platforms. More recently, adaptive CA methods[53, 99] have been derived to address this issue. In the next sections, each of the aforementioned CA categories will be briefly presented.

2.3 Non-Optimal CA

Even though most of the non-optimal CA methods discussed in this section have since been surpassed, they represented an important step in the CA development. In fact, some of the more advanced methods (like Active Sets [91]), have connections to these simpler methods, and additional insight can be gained by first discussing these approaches. The non-optimal CA methods considered in this section are the Generalized Inverse (GI), Iterative GI, Daisy Chaining (DS) and Direct Allocation (DA).

The first two methods focus only on finding efficient numeric procedures to meet the CA minimum requirements, i.e., generating the virtual control respecting the constraints $\mathcal{U}$. Therefore, the performance metric $J(\mathbf{u})$ is normally neglected, yielding non-optimal solutions. Some basic secondary objectives, like prioritisation, are addressed by the DS method, while the DA provides means to ensure the generation of the full admissible virtual control set, $\mathcal{V}$.

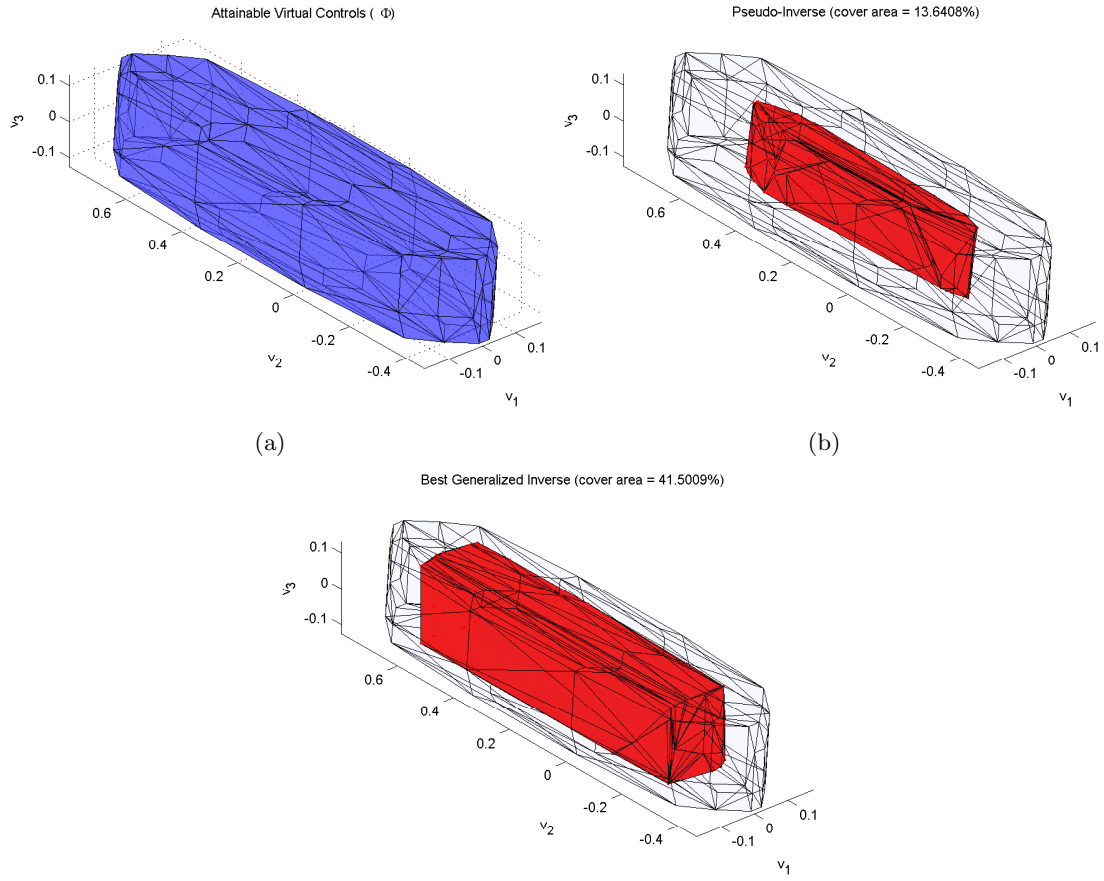

(a) (b)

(c)

Figure 2.4: Set of admissible virtual controls (a), attainable with pseudo-inverse (b) and with best generalised inverse (c) taken from a F-18 example (cf. [100] for the problem setting) with $n = 3$ and $m = 10$. It can be observed that, without violationing the constraints $\mathcal{U}$, the pseudo-inverse generates a fraction of the admissible set $\mathcal{V}$. On the other hand, the generalized inverse significantly increases the attainable set.

2.3.1 Generalized Inverse

The Generalized Inverse (GI) is one of the first practical approaches to solving the CA problem. This method divides the problem into two stages. In the first phase, the restriction $\mathcal{U}$ is ignored, no performance index is considered, and the interest rests on finding a solution to a system of underdetermined equations:

$$\mathbf{v}_d = \mathbf{B}\mathbf{u}, \qquad \mathbf{B} \in \mathbb{R}^{n \times m}, \quad m > n \tag{2.12}$$

A natural solution to the previous problem is to find the right inverse of the matrix $\mathbf{B}$, i.e., $\mathbf{B}\mathbf{P} = \mathbf{I}$, in order to easily calculate $\mathbf{u}$ by a matrix operation:

$$\mathbf{u} = \mathbf{P}\mathbf{v}_d, \qquad \mathbf{P} \in \mathbb{R}^{m \times n} \tag{2.13}$$

where $\mathbf{P}$ is defined in this chapter as Generalized Inverse (GI) of $\mathbf{B}$ [87]. Note that the solution (2.13) may not respect the constraints $\mathcal{U}$; this issue will be addressed in the second stage. First, let's take a look at the problem of choosing the $\mathbf{P}$ matrix. For a given $\mathbf{B}$

there are several ways to determine the GI; two of the most common solutions are:

Pseudo-Inverse

Also known as Penrose-Moore pseudoinverse, this solution assumes that $\mathbf{B}$ is full-rank and produces a minimum norm solution for (2.12), i.e. (2.13) with $\mathbf{P} = \mathbf{B}^{\dagger} = \mathbf{B}^T(\mathbf{B}\mathbf{B}^T)^{-1}$ is the solution of $\min_{\mathbf{Bu}=\mathbf{v}_d} \|\mathbf{u}\|$; (the previous result can be derived in several ways, for instance using the well-known projection theorem [101] or through the Lagrange multipliers theory [102]).

Weighted Pseudo-Inverse

Since the pseudo-inverse solution does not take into account the restrictions $\mathcal{U}$, unfeasible actuator values ($\mathbf{u} \notin \mathcal{U}$) are easily produced. In order to attenuate this issue, a weight matrix $\mathbf{W}$ can be introduced to penalise the use of some actuators: $\min_{\mathbf{Bu}=\mathbf{v}_d} \|\mathbf{Wu}\|$. The analytical solution to this problem is given by:

$$\mathbf{P} = (\mathbf{W}^T\mathbf{W})^{-1}\mathbf{B}^T\left(\mathbf{B}(\mathbf{W}^T\mathbf{W})^{-1}\mathbf{B}^T\right)^{-1} \tag{2.14}$$

For instance, [103] proposes the use of a diagonal $\mathbf{W}$ where each actuator is penalised by an amount inversely proportional to its maximum value (assuming actuator symmetry), $\mathbf{W} = (\mathbf{I}\overline{\mathbf{u}})^{-1}$. This way, the actuators with smaller operation range, and therefore more susceptible to breaching the constraints, are explicitly penalised and less requested.

Although numerically efficient, there is usually a large set of admissible virtual controls ($\mathbf{v}_d \in \mathcal{V}$) for which $\mathbf{u} = \mathbf{P}\mathbf{v}_d$ doesn't meet the constraints $\mathcal{U}$. To better understand this limitation, consider the set of virtual controls for which the GI solution does not violate the restrictions:

$$\Pi \;=\; \{\, \mathbf{v} \in \mathcal{V} \mid \mathbf{u} = \mathbf{P}\mathbf{v} \in \mathcal{U} \,\} \tag{2.15}$$

which depends, of course, on $\mathbf{P}$ selection. One way to quantify the GI performance is to analyse the size of the Π set, e.g., through the generalised volume of $V(\Pi)$ in an n-dimensional space. Analytical methods for calculating this volume can be found in [98, 100], as well as some numerical examples, showing that the Π generated by the pseudo-inverse method is sometimes a small fraction of the maximum attainable set $\mathcal{V}$ (see Figure 2.4). Spurred by this factor, [81] notice that the GI $\mathbf{P}$ can be chosen to satisfy $(m-n)n$ virtual controls. Therefore, this flexibility can be explored in:

Tailoring

This method improves the local volume of Π around a virtual control set-point [81], particularly useful if a group of set-points are known in advance. However, if $\mathbf{B}$ or $\mathbf{v}_d$ changes frequently, this can lead to abrupt reconfigurations of the actuators, impractical in real situations [100];

Best Generalized

As the name implies, the idea of this methods is to find the GI that maximises the volume of Π:

$$\mathbf{P}_{\text{best}} = \arg\max_{\mathbf{P}} V(\Pi(\mathbf{P})) \tag{2.16}$$

Like the "Tailoring" approach, if $\mathbf{B}$ is time-varying, undesirable abrupt changes in the actuators can occur [81].

Even though the use of the Best Generalized Inverse significantly increases the Π volume (see Figure 2.4), the totality of the admissible set may never be achieved. In other words, Π will always differ from $\mathcal{V}$ for any $\mathbf{P}$ selected (this claim was proofed in [81]). Therefore, there are admissible virtual controls ($\mathbf{v}_d \in \mathcal{V}$) for which the GI solution does not respect the actuators physical limits ($\mathbf{u} \notin \mathcal{U}$). In those situations, the easiest method to comply with $\mathcal{U}$ is to truncate the solution:

$$\mathbf{u} = \rho_{GI}(\mathbf{v}_d) = \text{sat}(\mathbf{P}\mathbf{v}_d) \tag{2.17}$$

where sat(.) is the saturation function, defined in (2.10). This truncation introduces troublesome consequences, most notably a significant tracking error on $\mathbf{v}_d$. Nevertheless, the GI simplicity is striking and still remains a practical tool to solve the basic CA requirements on some automotive [104] and aeronautic[105] applications.

2.3.2 Iterative GI

In order to overcome the truncation error of the GI, iterative methods have been proposed. This section briefly analyses the Cascading GI and the Null Space Intersection.

Cascading GI

The Cascading GI (CGI) [98] (a.k.a. Iterative GI [106]), is an iterative application of the GI method to handle the actuator truncation: when the solution obtained with (2.13) doesn't comply with the set $\mathcal{U}$, then the actuators that will be truncated in (2.17) are saturated and removed from the problem. The remaining actuators are then recalculated (using a new GI) in an attempt to generate the desired virtual control. During the new redistribution, other actuators may saturate, in which this procedure must be applied iteratively until the tracking error is zero or all the actuators are saturated.

Algorithm 1 Cascading GI (CGI)

Require: $\mathbf{v}_d, \mathbf{B}, \mathcal{U}$
  $\mathcal{I}_{sat} \leftarrow \emptyset$ {saturated actuators}
  repeat
    $\mathbf{B}_f \leftarrow [\mathbf{B}_i]_{i \notin \mathcal{I}_{sat}}$ {control eff. for free actuators}
    $\mathbf{e}_v \leftarrow (\mathbf{v}_d - \sum_{i \in \mathcal{I}_{sat}} \mathbf{B}_i u_i)$
    $[u_i]_{i \notin \mathcal{I}_{sat}} \leftarrow \mathbf{B}_f^{\dagger} \mathbf{e}_v$ {reconfigure non sat. actuators}
    $\mathcal{I}_{sat} \leftarrow \mathcal{I}_{sat} \cup \{\ i \notin \mathcal{I}_{sat} \mid u_i \leq \underline{u}_i$ **or** $u_i \geq \overline{u}_i;\ \}$
    $\mathbf{u} \leftarrow \text{sat}(\mathbf{u})$
  until $\mathbf{v}_d = \mathbf{B}\mathbf{u}$ **or** $\#\mathcal{I}_{sat} = m$

Algorithm 1 describes the CGI approach, where the notations $[u_i]_{i \notin \mathcal{I}_{sat}}$ and $[\mathbf{B}_i]_{i \notin \mathcal{I}_{sat}}$ represent the vector and matrix, respectively, associated with unsaturated actuators.

Despite an increase in the computational load, the CGI significantly improves the allocation performance over the GI (with truncation) and increases the volume of Π. In the original CGI [98], as described in Algorithm 1, all saturated actuators are removed in future iterations. However, more efficient heuristics can be used, for instance removing only one saturated component with the higher rate of $\mathcal{U}$ trespass [107], or the one that

minimises the distance to the desired virtual control [108]. A more rational approach, based on the optimisation theory and active set methods, is also discussed in this chapter, but is postponed to a later section.

Finally, it is important to note that even with an admissible virtual control, $\mathbf{v}_d \in \mathcal{V}$, the CGI can generate an actuator value with tracking error [82], i.e., $\mathbf{Bu} \neq \mathbf{v}_d$.

Null Space Intersection

Consider the solution obtained with the GI (cf. (2.13), which is referred to in this section as $\mathbf{u}_p$, i.e., $\mathbf{v}_d = \mathbf{B}\mathbf{u}_p$, and the Null Space generated by $\mathbf{B}$:

$$\mathcal{N}(\mathbf{B}) \quad = \quad \{\, \mathbf{u} \in \mathbb{R}^m \mid \mathbf{Bu} = 0 \,\} \tag{2.18}$$

which has dimension $m - n$ if $\mathbf{B}$ is full-rank. By the Null Space definition, we can add any element of $\mathcal{N}$ to $\mathbf{u}_p$, such that the resulting virtual control remains unchanged. This property can be useful to deal with unfeasible solutions produced by the GI, since the final actuator value, $\mathbf{u}_p + \mathbf{u}_n$, can be feasible. To put it another way, the idea is to find a $\mathbf{u}_n \in \mathcal{N}$ such that $\mathbf{u}_p + \mathbf{u}_n \in \mathcal{U}$, or, more generally, to find the set:

$$\mathcal{S} = \{\mathbf{u}_p + \mathcal{N}(\mathbf{B})\} \cap \mathcal{U} \tag{2.19}$$

If this set is non null, then we can find all the solutions to the inequality and equality constraints of the CA problem (2.9). The conceptual usefulness of this method is undeniable, but in practice it is laborious to implement, since the analytical characterisation of the set (2.19) is difficult and is also intractable for higher-dimension spaces [98].

2.3.3 Daisy Chaining (DC)

In avionics applications it is common to use redundant actuators with different maintenance costs. Hence, from an economic standpoint, it is convenient to just use the most expensive actuators when strictly necessary. This practical observation led to the proposal of the Daisy Chaining (DC) allocation method [93, 97], which defines a set of actuation banks, $\mathbf{u}^1$ (primary group), $\mathbf{u}^2$ (secondary), ..., $\mathbf{u}^p$, with different priority between them. For a given virtual control reference $\mathbf{v}_d$, the DC tries to satisfy the demand with the primary group, using, for example, the GI method. If the first actuator bank is not enough, then the secondary group is activated to fulfil the demand, and so on (see Figure 2.5). More formally:

$$\mathbf{u} = \begin{bmatrix} \mathbf{u}^1 \\ \mathbf{u}^2 \\ \vdots \end{bmatrix} = \rho_{DS}(\mathbf{v}_d) = \begin{bmatrix} \mathrm{sat}(\mathbf{P}_1\mathbf{v}_d) \\ \mathrm{sat}(\mathbf{P}_2(\mathbf{v}_d - \mathbf{B}_1\,\mathrm{sat}(\mathbf{P}_1\mathbf{v}_d))) \\ \vdots \end{bmatrix} \tag{2.20}$$

where $\mathbf{B}_i$ is the control effectiveness matrix associated with the group $i = 1, 2, \ldots, p$ and $\mathbf{P}_i$ the corresponding GI.

2.3.4 Direct Allocation (DA)

The direct allocation method, originally proposed in [81], relies on following geometric argument: for each virtual control $\mathbf{v}_d$ on the boundary of $\mathcal{V}$, there is only one actuator vector $\mathbf{u} \in \mathcal{U}$ that can generate $\mathbf{v}_d$. Based on this finding, the DA method calculates the actuator

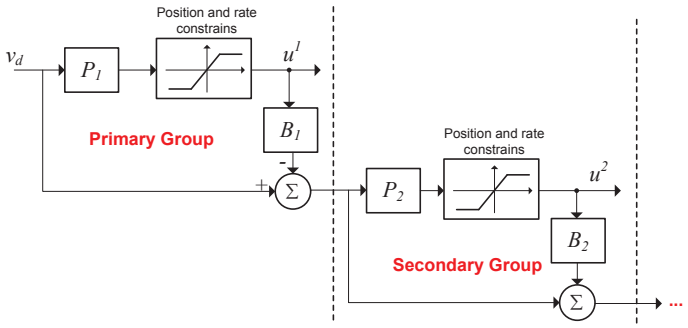

Figure 2.5: Daisy Chaining approach.

value for each virtual control by re-scaling the solution obtained on the boundary [100]. Compared with the GI-based approaches, the DA guarantees that the admissible set $\mathcal{V}$ is always attainable, and, due to the re-scaling operation, the directionality of the original virtual control is preserved. On the other hand, the dimension n can be an issue: for $n \leq 2$ it's relatively easy to calculate the solution [81], but for higher dimensions ($n \geq 3$) the problem becomes very complex, as illustrated in [109]. Moreover, [91] pointed out that the actuator redundancy in the DA is being used just to preserve the directionality of $\mathbf{v}_d$, while optimal-based CA methods, discussed in the next section, can be employed to explore more appealing objectives (for instance, energetic). More recently, Bodson [82], reformulated the DA geometric argument in an optimal problem setting, transferring, somehow, the DA to the optimal-based CA class.

2.4 Optimal CA

The non-optimal CA algorithms, described in the previous section, were developed in a context of strong computation constraints, and most of them do not guarantee that the reachable set $\mathcal{V}$ is totally attainable [81]. From the control point of view this is translated to a reduction of the control authority, introducing an undesirable decrease in the vehicle manoeuvrability range. Moreover, with the exception of DA, the non-optimal CA methods are unable to effectively address the constrained optimisation problem (2.9). For all these reasons, in the last decade numerical optimisation techniques began to be seen as an attractive alternative to the CA problem, strongly driven by the aerospace industry [82, 83, 110, 111]. Unsurprisingly, the performance index $J(\mathbf{u})$ plays a key role in the solution complexity, and the next section is devoted to analyse this issue. After that, the main numerical methods for solving the CA, based on Linear Programming, Quadratic Programming and Multi-parametric approaches, are revisited.

2.4.1 Performance Metric

Convexity is a fundamental property that $J(\mathbf{u})$ must hold, in order to guarantee global optimal solutions [112]. Consequently, the $l_p, 1 \leq p \leq \infty$, norm is a natural candidate to

the performance index:

$$\begin{aligned} \min_{\mathbf{u}} \quad & J(\mathbf{u}) = \|\mathbf{u} - \mathbf{u}_o\|_p^p \\ s.t. \quad & \mathbf{B}\mathbf{u} = \mathbf{v}_d \\ & \underline{\mathbf{u}} \leq \mathbf{u} \leq \overline{\mathbf{u}} \end{aligned} \tag{2.21}$$

where $\|.\|_p$ is the traditional l_p norm and $\mathbf{u}_o \in \mathbb{R}^m$ the "preferred" control set-point, to which the actuators should be attracted if the feasible set has more than one solution. For example, in aeronautical applications, $\mathbf{u}_o$ represents a set-point which minimises the drag, control deflections, wing loading, etc. [91], and, most of the time, is set to zero. The selection of the p norm influences the solution complexity, leading to Linear Programming (LP) problems for $p = 1$ and Quadratic Programming (QP) for $p = 2$. Naturally, the l_2 is the most popular choice given its relationship with the actuator energy consumption (even actuators with non-quadratic energy consumption can sometimes be reasonable approximated by l_2 norm [90]). Additionally, a very useful tool in the CA design is the inclusion of a weight matrix in the norm (similar to the Weighted Pseudo-Inverse discussed previously) in order to penalise the use of certain actuators. However, to simplify the presentation of the numerical methods, the weight matrix is not explicitly considered in the remainder of the chapter, although it can be easily accommodated in the solutions.

Another common technique when solving (2.21) is to formulate the problem as a multi-objective scheme:

Two-stage Optimisation

This scheme, also known as sequential optimisation, divides the CA problem into two stages [82, 83, 91]:

$$\mathcal{U}_A = \arg\min_{\underline{\mathbf{u}} \leq \mathbf{u} \leq \overline{\mathbf{u}}} J_1(\mathbf{u}) = \arg\min_{\underline{\mathbf{u}} \leq \mathbf{u} \leq \overline{\mathbf{u}}} \|\mathbf{B}\mathbf{u} - \mathbf{v}_d\|_p^p \tag{2.22a}$$

$$\mathbf{u} = \arg\min_{\mathbf{u} \in \mathcal{U}_A} \|\mathbf{u} - \mathbf{u}_o\|_p^p \tag{2.22b}$$

In the first stage, defined by (2.22a), a primary optimisation problem is solved, whose main interest is to assess whether the equality and inequalities constraints can be met. If the result of this first stage is non-zero ($J_1 \neq 0$), then the constraints cannot be fulfilled, and the problem ends returning the actuator value that best approximates the desired virtual control $\mathbf{v}_d$. On the other hand, if the result is zero ($J_1 = 0$), a second optimisation problem is formulated, defined by (2.22b), in order to explore the actuator redundancy to approximate the "preferred" control set-point.

Mixed Optimisation

The two-stage optimisation can be simplified by grouping the primary and secondary objective functions in the same cost function [82, 94]:

$$\min_{\underline{\mathbf{u}} \leq \mathbf{u} \leq \overline{\mathbf{u}}} \quad \alpha\|\mathbf{B}\mathbf{u} - \mathbf{v}_d\|_p^p + \epsilon\|\mathbf{u} - \mathbf{u}_o\|_p^p \tag{2.23}$$

where $\alpha, \epsilon \in \mathbb{R}_+$ represent the trade-off between the primary objective (produce the desired virtual control $\mathbf{v}_d$ with zero error), and the secondary objective (approximate the "preferred" control set-point). According to [82], the mixed optimisation can generally

be resolved more quickly than the two-stage optimisation and offers better numerical properties. In addition, the solution to (2.23) converges asymptotically to the solution of (2.22) [113].

Although the norm-based cost function (2.21) is the most popular choice for the performance index, there are, nevertheless, alternative metrics that can be used to explore the overactuation property:

Dynamic CA

Reference [94] proposed a cost function that penalises variations in the control compared with previous iterations:

$$J(\mathbf{u}) = \|\mathbf{u} - \mathbf{u}_o\|_p^p + \|\mathbf{W}(\mathbf{u} - \mathbf{u}[k-1])\|_p^p \tag{2.24}$$

where $\mathbf{u}[k-1] \in \mathbb{R}^m$ is the CA solution obtained in the previous sample, and $\mathbf{W}$ the weight matrix. The main idea behind this formulation is to include the actuators frequency response in the CA objective; e.g., through an appropriate choice of $\mathbf{W}$ matrix, we can shape the frequency response of the CA method, so that slow actuators respond to the low frequencies in the virtual control signal and fast actuators to the higher frequencies. If no saturation occurs, the CA solution to this problem can be seen as a linear filter, which, under the non-singularity condition on the $\mathbf{W}$ matrix, can be proved to be stable [91]. Moreover, the dynamic CA formulation can attenuate, to some extent, the effects of the fast actuator assumption that hampers most of the CA methods [94].

Slack Variable

Literature [85, 89, 90] formulate the mixed optimisation problem using slack variables:

$$\begin{aligned} \min_{\mathbf{u},\mathbf{s}} \quad & J(\mathbf{u}) = \|\mathbf{u}\|_p^p + \alpha\|\mathbf{s}\|_p^p \\ s.t. \quad & \mathbf{B}\mathbf{u} - \mathbf{s} = \mathbf{v}_d \\ & \underline{\mathbf{u}} \leq \mathbf{u} \leq \overline{\mathbf{u}} \end{aligned} \tag{2.25}$$

where $\mathbf{s} \in \mathbb{R}^n$ is the slack variable and $\alpha \in \mathbb{R}_+$ a adjust factor between the objectives. The motivation for this formulation is related with non-attainable virtual controls, i.e., $\mathbf{v}_d \notin \mathcal{V}$, which can lead to a violation of the equality constraint $\mathbf{B}\mathbf{u} = \mathbf{v}_d$. Thus, introducing the slack vector $\mathbf{s}$ allows a deviation between the virtual control requested ($\mathbf{v}_d$) and the real virtual control produced ($\mathbf{B}\mathbf{u}$), which must be minimised.

Singular Avoidance

A particularly challenging problem that can appear on some applications is the case of a nonlinear relation between the virtual control and the actuators' inputs:

$$\mathbf{v} = \mathbf{B}(\mathbf{u})\mathbf{u} \tag{2.26}$$

In this situation, it is of paramount importance to avoid control configuration that could lead to a loss of controllability in the vehicle, e.g., if one of the lines in $\mathbf{B}(\mathbf{u})$ is zero. This last property is equivalent to $\mathbf{B}(\mathbf{u})$ not being full-rank. Accordingly, a natural way to prevent the loss of controllability is to introduce a term in the performance index that

penalises the singularity condition of matrix $\mathbf{B}(\mathbf{u})$ [114]:

$$J(\mathbf{u}) = \|\mathbf{u}\|_2^2 + \frac{\alpha}{\epsilon + \det(\mathbf{B}(\mathbf{u})\mathbf{B}^T(\mathbf{u}))} \tag{2.27}$$

where $\alpha \in \mathbb{R}_+$ is a trade-off term between the norm minimisation and the singular avoidance condition and $\epsilon > 0$ is used to avoid divisions by zero. However, the second term in (2.27) complicates the optimisation problem, since this is a nonlinear problem. To simplify this issue, [114] suggests a linearization of (2.27), resulting in a QP, easily solvable through one of the numerical techniques discussed later in this section.

Non-convex Constraints

Besides the linear (equality and inequality) constraints with wich $\mathbf{u}$ must comply, there are cases where additional non-convex constraints have to be introduced in the problem (see [115] for a marine vessel application), making the solution much more difficult to obtain. A possible work-around to this issue is to transform the non-convex region into a union of convex regions (convexification technique), producing a set of several (convex) optimisation problems, which are easier to solve [115].

Summary

This section illustrated the fact that CA problems can be formulated with a variety of performance indices (cf. (2.21),(2.22),(2.23),(2.24),(2.25),(2.27)), which depend on the application/control requirements, practical issues and designer choices. Nevertheless, they all have a common factor: normally they can be posed as a linear or quadratic optimisation problem (even if the performance metric is not linear, linearization is a common practice). Therefore, in the next section numerical methods, based on LP, QP and Multi-Parametric approaches, will be presented in order to practically solve the CA problems. For the sake of brevity, just the main ideas and insights of these methods are provided.

2.4.2 Linear Programming (LP)

The typical LP formulation admits a cost function like $J(\mathbf{u}) = \mathbf{c}^T\mathbf{u}$ and affine constraints. Moreover, there are several ways to derive the CA problem as a LP [82, 83, 110, 111]. The first formulation is to transform the two-stage problem with l_1 norm:

$$\min \|\mathbf{B}\mathbf{u} - \mathbf{v}_d\|_1 \tag{2.28}$$

into a LP problem [111, 112]:

$$\min_{\mathbf{u},\xi} \quad \mathbf{1}^T\xi \qquad s.t. \quad -\xi \leq \mathbf{B}\mathbf{u} - \mathbf{v}_d \leq \xi, \quad \underline{\mathbf{u}} \leq \mathbf{u} \leq \overline{\mathbf{u}}$$

where $\xi \in \mathbb{R}^n$ is the slack variable and $\mathbf{1} \in \mathbb{R}^n$ a unity vector. A similar LP transformation can also be applied to the secondary objective (2.22b) [111]. Likewise, the Mixed optimisation can be posed as a LP problem, although requiring more involved calculations, since the cost function incorporates several objectives (see [82] for additional details). Another context where the LP can be used is in a recasting of the DA method as an optimisation problem. Recall that DA method exploits the actuation redundancy to preserve the virtual control directionality. Bodson [82] noticed that this property could be formulated in

the following elegant setting:

$$\min_{\mathbf{u}_1,\rho} \quad \rho \qquad s.t. \quad \mathbf{B}\mathbf{u}_1 = \rho\mathbf{v}_d \qquad \underline{\mathbf{u}} \leq \mathbf{u}_1 \leq \overline{\mathbf{u}} \tag{2.29}$$

where ρ is a scaling factor: if $\rho < 1$, then the virtual control $\mathbf{v}_d$ must be scaled down in order to respect the constraints; thus, it is unattainable (otherwise, $\rho \geq 1$, it is reachable). So, the optimal solution is given by:

$$\mathbf{u} = \begin{cases} \mathbf{u}_1/\rho, & \text{if } \rho > 1 \\ \mathbf{u}, & \text{otherwise} \end{cases} \tag{2.30}$$

It should be pointed out that the virtual control generated by the solution of (2.29), i.e., (**Bu**), is always in the same direction as the desired virtual control $\mathbf{v}_d$, thus maintaining the original ideas of the DA [81, 109, 116]. However, instead of the complicated geometric methods initially proposed to reach the DA solution, the formulation (2.29) opens new possibilities to solve the DA problem through LP solvers, which are known to be more robust and mature.

In the CA context, the most popular approach to solve the LP problem is the well-known Simplex method [102, Chap. 3]. Numerical experiments conducted by [82] indicate that, compared with the simpler CA strategies, like CGI, the simplex can reduce the mean tracking errors of the virtual controls in more than 20%, and, above all, ensure that all virtual admissible controls are produced, preserving the full vehicle manoeuvrability range. In contrast, the simplex implementation complexity is naturally higher and the execution times are typically an order of magnitude superior to the simpler methods (e.g., CGI); notwithstanding, with today's real-time controllers this is no longer a critical issue, as it was in the recent past. Additionally, for an effective simplex implementation it is necessary to take into consideration important practical details, such as the use of efficient matrix inversion methods and the introduction of anticycling schemes to avoid cycles between vertices with similar cost values [82].

2.4.3 Quadratic Programming (QP)

The QP formulation admits an objective function like $J(\mathbf{u}) = \frac{1}{2}\mathbf{u}^T\mathbf{W}\mathbf{u} + \mathbf{c}^T\mathbf{u}$, with $\mathbf{W} \in \mathbb{R}^{m\times m}$. Typically, the QP appears when (2.21) or (2.22) are considered with l_2 norm. Likewise, the mixed optimisation with $p = 2$ can also be easily transformed into a QP through the l_2 norm expansion (see, e.g., [88]); in fact, almost all the performance metrics considered in Section 2.4.1 can be transformed into a QP setting.

The main QP solvers used in the CA problem are the ellipsoidal approximation [83], fixed-point algorithm [117], active set methods [118] and interior point [88], which will be briefly reviewed in this section. Before we enter in the QP details, it should be highlighted that most of the methods use the well-known concept of the Karush–Kuhn–Tucker(KKT) first-order optimality conditions [102]; other important concepts, like polytope and polyhedra that appear in connection with linear constraints, as well as active set (of constraints) [102] are repeatedly mentioned throughout this section.

Ellipsoid Approximation [83]

The main idea of the method is to solve the problem (2.22a), with $p = 2$, using an ellipsoid to approximate the rectangular restriction($\underline{\mathbf{u}} \leq \mathbf{u} \leq \overline{\mathbf{u}}$):

$$\min_{\mathbf{u}} \quad \|\mathbf{B}\mathbf{u} - \mathbf{v}_d\|_2^2 \qquad s.t. \quad \frac{1}{2}\mathbf{u}^T\mathbf{Q}\mathbf{u} = 1 \tag{2.31}$$

where $\mathbf{Q} \in \mathbb{R}^{m\times m}$ characterises the ellipsoid. To solve the problem, a Lagrangian function is built: $\mathfrak{L}(\mathbf{u}, \mu) = \|\mathbf{B}\mathbf{u} - \mathbf{v}_d\|_2^2 + \mu(\frac{1}{2}\mathbf{u}^T\mathbf{Q}\mathbf{u} - 1)$, where $\mu \in \mathbb{R}$ is the Lagrange multiplier, and the first-order optimality conditions applied ($\partial\mathfrak{L}/\partial\mathbf{u} = \mathbf{0}$, $\partial\mathfrak{L}/\partial\mu = 0$). After some algebraic manipulation, the following relationships can be established [82, 83]:

$$\mathbf{u}(\mu) = \mathbf{B}^T\left(\mathbf{B}\mathbf{B}^T + \mu\mathbf{I}\right)^{-1}\mathbf{v}_d \tag{2.32}$$

$$\gamma(\mu) \triangleq \frac{1}{2}\mathbf{u}(\mu)^T\mathbf{Q}\mathbf{u}(\mu) = 1 \tag{2.33}$$

The main merit of this formulation is that the original m inequalities constraints are approximated by a single constraint (the ellipsoid), consequently, the number of Lagrange multipliers in the problem is reduced from m to just one, significantly simplifying the solution. Actually, [83] found out that the function $\gamma(\mu)$ is monotonically decreasing and the equation (2.33) can efficiently be solved with few iterations of the bisection method.

The final implementation of this method is divided into three steps: in the first attempt, (2.32) is solved with $\mu = 0$ (assuming that the constraint is not active); if the result failed to obey the constraints $\mathcal{U}$, then the equation $\gamma(\mu) = 1$ is solved and used in (2.32); finally, even with μ known, the solution can fail to meet the inequality constraints, since these restrictions were approximated by an ellipsoid; if that is the case, additional efforts must be executed, for instance saturating some commands [83].

Compared with simplex this method tends to use a higher number of actuators [110] and produces actuator values with higher norms [82]. Some of this performance degradation is due to the ellipsoidal approximation. On one hand, this approximation allows a significant reduction in complexity, since the number of Lagrange multipliers is decreased; but, on the other hand, it also introduces inaccuracies and non-optimal solutions. Nevertheless, this was a remarkable solution in transition phase between non-optimal to optimal CA methods.

Fixed Point(FXP)

Based on the mixed optimisation formulation (2.23), with $p = 2$, $\mathbf{u}_o = \mathbf{0}$, $0 < \epsilon < 1$, $\alpha = 1 - \epsilon$, and taking into account that this QP problem only has inequality constraints, then it is possible to derive a fixed-point (FXP) algorithm, which guarantees convergence to the optimal solution [117]:

$$\mathbf{u}^{(k+1)} = \text{sat}\left((1-\epsilon)\eta\mathbf{B}^T\mathbf{v}_d - (\eta\mathbf{M} - \mathbf{I})\mathbf{u}^{(k)}\right) \tag{2.34}$$

$$\mathbf{M} = (1-\epsilon)\mathbf{B}^T\mathbf{B} + \epsilon\mathbf{I} \qquad \eta = \left(\sum_i^m\sum_j^m M_{ij}\right)^{-1/2} \tag{2.35}$$

where $1/\eta$ is the Frobenius norm of $\mathbf{M}$ and $k = 0, 1, 2, \ldots$ is the iteration number. It can be shown that: *i*) the FXP solution satisfies the KKT optimality conditions; *ii*) by using

the contraction mapping theory, the recursive FXP equation converges to optimal solution (details about this proof can be found on [119] and [120, p. 94-96]).

The simplicity, numerical efficiency and the notable property of convergence to the optimal solution, constitute the major strengths of the FXP approach. Nonetheless, there are also some drawbacks: the convergence speed to the optimum is very sensitive to the virtual controls $\mathbf{v}_d$ magnitude, particularly for high values [88] and to the selection of the parameter ϵ ("trade-off between objectives). Moreover, when one or more elements of control $\mathbf{u}$ saturates in the FXP equation, the convergence may also be affected. To attenuate this issue, [75] established the "saturability" conditions, i.e., conditions ensuring that, when one of the components of $\mathbf{u}$ saturates, it will remain saturated in future iterations, and proposes that these saturated components be removed from the FXP equation (similar to the CGI). This method is denominated accelerated fixed-point (AFXP), with potential to decrease the number of iterations up to 50%[75, 120].

Active Set Method

Given the typical dimensionality of the CA problems ($m \leq 20, n \leq 6$), i.e., small to medium dimension, the application of Active Set Methods (ASM) [102, 113] is a promising alternative to effectively solve the QP problem. In algorithmic terms, the ASM is very similar to CGI: in each iteration, two groups of constraints are created. The first, associated with active constraints, assume that the inequalities are active; in other words they are at the boundary, e.g., the constraint $u_i \leq a$ is active if $u_i = a$. The second group, inactive constraints, are ignored in the ASM iterations [102]. As a consequence, the active inequalities produce an intermediate optimisation problem with only equality constraints, easily solvable with the Lagrangian approach.

The main difference between the CGI and the ASM is the managing of the active constraints. While in the CGI a heuristic algorithm is used (the selection of active constraints is based on testing which components of $\mathbf{u}$ are saturated), the ASM employs a more rational strategy, based on the constrained programming theory. In the ASM the selection of active constraints is based on the signal of the Lagrange multipliers: negative values are associated with a violation of the KKT conditions; consequently, they become active constraints.

The application of the ASM to the CA problem was initially evaluated in references [91, 118]. Simulation results performed on those works show that the implementation complexity of the ASM is similar to the CGI and FXP methods, but offers superior performance in tracking the virtual control. Finally, the ASM, and also FXP, need initial estimates to start the iteration search for the optimum. In both methods, the CA solution obtained in the previous sample is a good candidate, and has shown good results [91].

Interior Point

Further research on iterative solutions to the CA problem was carried out in [88], by exploring the Interior Point(IP) method. The main advantage of this method is that the relative distance to the optimum is always known, therefore we can leave the algorithm knowing how far we are from the optimum. However, according to [88], the computation burden of the IP is much higher than the ASM and, typically, only becomes competitive in high-dimension CA problems ($m > 15$).

2.4.4 Multi-Parametric (MP)

Motivated mainly by the Model Predictive Control problem, and its consequent practical implementation, the QP and LP problems have been recently solved explicitly [121]. This methodology is named Multi-Parametric (MP) and the novel idea is based on an association between each parametric set of the problem and the correspondent optimal active set. While in the ASM the optimal active set is found by iterative searches, the MP approach pre-calculates this set for each possible parameter of the problem, which offers important verifiability properties, as will be discussed shortly.

To assist in the explanation of the MP method, let us assume that the slack variable setting (2.25) is in use. Based upon this formulation, we can pose the following equivalent QP problem [89]:

$$\begin{array}{ll} \min\limits_{\mathbf{z}} & \frac{1}{2}\mathbf{z}^T\mathbf{H}\mathbf{z} \\ s.t. & \mathbf{G}\mathbf{z} \leq \mathbf{W} + \mathbf{S}\theta \end{array} \tag{2.36}$$

where $\mathbf{z} = [\mathbf{u}^T \quad \mathbf{s}^T]^T$, $\theta = [\mathbf{v}_d^T \quad \underline{\mathbf{u}}^T \quad \overline{\mathbf{u}}^T]^T$ and $\mathbf{H}, \mathbf{G}, \mathbf{W}, \mathbf{S}$ are matrices with appropriate dimension; the vector $\theta \in \Theta \subset \mathbb{R}^n \times \mathbb{R}^m \times \mathbb{R}^m$ contains the problem parameters and is normally defined in a polyhedral Θ. It can be shown that the optimal solution for (2.36), $\mathbf{z}^*(\theta)$, is a piecewise linear function (PWL) defined on Θ [121]. To illustrate this fact, further assume for a moment that: *i*) the parameter vector is fixed in θ_0; and *ii*) the active set (see Section 2.4.3) associated with the optimal solution of problem with θ_0 is known and defined by the set $\mathcal{I} \subset \{1, 2, ..., q\}$, where q is the number of inequalities in (2.36). By definition of active constraint, we can infer that:

$$\mathbf{G}^i\mathbf{z} = \mathbf{W}^i - \mathbf{S}^i\theta_0 \qquad i \in \mathcal{I} \tag{2.37}$$

where i represents the line of the vector/matrix. Grouping the previous relation in a matrix form, $\mathbf{G}^{\mathcal{I}}, \mathbf{W}^{\mathcal{I}}, \mathbf{S}^{\mathcal{I}}$, and applying the KKT conditions to the problem, we can derive the optimal solution [122]:

$$\lambda^{\mathcal{I}} = -\left[\mathbf{G}^{\mathcal{I}}\mathbf{H}(\mathbf{G}^{\mathcal{I}})^T\right]^{-1}(\mathbf{W}^{\mathcal{I}} + \mathbf{S}^{\mathcal{I}}\theta_0) \tag{2.38}$$

$$\mathbf{z}^* = -\mathbf{H}(\mathbf{G}^{\mathcal{I}})^T\lambda^{\mathcal{I}} \tag{2.39}$$

where $\lambda^{\mathcal{I}}$ is the Lagrange multiplier. Notice that the solution is under the assumption that the active set $\mathcal{I}$ is known. What if the optimal active set is known for all the possible parameters in Θ? In that case, we could easily apply (2.38),(2.39) and successfully solve the optimisation problem. The MP approach builds on this simple idea, and most of the effort is devoted to constructing the mapping between $\theta \in \Theta$ and the optimal active set $\mathcal{I}$, which can become very complicated if the dimension of the parametric space Θ is high. More formally, this mapping can be defined as $\varphi : \Theta \mapsto \mathfrak{I} \subset \{1, 2, ..., q\}$, thus $\mathcal{I} = \varphi(\theta)$. A common practice when building this mapping is to divide the parametric space into regions where φ is constant (see [121] and [122] for a description of efficient methods to construct this partitions). Fortunately, there are also some automated tools which help build this mapping, for example the Multi-Parametric Toolbox [123]. To summarise, the MP approach is defined as follows: given the parameter vector θ

1. calculate the optimum active set, using the mapping $\mathcal{I} = \varphi(\theta)$;

2. apply (2.38),(2.39) to determine the optimum solution.

As a result, the MP implementation is simple and can benefit greatly from calculating the mapping $\varphi(.)$ offline. This mapping can then be efficiently evaluated online, e.g., through binary search trees [124]. Moreover, the MP performance is predictable and the number of arithmetic operations bounded, which is a very desirable property for real-time systems. For problems with a reduced number of time-varying or unknown parameters, the MP approach is definitely an excellent candidate to solve the CA problem, as has been shown in [89, 115]. However, when the dimension of the parameter vector θ grows, the mapping $\varphi(.)$ may become very complicated and suffer from the curse of dimensionality.

2.5 Adaptive CA

The adaptive CA approach, pioneered by [99], and further developed in [80, 125], assumes a (possible) nonlinear CA optimisation problem with only equalities constraints:

$$\begin{aligned} \min_{\mathbf{u}} \quad & J(\mathbf{u}, \mathbf{x}) \\ s.t. \quad & g(\mathbf{x}, \mathbf{u}) = \mathbf{v}_d \end{aligned} \tag{2.40}$$

where $J(\mathbf{u}, \mathbf{x})$ can be any performance metric discussed in Section 2.4.1, but including an additional term to penalise the violation of the inequalities constraints, for instance through barrier functions. Consider the Lagrangian of (2.40):

$$\mathfrak{L}(\mathbf{u}, \mathbf{x}, \mu) = J(\mathbf{u}, \mathbf{x}) + \mu^T (g(\mathbf{x}, \mathbf{u}) - \mathbf{v}_d) \tag{2.41}$$

and the associated optimal set $\mathcal{O} = \{ \, (\mathbf{u}, \mathbf{x}, \mu) \mid \frac{\partial \mathfrak{L}}{\partial \mathbf{u}} = \mathbf{0}, \frac{\partial \mathfrak{L}}{\partial \mu} = \mathbf{0} \, \}$, derived from the first-order optimality conditions. Under the reasonable assumption that the outer controller makes the system (2.1) uniformly globally exponential stable, it can be shown (using the Lyapunov-based design approach [80, 99]) that the following adaptive law

$$\begin{bmatrix} \dot{\mathbf{u}} \\ \dot{\mu} \end{bmatrix} = \mathbf{\Gamma} \begin{bmatrix} \frac{\partial^2 \mathfrak{L}}{\partial \mathbf{u}^2} & -\left(\frac{\partial g}{\partial \mathbf{u}}\right)^T \\ -\frac{\partial g}{\partial \mathbf{u}} & \mathbf{0} \end{bmatrix} \begin{bmatrix} \frac{\partial \mathfrak{L}}{\partial \mathbf{u}} \\ \frac{\partial \mathfrak{L}}{\partial \mu} \end{bmatrix} - \mathbf{u}_{ff} \left(\mathfrak{L}, \frac{\partial \mathfrak{L}}{\partial \mathbf{u}}, \dots \right) \tag{2.42}$$

drives the system, with exponential convergence, to the optimal set $\mathcal{O}$. In the previous expression, $\mathbf{\Gamma}$ is a symmetric positive definite matrix and $\mathbf{u}_{ff}$ a (possible) nonlinear feedforward term, whose details are omitted in this chapter, for the sake of brevity. The complete details and proof of the previous claim can be found on [80, Chap. 3]. Furthermore, it can also be shown that, when $J(\mathbf{u}, \mathbf{x})$ is quadratic, the solution retrieved from (2.42) coincides with the pseudoinverse solution [99], discussed in Section 2.3.1.

In this context, the adaptive CA solution can be viewed as a nonlinear dynamic controller, which is very simple to implement and requires modest computational capabilities. It is also worth mentioning that this approach avoids the need to solve, in each sampling time, the CA optimisation problem; instead, a dynamic CA update law, defined by (2.42), searches for the solution in a gradient/Newton-like optimisation [99] (albeit guaranteeing exponential convergence). Moreover, this approach can be extended to deal with actuator dynamics and even handle uncertainty in the actuator model [126], proving an additional benefit compared to the numeric optimisation CA. More recently, this adaptive law was evaluated in the yaw-rate control of an overactuated ground vehicle [53], showing promising results in this cost-sensitive application.

2.6 Conclusions

In this chapter a comprehensive review of the non-optimal, optimal and adaptive control allocation (CA) methods was presented. Among these methods, the non-optimal CA are the most computationally efficient and simplest to implement. However, they also introduce significant errors in the virtual control generation and, in the last decade, were surpassed by the more effective optimal-based CA. A wide variety of solvers (simplex, active set, interior point) have been explored to numerically solve the CA constraint optimisation problem. Alternately, adaptive methods, based on the Lyapunov design-based approach, also represent a useful tool to derive practical solutions and also offer robustness to uncertainty in the actuators models.

In the context of EVs propelled by in-wheel motors (IWM), which is the main theme of the current work, the above-mentioned CA methods are useful in two types of problems. The first, briefly introduced in Section 1.1.1 and of a global character, is concerned with the allocation of forces and moments, required by the EV's motion controller, among the actuators available in the (over-actuated) vehicle. The second problem, of local character, is related with the (braking) torque allocation between IWM and friction brakes, necessary in the redundant braking system of EVs propelled by IWMs. The next chapter will be devoted to the latter problem, whereas the former will be tackled in Chapter 7.

Chapter 3

Hybrid ABS

Abstract: *Among the many opportunities offered by Electric Vehicles (EVs), the design of powertrains based on in-wheel electric motors represents, from the vehicle dynamics point of view, a very attractive prospect, mainly due the torque vectoring capabilities. However, this distributed propulsion also poses some practical challenges, owing to the constraints arising from motor installation in a confined space, to the increased unsprung mass weight and to the integration of the electric motor with the friction brakes. This last issue is the main theme of this chapter, which in particular focuses on the design of the Anti-lock Braking System (ABS). The proposed structure for the ABS is composed of a tyre slip controller, a wheel torque allocator and a braking supervisor. To address the slip regulation problem, an adaptive controller is devised, offering robustness to uncertainties in the tyre-road friction and featuring a gain-scheduling mechanism based on the vehicle velocity. Further, an optimization framework is employed in the torque allocator to determine the optimal split between electric and friction brake torque based on energy performance metrics, actuator constraints and different actuators bandwidth. Finally, based on the EV working condition, the priorities of this allocation scheme are adapted by the braking supervisor unit. Simulation results obtained with the CarSim vehicle model, demonstrate the effectiveness of the overall approach.*

3.1 Introduction

This chapter deals with Anti-Lock Braking Systems (ABS) design for EVs in which the powertrain does not contain a mechanical differential and the accelerating/braking torque transmitted to each driven wheel can be individually regulated. As discussed in Chapter 1, such class of powertrains can be found on vehicles with in-wheel electric motors [14, 15, 24] or with more simple solutions based on traditional electric motors coupled to the wheel through belts [18] or single-gear transmissions [17]. As a result, the ABS employed in these vehicles can be classified according to the type and number of actuators, thus we can have ABS based on: *i)* electric motor, *ii)* friction brakes and *iii)* combined/hybrid actuation (electric motor and friction brakes). From the control and energy efficiency point of view, the first approach, where the ABS solely relies on the electric motor [15, 17], is sound, but suffers from some practical limitations; for instance, the torque generated by the electric

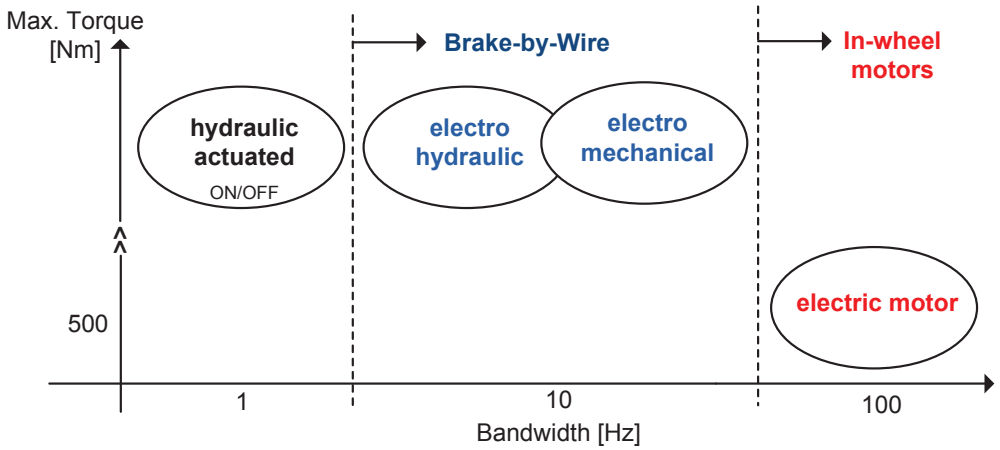

Figure 3.1: Qualitative features of the braking devices in the electric vehicles.

motor is severely reduced when the motor operates in the field weakening region or when the energy source is approaching the full charge state. Consequently, in these situations, the vehicle's braking ability is compromised, as well as the ABS functionality. From the robustness and reliability perspective, disabling the electric motor during the ABS and employing the traditional friction brakes, like hydraulic or electro-hydraulic [127], is the most simple approach to the ABS design [18]. The main motivation for the latter approach is due to the fact that, during emergency braking situations, the regenerative property of electric motor is not a top priority (the vehicle safety has precedence), so the electric motor can be safely disabled. However, this argument overlooks one important feature in the electric actuator: the fast torque response. As pointed out in Figure 3.1, the electric motor should be regarded as a braking device, which, although having a limited actuation authority, extends the bandwidth of the previous generations of friction brakes. Hence, to take full advantage of all the capabilities available in the braking devices, the most interesting configuration is the one where the electric motor and the friction brakes are simultaneously controlled by the ABS, which is named hybrid ABS in the present work. It should be noticed that the cooperation between the electric motor and friction brakes, during "normal braking" manoeuvres (i.e., when small values of wheel slip occur), was the subject of several works in recent years (see [12, 43] and references therein) . However, these studies are usually focused on maximizing the energy efficiency during the "normal braking" situations, and do not take into account the torque sharing strategies suitable for the ABS operation. Furthermore, the control of hybrid ABS configurations has received little attention in the literature. In the automotive industry we can find some hybrid ABS application examples, most notably the prototypes of Toyota with in-wheel motors [14], but these manufacturers, understandably, are not willing to disclose all the details of the control system.

The main objective of this work is to design a new control strategy for the hybrid ABS, capable of complementing the friction brakes with the quick, but limited, regenerative torque offered by the electric motor. To this aim, we propose a decoupled structure based on two layers. The first layer addresses the tyre slip regulation problem using a robust adaptive controller, able to cope with the parametric uncertainty in the tyre-road friction and other non-parametric disturbances. In the second layer, a torque allocator is responsible for distributing the torque requested by the ABS among the two braking

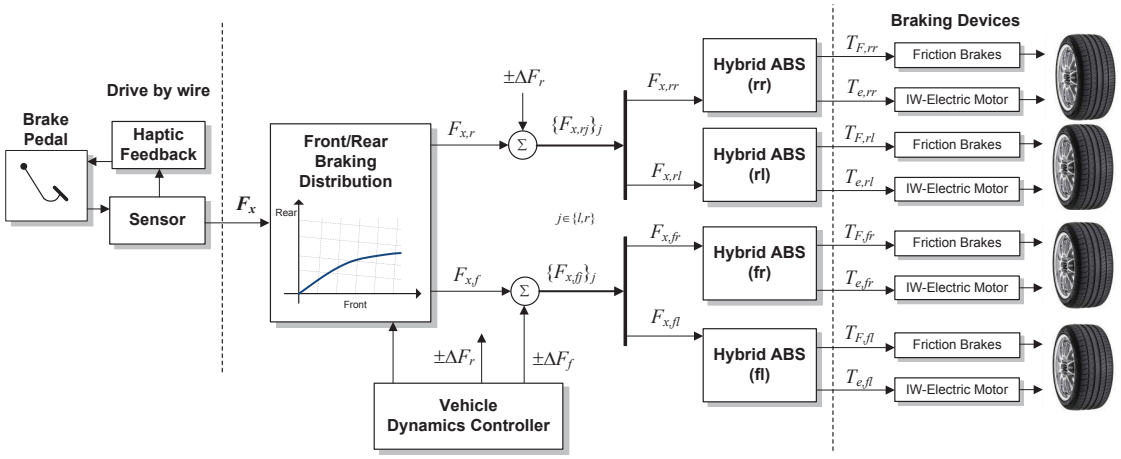

Figure 3.2: Generic architecture of the EV braking system with in-wheel electric motors and friction brakes; ΔF_f, ΔF_r represent differential braking signals and $F_{x,fl}, F_{x,fr}, F_{x,rl}, F_{x,rr}$ the desired braking forces for each wheel.

devices, taking into consideration the actuators limitations, i.e., torque range, rate limit and nonlinear constraints (e.g., field weakening in the electric motor), and performance metrics, such as energy efficiency and braking actuation bandwidth. This distribution is performed by a control allocation approach (see Chapter 2) and is formulated as an optimization problem, solved using an efficient numeric solver, suitable for realtime implementation. With this design approach we can decouple the slip regulation problem and the torque allocation one, and benefit from the full capabilities of the braking devices.

3.2 Overview of the Braking System

Generally, the braking system has the responsibility of safely decelerating the car in accordance with the braking force requested by the driver (F_x in Figure 3.2). The first step to achieve this goal consists of defining the amount of force that the front and rear axles will produce (see Figure 3.2). Historically, this distribution has been designed having in mind that, from the vehicle stability point of view, the rear wheels should never lockup before the front ones [3]. Consequently, optimal front-rear distributions can be devised in order to ensure the simultaneous locking of both axles, as discussed in [3]. After defining the front-rear distribution, the individual braking forces for each wheel are generated by adding/subtracting the differential braking signals required by the vehicle dynamics controller (e.g., the yaw-rate and/or side-slip controllers [40, 104]). A more recent trend, spurred by the increasing amount of actuation available in modern vehicles, is to bypass the front-rear distribution and use the EV's motion controller to generate the references for the individual (longitudinal and lateral) wheel forces, taking into account the requested forces, yaw moments, and tyre constraints (see Chapter 7 and references [128, 129]). In this chapter, it is assumed that the longitudinal force reference for each wheel is available, e.g., using one of the above methods, and our interest lies on the hybrid ABS problem, with particular emphasis on the following issues: *i*) understand how the longitudinal wheel force (or torque) should be distributed among the two braking devices and *ii*) ensure that, when a large wheel torque is applied, the tyre slip is regulated to a safe value.

3.2.1 Braking Devices: Control Oriented Models and Constraints

According to the hybrid braking configuration presented in Section 3.1, assume that each wheel is equipped with two braking devices: friction brakes and in-wheel electric motors (IWM). In both cases, the braking torque response can be approximated as a first-order system with delay:

$$\frac{T_i}{T_i^*}(s) = \frac{1}{\tau_i s + 1} e^{-\delta_i s} \tag{3.1}$$

where T_i^* is the reference torque, T_i the output torque, τ_i the dominant time constant, δ_i the pure delay and $i \in \{f, e\}$ (e=electric, f=friction). For the friction brakes, this continuous torque regulation can be accomplished by employing electro-hydraulic or electro-mechanic brakes, as discussed in Chapter 6. On the other hand, the IWM provides, in general, a much faster torque response [130], but the maximum torque is limited by two main factors: maximum regenerative power and battery state of charge (SoC). The first issue is related with the limited power (when compared with the friction brakes) that motor can regenerate, which restricts the braking torque in the high-speed zone. The second factor is the battery SoC: when the full charge condition is reached, the energy regeneration is no longer possible, which severely compromises the IWM braking torque. Thus, unlike the friction brakes, the maximum regenerative torque in IWM depends both on the wheel speed and battery SoC, thus yielding:

$$T_{e,max}(v, I_{q,max}, \omega) = p(v)\,(1 - I_{q,max}) \begin{cases} T_{e,n} & \omega \leq \omega_n \\ T_{e,n}\frac{\omega_n}{\omega} & \omega > \omega_n \end{cases} \tag{3.2}$$

where $I_{q,max} \in \{0, 1\}$ is an indicator for the full SoC condition, $T_{e,n}$ the peak braking torque and ω_n the motor nominal speed. The second branch in the above relation is due to the torque limitation introduced when the electric motor is operating in the constant power zone (also known as the field-weakening region in the electric drives field [9]), while $p(v)$ aims at disabling the regenerative braking when the vehicle is approaching the full stop; in this work, a simple sigmoid function

$$p(v) = \frac{1}{1 + e^{-k_v(v - v_o)}} \tag{3.3}$$

is used to model this mechanism, where k_v and v_o are tuning factors that define the speed zone and rate at which the electric motor is taken out of service.

Generally, both braking devices must also comply with range and rate limits:

$$T_{i,min} \leq T_i \leq T_{i,max}, \qquad -\dot{T}_{i,max} \leq \dot{T}_i \leq \dot{T}_{i,max}, \quad i \in \{e, f\} \tag{3.4}$$

where $T_{i,min}$, $T_{i,max}$ [Nm] represent the braking torque range and $\dot{T}_{i,max}$ [Nm/s] the maximum rate limit (assumed symmetrical). In the case of frictional brakes, the minimum torque is zero ($T_{f,min} = 0$ Nm), the maximum $T_{f,max}$ is normally very high and the rate limits may appear as a consequence of physical constraints on the variation rate at which the actuator change the pressure/force. As for the IWM, the highest regenerative torque $T_{e,max}$ was already discussed in (3.2), while the minimum (acceleration) torque is given by $T_{e,min} = -T_{e,max}(v, I_{q,min}, \omega)$, with $I_{q,min}$ representing a minimum SoC flag; the rate limit in this actuator is related with current rate constraints at which the EV batteries can be charged [42].

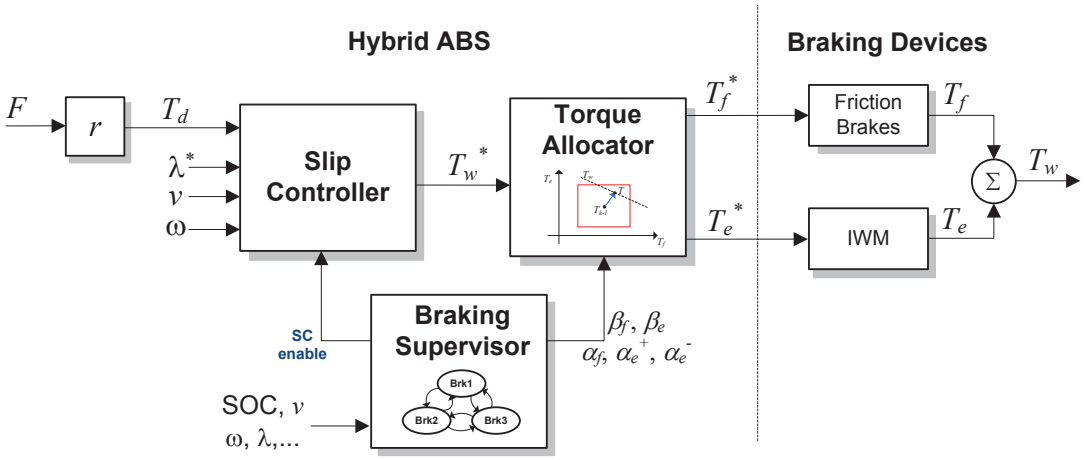

Figure 3.3: Block diagram of the proposed hybrid ABS structure.

3.2.2 Hybrid ABS

Hereafter, we concentrate on the design of the hybrid ABS, which is composed by three modules: (*i*) slip controller, (*ii*) torque allocator and (*iii*) a braking supervisor. As can be seen in Figure 3.3, there is a clear separation between the slip regulation task and the torque allocation, which was adopted with the aim of simplifying the control problem. For example, with this modular approach the design of the slip regulator can focus on the stability and robustness issues, e.g., due to friction variations and other disturbances, and only need to generate the desired wheel torque (T_w^*). On the other hand, the complexity associated with the split between electric/friction torque is deferred to a second block, the torque allocator, which handles the actuators range and rate limit constraints, energy performance metrics, different bandwidths, etc. This separation also allows the application of different tools to independently solve each of the above tasks, i.e., the stability and robustness issues can be addressed with Lyapunov-based techniques, while numerical optimization techniques are more appropriated to deal with the allocation problem (due to the multi-objective nature of this second task). As an added bonus, the torque allocator can also be used during normal braking manoeuvres. Finally, a braking supervisor is incorporated in the hybrid ABS in order to manage the different modes in which the torque allocator can operate, and, whenever necessary, enable/disable the slip controller. The next three sections will be devoted to the description and discussion of the three elements that compose the hybrid ABS.

3.3 Slip Controller

We will start the presentation of the hybrid ABS by tackling the problem of wheel slip control. Given that the braking actuators are (directly or indirectly) torque-controlled, it is convenient to first translate the desired longitudinal force for the tyre (F), generated by the hierarchical approach discussed in the previous section, in a "desired" wheel torque $T_d = F/r$, where r is the wheel radius (see Figure 3.3). For simplify the controller design, the actuators dynamics can be neglected and considered in the validation phase. Whereas the validity of this approximation is more than reasonable for the fast IWM, the delays present in the friction brakes actuator may raise some concerns. Nevertheless, as our ultimate goal is to blend the torque produced by both actuators, it will be shown

that by a careful design of the torque allocator block the above assumption holds (e.g., by making the IWM respond to the high frequency content of wheel torque).

3.3.1 Quarter Car Model

As a starting point for the design of the slip controller, the quarter car model (QCM) [15, 127, 131] is used to represent the vehicle longitudinal motion:

$$\begin{aligned} M\dot{v} &= -F_z\mu(\lambda) - \Delta_v(t,v) && \text{(3.5a)}\\ J\dot{\omega} &= rF_z\mu(\lambda) - T_w - \Delta_w(t,\omega), && \text{(3.5b)}\\ \lambda &= h(v,\omega) = \frac{v-\omega r}{v} && \text{(3.5c)} \end{aligned}$$

where $(v,\omega) \in \mathcal{D}$ are the system states, composed by the vehicle velocity v and the wheel speed ω, the braking torque T_w is the input and the tyre slip $\lambda \in \Lambda$ the output. The above model, valid in the (braking) domain $\mathcal{D} = (0,\infty)\times[0,\infty) \subset \mathbb{R}^2$, depends on the following parameters: wheel inertia (J), quarter car mass (M), wheel radius (r) and wheel vertical load (F_z). The function $\mu(\lambda)$ represents the nonlinear friction coefficient in the tyre-road interface, which is uncertain, and the terms $\Delta_v(t,v)$ and $\Delta_\omega(t,\omega)$ are force and torque disturbances resulting from unmodeled dynamics. For instance, the disturbance Δ_v can be described, in its simplest form, by a polynomial $\Delta_v(t,v) = a_1 + a_2 v + a_3 v^2$ to account for the total resistance to the vehicle motion, arising from aerodynamic drag, rolling resistance and grade force [3]. In this work it will be assumed that both disturbances are uniformly bounded:

$$|\Delta_v(t,v)| \le \overline{\Delta_v}, \qquad |\Delta_\omega(t,\omega)| \le \overline{\Delta_\omega}, \qquad \forall (t,v,\omega) \in [0,\infty)\times\mathcal{D} \tag{3.6}$$

where $\overline{\Delta_v}$ and $\overline{\Delta_\omega}$ are known constants.

The control objective is to design a state feedback control law that will bring, as fast as possible, the system output λ to a given set-point λ^*. Due to the nonlinear nature of the QCM (3.5), we will start by employing the concept of input-output linearization [96] and compute the relative degree of the system. The first time derivative of the output has the form:

$$\begin{aligned} \dot{\lambda} &= \frac{\partial h}{\partial v}\dot{v} + \frac{\partial h}{\partial \omega}\dot{\omega} && \text{(3.7a)}\\ &= -\frac{r\omega}{v^2}\left(\frac{F_z\mu(\lambda)+\Delta_v(t,v)}{M}\right) - \frac{r}{v}\left(\frac{rF_z\mu(\lambda) - T_w - \Delta_w(t,\omega)}{J}\right) && \text{(3.7b)}\\ &= -\frac{r/J}{v}\left((1+(1-\lambda)\frac{J}{Mr^2})r\mu(\lambda)F_z - T_w - \Delta_\omega(t,\omega) + (1-\lambda)\frac{J}{Mr^2}r\Delta_v(t,v))\right) \end{aligned}$$

Thus, defining the terms

$$p_1 = \frac{r}{J}, \qquad p_2 = \frac{J}{Mr^2}, \qquad \Psi(\lambda) = \big(1+(1-\lambda)p_2\big)r\mu(\lambda)F_z \tag{3.8}$$

the slip dynamics can be described as:

$$\dot{\lambda} = -\frac{p_1}{v}\Big(\Psi(\lambda) - T_w - \Delta_\omega(t,\omega) + (1-\lambda)p_2 r\Delta_v(t,v)\Big) \tag{3.9}$$

which allows us to conclude that the system has a relative degree one for any $(v, \omega) \in \mathcal{D}$. In order to derive an ideal control law, suppose, for a moment, that $\Psi(\lambda)$ is known and the disturbances can be neglected ($\Delta_v = \Delta_\omega = 0$). Based on these (very unlikely) assumptions, letting the braking torque be $T_w = \Psi(\lambda) - vk(\lambda - \lambda^*)$, where $k > 0$ is a constant, yields

$$\dot{\lambda} = -p_1 k(\lambda - \lambda^*) \tag{3.10}$$

i.e., a first order slip response with exponential convergence to λ^*. This simple control law, although fulfilling the control objectives, requires the knowledge of the $\Psi(\lambda)$ function, which is difficult to ensure given the uncertainties in the tyre-road friction $\mu(\lambda)$. Spurred by this difficulty, we will derive a robust adaptive method to handle the (parametric) uncertainty in $\Psi(\lambda)$ and cope, also, with the disturbances Δ_ω and Δ_v. Before describing the control law, a parametric representation for the Ψ function will be first outlined.

3.3.2 Approximation of $\Psi(\lambda)$ with a Linear Parameterization

In view of the fact that $Mr^2 \gg J$ (and thus p_2 in (3.8) is much smaller than 1) the function $\Psi(\lambda)$ can be re-written as

$$\Psi(\lambda) = rF_z\mu(\lambda) + \Delta_{\Psi 1}(t, \lambda), \qquad \Delta_{\Psi 1}(t, \lambda) = (1 - \lambda)p_2 r\mu(\lambda)F_z \tag{3.11}$$

where $\Delta_{\Psi 1}$ is a uniformly bounded disturbance, i.e,

$$\begin{aligned} |\Delta_{\Psi 1}(t, \lambda)| &\leq |(1 - \lambda)|p_2 r\mu(\lambda)F_z \\ &\leq p_2 r\mu_{max}\overline{F_z} \leq p_2 r\overline{\Delta_{\Psi 1}}, \qquad \forall (t, \lambda) \in [0, \infty) \times \Lambda \end{aligned} \tag{3.12}$$

with $\mu_{max} = \max_\lambda \mu(\lambda)$, $\overline{F_z} = \max_t F_z(t)$ and $\overline{\Delta_{\Psi 1}} \geq \mu_{max}\overline{F_z}$ a known constant. Notice that to establish the previous inequalities we employed the fact that, during a braking manoeuvre, $0 \leq r\omega \leq v$, which together with the definition of λ in (3.5c) restricts the slip domain to $\Lambda = [0, 1]$. In practice, the above bound μ_{max} can be obtained considering the highest possible grip in the tyre-road interface, while for $\overline{F_z}$ we can resort to well known relations of the front-rear load transfer and extract the maximum feasible vertical load that the tyre may experience during a braking manoeuvre [132]. Joining these two bounds, $\overline{\Delta_{\Psi 1}}$ can be seen as an upper bound for the maximum value of the longitudinal force produced by the tyre.

Continuing with the analysis of $\Psi(\lambda)$, rewritten as in (3.11), the main source of parametric uncertainty is in the friction coefficient $\mu(\lambda)$. For control design purposes, the tyre-road adhesion $\mu(\lambda)$ will be modelled as [133]:

$$\mu(\lambda) = c_1 + c_2\lambda + c_3 e^{-c_4\lambda} \tag{3.13}$$

where $c_i, i = 1, \ldots, 4$ are the parameters of the Burckhardt model, not known *a priori* and time-varying with the adhesion and tyre operation conditions. As we intend to build adaptive mechanisms to deal with the QCM parametric uncertainty, it is convenient to represent $\mu(\lambda)$ as a linear parameterization (LP). To this aim, notice that the first two terms in (3.13) are already linear in the parameters, while the nonlinearity is confined to the last term. Given that, for the most representative types of road surfaces, the parameter $c_4 \in \mathcal{C} = [4, 100]$, [133], the exponential term can be approximated as a sum of "fixed" exponentials, appropriately weighted, i.e., $e^{-c_4\lambda} \simeq \sum_{j=1}^{N} \theta_j e^{-w_j\lambda}$, where θ_j represent the linear parameters and w_j are fixed weights. In this approach, one natural question that

arises is how many fixed exponentials (or basis functions in the function approximation terminology) should be employed in the approximation, which is then coupled with the second question on how to determine the w_j. As discussed in Chapter 5, the Burckhardt model, for $c_4 \in \mathcal{C}$, can be accurately approximated by the following LP:

$$\mu(\lambda) = \boldsymbol{p}^T \Phi(\lambda)^T + \Delta_\mu(\lambda), \qquad |\Delta_\mu(\lambda)| \leq \overline{\Delta_\mu}, \quad \forall \lambda \in \Lambda \tag{3.14}$$

$$\boldsymbol{\Phi}(\lambda) = \begin{bmatrix} 1 & \lambda & e^{-4.99\lambda} & e^{-18.43\lambda} & e^{-65.62\lambda} \end{bmatrix}^T \tag{3.15}$$

where $\boldsymbol{p} \in \mathbb{R}^5$ is the set of linear parameters, $\boldsymbol{\Phi}(\lambda)$ is the (known) regressor and $\Delta_\mu(.)$ the approximation error introduced by the LP, bounded by a known constant $\overline{\Delta_\mu}$.

Finally, incorporating the LP approximation in (3.11), one may express $\Psi(\lambda)$ as:

$$\Psi(\lambda) = \boldsymbol{\theta}^T \boldsymbol{\Phi}(\lambda) + \Delta_{\Psi 1}(t, \lambda) + \Delta_{\Psi 2}(t, \lambda) \tag{3.16}$$

where $\boldsymbol{\theta} = r F_z \boldsymbol{p} \in \mathbb{R}^5$ is a set of linear parameters (recall that r and F_z represent scaling factors and can be incorporated in the parameter $\boldsymbol{\theta}$) and $\Delta_{\Psi 2}(t, \lambda) = r F_z \Delta_\mu(\lambda)$ is a disturbance uniformly bounded by a known constant $\overline{\Delta_{\Psi 2}}$, i.e.,

$$|\Delta_{\Psi 2}(t, \lambda)| \leq |r F_z \Delta_\mu(\lambda)| \leq r\overline{F_z}\,\overline{\Delta_\mu} \leq \overline{\Delta_{\Psi 2}}, \qquad \forall (t, \lambda) \in [0, \infty) \times \Lambda \tag{3.17}$$

Remark 3.1. in this section it was argued that, under reasonable assumptions, the $\Psi(.)$ function can be approximated by an LP based on the Burckhardt representation. Naturally, this is not the only parameterization on which the $\Psi(.)$ can rely and, as a matter of fact, due to the well known "universal approximation property" [134], we can also employ machine learning parameterizations, like neural networks and fuzzy approximators, to construct the LP. From a theoretical point of view, these approaches will affect the type and size of the regressor $\boldsymbol{\Phi}(\lambda)$, but the core theoretical results about stability and robustness of the slip controller (to be presented in the next section) will remain unchanged, since this study is independent of LP employed in the $\Psi(.)$ approximation. Therefore, it is interesting to note that the proposed slip controller can be effortless extended to contemplate LPs based on machine learning.

3.3.3 Robust Adaptive Slip Control

After presenting the system model, we now discuss a robust adaptive method to design the slip controller. To this aim, consider the regulation error

$$e = \lambda - \lambda^* \tag{3.18}$$

and redefine the control objective as the problem of finding the wheel torque T_w such that e converges to zero as fast as possible, in spite of uncertainties in Ψ and other disturbances. Before solving this problem, there are two issues that deserve preliminary discussion: (i) how to generate the slip set-point λ^*; and (ii) how to measure or estimate the slip λ in order to be used in feedback. Ideally, the slip set-point should be selected such that the tyre-road friction is maximized, i.e., $\lambda^* = \arg\max_\lambda \mu(\lambda)$, which is not easy due to the uncertainty in $\mu(\lambda)$. To overcome this hindrance, identification schemes to infer the friction peak before the slip control activation can be used (see, e.g. [135, 136]) or a fixed λ^* can be employed as a compromise value for the most representative road surfaces found in practice. Further, the vehicle speed v is not easy to measure during braking manoeuvres, hampering the λ calculation and feedback. To address this problem, it is common to

implement vehicle velocity observers, see e.g. [133, 136, 137, 138], and in what follows it is assumed that a sufficiently reliable speed estimate is available to the controller.

In view of (3.9), (3.16) and (3.18), the error dynamics are defined as:

$$\dot{e} = -\frac{p_1}{v}\left(\boldsymbol{\theta}^T\boldsymbol{\Phi}(\lambda) - T_w + \Delta(t,\lambda,v,\omega)\right) \tag{3.19}$$

where $\Delta(.)$ is a uniformly bounded disturbance torque, comprising all the model uncertainties, namely:

$$\begin{aligned} \Delta(t,\lambda,v,\omega) &= \Delta_{\Psi 1}(t,\lambda) + \Delta_{\Psi 2}(t,\lambda) - \Delta_{\omega}(t,\omega) + (1-\lambda)p_2 r\Delta_v(t,v) && \text{(3.20a)} \\ |\Delta(t,\lambda,v,\omega)| &\leq \overline{\Delta_{\Psi_2}} + \overline{\Delta_{\omega}} + p_2 r\left(\overline{\Delta_v} + \overline{\Delta_{\Psi 1}}\right) \leq \overline{\Delta} && \text{(3.20b)} \end{aligned}$$

for all $(t,\lambda,v,\omega) \in [0,\infty)\times\Lambda\times\mathcal{D}$. Compared with the torque applied to the wheel during an emergency braking, the value of $\Delta(.)$ is relatively small and tends to be neglected in the majority of the slip control designs reported in the literature [15, 127, 131, 139, 140, 141, 142, 143]. However, if the control law incorporates adaptive mechanisms to deal with the parameter uncertainty in $\boldsymbol{\theta}$ (which is the case in this work), the presence of these small disturbances may introduce parameter drifts and other stability issues, as discussed in [144]. With the aim of mitigating such problems, the adaptive controller will be endowed with a robust modification (the dead-zone), which, to be effective, requires the knowledge of a bound for the model disturbance and, as will be clear in the following, also plays an important role in the controller tuning. Another important issue in the slip controller design is related with the appearance of v in the denominator of (3.19), which makes the slip error dynamics infinitely fast as $v \to 0$ [131]. In practice, the controller must be disabled before the vehicle reaches a complete stop, and, in what follows, we will assume that the domain of interest during the slip regulation is constrained to $(v,\omega) \in \mathcal{D}^c = [v_o,\infty)\times[0,\infty) \subset \mathcal{D}$, where v_o is a positive speed threshold at which the slip controller is deactivated.

Inspired by the input-output linearization technique previously discussed, the stabilization of the error dynamics (3.19) will be achieved with the following control law:

$$T_w = \hat{\boldsymbol{\theta}}^T\boldsymbol{\Phi}(\lambda) - vke \tag{3.21}$$

where k is a positive tuning parameter and $\hat{\boldsymbol{\theta}}$ the estimate of $\boldsymbol{\theta}$, which will be defined by an adaptive mechanism. The first term in the previous relation can be interpreted, to some extent, as a compensation factor that deals with the non-linear tyre-road friction, while the second term represents a proportional term that improves the convergence. Substituting (3.21) in (3.19) yields:

$$\dot{e} = -p_1 ke - \frac{p_1}{v}\left(-(\hat{\boldsymbol{\theta}} - \boldsymbol{\theta})^T\boldsymbol{\Phi}(\lambda) + \Delta(.)\right) \tag{3.22}$$

To design the adaption law for $\hat{\boldsymbol{\theta}}$, consider the following candidate Lyapunov function:

$$V(e_\varepsilon, \tilde{\boldsymbol{\theta}}) = \frac{1}{2}e_\varepsilon^2 + \frac{p_1}{2\gamma}\tilde{\boldsymbol{\theta}}^T\tilde{\boldsymbol{\theta}} \tag{3.23}$$

where $\tilde{\boldsymbol{\theta}} = \hat{\boldsymbol{\theta}} - \boldsymbol{\theta}$ is the parametric estimation error, γ a constant tuning parameter and e_ε the regulation error with dead-zone (ε) [145]:

$$e_\varepsilon = g(e) = \begin{cases} 0 & \text{if } |e| < \varepsilon \\ e - \varepsilon \operatorname{sgn}(e) & \text{if } |e| \geq \varepsilon \end{cases}, \qquad \dot{e}_\varepsilon = g'(e)\dot{e} = \begin{cases} 0 & \text{if } e_\varepsilon = 0 \\ \dot{e} & \text{if } e_\varepsilon \neq 0 \end{cases} \tag{3.24}$$

In order to study the stability and transient behaviour of the system under closed-loop, the time derivative of V:

$$\dot{V} = e_\varepsilon \dot{e}_\varepsilon + \frac{p_1}{\gamma}\tilde{\boldsymbol{\theta}}^T\dot{\tilde{\boldsymbol{\theta}}} \tag{3.25}$$

will be analyzed in two parts. At first we consider $e_\varepsilon \neq 0$, which enables us to replace $\dot{e}_\varepsilon$ with $\dot{e}$ (see (3.24)), thus obtaining:

$$\begin{aligned} \dot{V} &= e_\varepsilon \dot{e} + \frac{p_1}{\gamma}\tilde{\boldsymbol{\theta}}^T\dot{\tilde{\boldsymbol{\theta}}}, \quad \forall e_\varepsilon \neq 0 && \text{(3.26a)} \\ &= -\frac{p_1}{v}e_\varepsilon\Big(- (\hat{\boldsymbol{\theta}} - \boldsymbol{\theta})^T\boldsymbol{\Phi}(\lambda) + vke + \Delta(.)\Big) + \frac{p_1}{\gamma}\tilde{\boldsymbol{\theta}}^T\dot{\tilde{\boldsymbol{\theta}}} && \text{(3.26b)} \\ &\leq -p_1 k e_\varepsilon e + \frac{p_1}{v}\overline{\Delta}|e_\varepsilon| + p_1\tilde{\boldsymbol{\theta}}^T\left(\frac{e_\varepsilon}{v}\boldsymbol{\Phi}(\lambda) + \frac{\dot{\tilde{\boldsymbol{\theta}}}}{\gamma}\right), \quad \forall e_\varepsilon \neq 0 && \text{(3.26c)} \end{aligned}$$

To cancel out the last term in the previous relation, the adaption law is selected as:

$$\hat{\boldsymbol{\theta}}(t) = \hat{\boldsymbol{\theta}}(t_i) - \int_{t_i}^{t} \gamma \frac{e_\varepsilon(\tau)}{v(\tau)}\boldsymbol{\Phi}(\lambda(\tau))d\tau \tag{3.27}$$

where $\hat{\boldsymbol{\theta}}(t_i)$ is the initial estimate of $\boldsymbol{\theta}$ and t_i the activation instant of the controller. It is worth pointing out that the adaption law described above is frozen when $e_\varepsilon = 0$, or equivalently $|e| \leq \varepsilon$, and the adaptation gain gets smaller as speed increases. Moreover, noticing that, for $e_\varepsilon \neq 0$, $e = e_\varepsilon + \varepsilon \operatorname{sgn}(e) = e_\varepsilon + \varepsilon \operatorname{sgn}(e_\varepsilon)$, one has:

$$\dot{V} \leq -p_1 k e_\varepsilon^2 - p_1 k|e_\varepsilon|\left(\varepsilon - \frac{\overline{\Delta}}{vk}\right), \qquad \forall e_\varepsilon \neq 0 \tag{3.28}$$

Since $(v, \omega) \in \mathcal{D}^c$, we can select the deadzone as $\varepsilon > \overline{\Delta}/(kv_0)$ to achieve: $\dot{V} \leq -p_1 k e_\varepsilon^2$ for any $e_\varepsilon \neq 0$, which concludes the analysis of the first case. In the second case, $e_\varepsilon = 0$ and it is easy to check that $\dot{V}(0, \tilde{\boldsymbol{\theta}}) = 0$. Hence, joining the two cases we get:

$$\dot{V} \leq -p_1 k e_\varepsilon^2, \qquad \forall e_\varepsilon \tag{3.29}$$

The next proposition states the stability properties of the closed-loop system.

Proposition 3.1. *Consider the control law* (3.21), (3.27) *applied to* (3.19) *with* $k > 0$, $\gamma > 0$ *and* $\varepsilon > \overline{\Delta}/(kv_0)$. *It holds that:*

(i) the signals e_ε *and* $\tilde{\boldsymbol{\theta}}$ *are bounded;*

(ii) the signal e_ε *is asymptotically vanishing, i.e.,* $\lim_{t\to\infty}|e_\varepsilon(t)| = 0$

(iii) the transient response performance can be quantified as follows:

$$\|e_\varepsilon\|_{\mathcal{L}_2} \leq \sqrt{\frac{e_\varepsilon(0)^2}{2p_1 k} + \frac{\|\tilde{\theta}(0)\|^2}{2k\gamma}} \tag{3.30}$$

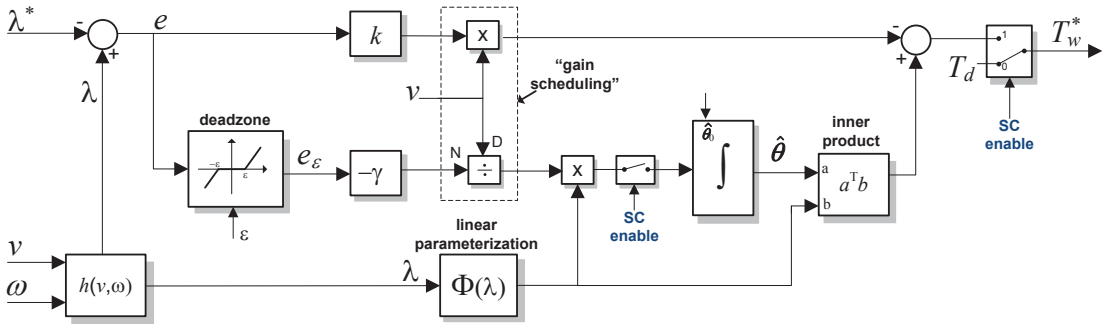

Figure 3.4: Block diagram of the proposed adaptive wheel slip control; the flag "SC enabled" is generated by the braking supervisor in order to activate/deactive the slip controller.

where $e_\varepsilon = g(e)$ *is the regulation error with deadzone defined in* (3.24).

Proof. the fact (i) can be deduced from the Lyapunov method: since (3.23) is positive definite, and the time derivative $\dot{V}(e_\varepsilon, \tilde{\boldsymbol{\theta}}) \leq -p_1 k e_\varepsilon^2 \leq 0$ is negative semidefinite, then e_ε and $\tilde{\boldsymbol{\theta}}$ belong to $\mathcal{L}_\infty$, thus being bounded. Furthermore, integrating (3.29), one has:

$$e_\varepsilon^2 \leq -\frac{\dot{V}}{p_1 k} \quad \Rightarrow \quad \lim_{t\to\infty} \int_0^t e_\varepsilon(\tau)^2 d\tau \leq \frac{V(0) - \lim_{t\to\infty} V(t)}{p_1 k} \leq \frac{V(0)}{p_1 k} \tag{3.31}$$

where the last inequality comes from the fact that V is lower bounded and $\dot{V} \leq 0$, which implies that $\lim_{t\to\infty} V(t)$ is finite [145]. It can also be straightforwardly verified that $\dot{V}$ is uniformly continuous ($\ddot{V} \leq -2p_1 k e_\varepsilon \dot{e}_\varepsilon$ is bounded), and by the application of Barbalat's Lemma [145]: $\lim_{t\to\infty} \dot{V}(t) = 0$, which implies (ii). Finally, from (3.31) an upper bound for the $\mathcal{L}_2$ norm of e_ε can be found as:

$$\|e_\varepsilon\|_{\mathcal{L}_2} = \sqrt{\lim_{t\to\infty} \int_0^t e_\varepsilon(\tau)^2 d\tau} \leq \sqrt{\frac{V(0)}{p_1 k}} = \sqrt{\frac{\frac{1}{2} e_\varepsilon(0)^2 + \frac{p_1}{2\gamma} \|\tilde{\boldsymbol{\theta}}(0)\|^2}{p_1 k}} \tag{3.32}$$

thus proving (iii). □

Remark 3.2. The results presented in the previous proposition characterize the controller performance and allow us to understand how the controller parameters (ε, k, γ) affect the slip error response. For instance, e_ε being vanishing implies that the steady-state regulation error e will converge asymptotically to the set $\{|e| \leq \varepsilon\}$. Therefore, the selection of the deadzone ε, besides the robustness considerations mentioned above, can also take into account the wheel slip measurement noise, e.g., letting $\varepsilon \geq \max(\sigma_\lambda, \overline{\Delta}/(kv_0))$, where σ_λ is the precision associated with the λ measure (or estimation). In terms of transient performance, (3.30) suggests that the designer can reduce the $\mathcal{L}_2$-norm of the regulation error by decreasing the initial estimation error ($\|\tilde{\boldsymbol{\theta}}(0)\|$) and initial regulation error ($e_\varepsilon(0)$), or by increasing the gains k, γ.

Remark 3.3. The slip controller will be switched on by the braking supervisor when excessive tyre slip is detected. Assuming that this activation occurs at $t = t_i$, we have $T_w(t) = T_d(t)$ for $t < t_i$, while for $t \geq t_i$ the wheel torque will be provided by (3.21). At the activation instant, the torque generated by the controller will be defined as $T_w(t_i) = \hat{\boldsymbol{\theta}}(t_i)^T \boldsymbol{\Phi}(\lambda(t_i)) - kv(t_i)e(t_i)$ and, as a result, if the controller is not carefully initialized, discontinuities in the wheel torque signal may occur (i.e., $T_d(t_i) \neq T_w(t_i)$). To

avoid this undesirable behaviour, the initial estimative of $\boldsymbol{\theta}$ is rescaled as follows:

$$\hat{\boldsymbol{\theta}}(t_i) = \boldsymbol{\theta}_N \frac{T_d(t_i) + kv(t_i)e(t_i)}{\boldsymbol{\theta}_N^T \boldsymbol{\Phi}(\lambda(t_i))} \tag{3.33}$$

where $\boldsymbol{\theta}_N$ is an initial parameter estimate chosen by the designer.

Remark 3.4. The vehicle speed plays a very important role in the slip controller response and robustness disturbances capabilities. For example, by analyzing the control law (3.21) it is clear that there is an equivalent proportional error term (vke) that is directly proportional to the vehicle speed, while an opposite influence is observed in the adaptation mechanism (3.27), i.e., the adaptation rate gets smaller at higher speed. In a way, this can be interpreted as a gain-scheduled mechanism, which was already discussed in previous works on wheel slip control within linear (or linearization) frameworks [15, 131, 139], and is extended in this work for the robust adaptive controller. Another aspect that is worth mentioning is the influence of v on the slip controller robustness. To explain this, consider the time derivative of the Lyapunov (3.28): the term associated with the disturbance (upper bound) $\overline{\Delta}$ decreases at higher speeds, and the minimum value for the deadzone ε also gets smaller. Consequently, these results suggest that the slip controller may deal more easily with the disturbances at higher vehicle speeds. From a practical point of view, these observations are in accordance with the fact that the speed estimation is affected by large errors as the vehicle velocity decreases, e.g., due to delays introduced by the wheel encoders signal processing phases [127].

Remark 3.5. It is also interesting to analyze the influence of the vehicle velocity v into the tyre slip dynamics (3.9) (or equivalently in the error dynamics (3.19)) from a different perspective, i.e., by looking at v as a slowly time-varying parameter. For example, in the ideal scenario of no uncertainty in the model (i.e., Ψ is known and $\Delta_v = \Delta_w = 0$), it was shown in Section 3.3.1 that the input-output (IO) linearization technique renders a closed-loop slip response independent of the vehicle speed and with exponential convergence to λ^* (see (3.10)). In this case, we can treat the vehicle velocity dynamics (3.5a) as the "zero dynamics" of the system [96], which is input-to-state stable during the slip control operation. On the other hand, when we take into account the model uncertainties and employ the adaptive controller, the IO linearization is no longer "perfect" and the vehicle speed appears in the slip closed-loop dynamics (see (3.22)), which is then incorporated in the adaptive law and, as discussed in the previous remark, attenuates the disturbance effects. Consequently, in this latter case, we can look again at the v dynamics as the "zero dynamics" of the system or, in alternative, neglect these dynamics and assume that v is a slow time-varying parameter. The latter approach, considered also in [15, 127, 131], is justified owing to the large difference of equivalent inertias between the wheel and the vehicle chassis.

3.4 Wheel Braking Torque Allocator

The wheel slip controller proposed in the previous section only specifies the desired wheel torque (T_w), but does not define how this torque should be split between the friction brakes (T_f) and the electric motor (T_e). This assignment is performed in a second step, after discretizing the slip controller, using a torque distribution strategy based on the control allocation (CA) concept, introduced in Chapter 2. As primary objective, the CA must

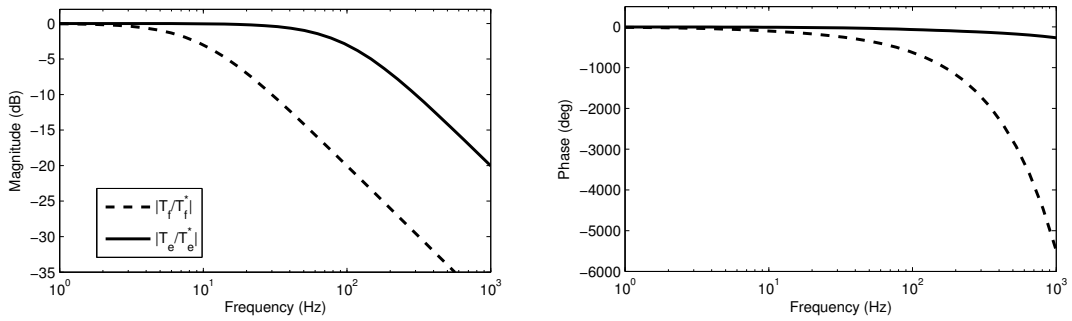

(a) (b)

Figure 3.5: Frequency response of the braking actuators, modelled with (3.1) and parameterized with the values given in Appendix (3.8).

ensure that the requested torque, T_w, is produced by the braking devices, i.e.

$$T_w = T_f + T_e \tag{3.34}$$

complying, at the same time, with the range and variation rate limits, defined in (3.4). Given that the system is discretized with a sampling time t_s, the derivative $\dot{T}_i$ can be approximated by the forward Euler method as $\dot{T}_i \simeq (T_i[k] - T_i[k-1])/t_s$, and the range and rate constraints can be joined together as:

$$\underline{T}_i \leq T_i \leq, \overline{T}_i, \qquad i \in \{e, f\} \tag{3.35a}$$

$$\underline{T}_i = \max(T_{i,min}, T_i[k-1] - t_s \dot{T}_{i,max}) \tag{3.35b}$$

$$\overline{T}_i = \min(T_{i,max}, T_i[k-1] + t_s \dot{T}_{i,max}) \tag{3.35c}$$

Thus, the number of inequalities constraints is reduced from 4 to only 2 per actuator. Notice that, for a given torque request T_w, there may be several pairs (T_f, T_e) that satisfy (3.34). Accordingly, this redundancy can be exploited by the CA to select the pair (T_f, T_e) that maximizes the energy efficiency and optimizes the (wheel) torque dynamic response. For instance, it is well known that the regenerative braking capabilities of IWMs are much more energy efficient than the friction brakes, hence the use of the latter braking device should be, whenever possible, penalized. Furthermore, the IWMs torque response offers a much larger bandwidth than the friction brakes (see Figure 3.5), albeit with less control authority, and the torque allocation should also take into account the frequency content of the T_w signal, e.g., making T_e more sensitive to the high-frequency content in T_w. Taking into consideration these ideas together with the constraints (3.34) and (3.35), the wheel torque allocation can be formulated as the following optimization problem:

$$\begin{aligned} \min_{T_f, T_e} \quad & \left(\alpha_f T_f^2 + \alpha_e(T_e) T_e^2\right) + \left(\beta_f (T_f - T_f[k-1])^2 + \beta_e (T_e - T_e[k-1])^2\right) \\ s.t. \quad & T_f + T_e = T_w, \qquad \underline{T}_i \leq T_i \leq, \overline{T}_i, \qquad i \in \{e, f\} \end{aligned} \tag{3.36}$$

The cost function of the previous problem can be divided into two components. The first term assigns a penalty to the use of each braking actuator, using for this purpose the weights α_f and $\alpha_e(.)$, which are associated with the frictional braking and IWM, respectively. As the IWM has two operational modes, i.e., regeneration and acceleration,

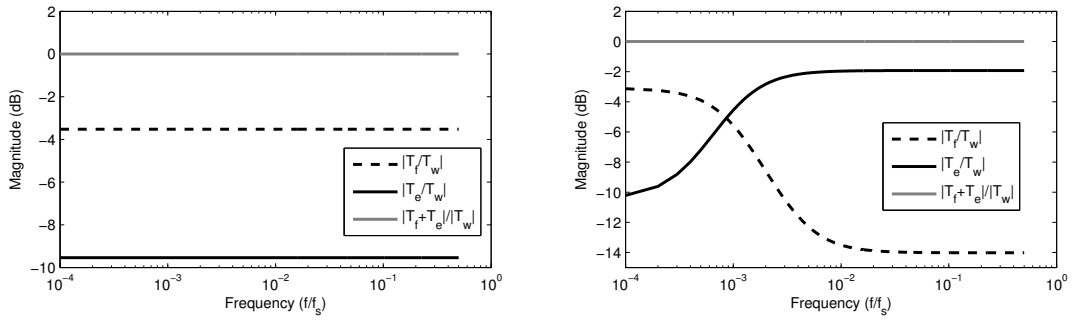

(a) Static Allocation (b) Dynamic Allocation

Figure 3.6: Frequency response of the wheel torque allocation: (a) static allocation, generated from the state 3 in Table 3.1 (b) dynamic allocation, generated from the state 4 in Table 3.1; The frequency scale is normalized with the sampling frequency ($f_s = 1/t_s$) and it is assumed that $\overline{T}_e > \underline{T}_e > 0$;

it is also helpful to assign different penalization values to each of these modes. To address this issue, we make the weight $\alpha_e(.)$ dependent on the T_e signal as

$$\alpha_e(T_e) = \begin{cases} \alpha_e^- & T_e < 0 \\ \alpha_e^+ & T_e \geq 0 \end{cases} \tag{3.37}$$

where the parameters α_e^+, α_e^- are related with the regeneration and acceleration mode, respectively. Despite being unusual, the IWM acceleration mode can also be employed during braking manoeuvres, and, in Section 3.6, some examples will be shown where this property is very useful to quickly reduce the wheel moment during the slip transients. Moreover, to exploit the different bandwidths of the braking devices, the second term in the cost function (3.36) assigns, via the weights β_i, penalties to torque variations in each actuator.

Albeit the complexity of (3.36) is not very high, the inclusion of nonlinearities, coupled with the inequality constraints, makes it difficult to find a closed-form solution. In order to gain some insight in the above problem, we start by considering a simplified case with $\alpha(T_e)$ constant and with no inequalities constraints, which yields an optimization linear problem. Then, the above assumptions will be removed and a numerical solver derived to handle the general case.

3.4.1 Linear Filtering Approximation

For the cases where none of the braking devices is saturated (including range and rate limits) and the electric torque limits satisfy

$$\operatorname{sgn}(\underline{T_e}) = \operatorname{sgn}(\overline{T_e}) \tag{3.38}$$

the solution of the allocation problem is a simple linear filter, as outlined in the next proposition.

Proposition 3.2. *Assume that* (3.38) *holds, which implies that* $\alpha_e(.) = \alpha_e$ *is constant, and that the inequality constraints in the CA problem* (3.36) *are inactive. Under these*

assumptions, the optimal solution of the control allocator is given by the following discrete-time filters

$$\frac{T_f}{T_w}(z) = \frac{\alpha_e + \beta_e}{l}\frac{z - a_f}{z - p}, \qquad \frac{T_e}{T_w}(z) = \frac{\alpha_f + \beta_f}{l}\frac{z - a_e}{z - p} \tag{3.39a}$$

$$a_f = \frac{\beta_e}{\alpha_e + \beta_e}, \qquad a_e = \frac{\beta_f}{\alpha_f + \beta_f}, \qquad p = \frac{\beta_f + \beta_e}{l} \tag{3.39b}$$

$$l = \alpha_f + \alpha_e + \beta_f + \beta_e \tag{3.39c}$$

where z represent the Z-transform operator.

Proof. Ignoring the inequality constraints in (3.36), the Lagrangian function of the resulting optimization problem is given by:

$$\begin{aligned}\mathcal{L}(T_f, T_e, \lambda_L) = \alpha_f T_f^2 + \alpha_e T_e^2 + \beta_f (T_f - T_f[k-1])^2 + \quad & \beta_e (T_e - T_e[k-1])^2 \\ & + \lambda_L (T_f + T_e - T_w)\end{aligned} \tag{3.40}$$

where λ_L is the Lagrange multiplier. Applying the first-order optimality conditions [102], we get:

$$\frac{\partial \mathcal{L}}{\partial T_f} = 2\alpha_f T_f + 2\beta_f (T_f - T_f[k-1]) + \lambda_L = 0 \tag{3.41a}$$

$$\frac{\partial \mathcal{L}}{\partial T_e} = 2\alpha_e T_e + 2\beta_e (T_e - T_e[k-1]) + \lambda_L = 0 \tag{3.41b}$$

$$\frac{\partial \mathcal{L}}{\partial \lambda_L} = T_f + T_e - T_w = 0 \tag{3.41c}$$

Solving the previous equations, the optimal solution has the form:

$$\begin{bmatrix} T_f \\ T_e \end{bmatrix} = \underbrace{\frac{1}{l}\begin{bmatrix} \beta_f & -\beta_e \\ -\beta_f & \beta_e \end{bmatrix}}_{\boldsymbol{A}} \begin{bmatrix} T_f[k-1] \\ T_e[k-1] \end{bmatrix} + \underbrace{\frac{1}{l}\begin{bmatrix} \alpha_e + \beta_e \\ \alpha_f + \beta_f \end{bmatrix}}_{\boldsymbol{B}} T_w \tag{3.42}$$

Defining the shift operator q, $q^{-1}T[k] = T[k-1]$, (3.42) can be written as

$$\begin{bmatrix} T_f[k] \\ T_e[k] \end{bmatrix} = \boldsymbol{A}\begin{bmatrix} T_f[k-1] \\ T_e[k-1] \end{bmatrix} + \boldsymbol{B}T_w[k] = q^{-1}\boldsymbol{A}\begin{bmatrix} T_f[k] \\ T_e[k] \end{bmatrix} + \boldsymbol{B}T_w[k] \tag{3.43}$$

which is equivalent to:

$$\begin{bmatrix} T_f[k] \\ T_e[k] \end{bmatrix} = (q\boldsymbol{I} - \boldsymbol{A})^{-1} q\boldsymbol{B}T_w[k] \tag{3.44}$$

where $\boldsymbol{I}$ is the identity matrix. Therefore, computing $(q\boldsymbol{I} - \boldsymbol{A})^{-1} q\boldsymbol{B}$, the filters given in (3.39) are obtained. □

Remark 3.6. The stability of (3.39) is ensured provided that the magnitude of p is less than one (e.g., by selecting $\alpha_i \neq 0$). Further, if the filter zero cancels the pole (e.g., by selecting $\beta_f = \beta_e = 0$ or $\alpha_f = \alpha_e = 0$) the filter reduces to a constant gain.

Additional understanding of the CA solution can be gained by inspecting the frequency response of the linear filters (3.39), depicted in Figure 3.6. The first plot (Figure 3.6a), illustrates the allocation among (T_f, T_e) when $\beta_f = \beta_e = 0$, and highlights that a "static",

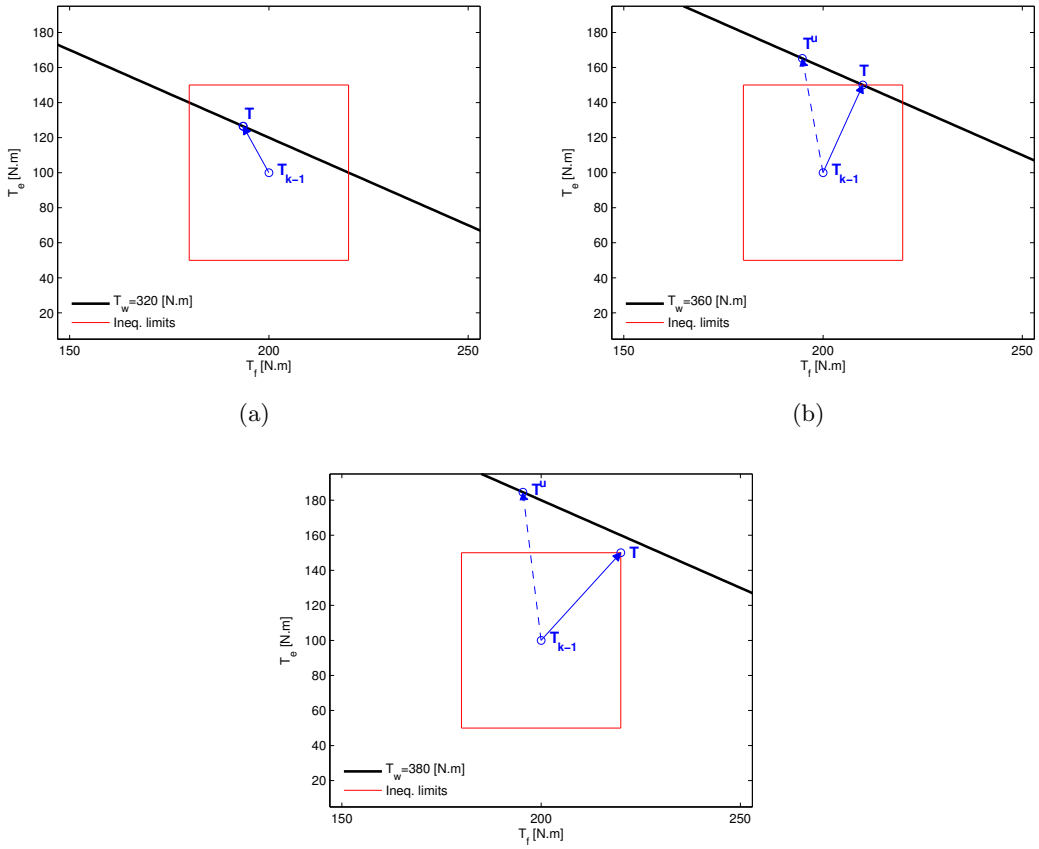

Figure 3.7: Example of operation for the wheel torque allocator: (a) unconstrained solution does not violate the constraints; (b) unconstrained solution is outside the acceptable domain and, as a result, it is necessary to activate one constraint; (c) T_w is unfeasible.

i.e., equal for all frequencies, is obtained. Actually, the steady-state gain of the filters (3.39) is given by

$$\frac{T_f}{T_w}(z=1) = \frac{\alpha_e}{\alpha_f + \alpha_e}, \qquad \frac{T_e}{T_w}(z=1) = \frac{\alpha_f}{\alpha_f + \alpha_e} \tag{3.45}$$

Thus, it is not surprising to verify that the β_i parameter has no influence on the DC gain. On the other hand, when non-zero β_i values are used, the allocation will be sensitive to the frequency spectrum of the input torque T_w; in the example illustrated in Figure 3.6b , T_e and T_f respond to the high and low frequency content, respectively. Therefore, the CA parameters can also be tuned from a frequency response perspective, and, in a later section, we will show that by a proper selection of α_i, β_i, the frequency response of (T_f, T_e) can be, somehow, shaped. As a side note, the frequency response plots also show that the magnitude of the combined torque response $(T_f + T_e)/T_w$ is always unitary, which is in accordance with the expectations associated with the equality constraint (3.34).

3.4.2 Numerical Solver for $\alpha_e(.)$ Constant

In this section we will continue to work under the assumption that (3.38) holds, but a numerical solver is introduced to handle the inequality constraints. Given that the CA

will be deployed in realtime control system, with limited computing resources, numerically efficient solvers, such as the active set methods [118], represent one of the possible candidates to calculate the solution of (3.36). Nonetheless, in view of the reduced number of inequalities (four), a simple solution can be found by following the next 3 steps:

1. check if the requested torque T_w is feasible:

$$\boldsymbol{T} = (T_f, T_e) = \begin{cases} (\overline{T}_f, \overline{T}_e), & \text{if } T_w > \overline{T}_f + \overline{T}_e \\ (\underline{T}_f, \underline{T}_e), & \text{if } T_w < \underline{T}_f + \underline{T}_e \\ \text{go to step 2} & \text{otherwise} \end{cases} \tag{3.46}$$

   (this step will ensure that, if T_w is unfeasible, the difference between the allocated torque and T_w is minimized, see Figure 3.7(c)).

2. compute the unconstrained optimal solution $\boldsymbol{T}^u = (T_f^u, T_e^u)$ by applying the difference equations resulting from (3.39); if this solution fulfils the inequality constraints, then $\boldsymbol{T} = \boldsymbol{T}^u$ and the solution is found (see Figure 3.7(a)), otherwise go to step 3;

3. in this case, the requested torque T_w is feasible, but $\boldsymbol{T}^u$ does not fulfil the inequality constraints and, as a consequence, at least one inequality is active. Notice, however, that the activation of one inequality, together with the equality constraint in (3.36), defines a unique solution. Activating individually each one of the problem inequalities results in the following candidate solutions: $\{(T_w - \overline{T}_e, \overline{T}_e), (T_w - \underline{T}_e, \underline{T}_e), (\overline{T}_f, T_w - \overline{T}_f), (\underline{T}_f, T_w - \underline{T}_f)\}$; among these, we neglect the ones that violate the problem inequalities and the optimal solution is the one that minimizes the cost function (see Figure 3.7(b)).

3.4.3 Numerical Solver for the General Case

This section addresses the general problem (3.36), dropping the assumption of constant $\alpha_e(T_e)$ suggested by condition (3.38). In order to deal with this situation, our approach consists in dividing the original allocation problem into two sub-problems. In the first we compute a solution assuming that the IWM can only produce regenerative braking, while in the second the opposite case will be considered, i.e., the IWM is only allowed to generate acceleration torque. Notice that in each of these sub-problems condition (3.38) is always verified, thus we can employ the solver described in the previous section. Based on these arguments, the final numerical solver is described as:

1. check the feasibility of the problem, as in (3.46). If it is feasible go to the next step, otherwise extract the closest point to T_w;

2. at this point we know that there is, at least, one feasible solution. The basic idea now, is to calculate two types of solutions:

   (i) determine $\boldsymbol{T}^+$, i.e., the best allocation with regenerative braking, using the solver in the previous section, configured with $\alpha_2 = \alpha_2^+$ and $T_{e,min} = 0$;

   (ii) determine $\boldsymbol{T}^-$, i.e., the best allocation by accelerating the electric motor, employing the solver described in the previous section, configured with $\alpha_2 = \alpha_2^-$ and $T_{e,max} = 0$.

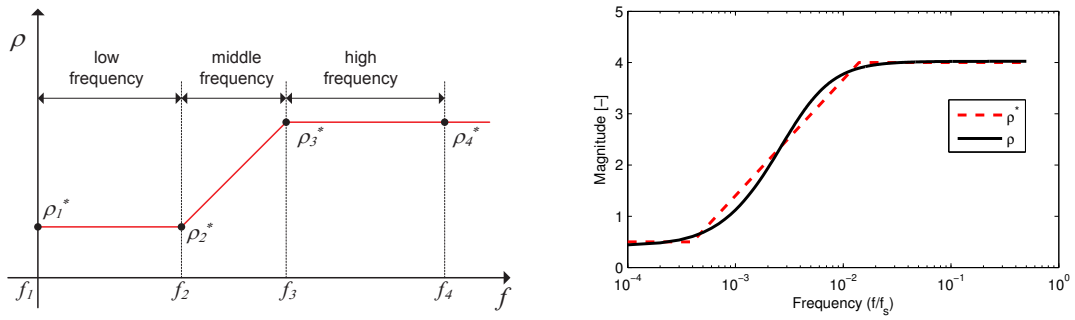

(a) (b)

Figure 3.8: a) shape of the desired torque sharing ratio ρ^*employed in this work; b) reference ρ^* employed to design the state 4 of the torque supervisor (see Table 3.1) and the approximating ρ (obtained after solving (3.50)) .

3. from the candidates $\{\boldsymbol{T}^+, \boldsymbol{T}^-\}$, discard the ones that violate the equality or inequalities constraints; for the resulting candidates, evaluate the cost function in (3.36): the optimal is the one with minimum cost.

Therefore, the above algorithm is numerically simple, has a well defined number of maximum iterations and it is suitable for realtime implementation.

3.4.4 Procedure to Select the Allocator Weights

One natural issue that emerges in the torque allocator implementation is the selection procedure of the weights α_i and β_i, which must take into account the actuators characteristics, designers preferences and the EV operational mode. To help the designer in this process, let us define the torque sharing ratio between the IWM and the friction brakes, as

$$\rho = \left| \frac{T_e}{T_f} \right| \tag{3.47}$$

Considering the linear filters (3.39), this variable can also be made frequency dependent, i.e.,

$$\begin{aligned} \rho(f) &= \left| \frac{T_e}{T_f}(z = e^{j2\pi f t_s}) \right| = \left| \left(\frac{\alpha_f + \beta_f}{\alpha_e + \beta_e} \right) \frac{e^{j2\pi f t_s} - \frac{\beta_f}{\alpha_f+\beta_f}}{e^{j2\pi f t_s} - \frac{\beta_e}{\alpha_e+\beta_e}} \right| \\ &= \left(\frac{\alpha_f + \beta_f}{\alpha_e + \beta_e} \right) \frac{\sqrt{1 + (\frac{\beta_f}{\alpha_f+\beta_f})^2 - 2\frac{\beta_f}{\alpha_f+\beta_f}\cos(2\pi f t_s)}}{\sqrt{1 + (\frac{\beta_e}{\alpha_e+\beta_e})^2 - 2\frac{\beta_e}{\alpha_e+\beta_e}\cos(2\pi f t_s)}} \end{aligned} \tag{3.48}$$

Now, assume that the designer specifies some desired torque sharing values (ρ_j^*) for a series of frequencies (f_j):

$$\mathcal{S} = \{(f_1, \rho_1^*), (f_2, \rho_2^*), \ldots, (f_N, \rho_N^*)\} \tag{3.49}$$

As an example, Figure 3.8(a) shows a possible shape for ρ^*, which provides the designer a simple framework to specify the low/high frequency gains, as well as a transition zone (middle frequencies). The question now is how we can select the parameters α_i, β_i in

Table 3.1: Example of operating modes for the braking supervisor

Num.	State	α_f	α_e^+	α_e^-	β_f	β_e	SoC	SC enable*
1	Series Braking	0.2	0	0.8	0	0	$< SoC_{th}$	0
2	Series ABS	0	0	0.024	0.8	0.2	$< SoC_{th}$	1
3	Paralell Braking	0.2	0.4	0.8	0	0	$\geq SoC_{th}$	0
4	Paralell ABS	0.002	0.005	0.01	0.8	0.2	$\geq SoC_{th}$	1
5	IWM Failure	0	1	1	0	0	–	0/1

* SC = slip controller

order to generate a torque sharing ratio ρ close to the desired ρ^*; given the mathematical expression for the frequency response (3.48), this selection is far from being trivial. To overcome this issue, we propose to solve the following nonlinear least squares problem:

$$\min_{\alpha_f,\alpha_e,\beta_f,\beta_e} \sum_{j=1}^{N} \left(\rho_j^* - \rho(f_j)\right)^2 \tag{3.50}$$

which, using a numerical solver enables us to find a suitable set of torque allocator weights. Figure 3.8(b) illustrates an application example of this methodology for the case of parallel braking (i.e., using both friction brakes and IWM).

3.5 Braking Supervisor

In order to take full advantage of wheel torque allocator, the parameters α_i, β_i should be modified depending on the EV running conditions. This adaptation is performed by the braking supervising unit (see Figure 3.3), which is also responsible for the activation/deactivation of the wheel slip controller (SC). As an illustrative example, Table 3.1 shows the braking operation modes considered in this work, which are divided into series/parallel braking with the SC enabled/disabled. The series terminology refers to the fact that, during normal braking, the friction brakes are only employed when the electrical torque saturates, while the parallel braking uses always both braking devices. The first mode, series braking, is available when the SoC of the energy source is not high (i.e., below a threshold SoC_{th}), and seeks to maximize the use of the regenerative braking; for that reason, the penalization of the friction brakes is higher than that for regenerative braking ($\alpha_f \gg \alpha_e^+$). On the other hand, when the SoC is close to the full charge, it may be convenient to reduce, gradually, the amount of regenerative braking and start to apply parallel braking (assigning higher penalization to the electric motor usage, α_e^+), which is addressed by the operational modes 3 and 4. A final state (number 5) is also added to contemplate the situation where the IWM fails and only the friction brakes are available.

It is worth mentioning that, in both series and parallel braking, when an emergency situation is detected and the SC enabled, the energy efficiency metric is no longer the main factor in the torque blending; in these scenarios, safety and a good slip regulation supersede the energy metric as the top priority. For those reasons, when the braking supervisor switches to the states 2 and 4, the weights associated with the dynamic allocation (β_i) assume preponderance in the torque allocation, and are tuned with the aim of exploiting the different actuation bandwidth offered by the braking devices (e.g., employing the procedure described in Section 3.4.4). A special mention is also due to the weight α_e^-. This parameter is responsible for the penalization assigned to the IWM acceleration mode and,

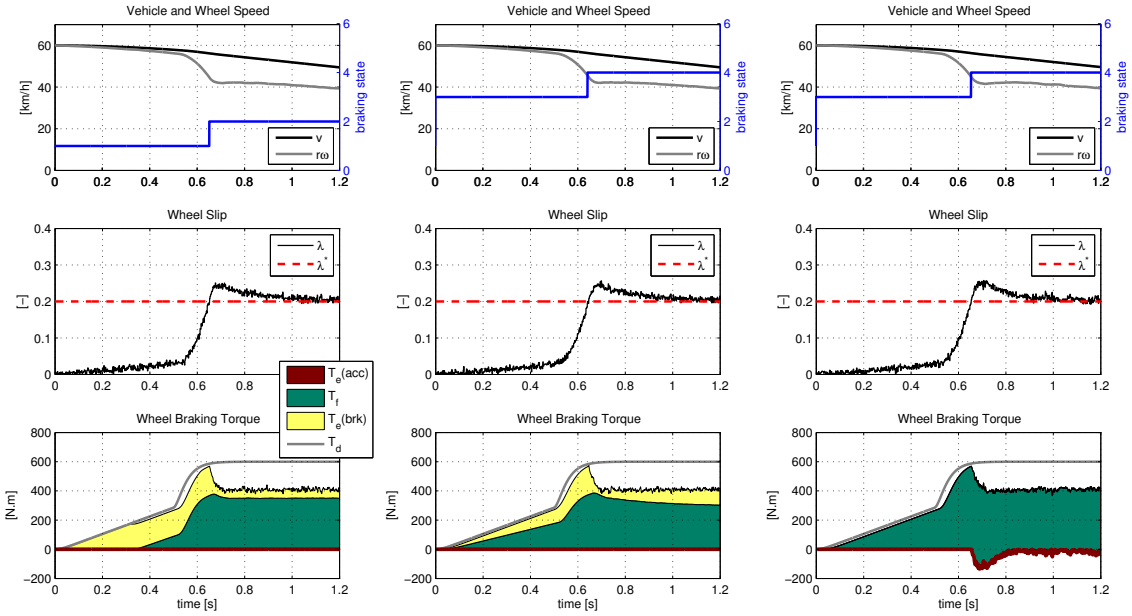

(a) $SoC < SoC_{th}$ (b) $SoC_{th} < SoC < 1$ (c) $SoC = 1.0$

Figure 3.9: Simulation results for braking on wet asphalt ($\mu_{max} = 0.6.$) for different values of SoC. The graphical representation of the wheel braking torque(T_w), and its allocation between electric and friction parts, is plotted in a stacked structure, where T_w is the result of summing $T_e(acc) + T_f + T_e(brk)$; for convenience of discussion and illustration, the electric torque was split into regenerative ($T_e(brk)$) and an acceleration ($T_e(acc)$) components.

except for the fault state, presents always a higher value than α_f and α_e^+, the penalties of friction and IWM braking. Even tough one may not expect to accelerate the IWM during normal braking manoeuvres, we will show in Section 3.6 that the SC can benefit from this feature.

To conclude, the proposed hybrid ABS structure is able to easily address the various scenarios that may affect the EV braking system (e.g., normal braking, emergency braking, low SoC, high SoC, full SoC, IWM fault, actuator constraints, etc.) and offers a simple tool to accommodate different braking approaches (series or parallel).

3.6 Simulation Results

The performance of the proposed control strategy was evaluated in a cosimulation between CarSim [146] and Matlab/Simulink. The former tool is responsible for the vehicle dynamics modelling and, compared with the QCM used in slip controller design, offers a more realistic environment to validate the braking control system. To complement CarSim, Matlab/Simulink is employed to implement the wheel slip controller, torque allocator, braking supervisor and the braking devices dynamics, parameterized with the values described in Appendix 3.8. A typical "A-class" hatchback vehicle, available in the CarSim library, was used as test car for the simulations, fitted with 175/70 R13 tyres and modelled with the magic tyre formula 5.2 [147]. Based on this simulation setting, several braking manoeuvres were carried out in a straight road, and, for simplicity, only the results of

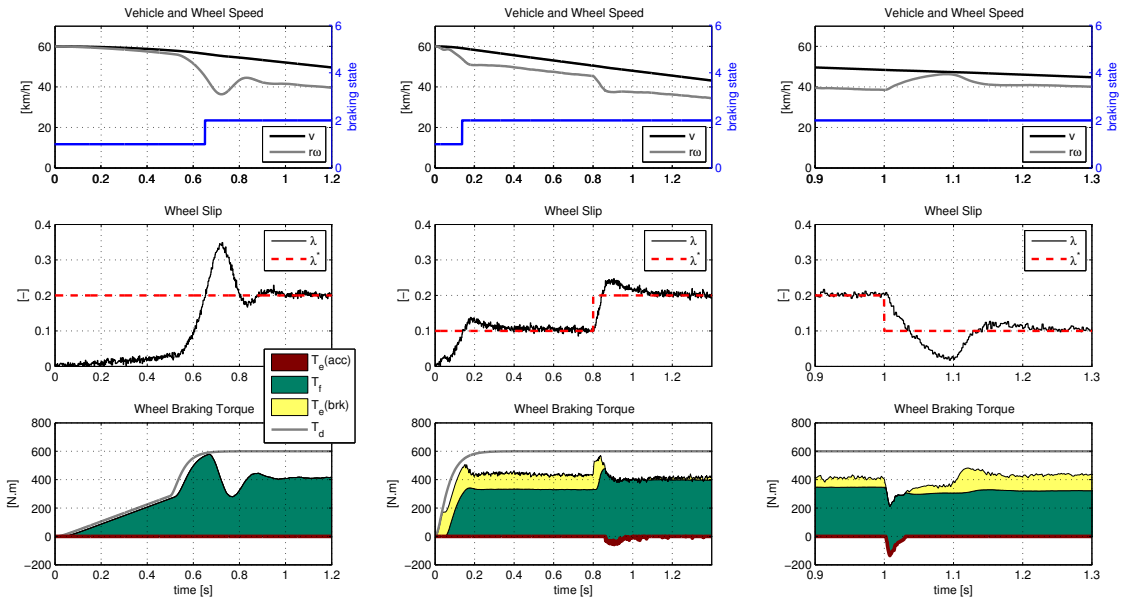

(a) IWM disabled (b) λ^* increase (c) λ^* decrease

Figure 3.10: Simulation results for braking on wet asphalt ($\mu_{max} = 0.6$.) for different setpoints and the special case with IWM disabled; the wheel torque is plotted using a stacked representation, discussed in Figure 3.9.

the left front wheel are shown (the other wheels have similar behaviour). To account for measurement errors, the slip λ was corrupted by a Gaussian noise with variance 0.005^2.

The first batch of tests, illustrated in Figure 3.9, aims at evaluating the hybrid ABS performance for three levels of battery SoC: low, high and full. Analyzing the low SoC case (Figure 3.9(a)), two phases can be identified. In the first section for $t \in [0, 0.65]$s a normal braking manoeuvre is performed: in order to maximize the energy efficiency, the torque allocator privileges the electric motor utilization; the friction brakes only start to be applied after the electric torque reaches saturation, i.e., a series braking approach is being applied. In the second part ($t > 0.65$s), the tyre slip reaches high values and the slip controller is activated (notice that the braking supervisor switches to the state 2): in this case the torque allocation strategy uses the electric actuator to quickly decrease the wheel moment and keep the tyre slip near the set-point, while the slow friction brakes torque is kept constant throughout the remaining of the manoeuvre. In the high SoC situation (Figure 3.9(b)), similar results to the low SoC case can be found, but with an important difference: since the beginning of the manoeuvre, a parallel braking policy is employed, enabling both electric and friction devices.

Lastly, when the SoC reaches the full charge, the IWM is no longer able to provide regenerative braking, but this does not necessarily mean that the IWM should be disabled during the slip control phase. In fact, it turned out (see Figure 3.9(c)) that we can still employ the IWM to produce, during some tenths of a second, acceleration torque and, as a consequence, quickly decrease the wheel moment required by the slip control after its activation; simultaneously, the friction torque is smoothly brought to its new steady-state value . Although this mode of operation, i.e., accelerating the IWM during a braking manoeuvre, may look counterintuitive, the simulation results highlights that, even if no

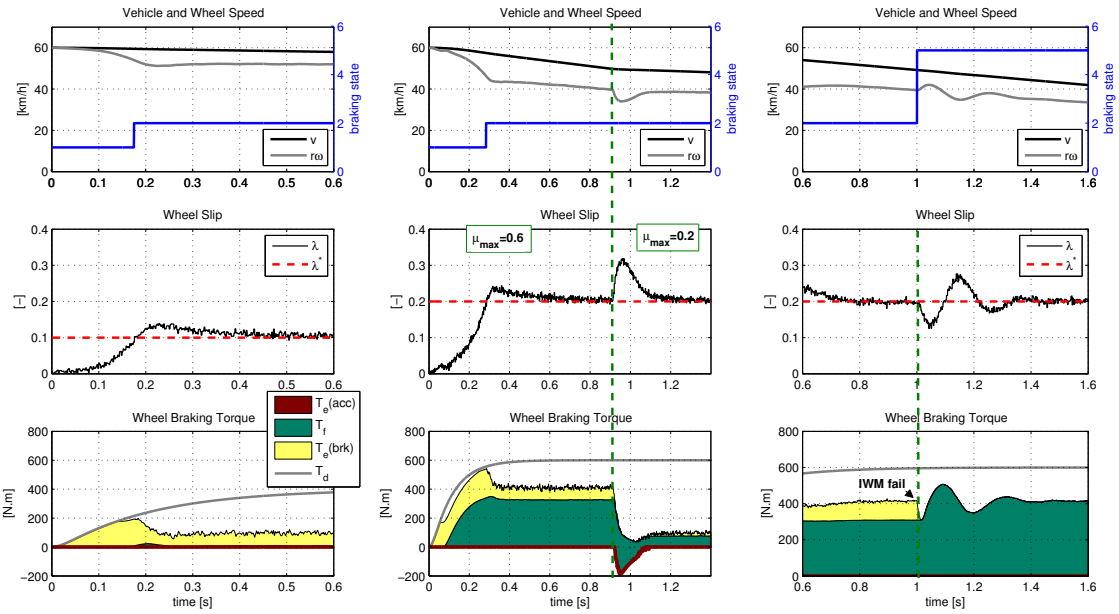

(a) snow test ($\mu_{max} = 0.2$) (b) μ jump (c) IWM Fail

Figure 3.11: Simulation results for braking on low μ and response to μ jumps ($SoC < SoC_{th}$); the wheel torque is plotted using a stacked representation, discussed in Figure 3.9.

energy recuperation is possible, the IWM usage is still pivotal to provide a fast slip response and ensure a braking behaviour independent of the battery SoC. To emphasize this last point, and also for comparison purposes, Figure 3.10(a) shows the braking performance when the IWM is, for some reason, disabled (for example, motivated by a fault before the braking). Examining these results, it is visible that employing only T_f is sufficient to perform the slip regulation, but, due to the large time constant and delays in the friction brake actuator dynamics, some degradation is introduced in the transient response (larger overshoot and oscillations).

There are also others scenarios, like the appearance of strong disturbances during the slip regulation process, where the IWM assistance is beneficial. Some of these situations are illustrated in Figure 3.10(b) and (c) for set-point changes, and in Figure 3.11(b) for a μ jump; in all these cases, it can be observed that the wheel slip regulator is able to cope with the disturbances and the IWM torque (acceleration and braking) is, again, exploited to quickly bring the slip to the set-point λ^*. As a matter of fact, analyzing more closely the test with a λ^* decrease (Figure 3.10(c)), it is interesting to note that the friction brake torque is kept constant at ~ 300 Nm, while the IWM torque is being modulated to respond to the disturbance, or, in other words, to provide the high frequency content of the T_w signal. From a braking intensity point of view, there are also some cases, such as decelerations on low μ roads, where the regenerative torque is enough to provide all the vehicle braking needs, as illustrated in Figure 3.11(a).

Along with the torque allocation features, the adaptive mechanism incorporated in the slip control is also a key aspect in handling the model parametric uncertainties. To explain how this adaption works, Figure 3.12 shows the evolution of $\hat{\boldsymbol{\theta}}$ during the snow and μ jump tests. Firstly, while a normal braking is detected the output of the estimator is the same

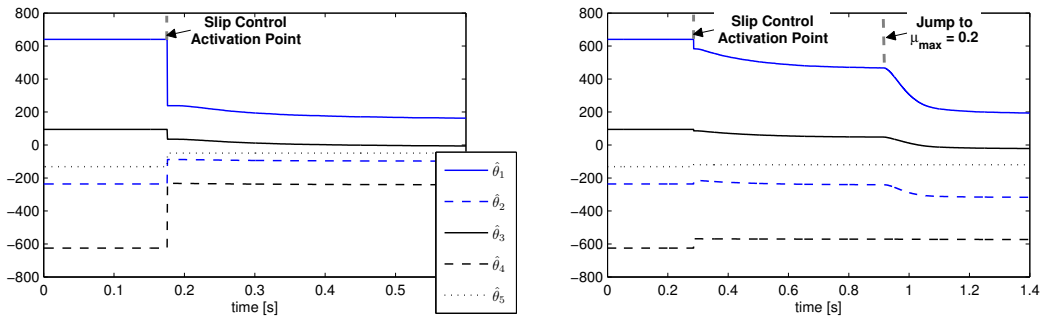

(a) snow test ($\mu_{max} = 0.2$) (b) μ jump

Figure 3.12: Simulation results: adaption of the estimates $\hat{\boldsymbol{\theta}}$ during the snow and μ jump test.

as the nominal estimate, $\boldsymbol{\theta}_N$, and the adaption is frozen. Next, once the slip control is activated the estimate is re-initialized with (3.33) in order to avoid wheel torque jumps, as explained in Section 3.3.3; after this step, the adaption begins and it can be observed a quick convergence to a steady-state value in the snow test, while in the μ jump case there is further activity to track the friction change that occurs at approximately $t = 0.9$s. Hence, these results indicate that, apart from the issue associated with the selection of the optimal λ^*, the proposed slip controller is robust to uncertainties in μ.

In a brake-by-wire system one of the most important issues is how to handle failures in the braking devices. As a preliminary test, consider the case depicted in Figure 3.11(c), where the IWM fails around 1s, forcing a rapid decrease of the electrical torque to zero. In that situation, the braking supervisor switches to a (IWM) fault mode (number 5), and reconfigures the torque allocator to employ only the remaining healthy actuator, the friction device. By inspecting the response after this fault injection, it can be seen that the friction actuator takes over the wheel torque and is, naturally, capable of recovering the slip control with minimum impact on the braking effectiveness. To a certain extent, the proposed braking structure is tolerant to some types of IWM failures, while more challenging failures scenarios (e.g., friction braking faults) will be tackled in future works.

3.7 Conclusion

In this Chapter, a hybrid ABS solution for electric and hybrid vehicles was proposed, endowed with IWMs and friction brakes. The proposed method relies on a robust adaptive wheel slip controller, and a wheel torque allocator to distribute the braking effort among the two actuators. Besides handling the actuators constraints, the torque allocator exploits the braking redundancy to optimize the energy efficiency and dynamic performance metrics. Simulation studies, carried out with the CarSim environment, highlighted that the IWM can assist the friction brakes, not only during normal braking manoeuvres, but also in emergency braking, contributing to a better transient response of the wheel slip controller. As future work, we plan to experimentally validate the hybrid ABS controller in the uCar EV prototype (see Appendix A) and investigate fault-tolerant schemes.

Table 3.2: Parameters of the vehicle, actuators and controller employed in the simulations

Parameter	Value
Quarter car mass (M) [kg]	1000/4
Wheel radius (r) [m]	0.3
Maximum electric torque $T_{e,n}$ [Nm]	200
Electric motor nominal speed ω_n [km/h]	50
Maximum torque of the friction brakes $T_{f,max}$ [Nm]	2000
Time constant of the friction brakes τ_f [ms]	16
Deadtime of the friction brakes δ_f [ms]	15
Time constant of the electric motor τ_e [ms]	1.5
Deadtime of the electric motor δ_e [ms]	0.5
Maximum torque variation rate of the friction brakes $\dot{T}_{f,max}$ [kN/s]	10
Maximum torque variation rate of the electric motor $\dot{T}_{e,max}$ [kN/s]	30
Speed threshold v_o [km/h]	5
k_v	1
deadzone ε	0.005
controller gain k	222*
adaption rate γ	300000*
initial estimate $\boldsymbol{\theta}_N = rF_z[1.22\ -0.45\, 0.18\ -1.19 - 0.25]^T$	
controller sampling time t_s[s]	1/500

* in case of electric motor failure, the control parameters are reduce to $k = 88.8$ and $\gamma = 200000$.

3.8 Appendix: Vehicle and Actuator Parameters

The values of the vehicle, actuators and controller parameters are defined in Table 3.2 and 3.1.

Chapter 4

Wheel Slip Control based on Sliding Modes and Conditional Integrator

Abstract: *This chapter is concerned with the design of a robust wheel slip controller based on the sliding mode framework. The robustness to parametric and modelling uncertainties is the main attraction in this design, thanks to a simple connection that was found between the driving torque request and the model uncertainty. To overcome the chattering issue, which arrives from the discontinuous nature of the sliding control, the conditional integrator approach was employed, enabling a smooth transition to a Proportional+Integral control law, with anti-windup, when the tyre slip is close to the setpoint. The controller asymptotic stability and robustness was analytically investigated through the Lyapunov method. Experimental results, obtained with a multi-motor EV prototype under low grip conditions, demonstrate a good slip regulation and robustness to disturbances.*

4.1 Introduction

The redundant braking system for EVs, proposed in the previous Chapter, can be decomposed into three sub-components: *i*) slip controller; *ii*) torque allocator and *iii*) braking supervisor (see Figure 3.3). This chapter will revisit the design of the slip controller, but, in contrast to the adaptive formulation derived in the section 3.3.3, we will follow an approach based purely on robust techniques. Before describing this approach, it is convenient to contextualize the wheel slip regulation within the controls that normally estabilize the longitudinal motion of the car, as is the case of Antilock Braking System (ABS) and the Traction Control (TC).

Traditionally, the adhesion control between the tyre and the road has been divided into two classes of driving aid systems: the TC, enabled during accelerating manoeuvres, and the ABS, active during decelerations. The motivation for introducing these systems is related to the difficulty that the drivers experience in controlling the throttle/brake pedal when the vehicle is running over slippery surfaces, such as snow or ice. In these conditions, it is tricky for the drivers to judge how much wheel torque to apply, and it is common to end up employing excessive wheel torque that results in skid (braking) or high tyre spin (acceleration), compromising the longitudinal force generation and reducing the ability of

the tyre to transmit lateral forces. It is the responsibility of the TC and ABS to avoid such pernicious operation modes by decreasing the magnitude of the torque requested by the driver, to levels where the tyre longitudinal force is maximized and the slip kept within a safe range that does not jeopardize the tyre lateral forces [127, 133]. However, such goals are not easy to achieve due to nonlinearities and model uncertainties associated with the vehicle and the road adhesion conditions. In fact, we can identify three fundamental issues that affect the TC/ABS design: *i*) the actuator dynamics; *ii*) the controlled variable and the available means to measure it; and *iii*) robustness to friction uncertainty in the tyre-road interface.

The first factor, related to actuator dynamics and delays, affected mainly the earliest generations of TC/ABS, since the traditional hydraulic-based friction brakes (used in the conventional ABS) are inherently slow and prone to exhibit limit cycles [148], while the internal combustion engine (ICE), for the TC case, presents a significant pure delay [149]. More recently, with the advent of electro-mechanical brakes (see Chapter 6 and references [131, 150]), faster torque responses started to be achieved, which eased off the delay problem in the controller design. In any case, for powertrains based on electric motors, which is the main focus of this work, the bandwidth of the electric motor surpasses the dynamics of any of the afore-mentioned traditional actuators [151], and the actuator delay is no longer a serious issue. An additional advantage provided by the electric motor is the torque bi-directionality, which enables the application of accelerating and regenerative torque; thus this actuator can be effectively used in both TC and ABS situations, a property explored in this chapter.

A second factor to take into account in the TC/ABS design is the selection of control variable, as well as its availability for feedback. From the control effectiveness point of view, the direct control of the tyre slip (λ) is advantageous, due to the intrinsic relationship between the friction force and the tyre slip, as shown by several friction models discussed in the specialised literature [133, 152]. Consequently, one of the most common approaches in the TC/ABS control problem is to make the tyre slip follow an optimum λ^* setpoint that, ideally, maximizes the longitudinal friction force [15, 131, 143, 153]. This method is very appealing for the accelerating mode of two-wheel drive (2WD) vehicles, because the vehicle speed, needed for the λ calculation, can be easily measured using the rotational speed of the non-driven wheels. On the other hand, for 4WD or for braking manoeuvres, the λ measure is difficult to acquire, because all the vehicle wheels are being driven, which obliges the application of observers for estimating the vehicle speed [133, 154], complicating the controller implementation and tuning. To partially mitigate this problem, alternative control variables, like the wheel acceleration [127, 133], easily derived from the wheel rotational speed, or a mix between the tyre slip and deceleration [150], helpful when the vehicle speed estimation is noisy, were also proposed in the literature. Another research line that dismisses the vehicle speed measurement or estimation includes the works pioneered by Prof. Hori and co-researchers [15, 155] where the Model-Following Control (MFC) [155], and the most recent Maximum Transmissible Torque Estimation (MTTE) [16], were employed to avoid excessive tyre slippage through disturbance observers' techniques.

In this work we followed the wheel slip control (SC) approach, and focused our attention on studying robust mechanisms to handle the model uncertainties, which constitute the third and final challenge in the TC/ABS design. Among the model uncertainties, the tyre-road friction (μ) is one of the most difficult variables to predict or measure. For this reason, ensuring robustness against this variation is an important requirement in the controller design that is not easy to accomplish. For instance, the linear Proportional+Integral (PI)

control proposed in [15, 155] is simple and very attractive from an implementation point of view, but suffers from the fact that the PI tuning is based on a linearization of the quarter-car model (QCM), thus only local stability can be ensured and robustness to model uncertainty is a concern. Based on a similar quarter-car linearized model, [149] employs a Model Predictive Control (MPC) setting, but there is no theoretical result that ensures the controller robustness to model uncertainties, which were only investigated with simulations.

In order to handle the model nonlinearities and uncertainties, the Sliding Mode Control (SMC) framework represents an attractive alternative, and it was the control technique employed in this Chapter. Albeit this control methodology has been previously applied to the TC/ABS problem (see [143, 156, 157, 158, 159, 160, 161]), there remain some challenging issues that are not easily solvable, such as finding the upper bound for the modelling error and the chattering problem. The former problem can be attenuated by employing SMC in conjunction with observers, based on neural-networks [159], fuzzy logic [160], recursive least-squares [162] or sliding modes [163], but they also increase the implementation complexity and the controller tuning effort, and it may be difficult to ensure a fast learning rate in real scenarios. To address the second problem, the chattering, the continuous approximation of the discontinuous control law [161, 162, 164] is the simplest approach to attenuate this issue, but, simultaneously, introduces a steady state error in the slip regulation. A more promising approach, recently applied to the TC/ABS problem, are the high-order sliding modes [143, 157], which confine the discontinuous action to a high-order time derivative of the control signal.

The first contribution of this chapter is related with a simple approach to design a SC based on sliding modes, without needing any friction observer. To this aim, we noticed that most of the previous works overlook the influence of driver torque requests (T_d), and, by studying the conditions that trigger the SC activation, we deduced a relation between T_d and the model uncertainty, which contributes to a simple tuning. To address the chattering problem, we employed the technique of sliding modes with conditional integrator [165], which allows us to keep the performance of the ideal SMC, outside a boundary layer, and switch to a PI-like controller, with anti-windup mechanism, when the slip is in the proximities of the slip setpoint. The asymptotic and robustness properties were analytically shown using the Lyapunov stability method, and experimentally validated in a multi-motor EV prototype.

4.2 Wheel Slip Control using Sliding Modes

As in the previous chapter, the starting point for the SC design is the quarter car model introduced in section 3.3.1. For our purposes here, lets consider that the main source of uncertainty lies in the friction model and the disturbances Δ_v and Δ_ω can be neglected, i.e., ($\Delta_v = \Delta_\omega = 0$). Under these assumptions, the tyre slip dynamics (3.9) can rewritten as:

$$\dot{\lambda} = -\gamma(v)\Big(\Psi(\lambda) - T_d u\Big) \tag{4.1a}$$

$$\Psi(\lambda) = \left(\frac{J}{Mr^2}(1-\lambda)+1\right) rF_z\mu(\lambda) \tag{4.1b}$$

$$\gamma(v) = \frac{1}{v}\frac{r}{J} \qquad T_w = T_d u \tag{4.1c}$$

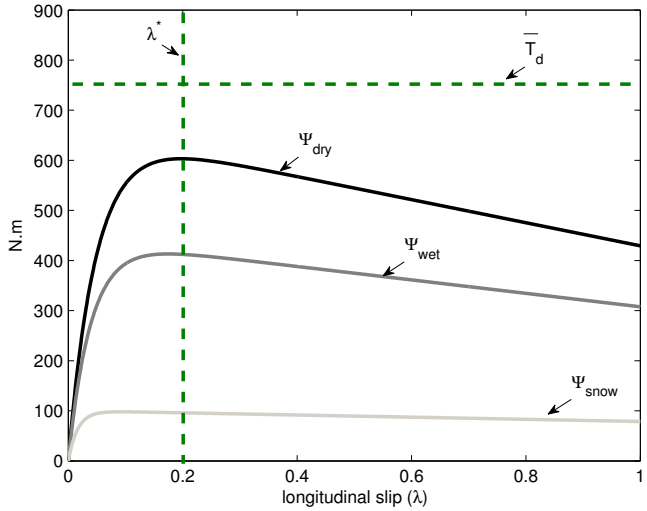

Figure 4.1: Example of the maximum braking torque $\overline{T_d}$, λ^* and $\Psi(\lambda)$ function for different adhesion levels, (Parameters: $M = 175$ kg, $r = 0.3$m, $J = 1\text{kg.m}^2$,$F_z = Mg$ and the Burckhardt friction curve [133]).

where $\lambda \in \mathcal{D} = [0, 1]$ is the tyre slip, $T_d \in \mathcal{T} = (0, \overline{T_d}] \subset \mathbb{R}$ the braking torque requested by the driver, positive and bounded by $\overline{T_d}$, and $u \in \mathcal{U} = [0, 1]$ the control input of the SC. During the SC design, we will not use any parametric model for the friction $\mu(\lambda)$, consequently the Ψ function is highly uncertain. We will only assume that Ψ is lower bounded by 0, upper bounded by $\overline{T_d}$ and passes though the origin, i.e., Ψ belongs to the set:

$$\begin{aligned} \mathcal{J} = \{\Psi(\lambda) \quad : \quad & \Psi(0) = 0 \text{ and} \\ & 0 < \Psi(\lambda) < \overline{T_d} \text{ for } \lambda \in \mathcal{D} \setminus \{0\} \ \} \end{aligned} \tag{4.2}$$

From the practical point of view, the upper bound $\overline{T_d}$ implies that the braking system has the ability to cover $\Psi(\lambda)$ function for every friction coefficient found in practice, as illustrated in Figure 4.1. There is also an interesting connection between $\Psi(\lambda)$ and the load torque that the wheel experiences: under the reasonable assumption that the wheel inertia J is much smaller than Mr^2, then $\Psi(\lambda) \simeq rF_z\mu(\lambda)$ [127]. Hence, $\Psi(\lambda)$ can be interpreted as a load torque applied to the wheel, which directly depends upon the friction coefficient and the normal load F_z (see Figure 4.1). Additionally, we work under the assumption of positive vehicle speeds $v > 0$, thus $\gamma(v) > 0$, the tyre slip λ is measured and that the torque requested by driver is nonzero (when $T_d = 0$, it does not make sense to apply the SC). On top of that, to simplify the controller presentation, it is further assumed that the vehicle is performing a braking operation, but the obtained results can be easily extended to the acceleration case, which will be illustrated in a later section.

In the author's opinion, the SC, when enabled, should not "take over" the brake signal, but it should instead work in cooperation with the braking torque requested by the driver, T_d. For that reason, the control input u is a multiplicative correction term that is inserted in the braking loop: during normal braking manoeuvres, $u = 1$, and the SC do not interfere in the braking process; on the other hand, when excessive (and potentially dangerous) tyre slips are detected, the SC will manipulate the u signal in order to reach

the maximum friction. It is further assumed that the traction force is maximized for a known optimum slip $\lambda^* = \arg\max_{\lambda\in\mathcal{D}} \mu(\lambda)$. Normally, λ^* is significantly affected by road adhesion conditions; experiences carried out in [166] indicate that $\lambda^* \in [0.08; 0.3]$ for the most common adhesion levels found in practice. In this work, we considered a constant value of $\lambda^* = 0.2$, but if a more precise value is needed a friction peak estimator can be applied to extract the optimum slip value (see Chapter 5 for additional details).

In the proposed SC design, the torque requested by the driver has a pivotal role in the controller operation and, for that reason, it is important to study the conditions that trigger, in the first place, the SC activation.

Lemma 4.1. *Consider $\lambda^* \in \mathcal{D}$, the set $\Omega_0 = [0, \lambda^*]$, $\lambda(0) \in \Omega_0$ and $u = 1$ (the SC is disabled). If $T_d \leq \Psi(\lambda^*)$, then the set Ω_0 is positively invariant, i.e., $\lambda(t) \in \Omega_0, \forall t \geq 0$*

Proof: In order to show the invariance of Ω_0 we will use the Lyapunov function $V(\lambda) = 1/2\lambda^2$. Analysing $\dot{V}(\lambda) = \lambda\dot{\lambda} = -\lambda\gamma(v)\left[\Psi(\lambda) - T_d\right]$ at the border of Ω_0, i.e., $\partial\Omega_0 = \{0, \lambda^*\}$, we have:

1. $\dot{V}(0) = 0$

2. $\dot{V}(\lambda^*) = -\lambda^*\gamma(v)\left[\Psi(\lambda^*) - T_d\right] \leq 0$

Since $\dot{V} \leq 0$ in $\partial\Omega_0$ we can state that Ω_0 is a positively invariant set. □

In order to explain the important of the previous Lemma, consider, for a moment, that the true λ^* is known, thus $\Psi(\lambda^*) = \max\Psi(\lambda)$. What Lemma 4.1 shows is that, while the driver is applying a torque $T_d \leq \max\Psi(\lambda) = \Psi(\lambda^*)$, the tyre slip will be kept in a "safe set" Ω_0, in this way preventing excessive slips, and the SC use will not be activated. Moreover, this result also give us an important insight about the conditions that will lead to the SC activation: it is relatively easy to see that if $T_d > \max\Psi(\lambda)$, then we can no longer guarantee the invariance property of Ω_0, thus excessive slip will be reached and the SC enabled. Consequently, when the SC is activated for the first time, the T_d is higher than the peak of $\Psi(\lambda)$, and, in this moment, we have valuable information about an upper bound for the unknown function $\Psi(\lambda)$, which will be of great importance to the robust design of the SC.

4.2.1 Ideal SMC

In the SMC framework adopted in this work, the control objective is to reach and remain in sliding surface $s = 0$, where

$$s = \lambda - \lambda^* \tag{4.3}$$

The control law obtained by the sliding approach is composed of two terms: the first is an equivalent control term that, ideally, would keep the system in the sliding surface, as long as the system model was completely known; since this hardly happens, a switching term is added to ensure the robustness to the modelling errors [96]. Applying this design method to the QCM, the sliding control law is defined as follows [17]:

$$u = \left(\frac{1}{T_d}\right)\left[\hat{\Psi}(\lambda) - T_d(\rho(\lambda) + \beta_0)\,\mathrm{sgn}(s)\right] \tag{4.4}$$

where $\hat{\Psi}$ is the estimative of the Ψ function, $\beta_0 > 0$ is a positive constant and ρ is the upper bound for the uncertainty:

$$\frac{|\Psi(\lambda) - \hat{\Psi}(\lambda)|}{T_d} \leq \rho(\lambda), \quad \forall \lambda \in \mathcal{D} \tag{4.5}$$

To show that, in spite of model disturbances, the closed loop system reaches $s = 0$ in finite time, consider the time derivative of the Lyapunov function $V(s) = 1/2s^2$:

$$\begin{aligned} \dot{V}(s) &= s\dot{s} \\ &= -\gamma(v)s\left[\Psi(\lambda) - \hat{\Psi}(\lambda) + T_d(\rho(\lambda) + \beta_0)\,\mathrm{sgn}(s)\right] \\ &\leq -\gamma(v)T_d\left[\rho(\lambda) + \beta_0 - \frac{|\Psi(\lambda) - \hat{\Psi}(\lambda)|}{T_d}\right]|s| \end{aligned} \tag{4.6}$$

assuming that (4.5) is satisfied, then:

$$\dot{V}(s) = s\dot{s} \leq -\gamma(v)T_d\beta_0|s| \tag{4.7}$$

Note that $\gamma(v), T_d$ and β_0 are all positive variables, which makes the relation (4.7), known as the sliding condition, negative definite in $\mathcal{D}$. Finally, employing the comparison lemma to the sliding condition, it can be shown that $s \to 0$ in finite time [96].

4.2.2 Relation between T_d and Model Uncertainty

The previous SMC needs the estimation $\hat{\Psi}$ and an upper bound ρ for the modelling uncertainty. Note that the biggest source of uncertainty in $\Psi(\lambda)$ is the friction coefficient $\mu(\lambda)$, which is time-varying and difficult to predict. One simple way to find $\hat{\Psi}$ and ρ involves exploiting the fact that $\Psi \in \mathcal{J}$, hence by construction is upper bounded by $\overline{T_d}$; if we select the estimation $\hat{\Psi}(\lambda) = \frac{\overline{T_d}}{2}$, then we can easily verify that $\frac{\overline{T_d}}{2T_d} \leq \rho(\lambda)$ is an upper bound for the modelling error, and meet the sliding condition. However, this choice leads to an excessive gain of the discontinuous term (4.4), which raises some practical concerns and may exacerbate the chattering problem. In other words, this is a very conservative approach and requires a large control effort.

In order to decrease the control effort and avoid $\mu(.)$ observers, what we propose is to use not the upper bound $\overline{T_d}$, but the torque requested by the driver, T_d, to build a simple estimator for $\Psi(\lambda)$, with a known maximum modelling error. The motivation for employing this strategy is to the results of Lemma 4.1, which gave us some hints about using T_d as an upper bound for the unknown function $\Psi(\lambda)$, when excessive slips are generated and the SC usage is needed. These ideas are formulated in the next theorem.

Theorem 4.1. *Consider the quarter car model* (4.1) *controlled by* (4.4). *Selecting the estimation* $\hat{\Psi}(\lambda) = \frac{T_d}{2}$ *and the upper bound* $\rho(\lambda) = \frac{1}{2}$ *we can ensure that, for any* $\Psi(\lambda) \in \mathcal{J}$, λ *reaches* λ^* *in finite time, as long as* $T_d \geq \max_{\lambda \in \mathcal{D}} \Psi(\lambda)$.

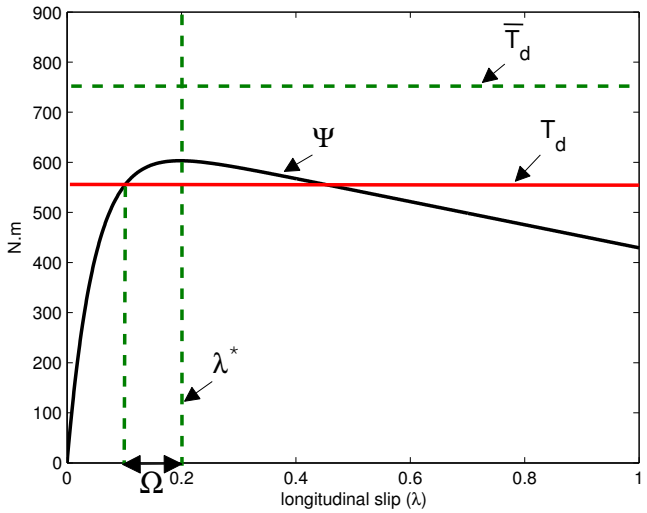

Figure 4.2: Representation of Ω set, defined in (4.15).

Proof: Since $\Psi \in \mathcal{J}$ and $\max_{\lambda\in\mathcal{D}} \Psi(\lambda) \leq T_d$ then

$$0 \leq \Psi(\lambda) \leq \max_{\lambda\in\mathcal{D}} \Psi(\lambda) \leq T_d \Leftrightarrow \tag{4.8}$$

$$-\frac{T_d}{2} \leq \Psi(\lambda) - \frac{T_d}{2} \leq \frac{T_d}{2} \Leftrightarrow \tag{4.9}$$

$$|\Psi(\lambda) - \frac{T_d}{2}| \leq \frac{T_d}{2} \Leftrightarrow \tag{4.10}$$

$$\frac{|\Psi(\lambda) - \frac{T_d}{2}|}{T_d} \leq \frac{1}{2} \tag{4.11}$$

Now compare the previous equation with (4.5): by choosing $\rho(\lambda) = 1/2$ and $\hat{\Psi} = \frac{T_d}{2}$, we can find an upper bound for the uncertainty, i.e., (4.5) is satisfied; thus the sliding condition (4.6) is also verified, which means that the sliding surface $s = \lambda - \lambda^* = 0$ will be reached in finite time, since $\dot{V}(s) = s\dot{s} \leq -\alpha_0|s|, \alpha_0 = \gamma(v)T_d\beta_0 > 0$. □

Making use of the previous Theorem, the resulting SMC control is given by:

$$u = \frac{1 - (1 + 2\beta_0)\,\mathrm{sgn}(s)}{2} \tag{4.12}$$

However, there remains a doubt: what happens when the driver is not requesting an excessive torque, i.e., $T_d < \max \Psi(\lambda)$, and the SC is still active? The next theorem answers this question.

Theorem 4.2. *Consider the same conditions as Theorem 4.1, but now assume that T_d can take any value in $\mathcal{T}$. Define the set:*

$$\Lambda(T_d) = \left\{ \lambda \in \mathcal{D} \ : \ T_d = \Psi(\lambda) \right\} \tag{4.13}$$

which represent the equilibrium points of (4.1) *when* $u = 1$*, and the scalar:*

$$\underline{\lambda} = \begin{cases} \min\{\lambda \in \Lambda(T_d)\} & \text{if } \Lambda(T_d) \neq \emptyset \\ \lambda^* & \text{if } \Lambda(T_d) = \emptyset \end{cases} \tag{4.14}$$

Using the control law (4.12)*, the following set*

$$\Omega = [\underline{\lambda}, \lambda^*] \cup \lambda^* = [\min(\underline{\lambda}, \lambda^*), \lambda^*] \tag{4.15}$$

will be reached in finite time for any $T_d \in \mathcal{T}$ *and any* $\Psi \in \mathcal{J}$*.*

Proof: For $T_d \in (\max_{\lambda\in\mathcal{D}} \Psi(\lambda), \overline{T_d}]$, $\Lambda(T_d) = \emptyset$, $\Omega = \{\lambda^*\}$ and we have the same conditions as Theorem 4.1, thus λ will reach $\lambda^* \in \Omega$ in finite time.

The remainder of the proof is concerned with the situation $T_d \in (0, \max_{\lambda\in\mathcal{D}} \Psi(\lambda)]$. In this case, $\Lambda(T_d) \neq \emptyset$ and, since $\underline{\lambda}$ is where T_d and $\Psi(\lambda)$ first intersect, we can state that: $T_d \geq \Psi(\lambda)$ for $\lambda \in [0, \underline{\lambda}]$, which will be useful later in the proof. The set Ω can be a single point $\{\lambda^*\}$, if $\underline{\lambda} \geq \lambda^*$, or an interval $[\underline{\lambda}, \lambda^*]$, if $\underline{\lambda} < \lambda^*$, and we will show, for both cases, that the set Ω will be reached in finite time. To assist this demonstration we will make use of the Lyapunov function $V = 1/2s^2$ and the control law (4.12), thus $\hat{\Psi}(\lambda) = \frac{T_d}{2}$, $\rho(\lambda) = \frac{1}{2}$ and $\dot{V}$ is defined by:

$$\dot{V}(s) = -\gamma(v)s\left[\Psi(\lambda) - \frac{T_d}{2} + T_d(\frac{1}{2} + \beta_0)\,\mathrm{sgn}(s)\right] \tag{4.16}$$

$$\leq -\gamma(v)T_d\left[\frac{1}{2} + \beta_0 - \frac{|\Psi(\lambda) - \frac{T_d}{2}|}{T_d}\right]|s| \tag{4.17}$$

Case I: $\underline{\lambda} \geq \lambda^*$, $\Omega = \{\lambda^*\}$. For studying the $\dot{V}$ function we will split the slip domain into two parts:

$$\mathcal{D} = [0, 1] = [0, \underline{\lambda}] \cup (\underline{\lambda}, 1] \tag{4.18}$$

In the first interval, $\lambda \in [0, \underline{\lambda}]$ and $0 \leq \Psi(\lambda) \leq T_d$, so we can easily verify (for instance following a similar reasoning as in the Theorem 4.1 proof) that

$$\frac{|\Psi(\lambda) - \frac{T_d}{2}|}{T_d} \leq \frac{1}{2}, \quad \forall\, \lambda \in [0, \underline{\lambda}] \tag{4.19}$$

Applying the previous relation to (4.17) results in:

$$\dot{V}(s) \leq -\gamma(v)T_d\beta_0|s|, \quad \forall\, \lambda \in [0, \underline{\lambda}] \tag{4.20}$$

Regarding the second interval of $\mathcal{D}$, $(\underline{\lambda}, 1]$, the sliding variable is positive, $s = \lambda - \lambda^* > 0, \quad \forall\, \lambda \in (\underline{\lambda}, 1]$ and $\dot{V}$ satisfies:

$$\dot{V}(s) = -\gamma(v)s\left[\Psi(\lambda) + T_d\beta_0\right)] \tag{4.21}$$

$$= -\gamma(v)\left[T_d\beta_0 + \Psi(\lambda))\right]|s|, \quad \forall\, \lambda \in (\underline{\lambda}, 1] \tag{4.22}$$

Therefore, by (4.20) and (4.22), we can state that:

$$\dot{V}(s) = s\dot{s} \leq -\alpha_0|s|, \quad \forall \lambda \in \mathcal{D} \tag{4.23}$$

where $\alpha_0 = \gamma(v)\min\{T_d\beta_0,\ T_d\beta_0 + \Psi(\lambda)\}$. Since $\Psi(\lambda) \in \mathcal{J}$ is positive definite over $\mathcal{D}$, $\alpha_0 = \gamma(v)T_d\beta_0 > 0$; as a result (4.23) implies that $s = 0$ ($\Leftrightarrow \lambda = \lambda^* \in \Omega$) will be reached in finite time.

Case II: $\underline{\lambda} < \lambda^*$, $\Omega = [\underline{\lambda}, \lambda^*]$. In this case, we are interested in studying $\dot{V}$ in $\mathcal{D} \setminus \Omega$, which can be decomposed into two intervals:

$$\mathcal{D} \setminus \Omega \quad = \quad [0, \underline{\lambda}) \cup (\lambda^*, 1] \tag{4.24}$$

For the first interval, we note that $[0, \underline{\lambda}) \subset [0, \underline{\lambda}]$, thus (4.19) and (4.20) hold in $[0, \underline{\lambda})$. Regarding the second interval, $s > 0, \forall\lambda \in (\lambda^*, 1]$, and (4.22) is valid in $(\lambda^*, 1]$. As a result,

$$\dot{V}(s) = s\dot{s} \quad \leq \quad -\alpha_0|s|, \quad \forall\lambda \in \mathcal{D} \setminus \Omega \tag{4.25}$$

which shows that Ω will be reached in finite time. □

Remark 4.1. (time-varying T_d) so far it was assumed that the T_d, the braking torque requested by the driver, is a constant (and known) parameter. However, in practice, T_d varies with time, and it is necessary to extend the previous results to address this situation. In the case of Lemma 4.1, this extension is straightforward because the invariance of Ω_0 remains valid, as long as $T_d(t)$ stays in the range $0 \leq T_d(t) \leq \max_{\lambda\in\mathcal{D}} \Psi(\lambda)$. Similarly, the convergence conditions of Theorem 4.1 are kept valid, if $T_d(t)$ complies with the lower bound $T_d(t) \geq \max_{\lambda\in\mathcal{D}} \Psi(\lambda)$. In addition, due to the time-varying nature of $T_d(t)$, the α_0 parameter must be recalculated as $\alpha_0 = \gamma(v)\underline{T_d}\beta_0$, where $\underline{T_d} = \min_t T_d(t)$ represent the minimum torque requested by the driver during the braking manoeuvre. Finally, Theorem 4.2 is still valid for time-varying T_d and, to illustrate this point, consider that $T_d(t) \in [\underline{T_d}, \overline{T_d}] \subset (0, \overline{T_d}]$. If $\underline{T_d} \geq \max_{\lambda\in\mathcal{D}} \Psi(\lambda)$, then we have the same conditions as Theorem 4.1, thus, we only need to investigate the case where $\underline{T_d} < \max_{\lambda\in\mathcal{D}} \Psi(\lambda)$. In this later case, Λ is a set, not empty, representing all the potential equilibrium points during the braking manoeuvre and, among these, the lowest equilibrium point $\underline{\lambda}$ is selected to build Ω. To show that λ is attracted to Ω, we can apply the same methodology employed in the Theorem 4.2 Proof, but with two small modifications. Firstly, for any $\lambda \in [0, \underline{\lambda}]$, $0 \leq \Psi(\lambda) \leq \underline{T_d} \leq T_d(t)$, hence (4.19) remains valid for the case of time-varying $T_d(t)$. Secondly, the parameters α_0, used to define the upper bound in $\dot{V}$, must be recalculated as: $\alpha_0 = \gamma(v)\min\{T_d(t)\beta_0,\ T_d(t)\beta_0 + \Psi(\lambda)\} = \gamma(v)\underline{T_d}\beta_0$.

The previous theorem highlights some very interesting properties of the ideal SMC (4.12): for any braking torque $T_d \in \mathcal{T}$ requested by the driver, and any friction curve found in practice (which is formulated as any $\Psi(\lambda) \in \mathcal{J}$), we can ensure that (4.12) will drive the system state to the "safe set" Ω. The Ω is characterized as "safe", because it only contains points to the "left" of λ^* (see Figure 4.2), preventing excessive slip. Eventually, if the driver applies excessive torque, Ω reduces to a single point, λ^*, and the sliding condition is verified (Theorem 4.1).

Although the ideal SMC has some attractive theoretical properties, there are some practical issues related to the chattering that pose practical obstacles to its implementation. These problems are induced by the discontinuous control law, which can cause undesirable high-frequency oscillations in the control signal, excite non-modelled dynamics, produce noise and wear in the mechanical system, etc.

4.2.3 Continuous SMC (CSMC)

A possible solution to attenuate the chattering problem is to replace the discontinuous sgn(.) function with a continuous approximation[96]:

$$\text{sat}(w) \quad = \quad \text{sgn}(w)\min(1, |w|) \tag{4.26}$$

which generates a Continuous SMC (CSMC):

$$u = \frac{1}{2} - \left(\frac{1}{2} + \beta_0\right) \text{sat}\left(\frac{s}{\varepsilon}\right) \tag{4.27}$$

where $\varepsilon > 0$ is the width of what is known as the boundary layer (BL). Albeit the CSMC alleviates the chattering problem, it also introduces a steady state tracking error, and only ultimate boundness of the error can be achieved [96, Theorem 14.1]. To overcome this issue, in the next section, the conditional integrator approach will be applied to this problem, which will eliminate the state error without exacerbating the chattering issue.

In summary, even if the practical applicability of the CSMC is limited, the robustness properties studied in this section are valuable and enable us to find a simple connection between the driver torque requests and the friction uncertainty. This finding will lay the foundation for exploring the conditional integrator endowed with an upper bound for the model uncertainty.

4.3 Wheel Slip Control with Conditional Integrator

In order to address the steady state error introduced by the CSMC, an integral action can be incorporated into the SMC. It is well known that by introducing integral control in the SMC, asymptotic regulation in the presence of constant disturbances can be ensured. Nevertheless, the transient performance is normally degraded with integral action and special care must be taken to avoid integrator windup. In the ABS/TC application area, several researchers have investigated SMC with integral control action [156, 161, 167]. However, these previous studies do not explicitly consider the anti-windup mechanism in the SMC design, which is analytically addressed in this work within the SMC + Conditional Integrator (CI) framework [165].

The main idea behind the SMC+CI is to introduce integral action only inside the boundary layer (BL), while outside the BL the performance and robustness of the ideal SMC is preserved. Moreover, while the CSMC only ensures asymptotic stability for an arbitrarily small BL, the CI satisfies the asymptotic property for a sufficiently small BL. Hence, with the CI there is more flexibility to increase the width of the BL and potentially attenuate the chattering problem. Position control of permanent magnet motor [168], marine vessel control [169] and the aircraft pitch control [170] are some recent examples of practical problems solved by the SMC+CI approach. In this chapter, we employed this method to tackle the SC problem and improve the performance of the CSMC, described in the previous section. The SMC+CI extension builds on the original sliding controller, and can be described in two steps:

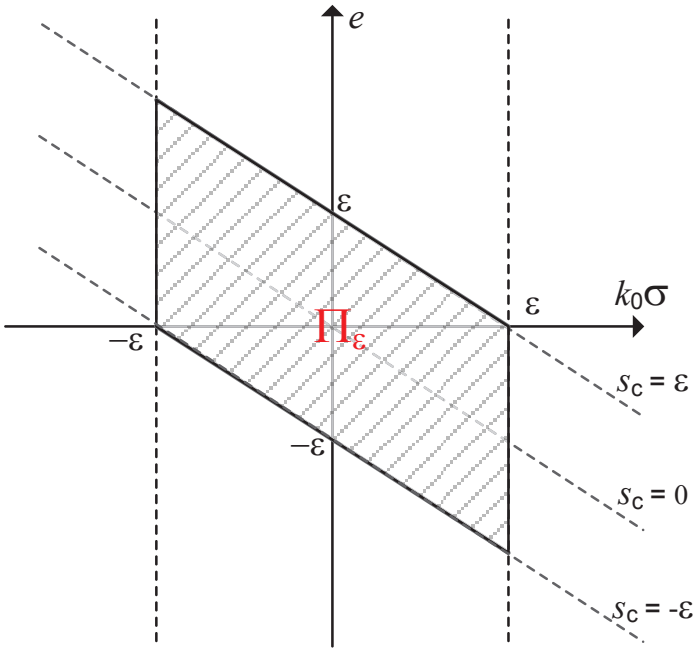

Figure 4.3: Representation of the Π_ε set, defined by (4.30), which constitutes the boundary layer for the SMC+CI.

1) the first step consists of adding a new term, the conditional integrator, to the original sliding surface:

$$s_c = e + k_0\sigma, \qquad e = \lambda - \lambda^* \tag{4.28a}$$

$$\dot{\sigma} = -k_0\sigma + \varepsilon \,\mathrm{sat}\left(\frac{s_c}{\varepsilon}\right), \quad |\sigma(0)| \leq \frac{\varepsilon}{k_0} \tag{4.28b}$$

where $s_c(e,\sigma) = 0$ is the new sliding surface, $\sigma \in \mathcal{D}_\sigma \subset \mathbb{R}$ the conditional integrator, $e \in \mathcal{D}_e = [-\lambda^*, 1-\lambda^*] \subset \mathbb{R}$ the tracking error, $k_0 > 0$ a tuning parameter and $\varepsilon > 0$ specifies the width of the boundary layer, to be defined later on.

2) the discontinuity in the original SMC control law is replaced with a continuous approximation:

$$u = \left(\frac{1}{T_d}\right)\left[\hat{\Psi}(\lambda) - T_d\beta(\lambda)\,\mathrm{sat}\left(\frac{s_c}{\varepsilon}\right)\right] \tag{4.29a}$$

$$\beta(\lambda) = \rho(\lambda) + \beta_0 \tag{4.29b}$$

In the sequel, we assume that the condition (4.5) is satisfied, for instance with the simple estimator proposed in Theorem 4.1, or by any other method. In addition, we will show that the control law (4.29) is able to ensure asymptotic regulation of λ for a sufficiently small ε. Before presenting the proof for this claim, we will derive some auxiliary results that will be helpful later on. To start with, it is convenient to analyze the domain of the function $s_c(e,\sigma) : \mathcal{D}_e \times \mathcal{D}_\sigma \mapsto \mathbb{R}$, in particular $\mathcal{D}_\sigma$. Given the bound on the initial condition $\sigma(0)$, this domain can be characterized as follows:

Lemma 4.2. *Consider the set $\mathcal{D}_\sigma = \{|\sigma| \leq \varepsilon/k_0\}$, the σ dynamics defined in (4.28b), and assume that the initial value satisfies $\sigma(0) \in \mathcal{D}_\sigma$. Under these conditions, $\mathcal{D}_\sigma$ is a positively invariant set, i.e., $\sigma(t) \in \mathcal{D}_\sigma, \forall t \geq 0$.*

Proof: the proof relies on the results presented in [165], replicated here for completeness. Making use of the Lyapunov function $V = 1/2\sigma^2$, the time derivative is given by $\dot{V} = \sigma(-k_0\sigma + \varepsilon \,\mathrm{sat}\left(\frac{s_c}{\varepsilon}\right)) \leq -k_0|\sigma|(|\sigma| - \epsilon/k_0)$, and it is clear that at the $\partial\mathcal{D}_\sigma$, i.e., at the boundary of the domain, $\dot{V} = 0$, thus the positively invariance is shown. □

With the domain of s_c specified, the next step is to investigate the properties of the $\mathrm{sat}(s_c/\varepsilon)$ function, which plays an important role in the generation of the control signal u. It can be easily seen, that inside the set:

$$\Pi_\varepsilon \;=\; \left\{ (e,\sigma) \in \mathcal{D}_e \times \mathcal{D}_\sigma : \quad |s_c(e,\sigma)| \leq \varepsilon \right\} \tag{4.30}$$

the saturation function is linear, and discontinuous outside. Since s_c is also linear and the domain is contained in $\mathbb{R}^2$, a graphical plot of Π_ε is readily available (see Figure 4.3). Similarly to the CSMC, this set can be interpreted as an equivalent boundary layer for the SMC+CI that establishes the limits where the original SMC discontinuous control law is applied.

Lemma 4.3. *For $(e,\sigma) \notin \Pi_\varepsilon$, the SMC+CI* (4.28),(4.29) *retrieves the same control law as the original SMC, defined in* (4.4).

Proof: We note that the only difference between the control law of the original SMC and the SMC+CI is the discontinuous function. Consequently, we must show that:

$$\mathrm{sat}\left(\frac{s_c}{\varepsilon}\right) = \mathrm{sgn}(e), \quad \forall (e,\sigma) \notin \Pi_\varepsilon \tag{4.31}$$

Outside the Π_ε, we have $|s_c| > \varepsilon$, thus:

$$\mathrm{sat}\left(\frac{s_c}{\varepsilon}\right) = \mathrm{sgn}(s_c) = \mathrm{sgn}(e + k_0\sigma), \quad \forall (e,\sigma) \notin \Pi_\varepsilon \tag{4.32}$$

Also note that Lemma 4.2 implies $\sigma \in \mathcal{D}_\sigma$. In summary, we are interested in studying the function $\mathrm{sgn}(e + k_0\sigma)$, over the domain:

$$\begin{aligned} \Xi \;&=\; \left\{ (e,\sigma) : \quad (e,\sigma) \notin \Pi_\varepsilon,\ \sigma \in \mathcal{D}_\sigma \right\} \\ &=\; \left\{ (e,\sigma) : \quad |e + k_0\sigma| > \varepsilon,\ k_0|\sigma| \leq \varepsilon \right\} \end{aligned} \tag{4.33}$$

which is carried out by dividing Ξ into two sub-domains: $\Xi = \Xi_+ \cup \Xi_-$, where Ξ_+ is the sub-domain with positive s_c and Ξ_- with negative s_c (we further note that $s_c = 0$ is not possible outside Π_ε, since $\varepsilon > 0$).

For the Ξ_+ sub-domain, we have $s_c = e + k_0\sigma > 0$, which produces the set:

$$\Xi_+ = \{\ (e,\sigma) : (e + k_0\sigma) > 0,\ |e + k_0\sigma| > \varepsilon,\ k_0|\sigma| \leq \varepsilon\} \tag{4.34}$$

consequently, $|e + k_0\sigma| = e + k_0\sigma$ and we can verify that:

$$e > \varepsilon - k_0\sigma > \min_{k_0|\sigma| \leq \varepsilon} (\varepsilon - k_0\sigma) = 0, \quad \forall (e,\sigma) \in \Xi_+ \tag{4.35}$$

thus $e > 0$ and $\mathrm{sgn}(e + k_0\sigma) = \mathrm{sgn}(e)$=1 for $(e,\sigma) \in \Xi_+$.

For the sub-domain Ξ_-, $(e + k_0\sigma) < 0$:

$$\Xi_- = \{\ (e,\sigma) : (e + k_0\sigma) < 0,\ |e + k_0\sigma| > \varepsilon,\ k_0|\sigma| \leq \varepsilon\} \tag{4.36}$$

This sub-domain is "symmetrical" to Ξ_+ and, following a similar reasoning used for the Ξ_+ sub-domain, we can straightforwardly conclude that $e < 0$ and $\text{sgn}(e+k_0\sigma) = \text{sgn}(e) = -1$ for $(e, \sigma) \in \Xi_-$.

As a consequence, joining these previous two cases, $\text{sgn}(e + k_0\sigma) = \text{sgn}(e), \forall (e, \sigma) \in \Xi_+ \cup \Xi_-$, hence (4.31) is satisfied and the Lemma proved. □

After showing the equivalence between the ideal SMC and the SMC+CI outside Π_ε, we move on to analyze the control law inside the BL. When the system enters in Π_ε, the conditional integrator σ becomes a simple error integrator:

$$\dot{\sigma} = -k_0\sigma + \varepsilon\frac{s_c}{\varepsilon} = e, \quad \forall (e, \sigma) \in \Pi_\varepsilon \tag{4.37}$$

and the control law is given by:

$$\begin{aligned} u &= \frac{\hat{\Psi}(\lambda)}{T_d} - (\rho(\lambda) + \beta_0)\left(\frac{e + k_0\sigma}{\varepsilon}\right) \\ &= \frac{\hat{\Psi}(\lambda)}{T_d} - \frac{(\rho(\lambda) + \beta_0)}{\varepsilon}\left(e + k_0\int e\right), \ \forall (e, \sigma) \in \Pi_\varepsilon \end{aligned}$$

If the observer $\hat{\Psi}(.)$ and the modelling error $\rho(.)$ are fixed, e.g., using the results of Theorem 4.1, then the control law inside Π_ε is composed by a feedforward term and a feedback component, which resembles the structure of a PI controller. Therefore, when the system enters the BL, the controller switches to a linear control law, with integral action, while outside it maintains the discontinuous law of the ideal SMC. In light of the above, the asymptotic stability conditions for the SMC+CI are the only missing parts in the controller design, which are established in the next Theorem.

Theorem 4.3. *Consider the control law defined by* (4.28),(4.29)*, and under the assumption of* (4.5)*.*

1. *For any* $(e(0), \sigma(0)) \in \mathcal{D}_e \times \mathcal{D}_\sigma$*, the set* Π_ε *will be reached in finite time.*

2. *Inside* Π_ε*, the equilibrium point*

$$\left(\overline{e} = 0, \ \overline{\sigma} = -\frac{\varepsilon}{k_0(\rho(\lambda^*) + \beta_0)}\Delta(\lambda^*)\right) \tag{4.38}$$
$$\Delta(\lambda) = \frac{\Psi(\lambda) - \hat{\Psi}(\lambda)}{T_d}$$

is asymptotically stable for a sufficiently small ε *(defined in the Theorem proof) and* $\Delta(\lambda)/(\rho(\lambda) + \beta_0)$ *Lipschitz on the set* $\mathcal{D}$*.*

Proof: For the first claim, we notice that in Lemma 4.2 the invariance of $\mathcal{D}_\sigma$ was shown, hence we only need to analyze the error (e) trajectory. Considering the time derivative of the Lyapunov function $V = 1/2e^2$, we have:

$$\begin{aligned} \dot{V} &= e\dot{e} = e\dot{\lambda} = -e\gamma(v)\left(\Psi(\lambda) - T_d u\right) \\ &= -e\gamma(v)\left(\Psi(\lambda) - \hat{\Psi}(\lambda) + T_d(\rho(\lambda) + \beta_0)\,\text{sat}\left(\frac{s_c}{\varepsilon}\right)\right) \end{aligned}$$

Using the result of Lemma 4.3

$$\begin{aligned}\dot{V} &= -e\gamma(v)\left(\Psi(\lambda)-\hat{\Psi}(\lambda)+T_d(\rho(\lambda)+\beta_0)\operatorname{sgn}(e)\right), \\ &\qquad\qquad \forall(e,\sigma)\notin\Pi_\varepsilon \\ &\leq -\gamma(v)T_d|e|\left(\rho(\lambda)+\beta_0-\frac{|\Psi(\lambda)-\hat{\Psi}(\lambda)|}{T_d}\right) \\ &\leq -\gamma(v)T_d\beta_0|e|, \quad \forall(e,\sigma)\notin\Pi_\varepsilon \end{aligned} \tag{4.39}$$

Since $\gamma(v), T_d, \beta_0$ are positive, the previous inequality ensures that Π_ε will be reached in finite time.

For the second part, we resort to the closed loop dynamics inside Π_ε:

$$\begin{cases}\dot{\sigma}=e \\ \dot{e}=-\gamma(v)T_d\left(\beta(e+\lambda^*)\frac{e+k_0\sigma}{\varepsilon}+\Delta(e+\lambda^*)\right)\end{cases}$$

$$\Delta(\lambda)=\frac{\Psi(\lambda)-\hat{\Psi}(\lambda)}{T_d}, \quad \beta(\lambda)=\rho(\lambda)+\beta_0$$

and with this formulation in mind, it is straightforward to deduce the equilibrium point defined in (4.38). To show the asymptotic stability we will make a change of variable:

$$\tilde{\sigma}=\sigma-\bar{\sigma}, \qquad \tilde{s}_c=s_c-\bar{s}_c \tag{4.40}$$

where $\bar{s}_c=\bar{e}+k_0\bar{\sigma}=k_0\bar{\sigma}$, and employ the Lyapunov function:

$$V=\frac{1}{2}\tilde{s}_c+\frac{1}{2}\tilde{\sigma} \tag{4.41}$$

Calculating the time derivative of V:

$$\begin{aligned}\dot{V} &= \tilde{s}_c\dot{\tilde{s}}_c+\tilde{\sigma}\dot{\tilde{\sigma}}=\tilde{s}_c\dot{s}_c+\tilde{\sigma}\dot{\sigma}=\tilde{s}_c(\dot{e}+k_0\dot{\sigma})+\tilde{\sigma}e \\ &= -\tilde{s}_c\gamma(v)T_d\left(\beta(e+\lambda^*)\frac{\tilde{s}_c+\bar{s}_c}{\varepsilon}+\Delta(e+\lambda^*)\right) \\ &\quad +\tilde{s}_ck_0e+\tilde{\sigma}(\tilde{s}_c-k_0\tilde{\sigma}) \end{aligned} \tag{4.42}$$

After some algebraic manipulation we get

$$\begin{aligned}\dot{V} &= -\left(\gamma(v)T_d\frac{\beta(e+\lambda^*)}{\varepsilon}-k_0\right)\tilde{s}_c^2 \\ &\quad -\gamma(v)T_d\beta(e+\lambda^*)\tilde{s}_c\left[\frac{\Delta(e+\lambda^*)}{\beta(e+\lambda^*)}-\frac{\Delta(\lambda^*)}{\beta(\lambda^*)}\right] \\ &\quad -\left(k_0^2-1\right)\tilde{s}_c\tilde{\sigma}-k_0\tilde{\sigma}^2 \\ &\leq -\left(\frac{\chi(e+\lambda^*)}{\varepsilon}-k_0\right)\tilde{s}_c^2-\left(k_0^2-1\right)\tilde{s}_c\tilde{\sigma}-k_0\tilde{\sigma}^2 \\ &\quad +\chi(e+\lambda^*)|\tilde{s}_c|\left|\frac{\Delta(e+\lambda^*)}{\beta(e+\lambda^*)}-\frac{\Delta(\lambda^*)}{\beta(\lambda^*)}\right| \end{aligned} \tag{4.43}$$

where $\chi(\lambda) = \gamma(v)T_d\beta(\lambda)$. Applying the Lipschitz property:

$$\begin{aligned}\left|\frac{\Delta(e+\lambda^*)}{\beta(e+\lambda^*)} - \frac{\Delta(\lambda^*)}{\beta(\lambda^*)}\right| &\leq L|e| = L|\tilde{s}_c - k_0\tilde{\sigma}| \\ &\leq L|\tilde{s}_c| + Lk_0|\tilde{\sigma}| \end{aligned} \tag{4.44}$$

where L is the Lipschitz constant, it then follows:

$$\begin{aligned}\dot{V} &\leq -\left(\frac{\chi(e+\lambda^*)}{\varepsilon} - k_0\right)\tilde{s}_c^2 - \left(k_0^2 - 1\right)\tilde{s}_c\tilde{\sigma} - k_0\tilde{\sigma}^2 \\ &\quad + \chi(e+\lambda^*)|\tilde{s}_c|(L|\tilde{s}_c| + L\,k_0|\tilde{\sigma}|) \\ &\leq -\left(\frac{\chi(e+\lambda^*)}{\varepsilon} - k_0 - \chi(e+\lambda^*)L\right)\tilde{s}_c^2 \\ &\quad + \left(k_0^2 + 1 + L\,k_0\,\chi(e+\lambda^*)\right)|\tilde{s}_c||\tilde{\sigma}| - k_0\tilde{\sigma}^2\end{aligned} \tag{4.45}$$

Rearranging the terms in the quadratic form, and noticing that $\chi(e+\lambda^*) > 0$, we can then write

$$\dot{V} \leq -\begin{bmatrix}|\tilde{\sigma}| & |\tilde{s}_c|\end{bmatrix}\underbrace{\begin{bmatrix} k_0 & -\frac{1+k_0^2+L\,k_0\,\chi(.)}{2} \\ -\frac{1+k_0^2+L\,k_0\,\chi(.)}{2} & \chi(.)\left(\frac{1}{\varepsilon} - L\right) - k_0\end{bmatrix}}_{\mathbf{P}}\begin{bmatrix}|\tilde{\sigma}| \\ |\tilde{s}_c|\end{bmatrix}$$

which is a negative definite if all the leading principal minors of $\mathbf{P}$ are positive:

1. $k_0 > 0$
2. $k_0\left(\chi(.)\left(\frac{1}{\varepsilon} - L\right) - k_0\right) - \left(\frac{1+k_0^2+L\,k_0\,\chi(.)}{2}\right)^2 > 0$

the first condition is naturally ensured by selecting a positive k_0, while the second is verified choosing ε smaller than:

$$\varepsilon^* = \min_{e\in\mathcal{D}_e} \frac{1}{L + \frac{k_0}{\chi(e+\lambda^*)} + \frac{1}{k_0\,\chi(e+\lambda^*)}\left(\frac{1+k_0^2+L\,k_0\,\chi(e+\lambda^*)}{2}\right)^2}$$

As a result, $\forall\varepsilon \in (0, \varepsilon^*)$ the system state will asymptotically converge to the point $(\tilde{\sigma} = 0, \tilde{s}_c = 0)$ (note that this point is equivalent to (4.38)), which concludes the second part of the Theorem proof. □.

At this point it is important to mention that the previous Theorem assumed that the $\Delta(.)$ function has the Lipschitz property, which was not previously discussed. Taking in account the QCM and the functions that constitutes $\Delta(.)$, it is reasonable to assume that the Lipschitz property holds, as long as these functions are sufficiently smooth. Furthermore, from the theoretical point of view, Theorem 4.3 provides the upper bound for the parameter ε that ensures the asymptotical stability of the closed loop system. However, in practice, finding this value (ε^*) is a challenging task, since there are some parameters in the problem, e.g., the Lipschitz constant L, that are not known with precision. Due to the fact that asymptotic stability is obtained when ε goes to zero, ε can be viewed as a tuning parameter in the controller, and should be gradually reduced until the transient performance is satisfactory, as suggested in [165]. And lastly, making use of the results in

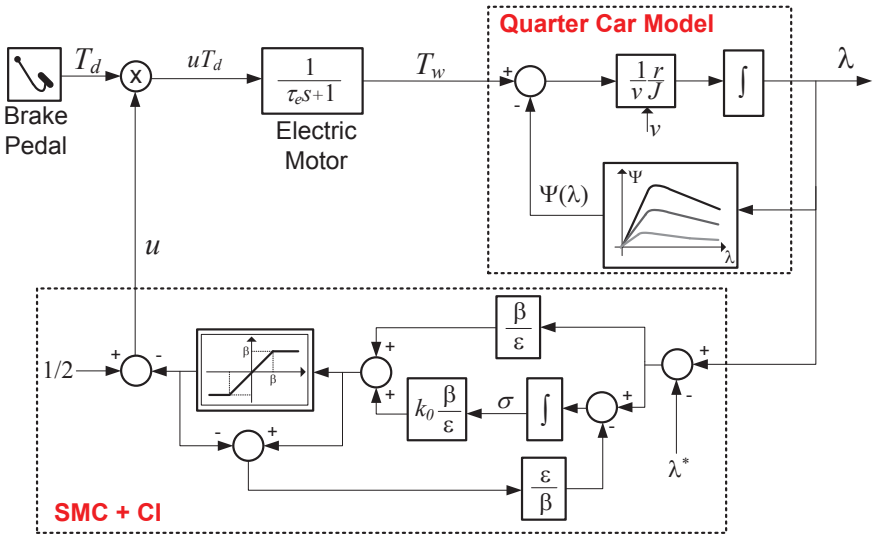

Figure 4.4: Block diagram of the wheel slip control based on the SMC+CI method.

Theorem 4.1, the final control law is given by (4.28) and:

$$u = \frac{1}{2} - \beta \,\mathrm{sat}\left(\frac{e + k_0\sigma}{\varepsilon}\right) \tag{4.46}$$

with $\beta = \frac{1}{2} + \beta_0$. This controller has 3 tuning parameters: ε, k_0 and β_0. The tuning rule for the first parameter was discussed above and the k_0 defines the convergence speed of the algorithm. Regarding the last parameter, β_0, it can be interpreted as a "slack" variable that gives some extra margin to the upper bound for the modelling error (4.5).

It worth pointing out that, although the controller as been designed with non-linear techniques, the resulting control law can be implemented as a simple PI with "anti-windup" [171] (see Figure 4.4).

Remark 4.2. The integration of the sliding mode slip controller within the Hybrid ABS structure (see Chapter 3) is perfectly possible, and was investigated by the author in [172]. However, as the main focus of this chapter is the robust wheel slip controller, the simulations and experimental validation present in the next sections employed a simplified braking setting, where a single actuator (the electric motor) generates the braking torque. The interested reader is referred to [172] for the validation of the sliding mode control with multiple actuators (IWM and friction brakes).

4.3.1 The Acceleration Case

The controller design presented in the previous sections focused only on the braking manoeuvres. Notwithstanding, some of previous results can be extended to the accelerating case, and, to assist in this observation, consider the quarter car model, valid for the acceleration manoeuvres (obtained after applying a process similar to the one described in

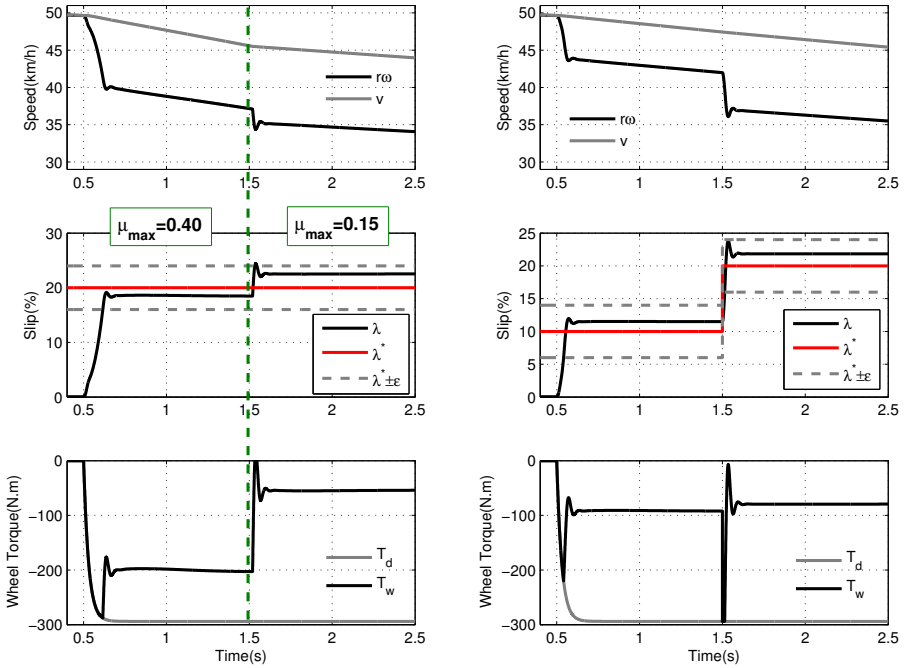

(a) μ step (b) λ^* step

Figure 4.5: Simulation results of the SC-based on CSMC ($\varepsilon = 0.04, \beta_0 = 0$) during deceleration manoeuvres (unless otherwise stated, $\mu_{max} = 0.2$ is the peak friction coefficient).

Section 3.3.1):

$$\dot{\lambda}_a = -\tilde{\gamma}(v, \lambda_a)\left(\tilde{\Psi}(\lambda_a) - T_a u\right) \tag{4.47a}$$

$$\tilde{\Psi}(\lambda_a) = \left(\frac{J}{Mr^2}\frac{1}{1-\lambda_a} + 1\right) rF_z\mu(\lambda_a) \tag{4.47b}$$

$$\tilde{\gamma}(v, \lambda_a) = \frac{1}{v}\frac{r}{J}(1-\lambda_a)^2 \qquad \lambda_a = \frac{\omega r - v}{\omega r} \tag{4.47c}$$

where T_a is the driving torque requested by the driver (bounded by $\overline{T_a}$) and λ_a the tyre slip (assuming $r\omega \geq v$). Comparing the previous formulation with (4.1), it is clear that both models share the same structure, with the $\gamma(.)$ and $\Psi(.)$ functions being replaced by $\tilde{\gamma}(.)$ and $\tilde{\Psi}(.)$. Albeit, $\tilde{\gamma}(.)$ depends also on λ_a, it remains always positive (as long as the vehicle speed is also positive), thus it has a similar role as the original $\gamma(.)$. The main difference between the formulations lies in the $\tilde{\Psi}(\lambda_a)$ function. While the original $\Psi(\lambda)$ can be approximated by $rF_z\mu(\lambda)$ for every $\lambda \in \mathcal{D}$, and it is bounded, the $\tilde{\Psi}(\lambda_a)$ function does not hold this property over $\mathcal{D}$, due to the $1/(1-\lambda_a)$ term that goes to infinity when λ_a gets closer to 1. As a consequence, for the accelerating case, the control law discussed in this Chapter only provides asymptotic stability in the subset $\mathcal{D}_a \subset \mathcal{D}$, with $\mathcal{D}_a$ being the slip range where $\tilde{\Psi}(\lambda_a)$ is bounded by $\overline{T_a}$.

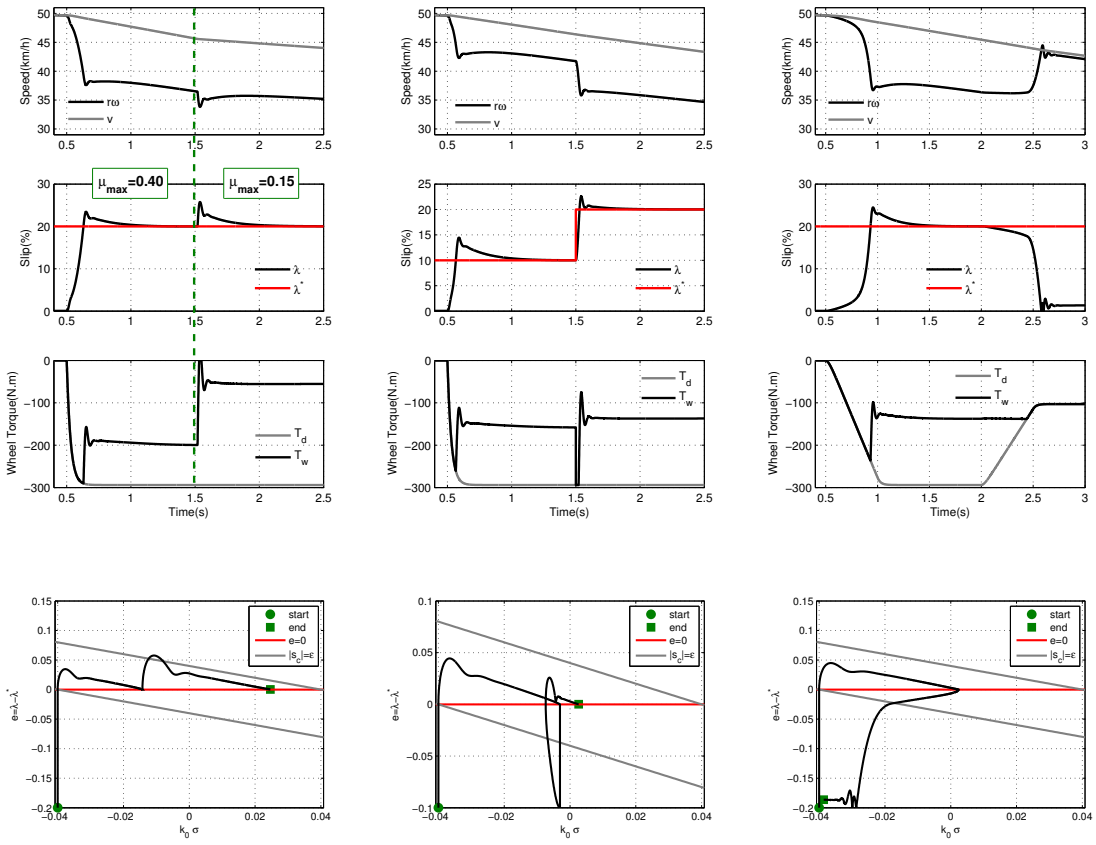

(a) μ step (b) λ^* step (c) T_d ramp

Figure 4.6: Simulation results of the SC based on SMC+CI ($k_0 = 5, \varepsilon = 0.04, \beta_0 = 0$) during deceleration manoeuvres (unless otherwise stated, $\mu_{max} = 0.3$ is the peak friction coefficient).

4.4 CarSim Simulations

The algorithms developed in this chapter were evaluated in a co-simulation between a vehicle dynamics simulator, the CarSim [146], and the Matlab/Simulink. The former tool provides a more realistic vehicle model than the simplified QCM used for designing the controller, while the latter allows the implementation of the control strategies. The simulations presented in this section were obtained using an A-class hatchback car (included in the CarSim library) modified as follows: *i*) the sprung mass properties (weight distribution, mass, etc.) were redefined to match the values of the experimental prototype discussed in Appendix A; *ii*) the original powertrain, based on the internal combustion engine, was replaced with two electric motors connected to the front wheels, having a torque response with a dominant time constant of 10ms; *iii*) the vehicle tyres, 175/70 R13, were modelled with the MTF 5.2 [147], employing the same dataset as the "Pacejka 5.2 example" available in the CarSim library. Based on this setting, several braking manoeuvres, performed in straight line and under different grip conditions, were carried out to evaluate the slip regulation performance of the CSMC and the SMC+CI.

Figure 4.5 shows the results of the CSMC for μ and λ^* steps disturbances and, in global terms, it can be seen that this controller offers a reasonable response, without chattering. However, taking a closer look at the steady state zone, it is clear that the boundary layer

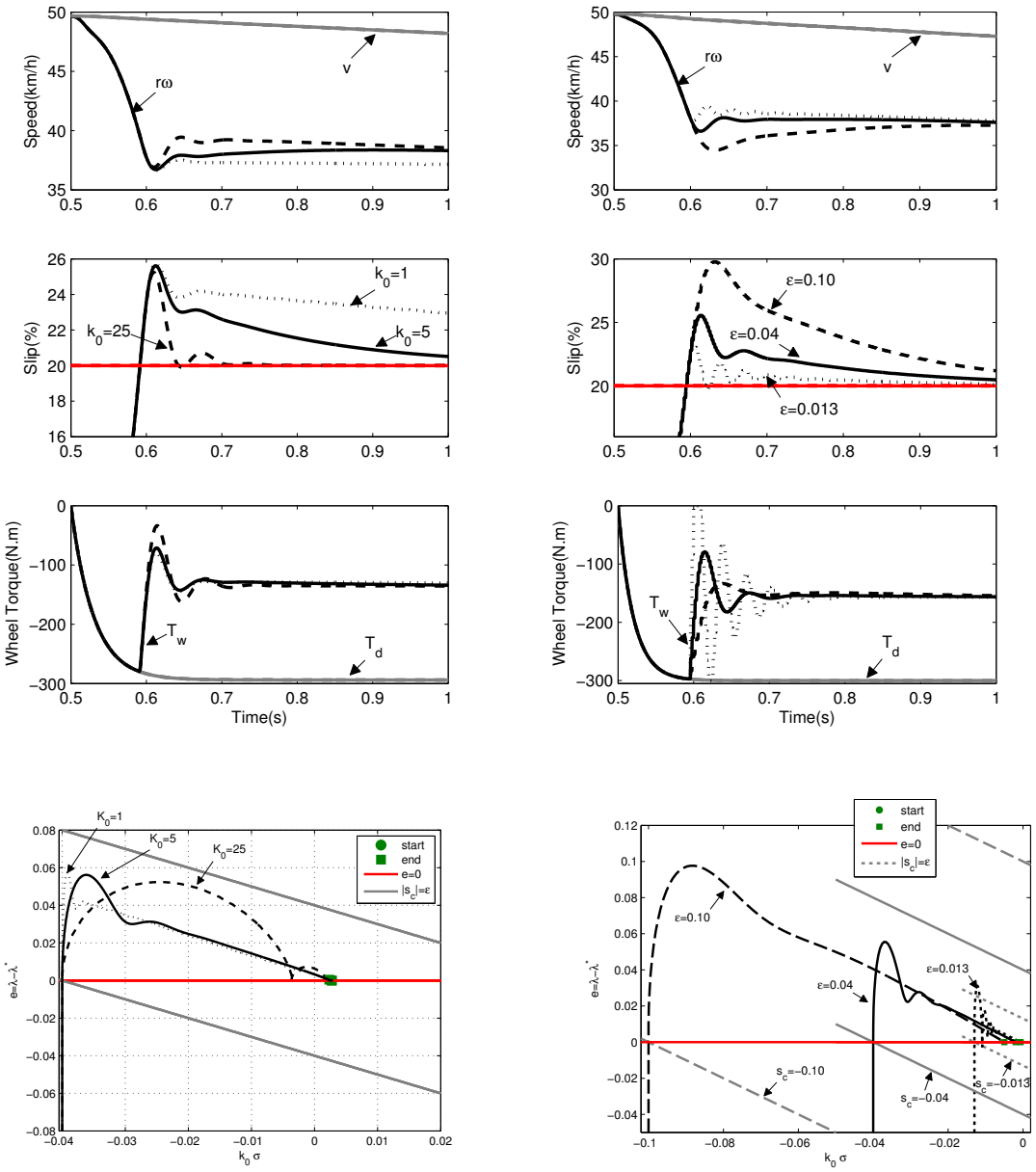

(a) k_0 sensitivity (b) ε sensitivity

Figure 4.7: Sensitivity of the SMC+CI to the parameters k_0 and ε (unless otherwise stated, $\mu_{max} = 0.3$ is the peak friction coefficient, $\beta_0 = 0.001$, $k_0 = 5$ and $\varepsilon = 0.04$).

introduces an error, which varies with adhesion conditions, among other factors. On the other hand, when the SMC+CI is employed (see Figure 4.6(a,b)), the conditional integral action retrieves a transient performance close to the CSMC, but with a significant improvement in the steady-state region, eliminating the tracking error. Moreover, analysing the (σ, e) trajectory, it can be noticed that the disturbances introduced by the μ and λ^* steps force the trajectory to leave the linear zone. Nonetheless, the controller manages to recover from this disturbance and keep the asymptotic attractiveness to the manifold $\{e = 0\}$. Regarding the μ step, it is interesting to note that the integral component in

(a) Braking (b) Accelerating

Figure 4.8: Experimental apparatus used to validate the wheel slip controller in a low μ surface.

the controller is increased in order to respond to the new friction condition, which further shows the controller adaptability to disturbances.

The interaction between the controller and the torque requested by the driver was investigated in Figure 4.6(c). These results highlight a natural cooperation between the driver and the controller: when the tyre loses adhesion the SC is quickly activated to constrain the wheel torque; on the other hand, the driver reassumes the full control when the braking pedal (or T_d) is decreased to the torque levels being generated by the SC. The (σ, e) trajectory plot shows that the SC activation (deactivation) coincides with the entering (leaving) of the controller linear zone. Finally, the sensitivity of the SMC+CI to the k_0 parameter was evaluated in Figure 4.7(a), where it can be observed a direct relation between the settling time of the slip response and the k_0 value. On the other hand, the overshoot and oscillation of the tyre slip response is mainly affected by the selection of the ε parameter [see Figure 4.7(b)].

4.5 Experimental Results

In this last section, the proposed wheel slip controllers are experimentally validated in the multi-motor electric vehicle prototype, with presented in Appendix A. The SMC+CI and CSMC were implemented in the FPGA based digital control system, and discretized with a sampling time of 2ms, which is quick enough to handle the tyre slip dynamics. The vehicle speed, needed for the λ calculation, was directly measured using the vehicle non-driven wheels. The maximum wheel torque that the driver can request was limited to $|\overline{T_d}| = 80$N.m, and set equal for both accelerating and braking manoeuvres, while the friction brakes were disabled during the experiments.

In order to assess the controller performance in challenging adhesion conditions, a slippery surface was artificially created using an experimental apparatus, depicted in Figure 4.8, composed of several wet plates and having a maximum μ of approximately 0.15. With this setting, several accelerating and braking manoeuvres were experimentally conducted with the following pattern: the first manoeuvre was performed without any control, i.e., manual driving, in order to assess how slippery the surface was; subsequently the CSMC, and then the SMC+CI, was enabled to investigate the SC effectiveness. During the preliminary experiments it was observed that, in order to avoid the chattering issue,

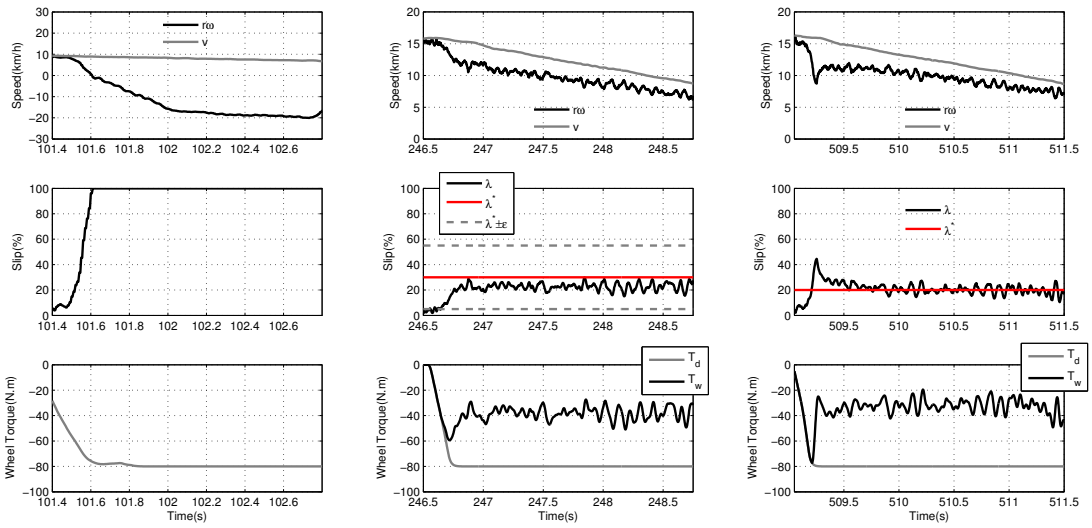

(a) No Control (b) CSMC ($\lambda^* = 0.3, \varepsilon = 0.25$) (c) SMC+CI($\lambda^* = 0.2, \varepsilon = 0.25, k_0 = 5$)

Figure 4.9: Experimental results of the SC during braking manoeuvres on a slippery surface. The left figure illustrates the high tyre slips that are reached with manual driving; in the middle figure, the CSMC is activated, which contributes to limiting the wheel torque and attaining a safer slip, although a significant steady state error is observed; with the SMC+CI (right) the steady state error is eliminated.

.

the CSMC boundary layer (BL) must have a thickness greater than 0.25. The reason for such a conservative value is related to the noise levels in the slip measurement and also to some non-modelled dynamics in the powertrain, in particular the transmission elasticity, which were neglected in this chapter (this issue is planned to be addressed in future works). For the same reason, the ε parameter in the SMC+CI was defined with the same value of 0.25; and fixing $k_0 = 5$ provided acceptable transient results.

Figure 4.9 shows the first batch of deceleration tests, carried out over the slippery surface. With the controller disabled, it can be observed that the regenerative torque applied by driver easily creates excessive tyre slip. With closer analysis of the evolution of the wheel rotational speed (ω), it is interesting to note that the wheel not only blocks, i.e., reaches zero speed, but starts to spin in the opposite direction of the vehicle movement, producing even higher slips (with the traditional frictional brakes the wheel would be kept at zero speed). When the CSMC is active (Figure 4.9(b)), the slip is constrained to a safer value (around 0.2) and it is clear that the driver torque reference is being effectively limited by the CSMC. Nevertheless, it should be pointed out that, albeit the CSMC is a sufficient mean to avoid excessive slip, the regulation performance is not satisfactory and a significant steady-state error is introduced, which is in accordance with theoretical expectations for this controller. For that reason, the slip reference was increased to 0.3 in order to obtain the desired slip value of 0.2. On the contrary, when the SMC+CI is employed (Figure 4.9(c)), the steady state error is reduced to almost zero, thanks to the conditional integral action, with a reasonable transient behaviour. The SMC+CI inner details, i.e., the error and the conditional integrator σ time evolution, are present in

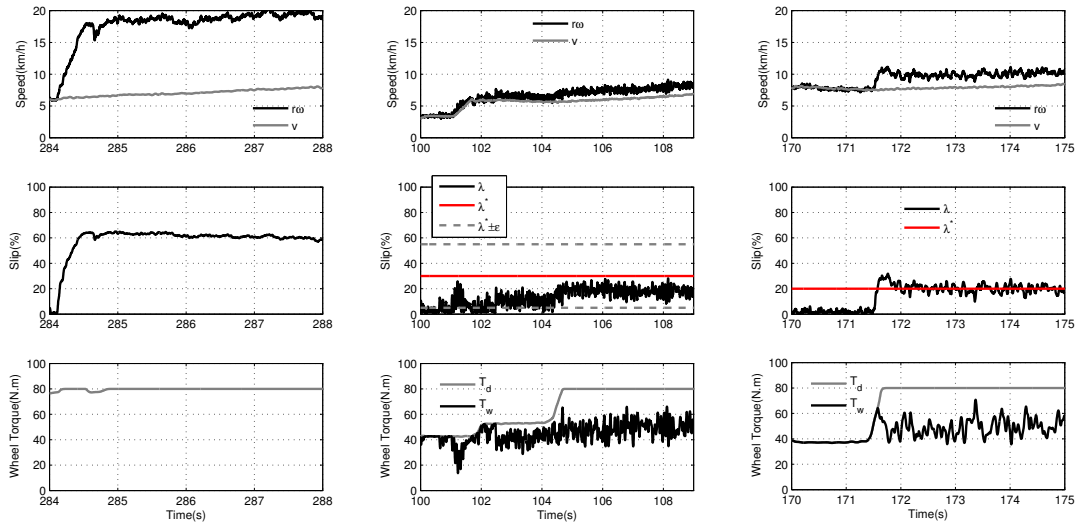

(a) No Control (b) CSMC($\lambda^* = 0.3, \varepsilon = 0.25$) (c) SMC+CI($\lambda^* = 0.2, \varepsilon = 0.25, k_0 = 5$)

Figure 4.10: Experimental results of the SC during accelerating manoeuvres. These results are "dual" of braking operation presented in Figure 4.9: with no control (left fig.) high tyre slips are reached; enabling the CSMC (middle fig.) reduces the slip, but has a steady state error, which is eliminated with the SMC+CI (right fig.)

.

Figure 4.11(a): initially the system state starts outside the BL, but due to the excessive wheel torque, is quickly attracted to the BL interior. Within the BL, the controller gradually increases the integral component until it reaches the manifold $\{e = 0\}$, which is in accordance with the asymptotical properties established in Theorem 4.3. In steady state operations, it was observed that the slip follows the reference with a tolerance of ± 0.04. Although this value may look excessive, in practice it is very difficult to achieve lower errors (due to the unavoidable measuring noise, non-modelled dynamics, and non-uniformities in the adhesion levels, among other factors), and these results are in line with the steady state performances previously reported in other experimental studies [15, 131]. Moreover, we would also like to stress the fact that, due to the reduced grip levels of the surface where the test was conducted (with $\mu_{max} < 0.15$), the maximum deceleration that we can impose to the vehicle is significantly limited.

In the second batch of experiments (Figure 4.10) the vehicle performs acceleration manoeuvres, achieving similar results to the braking case: (i) without control, high (and dangerous) tyre slips are reached; (ii) when the CSMC is active, the slip is constrained to a safe value, but presents a steady state error, which is eliminated with the SMC+CI activation. These results demonstrate a very satisfactory performance of the SMC+CI, with good slip regulation in both accelerating and braking operations, showing an (expected) superiority over the CSMC.

To further investigate the way the SMC+CI controller interacts with the driving torque requests (T_d), an additional experiment was conducted with the driver applying small increments in throttle signal (or, equivalently, in T_d). The obtained results (see Figure 4.12(a)) can be divided into three sections: 1) initially the driver is applying $45 - 50$

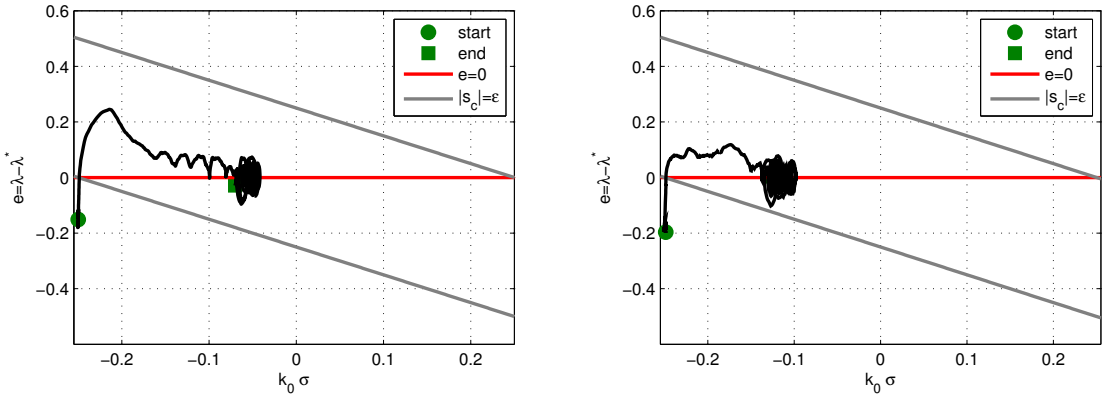

(a) Braking (b) Accelerating

Figure 4.11: Experimental results of (e, σ) trajectory for the SMC+CI, obtained during the braking and accelerating manoeuvres depicted in Figures 4.9 and 4.10.

N.m and the tyre is on the verge of losing grip; in this case the SC intervention is minimal; 2) at 402s, the driver increases the torque demand to 60 N.m which is now enough for the tyre to lose grip; the SC intervention starts to be more pronounced and, analysing the (e, σ) trajectory, it can be seen that the torque increase causes the system to enter the BL, although being close to the BL limit; and 3) finally, the full throttle is applied at 404s, which is equivalent to 80 N.m of torque demand; it can be noticed that the slip regulation is unaffected by this disturbance, and the controller responds by increasing the integral component, keeping the system close to the $\{e = 0\}$ manifold. Consequently, this experiment highlights another interesting property of the proposed SC system: our controller exhibits an elegant transition between the "manual driving" and the "SC operation mode", and is naturally prepared to gracefully switch between both modes. This natural cooperation between the "automatic/manual" drive contrasts with other integral-based controllers [127, 131], which, when the controller is activated, requires some special care with the integral component, e.g., integral resets with bumpless transfer.

As a final test, Figure 4.12(b) shows the controller response to a step change in the slip setpoint λ^*. Analysing the trajectory plot, it can be observed that the reference step from 0.3 to 0.15 makes the tracking error jump instantaneously to an error close to 0.15, which introduces a disturbance that drives the system to the limit of the BL. Nevertheless, the controller handles this disturbance satisfactory and, once again, brings the error to the manifold $\{e = 0\}$.

4.6 Conclusion

In this chapter, a sliding mode approach, based on conditional integrator, was proposed to control the wheel slip in electric vehicles. The main features of the proposed algorithm are a chattering-free operation, asymptotic stability, simple implementation and tuning. The asymptotic stability property, as well as the robustness to uncertainties and disturbances that affect the system model, were demonstrated through the Lyapunov method. Besides attenuating the chattering effect, the conditional integrator technique employed in the controller is simple to implement and also provides built-in anti-windup features. The wheel slip controller was further enhanced by exploring an intuitive relation between the model

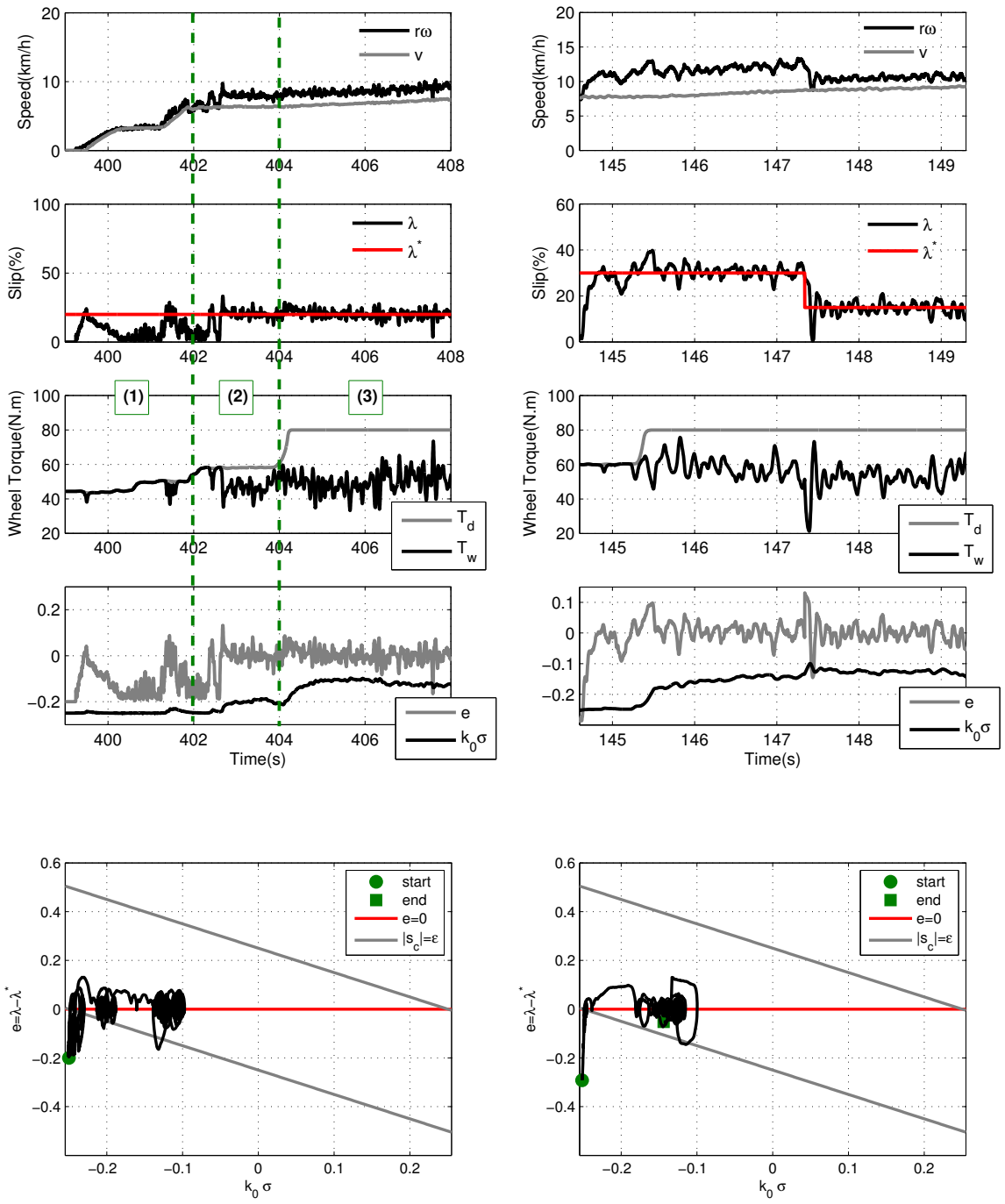

(a) T_d disturbances

(b) λ^* step from 0.3 to 0.15

Figure 4.12: Experimental results of the SMC+CI, when subject to disturbances: *a*) variations in the driver torque requests (T_d), and *b*) jumps in the slip setpoint.

uncertainty and the torque requested by the driver. Experimental results obtained with a multi-motor EV prototype showed good slip regulation and robustness to disturbances, in both accelerating and braking manoeuvres carried out over a slippery surface.

Chapter 5

Optimal Linear Parameterization for Friction Peak Estimation

Abstract: *Spurred by the problem of identifying, in real-time, the adhesion levels between the tyre and the road, a practical, linear parameterization (LP) model is proposed to represent the tyre friction. Toward that aim, results from the theory of function approximation, together with optimization techniques, are explored to approximate the nonlinear Burckhardt model with a new LP representation. It is shown that, compared with other approximations described in the literature, the proposed LP model is more efficient, i.e., requires a smaller number of parameters, and provides better approximation capabilities. Next, a modified version of the recursive least squares, subject to a set of equality constraints on parameters, is employed to identify the LP in real-time. The inclusion of these constraints, arising from the parametric relationships present when the tyre is in free-rolling mode, reduces the variance of the parametric estimation and improves the convergence of the identification algorithm, particularly in situations with low tyre slips. Simulation results obtained with the full-vehicle CarSim model under different road adhesion conditions demonstrate the effectiveness of the proposed LP and the robustness of the friction peak estimation method. Furthermore, experimental tests, performed with an electric vehicle under low-grip roads, provide further validation of the accuracy and potential of the estimation technique.*

5.1 Introduction

In automotive applications, the adhesion conditions present in the tyre-road interface have a strong influence in the tyre's ability to generate longitudinal and lateral forces and, under reduced grip conditions, represent a potential menace to the vehicle safety. With the recent proliferation of active safety systems (such as ABS, TC, and ESP) [40], the estimation of adhesion levels, characterized by the friction coefficient, has attracted growing interest in the research community since knowledge of this variable contributes significantly toward increasing the effectiveness of these safety systems. Additionally, intelligent vehicles, as is the case with autonomous vehicles, currently at an early stage of development, can also benefit from the friction estimation, adapting the control strategies to the maximum grip

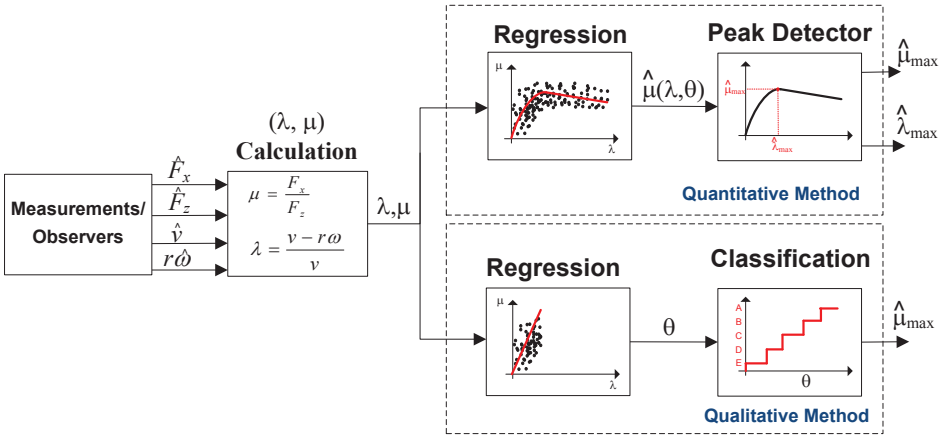

Figure 5.1: Estimation methods for detecting the longitudinal peak friction.

levels available on the road (see Chapter 7). Unlike other easily measurable variables, such as the vehicle acceleration, yaw rate, and wheel speeds, there is currently no economically viable sensor that can be installed in the vehicle to measure the friction coefficient. These difficulties have encouraged the development of virtual sensors to estimate this variable using easily measurable signals.

There are several approaches to tackling the friction estimation problem. In this chapter, we focus on the so-called slip-based techniques, i.e., the use of tyre force models based on the wheel slip to infer the adhesion levels [54], and constrain our study to the friction estimators active during longitudinal vehicle manoeuvres. These methods can be divided into two categories: qualitative and quantitative (see Figure 5.1). In both cases, the main objective is to obtain an estimation of the peak friction coefficient; however, the outputs of the two mentioned methods are very different. In the first case, qualitative, the output of the estimator is based on a grading system, providing an indicator of adhesion quality, for instance, qualifying the grip levels on a scale from 'A' (high grip) to 'E' (very slippery); in the second case, quantitative, a numeric output is generated to quantify the tyre-road adhesion in greater detail.

Examples of the qualitative methods can be found in references [54, 173, 174, 175, 176, 177]. The main driving force behind these approaches is the problem of persistence of excitation: in order to extract the peak friction, we need to apply high levels of tyre slip, which is not desirable from the safety point of view. To avoid this problem, the qualitative methods identify the tyre longitudinal stiffness, i.e., the friction slope for low slip values, and then infer the grip levels through a classification process that correlates the slope value with the peak friction (see Figure 5.1). Although these approaches solve the problem of persistence of excitation, they also introduce a new issue: the classification stage. This classification is very problematic to obtain in practice and, as pointed out by [173, 178] and [177], varies with the type of tyre, and the tyre wear, pressure, and temperature, among many other factors. Therefore, a significant experimental effort is required to tune the classification process, which makes these qualitative approaches very difficult to apply in practice.

On the other hand, the quantitative methods [133, 136, 179, 180, 181] extract the peak friction using only online curve-fitting techniques. Although the estimation is obtained at the expense of applying high tyre slips, the estimation process is more simple

and robust and also offers the possibility to identify the optimal slip reference λ_{max} associated with the maximum friction point. This last feature is very useful in generating the reference signal used in some antilock braking and traction control systems that rely on wheel slip control [15, 136]. Furthermore, since the most common tyre models, such as the magic tyre formula [147] or the Burckhardt representation [133], are nonlinear, the online identification of the model parameters tends to be very difficult. As a result, most of the quantitative methods use linear parameterization (LP), i.e., nonlinear models whose unknown parameters can be identified by linear techniques. Polynomials [180], rational functions [133, 182], exponentials [136], logistic sigmoids [183] and logarithmic functions [181, 184] are the most common LPs found in the literature.

In this chapter, we offer a contribution to the quantitative methods by proposing a more rational approach to deriving the LP. Unlike the aforementioned parameterizations, which are built using heuristics considerations, we employed optimal function approximation techniques to find an equivalent, but linear identifiable, model to the nonlinear Burckhardt representation. The resulting LP yields a more accurate approximation and, in some cases, requires a smaller number of parameters, which gives some practical advantages for online friction identification. A second contribution to the quantitative framework is related to the application of a new and more robust identification technique to the peak friction estimation problem. Due to its numeric efficiency and simplicity, the unconstrained recursive least squares (RLS) has become the most common method of estimating the friction parameters in real-time [133, 136], but as we will show in Section 5.4, under some parametric configurations, it may also introduce significant fitting error in the low-slip range and compromise the friction peak detection. To overcome this issue, we modify the RLS to comply with a set of (equality) constraints on the parameters, arising from the parametric relationships present when the tyre is in free-rolling mode. The inclusion of these constraints, which can be seen as a form of prior information on the system model, leads to a constrained RLS (CRLS) formulation and provides parameter estimates with less variance than the unconstrained version. Albeit the CRLS has been previously employed in other research fields (e.g., biomedical applications [185] and signal processing[186]), to the best of the author's knowledge, no previous study has applied this technique to the problem of estimating the friction peak. Several simulations, performed with CarSim under different road adhesion conditions, demonstrate the higher accuracy and robustness of the CRLS against the RLS, particularly for the λ_{max} estimation. Finally, the proposed optimal LP and CRLS were also experimentally tested with an electric vehicle.

5.2 Longitudinal Vehicle/Tyre Model

In this section, a brief introduction to the models related to the friction estimation methodology is provided. Since the longitudinal forces and slip are considered, the quarter car model, widely used in the literature on this field [133, 136, 152], is a sufficient mean for our study. For convenience, this quarter car model, already introduced in section 3.3.1, is restated here as:

$$J\dot{\omega} = rF_x - T_b \tag{5.1a}$$

$$M\dot{v} = -F_x \tag{5.1b}$$

where ω represents the wheel angular speed, v the longitudinal vehicle speed, T_b the braking torque applied to the wheel, F_x the friction force between tyre and the road, J

the wheel and transmission inertia, M the equivalent mass coupled to the wheel, and r the wheel radius. For simplicity, in this work we only consider braking manoeuvres, hence $v \geq r\omega$, but the obtained results can be effortlessly modified for the acceleration case.

Modelling the longitudinal friction force F_x is the main difficulty in (5.1). Generally, the friction force is proportional to the normal force that the wheel supports (F_z) and depends on a nonlinear function $\mu(.)$, known as the friction coefficient, which varies with the longitudinal tyre slip (λ), road adhesion conditions, and tyre pressure, temperature, and wear, among other factors, and can be grouped into a parameter vector $\boldsymbol{\beta} \in \mathbb{R}^d$:

$$F_x = F_z \mu(\lambda, \boldsymbol{\beta}) \tag{5.2}$$

$$\lambda = \frac{v - \omega r}{v} \tag{5.3}$$

The most common approaches to representing the friction coefficient $\mu(.)$ are based on two types of models: (i) static and (ii) dynamic. The static models, such as the Burckhardt [133] model:

$$\mu(\lambda, \boldsymbol{\beta}) = \beta_1(1 - e^{-\beta_2 \lambda}) - \beta_3 \lambda \tag{5.4}$$

and the magic tyre formula (MTF) [147]:

$$\mu(\lambda, \boldsymbol{\beta}) = \beta_1 \sin\left(\beta_2 \operatorname{atan}((1 - \beta_4)\beta_3 \lambda + \beta_4 \operatorname{atan}(\beta_3 \lambda))\right) \tag{5.5}$$

where the vector $\boldsymbol{\beta} = [\beta_1 \quad \beta_2 \quad ... \quad \beta_d]^T$ represents the model parameters, were developed by applying curve-fitting techniques to the experimental tyre data. The great advantage of the static models is their simplicity; however, they are limited to steady-state conditions, and the model parameters lack physical meaning. More recently, dynamic models, such as the LuGre [152], have been applied to represent the tyre-road friction, presenting promising features to capture the friction transient behaviour. A complete review of friction models is beyond the scope of this work, but a detailed discussion about this topic can be found in [152, 187] (and references therein).

It is worth stressing the fact that the present work is only concerned with finding more effective LPs in order to improve the performance of the online regression stage depicted in Figure 5.1. For this reason, we considered some practical assumptions, such as the access to the longitudinal and vertical tyre forces, vehicle velocity, and wheel angular speed values (see Figure 5.1), which is a common trend in the literature [136, 173, 175, 181]. Of these variables, ω and F_z are easily obtained; e.g., the wheel speed is measurable with low-cost sensors, whereas the tyre vertical load can be extracted from well-known weight transfer relations [133]. With regard to obtaining the longitudinal force information, there are two main possibilities: (i) direct measurement or (ii) observers. The former option can be accomplished through bearing units with load sensing [188, 189] or by putting accelerometers inside the tyre [190], but such sensors are generally costly and, as far as our knowledge goes, still remain largely in a prototype phase. To overcome the cost issue, longitudinal force observers represent an attractive prospect. For example, if the information about wheel torque is available, a simple force observer can be built from the model (5.1a), as discussed in [133] and [155]. Alternatively, the longitudinal vehicle dynamics (5.1b), together with the acceleration measurement, are also commonly employed to infer F_x [54, 175], whose performance can be further improved by applying the extended Kalman filter [191, 192]. Similarly to the longitudinal force information, the vehicle speed during braking can also be measured with dedicated sensors (e.g., with global

positioning system (GPS) [54]) or estimated, for instance, using Kalman filtering [191] or fuzzy logic [133]. The measurement/observation of F_x and v will be revisited later in the chapter when we experimentally validate the estimation algorithm.

5.3 Optimal Linear Parameterization

In this section, we present the derivation of an optimal LP, in the sense that it provides the best fit of a nonlinear friction model over a given parametric region of interest, as described in the next problem:

Problem 5.1. (Linear Approximation of μ) Consider a model $f(\lambda, \boldsymbol{\beta})$, typically nonlinear (such as (5.4) or (5.5)),

$$f\colon\ \mathcal{S} \times \mathcal{P} \to \mathbb{R} \tag{5.6}$$

describing the friction coefficient curve in the domain $(\lambda, \boldsymbol{\beta}) \in \mathcal{S} \times \mathcal{P} \subset [0, 1] \times \mathbb{R}^d$. The slip variable λ is the model input, and the $\boldsymbol{\beta}$ vector contains the model internal parameters, which are unknown and possibly time-varying. To approximate this nonlinear model, consider the parameterization:

$$\begin{aligned} \hat{f}(\lambda, \boldsymbol{w}, \boldsymbol{\theta}) &= \begin{bmatrix} h_1(\lambda, \boldsymbol{w}) & \dots & h_n(\lambda, \boldsymbol{w}) \end{bmatrix} \boldsymbol{\theta} && \text{(5.7a)} \\ &= \boldsymbol{H}(\lambda, \boldsymbol{w})^T \boldsymbol{\theta} && \text{(5.7b)} \end{aligned}$$

where $\{\boldsymbol{w}, \boldsymbol{\theta}\} \in \mathbb{R}^m \times \mathbb{R}^n$ is a vector of parameters, and $h_i(\lambda, \boldsymbol{w}), i = 1, ..., n$ are the basis functions. Under this setting, find the vector $\boldsymbol{w}^*$ that minimizes the modelling error[1] between $\hat{f}(\lambda, \boldsymbol{w}^*, \boldsymbol{\theta})$ and $f(\lambda, \boldsymbol{\beta})$ over a given domain of interest $[0, \overline{\lambda}] \times \mathcal{D} \subset \mathcal{S} \times \mathcal{P}$. □

Among the parameters $\{\boldsymbol{w}, \boldsymbol{\theta}\}$ of the approximator function, the $\boldsymbol{\theta}$ are easier to estimate, due to their linearity, while the $\boldsymbol{w}$ parameters have a nonlinear effect in the model and complicate the identification process. Spurred by these difficulties, we investigate the possibility of selecting, off-line, the best vector $\boldsymbol{w}^*$, in the sense that the fitting error is minimized, while $\boldsymbol{\theta}$ is estimated by online estimation methods in order to capture the variations of the unknown and time-varying internal parameters (β) of (5.6). Notice that, after finding $\boldsymbol{w}^*$, we can insert this vector in (5.7) and transform the nonlinear model into a LP, i.e., the model remains nonlinear, but it is linear in the parameters $\boldsymbol{\theta}$. To keep the problem tractable, it is assumed that the number (n) and type of basis functions are known beforehand (later we can evaluate the fitting performance for different numbers and types of basis functions).

At this stage, it is appropriate to discuss previous efforts toward solving Problem 5.1. Fixed basis functions (i.e., with $m = 0$), such as polynomials [180] and rational functions [179], have been successfully employed for approximating the nonlinear friction curve and have shown good performance in μ_{max} peak friction estimation. However, as pointed out by [183], the performance of these LPs deteriorates when λ_{max} estimations are needed. To overcome this difficulty, [136] proposed the use of exponential adaptive basis functions, which significantly boosts the μ_{max} and λ_{max} estimation. Despite this, there is an important drawback with the LP proposed in [136]: a heuristic approach was used to select the coefficients $\boldsymbol{w}$ in the adaptive function, which does not generate the most efficient LP,

[1] a performance metric to express the notion of modelling error will be presented shortly

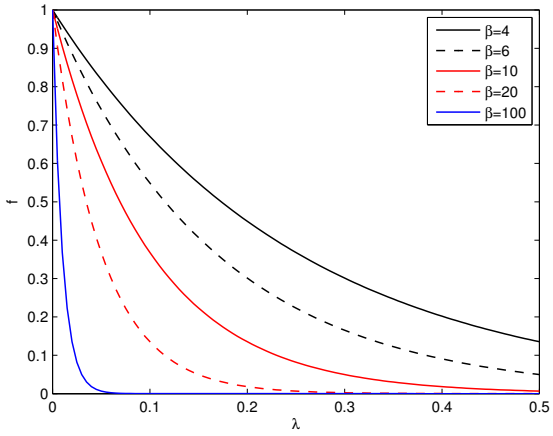

Figure 5.2: Nonlinear function $e^{-\beta\lambda}$, plotted for different values of β.

i.e., with a minimum number of basis functions. The present work extends these previous contributions by providing a systematic methodology to select the optimum value of the parameter $\boldsymbol{w}$, not only for exponentials but also for any type and number of basis functions.

The methodology presented in this chapter can be applied to various types of friction curves, but for simplicity, we use the Burckhardt parameterization as reference model and focus on finding a LP for the single nonlinear term in this representation:

$$f(\lambda, \beta) \quad = \quad e^{-\beta\lambda} \tag{5.8}$$

where $\lambda \in [0, \overline{\lambda}] \subset \mathbb{R}$ and $\beta \in \mathcal{D} = [\underline{\beta}, \overline{\beta}] \subset \mathbb{R}$. For now, the offset and linear gain of (5.4) is omitted in the LP but will be included in the final parameterization. According to [133], the parameter β shows a strong dependence on the road conditions (for example, dry tarmac, wet tarmac, snow, etc.) and, to represent the most common types of roads, varies between $\underline{\beta} = 4$ and $\overline{\beta} = 100$ (see Figure 5.2). In addition, since the LP will be used to extract the friction peak, it is reasonable to assume that the LP should minimize the fitting error in the slip range between 0 and $\overline{\lambda} = 0.5$ (notice that it is uncommon to have friction peaks for longitudinal slips higher than 0.5 [166]).

Before solving the above-mentioned approximation problem, it is helpful to revisit a simplified dual problem: of the two vectors $\{\boldsymbol{w}, \boldsymbol{\theta}\}$ that parameterize the approximator (5.7), admit that $\boldsymbol{w}$ is known and consider the problem of finding the best set of linear parameters $\boldsymbol{\theta}$. If $\boldsymbol{\beta}$ is also known, we can then apply well-known results from the theory of function approximation to transform this problem into a minimum norm problem and extract $\boldsymbol{\theta}$ (see Appendix 5.8). The approach to solve Problem 5.1 proposed in the next section, builds on these analytical results but drops the assumption of known $\boldsymbol{w}$ (and $\boldsymbol{\beta}$).

5.3.1 Optimal Method for Finding LP

To tackle Problem (5.1), we start by defining the fitting error of the approximator (5.7) for a given fixed triplet $(\beta, \boldsymbol{w}, \boldsymbol{\theta})$:

$$\varepsilon(\beta, \boldsymbol{w}, \boldsymbol{\theta}) = \int_0^{\overline{\lambda}} \big(f(\lambda, \beta) - \underbrace{\boldsymbol{H}(\lambda, \boldsymbol{w})^T \boldsymbol{\theta}}_{\hat{f}(\lambda, \boldsymbol{w}, \boldsymbol{\theta})}\big)^2 d\lambda \tag{5.9}$$

Considering fixed values of β and $\boldsymbol{w}$, the vector $\boldsymbol{\theta}$ that minimizes $\varepsilon(\beta, \boldsymbol{w}, \boldsymbol{\theta})$ can be found by direct application of Lemma 5.1, presented in Appendix 5.8:

$$\boldsymbol{\theta}(\beta, \boldsymbol{w}) = \boldsymbol{G}^{-1}(\boldsymbol{w})\boldsymbol{c}(\beta, \boldsymbol{w}) \tag{5.10}$$

$$[\boldsymbol{G}(\boldsymbol{w})]_{i,j} = \langle h_i(\boldsymbol{w}), h_j(\boldsymbol{w})\rangle = \int_0^{\overline{\lambda}} h_i(\lambda, \boldsymbol{w}) h_j(\lambda, \boldsymbol{w}) d\lambda \tag{5.11}$$

$$[\boldsymbol{c}(\beta, \boldsymbol{w})]_i = \langle f(\beta), h_i(\boldsymbol{w})\rangle \int_0^{\overline{\lambda}} f(\lambda, \boldsymbol{\beta}) h_i(\lambda, \boldsymbol{w}) d\lambda \tag{5.12}$$

where $i, j = 1, \ldots, n$. Replacing these relations in (5.9), the dependence on $\boldsymbol{\theta}$ can be eliminated and the fitting error redefined as:

$$\varepsilon(\beta, \boldsymbol{w}) = \int_0^{\overline{\lambda}} \left(f(\lambda, \beta) - \boldsymbol{H}(\lambda, \boldsymbol{w})^T \boldsymbol{G}^{-1}(\boldsymbol{w})\boldsymbol{c}(\beta, \boldsymbol{w})\right)^2 d\lambda \tag{5.13}$$

Given that β is known to belong to the set $\mathcal{D}$, it is reasonable to define a performance metric to sum all the fitting errors in this domain, which is obtained by integrating $\varepsilon(\beta, \boldsymbol{w})$ over $\mathcal{D}$. This new approximation metric, called total error, is defined by:

$$\varepsilon_T(\boldsymbol{w}) = \int_{\beta \in \mathcal{D}} \varepsilon(\beta, \boldsymbol{w}) d\beta \tag{5.14}$$

and depends only on $\boldsymbol{w}$. Thus, we can now pose an optimization problem to extract the $\boldsymbol{w}$ parameter that minimizes the total fitting error:

$$\begin{aligned} \min_{\boldsymbol{w} \in \mathbb{R}^m} \quad & \varepsilon_T(\boldsymbol{w}) = \min_{\boldsymbol{w} \in \mathbb{R}^m} \int_{\beta \in \mathcal{D}} \varepsilon(\beta, \boldsymbol{w}) d\beta \\ s.t. \quad & eq.(5.11), (5.12), (5.13) \end{aligned} \tag{5.15}$$

This problem assumes that the nonlinear function $f(\lambda, \beta)$, the domain $[0, \overline{\lambda}] \times \mathcal{D}$, and the structure of the adaptive basis functions $\boldsymbol{H}(\lambda, \boldsymbol{w})$ are known, and delivers the parameter $\boldsymbol{w}$ that minimizes the total fitting error, offering an optimal solution to Problem 5.1. Generally, the analytic treatment of the above problem is difficult, particularly when many basis functions are used. To overcome this issue, the integral (5.15) was discretized with a trapezoidal approximation and a numeric solver [193] employed to extract the optimal solution.

5.3.2 LPs for Approximating the Burckhardt Model

After presenting the methodology for deriving optimum LPs, we now evaluate the performance of different basis functions for approximating the single nonlinear term (5.8) in the Burckhardt friction model. The approximating domain $[0, \overline{\lambda}] \times \mathcal{D}$ of the LP is the same as that discussed in the previous section, and the basis functions under consideration are:

1. Polynomials: $\boldsymbol{H}_P(\lambda) = \begin{bmatrix} 1 & \lambda & \lambda^2 & \ldots & \lambda^{n-1} \end{bmatrix}^T$
2. Exponentials: $\boldsymbol{H}_E(\lambda, \boldsymbol{w}) = \begin{bmatrix} e^{w_1 \lambda} & \ldots & e^{w_n \lambda} \end{bmatrix}^T$
3. Logistic Sigmoid: $\boldsymbol{H}_L(\lambda, \boldsymbol{w}) = \begin{bmatrix} \frac{1}{1+e^{-w_1 \lambda - w_2}} & \ldots \end{bmatrix}^T$

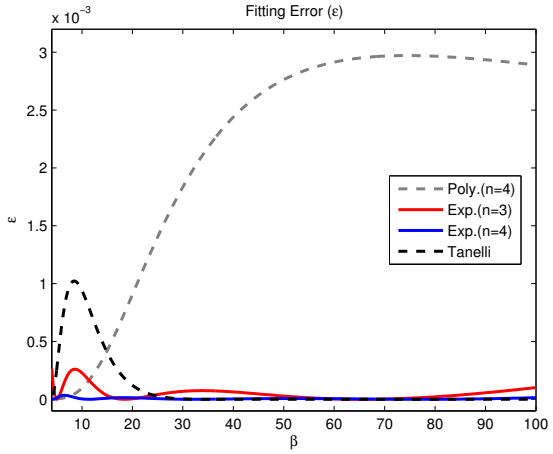

Figure 5.3: Fitting error $\varepsilon(\beta)$ evaluated for polynomials, exponentials, and the LP proposed in [136].

Table 5.1: Total error ε_T for fitting (5.8) with different LPs.

	Number of basis (n)			
Basis Type	1	2	3	4
Polynomial ($\boldsymbol{H}_P$)	-	0.6844	0.3857	0.2127
Log. Sigmoid ($\boldsymbol{H}_L$)	0.2849	0.0467	0.0212	0.0059
Exponential ($\boldsymbol{H}_E$)	0.2870	0.0362	0.0046	0.0005
Tanelli et al.[136]	-	-	-	0.0093

where $\boldsymbol{w} = \begin{bmatrix} w_1 & w_2 & \dots & w_m \end{bmatrix}^T \in \mathbb{R}^m$. Moreover, since we have a practical interest in minimizing the LP complexity, different numbers of bases ($n \in \{1, 2, 3, 4\}$) were also assessed.

A summary of the total error ε_T for the LPs under consideration can be found in Table 5.1. It is apparent from these results that the polynomial basis functions generate the worst fitting performance, and increasing n does not significantly reduce the error. On the contrary, the approximation error decreases considerably by employing adaptive functions, and among these, the exponentials gives the best LP. For comparison purposes, the total fitting error obtained with the parameterization defined in [136] is also provided: this LP produces a reasonable result, but it is clear that the total error can be decreased by using exponential basis functions, with optimum $\boldsymbol{w}$. Actually, we can even reduce the number of exponential functions to $n = 3$ and still obtain total errors less than the ones produced by [136].

To provide additional insight regarding the performance of the LP, Figure 5.3 shows the fitting error ε over the approximating domain $\mathcal{D}$. Inspecting the polynomial performance reveals that the fitting errors increase when β gets higher; this was expected since, in this parametric region, the nonlinear curve (5.8) starts to approach an impulse-like shape (see Figure 5.2) and a high-order polynomial is needed to capture this behaviour. Furthermore, although the LP proposed in [136] is globally better than the polynomial, it still presents some significant errors for low β. These errors are further reduced with (optimal) exponential basis functions, and using $n = 4$ basis generates the best LP over

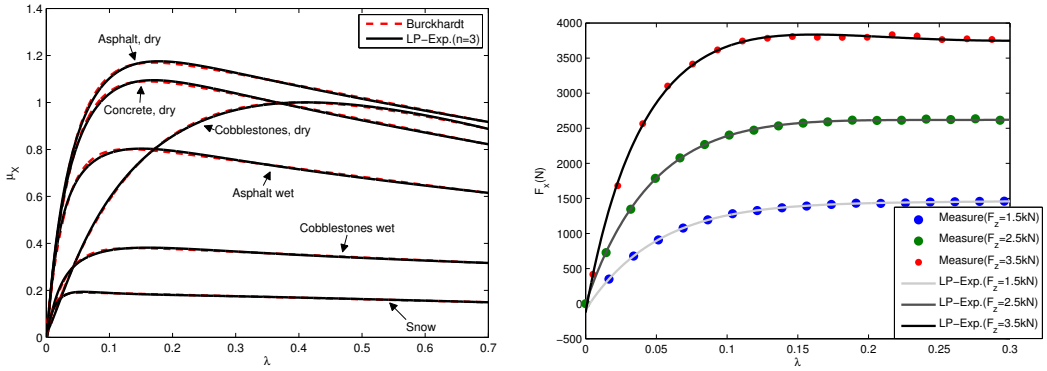

(a) (b)

Figure 5.4: a) Comparison of the Burckhardt model (cf. (5.4)) with the LP proposed in this chapter (cf. (5.18)) for the most representative types of roads found in practice [133]; b) Fitting of longitudinal force produced by a 205/55 R16 90 H tyre (experimental data were retrieved from [194]) using the LP (5.18).

the entire domain $\mathcal{D}$.

In summary, the optimal LP for approximating (5.8) was found to be exponential-based, with $n = 4$ and $n = 3$:

$$\boldsymbol{H}_{E4}(\lambda) = \begin{bmatrix} e^{-4.28\lambda} & e^{-11.37\lambda} & e^{-32.34\lambda} & e^{-77.05\lambda} \end{bmatrix}^T \tag{5.16}$$

$$\boldsymbol{H}_{E3}(\lambda) = \begin{bmatrix} e^{-4.99\lambda} & e^{-18.43\lambda} & e^{-65.62\lambda} \end{bmatrix}^T \tag{5.17}$$

Based on this result, we can now join the linear terms of (5.4) with the LP of (5.8) and obtain the optimum LP that better approximates the Burckhardt friction model: $\hat{\mu}(\lambda, \boldsymbol{\theta}) = \begin{bmatrix} 1 & \lambda & \boldsymbol{H}_E(\lambda)^T \end{bmatrix} \boldsymbol{\theta}$. Although the performance of $\boldsymbol{H}_{E4}$ surpasses the other LPs, the basis $\boldsymbol{H}_{E3}$ is enough to provide a good fitting of the original nonlinear model; on top of that, using $\boldsymbol{H}_{E3}$ enables us to eliminate one basis function, which may facilitate the online identification process. Accordingly, in the sequel, the LP

$$\hat{\mu}(\lambda, \boldsymbol{\theta}) = \boldsymbol{H}(\lambda)^T \boldsymbol{\theta} = \begin{bmatrix} 1 & \lambda & e^{-4.99\lambda} & e^{-18.43\lambda} & e^{-65.62\lambda} \end{bmatrix} \boldsymbol{\theta} \tag{5.18}$$

is used to approximate the Burckhardt friction model.

5.3.3 Off-line Validation

With the goal of validating the proposed LP, two "off-line" tests were conducted. The first is presented in Figure 5.4(a), which shows the performance of the LP defined in (5.18) against the original nonlinear Burckhardt parameterization (cf. (5.4)) for the most representative roads found in practice, as discussed in [133]. It can be noted that the LP and the Burckhardt curves are almost overlaid on each other, and little modelling error is introduced, thus providing additional evidence of the equivalence between both models.

An additional test was carried out to validate the LP with experimental data. This test is illustrated in Figure 5.4(b), which shows the LP curves after fitting with the classical least squares method, the experimental longitudinal force produced by a 205/55 R16 90 H tyre [194]. Once again, the fitting performance obtained with the LP was very satisfactory.

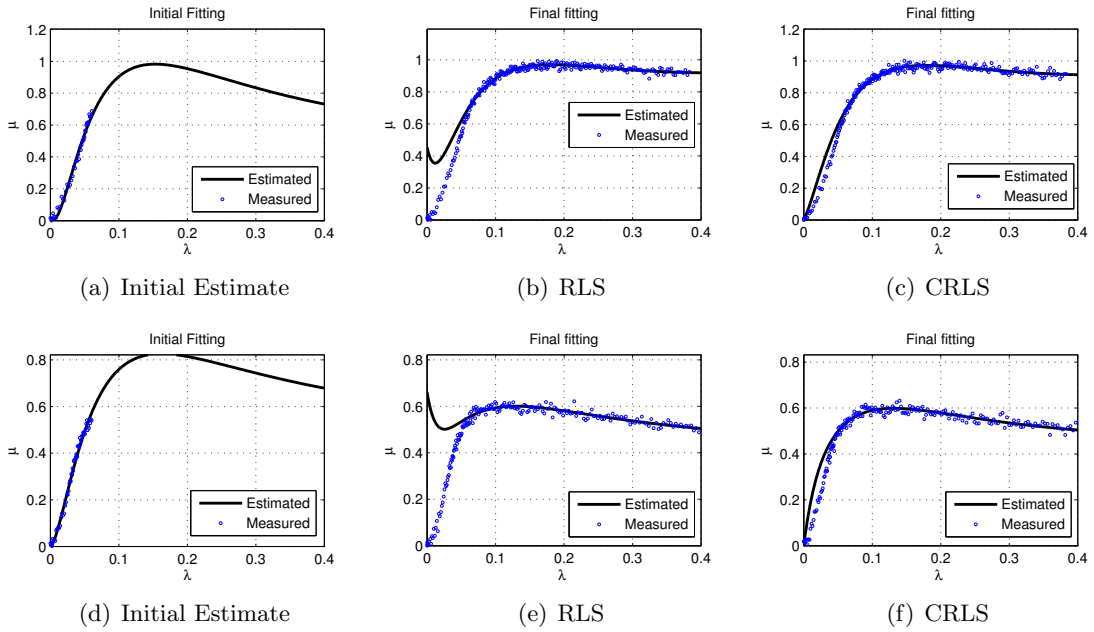

(a) Initial Estimate (b) RLS (c) CRLS

(d) Initial Estimate (e) RLS (f) CRLS

Figure 5.5: Identification of the friction curve during braking on dry asphalt with $\mu_{max} = 1.0$ (top figures) and on wet asphalt with $\mu_{max} = 0.6$ (bottom figures). The initial estimate for the friction curve, calculated from the samples with $\lambda \leq \underline{\lambda}$, is shown in (a,d); the final friction curve estimate obtained after processing all the samples (see Figure 5.6) with the RLS and CRLS is shown in (b,e) and (c,f), respectively.

5.4 Online Estimation Method

After finding a suitable LP representation of the friction model in the tyre-road interface, we will discuss in this section a modified version of the recursive least squares (RLS) [195], capable of handling equality constraints, to identify the friction parameters. This method is known as the constrained RLS (CRLS) and is particularly useful in the current work to improve the accuracy and robustness of the friction estimation in the low-slip range.

5.4.1 Motivation for CRLS

To illustrate the relevance of the CRLS, consider two sets of input/output samples, $\mathcal{Z} = \{(\lambda(1), \mu(1)), \ldots, (\lambda(N), \mu(N))\}$, obtained from braking tests conducted in the CarSim simulator; the first set was performed on dry asphalt and the second on wet (see Figure 5.5). The conditions under which these experiments were undertaken are described in the next section; for now, we merely discuss some of the potential pitfalls of the RLS. Due to the recursive nature of the identification process, an initial guess for $\hat{\boldsymbol{\theta}}_0$ needs to be defined, which, following the initialization procedure suggested in [136], was obtained by applying the traditional (batch) least squares to the first collected samples, $\mathcal{Z}_0(\underline{\lambda}) = \{(\lambda(k), \mu(k)) \in \mathcal{Z} \ : \ \lambda_k \leq \underline{\lambda}\}$, where $\underline{\lambda}$ is the minimum threshold (0.06 in this work) to start the identification. After this initialization step (Figure 5.5(a),5.5(d)), the remaining data in $\mathcal{Z}$ was processed with the RLS; the final fitting results are shown in Figure 5.5(b) for dry asphalt and in Figure 5.5(e) for wet asphalt. In the case of dry asphalt, it is clear that the RLS presents a very good fitting performance for tyre slips above 0.08 but is prone to exhibit significant fitting errors in the low-slip range. Although this issue does not affect the detection of the friction peak in dry asphalt, when the RLS is

evaluated in wet asphalt manoeuvres (Figure 5.5(e)), the fitting error in the low-slip range increases and compromises the estimation process: the peak of the identified friction curve is located at zero slip, $\hat{\lambda}_{max} = 0$, while the true peak is around 0.12. Accordingly, the peak friction estimation in wet asphalt has a significant error in the $\hat{\lambda}_{max}$, which makes its use impractical for safety systems, such as the traction controller (TC) or the ABS. This problem was also observed in other low-friction conditions, but for the sake of brevity, these results were omitted in this section.

The most natural choice to attenuate this problem is to modify the RLS forgetting factor in order to increase the weight of the initial samples. Note, however, that the forgetting factor employed in these results is already relatively high ($\rho = 0.999$), thus little improvement is observed by modifying this parameter. Alternatively, if the initial estimate $\hat{\boldsymbol{\theta}}_0$ is good, which is far from guaranteed, we may try to reduce the parameter in the RLS associated with the confidence in the initial guess (see [195] and $\boldsymbol{P}_0$ in (5.27d)) and, as a consequence, decrease the amount of parameter variation during the recursive adaptation. Although they are possible, these parametric changes in the RLS tend to slow down the identification process, colliding with the need to quickly produce accurate estimations of the friction peak, which must be available before the vehicle safety systems become enabled.

This set of difficulties urged us to find ways of improving the RLS performance. A well-known possibility to increase the estimation performance consists of the use of prior information about the system model, e.g., through a set of (equality and/or inequality) constraints on the model parameters [196, 197, 198, 199]. In the current friction estimation problem, the prior information comes from the fact that the ideal friction curve must pass though the origin of the coordinate system (λ, μ) or, equivalently, comply with an equality constraint, $\boldsymbol{H}(0)^T\boldsymbol{\theta} = 0$. In other words, this constraint means that when the tyre is in free-rolling mode (i.e., $\lambda = 0$), the friction force (and the instantaneous tyre-road friction coefficient μ) should be zero. The remainder of this section will be devoted to explaining how this equality constraint can be incorporated into the identification algorithm, called CRLS, and to highlighting some of its theoretical and practical advantages.

5.4.2 Description of the CRLS

Just like the RLS, the starting point of the CRLS formulation is a weighted least squares problem, but subject to an additional set of equality constraints:

$$\min_{\boldsymbol{\theta}\in\mathbb{R}^n} \sum_{k=1}^{t} \alpha(t,k) \left(\mu(k) - \mathbf{H}^T(\lambda(k))\,\boldsymbol{\theta}\right)^2, \qquad s.t. \quad \mathbf{C}\boldsymbol{\theta} = \mathbf{d} \tag{5.19}$$

where t is the number of samples being considered, $\alpha(.)$ is the weight assigned to each sample, and $\boldsymbol{C} \in \mathbb{R}^{p\times n}$ and $\boldsymbol{d} \in \mathbb{R}^p$ characterize the set of p linear constraints (it is assumed that $p < n$ and $\text{rank}(\boldsymbol{C}) = p$). Reformulating the optimization problem with the Lagrange multiplier, and taking into consideration the quadratic nature of the cost function, an analytical (batch) solution can be easily found [196, p. 225]:

$$\hat{\boldsymbol{\theta}}_t = \boldsymbol{R}_t^{-1}\boldsymbol{f}_t + \boldsymbol{R}_t^{-1}\boldsymbol{C}^T\left(\boldsymbol{C}\boldsymbol{R}_t^{-1}\boldsymbol{C}^T\right)^{-1}\left(\boldsymbol{d} - \boldsymbol{C}\boldsymbol{R}_t^{-1}\boldsymbol{f}_t\right) \tag{5.20}$$

$$\mathbf{R}_t = \sum_{k=1}^{t} \alpha(t,k)\tilde{\boldsymbol{H}}(k)\tilde{\boldsymbol{H}}^T(k), \qquad \mathbf{f}_t = \sum_{k=1}^{t} \alpha(t,k)\tilde{\boldsymbol{H}}(k)\mu(k) \tag{5.21}$$

where $\tilde{\boldsymbol{H}}(k) = \boldsymbol{H}(\lambda(k))$ is employed to simplify the notation.

Remark 5.1. From a convergence point of view, it is worth noting that, under some reasonable assumptions, the above batch estimator is unbiased and provides more precise results than the (unconstrained) least squares (LS). To prove these claims, we consider the following stochastic framework:

$$\mu(k) = \tilde{\boldsymbol{H}}^T(k)\boldsymbol{\theta} + e(k) \tag{5.22}$$

where $e(k)$ is the white noise measurement error, with mean $\mathrm{E}[e] = 0$ and variance σ^2. Further, it is assumed that $\{\tilde{\boldsymbol{H}}(k)\}$ and $\{e(k)\}$ are statistically independent, and, to simplify the mathematical treatment, a unitary weight $\alpha(t,k) = 1$ is taken. Using the parameter estimation error

$$\Delta\boldsymbol{\theta} = \hat{\boldsymbol{\theta}}_t - \boldsymbol{\theta} = \sum_{k=1}^{t} (\boldsymbol{I} - \gamma_t \boldsymbol{C})\, \mathbf{R}_t^{-1} \tilde{\boldsymbol{H}}(k) e(k) \tag{5.23}$$

where $\gamma_t = \boldsymbol{R}_t^{-1}\boldsymbol{C}^T \left(\boldsymbol{C}\boldsymbol{R}_t^{-1}\boldsymbol{C}^T\right)^{-1}$, we can determine the bias as:

$$\mathrm{E}[\Delta\boldsymbol{\theta}] = \sum_{k=1}^{t} \mathrm{E}\left[(\boldsymbol{I} - \gamma_t \boldsymbol{C})\, \mathbf{R}_t^{-1} \tilde{\boldsymbol{H}}(k) e(k)\right] = \sum_{k=1}^{t} \mathrm{E}\left[(\boldsymbol{I} - \gamma_t \boldsymbol{C})\, \mathbf{R}_t^{-1} \tilde{\boldsymbol{H}}(k)\right] \mathrm{E}[e(k)] \tag{5.24}$$

Thus, the estimator will be unbiased, i.e., $\mathrm{E}[\Delta\boldsymbol{\theta}] = 0$, if, besides the assumption of statistical independence, $\mathrm{E}[e(k)]$ is zero, and $\mathbf{R}_t$ and $\left(\boldsymbol{C}\boldsymbol{R}_t^{-1}\boldsymbol{C}^T\right)$ are non-singular. These last requirements represent the persistence of excitation conditions for the system. Next, consider the covariance of the parameter estimation error

$$\begin{aligned} \mathrm{cov}(\Delta\boldsymbol{\theta}) = \mathrm{E}\left[\Delta\boldsymbol{\theta}\Delta\boldsymbol{\theta}^T\right] &= \sum_{k=1}^{t}\sum_{j=1}^{t} \mathrm{E}\left[(\boldsymbol{I} - \gamma_t \boldsymbol{C})\, \mathbf{R}_t^{-1} \tilde{\boldsymbol{H}}(k) e(k) e(j) \tilde{\boldsymbol{H}}(j)^T \mathbf{R}_t^{-1} (\boldsymbol{I} - \gamma_t \boldsymbol{C})^T\right] && \text{(5.25a)} \\ &= \sigma^2\, \mathrm{E}\left[\mathbf{R}_t^{-1}\right] - \sigma^2\, \mathrm{E}\left[\gamma_t \boldsymbol{C} \mathbf{R}_t^{-1}\right] && \text{(5.25b)} \end{aligned}$$

and recall that the covariance matrix of the (unconstrained) LS is given by $\mathrm{cov}(\Delta\boldsymbol{\theta}^{LS}) = \sigma^2\, \mathrm{E}\left[\mathbf{R}_t^{-1}\right]$ [197, p. 236]. Replacing this relation in (5.25b), we get:

$$\mathrm{cov}(\Delta\boldsymbol{\theta}^{LS}) - \mathrm{cov}(\Delta\boldsymbol{\theta}) = \sigma^2\, \mathrm{E}\left[\gamma_t \boldsymbol{C} \mathbf{R}_t^{-1}\right] \geq 0 \tag{5.26}$$

Therefore, we can conclude that the constrained LS will be more efficient that the unconstrained LS, producing parameter estimates with smaller variance. □

Since this batch solution is of little use for online applications, it is necessary to find a recursive alternative. Following similar arguments to those in the RLS case, it is assumed that the weight function $\alpha(t,k)$ has the following properties [195]: (i) $\alpha(t,t) = 1$ and (ii) $\alpha(t,k) = \rho\alpha(t-1,k), \quad 0 \leq k \leq t-1$. These two properties can be satisfied using, for example, $\alpha(t,k) = \rho^{t-k}$, where ρ is the forgetting factor. Based on these properties, and employing the well-known matrix inversion lemma, a recursive solution to $\boldsymbol{R}_t$ and $\boldsymbol{f}_t$ can be derived, which, after some algebraic manipulation, results in the following iterative

solution of (5.20):

$$\hat{\boldsymbol{\theta}}_t = \hat{\boldsymbol{\theta}}_t^{RLS} + \gamma_t \left(\mathbf{d} - \mathbf{C}\hat{\boldsymbol{\theta}}_t^{RLS}\right) \tag{5.27a}$$

$$\hat{\boldsymbol{\theta}}_t^{RLS} = \hat{\boldsymbol{\theta}}_{t-1}^{RLS} + \boldsymbol{L}_t \left[\mu(t) - \tilde{\boldsymbol{H}}^T(t)\hat{\boldsymbol{\theta}}_{t-1}^{RLS}\right] \tag{5.27b}$$

$$\boldsymbol{L}_t = \frac{\boldsymbol{P}_{t-1}\tilde{\boldsymbol{H}}(t)}{\rho + \tilde{\boldsymbol{H}}^T(t)\boldsymbol{P}_{t-1}\tilde{\boldsymbol{H}}(t)} \tag{5.27c}$$

$$\boldsymbol{P}_t = \frac{1}{\rho}\left[\boldsymbol{P}_{t-1} - \frac{\boldsymbol{P}_{t-1}\tilde{\boldsymbol{H}}(t)\tilde{\boldsymbol{H}}^T(t)\boldsymbol{P}_{t-1}}{\rho + \tilde{\boldsymbol{H}}^T(t)\boldsymbol{P}_{t-1}\tilde{\boldsymbol{H}}(t)}\right] \tag{5.27d}$$

$$\boldsymbol{\gamma}_t = \boldsymbol{P}_t\boldsymbol{C}^T\left(\boldsymbol{C}\boldsymbol{P}_t\boldsymbol{C}^T\right)^{-1} \tag{5.27e}$$

It is interesting to note that the update equation (5.27a) of the recursive solution, is composed of two terms. The first ($\hat{\boldsymbol{\theta}}_t^{RLS}$) is in fact the solution to the unconstrained version of the problem, i.e., the traditional RLS, and because of this, (5.27b), (5.27c), and (5.27d) are the same as the RLS solution. The second term is a correction factor that ensures that the identified parameters respect the linear constraints in the iterations. Hence, from the numerical complexity point of view, the CRLS only demands an additional matrix equation (5.27e) to be evaluated, which, given the reduced number of unknown parameters (five) is not too penalizing. Nonetheless, the calculation of the $\boldsymbol{\gamma}_t$ matrix involves an undesirable operation for online implementation: the inversion of the $\boldsymbol{C}\boldsymbol{P}_t\boldsymbol{C}^T$ matrix. To avoid this inversion, consider the gain $\boldsymbol{\gamma}_t$, rewritten as:

$$\boldsymbol{\gamma}_t = \boldsymbol{\Gamma}_t\boldsymbol{\eta}_t \tag{5.28}$$

where $\boldsymbol{\Gamma}_t = \boldsymbol{P}_t\boldsymbol{C}^T$ and $\boldsymbol{\eta}_t = (\boldsymbol{C}\boldsymbol{\Gamma}_t)^{-1}$. Following the algebraic manipulation suggested in [186], a recursive version of $\boldsymbol{\Gamma}_k$ can be established by multiplying (5.27d) with $\boldsymbol{C}^T$, while the matrix inversion lemma is again applied to calculate $\boldsymbol{\eta}_k$ iteratively:

$$\boldsymbol{\Gamma}_t = \frac{1}{\rho}\left(\boldsymbol{\Gamma}_{t-1} - \boldsymbol{L}_t\tilde{\mathbf{H}}^T(k)\boldsymbol{\Gamma}_{t-1}\right) \tag{5.29a}$$

$$\boldsymbol{\eta}_t = \rho\left(\boldsymbol{\eta}_{t-1} + \frac{\boldsymbol{\eta}_{t-1}\boldsymbol{C}\boldsymbol{L}_t\tilde{\mathbf{H}}^T(k)\boldsymbol{\Gamma}_{t-1}\boldsymbol{\eta}_{t-1}}{1 - \tilde{\mathbf{H}}^T(k)\boldsymbol{\Gamma}_{t-1}\boldsymbol{\eta}_{t-1}\boldsymbol{C}\boldsymbol{L}_t}\right) \tag{5.29b}$$

Therefore, the final, numeric efficient, CRLS algorithm used in this work is described by (5.27a)-(5.27d), (5.28), and (5.29). Similar to the RLS, the CRLS also needs an initial guess for $\hat{\boldsymbol{\theta}}_0$ and $\boldsymbol{P}_0$, which are then used to initialize the remaining recursive variables ($\boldsymbol{\Gamma}_0 = \boldsymbol{P}_0\boldsymbol{C}^T$ and $\boldsymbol{\eta}_0 = (\boldsymbol{C}\boldsymbol{\Gamma}_0)^{-1}$).

5.4.3 CRLS Fitting Performance

Returning to the friction estimation, the CRLS was applied taking into account the single restriction in the problem:

$$\boldsymbol{H}(0)^T\boldsymbol{\theta} = \underbrace{\begin{bmatrix}1 & 0 & 1 & 1 & 1\end{bmatrix}}_{\boldsymbol{C}}\boldsymbol{\theta} = \underbrace{0}_{\boldsymbol{d}} \tag{5.30}$$

The CRLS performance, presented in Figure 5.5(c), 5.5(f), shows, as expected, that the identified friction curve always passes through the origin, which contributes to a much

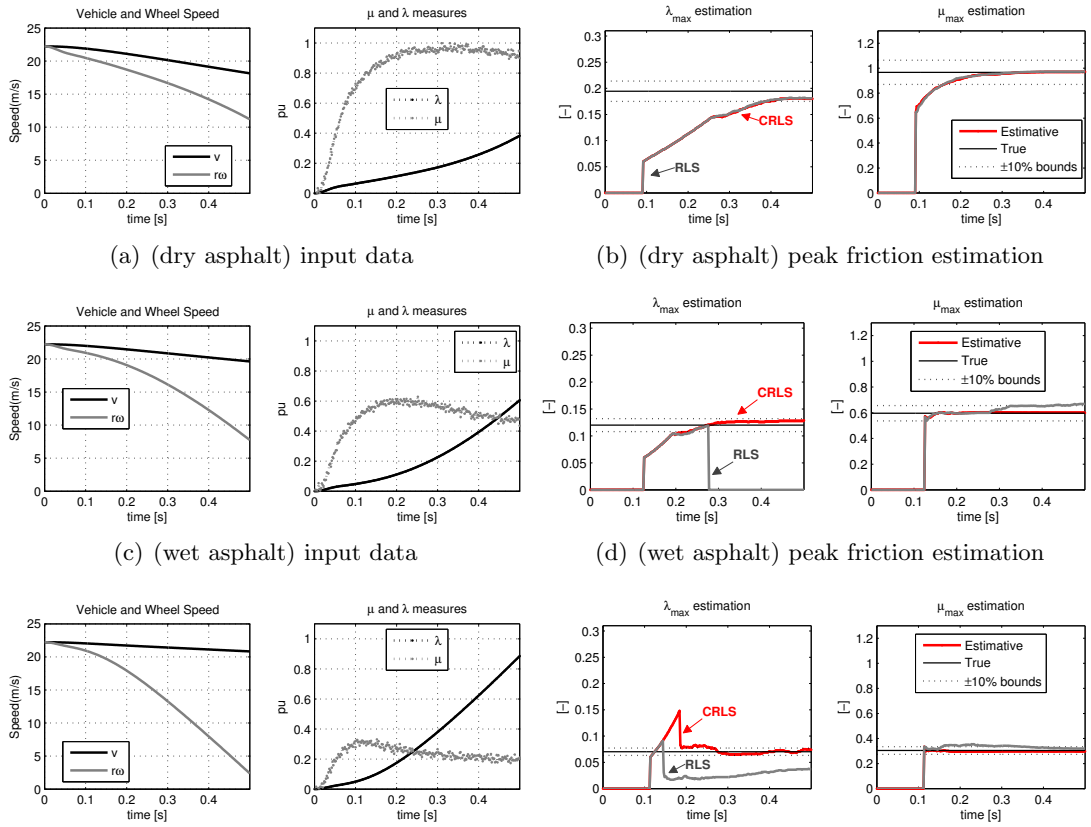

(a) (dry asphalt) input data

(b) (dry asphalt) peak friction estimation

(c) (wet asphalt) input data

(d) (wet asphalt) peak friction estimation

(e) (snow) input data

(f) (snow) peak friction estimation

Figure 5.6: Simulation results with the CarSim for different types of road adhesion: dry asphalt (top), wet asphalt (middle), and snow (bottom).

better fitting in the low-slip range, both on dry and wet asphalt. As will be shown in the next section, this CRLS feature is key to improving the identification robustness against the regression method parameters, e.g., the forgetting factor and the initial estimate, and extracts a precise estimation of the peak friction, particularly in low-grip conditions.

5.5 Simulation Results

To evaluate the performance of the peak friction estimation with the optimal LP and the CRLS identification method, this section presents the simulation results obtained with the CarSim simulator [146]. The estimation framework used is a quantitative one and, as shown in Figure 5.1, can be divided into 3 steps: (*i*)collection of λ and μ samples, (*ii*)fitting/regression, and (*iii*)peak detector. These steps were implemented as follows:

1. (μ, λ) collection

Regarding the first stage, it was assumed that the estimation algorithm has access to the samples $\mu(k)$ and $\lambda(k)$, where k is the sampling instant. In simulation tests, these variables are easily available.

2. Regression

For the regression step, the friction model adopted was the LP proposed in Section 5.3 (cf. (5.18)), which was used to evaluate two types of identification methods: the traditional RLS and the CRLS. To make a fair comparison, the algorithms had the same initial parameters, i.e., forgetting factor ($\alpha = 0.999$); $\boldsymbol{P}_0 = \delta \boldsymbol{I}$, where $\delta = 100$ and $\boldsymbol{I}$ is the identity matrix; and initial guesses $\hat{\boldsymbol{\theta}}_0 \in \mathbb{R}^n$ (which were obtained by the method suggested in [136] and described in Section 5.4.1).

3. Peak Extractor

The final step in the algorithm was obtained by computing the friction maximum point:

$$\hat{\mu}_{max} = \max_{\lambda} \hat{\mu}(\lambda, \hat{\boldsymbol{\theta}}) \tag{5.31a}$$

$$\hat{\lambda}_{max} = \arg\max_{\lambda} \hat{\mu}(\lambda, \hat{\boldsymbol{\theta}}) \tag{5.31b}$$

The identification algorithm presented above was evaluated using a typical A-class hatchback car, available in the CarSim library, having 175/70 R13 tyres, modelled with the MTF 5.2 [147]. The MTF 5.2 parameters are omitted here due to their high number (more than 80); in any case, the model reflects the steady-state behaviour of a real tyre and takes into account some simple dynamic transients, such as the relaxation length. The sampling time for the algorithm was set to 2 ms and, to contemplate the measuring errors that normally appear in this application, the variable μ was corrupted with Gaussian noise, with variance $\sigma_\mu^2 = 0.015^2$.

Based on these settings, three types of braking manoeuvres were performed in straight line, under different grip conditions: dry asphalt, wet asphalt and snow. The input data generated by these manoeuvres are shown on the left part of Figure 5.6, while the estimation results are on the right. Analyzing the estimations $\hat{\lambda}_{max}$ and $\hat{\mu}_{max}$ for all the tests, it can be observed that no value is generated in the first ~ 0.1s; during this period of time, the estimator is disabled because the slip is below the threshold activation point $\underline{\lambda}$, and these initial samples are used to calculate an initial guess for $\hat{\boldsymbol{\theta}}_0$. Inspecting the peak friction estimation for dry asphalt, shown in Figure 5.6(b), one can find that the RLS and the CRLS present an almost equal performances and converge, in less than 0.4s, to the proximities of the true values of μ_{max} and λ_{max}. This similar behaviour can be explained by the fact that the true friction peak is moderately high ($\lambda_{max} \simeq 0.2$), while the fitting error introduced by the RLS (see Figure 5.5(b)) mainly affects the low-slip regime ($\lambda \leq 0.08$). On the other hand, when the manoeuvre is performed on wet asphalt (Figure 5.6(d)), the $\hat{\lambda}_{max}$ estimation obtained with the RLS shows a severe estimation error after 0.3s, while the CRLS maintains a very satisfactory performance. Unlike in the previous case (dry), on wet asphalt the λ_{max} is relatively low (~ 0.12), and the fitting error introduced by the RLS (see Figure 5.5(e)) is sufficiently high to compromise the peak friction estimation. The snow test (Figure 5.6(f)) also shows a significant estimation error in $\hat{\lambda}_{max}$, albeit less severe than on wet asphalt. It is also worth mentioning that the $\hat{\mu}_{max}$ estimation is less sensitive to the fitting errors in low slip, and for that reason, both the RLS and the CRLS show similar performances in $\hat{\mu}_{max}$ in all the adhesion conditions under test.

In conclusion, these simulation results highlight the robustness of the CRLS over the traditional RLS in the peak friction estimation. Moreover, we can also conclude that by employing the CRLS, the designer has more freedom to select the forgetting factor (ρ)

and decrease the confidence ($\boldsymbol{P}_0$) in the initial guess without fear of the fitting problems in the low-slip region that appear in the RLS and mainly affects the λ_{max} estimation in low-grip roads.

5.6 Experimental Results

The peak friction estimator presented in the previous sections was experimentally validated in a neighborhood electric vehicle, which belongs to a class of low-speed vehicles suitable for urban mobility whose main feature is a decoupled powertrain structure with two electric motors individually connected to the front wheels (see Appendix A for additional details). The implementation of the peak friction estimator again followed the three steps described in the previous section but with some important modifications. First, while in the simulations the μ measures are easily obtained, in the experimental validation, such information must be estimated. Consequently, the μ samples were extracted from the quarter car model (5.1a), (5.2):

$$\mu = \frac{T_b}{rF_z} - \frac{J}{rF_z}\left(\frac{s}{\tau_f s + 1}\right)\omega \tag{5.32}$$

where s is the Laplace operator. The model parameters are the wheel radius ($r = 0.26$m) and the wheel inertia ($J = 0.6$kg.m^2), which are assumed constant throughout the experimental tests. To avoid the noise issues with the differentiation, this operator was approximated with a high-pass filter, having a time constant of $\tau_f = 40$ms (this approximation is also known as the "dirty differentiation" [200]), and discretized with the bilinear transformation. The vertical load supported by the wheel (F_z) can be extracted from simple weight transfer relations [133], while the braking torque is easily inferred from the motor current measures. The wheel slip samples λ were calculated using (5.3) and the vehicle speed was obtained from the non-driven wheels (note that during the experimental tests, only the EV front wheels were driven).

A second factor to be taken in consideration is the initial guess for the parameters $\hat{\boldsymbol{\theta}}_0$; two types of initial guesses were assessed:

- Initialization A: the Burckhardt dry curve (cf. Figure 5.4(a)) is used as the initial guess of $\hat{\boldsymbol{\theta}}_0$:

$$\hat{\boldsymbol{\theta}}_0 \;=\; \begin{bmatrix} 1.22 & -0.45 & 0.18 & -1.19 & -0.25 \end{bmatrix}^T \tag{5.33}$$

- Initialization B: $\hat{\boldsymbol{\theta}}_0$ is obtained following the procedure suggested in [136], used in the simulations and described in Section 5.4.1;

Although the second option may give more accurate (initial) estimates and contribute to faster convergence, from the implementation point of view, it requires higher computational effort since the batch least squares (LS) must be executed before the RLS. In the simulation and experimental tests performed in this work, we noticed that, depending on the manoeuvre, the size of the initial set of samples that the LS must handle (see the set $\mathcal{Z}_0$ in Section 5.4.1) can vary from 20 to 30 samples, which, for real-time applications with limited computational resources, may pose a serious computational burden. On the other hand, initialization A does not require any extra calculations, but there are some doubts about the algorithm convergence speed under low-grip conditions. To dissipate

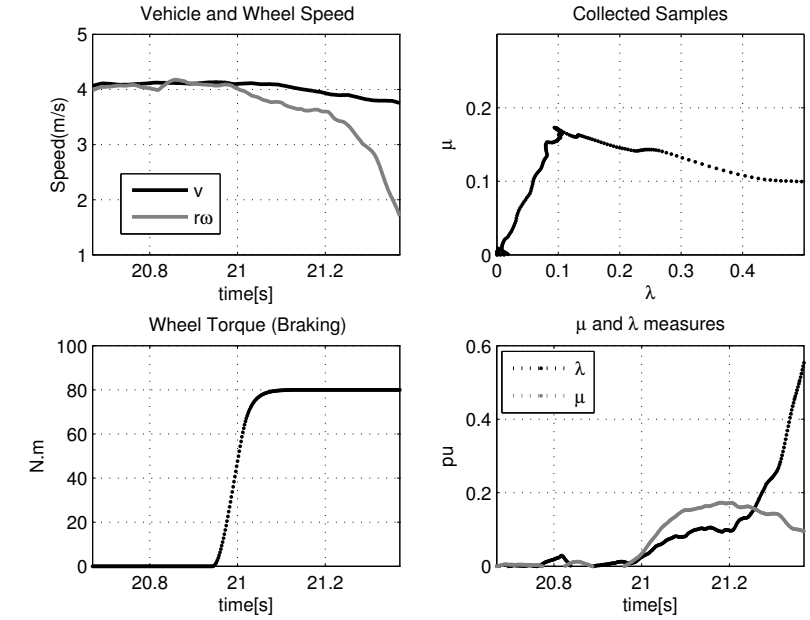

(a) acquired data

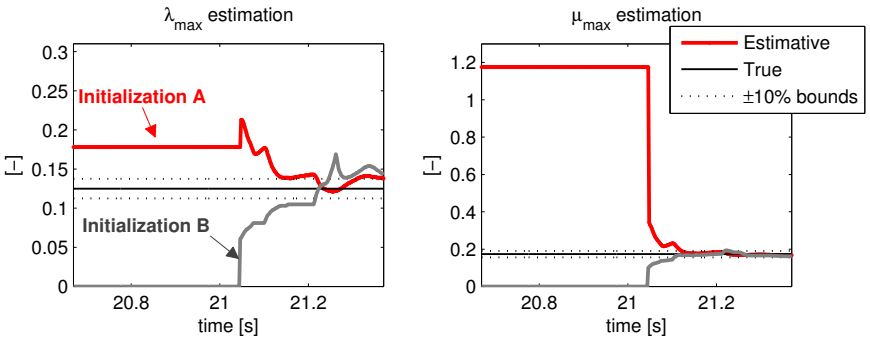

(b) peak friction estimation with CRLS

Figure 5.7: Experimental results for the left wheel during a braking manoeuvre on a low-grip surface.

such doubts, the performances of these two initializations are assessed in the experimental tests. Moreover, since the superiority of the CRLS has been established in the simulations, only this identification method is implemented (with the same configurations and sampling time as the ones used in the previous sections).

Figure 5.7 shows the acquired data on the left wheel during a braking operation performed on a low-grip surface, as well as the peak friction estimation, obtained with the slip control disabled. Before the driver applies a torque, both estimators are disabled because the slip does not reach the minimum threshold $\underline{\lambda}$, and for these reasons, initialization A outputs a nominal dry estimate, while initialization B does not provide any estimate. At around 21s, a significant braking torque is applied, which enables the CRLS adaptation, and after 0.3s of iterations, both initializations produce satisfactory results in the $\hat{\mu}_{max}$ estimation. Regarding $\hat{\lambda}_{max}$, it is interesting to point out the following: (i) during the initial transient, initialization A has a tendency to overestimate the peak friction, while initialization B is more prone to underestimation, which are expected given the $\hat{\boldsymbol{\theta}}_0$ employed

in each case (this observation also applies to $\hat{\mu}_{max}$); and (ii) initialization A provides a slightly more accurate final estimation of $\hat{\lambda}_{max}$ and, after $21.1s$, stays inside the predefined tolerance band of $\pm 10\%$, while initialization B shows a slightly larger estimation error. Hence, based on this second observation, we can state that although initialization B provides a better initial fitting for the slip range below $\underline{\lambda}$, this is no guarantee that the (final) identified friction curve will generate a better peak friction estimate. Moreover, this challenging experimental test highlights that the most computation-efficient initialization (A), together with the optimal LP and the CRLS, is sufficient to generate good peak friction estimation without penalizing the convergence speed or final accuracy.

5.7 Conclusions

In this work, a systematic methodology to extract an optimal linear parameterization (LP) to represent the tyre-road friction was developed. Toward this aim, we exploited the fact that the structure of the nonlinear friction model is known beforehand, such as the Burckhardt representation, and applied analytic, as well as numeric, optimization techniques to extract the LP with minimum fitting error along a given parametric range of interest. It was shown that the modelling error introduced by the optimum LP is almost negligible and outperforms others LPs previously proposed in the literature. The linear structure featured by the LP simplifies the real-time friction identification process since we can rely on linear regression methods to accomplish this task. A constrained version of the RLS was then employed to further increase the robustness of the peak friction identification against initial errors in the (linear) parameters and the RLS tuning parameters, e.g., the forgetting factor. Simulation results, obtained with the CarSim simulator, showed that the optimal LP identified with the CRLS provides a satisfactory performance in the estimation of $\hat{\lambda}_{max}$ and $\hat{\mu}_{max}$ under different tyre-road adhesion levels. These results were further validated with experimental tests, obtained with a neighborhood electric vehicle on a low-grip surface.

As future endeavours, we plan to extend the experimental work to address different types of surfaces, and study further extensions of the LP to handle situations with lateral and combined tyre slip.

5.8 Appendix: Classic Approximation Result

This section reviews a simple result from the theory of function approximation, which is helpful in establishing the optimal LP. For this purpose, consider the problem of approximating (5.6) with (5.7), assuming that β and $\boldsymbol{w}$ are fixed and known. Our intention is to find the linear parameters $\boldsymbol{\theta}$, such that the fitting performance, defined as the integral of the square fitting error (ε), is minimized:

$$\min_{\boldsymbol{\theta}\in\mathbb{R}^n} \varepsilon(\boldsymbol{\theta}) = \min_{\boldsymbol{\theta}\in\mathbb{R}^n} \int_0^{\overline{\lambda}} (f(\lambda) - \underbrace{\boldsymbol{H}(\lambda)^T\boldsymbol{\theta}}_{\hat{f}(\lambda,\boldsymbol{\theta})})^2 d\lambda \tag{5.34}$$

Note that, to simplify the notation, the dependence of β in f (and of $\boldsymbol{w}$ in $\boldsymbol{H}$) is omitted in this section, which is reasonable as these parameters are assumed to be constant. The previous optimization problem can be formulated in the vector space $L_2\left([0,\overline{\lambda}],\mathbb{R}\right)$, i.e.,

square-integrable functions over the interval $[0, \overline{\lambda}]$, making use of the L_2 norm:

$$\varepsilon(\boldsymbol{\theta}) \quad = \quad \|f - \hat{f}\|^2 = \int_0^{\overline{\lambda}} (f(\lambda) - \hat{f}(\lambda, \boldsymbol{\theta}))^2 d\lambda \tag{5.35}$$

Since the vector $\hat{f}$ is a linear combination of L_2 vectors (cf. (5.7)), the optimization problem (5.34) can be reformulated as a minimum norm problem in the L_2 space, which has a simple analytical solution, as described in the following lemma:

Lemma 5.1. *Consider the vector space $L_2\left([0, \overline{\lambda}], \mathbb{R}\right)$, a vector $f \in L_2$ and a subspace $\mathcal{M} \subset L_2$ generated by the linear combination of n basis functions $h_i \in L_2$:*

$$\mathcal{M} = \left\{ \hat{f} \in L_2 \ : \ \hat{f} = \sum_{i=1}^{n} h_i \theta_i, \quad h_i \in L_2, \quad \theta_i \in \mathbb{R} \right\} \tag{5.36}$$

Then, the minimum norm problem

$$\min_{\hat{f} \in \mathcal{M}} \|f - \hat{f}\|^2 \tag{5.37}$$

has the following solution:

$$\hat{f}_o(\lambda) \quad = \quad \begin{bmatrix} h_1(\lambda) & \dots & h_n(\lambda) \end{bmatrix} \boldsymbol{\theta_o} \qquad \boldsymbol{\theta_o} = \boldsymbol{G}^{-1} \boldsymbol{c} \tag{5.38a}$$

$$[\boldsymbol{G}]_{i,j} \quad = \quad \langle h_i, h_j \rangle = \int_0^{\overline{\lambda}} h_i(\lambda) h_j(\lambda) d\lambda \tag{5.38b}$$

$$[\boldsymbol{c}]_i \quad = \quad \langle f, h_i \rangle = \int_0^{\overline{\lambda}} f(\lambda) h_i(\lambda) d\lambda \tag{5.38c}$$

where $i, j = 1, \dots, n$, $\boldsymbol{G} \in \mathbb{R}^{n \times n}$, $\boldsymbol{c} \in \mathbb{R}^n$, $\langle , \rangle$ is the L_2 inner product, and $[.]_{i,j}$ refers to row i, column j of a given matrix. Moreover, the solution is unique if the basis functions h_i are linear independent. □

Proof: Given the fact that L_2 is a Hilbert space, we can apply the projection theorem to solve this minimum norm problem (see [101, Chap. 3.6] for details).

Chapter 6

Adaptive-Robust Friction Compensation in a Hybrid Brake-by-Wire Actuator

Abstract:

The present chapter focuses on the development of a pressure loop controller for a hybrid brake-by-wire (BBW) system, composed of a hydraulic link and an electro-mechanical actuator. Toward this goal, we will start by constructing a reduced model that is capable of capturing the fundamental dynamics of the actuator, being particular useful for control design purposes. Motivated by the large friction disturbances that affect the system, linear-in-the-parameters (LP) models suitable for (on-line) model-based friction compensation are also investigated. More specifically, results from the theory of function approximation, together with optimization techniques, are explored to approximate the Stribeck friction model through a LP. This new LP is then employed in the design of a control law for tracking the braking pressure of the hybrid BBW. The main features of this controller are the robustness to parametric uncertainties, thanks to the inclusion of a switching-σ adaptive mechanism, while non-parametric disturbances are attenuated with a continuous sliding mode action. The stability and robustness properties of the closed-loop system are investigated with the help of the Lyapunov method. Finally, experimental tests demonstrate the effectiveness of the proposed approach, and its ability to handle disturbances.

6.1 Introduction

With the progressive increase in the safety, comfort and performance requirements demanded by modern vehicles, brake-by-wire (BBW) approaches are being considered by the automotive industry as an attractive option to replace the hydraulic-based brakes systems. For example, in contrast to the traditional brakes systems based on solenoid valves that only admit discrete control actions (e.g., increase, hold, decrease), the BBW actuators allows an accurate and continuous action over the braking torque. This feature, together with the higher bandwidths provided by the BBW, is a great asset for: *i*) improving the effectiveness of braking assistance functionalities, like anti-lock braking systems [127, 131]; *ii*) providing better actuation capabilities for the vehicles' lateral safety systems that may

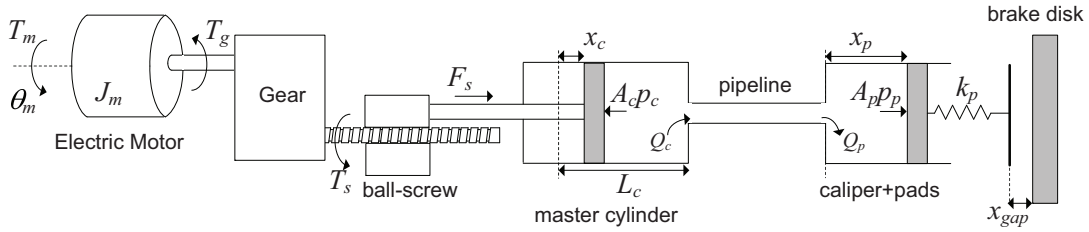

Figure 6.1: Block diagram of the BBW actuator.

depend on differential braking [201], and *iii*) facilitating the torque blending between friction brakes and regenerative torque available in electric vehicles, as discussed in Chapter 3. Another significant feature of the BBW system is the elimination of the mechanical link between the brake pedal and the wheel brakes. This isolation is beneficial from a comfort perspective, since it enables the implementation of haptic pedal feedback with custom brake feel; but, on the other hand, it also introduces major challenges to ensuring fail-safe operation[45].

Generally, there are two main options for the BBW implementation: electro-hydraulic braking (EHB) [202, 203] and electro-mechanical braking (EMB)[204, 205]. The main attractiveness in the former option is the possibility of maintaining a significant portion of the components used in the braking system of today's vehicles, such as callipers, hydraulic link, accumulators, etc. [202, 203, 206]. Given that most of these components have already reached a mature state of development, this normally brings cost and reliability advantages to the EHB solution. The second option, EMB, relies on a pure mechanical link between the actuator and the brake disk, and, in comparison with the EHB, allows a significant decrease in the volume, weight and component number, and also offers faster response times [205, 207]. However, the EMB requires a major redesign of today's braking systems, and, while such actuators do not reach a mass-production stage, the cost will remain an issue. Therefore, this factor, together with the fail-safe concerns, still represents a significant obstacle for the widespread use of pure EMB designs.

Spurred by these challenges, in recent years, the automotive industry has dedicated considerable efforts toward the improvement of EHB and EMB designs. In this chapter, we will explore an emerging BBW prototype, under development by an Italian brake manufacturer, which intends to hybridize the EHB and EMB approaches. The main idea behind this hybrid BBW, illustrated in Figure 6.1 and 6.2, is, just like the EHB, to keep intact the callipers and the braking lines of today's vehicles. However, instead of using electro-valves, accumulators and pumps to regulate the braking pressure (as is done in EHB), an electro-mechanical actuator, i.e., electric motor-gear-ball-screw, is directly connected to the piston of the master cylinder to generate the braking pressure. With this approach, the cost and the number of components can be kept relatively low, since we only need to fit one additional element - the electro-mechanical actuator - in the braking system. This latter feature is also very beneficial for vehicles subject to strong space constraints, e.g., motorbikes [208, 209]. Further, given the high bandwidth of the electro-mechanical actuator, the response times of the hybrid configuration are expected to be faster than the ones obtained with the EHB (but slower than the pure EMB, due to the hydraulic link). The presence of the hydraulic link also facilitates the incorporation of backup braking systems, which may be important to ensure fail-safe operation.

In this context, the main goal of the present chapter is to develop an electronic controller for the above-mentioned hybrid BBW, capable of robustly regulating the braking

force. In the literature there are several studies on the design of braking (or clamping) force control for pure EMB designs, ranging from linear PID techniques [210], force-speed cascaded loops [211], model predictive controllers [205] or robust time-optimal approaches [212]. Despite being useful for pure EMB actuators, the controllers' designs presented in these studies cannot be directly applied to the hybrid BBW configuration under study here. This is due to the existence of the hydraulic link in the actuator, which introduces non-negligible dynamics that must be taken into account at the controller's design stage. To overcome this limitation, in this work, we will propose a practical controller for the hybrid BBW actuator that considers these non-negligible dynamics.

Besides the hydraulic link, friction represents another major source of disturbance in the BBW actuator, which may lead to the appearance of limit cycles, stick-slip and steady-state tracking errors. From a control-perspective, there are several approaches that can be used to mitigate the friction effects, such as dither, position-error dead band and model-based compensation techniques [213]. Among these techniques, the model-based compensation, i.e., incorporation in the controller of a feedforward component to cancel the friction disturbance [213], has emerged in recent years as the most promising technique. As explained in Appendix 6.8, one of the main reasons for this interest lies in the possibility to combine model-based friction compensation with adaptive control methods, which enables the controller to handle, on-line, with parameter changes in the friction disturbance (which may appear as a result of variations in temperature, wear, etc.). Since the friction model is generally nonlinear, particularly the Stribeck effect, the construction of the adaptation laws is also greatly simplified if the (friction) disturbance can be represented with a *linear-in-the-parameters* (LP) structure [145], i.e., linear in the unknown parameters. The recent literature contains several works that approximate the nonlinear friction map with LPs based on linearization techniques [214, 215], polynomials [216, 217], Lorentzian [213, 218], and piecewise linear functions [219, 220, 221]. However, most of these approaches assumes an accurate knowledge of the so-called Stribeck velocity, a parameter that characterizes the transition speed between the static and kinetic (Coulomb) friction regimes. In practice, however, due to parametric variation resulting from various factors (temperature, humidity, etc.) this assumption does not always hold.

An additional contribution of this work is to offer a new LP, composed of a sum of normalized exponentials, which is capable of approximating the nonlinear friction map with a significant uncertainty in the Stribeck velocity. This new LP, obtained through optimal function approximation techniques, provides a higher accuracy than the LPs previously proposed in the literature [214, 215, 216, 221], and with a reduced number of basis functions (six). In the second part of the work, the optimal LP is employed in the development of an adaptive-robust controller for the hybrid BBW actuator. Toward that aim, it is showed that, under some reasonable assumptions, the actuator can be modelled as an uncertain second-order system, affected by two types of disturbances: parametric and non-parametric. The former, arising from the approximation of friction with a LP, is compensated using a switching-σ adaptation mechanism, while the latter, resulting from modelling approximations, is attenuated with a continuous sliding mode term. The robust stability and ultimate boundedness of the proposed controller is established analytically through the Lyapunov method, and confirmed with experimental tests.

The remainder of this chapter is structured as follows: Section 6.2 introduces the full actuator model, which is then used to develop a control-oriented model in Section 6.3. The friction characterization of the actuator, together with the derivation of the optimal LP, is presented in Section 6.4. Section 6.5 is concerned with the design of the adaptive-robust

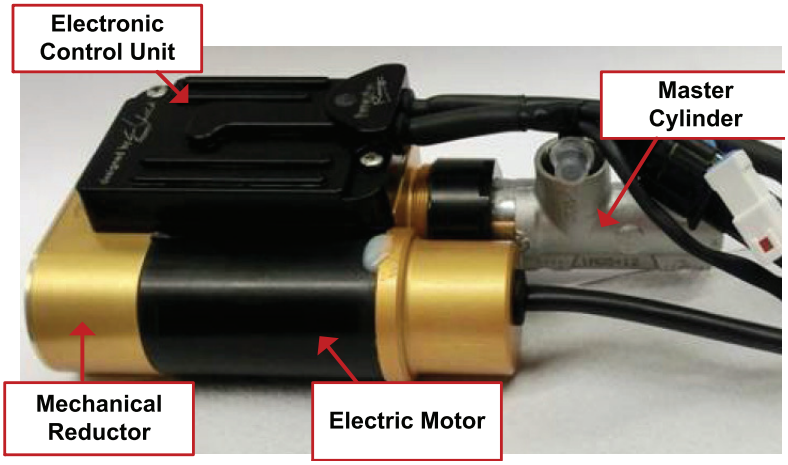

Figure 6.2: Brake-by-wire prototype developed by Brembo.

controller for tracking the pressure in the hybrid BBW actuator. Section 6.6 contains the experimental validation of the controller, while Section 6.7 presents the conclusions and the outlook for future work.

6.2 Actuator Model

As depicted in Figure 6.1, the BBW actuator under consideration is composed of different types of physical sub-systems, involving electrical, mechanical and hydraulical domains. The main source of motion lies in the electric motor (DC motor, with 200W), which is connected to a fixed reduction-gear to increase the output torque. This rotational motion is then converted in linear displacement, e.g., using a ball-screw device, pushing the master cylinder piston and building up the necessary braking pressure. The hydraulic pressure is conducted through a small pipeline (i.e., the brake lines) to the pads, which then presses the braking disk to generate the clamping force.

6.2.1 Mathematical Model

Starting with the electro-mechanical part of the actuator, we have:

$$J_m\ddot{\theta}_m = T_m - T_g - T_f(.) \tag{6.1a}$$
$$m_c\ddot{x}_c = F_s - p_c A_c \tag{6.1b}$$
$$T_g = \frac{F_s}{G}, \quad \theta_m = G x_c \tag{6.1c}$$
$$\tau_m\dot{i}_m = -i_m + i_m^*, \quad T_m = k_m i_m \tag{6.1d}$$

The first equation represents the rotational dynamics of the motor, where θ_m is the motor position, J_m the motor-reduction gear inertia, T_m is the torque generated by the electric motor, T_g the torque at the gearbox input, and T_f the equivalent friction torque. To simplify the model, it is presumed that the main friction forces that affect the actuator (e.g., the friction in reduction gear, ball-screw, piston, pipeline, etc.) can be referred to the electric motor side; we postpone the mathematical definition of T_f to a later section. The second equation models the linear displacement of the cylinder, with m_c representing the piston mass, x_c the position, F_s the linear force applied by the ball-screw, p_c the

master cylinder pressure, and A_c its area. The third set of equations describes the relation between torque/force and rotation/linear position in the reduction gear and ball-screw mechanisms, having G [rad/m] as the overall gain factor. Finally, (6.1d) contemplates the closed loop response of the motor current controller, where i_m is the motor current, i_m^* the setpoint, τ_m the dominant time constant and k_m [Nm/A] the current/torque gain. For the sake of brevity, the details regarding the design of inner current loop are omitted in this work (the interested reader is referred to [208, 222] for additional information on this inner loop).

After specifying the electro-mechanical model, we now move on to the modelling of the hydraulic section. Following similar arguments as the ones exposed in [208], the pressure dynamics in the master and pad cylinders can be established by the direct application of the continuity equation [223]:

$$-Q_c = \dot{V}_c + \frac{V_c}{\beta}\dot{p}_c \tag{6.2a}$$

$$Q_p = \dot{V}_p + \frac{V_p}{\beta}\dot{p}_p \tag{6.2b}$$

$$V_c = (L_c - x_c)A_c, \quad V_p = A_p x_p, \tag{6.2c}$$

where Q_c represents the volumetric flow rate getting out of the master cylinder chamber, Q_p the volumetric flow entering the pad's cylinder, V_c and V_p represent the volume of the master and pad cylinders, respectively, A_p the area of the pad cylinder piston and β the bulk modulus of the brake fluid. Neglecting the pipeline dynamics, and assuming laminar flow, we can further derive the pressure drop in the pipeline as:

$$p_c - p_p = K_{cp}Q, \qquad Q = Q_c = Q_p \tag{6.3}$$

where K_{cp} is the laminar flow coefficient of the pipeline (which depends on the conduct geometry and fluid properties [223]). Finally, the clamping force applied to the brake disk can be described by the following dynamic model:

$$m_p\ddot{x}_p = p_p A_p - F_c(x_p) \tag{6.4a}$$

$$F_c(x_p) = \begin{cases} 0, & \text{if } x_p < x_{gap} \\ k_p(x_p - x_{gap}), & \text{if } x_p \geq x_{gap} \end{cases} \tag{6.4b}$$

where m_p is pad mass, x_p the pad displacement, x_{gap} the air gap between the brake disk and the pad, k_p the stiffness of the pad and F_c the clamping force. Table 6.1 contains a list of the known values of some of the actuator's physical parameters.

6.3 Development of a Control-Oriented Model

This section aims to develop a practical mathematical model that can be helpful in the design of feedback controllers for the BBW actuator. Spurred by this idea, and in order to clarify the role of the numerous variables introduced in the previous section (i.e., define states, parameters, disturbances, etc.), it is convenient to first rewrite the system model (6.1)-(6.4) in a state space formulation. Accordingly, let's consider the following

Table 6.1: Physical parameters of the BBW actuator

Variable	Symbol	**Value**
inertia of motor + gear	J_m	1.1×10^{-5} kg m^2
mass of the master cylinder piston	m_c	1×10^{-2} kg
combined reduction ratio	G	3.294×10^{3} rad/m
time constant of the current loop	τ_m	15.9×10^{-3} s
current/torque gain	k_m	16.8×10^{-3} Nm/A
area of the master cylinder	A_c	1.13×10^{-4} m^2
length of the master cylinder	L_c	29×10^{-3} m
bulk modulus of the brake fluid [1]	β	1.6×10^{9} Pa
area of the pad's cylinder	A_p	3.22×10^{-3} m^2
stiffness of the pad [1]	k_p	1.28×10^{8} N/m
pipeline width	-	8×10^{-3} m
pipeline length	-	0.8 m

[1] nominal value

state variables:

$$x_1 = \theta_m, \quad x_2 = \dot{\theta}_m = \omega_m, \quad x_3 = p_c, \tag{6.5a}$$

$$x_4 = p_p, \quad x_5 = x_p, \quad x_6 = \dot{x}_p, \quad x_7 = i_m \tag{6.5b}$$

$$\mathbf{x} = \begin{bmatrix} x_1 & x_2 & x_3 & x_4 & x_5 & x_6 & x_7 \end{bmatrix}^T \tag{6.5c}$$

Replacing these variables in (6.1)-(6.4), and considering the motor current setpoint as the control input for the system, i.e., $u = i_m^*$, the system dynamics is given as:

$$\dot{x}_1 = x_2 \tag{6.6a}$$

$$J_{eq}\dot{x}_2 = k_m x_7 - \frac{A_c}{G} x_3 - T_f(.) \tag{6.6b}$$

$$\dot{x}_3 = \frac{\beta}{L_c - \frac{x_1}{G} A_c} \left(\frac{A_c}{G} x_2 - \frac{x_3 - x_4}{K_{cp}} \right) \tag{6.6c}$$

$$\dot{x}_4 = \frac{\beta}{A_p x_5} \left(\frac{x_3 - x_4}{K_{cp}} - A_p x_6 \right) \tag{6.6d}$$

$$\dot{x}_5 = x_6 \tag{6.6e}$$

$$m_p \dot{x}_6 = (x_4 A_p - F_c(x_5)) \tag{6.6f}$$

$$\tau_m \dot{x}_7 = (-x_7 + u) \tag{6.6g}$$

where $J_{eq} = J_m + \frac{m_c}{G^2}$ is the equivalent inertia of the motor, gear, ball-screw and mass of master cylinder's piston. As can be seen from the above equations, this seven-state model presents a complicated structure, with several nonlinearities in the state dynamics, most notably in (6.6c),(6.6d), and (6.6f). From a parametric perspective, it is worth pointing out that, while some parameters in the model depend on geometric properties, easily measured, such as the cylinder's areas A_c, A_p, length L_c or the reduction-gain G (see

Table 6.1), there are other parameters that are subject to a significant level of uncertainty. For example, it is well known that the bulk-module of the braking fluid, β, is sensitive to temperature variations [223], while the pad's stiffness k_p (that affects the function F_c) changes, not only according to temperature, but also with the pad's wear (among other factors). Moreover, the model is also affected by other disturbances, such as the friction T_f, which, as we will see shortly, plays a relevant role in the system dynamics. In light of these nonlinearities, parameter uncertainties and disturbances, constructing a robust and high-performance feedback controller for the BBW actuator is a challenging task. Motivated by these difficulties, we will develop in the remainer of this section a control-oriented model for the actuator, which can help the designer construct and tune practical controllers.

Before presenting the development of the reduced model, it is pertinent to discuss some of the possible control variables that can be used by the BBW controller. Ideally, the BBW controller should use the braking torque (or, alternatively, the clamping force F_c) as the controlled variable. However, due to the package and cost constraints, it is not always desirable/possible to have dedicated sensors to measure these variables. Therefore, in practice, it is more convenient to exert an indirect control over the braking torque using easily measurable variables, such as hydraulic pressure. In the BBW actuator employed in this work, and taking into account our goal of keeping intact the callipers used in today's vehicles, the variable that is more easily measurable and which, simultaneously, has a strong connection with the braking torque, is the pressure in the master cylinder, $x_3 = p_c$. Consequently, in the sequel, we will regard x_3 as the main output of the actuator's reduced model.

6.3.1 Simplification of the Hydraulic and Pads Model

Starting with the pad's model, it is noteworthy to verify that (6.6f) is a hybrid/switching system, in the sense that the model's vector field is dependent on the value of the binary condition

$$c_g = (x_5 \geq x_{gap}) \in \{0, 1\} \tag{6.7}$$

Generally, this condition will affect the control strategy employed in the electro-hydraulic braking actuator. For example, in situations where $c_g = 0$, an air-gap management algorithm is normally used to overcome the clearance gap between the pads and braking disk. This operation, seen as an initial procedure to prepare the actuator for the braking manoeuvre, can be achieved with the help of prefilling functionalities [224] or by controlling the pad's position [209, 210, 212, 225]. On the other hand, after putting the pads in direct contact with the braking disk (i.e., $c_g = 1$), the control goal is to track the (hydraulic brake) pressure setpoint. Throughout this work it will be considered that

Assumption 6.1. the pads are always in direct contact with the braking disk, i.e., $x_p = x_5 \geq x_{gap}$. Thus, the control-oriented model will be valid in the domain:

$$\mathcal{X} = \{\mathbf{x} \mid x_5 \geq x_{gap}\} \tag{6.8}$$

This assumption can be ensured by employing a suitable gap clearance management every time the BBW controller is active, as mentioned above. Additionally, to further simplify (6.6f) we will consider that

Assumption 6.2. after the pad encounter the braking disk, the inertial force of the pads ($m_p \dot{x}_6$) can be neglected.

This simplification allows us to find an (approximate) algebraic relation between the pad's pressure and position, as well as its time derivative:

$$k_p(x_p - x_{gap}) \approx p_p A_p, \quad k_p \dot{x}_p \approx \dot{p}_p A_p, \quad \forall x_p \geq x_{gap} \tag{6.9}$$

By replacing the above relations in (6.6c)-(6.6f), the equations associated with the pad position (x_5) and speed (x_6) can be dropped, and the dynamics of the master cylinder pressure (x_3) and the pad's pressure (x_4) posed with the following representation:

$$\dot{x}_3 = \Gamma(x_1)\left(x_2 - \alpha_1(x_3 - x_4)\right) \tag{6.10a}$$
$$\dot{x}_4 = \alpha_2 \Xi(x_4)(x_3 - x_4) \tag{6.10b}$$

$\mathbf{x} \in \mathcal{X}$, which depends on two parameters:

$$\alpha_1 = \frac{G}{A_c K_{cp}}, \quad \alpha_2 = \frac{k_p}{K_{cp} A_p^2} \tag{6.11}$$

and two nonlinear functions:

$$\Gamma(x_1) = \frac{\beta}{L_c G - x_1}, \quad \Xi(x_4) = \left(1 + \frac{x_4 + x_{gap}\frac{k_p}{A_p}}{\beta}\right)^{-1}$$

Inspecting more closely the last function, $\Xi(x_4)$, one can find that the pad's pressure (x_4) and the bulk modules of the braking fluid β are the most relevant variables in the function. Since, in practice, β takes very high values (see, e.g., the nominal value of β presented in Table 6.1), we can use the following result

Assumption 6.3. [high value of the bulk modulus]

$$\beta \gg x_4 + x_{gap}\frac{k_p}{A_p} \tag{6.12}$$

to approximate the function $\Xi(x_4)$ with a constant, unitary value that is $\Xi(x_4) \approx 1$. Consequently, (6.10) can be further simplified as:

$$\dot{x}_3 = \Gamma(x_1)\left(x_2 - \alpha_1(x_3 - x_4)\right), \quad \dot{x}_4 = \alpha_2(x_3 - x_4) \tag{6.13}$$

From these relations, it worth underlining the fact that the main driving forces behind x_3 dynamics are the motor speed (x_2) and the pressure difference $x_3 - x_4$ in the pipeline. Since this last quantity also plays an important role in the dynamics of the pad's pressure x_4, it seems reasonable to consider the pressure difference

$$\Delta_p = x_3 - x_4 \tag{6.14}$$

as an alternative state variable to x_4. In particular, introducing Δ_p in (6.13), we obtain

$$\dot{x}_3 = \Gamma(x_1)\left(x_2 - \alpha_1 \Delta_p\right), \tag{6.15a}$$
$$\dot{\Delta}_p = \Gamma(x_1)x_2 - \left(\Gamma(x_1)\alpha_1 + \alpha_2\right)\Delta_p \tag{6.15b}$$

By joining these last two equations, the master cylinder dynamics can be expressed as:

$$\dot{x}_3 = \frac{\alpha_2}{\alpha_1 + \frac{\alpha_2}{\Gamma(x_1)}} x_2 + \frac{\alpha_1}{\alpha_1 + \frac{\alpha_2}{\Gamma(x_1)}} \dot{\Delta}_p, \tag{6.16a}$$

$$= \frac{\alpha_2}{\alpha_1} x_2 + \underbrace{\frac{1}{1 + \frac{\alpha_2}{\alpha_1 \Gamma(x_1)}} \left(\dot{\Delta}_p - \frac{\alpha_2^2}{\alpha_1^2 \Gamma(x_1)} x_2 \right)}_{\delta(x_1, x_2, \dot{\Delta}_p)} \tag{6.16b}$$

$$= \frac{\alpha_2}{\alpha_1} x_2 + \delta(x_1, x_2, \dot{\Delta}_p) \tag{6.16c}$$

Assumption 6.4. for control purposes, we will regard the term $\delta(x_1, x_2, \dot{\Delta}_p)$ as a bounded disturbance that the BBW controller should attenuate. It is also convenient to consider that this disturbance has a bounded time-derivative, which means that, from now on, we will work under the premise that:

$$|\delta(.)| \leq \overline{\delta}_0, \qquad |\dot{\delta}(.)| \leq \overline{\delta}_1, \qquad \forall \mathbf{x} \in \mathcal{X} \tag{6.17}$$

where $\overline{\delta}_0$ and $\overline{\delta}_1$ are known upper bounds.

Assumption 6.5. in light of the fast response of the inner current loop, the dynamics of this loop will be neglected, thus $x_7 = i_m \approx i_m^* = u$

Using these last assumptions, together with (6.16c) and (6.6b), the control-oriented model that we propose for the actuator is described by the following uncertain second-order system:

$$J_{eq} \dot{x}_2 = k_m u - \frac{A_c}{G} x_3 - T_f(.) \tag{6.18a}$$

$$\dot{x}_3 = \frac{\alpha_2}{\alpha_1} x_2 + \delta(.) \tag{6.18b}$$

which is valid for $\mathbf{x} \in \mathcal{X}$. In comparison with (6.6), the above reduced representation, albeit less accurate, is a much more tractable model for control design purposes.

6.3.2 Validation of the Reduced Hydraulic Model

The structure proposed in (6.18) is composed of two parts: *i*) the x_2 dynamics, associated with the electro-mechanical part, and *ii*) the x_3 dynamics, related to the hydraulic pressure in the master cylinder. With regard to the electro-mechanical part, and given that we did not make any special simplifications to (6.18a), it is expected that this relation will be sufficient to characterize the response of the motor speed. On the other hand, the cylinder's reduced model, (6.18b), was subjected to a series of strong simplifications in the hydraulics and pads dynamics, and there are legitimate concerns about the validity of such approximations. In order to dissipate such concerns, we will demonstrate, through experimental tests, that (6.18b) is able to capture the fundamental dynamics of the actuator, and that the assumptions employed in the model's derivation are valid.

Recall that (6.18b) builds on the hypothesis that the fundamental relation between the motor speed x_2 and the pressure x_3 is described by an integral relation (assuming the undisturbed situation $\delta \approx 0$):

$$\dot{x}_3 \approx \frac{\alpha_2}{\alpha_1} x_2, \qquad \mathbf{x} \in \mathcal{X} \tag{6.19}$$

To validate this hypothesis, it is helpful to regard the motor speed $x_2 = \omega_m$ as a "pseudo-input" for the hydraulic model, while the pressure $x_3 = p_c$ is the output. Of course, in practice, the true control input for the BBW controller will be the motor current setpoint, and we will also have to take into consideration the motor dynamics, i.e., (6.18a). Nonetheless, for validating the candidate model (6.19), it is much more interesting to decouple the hydraulics from the electro-mechanical part, as this latter sub-block is subject to difficult-to-model nonlinearities, like friction (topic to be addressed in the next section), which brings unnecessary complications to the identification process.

Since (6.19) only depends on one parameter, i.e., the ratio $\vartheta = \alpha_2/\alpha_1$, the identification process of this model is relatively straightforward. In fact, considering a continuous-time identification approach, the parameter ϑ can be estimated by solving the following least-squares problem:

$$\min_{\hat{\vartheta}} \int_0^T \left(p_c(t) - \underbrace{\left(\hat{\vartheta} \int_0^t \omega_m(\tau) d\tau + p_c(0) \right)}_{\hat{p}_c(t)} \right)^2 dt \tag{6.20}$$

where T is the duration of the test, $\omega_m(t)$ the measured motor speed (model input), $p_c(t)$ the measured pressure in the master cylinder (model output) and $\hat{p}_c(t)$ the estimated pressure.

For experimentally validating the simplified hydraulic model, the BBW actuator was installed in a testbench, whose details are provided in Section 6.6. A pseudo-random binary signal was applied to the motor current, having a significant power spectrum up to 10Hz (see Figure 6.3(a)), which represents the intended working range for the actuator. After collecting the measurements p_c and ω_m, the fitting problem (6.20) was discretized and then numerically solved, producing the estimative $\hat{\vartheta} = 2.99$ bar/rad. As illustrated in Figure 6.3(b), the overall performance of the simplified hydraulic model is very reasonable, and the estimate $\hat{p}_c$ is able to follow the general trend of the measured pressure p_c. These results demonstrate that the proposed control-oriented model is, indeed, a good candidate for capturing the fundamental dynamics of the hydraulic part of the BBW actuator.

6.4 Friction Characterization and Modelling

After establishing a practical model for the BBW actuator, we will now characterize in more detail the friction disturbance T_f. From a physical point of view, friction is a ubiquitous phenomenon that is present in almost every part of the BBW actuator, being particularly intense in the reduction gear-ball-screw system (due to the high reduction ratio) and in the master cylinder (as a result of tight sealing used in the cylinder). In order to gain some insight on how this issue affects our application, a series of open-loop experiences in the BBW actuator were prepared. The idea is to apply a relatively slow ramp (2.4 A/s) to the motor current and observe the response of the system states, such as motor speed and hydraulic pressure. As it can be seen Figure 6.4(a), the BBW actuator exhibits the typical stick-slip motion, which can be qualitatively described as follows: *i*) the increasing motor torque eventually overcomes the static friction load (see the green circles in Figure 6.4(a)) and starts moving the master cylinder's piston (slip phase); *ii*) by pushing the piston, the pressure in the master cylinder increases, which in turn raises the motor load, and, more importantly, the friction levels (as we will see shortly, friction

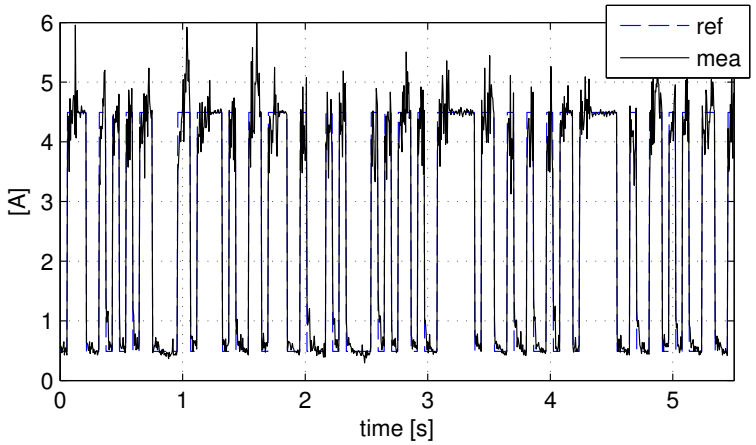

(a) input current

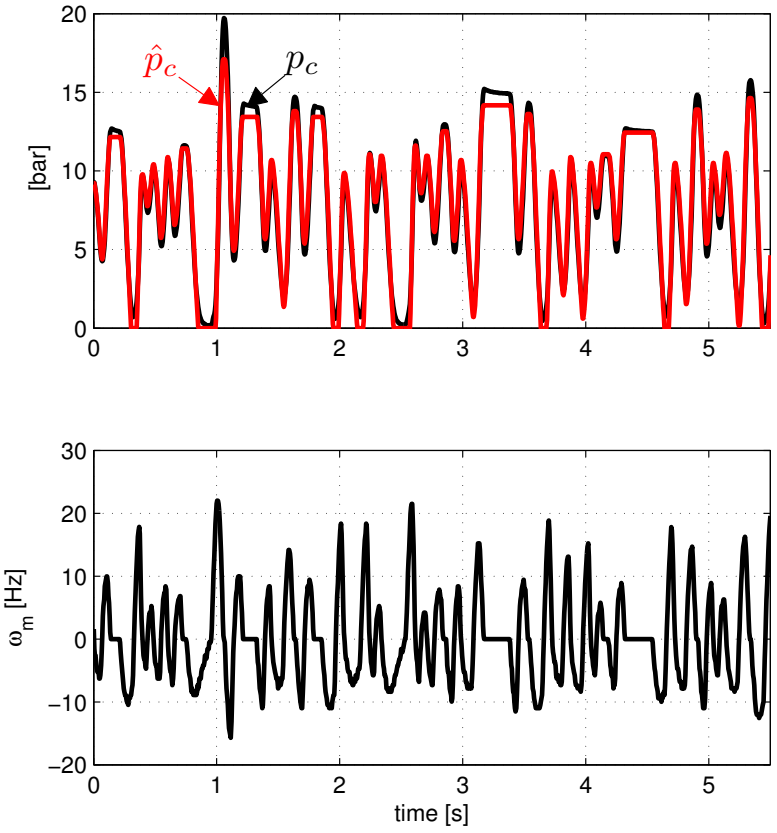

(b) id. test: p_c=measured pressure; $\hat{p}_c$=estimated from the model

Figure 6.3: Experimental validation of the hydraulic sub-block of the control-oriented model (note that, in this test, ω_m is regarded as the pseudo-input for the hydraulic model, while p_c is the output).

displays a load-dependent behaviour); *iii*) this increment in the total load will, at some point, surpass the motor torque, which will decelerate the piston and, ultimately, stop it (stick phase). This stick-slip pattern then repeats periodically throughout the test.

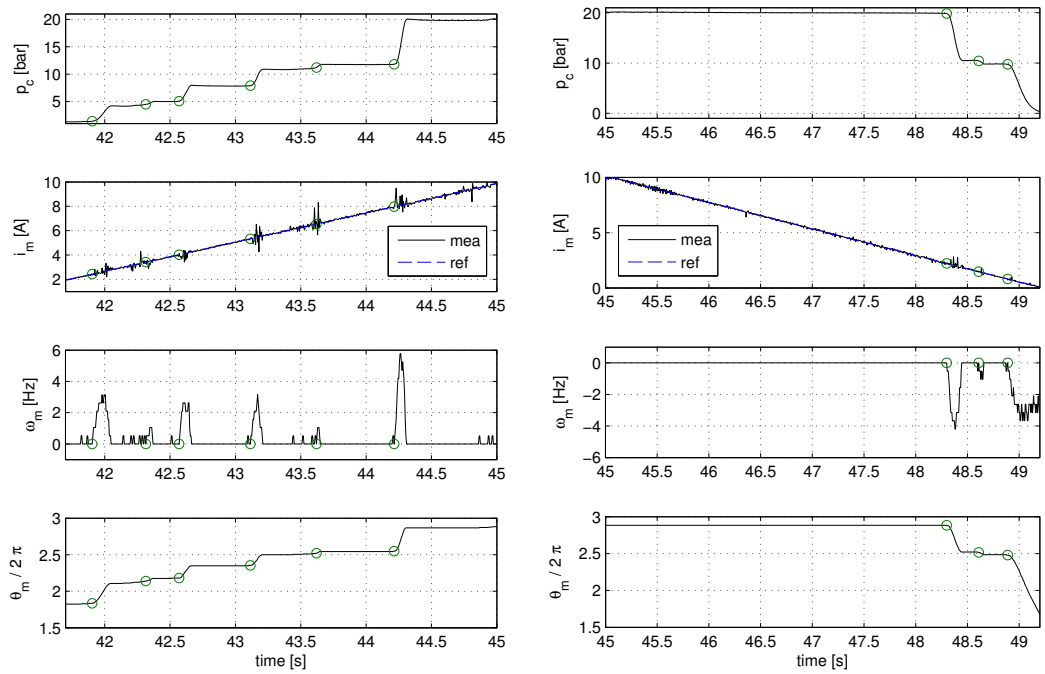

(a) (b)

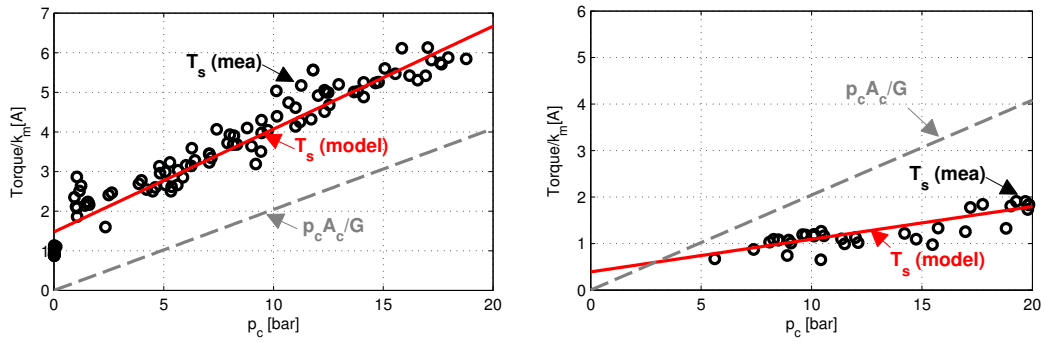

(c) breakaway torque ($di_m/dt > 0$)) (d) breakaway torque ($di_m/dt < 0$))

Figure 6.4: Experimental characterization of the breakaway torque in the BBW actuator. Notice: *i*) for convenience, the torque variables are translated to current, using the current/torque motor gain k_m; *ii*) the green circles represent the time instances where the breakaway occurs.

Besides the qualitative analysis of the actuator motion, this open-loop test can also be explored to infer the values of breakaway friction torque, i.e., the minimum value that will overcome the static friction. Toward that goal, it is necessary to estimate the friction torque and the time instants where the breakaway happens. The first estimative can be performed with the help of the relation (6.18a), while the breakaway's time instants are defined as

$$\Omega = \{t \mid \omega_m(t-i) = 0, \quad \omega_m(t+i) > 0, \quad \forall i \in (0, \overline{T}]\}$$

where $\overline{T}$ is the length of a time window where the piston motion is evaluated; for illustration purposes, the Ω set is highlighted by green circles in Figure 6.4. Assuming that the motor acceleration ($\dot{\omega}_m$) is relatively low in the domain Ω, thus the term $J_{eq}\dot{\omega}_m$ can be neglected

in (6.18a), the breakaway torque T_S can be approximated by

$$T_S(t) \approx k_m i_m(t) - \frac{A_c}{G} p_c(t), \qquad t \in \Omega \tag{6.21}$$

Figure 6.4(c) shows the experimental results obtained with this estimator, plotted against the pressure p_c, during the rising part of the current ramp (i.e., $di_m/dt > 0$). These results suggest that T_S increases with the pressure in the master cylinder p_c. To some extent, this is a reasonable behaviour, since the type of actuator under study is expected to display "load-dependence" friction, as explained in [226]. Furthermore, taking into account the (almost) linear increase of T_s with the p_c, shown by the experimental data, it is appropriate to consider an affine model for the breakaway torque T_s, that is

$$\hat{T}_S(p_c) = T_{S0} + T_{Sp} p_c \tag{6.22}$$

where T_{S0}, T_{Sp} are parameters. As shown in Figure 6.4(c), there is a reasonable agreement between the measurements and this affine model. Another point worth stressing is related to the control effort that the motor needs to develop in order to overcome the (static) friction. To better explain this point, recall that, in steady state conditions ($\dot{\omega}_m = 0$), and in light of (6.18a), we will have the following condition

$$k_m i_m = \frac{A_c}{G} p_c + T_f \tag{6.23}$$

This means that the torque developed by the motor ($k_m i_m$) will be used to generate the braking pressure ($\frac{A_c}{G} p_c$) and overcome the friction disturbance T_f. Now, inspecting again Figure 6.4(c), we can observe that the (breakaway) friction disturbance is significantly higher ($2-3$ times) than the expected load torque associated with the braking pressure. This result clearly emphasizes the dominant role that friction disturbance have in the BBW actuator.

It is also useful to analyse the results of the open-loop test when the motor current is decreasing ($di_m/dt < 0$), which are illustrated in Figure 6.4(b). The most striking result to emerge from the data is that, for $t \in [45, 48.3]$s the motor current diminishes from 10 A (equivalent to 100% of the nominal torque) to 2A, but the motor position and the pressure remain unchanged. This loss of control authority can be, again, explained by the strong effect of friction. Interestingly, the breakaway torque for this situation ($\omega_m < 0$) shows much lower friction levels than the situation where the piston is being pushed (see Figure 6.4(d)), which puts in evidence the large friction asymmetries in the actuator.

6.4.1 Friction Map

The analysis carried out thus far has focused on the characterization of the breakaway friction torque; we will now move our attention to the friction study when the actuator is moving, i.e., $|\omega_m| > 0$. In this operation mode, the most relevant factors that need to be considered are the well-known Coulomb friction, viscous friction and Stribeck effects [213]. Classically, these factors can be modelled though a static map, having as main input the speed difference between the contact bodies in the actuator (ω_m). In addition, given the load-dependent friction that affects the actuation, illustrated in Figure 6.4, it seems appropriate to also conjecture the possibility of having some terms in the friction map that increase linearly with hydraulic pressure p_c. Accordingly, the friction map under

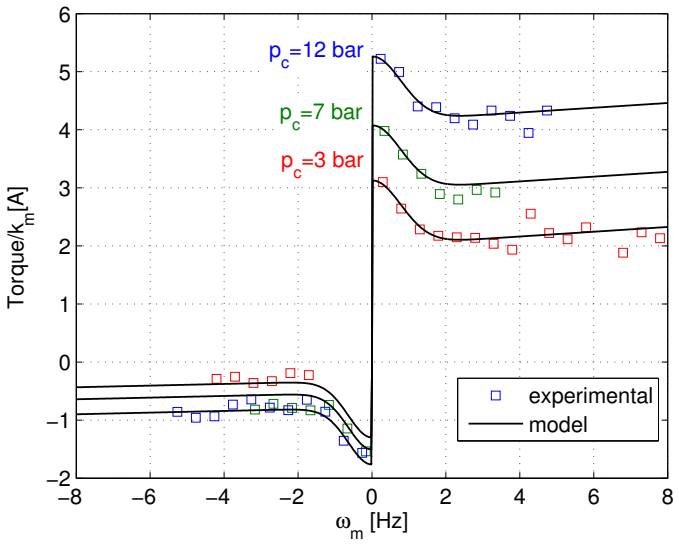

Figure 6.5: Comparison between the experimental friction map and the model (6.24).

Table 6.2: Nominal values of the friction model.

Mode	T_{C0} [A]	T_{Cp} [A/bar]	σ_2 [A/rad/s]	ΔT [A]	ω_s [rad/s]
$\omega_m > 0$	1.28	0.23	0.0065	1.12	6.9
$\omega_m < 0$	0.16	0.05	0.0023	0.97	5.6

consideration for the BBW actuator is given by:

$$T_f(\omega_m, p_c) = (T_{C0} + T_{Cp} p_c)\,\mathrm{sgn}(\omega_m) + \sigma_2 \omega_m + \Delta T e^{-\left(\frac{\omega_m}{\omega_s}\right)^2} \mathrm{sgn}(\omega_m) \qquad (6.24)$$

where T_{C0} is the (no-load) Coulomb friction torque, T_{Cp} the Coulomb friction increase due to pressure in the master cylinder, ΔT a torque difference between the breakaway and the Coulomb torque, ω_s the Stribeck speed and σ_2 the viscous friction coefficient.

Notice that, in practice, the hydraulic pressure affects, not only the Coulomb term, but also the viscous and Stribeck terms, i.e., the parameters σ_2 and ΔT may change with p_c. However, we verified that the load-dependence is more pronounced in the Coulomb term, and, to avoid over-complicating the friction model, the load effects in the viscous and Stribeck terms were neglected. Another aspect needing special attention is the friction asymmetries with respect to the direction of movement. To address this issue, the model's parameters in (6.24) must be switched in accordance with the direction of movement, i.e.,

$$\circ = \begin{cases} \circ^+, & \text{if } \omega_m > 0 \\ \circ^-, & \text{otherwise} \end{cases} \qquad (6.25)$$

where $\circ$ represents one of the parameters $T_{C0}, T_{Cp}, \sigma_2, \Delta T, \omega_s$.

Toward the experimental validation of (6.24), we arranged another series of open-loop experiments with the BBW actuator, which follows a similar pattern to the ones employed in the breakaway test. More specifically, after imposing in the motor current a ramp

setpoint (2.4 A/s), the pressure and speed measures were used to estimate the friction torque through the relation (6.18a). The experimental results depicted in Figure 6.5 show two features that were already noticed in the breakaway torque tests, namely i) the friction torque increases with the hydraulic pressure p_c, and ii) the direction of motion plays a major role in the friction levels (in particular, the friction disturbance is much more severe in the domain $\omega_m > 0$). Moreover, by fitting the experimental data with (6.24) we can also observe a very satisfactory agreement between the measures and the friction model (the parameters of the model, obtained with non-linear fitting techniques, are shown in Table 6.2).

Remark 6.1. it is a well-known fact that the friction map (6.24) will not be able to capture some features of the friction disturbance, such as presliding displacement, frictional lag or the variable break-away force [213]. For representing these features, we would need to use a more complicated friction model, such the LuGre model [226, 227]. Nonetheless, our main focus here is to employ practical control-oriented models, which, albeit only providing an approximation of the reality, are easier to treat at the control design stage. As a result, we will assume that the friction can be modelled by a static map, and endow the BBW controller with robust mechanisms to cope with modelling errors.

6.4.2 A Practical LP for Friction Compensation

The friction torque model (6.24), in addition to the nonlinearities, also depends on a set of parameters $(T_{C0}, T_{Cp}, \sigma_2, \Delta T, \omega_s)$ that are subject to uncertainty. In order to facilitate the effective handling of this uncertainty by the BBW controller, we will present in this section a Linear Parameterization (LP), suitable for (model-based) friction compensating with adaptive methods. With this objective in mind, it is worth highlighting the fact that the parameters $(T_{C0}, T_{Cp}, \sigma_2)$ have a linear effect in (6.24) and, as a result, they are already in a proper format to be incorporated in the LP. However, the exponential $f_e(\omega_m, \omega_s) = e^{-\left(\frac{\omega_m}{\omega_s}\right)^2}$, related with the Stribeck effect, is nonlinear in the parameter ω_s. In order to derive a LP to this term, in the sequel, we will consider that the Stribeck speed is constrained to the domain: $\underline{\omega_s} \leq \omega_s \leq \overline{\omega_s}$.

Normalization of the Stribeck effect

In general, the Stribeck speed is a parameter that varies from application to application and is subject to a wide range of variation, e.g. [228] argues that ω_s can vary between 0.00001 to 0.1 m/s (equivalent linear motion). In order to keep our approach general, it is useful to introduce a normalization factor in the parameter ω_s. With this goal in mind, let us re-parameterize the ω_s range as

$$\omega_s \in [\underline{\alpha}\hat{\omega}_s, \overline{\alpha}\hat{\omega}_s] = [\underline{\omega_s}, \overline{\omega_s}] \tag{6.26}$$

where $\hat{\omega}_s \in [\underline{\omega_s}, \overline{\omega_s}]$ is the (nominal) estimative for the Stribeck speed and $\underline{\alpha} \in (0, 1], \overline{\alpha} \in (1, \infty)$ are selected in order to keep the original range intact. Introducing this normalization in the exponential term:

$$f_{en}(\omega_m, \alpha) = f_e(\omega_m, \alpha\hat{\omega}_s) = e^{-\left(\frac{1}{\alpha}\right)^2\left(\frac{\omega_m}{\hat{\omega}_s}\right)^2} \tag{6.27}$$

where $\alpha \in [\underline{\alpha}, \overline{\alpha}]$, and defining the additional normalization variables:

$$X = \left(\frac{\omega_m}{\hat{\omega}_s}\right)^2, \quad \eta = \left(\frac{1}{\alpha}\right)^2 \tag{6.28}$$

the nonlinear Stribeck effect can be represented with the equivalent function:

$$f(X, \eta) = e^{-\eta X} \tag{6.29}$$

where $\eta \in [\underline{\eta}, \overline{\eta}] = \left[\frac{1}{(\overline{\alpha})^2}, \frac{1}{(\underline{\alpha})^2}\right]$ is an unknown parameter, which models the uncertainty in the estimation $\hat{\omega}_s$, and X the normalized input.

Remark 6.2. normally, the Stribeck effect is represented by the generic expression: $e^{-|\omega_m/\hat{\omega}_s|^\chi}$, with typical values of $\chi = 1$ (Tustin model), $\chi = 2$ (Gaussian model) and in general $\chi \in [0.5, 1] \cup \{2\}$ [228, 229]. In this work, it was assumed $\chi = 2$, but the described method to derive the optimal LP can easily be adapted to other values of χ, by changing the normalized variables as $X = |\omega_m/\hat{\omega}_s|^\chi, \eta = 1/\alpha^\chi$.

Formulation of the Optimal LP problem

In order to approximate (6.29) with a LP, we will consider functions with the following format:

$$f_{LP}(X, \boldsymbol{\theta}, \mathbf{w}) = \underbrace{\begin{bmatrix} h_1(X, \mathbf{w}) & \dots & h_d(X, \mathbf{w}) \end{bmatrix}}_{\boldsymbol{h}^T(X, \mathbf{w})} \boldsymbol{\theta} \tag{6.30}$$

where $h_i(X, \mathbf{w}), i = 1, \dots, d$ are the basis functions, $\boldsymbol{\theta} \in \mathbb{R}^d$ the linear parameters, $\mathbf{w} \in \mathbb{R}^m$ the weights that characterize the (possible) nonlinear basis functions. The selection of these weights will be carried out through the following procedure:

Proposition 6.1. *The weight* $\mathbf{w}^*$ *that minimizes the fitting error between the LP* $f_{LP}(X, \boldsymbol{\theta}, \mathbf{w}^*)$ *and* $f(X, \eta)$ *over the parametric range of interest* $(X, \eta) \in [0, \overline{X}] \times [\underline{\eta}, \overline{\eta}]$*, is defined as the solution of the following optimization problem:*

$$\begin{aligned}
&\min_{\mathbf{w} \in \mathbb{R}^d} \epsilon_T(\mathbf{w}) \\
&s.t. \qquad \epsilon_T(\mathbf{w}) = \int_{\underline{\eta}}^{\overline{\eta}} \epsilon(\eta, \mathbf{w}) d\eta \\
&\epsilon(\eta, \mathbf{w}) = \int_0^{\overline{X}} \left(f(X, \eta) - \boldsymbol{h}^T(X, \mathbf{w}) \mathbf{G}^{-1}(\mathbf{w}) \mathbf{c}(\eta, \mathbf{w}) \right)^2 dX \\
&[\mathbf{G}(\mathbf{w})]_{ij} = \int_0^{\overline{X}} h_i(X, \mathbf{w}) h_j(X, \mathbf{w}) dX \\
&[\mathbf{c}(\eta, \mathbf{w})]_i = \int_0^{\overline{X}} h_i(X, \mathbf{w}) f(X, \eta) dX, \quad i, j = 1, \dots, d
\end{aligned}$$

where $\epsilon_T(\mathbf{w})$ *is defined as the total fitting error.*

The motivation and proof of the previous result was derived in Chapter 5.

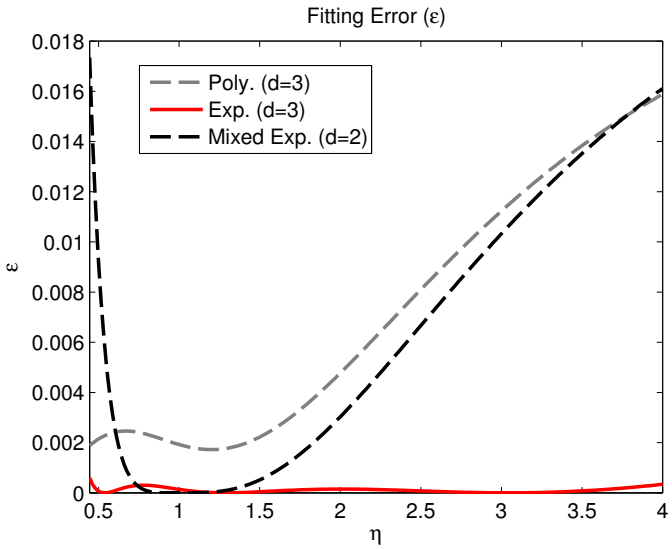

Figure 6.6: Fitting error $\epsilon(\eta, \mathbf{w}^*)$ evaluated for polynomials, exponentials and mixed exponentials (see Table 6.3).

Table 6.3: Total error ε_T for fitting (6.29) with different LPs.

	Number of basis (d)		
Basis Function	1	2	3
Lorentzian [218]	0.2833	-	-
Mixed Exponentials [214]	-	0.0224	-
Polynomial [216, 217]	-	0.197	0.0256
Exponentials	0.0976	0.0087	0.0004

Numerical Evaluation

In the remainder of the chapter, we will consider that the nominal/estimated Stribeck speed, $\hat{\omega}_s$, has an uncertainty of $\pm 50\%$, which is equivalent to $\underline{\alpha} = 0.5$, $\overline{\alpha} = 1.5$, and $\underline{\eta} = 0.444$, $\overline{\eta} = 4$. Further, we fixed $\overline{X} = 5$, since this is generally enough to cover the range where the Stribeck effect is pronounced. Due to the exponential nature of the Stribeck curve, the basis functions employed in this work also rely on exponentials

$$\boldsymbol{h}_E(X, \mathbf{w}) = \begin{bmatrix} e^{-w_1 X} & e^{-w_2 X} & \dots & e^{-w_d X} \end{bmatrix}^T \tag{6.31}$$

Next, the problem described in Proposition 6.1 was discretized and then tackled with a numerical solver [193], which enabled us to obtain the optimal weights $\mathbf{w}^*$.

To investigate the performance of the optimal LP, Table 6.3 represents the total fitting error metric, $\epsilon_T(\mathbf{w})$, evaluated for different types (and number) of basis functions. It is interesting to note that, from the LPs previously proposed in the literature, the Mixed Exponentials [214] provide a respectable fitting result when compared with the Lorentzian function [218] and the polynomial approach [216, 217]. Nevertheless, employing the fixed exponentials ($\boldsymbol{h}_E$), with the optimal selection of weights, a significant improvement is observed: incorporating two fixed exponentials contributes to a reduction of almost 60%

in the total fitting error, while three exponential produces an almost negligible error.

To further investigate the performance of these LPs, Figure 6.6 shows the evolution of the fitting error, $\epsilon(\eta, \mathbf{w}^*)$, for different values of η. Inspecting the Mixed Exponentials (ME) basis functions, it is clear that the fitting error is almost zero when η approaches 1 (i.e., α is near to 1), implying a small error in $\hat{\omega}_s$. These results are in accordance with the theoretical expectations for this approximation: the MEs were derived based on linearization techniques, thus it should present good results when $\hat{\omega}_s$ is close to the nominal point. However, these good results do not extend to situations when η departs from 1, and the ME ends up introducing significant fitting errors. On the other hand, employing fixed exponentials ($d = 3$), it can be observed that the fitting error is almost zero everywhere, which highlights the robustness of this LP against uncertainty in η (or in $\hat{\omega}_s$ estimation).

In summary, the optimal LP for approximating the normalized Stribeck effect (6.29), was found to be exponential based, with $d = 3$:

$$\boldsymbol{h}_{E3}(X) = \begin{bmatrix} e^{-0.538X} & e^{-1.289X} & e^{-3.043X} \end{bmatrix}^T \tag{6.32}$$

This enables us to approximate the original nonlinear friction map (6.24) with the following LP:

$$\begin{aligned} T_f(\omega_m, p_c) &= \boldsymbol{\theta}^T \boldsymbol{\varphi}(\omega_m, p_c)\,\mathrm{sgn}(\omega_m) \\ \boldsymbol{\varphi}(\omega_m, p_c) &= \begin{bmatrix} 1 & p_c & |\omega_m| & \boldsymbol{h}_{E3}^T\left(\left(\dfrac{\omega_m}{\hat{\omega}_s}\right)^2\right) \end{bmatrix}^T \end{aligned} \tag{6.33}$$

where $\boldsymbol{\theta} \in \mathbb{R}^n$, $n = 6$ and $\boldsymbol{\varphi}(\omega_m)\,\mathrm{sgn}(\omega_m)$ is the regressor.

There are two important factors that should be taken into consideration when implementing the above LP. First, the regressor function depends on the discontinuous function $\mathrm{sgn}(\omega_m)$, which makes the numerical calculation of this regressor sensitive to measurement errors and may excite high-frequency modes neglected during the modelling phase [230]. To mitigate this issue, the term $\mathrm{sgn}(\omega_m)$ will be approximated by a continuous function, based on a logistic sigmoid $c(\omega_m) = -1 + 2/(1 + e^{-k_c\omega_m}), k_c > 0$. This allows us to approximate the LP through the following continuous map:

$$T_f(\omega_m, p_c) \approx \boldsymbol{\theta}^T \boldsymbol{\Phi}(\omega_m, p_c), \tag{6.34a}$$

$$\boldsymbol{\Phi}(\omega_m, p_c) = \boldsymbol{\varphi}(\omega_m, p_c) c(\omega_m) \tag{6.34b}$$

The second factor that deserves special attention is related to the asymmetric levels of friction present in the actuator. These asymmetries make it convenient to switch the LP's parameters according to the direction of motion, i.e.,

$$\boldsymbol{\theta} = \begin{cases} \boldsymbol{\theta}^+, & \text{if } \omega_m > 0 \\ \boldsymbol{\theta}^-, & \text{otherwise} \end{cases} \tag{6.35}$$

where $\boldsymbol{\theta}^+$,$\boldsymbol{\theta}^-$ are the friction parameters associated with positive and negative speeds, respectively.

6.5 Controller Design

In this section, a control strategy for the BBW braking actuator will be developed. The control objective is a tracking one: design a control law for the motor current u such that the hydraulic pressure $x_3 = p_c$ follows, as fast as possible, the reference x_3^*. This pressure setpoint, normally defined by the driver or by an auxiliary safety system (like the ABS), is supposed to have known first ($\dot{x}_3^*$) and second ($\ddot{x}_3^*$) time derivatives. In accordance with the discussion presented in the previous sections, the design of this controller will rely on the reduced model (6.18) and in the optimal LP (6.34), i.e.,

$$\begin{aligned} \dot{x}_2 &= \frac{1}{J_{eq}}\left(k_m u - \alpha_3 x_3 - \boldsymbol{\theta}^T \boldsymbol{\Phi}(x_2, x_3)\right) && \text{(6.36a)} \\ \dot{x}_3 &= \frac{\alpha_2}{\alpha_1} x_2 + \delta(t) && \text{(6.36b)} \\ y &= x_3 - x_3^* && \text{(6.36c)} \end{aligned}$$

where y is the model output and $\alpha_3 = A_c/G$.

6.5.1 Input-Output Linearization and Normal Form

To gain additional insight regarding the model (6.36), it is helpful to determine its relative degree. Recall that, broadly speaking, the relative degree of single-input-single-output system is equal to number of times the output y needs to be differentiated until the control input u appears, for the first time, in the derivatives of y [96]. By considering the first and second time derivatives of the output:

$$\begin{aligned} \dot{y} &= \dot{x}_3 - \dot{x}_3^* = \frac{\alpha_2}{\alpha_1} x_2 + \delta(t) - \dot{x}_3^* \\ \ddot{y} &= \underbrace{\frac{\alpha_2}{\alpha_1 J_{eq}}}_{w^{-1}} \left(k_m u - \alpha_3 x_3 - \boldsymbol{\theta}^T \boldsymbol{\Phi}(.) + \underbrace{\frac{\alpha_1 J_{eq}}{\alpha_2} \dot{\delta}(t)}_{\gamma(t)} \right) - \ddot{x}_3^* \\ &= \frac{1}{w}\Big(k_m u - \alpha_3 x_3 - \boldsymbol{\theta}^T \boldsymbol{\Phi}(x_2, x_3) + \gamma(t) \Big) - \ddot{x}_3^* \qquad \text{(6.37)} \end{aligned}$$

it can be concluded that the actuator has relative degree two. Furthermore, according to the input-output (IO) linearization technique, the nonlinear terms in the previous relation can be cancelled by selecting the control input as

$$k_m u = \alpha_3 x_3 + \boldsymbol{\theta}^T \boldsymbol{\Phi}(x_2, x_3) - \gamma(t) + w\,(v + \ddot{x}_3^*) \qquad \text{(6.38)}$$

where v is a new control term. Replacing this law in (6.37) produces a second-order linear dynamic, i.e., $\ddot{y} = v$, which can straightforwardly stabilized by a suitable selection of v. Moreover, given that (6.36) has relative degree two (equal to the number of states), this control-oriented model does not have zero-dynamics. This result is also evident from the normal form associated with the reduced model (6.36):

$$\begin{aligned} \dot{e}_1 &= e_2 && \text{(6.39)} \\ \dot{e}_2 &= \frac{1}{w}\Big(k_m u - \alpha_3 x_3 - \boldsymbol{\theta}^T \boldsymbol{\Phi}(x_2, x_3) + \gamma(t) - w\ddot{x}_3^* \Big) \end{aligned}$$

where $e_1 = y = x_3 - x_3^*$ and $e_2 = \dot{y}$.

6.5.2 Adaptive-Robust Controller

The control law (6.38), although effective in handling the model nonlinearities, is dependent on the exact knowledge of the friction parameters ($\boldsymbol{\theta}$) and it needs the value of the function $\gamma(t)$. In practice, both $\boldsymbol{\theta}$ and $\gamma(t)$ may change throughout the actuator's operation conditions (e.g., with temperature, mechanical wear, etc.) and are also subject to uncertainty. To cope with these uncertainties the ideal controller will be modified in two directions. Firstly, adaptive mechanisms will be included in the controller to deal with the parametric uncertainty in $\boldsymbol{\theta}$; and, secondly, $\gamma(t)$ will be treated as a disturbance that the controller should robustly attenuate.

Taking into account the normal form (6.39), the design of this adaptive-robust controller can be simplified by using a "sliding-like" variable s:

$$s = e_2 + L_1 e_1 \tag{6.40}$$

where L_1 is a positive constant. It is easy to see that if s is maintained at zero, then the pressure error will decrease to zero with a first order dynamic, i.e., $\dot{e}_1 = -L_1 e_1$. Consequently, the controller design can be based on the s variable, which is a common practice in servo control applications[145, 221, 230]. For control design purposes, it is also convenient to determine the sliding variable dynamics:

$$\dot{s} = \frac{1}{w}\left(k_m u - \alpha_3 x_3 - \boldsymbol{\theta}^T \boldsymbol{\Phi}(x_2, x_3) + \gamma(t) - w\left(\ddot{x}_3^* - L_1 e_2\right) \right) \tag{6.41}$$

In order to stabilize this s dynamic we propose the following control law:

$$k_m u = \alpha_3 x_3 + \hat{\boldsymbol{\theta}}^T \boldsymbol{\Phi}(x_2, x_3) + \hat{w}\left(\ddot{x}_3^* - L e_2\right) - \rho \tanh\left(\frac{s}{\varepsilon}\right) - L_2 s \tag{6.42}$$

where L_2 is a positive tuning constant, and $\hat{\boldsymbol{\theta}}$, $\hat{w}$ are estimates of $\boldsymbol{\theta}$ and w, which will be defined by an adaptive mechanism (to be introduced shortly). From an engineering standpoint, the structure of the proposed controller can be explained as follows: the first two terms attempt to cancel the load torque resulting from the friction and the generation of the hydraulic braking pressure. The third term appears due to tracking formulation of the problem and the sliding variable definition. The fourth term employs a continuous sliding mode action to attenuate the effect of the disturbance $\gamma(t)$, where $\varepsilon > 0$ is the width of the boundary layer; finally, the last term is incorporated to improve the transient response.

At this stage, it is worth pointing out that, besides the friction parameters $\hat{\boldsymbol{\theta}}$, the proposed controller will also perform an on-line adaptation of the w parameter. From a practical perspective, this adaption is also relevant, because w constitutes another source of parametric uncertainty (e.g., w depends on the pad's stiffness k_p, which, as already discussed, varies in time). With regard to the other two parameters in the control law (k_m, α_3), we treat them as known constants; in our view, this approach is justified by the fact that both variables are known with a reasonable accuracy, e.g., $\alpha_3 = A_c/G$ depends only on the actuator's geometric properties, while the current/torque gain k_m is generally a well-known quantity.

6.5.3 Stability and Adaptive Laws

As commonly done in the construction of robust controllers, we will work under the premise that the disturbance $\gamma(t)$ and the parameters $\boldsymbol{\theta}, w$ are upper bounded

$$|\gamma(t)| = |\frac{\alpha_1 J_{eq}}{\alpha_2}\dot{\delta}(t)| \ \leq \ \frac{\alpha_1 J_{eq}}{\alpha_2}\overline{\delta}_1 \ \leq \ \rho, \tag{6.43}$$

$$0 < w \leq M_w, \quad \|\boldsymbol{\theta}\| \leq M_\theta \tag{6.44}$$

where ρ, M_w, M_θ are constants. To investigate the stability of the proposed adaptive-robust controller, as well as to find the adaptive laws for the parameters' estimates $\hat{\boldsymbol{\theta}}$, $\hat{w}$, consider the following candidate Lyapunov function:

$$V(s, \tilde{\boldsymbol{\theta}}, \tilde{w}) = \frac{w}{2}s^2 + \frac{1}{2}\tilde{\boldsymbol{\theta}}^T \boldsymbol{\Gamma}_\theta^{-1}\tilde{\boldsymbol{\theta}} + \frac{1}{2\Gamma_w}\tilde{w}^2 \tag{6.45}$$

where $\tilde{\boldsymbol{\theta}} = \hat{\boldsymbol{\theta}} - \boldsymbol{\theta}$ and $\tilde{w} = \hat{w} - w$ represent the parametric estimation errors, and $\boldsymbol{\Gamma}_\theta$, Γ_w are positive-definite gains. Calculating the time derivative of V, it can be shown that:

$$\begin{aligned} \dot{V} \ &= \ -L_2 s^2 + \tilde{\boldsymbol{\theta}}^T \left[\boldsymbol{\Phi}(x_2, x_3)s + \boldsymbol{\Gamma}_\theta^{-1}\dot{\hat{\boldsymbol{\theta}}}\right] \\ &\quad +\tilde{w}\left[(\ddot{x}_3^* - Le_2) + \Gamma_w^{-1}\dot{\hat{w}}\right] + s\left[\gamma(t) - \rho\tanh\left(\frac{s}{\varepsilon}\right)\right] \end{aligned} \tag{6.46}$$

The adaptation law adopted in this work is based on the switching-σ method[231]:

$$\dot{\hat{\boldsymbol{\theta}}} = -\boldsymbol{\Gamma}_\theta\left(\boldsymbol{\Phi}(x_2, x_3)s + \sigma_\theta(\hat{\boldsymbol{\theta}})\hat{\boldsymbol{\theta}}\right), \ \sigma_\theta = \begin{cases} 0, \text{ if } \|\hat{\boldsymbol{\theta}}\| \leq M_\theta \\ \sigma_0 \text{ otherwise} \end{cases}$$

$$\dot{\hat{w}} = -\Gamma_w\left(s\left(\ddot{x}_3^* - Le_2\right) + \sigma_w(\hat{w})\hat{w}\right), \sigma_w = \begin{cases} 0, \text{ if } |\hat{w}| \leq M_w \\ \sigma_0 \text{ otherwise} \end{cases} \tag{6.47}$$

where $\sigma_0 > 0$ is a tuning parameter. The idea behind the switching terms is to introduce leakage in the integration process of the adaption law, whenever excessive estimates are present; this leakage ends up attenuating the parameter-drift issues, which is one of the main concerns in this approach. Replacing (6.47) in $\dot{V}$ and by noticing that $|s\gamma(t)| \leq \rho|s|$, one has:

$$\dot{V} \leq -L_2 s^2 - \sigma_\theta(.)\tilde{\boldsymbol{\theta}}^T\hat{\boldsymbol{\theta}} - \sigma_w(.)\tilde{w}\hat{w} + \rho\left(|s| - \tanh\left(\frac{s}{\varepsilon}\right)s\right)$$

Now, consider the following auxiliary results

$$\begin{aligned} \text{A.} \quad -\sigma_\theta(.)\tilde{\boldsymbol{\theta}}^T\hat{\boldsymbol{\theta}} \leq -\sigma_0\tilde{\boldsymbol{\theta}}^T\hat{\boldsymbol{\theta}} + 2\sigma_0 M_\theta^2 \leq \\ -\frac{\sigma_0}{2}\|\tilde{\boldsymbol{\theta}}\|^2 + \frac{\sigma_0}{2}\|\boldsymbol{\theta}\|^2 + 2\sigma_0 M_\theta^2 \end{aligned} \tag{6.48}$$

$$\begin{aligned} \text{B.} \quad -\sigma_w(.)\tilde{w}\hat{w} \leq -\sigma_0\tilde{w}\hat{w} + 2\sigma_0 M_w^2 \leq \\ -\frac{\sigma_0}{2}\tilde{w}^2 + \frac{\sigma_0}{2}w^2 + 2\sigma_0 M_w^2 \end{aligned} \tag{6.49}$$

$$\text{C.} \quad 0 \leq |s| - s\tanh\left(\frac{s}{\varepsilon}\right) \leq 0.2785\varepsilon = \tilde{k}\varepsilon \tag{6.50}$$

The first inequality of (6.48) and (6.49) is a well-known result for the switching-σ method [231, p. 561], while the second inequality follows from the completion of squares; inequalities (6.50) are demonstrated in [232, Lemma A.5.1]. Using these three auxiliary results, $\dot{V}$ can be further bounded by:

$$\dot{V} \leq -L_2 s^2 - \frac{\sigma_0}{2}\|\tilde{\boldsymbol{\theta}}\|^2 - \frac{\sigma_0}{2}\tilde{w}^2 + \underbrace{\frac{5\sigma_0}{2}\left(M_w^2 + M_\theta^2\right) + \rho\tilde{k}\varepsilon}_{\lambda_2}$$

where $\tilde{k} \geq 0.2785$. Selecting $\lambda_1 = \min\left(\frac{2L_2}{w}, \frac{\sigma_0}{\lambda_{min}(\boldsymbol{\Gamma}_\theta^{-1})}, \sigma_0\Gamma_w\right)$, where $\lambda_{min}(\boldsymbol{\Gamma}_\theta^{-1})$ is the smallest eigenvalue of $\boldsymbol{\Gamma}_\theta^{-1}$, we finally get

$$\dot{V} \leq -\lambda_1 V + \lambda_2 \tag{6.51}$$

This inequality paves the way for the main result of this section:

Proposition 6.2. *Consider the system* (6.41) *controlled by* (6.42), (6.47). *It holds that:*

1. *the signals s, $\hat{\boldsymbol{\theta}}$, $\hat{w}$ are bounded; in particular:*

$$|s(t)| \leq \sqrt{\frac{2}{w}\max\left(V(0), \frac{\lambda_2}{\lambda_1}\right)} \tag{6.52}$$

2. *the signal s is ultimately bounded by:*

$$\lim_{t\to\infty}|s(t)| \leq \sqrt{\frac{5\sigma_0\left(M_w^2 + 2M_\theta^2\right) + 2\rho\tilde{k}\varepsilon}{w \times \min\left(\frac{2L_2}{w}, \frac{\sigma_0}{\lambda_{min}(\boldsymbol{\Gamma}_\theta^{-1})}, \sigma_0\Gamma_w\right)}} \tag{6.53}$$

Proof. By the comparison Lemma [96], the differential inequality (6.51) implies that $V(t)$ is upper bounded by:

$$V(t) \leq \frac{\lambda_2}{\lambda_1} + e^{-\lambda_1 t}\left(V(0) - \frac{\lambda_2}{\lambda_1}\right) \leq \max(V(0), \frac{\lambda_2}{\lambda_1}) \tag{6.54}$$

Since, $V(t)$ is also lower bounded:

$$\frac{w}{2}s^2 + \frac{\lambda_{min}(\boldsymbol{\Gamma}_\theta^{-1})}{2}\|\tilde{\boldsymbol{\theta}}\|^2 + \frac{1}{2\Gamma_w}\tilde{w}^2 \leq V(t) \tag{6.55}$$

we can conclude that: $|s(t)| \leq \sqrt{\frac{2}{w}V(t)}$, yielding (6.52); the boundedness of the estimates $\hat{\boldsymbol{\theta}}$, $\hat{w}$ is evident from the "leaky" integrator adopted in the adaption law (6.47). As for the ultimate boundedness of s: it follows from the fact that $\lim_{t\to\infty}|s(t)| \leq \lim_{t\to\infty}\sqrt{\frac{2}{w}V(t)} \leq \sqrt{\frac{2}{w}\frac{\lambda_2}{\lambda_1}}$. □

Table 6.4: Controller's parameters.

Variable	Symbol	**Value**
controller gain	L_1	38
controller gain	L_2	38
upper bound for $\|\gamma(t)\|$	ρ	0.014
width of boundary layer	ε	150
leakage factor	σ_0	0.1
Adaptive gains:		
$\mathbf{\Gamma}_\theta^+ = \text{diag}\left(\begin{bmatrix}2 & 2 & 0.1 & 1.4 & 1.4 & 1.4\end{bmatrix}\right) \times 10^{-3}$		
$\mathbf{\Gamma}_\theta^- = \text{diag}\left(\begin{bmatrix}2 & 2 & 0.1 & 1.4 & 1.4 & 1.4\end{bmatrix}\right) \times 10^{-4}$		
$\Gamma_w = 10^{-9}$		

* $\mathbf{\Gamma}_\theta^+$ represents the adaptation gains employed during positive velocity range, and $\mathbf{\Gamma}_\theta^-$ contains the gains for the negative velocities.

Remark 6.3. given that s will eventually enter inside the set $\{|s| \leq \sqrt{\frac{2}{w}\frac{\lambda_2}{\lambda_1}}\}$, it can also be shown that the pressure tracking error is ultimately bounded by [145]:

$$\lim_{t\to\infty} |e_1| \leq \frac{1}{L_1}\sqrt{\frac{2}{w}\frac{\lambda_2}{\lambda_1}}, \tag{6.56}$$

Inspecting this relation, together with (6.53), reveals that as long as L_1, L_2 and the adaption gains (i.e., the terms in the denominator of (6.56)) are sufficiently high, the tracking errors can be made smaller. Nevertheless, due to practical limitations (control saturation, noise sensibility, etc.) these gains cannot be set too high, and the adaptive approach is only viable as long as the term λ_2 (the numerator in (6.56)) presents a moderate value.

6.6 Experimental Validation

The validation of the adaptive-robust controller was performed through a series of experimental tests carried out in a test bench, whose results and discussion presented in this section. Throughout these tests, the BBW actuator, already introduced in Section 6.2, was controlled through a low-cost digital signal processor (DSP), Freescale MC9S12XE. This controller samples the measurements from the master cylinder's pressure and motor position (through an encoder with 100 pulses per revolution) at a rate of 200 Hz, which is also the update rate of the discretized version of the pressure controller. Since the controller needs information about the motor speed, and given that this variable is not measured, it becomes necessary to calculate it through the derivation of the position signal. To robustify the derivative operation against measurement noise, we employed the well-known polynomial fitting technique [233], which, for our application, was set up to fit the past three position samples with a second-order polynomial. Finally, the DSP is also responsible for implementing the inner loop for the motor current; this inner loop in executed in

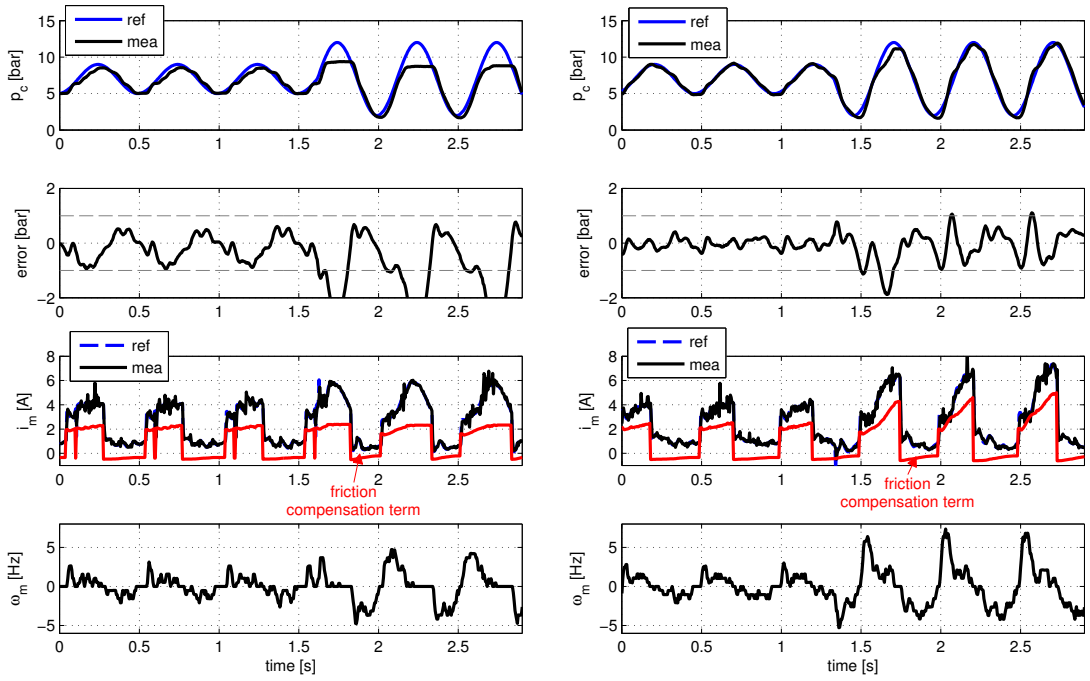

(a) PD with nominal friction compensation

(b) adaptive-robust controller

Figure 6.7: Experimental comparison between two control strategies for tracking the braking pressure.

the DSP at a faster rate (1000Hz) and generates, through a Proportional+Integral (PI) control law, the switching signals for a H-bridge power converter that feeds the electric motor. Additional details on this inner loop can be found on references [208, 222].

In what follows, the presentation and discussion of the experimental tests are divided into four parts. In the first two, we will investigate how the proposed adaptive-robust controller performs in comparison with other friction-compensation techniques, namely: *i*) Proportional+Derivative (PD) control law+nominal friction, and, *ii*) dither-based friction compensation. The final two experimental tests will show the response of the proposed controller to general setpoints (steps and ramps), as well as real-life braking setpoints.

6.6.1 Nominal vs Adaptive Friction Compensation

As an initial attempt to comply with the control specifications, we start by implementing a simple PD control, with nominal friction compensation. This is a reasonable approach to start with, since, in practice, some preliminary experiments can be performed in order to construct an estimative for the steady-state friction map (as discussed in Section 6.4.1). The PD control law was built from (6.42), with the adaptive mechanism disabled, i.e., $\boldsymbol{\Gamma}_\theta = \mathbf{0}, \Gamma_w = 0$, gains $L_1 = L_2 = 38$ and fixed estimates $\hat{w} = w$, $\rho = 0$; the (fixed) estimative of the friction parameters $\hat{\boldsymbol{\theta}}$ was obtained by fitting the nominal friction map shown in Figure 6.5 with the LP (6.34). From the sinusoidal tracking results presented in Figure 6.7(a) one can observe that, as long as the friction levels are close to the nominal ones ($t \in [0, 1.5]s$), this control law ensures a satisfactory tracking performance, with pressure error inferior to 1 bar. However, at $t \geq 1.5s$, the operation window to which the nominal friction model is valid changed (the sine amplitude of the pressure setpoint

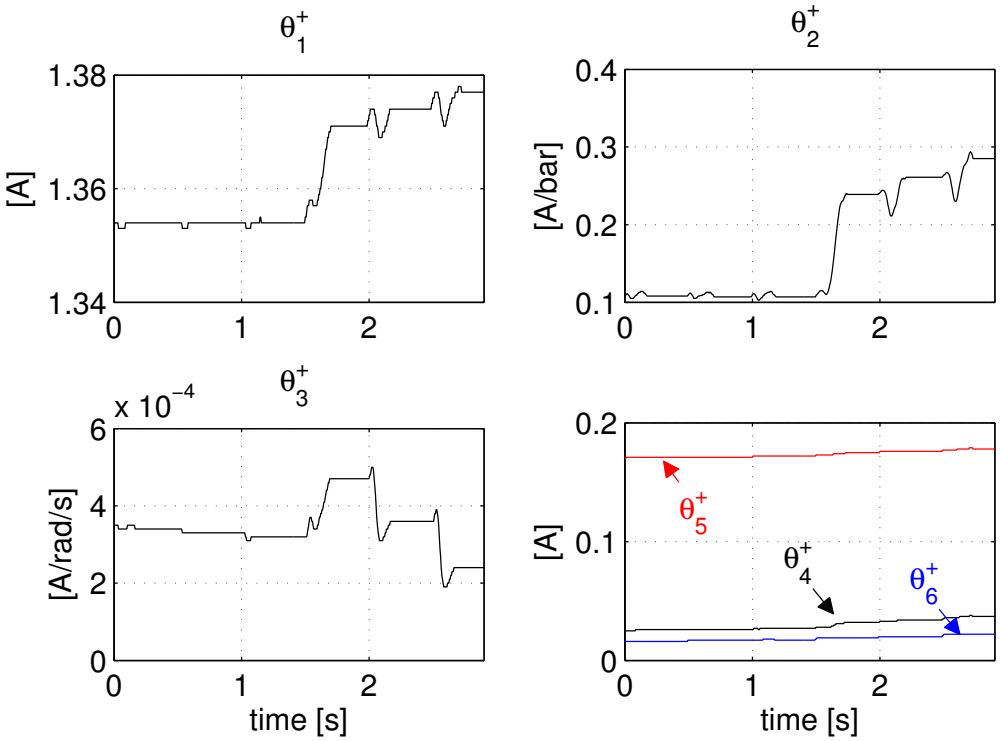

Figure 6.8: Parameter adaption of the friction parameters $\hat{\boldsymbol{\theta}}^{+}$ (positive velocities) during the experimental test shown in Figure 6.7.

increases), which introduces a parametric disturbance that the PD controller is unable to handle, generating significant errors in the pressure control (see the time-period $t \geq 1.5s$).

Next, the adaptive-robust controller was evaluated using the parameters configuration specified in Table 6.4. Just like the PD control, the adaptive law offers good tracking capabilities for the nominal friction situation (see Figure 6.7(b) for $t \in [0, 1.5]s$), but, this time, the proposed controller is able to successfully cope with the parametric disturbance ($t \geq 1.5s$), showing a quick transient response and low tracking error in steady state. The evolution of the parameter estimation during this test is also represented in Figure 6.8; for the sake of brevity, we only show the parameter adaption of the friction parameter $\hat{\boldsymbol{\theta}}^{+}$ (positive speeds), as these are the ones that have higher uncertainty. Interestingly, these data reveal that, after introducing the setpoint disturbance at $t = 1.5s$, there is a significant change in the parameter estimation, particularly in θ_2^{+}, in an effort to track the new friction conditions. Notice that the main objective of the controller is just the pressure tracking, and not parametric estimation (which will only be met if the reference signal has the persistence of excitation property [145]).

6.6.2 Dither vs Adaptive Friction Compensation

Dither is another common approach to mitigate friction disturbances [213], and was used in previous research on the development of BBW control systems (see, e.g., [208], [209]). The idea behind this technique is to inject in the motor torque a high-frequency auxiliary signal, e.g., sinusoidal, such that the actuator is always on the move (or on the verge of movement), in an effort to attenuate the effects of the static friction phenomenon, which is one of the most difficult disturbances with which the controller has to cope. In the scope of

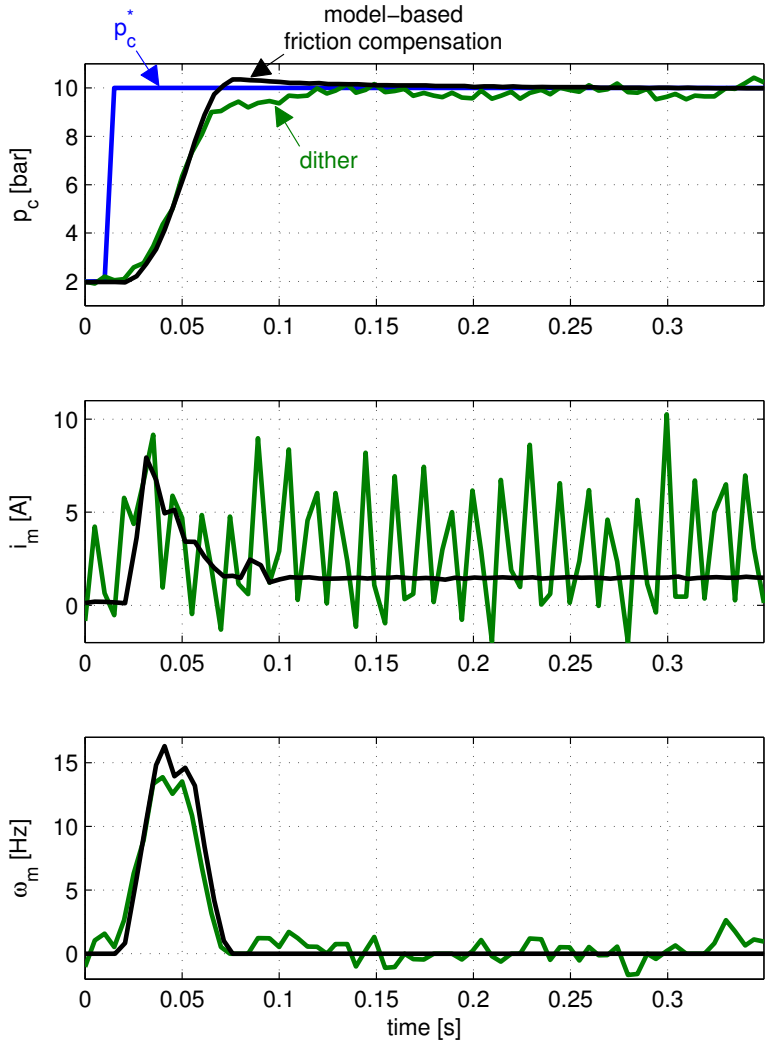

(a) Transient response

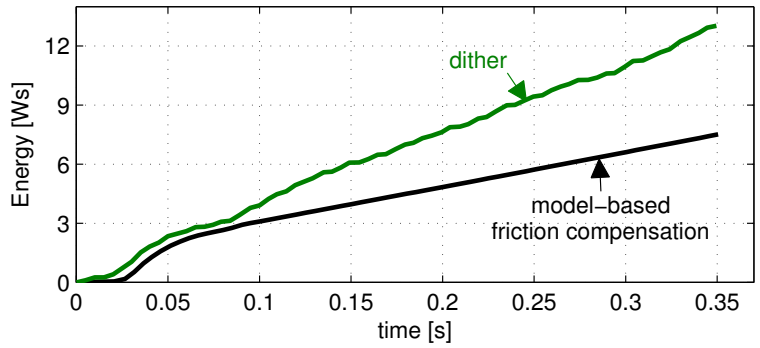

(b) energy consumption of the actuator

Figure 6.9: Experimental comparison between the dither technique and the model-based friction compensation (employed in the adaptive-robust controller).

the BBW controller development, it is useful to investigate how the model-based friction compensation, employed in our controller, performs in comparison with the dither friction compensation used in previous research. Accordingly, in this section, we will compare the performance of the adaptive-robust controller against a PD controller endowed with dither friction compensation. The latter controller is constructed by disabling the friction parameters ($\hat{\boldsymbol{\theta}} = 0, \boldsymbol{\Gamma}_\theta = \mathbf{0}, \Gamma_w = 0$) and adding a sinusoidal dither term $i_d sin(\omega t)$ to the control law (6.42). The parameters of the dither signal, $\omega = 2\pi 71.5$ rad/s and $i_d = \min(7, 4 + p_c)$, were selected based on the previous studies [208] and [222].

From the experimental results shown in Figure 6.9(a), it can be verified that the pressure responses of the controllers under consideration are very similar: in both cases, the tracking error reaches the ± 1 [bar] range in approximately 50ms and the steady-state is close to zero. The major differences lie in the control action, i.e., the motor current. In order to keep the motor always on the move, the high-frequency signal injected by the dither generates chattering in the current, which then cause vibrations, audible noise and, given that the actuator is always moving, i.e., $\omega_m \neq 0$, an increase in mechanical wear of the system. On the other hand, the model-based friction compensation does not suffers from such hurdles and produces a much smoother control action. These differences in control action also have an important consequence for the energy consumption in the actuator. As shown in Figure 6.9(b), the dither controller consumes 13 Ws of electrical energy during the test, while the model-based friction compensation (incorporated in the adaptive-robust controller) uses only 7.5 Ws. Hence, these results demonstrate that the model-based friction compensation can reduce the energy consumption of the BBW actuator up to 42.3%. Although the energy consumption is not the main priority in the BBW system, the higher energy efficiencies offered by the model-based friction compensation is an attractive feature for energy-sensitive applications, as is the case of the automotive field in which the actuator will be employed.

6.6.3 Transient Response

After demonstrating the energy and performance advantages of the adaptive-robust pressure controller against other strategies, we will now investigate more closely the transient response of this controller. Toward that goal, additional experiments with square and triangular waveform setpoints were carried out. From the results shown in Figure 6.10(a), it can be seen that the transient response to the positive ($2 \rightarrow 10$bar) and negative ($10 \rightarrow 2$ bar) steps is very good: the time to reach the setpoint is less than 50 ms, and the steady-state pressure error is close to zero. There is also a small overshoot during the positive step (0.5 bar), but it still lies within reasonable range.

The response of the controller to ramp setpoints, illustrated in Figure 6.10(b), also displays a satisfactory performance, with tracking errors below 0.6 bar. From these results, we also can observe that the peak tracking error occurs when the ramp switches from decrease to increase mode (see, e.g., $t = 0.26$s or $t = 1.02$s). During these time instants, it becomes necessary to reverse the direction of the motor speed ω_m, which is one of the most challenging operation points for the controller, as it will have to cope with the static/breakaway force disturbances.

6.6.4 Validation with Realistic Setpoints

For the final evaluation of the BBW controller we employed a pressure setpoint generated by a professional racing pilot, which was acquired during an experimental test session

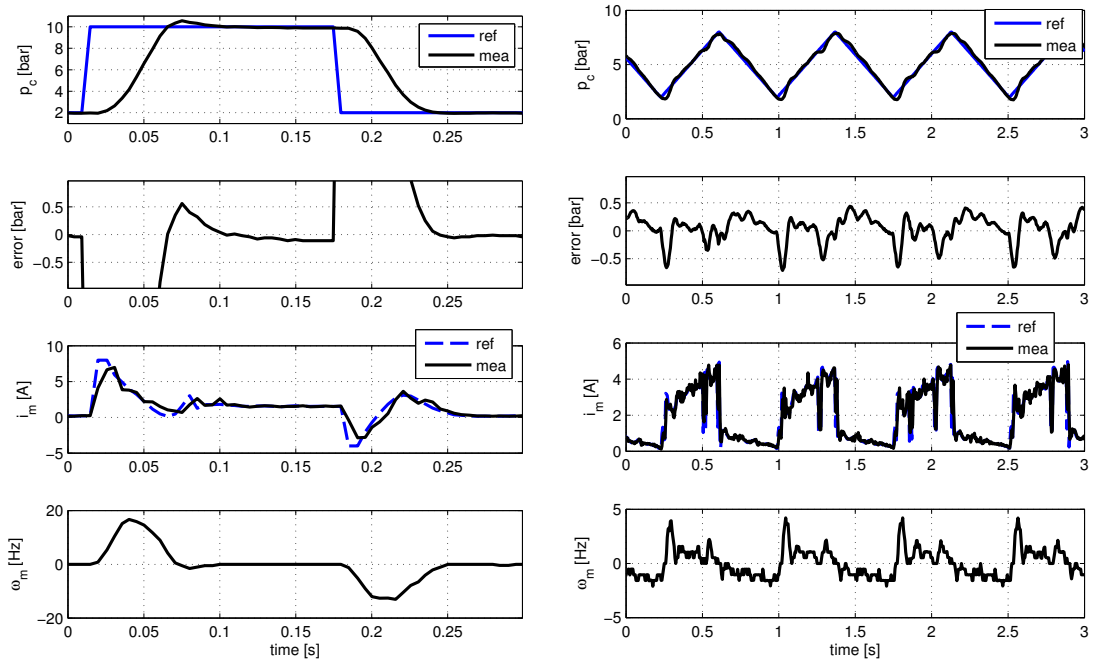

(a) response to steps in the pressure setpoint

(b) response to triangular setpoints

Figure 6.10: Experimental response of the adaptive-robust controller for step and ramps pressure setpoints.

carried out on an instrumented motorbike. Figure 6.11 show a typical example of a pressure braking setpoint produced by a racing pilot. This signal can be decomposed into three phases: *i*) from $t \in [0, 0.35]s$ we have a strong, and fast, brake increase in the pressure setpoint (35 bar/s); *ii*) during the modulation phase, $t \in [0.35, 4]$s, the average pressure is kept approximately constant (8 bar in this example), and the driver introduces small oscillations in the braking pressure setpoint in order to seek the maximization of the tyre-road friction force; *iii*) finally, for $t \geq 4$s, the driver starts releasing the brakes in order to allow the vehicle to negotiate the corner.

Inspecting the results presented in Figure 6.11 it can be concluded that the proposed BBW presents a good tracking performance, with the pressure setpoint being imposed with an accuracy of ± 0.5 bar. As for the control action generated by the controller, one can observe the existence of some current spikes, with amplitude varying between 4 and 6A. These spikes are a consequence of the high-level (and asymmetric) friction present in the BBW system. For example, given that the friction disturbance is smaller for negative speeds (see the discussion in Section 6.4), it is no surprise that during the periods where the pressure setpoint decreases slowly, e.g, $t \in [0.72, 1.25] \cup [1.8, 2.5]s$, thus with negative speeds, the motor current is low and relatively smooth (notice that, this behaviour is also present in the tracking of the ramp setpoints, illustrated in Figure 6.10(b)). However, for the periods of time when the pressure setpoint increases (e.g., $t \in [1.62, 1.82] \cup [2.54, 2.68]s$), and since the friction disturbance for positive speeds is very significant, the controller needs to apply a large control effort, making unavoidable the presence of the current spikes shown in the bottom plot of Figure 6.11. Despite these difficulties, the experimental tests shown in this section demonstrated that the proposed controller is able to cope well with the friction disturbances.

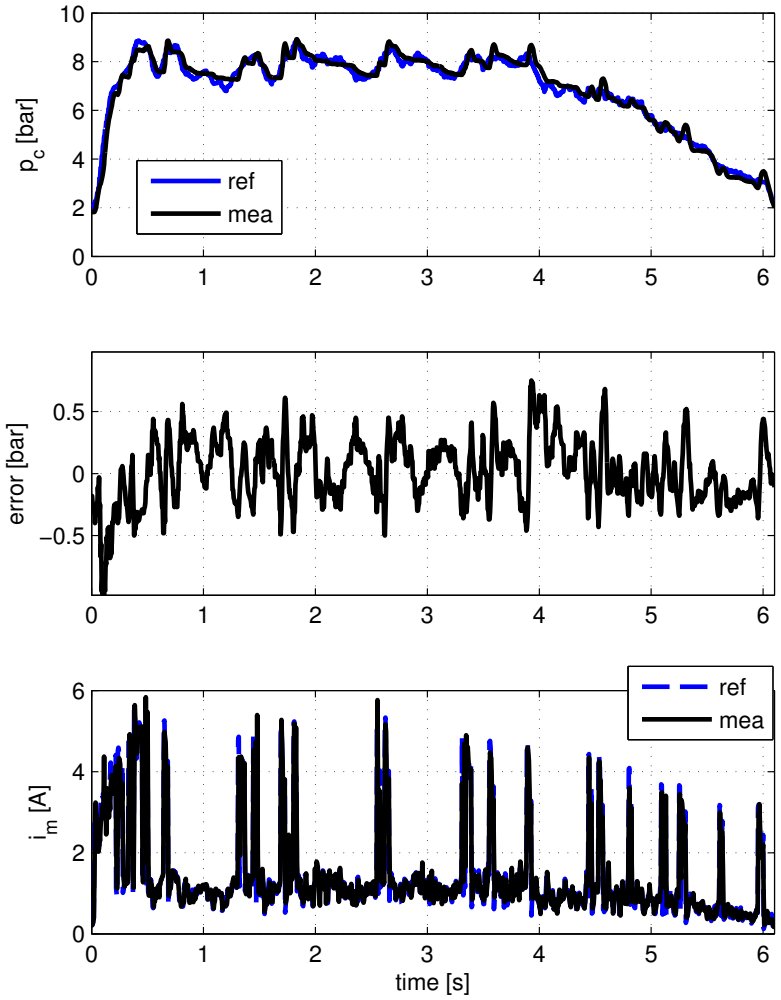

Figure 6.11: Experimental test of the adaptive-robust controller with a realistic pressure setpoint.

6.7 Conclusion

In this chapter, an adaptive-robust controller for tracking the braking pressure of a BBW actuator was proposed. In order to facilitate the design of this controller, we start by deriving a practical model for the actuator, putting particular focus on the simplification of the hydraulic dynamics. By exploring pragmatic assumptions we were able to reduce the original actuator model, based on a seven-state representation, to a (uncertain) second-order system. Experimental tests provided strong evidence that this reduced model is able to capture the fundamental dynamics of the actuator, making it very attractive for control purposes. In order to cope with friction disturbance, results from the theory of optimal approximation of functions were used to approximate the nonlinear friction map with a simpler and more practical LP. It was shown that, compared with the parameterizations previously proposed in the literature, the optimal LP reduces the total fitting error and tolerates a significant uncertainty in all friction parameters, most notably the Stribeck speed. Furthermore, given that the friction (and the LP) is subject to parametric uncertainty, adaptive mechanisms based on switching-σ were incorporated in the BBW

controller, while robustness to non-parametric disturbances, arising from modelling simplifications, were handled by a continuous sliding mode action. The stability and ultimate boundedness of the proposed adaptive-robust controller were demonstrated with the help of the Lyapunov method.

Experimental results demonstrated that, in comparison with the nominal friction compensation technique, the proposed BBW controller is able to offer superior robustness to parametric variations. It was also shown that, when compared with the classical dither-based friction compensation, the proposed controller enables a reducing in the energy consumption of the actuator by more than 40%. Finally, the effectiveness and performance of the adaptive-robust controller were confirmed using realistic pressure setpoints. As future work it is our intention to address the always important failsafe operation of the BBW actuator, and test the controller in a real vehicle.

6.8 Appendix: Overview of Model-based Friction Compensation

This section aims to provide a general overview of the model-based friction compensations presented in the recent literature. The simplest approach to achieving friction compensation is to apply offline methods [217, 234, 235, 236, 237, 238, 239, 240, 241]. These methods rely on the assumption of a time-invariant friction model, which is obtained through preliminary identification tests conducted during the calibration phase (before the controller activation). Although the computational effort of this approach is reduced, e.g., a look-up table, it turns out that the friction depends on several time-varying parameters, like humidity, temperature and lubricant condition [228], deteriorating the compensation provided by the nominal model, estimated *a priori*. For this reason, it is highly desirable that the controller possess adaptive mechanisms, capable of dealing, on-line, with the above-mentioned parametric disturbances.

Most of the on-line compensation methods rely on two types of friction models: static and dynamic. The former considers a static relation between the relative velocity and the friction force (or torque), incorporating Coulomb, viscous and Stribeck effects [214, 216, 219, 221, 242, 243, 244]. The latter approach extends the static models to contemplate important dynamic and position-dependent effects, like presliding displacement, frictional lag and variable break-away force, which can be modelled by the LuGre [229] and, more recently, by the Leuven [245] and the generalized Maxwell slip [246] models. Comparing the static and dynamic models for on-line friction compensation, it is undeniable that the dynamic friction models are better equipped to perform friction compensation, in particular for low-speed motion where the dynamics effects are more relevant [247]. Despite this theoretical advantage, the implementation of on-line friction compensation with dynamic models (particularly the LuGre), on platforms with limited computational resources, has revealed some practical difficulties. Firstly, the LuGre-based friction compensation requires the implementation of observers for the non-measurable state (an idealized average bristle deflection), which, when discretized with typical Euler approximations, is prone to exhibit numerical instability in the high-speed zone [248, 249]. Secondly, the dynamic models depend on unknown friction parameters, which coupled with the non-measurable state and nonlinear nature of the LuGre model, presents several challenges to devising controllers capable of simultaneously handling the parametric uncertainty and the bristle deflection observer. As a result, the majority of friction compensations based on the LuGre model assume a partial knowledge of the parameters, i.e., only the parameters with a

linear effect in the model are estimated on-line, while the others (e.g., the Stribeck speed) are assumed to be constant and known (see [247, 250, 251]). Naturally, due to the time-varying nature of friction, the assumption of constant parameters does not always hold. On the other hand, the on-line friction compensation with static maps, while ignoring the dynamics effects, is considerably simpler to implement and design, which represents important advantages for low-cost applications, where the computational resources and sensor resolution are limited.

In light of the above, the ultimate decision on the most suitable type of model-based compensation technique (off-line, on-line with static friction model or on-line with dynamic friction model) varies from application to application and is dependent on the sensors' costs and precision, control specifications, such as the tolerable tracking error, and computational resources of the control platform [252]. In this work, we restrict our attention to the class of on-line friction compensation with static maps (OFCSM). This is helpful in applications with time-varying friction parameters, hence the off-line compensation is unsuitable, and with negligible friction dynamics (this latter issue can also be handled with robust methods). Several practical examples can be found in recent literature, which meet these requirements, e.g., see [216, 219, 230, 244, 252, 253, 254].

In the framework of OFCSM, there are two main issues that must be addressed: *i*) what model should be used in the friction map? and *ii*) what "on-line" learning/update method should be employed to tune the map parameters during the system operation? In fact, the answer to the first question is intrinsically connected with second one: the most common approach to derive learning methods is through adaptive mechanisms, which normally demand that the unknown disturbance, in this case the friction, must have a *Linear Parameterization* (LP) structure, i.e., linear in the unknown parameters. As a result, LPs constitute the most common and practical structure for modelling the friction map.

Due to the well-known property of universal function approximation, Neural Networks (NN), with single hidden-layer [253, 255, 256, 257] or multiple layers [258], present an attractive structure to approximate the static friction map. In order to obtain a LP from the NN, the parameters associated with the hidden-layer(s), which have a nonlinear effect in the model, must be fixed off-line before the controller activation. For example, if radial basis functions are used as the activation function, this means that the "centres" and the "variance" parameters must be fixed *a priori*. This selection is not always obvious, and, albeit some preliminary tests can be conducted to guide this choice [253], it is not clear that the generated LP is the most efficient, i.e., with the minimum number of neurons, and normally requires NNs with a high number of neurons, ranging from 20 to 100 (radial) basis functions [253, 255, 256, 257]. Despite the good approximation capabilities of these NNs, also known as a "model free approach", for systems where the friction is the main disturbance, the high number of unknown parameters may present an unnecessary complexity and be an issue for cost-sensitive applications with real-time requirements, which is a common trend in industry applications. Furthermore, the high number of parameters is also a limiting factor for obtaining fast transient responses in adaptive controllers, of which the OFCSM normally relies.

An alternative possibility to overcoming the complexity of the LPs obtained from the NNs is to explore the structure of nonlinear (steady-state) model associated with the friction map, e.g., the Tustin model or the generalized exponential model [228]. To approximate these models, several LPs were proposed in the literature, based on linearization of the static friction curve [214, 215] or on polynomial approaches [216, 217], Lorentzian

[213, 218] and piecewise linear functions [219, 220, 221, 259, 260]. However, most of these approaches assume an accurate knowledge of the so-called Stribeck velocity, which is not always possible to ensure, due to parametric variation resulting from various factors (temperature, humidity, etc.). As already mentioned in Section 6.1, one of the main contributions of this work is to offer a new LP: *i*) capable of tolerating a significant uncertainty in the Stribeck velocity; *ii*) which provides a higher accuracy than the LPs previously proposed in the literature [214, 215, 216, 217, 219, 220, 221, 259, 260] and, *iii*) unlike the LPs based on NNs [253, 255, 256, 257], has a small number of basis functions.

Chapter 7

Minimum-time Path Following in Highly Redundant Vehicles

Abstract:

This chapter is concerned with the development of path following algorithms for redundant vehicles, endowed with four wheel steer and four in-wheel motors. The ultimate goal is to find the wheels' torques and steers such that the vehicle performs a pre-specified geometric path in minimum time. The main challenges are the nonlinear and complex models of the tyre-road friction forces, as well as the power limitations of the electric motors. By regarding the centre-of-gravity forces as pseudo-control inputs, it is shown that this problem can be transformed into a convex optimization setting, and effectively solved by numerical techniques. Further, the proposed controller also incorporates tuning factors that enable the designer to trade off lap-time and energy consumption. To cope with model approximation errors and disturbances, a robust sliding mode controller, based on conditional integrators, is also presented. Finally, for distributing the forces among the tyres, two control allocation approaches are investigated. The first, based on the extension of the cascading generalized inverse method, is computational efficient, but displays difficulties coping with unfeasible forces. This issue is mitigated in the second allocation algorithm, which relies on the linearization of the friction constraints. Several simulations, carried out in the CarSim vehicle model, demonstrate the effectiveness of the proposed strategy, both in single-corner manoeuvres and longer road courses.

7.1 Introduction

Up to now, our study focused on the development of control and estimation techniques to regulate the longitudinal force produced by each wheel of the electric vehicle (EV). In what follows, we will move our attention from the "wheel domain" to the "vehicle domain", and address the design of advanced motion controllers for highly redundant EVs, equipped, not only with IWMs, but also with independent wheel steer mechanisms. To implement such control systems, there are two fundamental issues that should be investigated: *i*) we must find suitable allocation methods for distributing the control effort among the vehicle's

several actuators; and, *ii*) it is also necessary to design control strategies that can have an active control over the vehicle motion (e.g., through the control of the longitudinal, lateral and yaw velocities). Normally, the ultimate goal of these systems is to ensure the safe motion of the vehicle [15], improve its handling and maneuverability [18], and/or guarantee fail-tolerant operation [261]. In this chapter, the motion-control problem of redundant EVs will be approached from a different point of view. More specifically, we will investigate the potential benefit of redundant actuation configurations in the path following problem of autonomous vehicles. As explained in the paragraphs below, it is expected that the next generation of driver's electronic aids will evolve toward the full automation of the vehicle. In view of the high manoeuvrability offered by the IWMs and independent wheel steer mechanisms, we believe that the redundant actuation configurations can have a key role in the development of future autonomous vehicles, and the present chapter represents our contribution to this goal.

The full automation of the EV can bring enormous benefits to its users. To start with, releasing the driver from the tedious manual driving operations may allow him to focus on more productive and enjoyable tasks [262]. From a safety point of view, we may also envisage the development of cars that are "impossible" to crash [263], which can further reduce road fatalities. From a social standpoint, the possibility of having disabled people (e.g., visually impaired) driving without assistance of other humans [264] represents another example of the impact that such technologies can bring to people's lives. However, the development of fully autonomous vehicles still faces many techniques challenges, particularly in areas such as environmental sensing and perception, motion/path planning and motion control [264, 265]. In this work, our attention will lie only on the development of the motion-control layer, with particular focus on vehicle configurations with highly redundant actuators.

According to [266, 267], the motion control layer is composed of three main problems. The first, known as a path following problem, intends to determine the actuators' setpoints (e.g., wheels' torques and steer) such that the vehicle follows a pre-defined geometric path, possibly with a constant velocity. The second, called trajectory tracking, has a similar goal to the previous problem, but features an important difference: the geometric path is parameterized in time. And finally, there is also the point-to-point motion, which, as the name suggests, aims to move the vehicle from an initial to a final (Cartesian) point. In the remainder of this work our efforts will be entirely devoted to the path following subproblem. Further, we will also work under the assumption that the referenced geometric path is produced, for example, from a higher-level motion planner [187] (not addressed here).

The main challenge in the development of path following algorithms lies in the complexity of the vehicle's models, in particular, the nonlinear mechanisms associated with the friction forces between the tyre and road. One way to relax these complexities involves exploring idealized assumptions, imported mainly from the mobile robots, such as pure rolling of the tyres and no side-slip, to derive simple, but practical, vehicle kinematic models. This way, the vehicle movement can be described using only the wheels' velocities, steer angles and geometric properties of the car [266]. Techniques such as pure-pursuit [268], "Stanley's method" [269], or nonlinear feedback laws, based on the transformation of the vehicle model to the so-called chain-form (see [266] and references therein), represent some of the pragmatic approaches that were proposed and experimentally tested within this kinematic setting. Nonetheless, since these approaches do not take into account the tyre-road friction forces, together with the limited validity of pure-rolling and zero

side-slips assumptions, they end up confining the applicability of kinematic-based controllers to low-speed manoeuvres [270, 271]. To handle high-speed manoeuvres, several path following algorithms have been developed based on the single-track bicycle model, a linearized model for the vehicle dynamics and lateral forces [133]. The uncertainties affecting this bicycle model, most notably in the cornering stiffness parameters, has also instigated the application of several robust techniques to the path following problem, such as sliding mode [272], H_∞ [273], and nonlinear Lyapunov-based laws [274]. Alternatively, linear control techniques, like state feedback [275] and PIDs [276], can also be used, and their robustness to parameter uncertainty verified at the end of the design stage, e.g., through Lyapunov methods [275, 277].

From a theoretical point of view, the main shortcoming of the designs based on the bicycle model is related to the assumption that the lateral and longitudinal vehicle dynamics are decoupled. As a result, the majority of these works design the path following algorithm under the hypothesis that the vehicle longitudinal speed is constant through the corners, imposed by a (longitudinal) velocity controller that operates independently from the lateral motion controller. While this is reasonable for moderate driving scenarios, when we consider more aggressive manoeuvres, involving, for example, combined steer and acceleration, it becomes imperative to incorporate the effects of the lateral-longitudinal coupling[1]. One pragmatic solution to mitigate this issue was presented in [275, 278, 279]; their idea is to explore the *gg* diagram (a tool that generalizes the tyre friction circle concept to the vehicle's CoG forces/accelerations [132]) together with the information of the path's curvature, to infer the maximum longitudinal speed and acceleration so that the vehicle operate always within the limit of the gg diagram. Based on this information, a feedforward term for the longitudinal controller is generated, which is then combined with a wheel-slip controller to cope with modelling errors and disturbances. The present work shares the same goals as the ones mentioned above, but will follow an alternative route. More specifically, instead of relying on simple kinematic [266, 268, 269] or the single-track bicycle models [274, 275, 276] to regulate the lateral vehicle's dynamics, or the *gg* diagram to infer the maximum longitudinal accelerations [275, 279], our path following controller will employ a full nonlinear two-track vehicle model, with nonlinear tyre forces and contemplating vertical load movement. Although this inevitably leads to increased modelling complexity, this report will demonstrate that, by bringing together different control and optimization tools, such as time-to-space transformations, convex optimization, robust and control allocation techniques, this complex system can be effectively tackled. It will also be shown that the two-track nonlinear model is instrumental to allow the path-follow controller to operate the vehicle near its adhesion limits.

The four in-wheel-motors (4IWM) and four wheel-steer (4WS) represent the key enabling technologies that allow us to handle, within a nonlinear framework, the min-time path following problem. To start with, notice that this redundant actuation structure allows us to actively regulate the longitudinal and lateral forces that each wheel produces [280]. This property paves the way for using the centre of gravity's forces and moments as the pseudo-controls, which introduces major simplifications to the motion controller's design [75, 280]. In addition, the high degree of manoeuvrability introduced by the 4WS also facilitates the generation of feasible paths for the vehicle, e.g., with this structure it is possible to impose zero side-slip motions or perform parallel manoeuvres [281].

[1] for example, it is well known that the bicycle model is generally only valid for lateral accelerations below 0.4g, and constant longitudinal velocity [133]

The contributions of this work can be divided in three main areas. First, we bring to the automotive applications the convex formulation of the minimum-time path following problems that has been used, for some time, in robotics [282][283]. In particular, we will show that, in comparison with the robotics, the vehicular applications introduce additional complications related to the frictional forces and power limits of the IWMs. In order to preserve the problem's convexity, we applied convexification techniques to the friction and power limit constraints, which then enabled us to tackle the resulting min-time path following problem with practical direct optimization methods [284]. Another important contribution of our controller is the possibility of exploring trade-offs between performance and energy consumption. The idea is that, for a given pre-specified path, the user (or the designer) can configure the controller so that the vehicle travels through the path *i*) in minimum-time; *ii*) with minimum-energy[2]; or, a *iii*) trade-off between the travel time and energy consumption. Consequently, in contrast to the classical path following setting where the vehicle velocity is kept constant [266], our controller is able to generate appropriate speed profiles that take into account the adhesion limits of the car and the user/designer preferences (lap-time *vs* energy consumption).

The solution of the above optimization approach is then used as a feedforward term for the motion controller, i.e., a setpoint for the (centre of gravity) force that, under ideal conditions, would be enough to keep the vehicle circulating along the path. However, in practice, the vehicle's model is subject to uncertainties, which makes the feedforward term insufficient to meet the control goals. To overcome this limitation, the motion controller contains feedback mechanisms, based on the cascade of a position and speed loops, which are derived with the help of sliding mode law, endowed with conditional integrators [165, 171]. Besides the implementation and tuning simplicity, robustness to disturbances, and built-in anti-windup mechanisms, the conditional integrators also offer a chattering-free operation, which is one of the main issues in the traditional sliding control laws. The application of sliding modes, with conditional integrator, to the vehicle-motion layer represents the second contribution of this work.

Finally, the motion controller needs to determine the wheel's torque and steers, so that the (centre of gravity) forces and moments requested by the path following controller are effectively applied to the vehicle. Given the high degree of actuation redundancy, there are many allocation solutions for this problem. In this work, the actuation redundancy is explored by a control allocation technique that intends to minimize the tyre's friction use, satisfying, simultaneously, the actuation limits. To solve this problem, two techniques are investigated. The first extends the cascading generalized inverse (CGI) [106, 108], a well-known technique borrowed from aeronautical application (see also the discussion in Chapter 2.3.2), to the force allocation problem in vehicular applications. More specifically, it is shown that, by fixing *a-priori* the force's angles of each tyre (obtained from the pseudo-inverse solution of the unconstrained optimization problem), the allocation problem can be transformed into a practical quadratic-programming (QP) problem. Simulation results demonstrate that, as long as the requested forces are feasible, this approach is capable of generating accurate solutions in less than 400 us (average values). However, for unfeasible forces requests, the performance of this allocation strategy degrades. This issue motivated us to develop a second approach, based on the linearization of the friction constraints. Albeit requiring $2-3$ times higher computational times, the linearization-based approach

[2]due to reasons that will be clear later on, our approach only indirectly minimizes the energy consumption of the vehicle

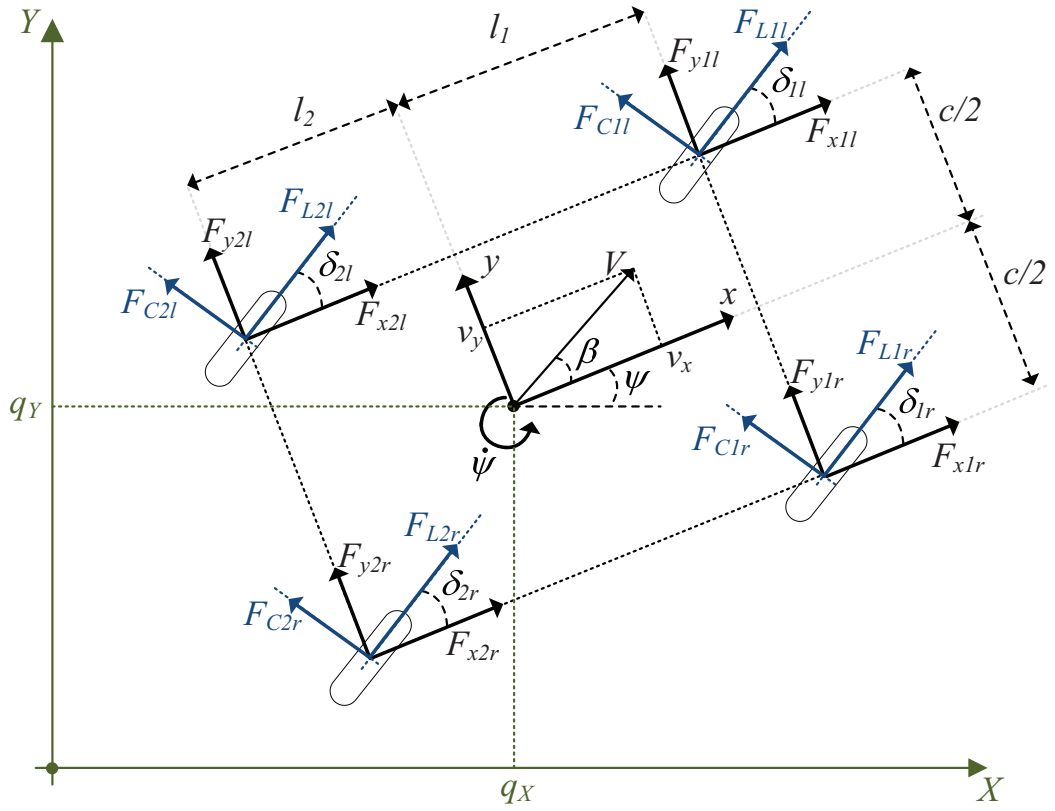

Figure 7.1: Two-track vehicle model.

produces lower allocation errors than the extended CGI, particularly for unfeasible forces requests.

The effectiveness of the proposed path following controller is demonstrated with simulation tests, carried out with the help of the CarSim simulator.

7.2 Vehicle Modelling

In this section, a two-track nonlinear vehicle model will be presented, which will be used for the development of the vehicle's motion controller. The vehicle under study is composed of 4 independent wheel drive, and 4 independent wheel steering. To make the mathematical model tractable, we will adopt a pragmatic approach, and neglect the roll and pitch dynamics of the EV, which is a typical assumption in the development of control-oriented models for the vehicle dynamics [35, 75, 285].

7.2.1 Preliminaries

Let us start by introducing the most important notation that is employed throughout the document. As shown in Figure 7.1, the vehicle's modelling involves several physical quantities, specified in three coordinate systems. The starting point is the XY axis, fixed with the Earth, which is used to define the position and orientation of the vehicle

$$\mathbf{p} = \begin{bmatrix} p_X & p_Y & p_\psi \end{bmatrix}^T \tag{7.1}$$

where p_X, p_Y are the X and Y components of the position, respectively, and p_ψ is the angle between the vehicle orientation and the X axis, i.e., the yaw-angle. The second axis system, xy, is fixed to the centre of gravity (CoG) of the vehicle, and is used to specify the CoG's velocities and forces:

$$\mathbf{v} = \begin{bmatrix} v_x & v_y & \dot{\psi} \end{bmatrix}^T \in \mathbb{R}^3 \tag{7.2}$$

$$\mathcal{F} = \begin{bmatrix} F_x & F_y & M_z \end{bmatrix}^T \in \mathfrak{F} \subset \mathbb{R}^3 \tag{7.3}$$

where F_x is the longitudinal force applied to the vehicle's CoG, v_x the longitudinal speed, F_y the lateral force, v_y the lateral speed, M_z the yaw-moment and $\dot{\psi}$ the yaw-rate. The set $\mathfrak{F}$ represents the admissible set of force/moments that can be applied to the CoG.

During the development of the vehicle dynamic model, it is helpful to represent the velocities (and forces) in both xy and XY axes, which can be performed with the help of the following transformation:

$$\frac{d\mathbf{p}}{dt} = \underbrace{\begin{bmatrix} \cos(p_\psi) & -\sin(p_\psi) & 0 \\ \sin(p_\psi) & \cos(p_\psi) & 0 \\ 0 & 0 & 1 \end{bmatrix}}_{\mathbf{T}(\mathbf{p})} \mathbf{v} \tag{7.4}$$

The inverse relation can also be straightforwardly obtained by applying $\mathbf{T}^{-1}(\mathbf{p})$ to the previous relation; notice that $\mathbf{T}^{-1}(\mathbf{p})$ is well-defined for any value of p_ψ.

The generalized forces/moments ($\mathcal{F}$) applied to the CoG is the aggregated result of the individual friction forces generated by each one of vehicle's tyres, and is expressed as

$$\mathcal{F} = \mathbf{B}\mathbf{F}_{xy} \tag{7.5}$$

$$\mathbf{B} = \begin{bmatrix} B_x \\ B_y \\ B_\psi \end{bmatrix} = \begin{bmatrix} 1 & 0 & 1 & 0 & 1 & 0 & 1 & 0 \\ 0 & 1 & 0 & 1 & 0 & 1 & 0 & 1 \\ -\frac{c}{2} & l_1 & \frac{c}{2} & l_1 & -\frac{c}{2} & -l_2 & \frac{c}{2} & -l_2 \end{bmatrix}$$

where l_1 is the distance between the front axle and the CoG, l_2 the distance between the rear axle and the CoG, c the trackwidth and $\mathbf{F}_{xy}$ the friction forces of each tyre, defined in the xy frame (see Figure 7.1):

$$\mathbf{F}_{xy} = \begin{bmatrix} F_{x1l} & F_{y1l} & F_{x1r} & F_{y1r} & F_{x2l} & F_{y2l} & F_{x2r} & F_{y2r} \end{bmatrix}^T$$

In terms of notation, throughout this work the front tyres will be referred with the sub-index 1, the rear with 2, the left with l and the right with r. They will be compactly grouped in the set $\mathfrak{T} = \{1l, 1r, 2l, 2r\}$. To extract from $\mathbf{F}_{xy}$ the x and y force components of the tyre $i \in \mathfrak{T}$ we will apply the diagonal matrix $\mathbf{E}_i \in \mathbb{R}^{2\times 8}$, e.g.

$$\begin{bmatrix} F_{x1l} & F_{y1l} \end{bmatrix}^T = \mathbf{E}_{1l}\mathbf{F}_{xy} \tag{7.6}$$

$$\mathbf{E}_{1l} = \mathrm{diag}(\begin{bmatrix} 1 & 1 & 0 & 0 & 0 & 0 & 0 & 0 \end{bmatrix})$$

Finally, the frictional forces generated by each tyre are usually modelled in the coordinates LC, fixed with the wheel (see blue axes in Figure 7.1). The variables in the LC

coordinates are related to the xy by the following transformation:

$$\begin{bmatrix} F_{xi} \\ F_{yi} \end{bmatrix} = \underbrace{\begin{bmatrix} \cos(\delta_i) & -\sin(\delta_i) \\ \sin(\delta_i) & \cos(\delta_i) \end{bmatrix}}_{\mathbf{W}(\delta_i)} \begin{bmatrix} F_{Li} \\ F_{Ci} \end{bmatrix}, \quad i \in \mathfrak{T} \tag{7.7}$$

where F_{Li} is the force generated in the tyre's orientation, F_{Ci} the cornering force (orthogonal to the tyre's orientation) and δ_i the steering angle of the wheel. Notice that the inverse $\mathbf{W}^{-1}(\delta_i)$ is also well-defined for all values of δ_i.

7.2.2 Equation of Motion

By direct application of the Newton's second law, and taking into account the notation introduced in the previous sub-section, the dynamic evolution of vehicle position $\mathbf{p}$ is defined as:

$$\mathbf{M}\ddot{\mathbf{p}} = \mathbf{T}(\mathbf{p})\left(\mathcal{F} - \mathcal{R}(\mathbf{p}, \dot{\mathbf{p}}) + \mathcal{D}\right) \tag{7.8}$$

where $\mathbf{M} = \text{diag}([m, m, I_z])$, m is the vehicle mass, I_z the yaw inertia, $\mathcal{D} \in \mathbb{R}^3$ a generalized force due to the effect non-modelled dynamics and disturbances, and $\mathcal{R}(.) \in \mathbb{R}^3$ the resistance forces that affect the vehicle motion. As shown in Appendix 7.8, the resistance forces can be decomposed into two components:

$$\mathcal{R}(\mathbf{p}, \dot{\mathbf{p}}) = \mathcal{R}_1 + \mathcal{R}_2(\mathbf{p}, \dot{\mathbf{p}})\dot{\mathbf{p}} \tag{7.9}$$

where $\mathcal{R}_1 \in \mathbb{R}^3$ is a constant term due to rolling resistance and $\mathcal{R}_2(\mathbf{p}, \dot{\mathbf{p}}) \in \mathbb{R}^3$ is a resistance term due to aerodynamic drag. With respect to this last component it is worth noticing that

Remark 7.1. for $\alpha \geq 0$, $\mathcal{R}_2(\mathbf{p}, \alpha\dot{\mathbf{p}}) = \alpha\mathcal{R}_2(\mathbf{p}, \dot{\mathbf{p}})$

which can be straightforwardly verified using the aerodynamic drag model presented in Appendix 7.8.

7.2.3 Friction Forces

As already mentioned, the generalized force/moments $\mathcal{F}$ are a direct consequence of the individual friction forces, F_{Li}, F_{Ci}, generated by each tyre. To model these forces, a simplified version of the well-known magic tyre formula [147] will be employed here. The main inputs for this model are: *i*) the longitudinal tyre slip κ_i, a normalized difference between the wheel rotation speed (ω_i) and the wheel linear speed (v_{Li}); and *ii*) the tyre side-slip angle α_i, which is the angle between the wheel orientation (δ_i) and the wheel's velocity vector. Mathematically, these variables are defined as

$$\kappa_i = \frac{\omega_i r_i - v_{Li}}{v_{Li}}, \qquad \tan\alpha_i = -\frac{v_{Ci}}{v_{Li}}, \quad i \in \mathfrak{T} \tag{7.10}$$

where r_i effective radius of the wheel, and v_{Li}, v_{Ci} the tyre's longitudinal and cornering speeds. Given that the velocity of the wheels is the consequence of the superposition of (v_x, v_y) and rotational motion (yaw-rate), one can express v_{Li}, v_{Ci} according to the following map [133]:

$$\begin{bmatrix} v_{Li} \\ v_{Ci} \end{bmatrix} = \mathbf{W}^{-1}(\delta_i) \begin{bmatrix} 1 & 0 & \chi_{Li} \\ 0 & 1 & \chi_{Ci} \end{bmatrix} \mathbf{v}, \quad i \in \mathfrak{T} \tag{7.11}$$

$$\begin{bmatrix}\chi_{L1l} & \chi_{L1r} & \chi_{L2l} & \chi_{L2r}\end{bmatrix} = \begin{bmatrix}-\frac{c}{2} & \frac{c}{2} & -\frac{c}{2} & \frac{c}{2}\end{bmatrix}$$
$$\begin{bmatrix}\chi_{C1l} & \chi_{C1r} & \chi_{C2l} & \chi_{C2r}\end{bmatrix} = \begin{bmatrix}l_1 & l_1 & -l_2 & -l_2\end{bmatrix}$$

To incorporate the combined slip conditions, i.e., situations where traction and steering are simultaneously applied, the so-called "theoretical slips" [147] are considered:

$$\sigma_{Li} = \frac{\kappa_i}{1+\kappa_i}, \quad \sigma_{Ci} = \frac{\tan\alpha_i}{1+\kappa_i}, \quad \sigma_i = \sqrt{\sigma_{Li}^2 + \sigma_{Ci}^2}, \quad i \in \mathfrak{T}$$

These theoretical slips represent the main factors in generating the longitudinal (F_{Li}) and cornering forces (F_{Ci}) of the tyre:

$$F_{Li} = \frac{\sigma_{Li}}{\sigma_i} F_i(\sigma_i, F_{zi}) \qquad F_{Ci} = \frac{\sigma_{Ci}}{\sigma_i} F_i(\sigma_i, F_{zi})$$

$$F_i(\sigma_i, F_{zi}) = \mu_{max} F_{zi} \sin\left(C \operatorname{atan}(B\sigma_i)\right), \quad i \in \mathfrak{T} \tag{7.12}$$

where C, B are parameters of the friction model, μ_{max} the tyre-road friction peak and F_{zi} the vertical force. From the above relation, it is interesting to note that

Remark 7.2. the longitudinal (F_{Li}) and cornering (F_{Ci}) forces of the tyre must fulfil

$$F_{Li}^2 + F_{Ci}^2 = F_i^2 \leq (\mu_{max} F_{zi})^2, \quad i \in \mathfrak{T} \tag{7.13}$$

This is known in the literature as the friction circle constraint, and essentially states that the force generated by the tyre must lie within a circle with a radius defined by the vertical load and the friction peak. The friction circle constraint also puts in evidence several key limiting factors in the tyre's force generation. First, as the grip level deteriorates, i.e., as μ_{max} decreases, the radius of the friction circle becomes smaller, and, as a consequence, the force capability of the tyre (in both directions) diminishes. This introduces important limitations in the control authority that the driver (and the automatic controller) have over the vehicle. Similarly, the vertical load of the tyre also plays a relevant role in the circle's radius, and, by inspecting (7.13) one can find that the radius is proportional to F_{zi}. From a practical perspective, this means that the tyres with more vertical load will have higher force capabilities, which is particularly useful when allocating the traction forces among the tyres (e.g., torque vectoring systems [28]). Another factor that deserves to be underlined is the limitations that appear when the tyre develops simultaneous longitudinal ($|F_{Li}| > 0$) and lateral forces ($|F_{Ci}| > 0$). More specifically, the friction circle constraint implies that the maximum longitudinal (lateral) force is only achievable if the tyre does not produce any lateral (longitudinal) force. In other words, the friction force must be shared by the longitudinal and lateral components, which poses important challenges when combined traction and steering is needed.

For simplicity, the representation of the tyre-road friction forces considered here assumes an isotropic condition, which leads to the friction circle constraint. It is also worth mentioning that the simplified magic tyre formula is just an approximation of the real friction phenomena, and, in practice, the tyre forces are governed by more complex mechanisms (see [147] for additional details). Nonetheless, our focus here is to employ control-oriented models that can capture the fundamental properties of the tyre's forces, and which can be used to design practical motion controllers.

The friction circle constraint also holds for the forces defined in the xy coordinates:

Remark 7.3. the forces F_{xi}, F_{yi} are confined to the following set:

$$F_{xi}^2 + F_{yi}^2 = \left\| \mathbf{W}(\delta_i) \begin{bmatrix} F_{Li} \\ F_{Ci} \end{bmatrix} \right\|_2^2 = F_i^2 \leq (\mu_{max} F_{zi})^2, \quad i \in \mathfrak{T}$$

This property results from the fact that the change of coordinates $\mathbf{W}(\delta_i)$ does not affect the tyre's force magnitude.

7.2.4 Vertical Forces

The tyre's vertical forces F_{zi} are affected by the load movement between front-rear axle, and left-right wheels, that the vehicle experiences when subjected to longitudinal and lateral accelerations. To model these factors, we will employ the following quasi-static mapping [133]:

$$\mathbf{F}_z = \mathbf{F}_z^0 + \varrho_x a_x + \varrho_y a_y \tag{7.14}$$

$$\begin{aligned} \mathbf{F}_z &= \begin{bmatrix} F_{z1l} & F_{z1r} & F_{z2l} & F_{z2r} \end{bmatrix}^T \\ \mathbf{F}_z^0 &= \frac{mg}{2(l_1+l_2)} \begin{bmatrix} l_2 & l_2 & l_1 & l_1 \end{bmatrix}^T \\ \varrho_x &= \frac{mh}{2(l_1+l_2)} \begin{bmatrix} -1 & -1 & 1 & 1 \end{bmatrix}^T \\ \varrho_y &= \frac{mh}{c(l_1+l_2)} \begin{bmatrix} -l_2 k_f & l_2 k_f & -l_1 k_r & l_1 k_r \end{bmatrix}^T \end{aligned}$$

where $\mathbf{F}_z^0$ is the static force distribution, h the height of the CoG, k_f, k_r represent the front and rear coefficients associated with the lateral load transfer due to vehicle roll (see [132]), g the gravitational acceleration and a_x, a_y the vehicle's longitudinal and lateral accelerations, respectively:

$$\begin{bmatrix} a_x \\ a_y \end{bmatrix} = \begin{bmatrix} \frac{1}{m} & 0 & 0 \\ 0 & \frac{1}{m} & 0 \end{bmatrix} \left(\mathcal{F} - \mathcal{R}(\mathbf{p}, \dot{\mathbf{p}}) \right) \tag{7.15}$$

7.2.5 Wheel Dynamics and Actuator's Limits

The rotational dynamics of each wheel in the vehicle is given by:

$$J\dot{\omega}_i = T_i - r_i F_{Li}, \qquad i \in \mathfrak{T}$$

where J is the wheel inertia, and T_i the wheel torque. It is considered that the wheel torque is generated by a combination of in-wheel motors ($T_{m,i}$) and brake-by-wire actuators ($T_{b,i}$), i.e., $T_i = T_{m,i} + T_{b,i}$. The main limiting factors in these actuators are the acceleration power and acceleration torque limits associated with the in-wheel motors:

$$\underline{T} \leq T_i \leq \overline{T}, \quad T_i \omega_i \leq \overline{P}, \qquad i \in \mathfrak{T} \tag{7.16}$$

where $\overline{T} \in \mathbb{R}_+$ is the maximum acceleration torque that the motor can develop, $\underline{T} \in \mathbb{R}_-$ the maximum braking torque of the brake-by-wire system, and $\overline{P}$ the maximum acceleration power, which are equal for all the wheels. The braking power limits are not explicitly considered here, since, due to safety concerns, modern braking system are generally able

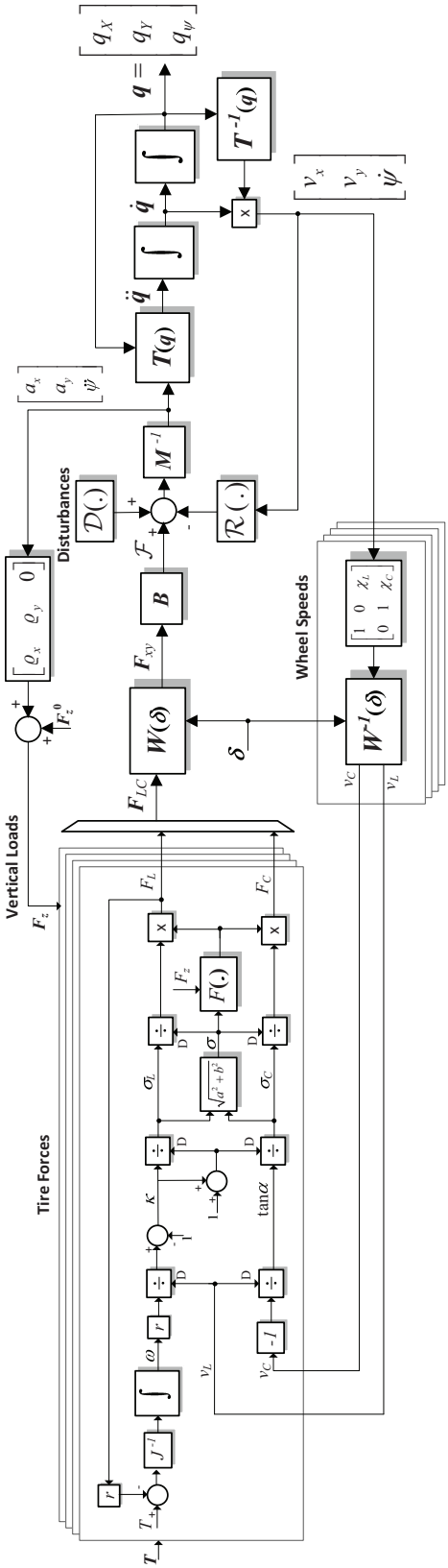

Figure 7.2: Block diagram of the vehicle model.

to overcome the friction limits. In other words, the constraints introduced by the friction circle (7.13) will be the dominant factor in the generation of the braking torque (and not the power limits of the braking system).

Regarding the steering, it is assumed that each wheel has independent steer capabilities, constrained to the following sets:

$$-\overline{\delta} \leq \delta_i \leq \overline{\delta}, \qquad i \in \mathfrak{T} \tag{7.17}$$

where $\overline{\delta}$ is the maximum steering range. The dynamics of all the actuators are neglected here, since, in practice, their bandwidth is normally much higher than the vehicle's dynamics.

7.2.6 Compact Representation

In summary, the vehicle model can be compactly represented as:

$$\begin{aligned}
\mathbf{M}\ddot{\mathbf{p}} &= \mathbf{T}(\mathbf{p})\left(\mathcal{F} - \mathcal{R}(\mathbf{p}, \dot{\mathbf{p}}) + \mathcal{D}\right) && \text{(7.18a)}\\
\mathcal{F} &= \mathbf{B}\mathbf{F}_{xy} && \text{(7.18b)}\\
\mathbf{F}_{xy,i} &= \mathbf{W}(\delta_i)\begin{bmatrix} F_{Li} & F_{Ci}\end{bmatrix}^T, \quad i \in \mathfrak{T} && \text{(7.18c)}\\
\begin{bmatrix} F_{Li} \\ F_{Ci}\end{bmatrix} &= \tilde{\mathbf{F}}_i(\mathbf{p}, \dot{\mathbf{p}}, \omega_i, \delta_i, F_{zi}, \theta_T), \qquad i \in \mathfrak{T} && \text{(7.18d)}\\
\mathbf{F}_z &= \mathbf{F}_z^0 + \frac{\varrho_x}{m}\mathbf{e}_1^T(\mathcal{F} - \mathcal{R}) + \frac{\varrho_y}{m}\mathbf{e}_2^T(\mathcal{F} - \mathcal{R}) && \text{(7.18e)}\\
J\dot{\omega}_i &= T_i - r_i F_{Li}, \qquad i \in \mathfrak{T} && \text{(7.18f)}
\end{aligned}$$

$$\underline{T} \leq T_i \leq \overline{T}, \quad T_i\omega_i \leq \overline{P}, \quad -\overline{\delta} \leq \delta_i \leq \overline{\delta}, \quad i \in \mathfrak{T} \tag{7.18g}$$

where $\tilde{\mathbf{F}}_i \in \mathbb{R}^2$ is the friction force, which groups the expressions (7.10)-(7.12)), θ_T represents the parameters of the friction model, $\mathbf{F}_{xy,i}$ refers to the x and y force components of the tyre $i \in \mathfrak{T}$, and $\mathbf{e}_1^T = \begin{bmatrix}1 & 0 & 0\end{bmatrix}^T$, $\mathbf{e}_2^T = \begin{bmatrix}0 & 1 & 0\end{bmatrix}^T$.

From a control perspective, we can identify T_i, δ_i as the model inputs, and $\mathbf{p}, \dot{\mathbf{p}}, \omega_i$ as the states; the compact model also contains a series of auxiliary variables and algebraic equalities that are employed to facilitate the presentation of the model and the controller design. Moreover, it is also important to clarify that the vehicle's motion controller will be designed under the assumption that the wheel's torques T_i can be individually regulated. Given that T_i is a result of the IWM ($T_{b,i}$) and the brake-by-wire system ($T_{m,i}$), this means that it will be necessary to perform a torque allocation among these actuators, particularly, for $T_i < 0$. Throughout this chapter, we will assume that the torque allocation is performed by the hybrid ABS algorithm presented in Chapter 3.

Despite all the model simplifications adopted in this section, the control-oriented model (7.18) still features difficult nonlinearities, whose complexity is well reflected in the block diagram presented in Figure 7.2.

7.3 Controller Specification and Architecture

After introducing the vehicle modelling, we will now discuss in more detail the controller structure. The main goal of the vehicle's controller is to determine the torque and steer

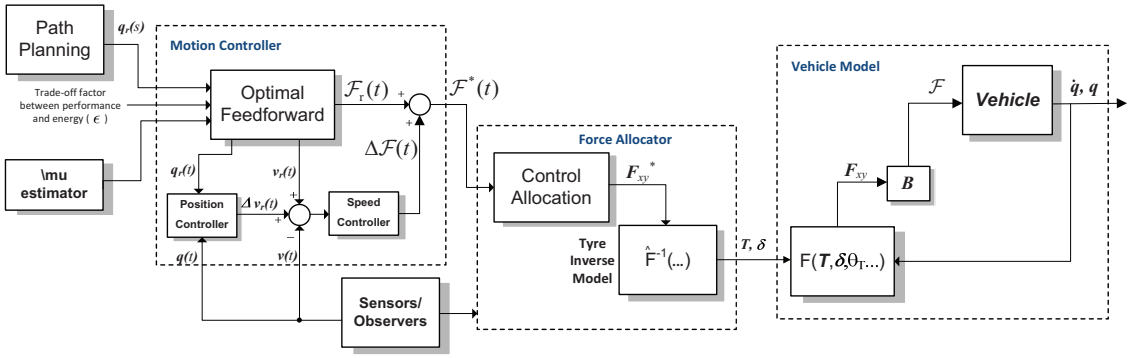

Figure 7.3: Block diagram of the proposed control algorithm.

values of each wheel, T_i, δ_i, so that the vehicle follows a given reference path, while respecting the dynamic constraints of the model. The speed at which the vehicle follows this reference path will be dependent on a tuning parameter, which will enable the user to explore trade-offs between performance (i.e., execute the path in minimum time) and energy consumption of the actuators. Further, if the information about the friction conditions is available, the motion controller should adapt its control actions to take into account the grip levels available in the tyre-road interface. Before presenting the design of this controller, it is pertinent to clarify some issues that may appear during the generation of the reference path.

7.3.1 Reference Path

Mathematically, the vehicle's desired position along the (geometric) path reference can be described by the vector $(p_{rX}(s), p_{rY}(s)) \in \mathbb{R}^2$, which is parameterized by the path coordinate $s \in \mathbb{R}_+$. Notice that this vector can be straightforwardly generated if the goal is to follow a known road (as is commonly done in lanekeeping system [277]), or if we want to develop an automatic driving system to follow a reference path set by a "leading car"[262]. Given that our interest here lies only on controlling the vehicle motion, in what follows, we will regard the path reference as known information.

In order to ensure that the vehicle follows the reference path $(p_{rX}(s), p_{rY}(s))$, its speed must be tangential to the path, i.e., parallel to the vector $\left(\frac{d}{ds}p_{rX}(s), \frac{d}{ds}p_{rY}(s)\right) = \rho_{XY}(s)e^{j\vartheta_r(s)}$. On the other hand, the angle of vehicle speed (with respect to the X axis) is equal to the sum of the side-slip (β) and yaw-angle(ψ), as illustrated in Figure 7.1. Therefore, to keep the vehicle in the desired path, the reference yaw-angle should fulfil:

$$p_{r\psi}(s) = \vartheta_r(s) - \beta_r(s) \tag{7.19}$$

where $\vartheta_r(s)$ is the (known) angle of the vector tangent to the reference path, and $\beta_r(s)$ is the desired side-slip that is intended to apply to the vehicle at position s. There are two main approaches to specifying the side-slip reference:

1. zero side-slip, $\beta_r(s) = 0$: this is a perfectly reasonable approach for vehicles with 4WS, as discussed in [286], [287], [288],

2. non-zero side-slip, $\beta_r(s) \neq 0$, is useful to perform parallel manoeuvres [281] or to explore the active control of β to carry out "controlled drift".

Hereafter, it will be assumed that a smooth, feasible reference path $\mathbf{p}_r(s) = [p_{rX}(s)\ p_{rY}(s)\ p_{r\psi}(s)]^T$ is known, as well as its first and second derivatives, $\mathbf{p}'_r(s), \mathbf{p}''_r(s)$.

7.3.2 Discussion on the Controller Architecture

In light of the nonlinearities that affect the vehicle model, the design of a control law for T_i, δ_i that will make $\mathbf{p}$ follow $\mathbf{p}_r$ in minimum time (or with minimum energy) is not obvious or trivial. The main reason for this difficulty lies in the complicated mechanism that governs the generation of the friction forces, specified by (7.18b)-(7.18d). To cope with these difficulties, in this work we will adopt a model-inversion approach for the friction forces. The idea is to design the controller under the assumption that the CoG forces and moments $\mathcal{F} \in \mathfrak{F}$ can be individually regulated. Inspecting (7.18), one can immediately conclude that using $\mathcal{F}$ as the virtual control input (instead of the true inputs, T_i and δ_i) enables us to decouple the generation of friction forces from the vehicle dynamics $(\mathbf{p}, \dot{\mathbf{p}})$, bringing undeniable advantages for the design of the motion controller. Accordingly, the controller proposed in this work will track the vehicle position $\mathbf{p}$ using $\mathcal{F}$ as the virtual control input (see block diagram presented in Figure 7.3). The generation of the true inputs, T_i and δ_i, will be then performed by the force allocation block, which is based on the control allocation concepts. In the next section, these two blocks will be presented with more detail.

Another important aspect that deserves some additional discussion is the availability of the feedback signals. In this work, it is assumed that the model's states, i.e., the vehicle position and orientation ($\mathbf{p}$), the vehicle speed $\mathbf{v}$, represented in the local coordinates, and the wheels' rotational velocity (ω_i), are available for feedback. While some of these signals are easily acquired, such as $\dot{\psi}$ and ω_i, others require expensive sensors or the development of advanced observers, such as lateral speed v_y and the vehicle position. Even if it is unusual to have all these signals available in today's cars, the trend in the automotive industry is toward the increased automation of the vehicle, particular with totally autonomous vehicles, and it is expected that in the near future these signals will become common measures [75, 277]. For example, today, there already commercial products (albeit expensive) that are capable of generating position and heading estimations with an accuracy of 2 cm and 0.1 degrees, respectively (see [289]).

.

7.4 Motion Controller

As shown in Figure 7.3, the motion controller proposed in this work is composed of three components: *i*) an optimal feedforward (FF) term; *ii*) a position loop; and *iii*) a speed loop, operating with the vehicle's local coordinates. The reasoning behind this approach is as follows. The vehicle's motion controller receives as main input the reference path $\mathbf{p}_r(s)$ that the vehicle should follow. To qualitatively specify how fast the vehicle should go through the reference path, the user (or the path planning layer) provides the parameter $\epsilon \in [0, 1]$, which represents a trade-off factor between the journey time and the energy consumption of the vehicle. This information is then used by the optimal FF to generate a suitable speed profile $\mathbf{v}_r(t)$ that must be imposed in the vehicle. In the calculation of $\mathbf{v}_r(t)$, the algorithm, besides the vehicle dynamics constraints, also takes into account the adhesion levels present in the tyre-road interface $\hat{\mu}_{max}$, which may be provided from a dedicated friction peak observer (see, e.g. [290]). Additionally, the optimal FF also

produces an estimative of the CoG forces and moments $\mathcal{F}_r$, which, if the vehicle model was perfect, would be enough to impose $\mathbf{v}_r(t)$ in the vehicle. Since, in practice, the model employed in the optimal FF contains approximation errors, besides the disturbances that affect the system, $\mathcal{F}_r$ is not sufficient to ensure the desired motion. Consequently, to cope with these uncertainties we added two additional loops to correct the vehicle speed and position. These loops are configured in a cascade setting, operating in parallel to the optimal FF. More specifically, the position loop generates speed increments to be superimposed in the speed profile $\mathbf{v}_r(t)$, while the speed loop manipulates force increments that are added to $\mathcal{F}_r(t)$.

In the remainder of this section, we will describe in detail the design of the three components that constitute the motion controller.

7.4.1 Optimal Feedforward

Construction of the Attainable Set of Forces

As already mentioned, the motion controller regards the CoG forces/moments $\mathcal{F} \in \mathfrak{F}$ as the virtual input for the system. Consequently, the first issue that needs to be addressed is the construction of the admissible set of forces and moments, i.e., $\mathfrak{F} \subset \mathbb{R}^3$; at first glance, it is not obvious how $\mathfrak{F}$ can be mathematically defined. Nonetheless, from the analysis carried out in Section 7.2, it is reasonable to expect that the attainable set will be dominated by the friction constraints ($\mathfrak{F}_f$) and the torque and power limits imposed by the IWMs ($\mathfrak{F}_T$):

$$\mathfrak{F} = \mathfrak{F}_f \bigcap \mathfrak{F}_T \tag{7.20}$$

As far as the friction constraints are concerned, it is worth recalling the result of Remark 7.3, which states that the tyre's friction limits in xy components are dependent on the friction peak μ_{max} and the vertical load (F_{zi}). In light of this result, one possible attempt to mathematically define $\mathfrak{F}_f$ is to consider:

$$\begin{aligned} \mathfrak{F}_f = \{\, \mathcal{F} = \mathbf{B}\mathbf{F}_{xy} \in \mathbb{R}^3 \quad | \quad \forall i \in \mathfrak{T} \\ \|\mathbf{E}_i \mathbf{F}_{xy}\|_2 \leq \mu_{max} F_{zi} \\ \approx \mu_{max} \left(F_{zi}^0 + \left(\frac{\varrho_{xi}}{m} \mathbf{e}_1^T + \frac{\varrho_{yi}}{m} \mathbf{e}_2^T \right) \mathcal{F} \right) \\ = \mu_{max} \left(F_{zi}^0 + \left(\frac{\varrho_{xi}}{m} \mathbf{e}_1^T + \frac{\varrho_{yi}}{m} \mathbf{e}_2^T \right) \mathbf{B}\mathbf{F}_{xy} \right) \} \end{aligned} \tag{7.21}$$

where $\mathbf{E}_i \in \mathbb{R}^{2\times 8}$ is a matrix that extracts the x and y components associated with the tyre $i \in \mathfrak{T}$. To keep the analysis simple, the influence of the resistance forces $\mathcal{R}$ were neglected in the calculation of the vertical forces F_{zi}.

Remark 7.4. $\mathfrak{F}_f$ is a convex set in $\mathbb{R}^3$.

The above claim can be verified by firstly noticing that each one of the four inequalities in (7.21) represents a second-order cone in $\mathbf{F}_{xy} \in \mathbb{R}^8$, which are convex constraints [112]. Remark 7.4 then follows from the fact that the $\mathfrak{F}_f$ is obtained by a linear transformation of a convex set (intersection of second order cones in $\mathbb{R}^8$), which is known to preserve the convexity property [112]. This property is also evident from the 3D geometric figure of the attainable set, shown in Figure 7.4. Moreover, it is interesting to note the important impact that μ_{max} has on the size of $\mathfrak{F}_f$, which is depicted in Figure 7.5.

While the torque and power constraints introduced by IWM are easily characterized in the domain (T_i, ω_i) (see (7.16)), transferring these constraints to the CoG forces/moments

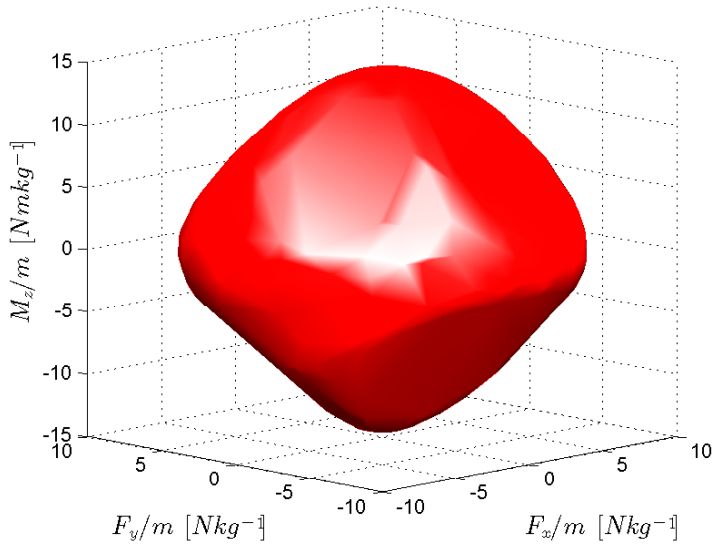

Figure 7.4: Attainable set of forces due to friction in the tyre-road interface, $\mathfrak{F}_f$, with $\mu_{max} = 1.0$.

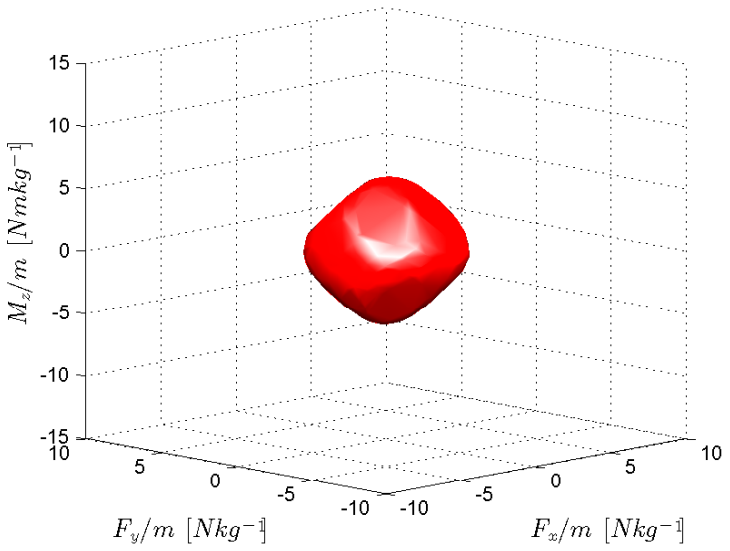

Figure 7.5: Attainable set of forces due to friction in the tyre-road interface, $\mathfrak{F}_f$, with $\mu_{max} = 0.4$.

$\mathcal{F}$ is not straightforward. The main reason for these hurdles is due to the complicated relations that exist between T_i and $\mathcal{F}$, as described in (7.18b)-(7.18f). Driven by the aim of finding a practical formulation for $\mathfrak{F}_T$, we will make three pragmatic assumptions. First, we will consider steady conditions for the wheel dynamics (7.16), that is

$$T_i \approx r_i F_{Li}, \quad i \in \mathfrak{T} \tag{7.22}$$

Second, the tyre longitudinal slips will be neglected, which allows us to approximate the wheel rotational velocity as $\omega_i \approx v_x/r_i$. Lastly, it will be assumed that the wheel steering

angles δ_i are small, enabling us to approximate $\mathbf{W}(\delta_i) \approx \mathbf{I}$, where $\mathbf{I}$ is the identify matrix. With these assumptions in mind, the effect of the power and torque limits (7.16) can be approximated as

$$\begin{aligned}\mathfrak{F}_T(v_x) &\approx \{\mathcal{F} = \begin{bmatrix}F_x & F_y & M_z\end{bmatrix}^T \in \mathbb{R}^3 \mid F_x = \sum_{i\in\mathfrak{T}} F_{Li} \\ &\qquad F_{Li} \leq \overline{T}/r_i \quad F_{Li} \leq \overline{P}/v_x, \forall i \in \mathfrak{T}\} \qquad (7.23)\\ &\approx \{\mathcal{F} = \begin{bmatrix}F_x & F_y & M_z\end{bmatrix}^T \in \mathbb{R}^3 \mid \\ &\qquad F_x \leq n_T\overline{F}, \quad F_x v_x \leq n_T\overline{P}\} \qquad (7.24)\end{aligned}$$

where $n_T = 4 = \#\mathfrak{T}$ and $\overline{F} = \overline{T}/r_i$. The above set provides a very reasonable approximation of the torque/power constraints in straight-line conditions, but its accuracy deteriorates when the cornering manoeuvres become more aggressive (i.e., when δ_i increases). Since during cornering conditions the longitudinal accelerations are normally low, it is expected that the approximation errors in $\mathfrak{F}_T(v_x)$ will be reduced.

Path Following Problem

The optimal FF controller proposed in this work will be designed with the help of a path following setting. Accordingly, we start by noticing that if the equations of motion are ideal ($\mathcal{D} \equiv 0$), and if the position error at the initial instant is zero ($\mathbf{p}(0) = \mathbf{p}_r(0)$, then the perfect tracking of $\mathbf{p}_r$ can be ensured if the following condition holds:

$$\left(\mathbf{T}^{-1}(\mathbf{p}_r)\mathbf{M}\right)\ddot{\mathbf{p}}_r + \mathcal{R}_2(\mathbf{p}_r, \dot{\mathbf{p}}_r)\dot{\mathbf{p}}_r + \mathcal{R}_1 = \mathcal{F}_r, \quad \mathcal{F}_r \in \mathfrak{F} \qquad (7.25)$$

where $\mathcal{F}_r$ is the feedforward force term. Given that the reference path is specified with the path coordinate s, i.e., $\mathbf{p}_r(s)$, we can apply the composite rule for the derivate operator to express the first and second time derivative of $\mathbf{p}_r$ as:

$$\dot{\mathbf{p}}_r(s) = \frac{d\mathbf{p}_r(s)}{dt} = \frac{d\mathbf{p}_r(s)}{ds}\frac{ds}{dt} = \mathbf{p}_r'(s)\dot{s} \qquad (7.26)$$

$$\ddot{\mathbf{p}}_r(s) = \frac{d^2\mathbf{p}_r(s)}{dt^2} = \mathbf{p}_r''(s)\dot{s}^2 + \mathbf{p}_r'(s)\ddot{s} \qquad (7.27)$$

Inserting these relations in (7.25), and after some straightforward algebraic manipulations, we obtain:

$$\mathbf{m}(s)\ddot{s} + \mathbf{r}_2(s)\dot{s}^2 + \mathbf{r}_1 = \mathcal{F}_r, \quad \mathcal{F}_r \in \mathfrak{F} \qquad (7.28)$$

where

$$\begin{aligned}\mathbf{m}(s) &= \mathbf{T}^{-1}(\mathbf{p}_r(s))\mathbf{M}\mathbf{p}_r'(s)\\ \mathbf{r}_2(s) &= \mathbf{T}^{-1}(\mathbf{p}_r(s))\mathbf{M}\mathbf{p}_r''(s) + \mathcal{R}_2(\mathbf{p}_r(s), \mathbf{p}_r'(s))\mathbf{p}_r'(s)\\ \mathbf{r}_1 &= \mathcal{R}_1 \qquad (7.29)\end{aligned}$$

Notice that we made use of Remark 7.1, together with the fact that $\dot{s} > 0$ (speed reverses along the reference path are not allowed), to determine the term $\mathbf{r}_2$. In addition, we must also point out that the use of the composite rule to reach the formulation (7.28) has been widely used in the motion control of robotic arms [282, 283]. Our idea here is to explore this formulation for a slightly different problem: path following in highly redundant vehicles. Finally, the vehicle speed (in the local coordinates) can also be expressed as a function of

s:

$$\mathbf{v}_r(s) = \mathbf{T}^{-1}(\mathbf{p}_r(s))\mathbf{p}_r'(s)\dot{s} = \tilde{\mathbf{v}}_r(s)\dot{s} \tag{7.30}$$

With this setting, we are now in the condition of defining the minimum-time path following problem:

$$\begin{aligned} &\min_{\mathcal{F}_r,s,\dot{s},\ddot{s},T} T \\ &s.t. \quad \mathbf{m}(s(t))\ddot{s} + \mathbf{r}_2(s(t))\dot{s}^2 + \mathbf{r}_1 = \mathcal{F}_r(t) \\ &\qquad s(0) = 0, \quad s(T) = 1, \quad \dot{s}(0) = \dot{s}_0 \\ &\qquad \dot{s}(t) > 0 \\ &\qquad \mathcal{F}_r(t) \in \mathfrak{F}_f \bigcap \mathfrak{F}_T, \qquad t \in [0, T] \end{aligned} \tag{7.31}$$

Going through the problem constraints, one can find that the first equality is due to the path following setting; the second set of equalities expresses the boundary constraints for the problem ($\dot{s}_0$ is the initial normalized speed); in the third we make $\dot{s}$ positive, as speed reversals are not allowed, and the last constraint is related to the admissible set of forces/moments that can be applied to the vehicle.

Convexification

In order to facilitate the resolution of the optimization problem we will now discuss a series of practical modifications, which will ultimately lead to a convex formulation. First, we will adopt the change of independent variable suggested in [282, 283]: instead of time (t), we will consider the normalized distance in the reference path, s, as the new independent variable. This means that $\dot{s} = ds/dt$, which enables us to rewrite the cost function as:

$$T = \int_0^T 1dt = \int_{s(0)}^{s(T)} \frac{ds}{\dot{s}} = \int_0^1 \frac{1}{\dot{s}} ds \tag{7.32}$$

Furthermore, with this change of variable, the terms $\ddot{s}$ and $\dot{s}^2$ appear linearly in (7.28). This observation leads [282, 283] to introduce a second change of variable

$$a(s) = \ddot{s}^2, \quad b(s) = \dot{s}^2 \tag{7.33}$$

which are related through a linear differential equation:

$$a(s) = \frac{d\dot{s}}{dt} = \dot{s}\frac{d\dot{s}}{ds} = \frac{1}{2}\frac{d\dot{s}^2}{ds} = \frac{1}{2}\frac{d(b(s))}{ds} \tag{7.34}$$

Thus, with the introduction of $a(s)$ and $b(s)$, the nonlinear differential relation (7.28) is decoupled into two parts: one affine constraint ($\mathbf{m}(s)a + \mathbf{r}_2(s)b + \mathbf{r}_1 = \mathcal{F}_r$), and one linear differential equation (7.34). This decoupling brings obvious advantages to the resolution of (7.31).

Another aspect that deserves discussion is the convexity of the admissible set $\mathfrak{F}$, which is the result of the friction limits ($\mathfrak{F}_f$) and the torque/power constraints of the electric motors ($\mathfrak{F}_T(v_x)$). While the convexity of $\mathfrak{F}_f$ was already established in Remark 7.4, the set $\mathfrak{F}_T(v_x)$ requires further analysis. From (7.24) it is clear that the power and torque limits affect mainly the F_x component of $\mathcal{F}$; thus, it is more practical to analyse these constraints in the domain (v_x,F_x):

$$\Omega_T = \{(v_x, F_x) \in \mathbb{R}^2 \ : \ F_x v_x \leq n_T \overline{P}, \quad F_x \leq n_T \overline{F}\} \tag{7.35}$$

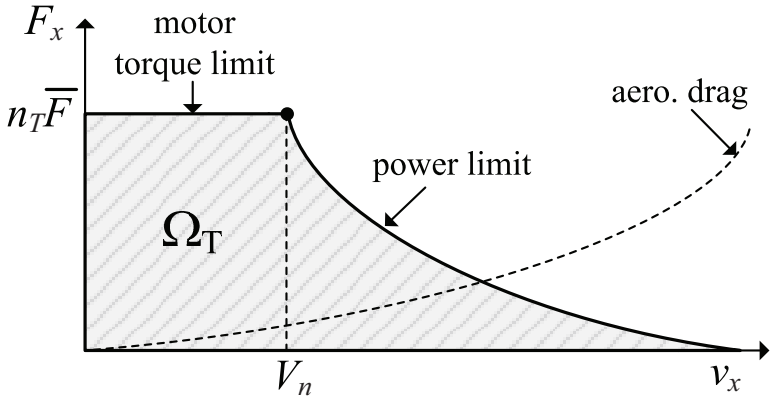

(a)

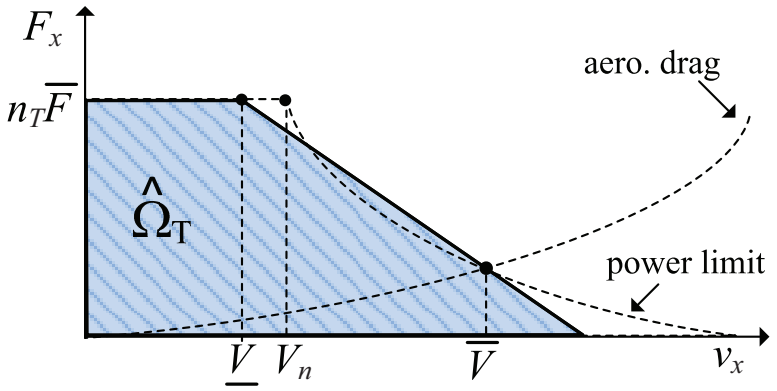

(b)

Figure 7.6: Non-convex (a) and convex approximation (b) of the power limits introduced by the electric motors.

As depicted in Figure 7.6(a), when the vehicle exceeds the nominal speed $V_n = \overline{P}/\overline{F}$ the power constraints makes the Ω_T non-convex, which is a relevant obstacle to the establishment of global optimal solution for the optimization problem [112]. To mitigate this issue, we will apply a convexification technique to handle the power constraint. The idea is to approximate the non-convex constraint $F_x v_x \leq n_T \overline{P}$ with a linear inequality characterized by the points $(\underline{V}, n_T\overline{F})$, and $(\overline{V}, n_T\overline{P}/\overline{V})$, as illustrated in Figure 7.6(b). The points $\underline{V} \leq V_n$ and $\overline{V} \geq V_n$ are parameters that the designer can choose to tune the approximation; for example, a good rule of thumb is to select $\overline{V}$ close to the point where the aerodynamic drag overcomes the maximum power of the vehicle. The linear approximation of Ω_T can also be expressed as

$$\hat{\Omega}_T = \{(v_x, F_x) \ : \ F_x \leq (v_x - \underline{V})\tilde{\gamma}_p + n_T\overline{F}, \quad F_x \leq n_T\overline{F}\}$$

where $\tilde{\gamma}_p = n_T \frac{\overline{P}/\overline{V} - \overline{F}}{\overline{V} - \underline{V}}$.

Now, notice that after introducing the new variable b, and taking into account (7.30), the vehicle longitudinal speed is given by $v_x = \mathbf{e_1}^T \tilde{\mathbf{v}}_r(s)\dot{s} = \mathbf{e_1}^T \tilde{\mathbf{v}}_r(s)\sqrt{b(s)}$. This implies that the power constraints in $\hat{\Omega}_T$, although being linear in v_x, become nonlinear when

we include the new variable $b(s)$; in fact, it also loses the convexity property[3], which is even more worrying for our purposes here. This issue spurred us to find an alternative convexification technique that can be applied to the space $(F_x, b(s))$. With this goal in mind, it is convenient to first relate v_x and b as:

$$b = \left(\frac{v_x}{\mathbf{e_1}^T \tilde{\mathbf{v}}_r(s)} \right)^2 \tag{7.36}$$

Now, recall that the linear approximation in (F_x, v_x) was characterized by a half-plane that passes through the points $(\underline{V}, n_T\overline{F})$, $(\overline{V}, n_T\overline{P}/\overline{V})$. One alternative way of dealing with the linear approximation with $b(s)$ is to translate this half-plane to the space $((F_x, b(s))$, using, for that purpose, the relation (7.36):

$$(v_x, F_x) \quad \longrightarrow \quad (b(s), F_x) \tag{7.37}$$
$$(\underline{V}, n_T\overline{F}) \quad \longrightarrow \quad (\underline{b}(s), n_T\overline{F}) \tag{7.38}$$
$$(\overline{V}, n_T\overline{P}/\overline{V}) \quad \longrightarrow \quad (\overline{b}(s), n_T\overline{P}/\overline{V}) \tag{7.39}$$

where

$$\overline{b}(s) = \left(\frac{\overline{V}}{\mathbf{e_1}^T \tilde{\mathbf{v}}_r(s)} \right)^2, \quad \underline{b}(s) = \left(\frac{\underline{V}}{\mathbf{e_1}^T \tilde{\mathbf{v}}_r(s)} \right)^2 \tag{7.40}$$

The resulting linear approximation of the power constraint is then obtained as:

$$F_x \leq \gamma_p(s)(b - \underline{b}(s)) + n_T\overline{F}, \quad \gamma_p(s) = n_T \frac{\overline{P}/\overline{V} - \overline{F}}{\overline{b}(s) - \underline{b}(s)} \tag{7.41}$$

Although this constraint will inevitably introduce approximation errors, we believe this is a practical approach to handling the power limitation of the electric motors.

In summary, the path following problem can be recast as:

$$\begin{aligned}
\min_{\mathcal{F}_r, a, b} \ & \epsilon \int_0^1 \frac{1}{\sqrt{b(s)}} ds + (1-\epsilon) \int_0^1 \mathcal{F}_r(s)^T \mathbf{W} \mathcal{F}_r(s) ds \\
s.t. \quad & \mathbf{m}(s)a(s) + \mathbf{r}_2(s)b(s) + \mathbf{r}_1 = \mathcal{F}_r(s) \\
& \frac{d}{ds}b(s) = 2a(s), \quad b(0) = \dot{s}_0^2, \qquad b(s) > 0 \\
& \mathcal{F}_r(s) \in \mathfrak{F}_f, \qquad \mathbf{e}_1^T \mathcal{F}_r(s) \leq n_T\overline{F} \\
& \mathbf{e}_1^T \mathcal{F}_r(s) \leq \gamma_p(s)(b(s) - \underline{b}(s)) + n_T\overline{F} \\
& s \in [0, \overline{s}]
\end{aligned} \tag{7.42}$$

Notice that, to (indirectly) penalize the energy consumption of the vehicle, a quadratic term in the forces $\mathcal{F}_r$ was incorporated into the cost function. This penalization is controlled through the diagonal weight matrix $\mathbf{W} = \text{diag}\{w_1, w_2, w_3\}$ and the parameter ϵ, which represents a trade-off factor between the min-time and the energy consumption goals. Of course, in practice, the real energy consumption of the vehicle will not be described by this quadratic-term, and will require more complex relations, involving control

[3] to briefly demonstrate the loss of convexity, notice that power constraint can be expressed as: $F_x + k_0\sqrt{b(s)} \leq k_1$, where $k_0 = -\tilde{\gamma}_p \mathbf{e_1}^T \tilde{\mathbf{v}}_r(s), k_1$ are positive constants. This inequality is not convex due to the presence of $k_0\sqrt{b(s)}$, a concave function (see [112] for further details).

variables that are not addresses at this layer (e.g., motor torques). Nonetheless, to keep the problem tractable, and given that $\mathcal{F}_r$ is regarded as a pseudo-input at this stage, we opted to indirectly penalize the energy consumption of the vehicle through the quadratic term in $\mathcal{F}_r$.

Remark 7.5. The above optimization problem is convex.

This property was already pointed out by [282] in a robotics context, and is extended here for the minimum-time path following of autonomous vehicles. In fact, in comparison with the minimum-time path-following problem of robotic manipulators [282, 283], the main differences in the vehicle's case lie in the friction circle ($\mathfrak{F}_f$) and power limits constraints ($\mathfrak{F}_T$), which generally are not relevant for robotics applications.

In order to gain additional insight into the problem (7.42), it is also useful to determine the maximum operation envelope of the vehicle throughout the reference path. Such envelope can be constructed by exploiting the link between the force $\mathcal{F}$, pseudo-acceleration (a) and pseudo-velocity (b). In particular, by referring the friction and power limits of $\mathcal{F}$ to the (a,b) space, the maximum operation envelope can be defined as:

$$\begin{aligned}\Phi(s) \;=\; \{(a,b)\in\mathbb{R}^2 \mid\quad & \mathbf{m}(s)a+\mathbf{r}_2(s)b+\mathbf{r}_1=\mathcal{F}_r,\\ & \mathcal{F}_r\in\mathfrak{F}_f,\quad \mathbf{e}_i^T\mathcal{F}_r\le n_T\overline{F},\quad b>0\\ & \mathbf{e}_i^T\mathcal{F}_r\le\gamma_p(s)(b-\underline{b}(s))+n_T\overline{F}\quad\}\end{aligned}$$

For a fixed s, $\Phi(s)$ gives the domain of the pseudo-acceleration and pseudo-speed that can be applied to the vehicle. For example, Figure 7.7 illustrates the evolution of this domain when the vehicle negotiates a 180-degree corner. It can be observed that during straight-line conditions ($s\in[0,40]\cup[110,150]m$), the $\Phi(s)$ set presents, as expected, a large operation window, both in the vehicle (pseudo) velocity and acceleration. On the other hand, for $s\in[45,105]$ the vehicle enters in the corner, and one can find that the size of the $\Phi(s)$ decreases significantly, particularly the maximum allowed pseudo-velocity. This evolution mimics well the typical feeling of the vehicle's driver, which generally reduces the velocity of the car when negotiating corners.

Collocation Method

Despite the convexity property of (7.42), the vehicle model still contains difficult nonlinearities, particularly in the constraints of the friction forces, which complicates the analytical establishment of the optimality conditions for the continuous problem. Consequently, to facilitate the resolution of this problem, we adopted a direct optimization approach, also known as the collocation formulation [284, 291]. The main idea is to discretize the path coordinate into a grid with $N+1$ points: $s^0<s^1<...<s^N$; the value of the variable a at the grid points will be referred as $a(s^k)=a^k$, $k=0,\ldots,N$; this notation is also extended to the remaining variables in the problem, i.e., $\mathcal{F}_r^k, b^k, \mathbf{m}^k, \mathbf{r}_2^k, \mathbf{r}_1^k, \underline{b}^k, \overline{b}^k, \gamma_p^k$. The discretization of the integral and the (single) differential equation will be performed using the well-known trapezoidal method. As a result, the relation $\frac{dx(s)}{ds}=f(x(s))$ is approximated with

$$x^{k+1}=x^k+\frac{\Delta s^k}{2}\Big(f(x^{k+1})+f(x^k)\Big) \tag{7.43}$$

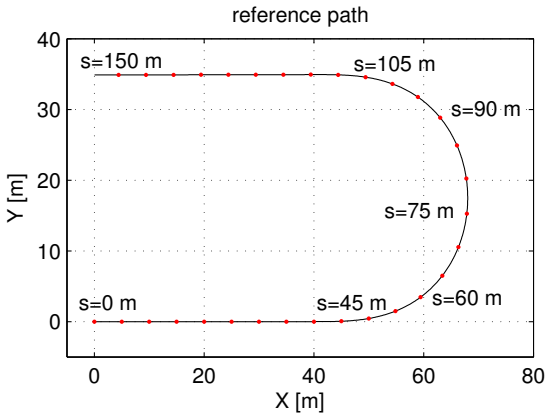

(a)

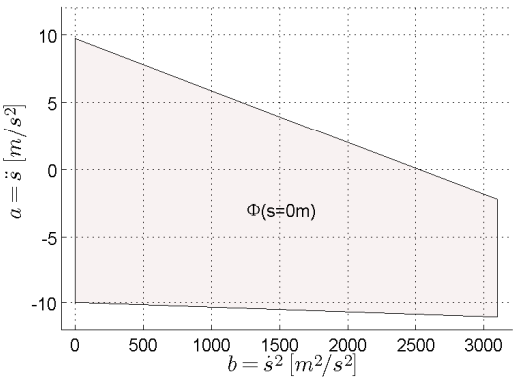

(b) $s = 0m$

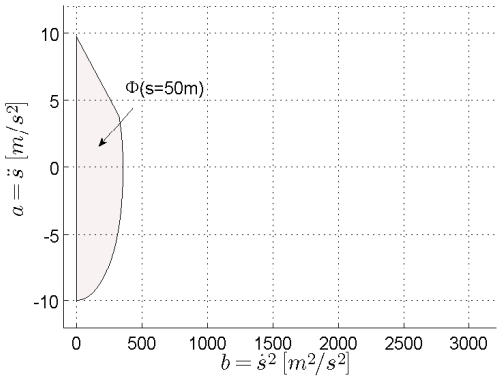

(c) $s = 50m$

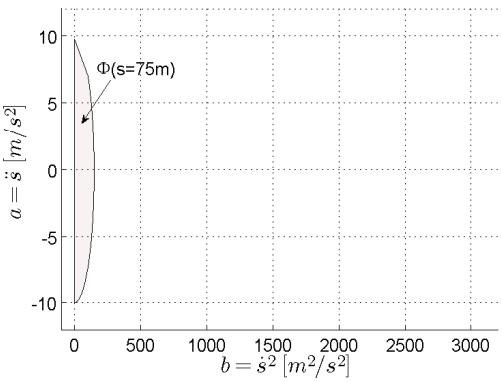

(d) $s = 75m$

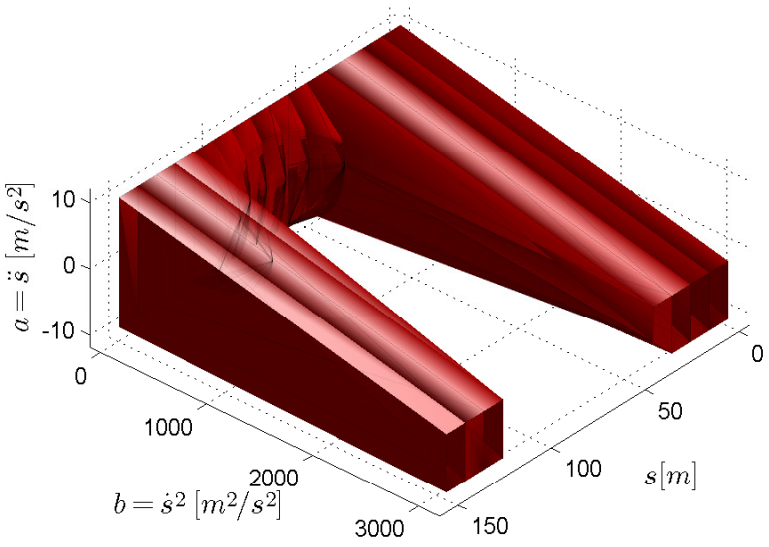

(e)

Figure 7.7: Maximum operation envelope of the vehicle when negotiating a 180° corner ($\mu_{max} = 1.0$).

where $\Delta s^k = s^{k+1} - s^k$. Applying this discretization approach to (7.42), we obtain:

$$\begin{aligned}
\min \sum_{k=0}^{N-1} & 0.5\Delta s^k \Bigg(\epsilon \left(\frac{1}{\sqrt{b^{k+1}}} + \frac{1}{\sqrt{b^k}} \right) \\
& \qquad + (1-\epsilon) \left((\mathcal{F}_r^k)^T \mathbf{W} \mathcal{F}_r^k + (\mathcal{F}_r^{k+1})^T \mathbf{W} \mathcal{F}_r^{k+1} \right) \Bigg) \\
s.t. \quad & \mathbf{m}^k a^k + \mathbf{r}_2^k b^k + \mathbf{r}_1 = \mathcal{F}_r^k \\
& b^{k+1} = b^k + \Delta s^k (a^{k+1} + a^k), \quad b^0 = \dot{s}_0^2, \qquad b^k > 0 \\
& \mathcal{F}_r^k \in \mathfrak{F}_f, \qquad \mathbf{e}_1^T \mathcal{F}_r^k \leq n_T \overline{F} \\
& \mathbf{e}_1^T \mathcal{F}_r^k \leq \gamma_p^k (b^k - \underline{b}^k) + n_T \overline{F}, \qquad k = 0, 1, \ldots, N-1
\end{aligned} \tag{7.44}$$

To avoid overloading the notation in the above problem, we opted to omit the explicit definition of $\mathfrak{F}_f$. Nonetheless, the discrete implementation of $\mathcal{F}_r^k \in \mathfrak{F}_f$ is not problematic, and, as a matter of fact, it only requires an addition equality and 4 second-order cone constraints (see (7.21)). As for the numerical solution of the optimization problem, it is worth pointing out that (7.44) adheres to the disciplined convex rules, a concept introduced in [292] to facilitate the resolution of convex optimization problems. Consequently, the above problem can be coded in the CVX environment [293] and efficiently solved with the help of the SDPT3 numerical solver [294]. Finally, after extracting the numerical solution, the time-domain variables can then be recuperated using the relation (7.32); variables of particular interest are the feedforward term $\mathcal{F}_r(t)$, the reference trajectory $\mathbf{p}_r(t)$ and the speed profile $\mathbf{v}_r(t)$.

7.4.2 Speed Controller

Due to disturbances and modelling errors, the feedforward force term $\mathcal{F}_r(t)$ is generally not sufficient to ensure the tracking of $\mathbf{p}_r$. One possible way to robustly control the motion controller is to incorporate feedback loops that can track the speed profile $\mathbf{v}_r(t)$ and the reference trajectory $\mathbf{p}_r(t)$ obtained during the optimization process. In fact, the direct control of the vehicle speed $\mathbf{v}$ is a very appealing prospect, and it is already performed in today's cars, e.g., v_x is controlled by cruise control systems [187], while the yaw-rate ($\dot{\psi}$) and the lateral speed (v_y) are normally controlled (or, at least, stabilized) during emergency situations [40]. So, from this perspective, it seems reasonable to keep this speed-control layer in the motion control of the vehicle.

In order to construct the speed loop, it is convenient to represent the vehicle dynamics in the local coordinates fixed with the CoG, i.e., xy frame. Toward that goal, the vehicle equation of motion (7.8) can be rearranged as:

$$\mathbf{M} \left(\mathbf{T}^{-1}(p_\psi) \ddot{\mathbf{p}} \right) = \mathcal{F} - \mathcal{R}(.) + \mathcal{D} \tag{7.45}$$

By working out the left part of the equation we obtain

$$\begin{aligned}\mathbf{T}^{-1}(p_\psi)\ddot{\mathbf{p}} &= \mathbf{T}^{-1}(p_\psi)\frac{d}{dt}\left(\mathbf{T}(p_\psi)\mathbf{v}\ \right) \\ &= \mathbf{T}^{-1}(p_\psi)\left(\left(\frac{d}{dt}\mathbf{T}(p_\psi)\right)\mathbf{v} + \mathbf{T}(p_\psi)\dot{\mathbf{v}}\ \right) \\ &= \mathbf{T}^{-1}(p_\psi)\left(\mathbf{T}'(p_\psi)\dot{p}_\psi\mathbf{v}\right) + \dot{\mathbf{v}} \\ &= \underbrace{\begin{bmatrix} -v_y\dot{\psi} \\ v_x\dot{\psi} \\ 0 \end{bmatrix}}_{g(\mathbf{v})}\mathbf{v} \quad + \quad \dot{\mathbf{v}}\end{aligned} \tag{7.46}$$

Replacing this term in (7.45), we get the vehicle dynamics, expressed in the local coordinates,

$$\mathbf{M}\left(g(\mathbf{v}) + \dot{\mathbf{v}}\right) = \mathcal{F} - \mathcal{R}(\mathbf{v}) + \mathcal{D} \tag{7.47}$$

which uses the resistance force model $\mathcal{R}(\mathbf{v})$, parameterized with the vehicle velocity (see (7.84)). Following the procedure initiated in the previous section, the speed controller design will be performed under the assumption that forces and moments of the CoG, $\mathcal{F}$, can be regarded as the virtual control inputs. Accordingly, the control goal is to design a law for $\mathcal{F}$ that will make the vehicle velocity $\mathbf{v}$ follow the speed profile $\mathbf{v}_r$, in spite of the disturbance $\mathcal{D}$. For the undisturbed case($\mathcal{D} \equiv 0$), the control task can be accomplished by using the feedforward term $\mathcal{F}_r$; this is,

$$\mathbf{M}\left(g(\mathbf{v}_r) + \dot{\mathbf{v}}_r\right) = \mathcal{F}_\mathbf{r} - \mathcal{R}(\mathbf{v}_r) \tag{7.48}$$

Since, in practice, the vehicle is subject to modelling errors and disturbance, it is inevitable the appearance of non-zero tracking errors $\mathbf{e}_v = \mathbf{v} - \mathbf{v}_r$. These errors have the following dynamics:

$$\mathbf{M}\dot{\mathbf{e}}_v = \mathcal{F} - \mathcal{F}_r + \mathbf{M}\left(g(\mathbf{v}_r) - g(\mathbf{v})\right) + \mathcal{R}(\mathbf{v}_r) - \mathcal{R}(\mathbf{v}) + \mathcal{D} \tag{7.49}$$

Spurred by the input-output linearization technique [96], the most relevant nonlinearities in the above model can be cancelled by selecting the CoG force as:

$$\mathcal{F} = \underbrace{\mathbf{M}\Delta a}_{\Delta\mathcal{F}} + \mathcal{F}_r - \mathbf{M}\left(g(\mathbf{v}_r) - g(\mathbf{v})\right) - \mathcal{R}(\mathbf{v}_r) + \mathcal{R}(\mathbf{v}) \tag{7.50}$$

where $\Delta a \in \mathbb{R}^3$ represents acceleration increments (a new virtual control) that will be directly manipulated by the controller. This cancellation brings considerable simplification to the error model:

$$\dot{\mathbf{e}}_v = \Delta a + \mathcal{D}_a \tag{7.51}$$

where $\mathcal{D}_a = \mathbf{M}^{-1}\mathcal{D} \in \mathbb{R}^3$ is the equivalent accelerations due to $\mathcal{D}$. Note that, albeit (7.50) assumes exact knowledge of some model parameters (e.g., $\mathbf{M}$), in practice the influence of these parametric errors can be effortlessly embedded in $\mathcal{D}_a$. To facilitate the design of the controller, it is convenient to represent the above MIMO (multiple input, multiple output) system as a set of 3 SISOs (single input, single output):

$$\dot{e}_{vj} = \Delta a_j + \mathcal{D}_{aj} \tag{7.52}$$

where $j \in \mathfrak{J} = \{x, y, \psi\}$ represents the sub-index associated with each one of the degrees of

freedom in the vehicle's local coordinate system. The main challenge in the design of the speed controller lies in the effective attenuation of $\mathcal{D}_{aj}$. To cope with this difficulty, we will explore here a sliding-mode formulation, endowed with conditional integrators [165, 171] (which was already introduced in Chapter 4 for the design of the wheel-slip controller). The proposed control law is given by:

$$\Delta a_j = -k_{aj}\,\mathrm{sat}\left(\frac{\sigma_j}{\varepsilon_j}\right) \tag{7.53a}$$

$$\sigma_j = e_{vj} + k_{\eta j}\eta_j \tag{7.53b}$$

$$\dot{\eta}_j = -k_{\eta j}\eta_j + \varepsilon_j\,\mathrm{sat}\left(\frac{\sigma_j}{\varepsilon_j}\right), \qquad j \in \mathfrak{J} \tag{7.53c}$$

where k_{aj}, $k_{\eta j}$, ε_j are the controller's parameters, η_j the value of the (conditional) integrator, σ_j the sliding variable and $\mathrm{sat}(w) = \mathrm{sgn}(w)\min(1, |w|)$ the saturation function. The properties of the resulting closed loop system are as follows:

Proposition 7.1. *Consider the system* (7.52)*, controlled by* (7.53)*. It holds that:*

1. *if* $|\eta_j(0)| \leq \frac{\varepsilon_j}{k_{\eta j}}$*, then* $|\eta_j(t)| \leq \frac{\varepsilon_j}{k_{\eta j}}$*, for* $t \geq 0$

2. *for an arbitrary bounded disturbance* $\mathcal{D}_{aj} \leq \overline{\mathcal{D}}_{aj}$*, and assuming*

$$k_{aj} > \overline{\mathcal{D}}_{aj} + 2k_{\eta j}\varepsilon_j, \qquad j \in \mathfrak{J} \tag{7.54}$$

then system state will reach in finite time the set:

$$\Xi_j = \{|e_{vj}| \leq 2\varepsilon_j, \quad |\sigma_j| \leq \frac{\varepsilon_j}{k_{\eta j}}\} \subset \mathbb{R}^2, \qquad j \in \mathfrak{J} \tag{7.55}$$

3. *in addition, if i) the disturbance is Lipchitz in the domain* Ξ_j*, i.e.,*

$$|\mathcal{D}_{aj}(e_a) - \mathcal{D}_{aj}(e_b)| \leq L_j|e_a - e_b|, \quad \forall e_a, e_b \in \{|x| \leq 2\varepsilon_j\}$$

where L_j *is the Lipchitz constant,* $j \in \mathfrak{J}$*; and ii) the controller's parameters fulfil:*

$$k_{\eta j} > 0, \quad 0 < \varepsilon_j < \frac{4k_{\eta j}k_{aj}}{4k_{\eta j}L_j + (L_j k_{\eta j} + 1)^2} \tag{7.56}$$

then, the tracking error, besides reaching Ξ_j*, will asymptotically converge to zero, i.e.,* $e_{vj} \to 0$*.*

Proof. the above result is demonstrated in Appendix 7.9 (which is reformulated with a friendlier notation, without the sub-indexes j). □

In summary, the results presented in the above proposition showed that for (general) bounded disturbances the absolute value of the tracking error e_{vj} will ultimately be bounded by $2\varepsilon_j$. Asymptotic convergence to zero can be ensured for the (particular) case where $\mathcal{D}_{aj}$ is locally Lipchitz. Regarding the tuning of the controller's parameters, it is instructive to start analysing the controller when it operates in the linear range. In particular, for $|\sigma_j| \leq \varepsilon_j$ one can find that the saturation functions in (7.53) become linear,

resulting in the following control law:

$$\Delta a_j = -\frac{k_{aj}}{\varepsilon_j} e_{vj} - \frac{k_{aj}}{\varepsilon_j} k_{\eta j} \eta_j \tag{7.57}$$

$$\dot{\eta}_j = e_{vj}, \qquad |e_{vj} + k_{\eta j}\eta_j| \leq \varepsilon_j \tag{7.58}$$

Thus, the proposed controller operates as a simple proportional+integral controller when the sliding variable is small. In light of this interpretation, we can now appreciate the practical benefits of the first claim in the Proposition 7.1: the bound $|\eta_j(t)| \leq \frac{\varepsilon_j}{k_{\eta j}}$ endows the controller with anti-windup mechanisms to cope with the saturation of the integral action. Moreover, within the controller's linear operation, the closed-loop dynamics can be expressed as:

$$\begin{bmatrix} \dot{\eta}_j \\ \dot{e}_{vj} \end{bmatrix} = \begin{bmatrix} 0 & 1 \\ -\frac{k_{aj}}{\varepsilon_j} k_{\eta j} & -\frac{k_{aj}}{\varepsilon_j} \end{bmatrix} \begin{bmatrix} \eta_j \\ e_{vj} \end{bmatrix} + \begin{bmatrix} 0 \\ \mathcal{D}_{aj} \end{bmatrix} \tag{7.59}$$

which has the following second-order characteristic polynomial:

$$\lambda^2 + \underbrace{\frac{k_{aj}}{\varepsilon_j}}_{2\zeta_j\omega_{nj}} \lambda + \underbrace{\frac{k_{aj}}{\varepsilon_j} k_{\eta j}}_{\omega_{nj}^2} = 0, \qquad j \in \mathfrak{J} \tag{7.60}$$

where ω_{nj}, ζ_j are the natural frequency and damping, respectively, of the (undisturbed) closed loop dynamics. This means that the designer can also employ pole-placement techniques to guide the selection of the parameters k_{aj}, $k_{\eta j}$, ε_j. For instance, assuming a given specification for the controller's transient response, through the variables ζ_j, ω_{nj}, the selection of parameters can take into account the relations:

$$k_{\eta j} = \frac{\omega_{nj}}{2\zeta_j}, \qquad \frac{k_{aj}}{\varepsilon_j} = 2\zeta_j\omega_{nj}, \qquad j \in \mathfrak{J} \tag{7.61}$$

while the bounds (7.54),(7.56) ensure the controller's robust operation.

7.4.3 Position Controller

The use of the speed loop, although improving the robustness of the feedforward controller, is, in general, not enough to cope with all the disturbances and model mismatches. For example, the speed loop is not able to attenuate a simple initial error in the vehicle position, $\mathbf{p}(0) \neq \mathbf{p}_r(0)$ (the difference in initial conditions will impose an offset in the vehicle motion). In order to overcome these difficulties, we will add a second feedback loop, based on the vehicle position and orientation, which is connected in cascade with the speed controller, presented above (see Figure 7.3). The goal of the position loop is to make $\mathbf{p}(t)$ follow $\mathbf{p}_r(t)$ as fast as possible, using, for that purpose, speed increments. As the vehicle speed is being regulated in a lower level, the design of the position loop can be carried out in a kinematic setting, i.e., employing the speeds as pseudo-controls. Accordingly, using the vehicle kinematic model (7.4) and the position error $\mathbf{e}_p = \mathbf{p} - \mathbf{p}_r$, the error dynamic is defined as:

$$\dot{\mathbf{e}}_p = \mathbf{T}(\mathbf{p})\mathbf{v} - \mathbf{T}(\mathbf{p}_r)\mathbf{v}_r + \mathcal{D}_v \tag{7.62}$$

where $\mathcal{D}_v \in \mathbb{R}^3$ represents speed disturbances. Given that the change of variable $\mathbf{T}(\mathbf{p})$ is invertible, one possible way to simplify the error dynamics is to apply, again, the input-output linearization technique. With this goal in mind, the nonlinearities in (7.62) can be cancelled by imposing

$$\mathbf{v} = \mathbf{T}^{-1}(\mathbf{p})\left(\mathbf{T}(\mathbf{p}_r)\mathbf{v}_r + \Delta\nu\right) \tag{7.63}$$

where $\Delta\nu \in \mathbb{R}^3$ is a speed increment. This change of variable yields the following simplified error dynamics:

$$\dot{\mathbf{e}}_p = \Delta\nu + \mathcal{D}_v \tag{7.64}$$

which can also be represented through a set of three SISO systems:

$$\dot{e}_{pk} = \Delta\nu_k + \mathcal{D}_{vk} \tag{7.65}$$

where $k \in \mathfrak{K} = \{X, Y, \psi\}$ represents the three degrees of freedom of the vehicle in the 2D plane. Given the similarities between the above model and (7.51), we will apply the same sliding mode control with the conditional integrators technique to stabilize the error dynamics, that is:

$$\Delta\nu_k = -k_{vk}\,\mathrm{sat}\left(\frac{\sigma_k}{\varepsilon_k}\right) \tag{7.66a}$$

$$\sigma_k = e_{vj} + k_{\eta k}\eta_k \tag{7.66b}$$

$$\dot{\eta}_k = -k_{\eta k}\eta_k + \varepsilon_k\,\mathrm{sat}\left(\frac{\sigma_k}{\varepsilon_k}\right), \qquad k \in \mathfrak{K} \tag{7.66c}$$

where σ_k, η_k are the sliding variable and integral error (for the position) and $k_{vk}, k_{\eta k}, \varepsilon_k$ the controller's parameters. The closed-loop properties of the position controller are equivalent to the ones established in Proposition 7.1; the only difference lies, obviously, on the bounds of the disturbances (e.g., we regard $\overline{\mathcal{D}}_{vk}$, instead of $\overline{\mathcal{D}}_{aj}$) and in the sub-indices ($k \in \mathfrak{K}$ instead of $j \in \mathfrak{J}$).

As for the tuning of the controller, we may, again, follow the same general guidelines established in the previous sub-section. It is only necessary to take into account that, as the position loop will be placed in cascade configuration, its bandwidth should be considerably lower than the speed loop (this way, the position loop tuning may safely neglect the error dynamics of the lower-level controllers).

7.5 Force Allocation

After the motion controller specifies the value of forces/moments to be applied to the vehicle's CoG, $\mathcal{F}^* = \mathcal{F}_r + \mathbf{M}\Delta a$, it becomes necessary to allocate the value of wheel torques T_i and steer angles δ_i capable of producing $\mathcal{F}^*$. In this work, the allocation will be performed through the force allocation layer depicted in Figure 7.3. Given the high level of redundancy in the vehicle, the allocation solution is, in general, not unique, which opens the door to pursue secondary goals, such as the minimization of the energy consumption of the actuators and/or friction utilization of tyres. In the literature, this type of problem

is known as control allocation (see Chapter 2) and can be mathematically formulated as:

$$\min_{T_i,\delta_i,\mathbf{F}_{xy},F_{Li},F_{Ci},\mathbf{F}_z,\omega_i} \quad L(.) + \|\mathbf{Qz}\|_p^p \tag{7.67a}$$

$$\mathcal{F}^* = \mathbf{BF}_{xy} + \mathbf{z} \tag{7.67b}$$

$$\mathbf{F}_{xy,i} = \mathbf{W}(\delta_i)\begin{bmatrix} F_{Li} & F_{Ci}\end{bmatrix}^T, \quad i \in \mathfrak{T} \tag{7.67c}$$

$$\begin{bmatrix} F_{Li} \\ F_{Ci}\end{bmatrix} = \tilde{\mathbf{F}}_i(\mathbf{v},\omega_i,\delta_i,F_{zi},\theta_T), \qquad i \in \mathfrak{T} \tag{7.67d}$$

$$\mathbf{F}_z = \mathbf{F}_z^0 + \left(\frac{\varrho_x}{m}\mathbf{e}_1^T + \frac{\varrho_y}{m}\mathbf{e}_2^T\right)\mathbf{BF}_{xy} \tag{7.67e}$$

$$\mathbf{F}_z > 0 \tag{7.67f}$$

$$T_i = r_i F_{Li}, \quad i \in \mathfrak{T} \tag{7.67g}$$

$$\underline{T} \leq T_i \leq \overline{T}, \quad T_i\omega_i \leq \overline{P}, \quad -\overline{\delta} \leq \delta_i \leq \overline{\delta}, \quad i \in \mathfrak{T} \tag{7.67h}$$

The function $L(.)$ is a performance metric associated with the secondary goals of the allocation (to be defined shortly), $\mathbf{z} \in \mathbb{R}^3$ a slack variable to tolerate situations where non-feasible $\mathcal{F}^*$ are requested, $p \in \{1,2\}$ the type of norm, and $\mathbf{Q} = \text{diag}(\begin{bmatrix} Q_x & Q_y & Q_z\end{bmatrix}) \in \mathbb{R}^{3\times3}$ a diagonal matrix, which assigns individual penalizations to allocation errors. The problem constraints are related to the friction force mechanism and limitations of the actuators, already introduced in Section 7.2; the main points that deserve attention are related to the fact that: *i*) the vehicle speed $\mathbf{v}$ is considered here as a known parameter in the optimization problem, and *ii*) the vertical forces $\mathbf{F}_z$ are constrained to positive values (in order to avoid the wheel lift). Moreover, to keep the allocation problem practical, we assumed steady-state conditions for the wheel rotational dynamics. This means that the torque and the longitudinal tyre force are related by the static map (7.67g), while the wheel rotational ω_i is used as an additional optimization variable (that affects directly the wheel longitudinal slip and the friction force).

Due to the nonlinearities in (7.67), obtaining a numerical solution for this problem is difficult, particularly for real-time applications. In the control allocation literature dedicated to the automotive applications, there are two main approaches to overcome this issue. The first idea is to linearize the friction model around the vehicle's current operating point. For instance, by joining all the friction-related constraints of (7.67), one may find a compact nonlinear map between $\mathcal{F}^*$, the vehicle speed ($\mathbf{v}$) and the control inputs $\mathbf{u} = [T_i, \delta_i, ...]$, that is $\mathcal{F}^* = \mathbf{f}(\mathbf{v},\mathbf{u})$. Linearizing the model around $(\mathbf{v}^{eq},\mathbf{u}^{eq})$,

$$\mathcal{F}^* \approx \mathbf{f}(\mathbf{v}^{eq},\mathbf{u}^{eq}) + \left.\frac{\partial \mathbf{f}(\mathbf{v},\mathbf{u})}{\partial \mathbf{u}}\right|_{\mathbf{v}^{eq},\mathbf{u}^{eq}} \Delta\mathbf{u} \tag{7.68}$$

we can approximate the nonlinear friction model by an affine relation, and use the increment $\Delta\mathbf{u}$ as the new control input; the final control value is then recuperated as $\mathbf{u} = \mathbf{u}^{eq} + \Delta\mathbf{u}$, where $\mathbf{u}^{eq}$ is the nominal operation point of the controller (obtained, for example, in the previous control iteration), and $\mathbf{v}^{eq}$ is the current vehicle speed. With this approach, the nonlinear constraints are relaxed to linear relations, which enables the application of practical linear programming or quadratic programming solvers for the problem (assuming that the cost function is linear or quadratic, respectively), as discussed in [75, 86, 295].

The second possibility to solve (7.67) builds on the idea of exerting a direct control over

the xy forces of tyres, i.e., $\mathbf{F}_{xy}$ is considered as a second virtual control. This approach is very attractive for vehicles with independent wheel steer and independent wheel drive (e.g., with in-wheel motors), since, in theory, each tyre can generate force in an arbitrary direction. Additionally, the use of $\mathbf{F}_{xy}$ as a virtual control enables us to decompose the allocation problem in two steps. The first determines the xy force distribution among the tyres in order to fulfil the force/moment requested to the CoG,

$$\min_{\mathbf{z},\mathbf{F}_{xy},\mathbf{F}_z} \quad L(.) + \|\mathbf{Q}\mathbf{z}\|_p^p \tag{7.69a}$$

$$\mathcal{F}^* = \mathbf{B}\mathbf{F}_{xy} + \mathbf{z} \tag{7.69b}$$

$$\|\mathbf{E}_i\mathbf{F}_{xy}\|_2 \leq \mu_{max} F_{zi}, \quad i \in \mathfrak{T} \tag{7.69c}$$

$$\mathbf{F}_z = \mathbf{F}_z^0 + \left(\frac{\varrho_x}{m}\mathbf{e}_1^T + \frac{\varrho_y}{m}\mathbf{e}_2^T\right)\mathbf{B}\mathbf{F}_{xy} \tag{7.69d}$$

$$\mathbf{F}_z > 0 \tag{7.69e}$$

$$\begin{bmatrix}1 & 0\end{bmatrix}\mathbf{E}_i\mathbf{F}_{xy} \leq \min\left(\frac{\overline{T}}{r_i}, \frac{\overline{P}}{v_x}\right), \quad \forall i \in \mathfrak{T} \tag{7.69f}$$

where the friction circle constraints were extracted from (7.21), and the torque and power limits of the motors were approximated through the relation (7.23) (the steering angle constraints were neglected). Notice that the above constraints are convex: (7.69c) can be posed as a second-order cone, while the remaining is linear. Consequently, if the performance metric $L(.)$ is convex, the resulting optimization problem is also convex [112], which brings undeniable theoretical advantages in comparison to (7.67) (e.g., any local solution is also global). After solving the above problem, the second step in the allocation process relies on inversion of the tyre forces, i.e., using the $\mathbf{F}_{xy}$ obtained from (7.69), and the vehicle state $\mathbf{v}$, find the torque (T_i) and steer (δ_i) that produces the necessary tyre forces. As shown in Appendix 7.10, for the slip-based friction model under consideration here, such inversion is possible and its calculations are not too difficult. Different variants of this approach have been reported in the literature [129, 280, 296, 297].

In comparison with the linearization approach, the main advantage of using $\mathbf{F}_{xy}$ as a second virtual control is the possibility to fully handle the nonlinearities in the friction model. On the other hand, the formulation (7.69) makes more difficult to translate the physical actuator limits (torque and steer) to the xy force components, which generally makes inevitable the approximation of the actuator's constraints (as explained in (7.24)). Interestingly, the introduction of the physical actuator's limits is not an issue for the linearization approach, and can easily be incorporated in the allocation problem. In summary, the designer has two practical routes to formulate the force-allocation problem: *i*) linearize the friction model, and use the true physical limits of the actuators [75, 86, 295]; or *ii*) employ the full nonlinear friction model, and approximate the physical actuator limits [129, 280, 296, 297]. In this work we will follow the second approach, and concentrate our attention on the application of fast numerical techniques to handle the control-allocation problem, and which can be used in real-time applications.

7.5.1 Performance Metric and Control Allocation Problem

Due to the high degree of actuation in the vehicle, there are many possibilities to allocate the forces between the tyres. To explore this actuation redundancy, we will consider, as a

secondary performance metric, the minimization of the friction use in the tyre:

$$\begin{aligned} L(\mathbf{F}_{xy}, \mathbf{F}_z) &= \sum_{i\in\mathfrak{T}} \| \frac{1}{\mu_{max} F_{zi}} \mathbf{E}_i \mathbf{F}_{xy} \|^2 \\ &= \sum_{i\in\mathfrak{T}} \| \begin{bmatrix} \frac{1}{\mu_{max} F_{zi}} & 0 \\ 0 & \frac{1}{\mu_{max} F_{zi}} \end{bmatrix} \begin{bmatrix} F_{xi} \\ F_{yi} \end{bmatrix} \|^2 \\ &= \|\mathbf{R}^*(\mathbf{F}_z)\mathbf{F}_{xy}\|^2 \end{aligned} \tag{7.70}$$

where $\mathbf{R}^*(\mathbf{F}_z)$ is a diagonal matrix, which assigns the weight $\frac{1}{\mu_{max} F_{zi}}$ to the x and y forces of the tyre $i \in \mathfrak{T}$. The idea behind the performance metric L is to assign to each tyre a penalization inversely proportional to the vertical force that each wheel support. Consequently, the tyres with higher vertical forces, thus capable of delivering higher force, will have lower penalization, while the lighter tyres will be incited to produce less force. Since this allocation policy discourages the full use of friction forces, it can also be viewed, to some extent, as maximization of a safety margin in the force allocation. In order to facilitate the practical use of this cost function, it will be further assumed that the allocation errors, $\mathbf{z}$, are not very high, which enables us to approximate the weight matrix, by:

$$\begin{aligned} \mathbf{R}^*(\mathbf{F}_z) &= \mathbf{R}^* \left(\mathbf{F}_z^0 + \left(\frac{\varrho_x}{m} \mathbf{e}_1^T + \frac{\varrho_y}{m} \mathbf{e}_2^T \right) (\mathcal{F}^* - \mathbf{z}) \right) \\ &\approx \mathbf{R}^* \left(\mathbf{F}_z^0 + \left(\frac{\varrho_x}{m} \mathbf{e}_1^T + \frac{\varrho_y}{m} \mathbf{e}_2^T \right) \mathcal{F}^* \right) \\ &= \mathbf{R}(\mathcal{F}^*) \end{aligned} \tag{7.71}$$

Notice that, for the cases where non-feasible forces are requested, the variable $\mathbf{z}$ may not comply with the assumption of small allocation errors. Notwithstanding, to handle such cases, we may saturate the calculation of the vertical forces used in the previous relation, avoiding, this way, negative or excessive vertical loads that appear when dealing with unfeasible forces. Albeit this approach will introduce errors, the resulting weight matrix is still in line with our original goal of assigning higher penalization to the tyres that will have (presumably) lower vertical loads. With this approximation, the $\mathbf{F}_z$ dependence can be dropped in the cost function, $L \approx \|\mathbf{R}(\mathcal{F}^*)\mathbf{F}_{xy}\|^2$; the final control allocation then follows from joining (7.69),(7.70),(7.71), i.e.,

$$\begin{aligned} \min_{\mathbf{z}, \mathbf{F}_{xy}, \mathbf{F}_z} \quad & \|\mathbf{R}(\mathcal{F}^*)\mathbf{F}_{xy}\|^2 + \|\mathbf{Q}\mathbf{z}\|^2 \\ \text{s.t.} \quad & (7.69\text{b}) - (7.69\text{f}) \end{aligned} \tag{7.72}$$

which makes use of $p = 2$ for the norm calculation. Notice that $\mathcal{F}^*$ is a parameter in the control allocator; thus, for each control update, the weight matrix $\mathbf{R}(\mathcal{F}^*)$ is constant, and the cost function quadratic. The main difficulty for the numerical solution of the above problem lies in the second-order cone constraints(7.69c), which although being convex, are not in a suitable format to be handled by real-time QP solvers, like the CVXGEN [293]. In the next sub-section, we will discuss two practical algorithms to transform the allocation problem into a QP.

7.5.2 Algorithm 1: Fix Tyre's Force Angles and Then Optimize

The first algorithm that we will develop is inspired by the cascading generalized inverse (CGI) method, a widely used allocation strategy in aeronautical applications [106, 108]. Our idea builds on the following reasoning: *i*) first, we will determine a suitable direction for the F_{xi} and F_{yi} forces of each tyre; *ii*) then, the force's direction is kept fixed, and the magnitude of the tyre's force is recalculated in an effort to fulfil the problem constraints. As we will see shortly, by fixing the force's angles, the second-order cone constraints associated with the friction circle can be transformed into linear inequalities, which are easier to treat numerically. This algorithm is implemented as follows:

STEP 1: to start with, let's consider that the power, torque and friction constraints are not active, and that $\mathcal{F}^*$ is feasible, so $\mathbf{z} = 0$. Under these assumptions, the control allocation problem (7.72) can be recast as a minimum-norm problem, subject to equality constraints:

$$\min_{\mathbf{F}_{xy}} \quad \|\mathbf{R}(\mathcal{F}^*)\mathbf{F}_{xy}\|^2, \qquad \text{s.t.} \quad \mathcal{F}^* = \mathbf{B}\mathbf{F}_{xy} \tag{7.73}$$

By constructing the Lagrangian function for the above problem, $\mathcal{L}(\mathbf{F}_{xy}, \lambda) = \|\mathbf{R}(\mathcal{F}^*)\mathbf{F}_{xy}\|^2 + \lambda\left(\mathbf{B}\mathbf{F}_{xy} - \mathcal{F}^*\right)$, and applying the first-order optimality conditions ($\partial\mathcal{L}/\partial\mathbf{F}_{xy} = 0, \quad \partial\mathcal{L}/\partial\lambda = 0$), the following analytical solution can be established:

$$\mathbf{F}^0_{xy} = (\mathbf{R}^T\mathbf{R})^{-1}\mathbf{B}^T\left(\mathbf{B}(\mathbf{R}^T\mathbf{R})^{-1}\mathbf{B}^T\right)^{-1}\mathcal{F}^* \tag{7.74}$$

which is known in the control-allocation literature as the weighted pseudo-inverse solution. To simplify the notation, we omitted the dependence of $\mathcal{F}^*$ in the weight matrix $\mathbf{R}$.

STEP 2: it is obvious that the assumptions made in step 1 do not always hold, and, in practice, the vehicle may have to operate in the boundaries of the friction/power/torque limits. Consequently, the solution (7.74) may violate some of the constraints in the problem, and it becomes necessary to rearrange the allocation solution to comply with the constraints. Before explaining how this issue was handled, it is helpful to express the tyre's forces in polar coordinates:

$$\mathbf{F}_{xy,i} = \begin{bmatrix} F_{xi} \\ F_{yi} \end{bmatrix} = \rho_i \begin{bmatrix} \cos(\theta_i) \\ \sin(\theta_i) \end{bmatrix}, \qquad i \in \mathfrak{T} \tag{7.75}$$

where ρ_i is the force magnitude of the tyre $i \in \mathfrak{T}$ and θ_i its angle. Applying the polar representation to all the tyre's forces $\mathbf{F}_{xy}$ we obtain:

$$\begin{aligned} \mathbf{F}_{xy} &= \underbrace{\begin{bmatrix} \cos(\theta_{1l}) & 0 & 0 & 0 \\ \sin(\theta_{1l}) & 0 & 0 & 0 \\ 0 & \cos(\theta_{1r}) & 0 & 0 \\ 0 & \sin(\theta_{1r}) & 0 & 0 \\ 0 & 0 & \cos(\theta_{2l}) & 0 \\ 0 & 0 & \sin(\theta_{2l}) & 0 \\ 0 & 0 & 0 & \cos(\theta_{2r}) \\ 0 & 0 & 0 & \sin(\theta_{2r}) \end{bmatrix}}_{\mathbf{H}^*(\theta)} \underbrace{\begin{bmatrix} \rho_{1l} \\ \rho_{1r} \\ \rho_{2l} \\ \rho_{2r} \end{bmatrix}}_{\rho} \\ &= \mathbf{H}^*(\theta)\rho \end{aligned} \tag{7.76}$$

where $\theta = [\theta_{1l}\ \theta_{1r}\ \theta_{2l}\ \theta_{2r}]$ and $\rho \in \mathbb{R}^4_+$. Now, notice that, if the angles of the tyre's forces θ are fixed then there is a linear relation between the force's magnitude ρ and the $\mathbf{F}_{xy}$; more importantly, the second-order cone constraints associated with the friction's limits $\| [F_{xi}\ F_{yi}]^T \|_2 \leq \mu_{max} F_{zi}$ become simple linear inequalities, i.e., $\rho_i \leq \mu_{max} F_{zi}$. Spurred by these observations, our approach to handle the problem's constraints will consider fixed tyre's forces angles,

$$\mathbf{H} = \mathbf{H}^*(\theta^0), \tag{7.77}$$

where θ^0 are the angles obtained from the weighted pseudo-inverse (7.74). The force magnitude ρ will then be redistributed to comply with the friction/power/torque constraints. This redistribution is obtained by inserting (7.76) in (7.72) and solving the following problem:

$$\min_{\mathbf{z},\rho,\mathbf{F}_z} \quad \|\mathbf{R}\mathbf{H}\rho\|^2 + \|\mathbf{Q}\mathbf{z}\|^2 \tag{7.78a}$$

$$\mathcal{F}^* = \mathbf{B}\mathbf{H}\rho + \mathbf{z} \tag{7.78b}$$

$$\mathbf{0} \leq \rho \leq \mu_{\max}\mathbf{F}_z, \qquad \mathbf{F}_z > 0 \tag{7.78c}$$

$$\mathbf{F}_z = \mathbf{F}_z^0 + \left(\frac{\varrho_x}{m}\mathbf{e}_1^T + \frac{\varrho_y}{m}\mathbf{e}_2^T\right)\mathbf{B}\mathbf{H}\rho \tag{7.78d}$$

$$\begin{bmatrix}1 & 0\end{bmatrix}\mathbf{E}_i\mathbf{H}\rho \leq \min\left(\frac{\overline{T}}{r_i}, \frac{\overline{P}}{v_x}\right), \quad \forall i \in \mathfrak{T} \tag{7.78e}$$

It is worth pointing out that all the constraints in the above problem are linear, and the cost function is quadratic[4]; so, we are now in conditions to handle the allocation problem with fast QP solvers. The final allocation solution is then obtained by $\mathbf{F}_{xy} = \mathbf{H}\rho$.

In what follows, the above algorithm will be referred to as PINV+QP.

7.5.3 Algorithm 2: Linear Approximation of the Friction Circle

The second algorithm that we will employ to transform (7.72) into a QP is based on the linearization of the friction circle constraint. In particular, the main idea is to approximate the circle constraint:

$$\left\| \begin{bmatrix} F_{xi} \\ F_{yi} \end{bmatrix} \right\|_2 \leq \mu_{max} F_{zi}, \qquad i \in \mathfrak{T} \tag{7.79}$$

by a polytope, characterized by N half-spaces:

$$\mathbf{C}\begin{bmatrix} F_{xi} \\ F_{yi} \end{bmatrix} \leq \mathbf{D}\mu_{max} F_{zi}, \qquad i \in \mathfrak{T} \tag{7.80}$$

where $\mathbf{C} \in \mathbb{R}^{N\times 2}$, $\mathbf{D} \in \mathbb{R}^N$ are matrices that characterize the half-spaces; the definition of these matrices is present in Appendix 7.11. From a qualitative perspective, one can find that, as we increase the number of half-spaces N, the friction circle constraint can be approximated with a rather high accuracy (see, e.g., Figure 7.8 for $N = 12$). However, for the real-time implementation of the allocator, N cannot be too large, as the total number of linear inequalities associated with the friction constraints, taking into account all the tyres, is $4N$. Hence, in practice, we may need to find a trade-off value for N, capable of providing a reasonable accuracy in the friction circle approximation, but, simultaneously,

[4] notice that the cost function can be rewritten as $\left\| \begin{bmatrix} \mathbf{R}\mathbf{H} & \mathbf{0} \\ \mathbf{0} & \mathbf{Q} \end{bmatrix} \begin{bmatrix} \rho \\ \mathbf{z} \end{bmatrix} \right\|^2$

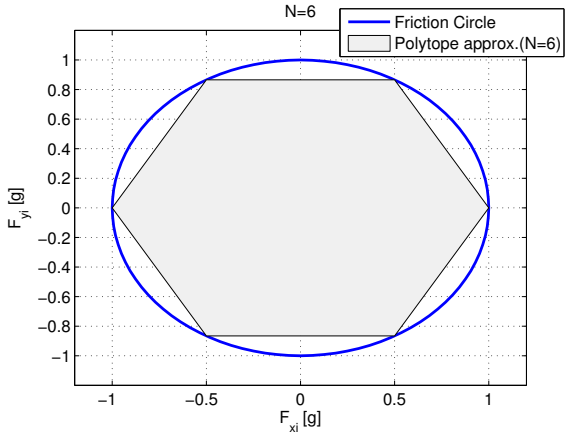

(a)

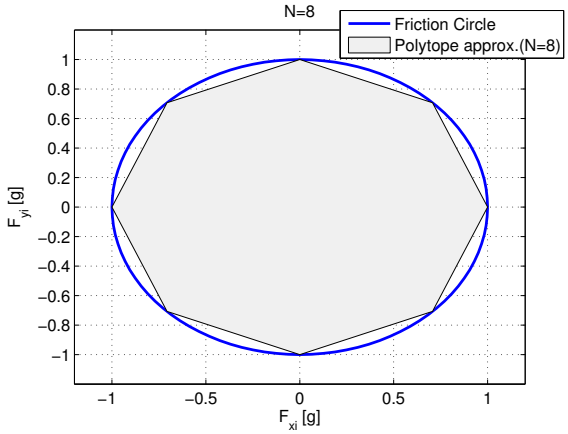

(b)

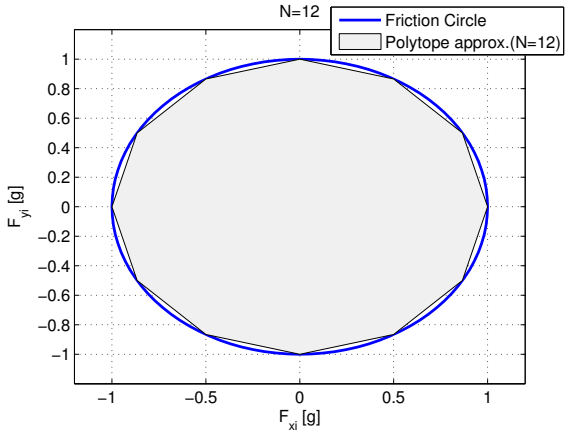

(c)

Figure 7.8: Linear approximation of the friction circle constraints.

without compromising too much the computational time of the numerical solver (which may be affected by the number of constraints).

Based on the approximation (7.80), the allocation problem can be posed as:

$$\min_{\mathbf{z},\mathbf{F}_{xy},\mathbf{F}_z} \quad \|\mathbf{R}\mathbf{F}_{xy}\|^2 + \|\mathbf{Q}\mathbf{z}\|^2 \tag{7.81a}$$

$$\mathcal{F}^* = \mathbf{B}\mathbf{F}_{xy} + \mathbf{z} \tag{7.81b}$$

$$\mathbf{C}\mathbf{E}_i\mathbf{F}_{xy} \leq \mathbf{D}\mu_{max}F_{zi}, \qquad i \in \mathfrak{T} \tag{7.81c}$$

$$\mathbf{F}_z = \mathbf{F}_z^0 + \left(\frac{\varrho_x}{m}\mathbf{e}_1^T + \frac{\varrho_y}{m}\mathbf{e}_2^T\right)\mathbf{B}\mathbf{F}_{xy} \tag{7.81d}$$

$$\mathbf{F}_z > 0 \tag{7.81e}$$

$$\begin{bmatrix}1 & 0\end{bmatrix}\mathbf{E}_i\mathbf{F}_{xy} \leq \min\left(\frac{\overline{T}}{r_i}, \frac{\overline{P}}{v_x}\right), \quad \forall i \in \mathfrak{T} \tag{7.81f}$$

Since all the constraints are linear, and the cost function is quadratic [5] , the above problem can be tackled by QP solvers. In comparison with the Algorithm 1, the linear approximation requires a higher number of inequalities and optimization variables, which has an important impact on the computational time of the solver. On the other hand, the linear approximation has more freedom to select the tyre's forces orientation (recall that in Algorithm 1 the orientation is fixed by the weighted pseudo-inverse), which may be beneficial in situations where non-feasible forces are requested. These properties will be further investigated in the next section, where a detailed comparison between the two algorithms is provided.

It is also worth pointing out that, in the context of the control allocation of forces, the linear approximation of the friction circle was an idea initially developed by [280]. However, this previous work failed to take into account the important influence of the longitudinal and lateral acceleration in the friction circle's radius, i.e., (7.81d), as well as additional power and torque constraints introduced by the in-wheel motors, which are addressed here. Furthermore, we will also investigate how the algorithm performs for different values of N, which is important for the real-time implementation.

In the remainder of this work, the allocator (7.81) will be named as QP(N), where N refers to the number of linear inequalities employed in the approximations.

7.5.4 Comparison between Allocation Algorithms

To investigate the performance of the two allocation algorithms described above, we will now perform a series of simulation tests. The goal is to evaluate the allocation results during the path following of the Norising track (with 2.2 km of length). The reference force $\mathcal{F}^*$ and the vehicle speed profile $\mathbf{v}$ were generated through the feedforward controller, described in Section 7.4.1, without activating the feedback speed and position loops. Since, for now, our concern is merely focused on the allocation problem, this idealized setting (i.e., working under the assumption of a perfect vehicle model, without disturbances) constitutes a pragmatic way of gaining insight on the merits and drawbacks of the allocation algorithms. Regarding the numerical solver to handle the QP numerical problems, we employed the CVXGEN, a code-generator tool for embedded linear-programming (LP) and QP optimization (see [298] for additional details). We also reduced the number of decision variables in both optimization problems, by eliminating the equality constraints

[5] notice that the cost function can be rewritten as $\left\| \begin{bmatrix}\mathbf{R} & \mathbf{0}\\ \mathbf{0} & \mathbf{Q}\end{bmatrix}\begin{bmatrix}\mathbf{F}_{xy}\\ \mathbf{z}\end{bmatrix}\right\|^2$;

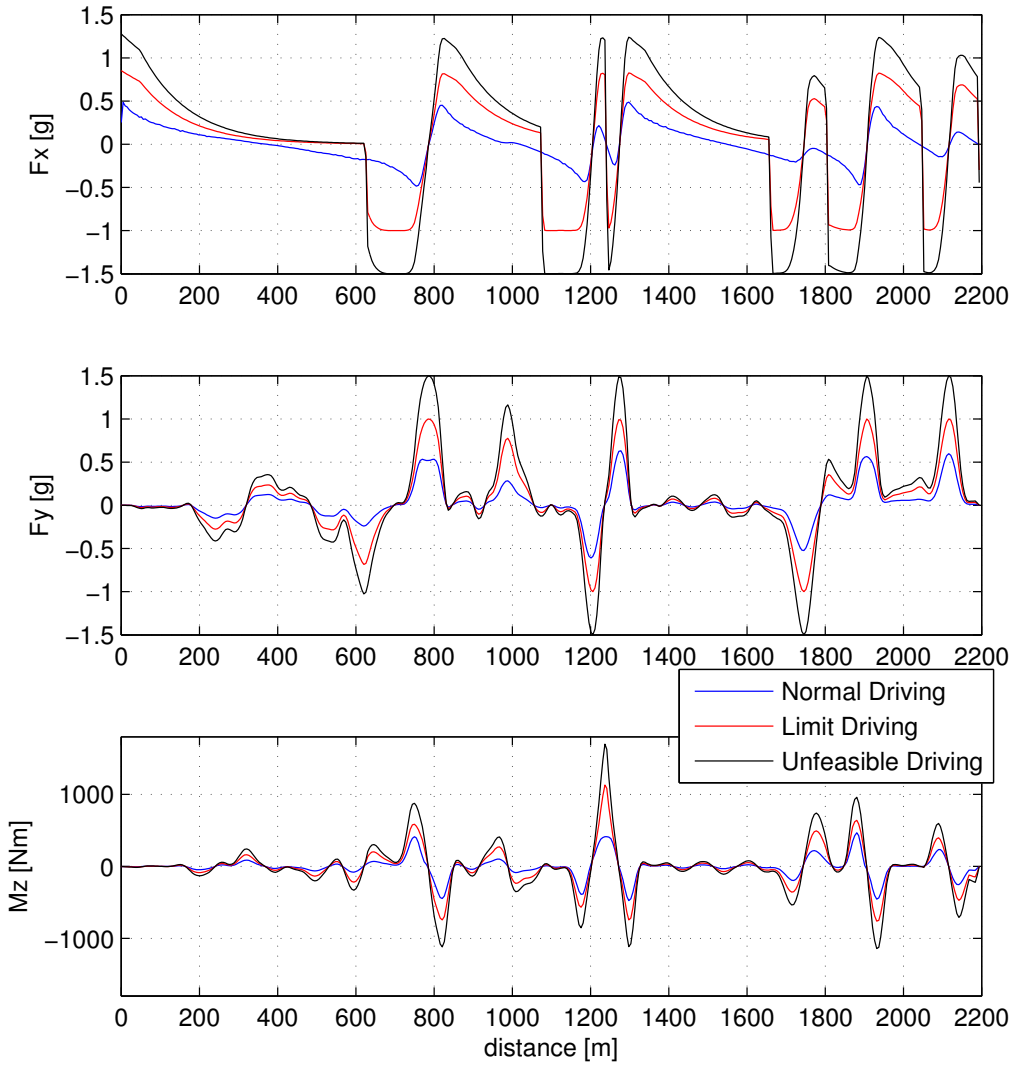

Figure 7.9: Reference values of $\mathcal{F}^*$ employed in the evaluation of the control allocation algorithms.

associated with the $\mathbf{z}$ and $\mathbf{F}_z$ variables (e.g., the (7.81b) was dropped, and the term $\|\mathbf{Qz}\|^2$ replaced by $\|\mathbf{Q}\left(\mathbf{BF}_{xy} - \mathcal{F}^*\right)\|^2$).

For the performance evaluation of the allocation algorithms, three test cases were considered (see Figure 7.9):

- Normal driving: $\mathcal{F}^* = \mathcal{F}_r$, obtained with $\epsilon = 0.8$
- Limit driving: $\mathcal{F}^* = \mathcal{F}_r$, obtained with $\epsilon = 1.0$
- Unfeasible driving: $\mathcal{F}^* = 1.5\mathcal{F}_r$, obtained with $\epsilon = 1.0$

The normal driving scenario corresponds to the situation where the vehicle is driven around the track with moderate levels of acceleration. The second case, limit driving, is related to the minimum-time path following, where the vehicle operates very close to the friction and power boundaries; the aim of this test is to assess if the control allocator is able to reach the maximum operation envelope of the vehicle. In the last scenario, the allocator is asked to produce unfeasible forces, beyond the friction adhesion limits, which is the most challenging task.

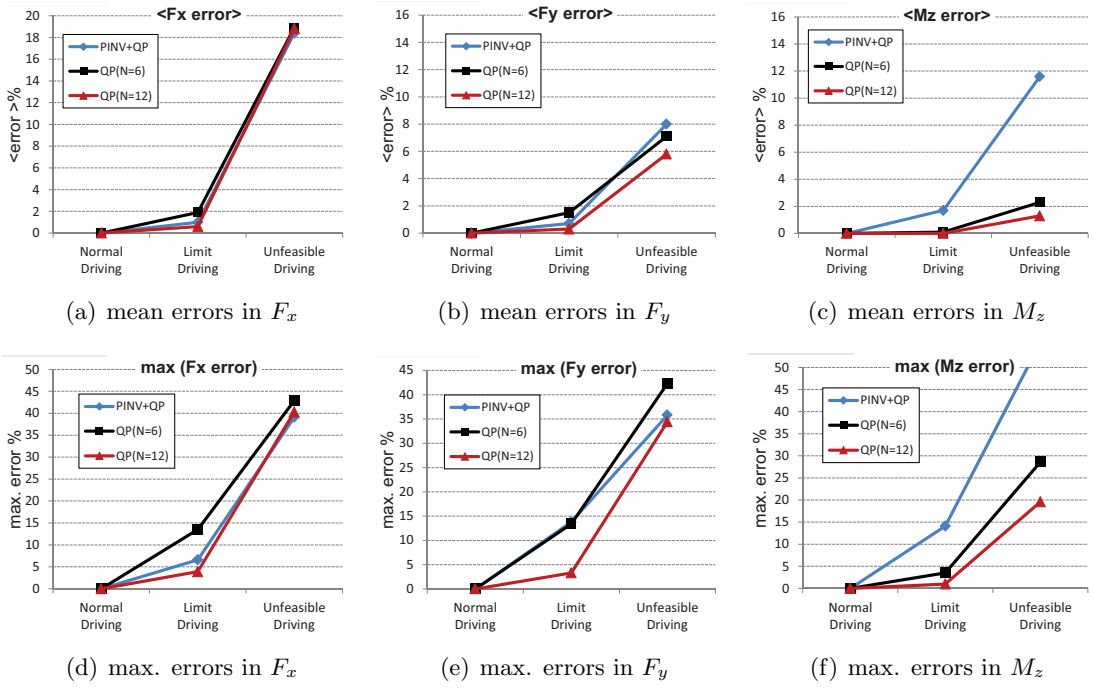

(a) mean errors in F_x (b) mean errors in F_y (c) mean errors in M_z

(d) max. errors in F_x (e) max. errors in F_y (f) max. errors in M_z

Figure 7.10: Evaluation of the force errors produced by the allocation algorithms.

For each one of these test cases, we will assess three types of allocators: *i*) PINV+QP, *ii*) Q(N=6), and *iii*) Q(N=12). The latter two were included with the aim of investigating how the parameter N affects the QP performance. Further, to keep the comparison fair, all three algorithms share the same weight matrices.

Figure 7.10 depicts the mean and maximum allocation errors of the algorithms along the test cases under study. These results show that, for normal driving scenarios, each allocator presents a very satisfactory performance, with zero errors. With regard to the limit driving conditions, one can find that the average performance of all the allocators is also acceptable, with average errors inferior to 2%. However, the maximum allocation errors for the PINV+QP and QP(N=6) are much higher than the QP(N=12); for example, the peak error in the generation of F_y is 14% for both QP(N=6) and PINV+QP, while the QP(N=12) shows only 4%. These results suggests that the full potential of the vehicle may not be reached with the pseudo-inverse allocation and the QP(N=6) strategies; the QP(N=12) method will also be unable to reach the maximum operation envelope, but will be very close. Finally, during the unfeasible driving conditions, the performance of all the allocation algorithms suffers a significant degradation, which was expected given the non-feasible requests. Nonetheless, it can be observed that the QP(N=12) allocation strategy copes better with the infeasibility than the other methods, particularly in the tracking of F_y and M_z. On average, the QP(N=12) features tracking errors of 6% in F_y and 1.8% in M_z, which contrasts with 8% and 11.8% generated by the PINV+QP, and 7% and 2.1% for the QP(N=6).

From these results, it becomes clear that the QP(N=12) is the allocation strategy with better performance. The only drawback of this strategy is related to the increase of the computational time; while the difference to the QP(N=6) is not very high (on average, QP(N=12) requires 30% more computation time), the QP(N=12) is 2-2.5 times slower than the pseudo-inverse, as shown in Figure 7.11. Notwithstanding, the total computational

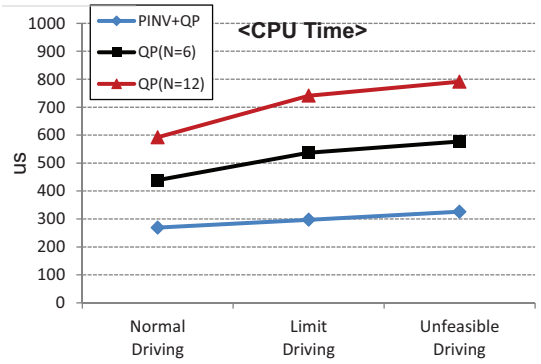

(a) mean CPU time

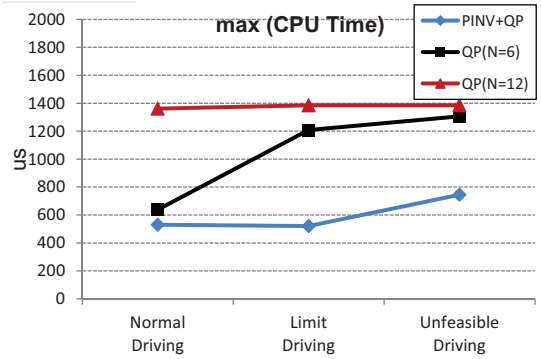

(b) max. CPU time

Figure 7.11: Computational time for the control allocation algorithms.

time of the QP(N=12) is, on average, less than $1ms$, which is still acceptable for real-time implementation in a vehicle, where the update rates of the vehicle's motion controller are normally lower than 100Hz (10ms).

In light of the performance superiority offered by the QP(N=12), we will use this allocation strategy in the remainder of this chapter.

7.5.5 Tyre Force Inversion

After determining the desired x and y forces of each tyre, it is necessary to calculate the corresponding torque T_i and steer angle δ_i, capable of delivering the requested forces. As explained in Appendix 7.10, this transformation can be performed using the tyre inverse model. However, since, in practice, the tyre model is subject to uncertainty, the tyre inversion will not be "perfect" and, as a result, allocation errors will emerge. In any case, such approximation errors can be embedded in the disturbance term ($\mathcal{D}$), and mitigated by the robust feedback loops discussed in the previous section.

7.6 Simulations

In order to evaluate the performance of the controller proposed in the previous sections, a series of tests were carried out with the help of a high-fidelity simulator, the CarSim [146]. Since the CarSim contemplates dynamics neglected at the controller's design stage, e.g.,

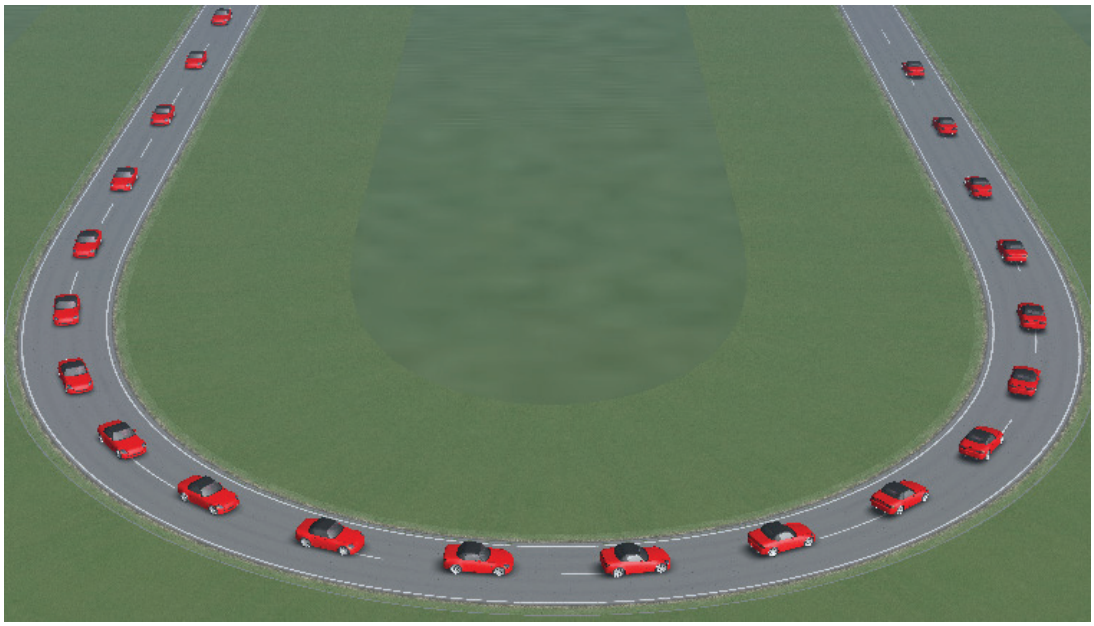

(a) approach with $\beta_r = 0$

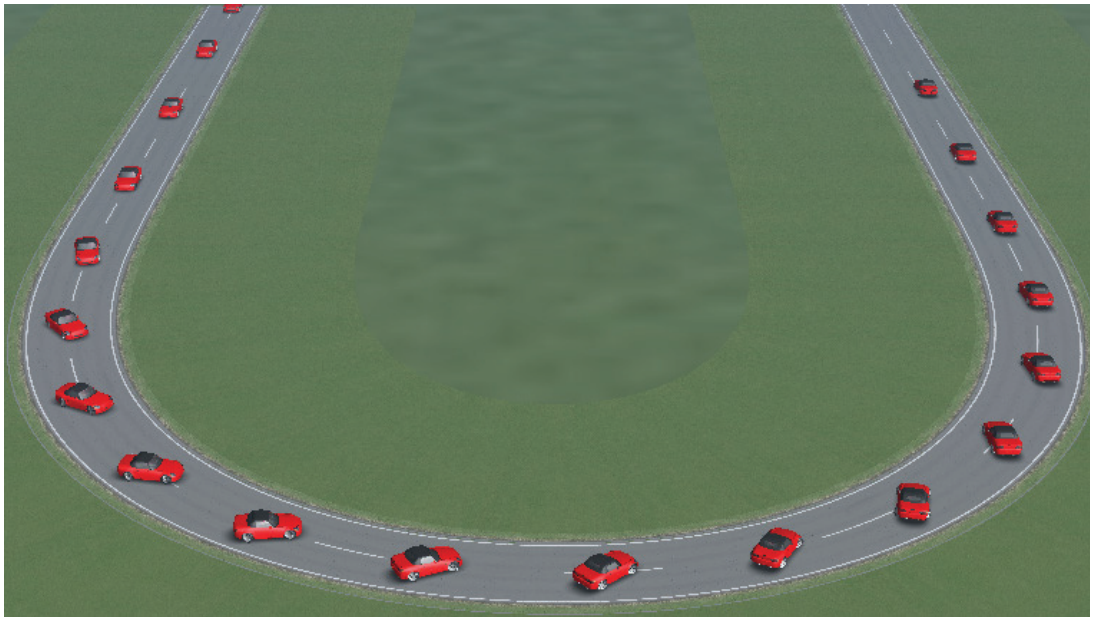

(b) approach with $\beta_r \neq 0$

Figure 7.12: Path following of a 180° corner; the dashed white lines (centre of the road) represent the reference path that the vehicle should follow.

nonlinear suspensions dynamics, compliance effects, roll and pitch motions, etc., this simulation setting will enable us to evaluate the robustness of the controller against some of these disturbances. The vehicle used in the simulations is based on a B-Class sports car, available in the default library of the CarSim, with the parameters shown in Appendix 7.12. For our purposes here, it is assumed that the reference path is pre-specified before the start of the simulation; based on this information, the convex optimal problem (7.42) is then solved (off-line) with the help of SDPT3 [294], generating the feedforward components $\mathcal{F}_r$,

$\mathbf{v}_r$, $\mathbf{p}_r$. It is the responsibility of the speed and position feedback loops, together with the control-allocation layer, to impose (on-line) in the vehicle this pre-specified motion. Unless otherwise stated, the default settings employed in the simulation are:

- $\beta_r(s) = 0$: zero side-slip reference;
- $\mu_{max} = 1$: dry asphalt;
- $\epsilon = 1$: minimum-time goal
- $\mathbf{W} = \text{diag}\{1, 1, 1\}$: equal penalization for all the forces

It is also important to mention that the friction peak estimation considered by the controller is 20% less than the true value, i.e., $\hat{\mu}_{max} = 0.8$. The use of an underestimated μ_{max} is imperative to preserve control authority when the vehicle's model is subject to uncertainty and disturbances (notice that, if we employ $\hat{\mu}_{max} = \mu_{max}$ within the minimum-time goal, then the friction forces will operate close to saturation, and the controller may not have enough margin to deal with unexpected disturbances). Furthermore, with the aim of making the simulation setting more realistic, we added Gaussian noise to the feedback measurements, with variance of (0.14 m/s, 0.14 m/s, 0.0052 rad/s)^2 for the velocities $v_x, v_y, \dot{\psi}$, and (0.1 m, 0.1m, 0.009 rad)^2 for the position X, Y, ψ.

7.6.1 Hairpin Corner

To gain some insight on controller performance, we start by considering a 180^o corner, also known as hairpin corner, with the steady-state radius of 30m. The initial vehicle speed was set at 90 km/h, and the sampling rate employed in the discretization was $\Delta s = 5$m.

Normal approach ($\beta_r = 0$)

As illustrated in Figure 7.12(a) and 7.13(a), the vehicle follows with a reasonable accuracy the pre-specified path: the absolute tracking errors are inferior to 0.5m in the X and Y components, while the heading errors do not exceed 0.4^o. Inspecting the CoG forces and velocities shown in Figure 7.13(b), the manoeuvre can be further decomposed into three main zones: *i*) during pre-corner conditions, the controller applies high braking in a straight line ($s \in [45, 75]m$), in order to prepare the vehicle speed to the conditions that will be found in the corner ahead; *ii*) during corner conditions $s \in [75, 200]$m, there is a smooth exchange between the longitudinal and lateral forces (F_x, F_y), which is a consequence of the friction circle limits; and *iii*) from $s \geq 200$m the controller applies maximum acceleration, constrained by limited power of IWMs. From these data, it is also worth pointing out that the feedforward (FF) components, generated by the optimal formulation (dashed lines), are close to the values produced by the feedback (FB+FF), particularly the speeds and forces F_x and F_y. The main difference between the FF and the FF+FB is present in the yaw-moment of the vehicle (M_z), which suggests that the reduced model employed in the optimal problem is less accurate for the yaw-rate dynamics. Nonetheless, the simulation results also demonstrate that the feedback controller is able to compensate for these model mismatches.

To assist in the analysis of the torque allocation results produced by the controller, it is convenient to introduce three auxiliary variables, i.e., the allocation ratios between

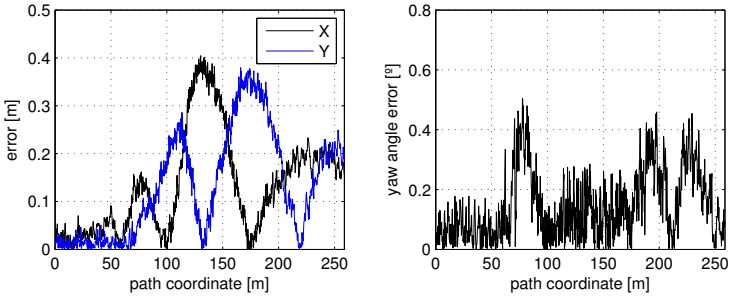

(a) Position and orientation errors

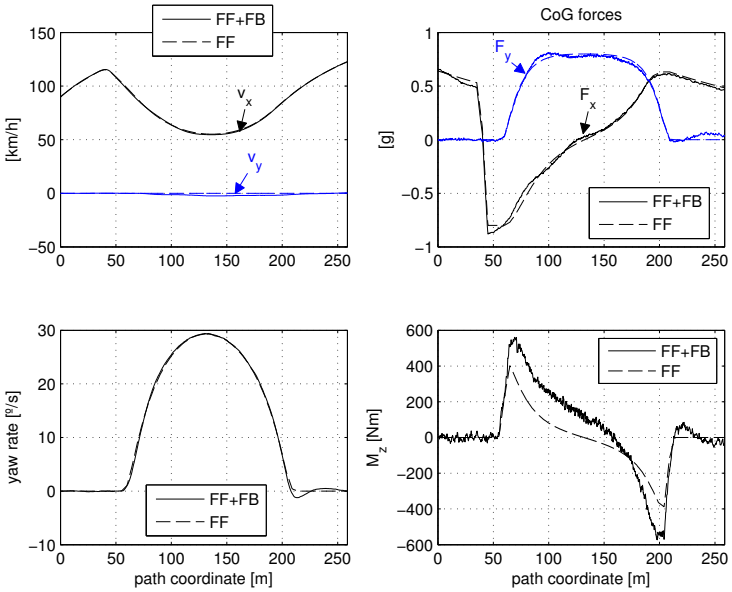

(b) Motion Control (solid line = feedforward reference; dashed line = feedforward + feedback)

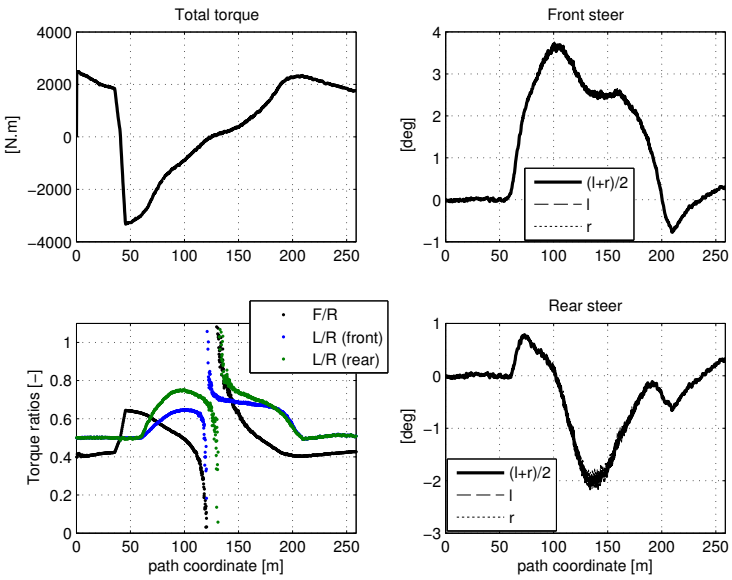

(c) Allocation Results

Figure 7.13: Simulation results for negotiating a 180° corner in minimum-time (zero side-slip, $\beta_r = 0$).

front/rear axles (γ_0) and left/right wheels (γ_1, γ_2). These variables are defined as:

$$\begin{aligned} T &= T_{1l} + T_{1r} + T_{2l} + T_{2r} && (7.82) \\ T_{1l} &= T\gamma_0 (1-\gamma_1) \qquad T_{1r} = u_T \gamma_0 \gamma_1 && (7.83) \\ T_{2l} &= T (1-\gamma_0)(1-\gamma_2) \qquad T_{2r} = u_T (1-\gamma_0)\gamma_2 \end{aligned}$$

where

- γ_0 is the front/rear allocation ratio ($\gamma_0 = 1$ means all the torque is applied to the front axle)
- γ_1 is the left/right allocation ratio of the front axle ($\gamma_1 = 1$ means all the front axle torque is on the right wheel)
- γ_2 is the left/right allocation ratio of the rear axle
- T is the total torque

Notice that, in conventional vehicles, the ratio γ_0 is a well-known quantity for distributing the braking force among the front/rear axles [3]; so, it seems pertinent to extend this concept to the torque split between the left/right wheels. Analysing the torque ratios throughout the hairpin corner, illustrated in Figure 7.13(c), reveals a fairly intuitive result: during the strong braking phase, $s \in [45, 85]$m, the controller applies a higher braking torque to the front axle, while the opposite is verified in the accelerating phase, i.e., rear wheels receive higher torques in the region $s \in [167, 200]$m. Similarly, we can also verify that, during cornering conditions, the left/right allocation ratios are higher than 0.5, which implies that the outer wheels (the right wheels in this particular example) receive a greater torque magnitude than the inner wheels, i.e., $|T_{1r}| \geq |T_{1l}|$,$|T_{2r}| \geq |T_{2l}|$. In light of the well-known load movement between the front-rear axle and left-right wheels that the vehicle experiences when subjected to longitudinal and lateral accelerations, these allocation results seem very reasonable. Notice that, in order to keep the friction use at acceptable levels (which was one of the goals established in the control allocation layer), the controller is applying higher torque levels to the wheels with greater vertical loads.

With regard to the steer allocation, depicted in Figure 7.13(c), there are two noteworthy facts. First, the differences between left and right steering are very little. Second, during cornering conditions, the rear steer is driven in the opposite direction from that of the front. As we will show in later simulations, this difference in steer directions ends up inducing an additional yaw-moment in the vehicle, which is important to negotiate tight corners such as the one under study here.

Sliding approach $\beta_r \neq 0$

For the second test, we considered the same conditions as the previous one, but with an important exception: a significant side-slip reference (see Figure 7.15) is imposed on the controller, so that the vehicle slides throughout the corner. The goal of this test is to demonstrate that the path following controller can emulate advanced driving techniques that, generally, are only mastered by professional drivers. The results depicted in Figure 7.12(b) and 7.14 show that the controller, despite the high-beta range, is able to keep low position errors. In addition, we can also verify that, in order to keep the vehicle drifting in minimum time, the longitudinal force F_x and the yaw-moment M_z applied to the vehicle are much higher than is the case with $\beta_r = 0$ (see Figure 7.14(b)). To some

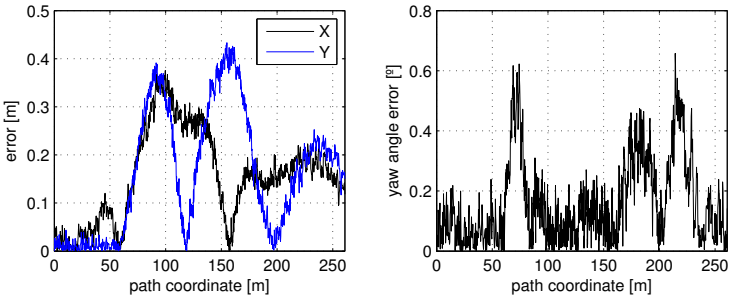

(a) Position and orientation errors

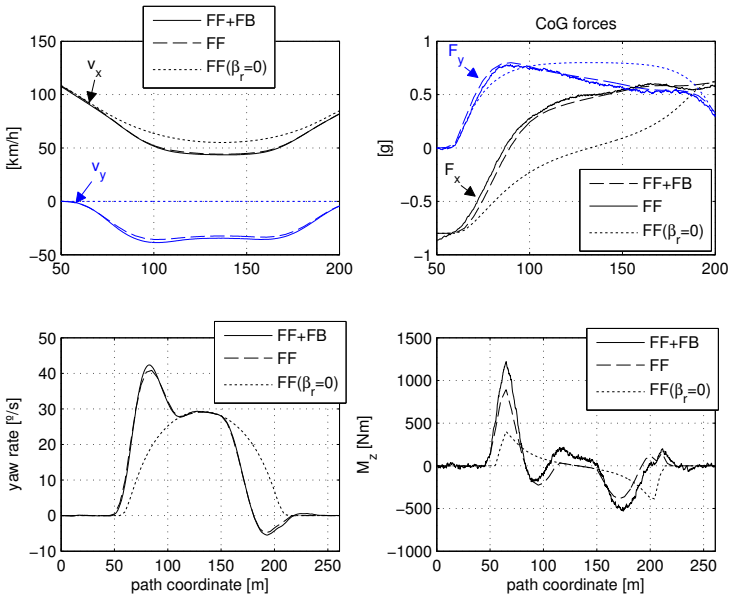

(b) Motion Control (solid line = feedforward reference; dashed line = feedforward + feedback; dotted =feedforward when $\beta_r = 0$)

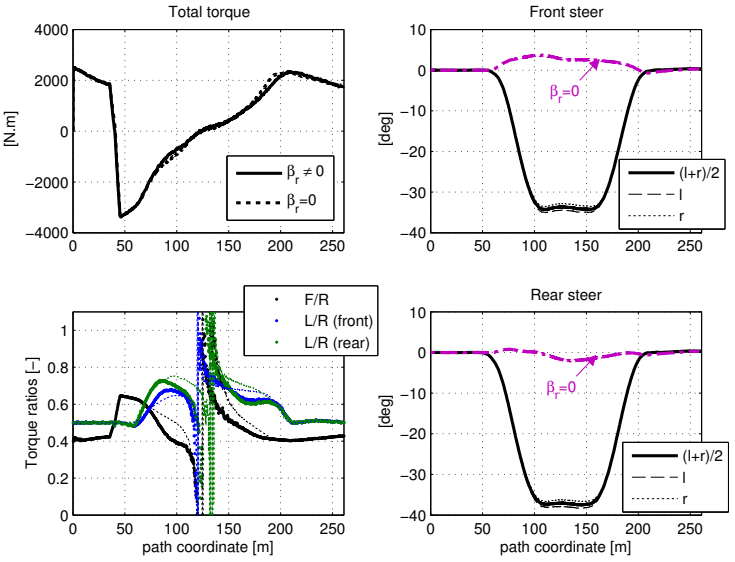

(c) Allocation Results

Figure 7.14: Simulation results for negotiating a 180° corner in minimum-time (non-zero side-slip, $\beta_r \neq 0$

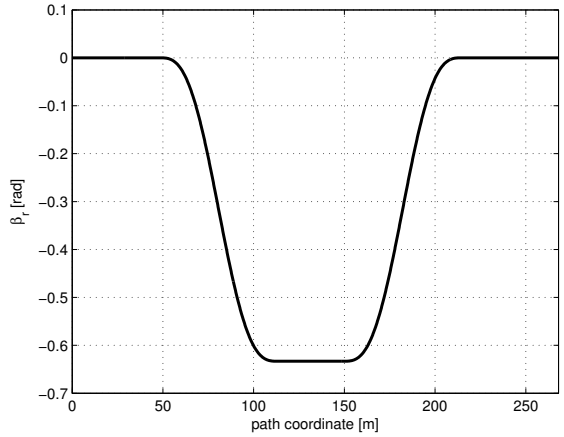

Figure 7.15: Side-slip reference (β_r) employed in the sliding test.

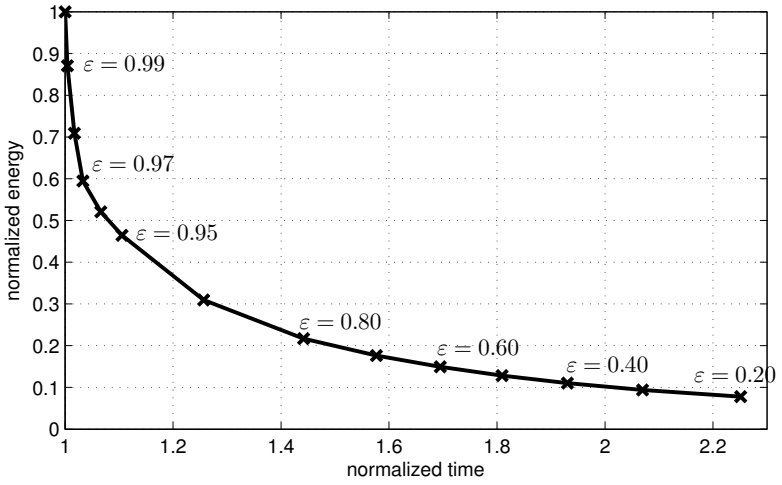

Figure 7.16: Influence of the trade-off parameter ϵ in the vehicle performance and energy consumption, during the hairpin corner. To facilitate the analysis, the time and energy were normalized, using as reference the solution obtained with $\epsilon = 1$ (i.e., min-time solution).

extent, the imposition of these extreme forces and yaw-moments is greatly facilitated by the presence of the four-wheel steer and the four-in-wheel motors in the vehicle. In particular, inspecting the allocation results present in Figure 7.14(c), it can be found that the front and rear steers, besides a very significant magnitude (when compared with the situation $\beta_r = 0$), point in the opposite direction of the corner, which is instrumental in keeping the vehicle sliding throughout the hairpin corner.

Performance vs Energy Consumption

Another interesting feature of the path following controller is its ability to trade off performance and energy consumption. To illustrate this feature we have evaluated the hairpin corner for various trade-off factors ϵ, as shown in Figure 7.16. The results illustrate a clear trend: as we approach the min-time solution, the energy consumption rises significantly, which is in accordance with our engineer intuition. However, if the user is willing to

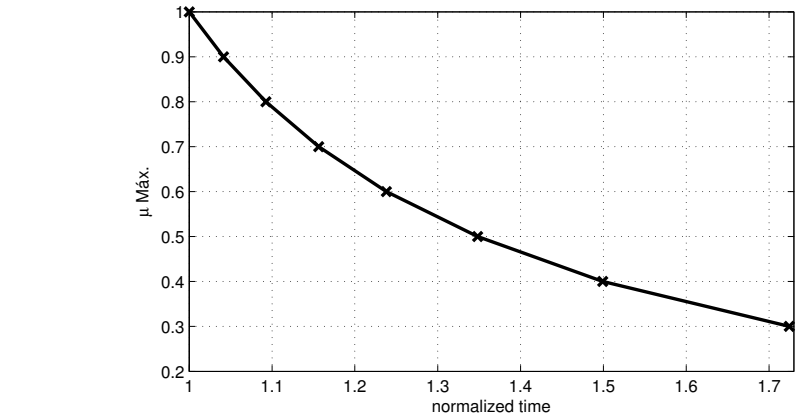

(a)

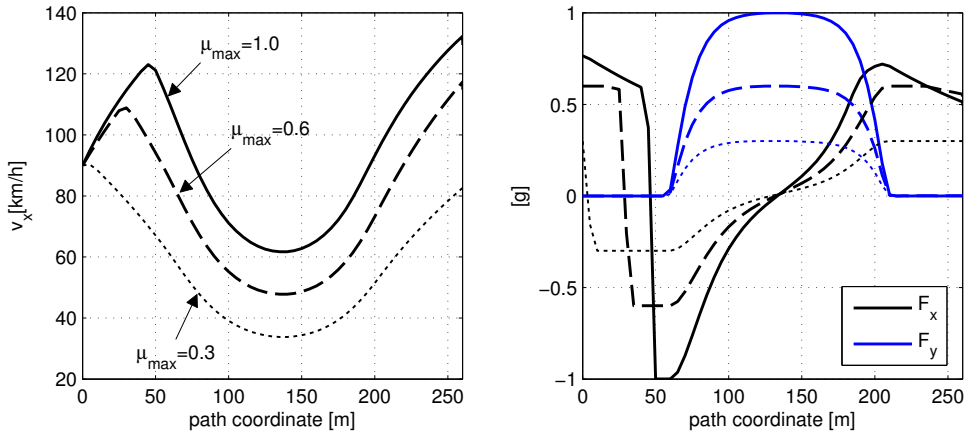

(b)

Figure 7.17: Influence of the μ_{max} in the normalized manoeuvre time (a) and speed and forces (b).

perform the path in non-minimum time, the energy gains can be quite significant. For example: *i*) a 20% increase in the manoeuvre time will decrease the consumption by almost 70%; *ii*) doubling the journey time decreases the energy consumption by 10 times.

μ_{max} influence

If the information about the tyre-road conditions are available, the path following controller can also adapt the vehicle motion accordingly, particularly the feedforward component. For example, Figure 7.17(a) shows the sensitivity of the manoeuvre time to different values of μ_{max}. These results suggests an almost linear relation between the μ_{max} and the manoeuvre time, e.g. on wet road ($\mu_{max} = 0.6$) the manoeuvre time will increase 24%, while for snow conditions (μ_{max}=0.3), the time increase reaches almost 70%. Furthermore, analysing the speeds and forces produced by the feedforward component (see Figure 7.17(b)), it is interesting to note that as μ_{max} is reduced, the vehicle brakes earlier, and the approach to the corner is much more careful.

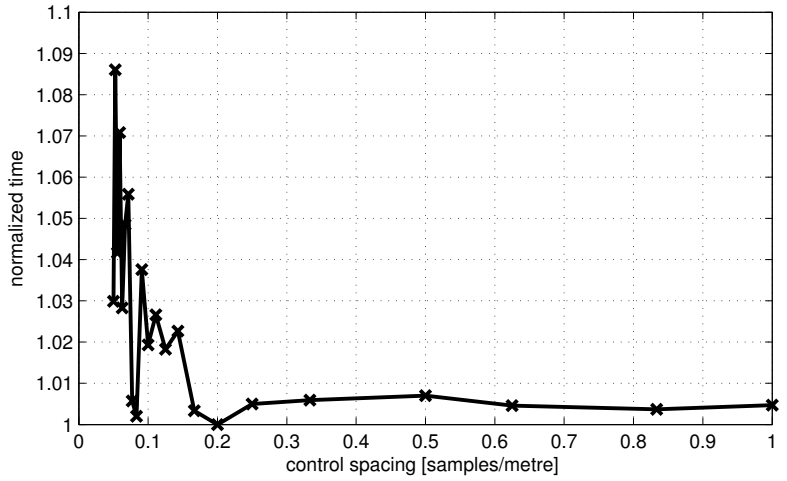

(a)

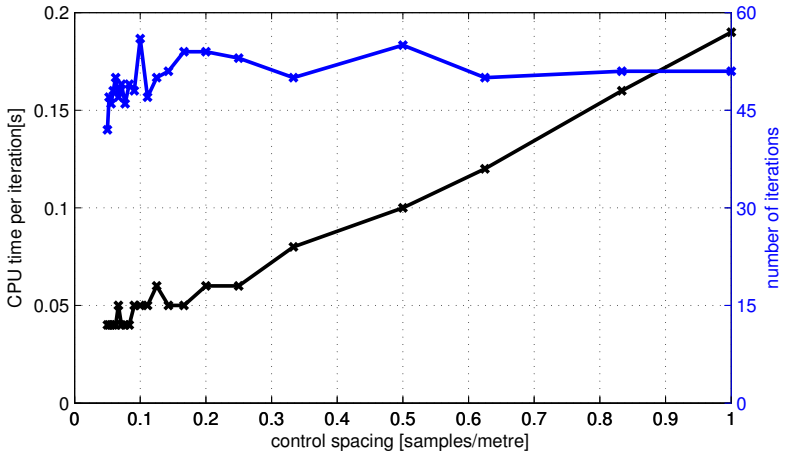

(b)

Figure 7.18: Influence of the sampling distance in the manoeuvre time (a) and computation time (b).

Computational Performance

From a practical perspective, the distance between sampling points (Δs) plays a key role in the solution precision and computation time. To investigate the effect of this parameter in the solving process, we conducted a set of simulations with different Δs, as illustrated in Figure 7.18. From these plots, one can find that, for sampling rates higher that 0.2 samples/metre, the solution precision is quite good and does not change much. As for the computational performance, it is apparent that the computation time per iteration rises almost linearly with the increase in the sampling rate. Thus, in light of these results, we can conclude that 0.2 samples/metre (i.e., $\Delta s = 5$m) represents a good compromise between solution accuracy and computational time.

7.6.2 Track Evaluation

As a final evaluation test, we consider the path following of a longer course, based on the 2.2km Norising track, which will enable us to evaluate the controller performance with

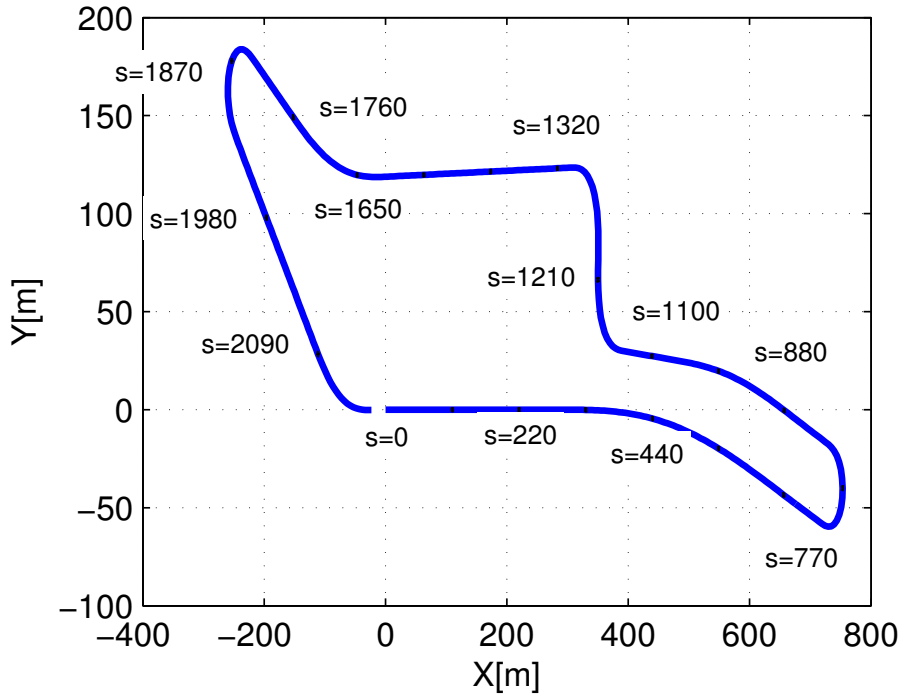

Figure 7.19: Track layout employed in the simulations.

different types of corners (see Figure 7.19).

Min-time approach

The results of the minimum-time path following for this track are presented in Figure 7.20. Broadly speaking, this test confirms the good indicators already observed in the hairpin corner; in particular, *i*) the tracking errors are low, with peak position error inferior to 0.5m, *ii*) the feedforward components generated by the optimal (FF) approach produce a control action that is very close to the feedback term (particularly in v_x and v_y), which demonstrates the usefulness of the FF in achieving high control performances; and *iii*) the torque distribution between the four wheels is largely based on the load movement that the vehicle is subject to, i.e., the wheels with higher vertical load receive more torque, in order to keep the overall friction use low. Taking into account the control allocation formulation, which intends to minimize the friction use, the allocation results are in accordance with our expectations.

The longer course also enables us to extract additional insight into the performance of the path following controller. For example, it can be observed that the vehicle's top speed is approximately 180km, which is limited by the power constraints in the IWMs. This limitation puts in evidence the importance of including the IWM's power constraints in the optimal formulation adopted for the min-time problem. Furthermore, the steer-allocation results also exhibit an interesting pattern: during fast corners, e.g., $s \in [300, 600] \cup [1600, 1750]$m, both front and rear steers point in the same direction, while for tight-corners, e.g., $s \in [700, 800] \cup [1820, 1920]$m, the rear steer points in the opposite direction from the front steer. From a practical perspective, we believe these allocation results are directly linked with the yaw-rate requested by the controller. To better explain

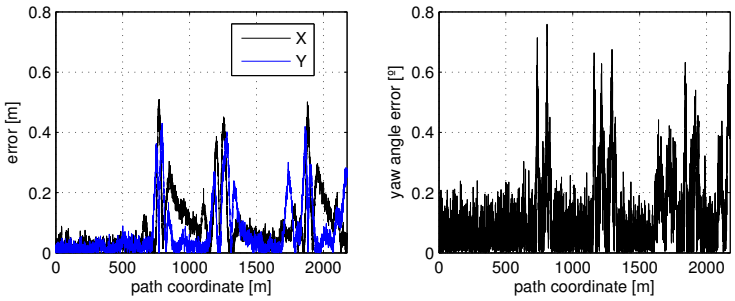

(a)

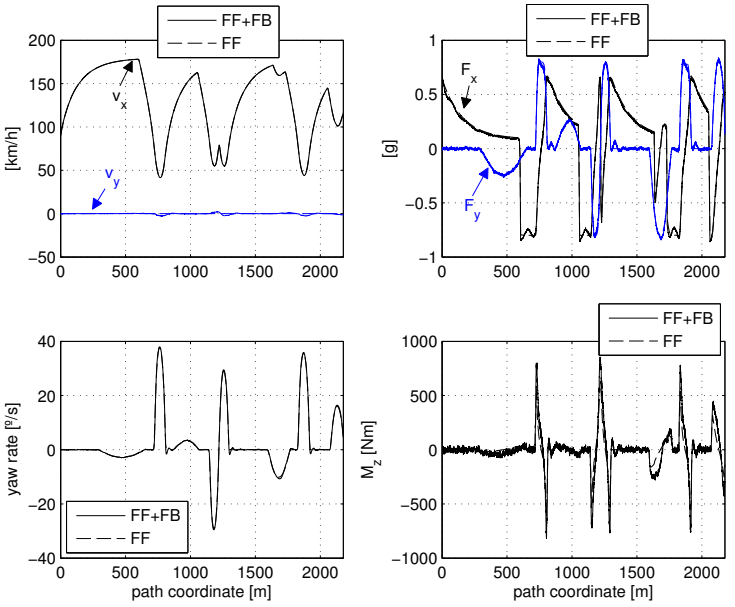

(b)

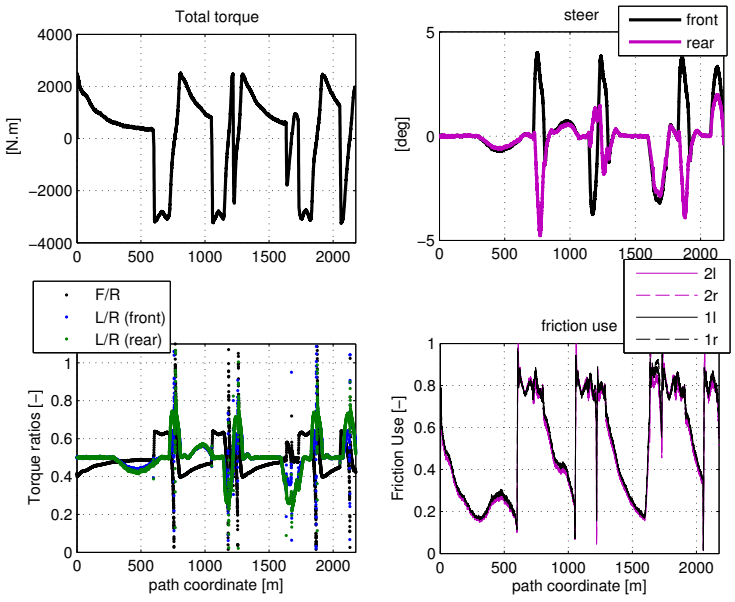

(c)

Figure 7.20: Simulation results for the track evaluation.

this claim, notice that during tight corners the vehicle undergoes a significant change of direction, requiring a large yaw-rate, with peaks of 30-40^o/s. Consequently, by steering the front and rear in opposite directions, the controller can apply a significant yaw-moment (M_z) and quickly rotate the vehicle to negotiate the slow corner. On the other hand, for fast corners, the yaw-rate requirements are much lower, and, as a result, there is no need to apply large yaw-moments, which makes the front/rear steering in the same direction more suitable.

Finally, it is also worth discussing the results associated with the friction use of the tyres, which is depicted in Figure 7.20(c). In general terms, it can be verified that, during cornering conditions, the friction use does not exceed $80-90\%$ of the tyre's potential (recall that we left a 20% friction margin to enable the controller to cope with uncertainties). Conversely, in straight-line operation, there is a marked decrease in the friction use, which can be attributed to the dominant role of the IWM's power constraints.

Energy/performance trade-offs

It is also pertinent to evaluate trade-offs between energy and performance metrics along the track. For example, Figure 7.21 illustrates the speeds and forces obtained with two different weights: $\epsilon = 1.0$ and $\epsilon = 0.9$. From the results obtained with $\epsilon = 0.9$, we can find some traces of the "coasting technique", i.e., the controller decreases the accelerating force well in advance of the corners, and takes advantage of the aero and rolling drag to reduce the vehicle speed. Further, Figure 7.22 illustrates the energy-performance trade-off curve along the track, which confirms a similar trend to the one discussed in the hairpin-corner, that is, if the user is willing to sacrifice lap-time, the energy gains can be very significant, e.g., increasing the journey time by 20% allows energy savings up to 55%.

7.7 Conclusion

In this work, a path following algorithm, suitable for highly redundant vehicles, composed of 4IWMs and 4WS, was proposed. By combining different tools, such as time-to-space transformation, convex optimization, robust control methods and control allocation techniques, we were able to decompose the path following problem into several sub-layers. To start with, we developed a convex formulation for the minimum-time path following problem for autonomous vehicles. This formulation builds on the idea that the CoG forces can be regarded as pseudo-inputs, and explores convexification techniques to approximate the nonlinear power constraints associated with the IWMs. The resulting problem was then tackled with a direct optimization method, i.e., by discretizing the control and states variables, the original (continuous) formulation was transformed into a large discrete (but convex) optimization problem, and then solved by numerical means. The solution of this problem was employed as a feedforward term by the motion controller. Robustness to model uncertainties and disturbances were ensured thanks to the inclusion of a cascade position-speed feedback loop, which relies on sliding-modes technique, endowed with conditional integrators. The final layer in the motion controller is related to the allocation of the CoG forces between the wheel's torques and steer, targeting the minimization of the tyre's friction use. Toward that goal, two control allocation techniques were investigated. The first method is based upon the idea that, using the pseudo-inverse solution, the force's angles can be fixed and then the force magnitude recalculated with the help of fast quadratic

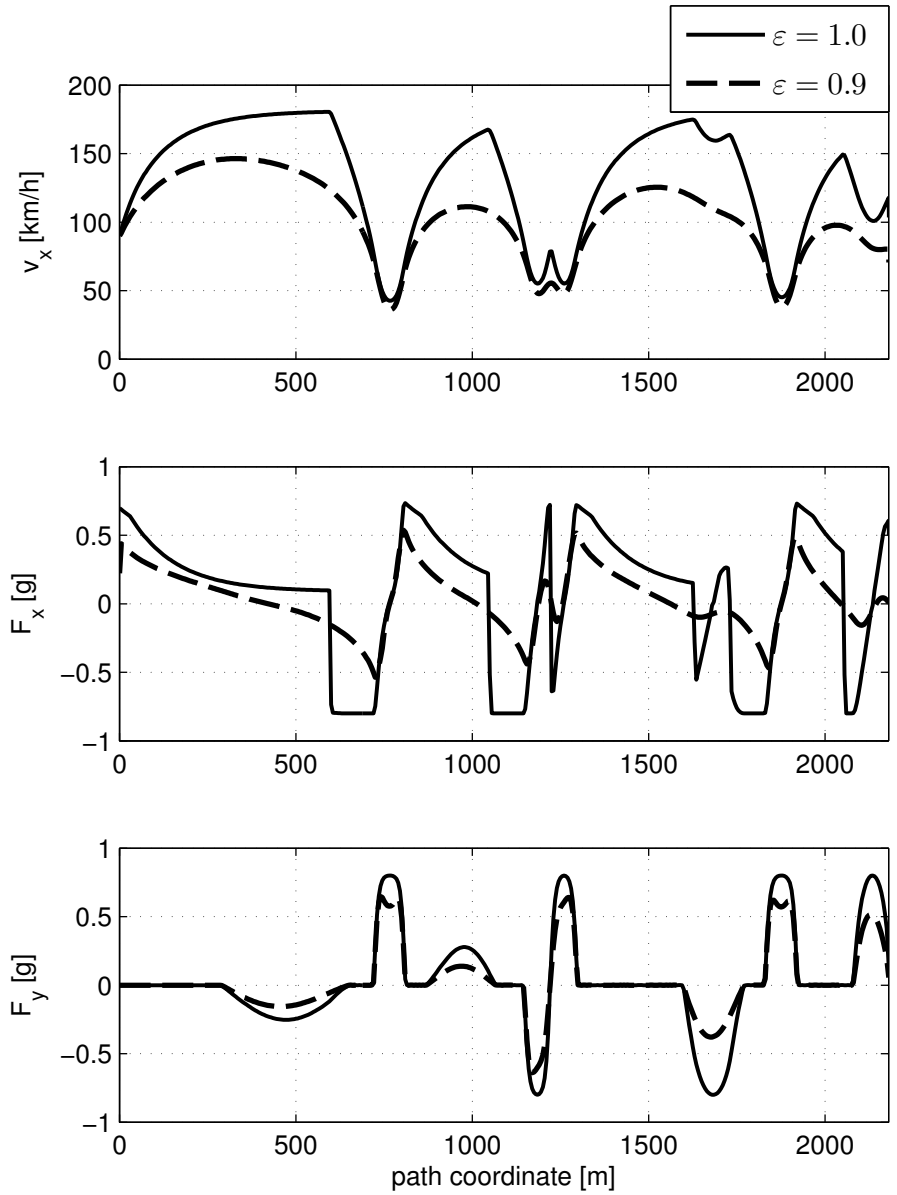

Figure 7.21: Influence of the trade-off parameter ϵ in the velocity and forces, during the track simulation.

programming solvers. On the other hand, the second method relies mainly on the linearization of the friction constraints. It was shown that the first method is faster, but less accurate when unfeasible forces setpoints are requested; the second method copes better with the unfeasible forces, but requires $2-3$ times more computational time. Nonetheless, given that the absolute computation times of the linearization approach are still acceptable for real-time purposes (less than 1 ms on average), this method was selected to be included in the path following controller. Simulation results carried out in the high-fidelity CarSim simulator demonstrated the effectiveness of the approach, both in normal driving condition, and in extreme conditions (with high side-slip). Sensitive studies also revealed the trade-offs between lap-time and energy consumption that the path following controller can provide.

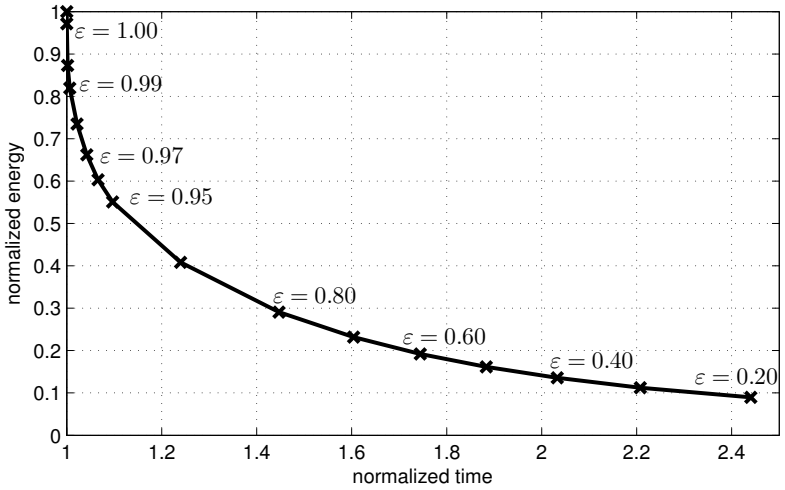

Figure 7.22: Influence of the trade-off parameter ϵ in the energy consumption and lap-time,during during the track simulations.

Future works should address the incorporation of the path following approach with the path-planning layer. Coupled with this issue, we also aim to apply real-time solvers for the generation of the feedforward component, and also address the fail-safe operation.

7.8 Appendix: Resistance Forces

This work considers that the main resistance forces that affect the vehicle motion are the rolling friction and aerodynamic drag; for simplicity, the grade forces were neglected, since only planar motion is being considered. This means that the resistance force can be expressed as

$$\mathcal{R}(v_x, v_y) = \begin{bmatrix} \mathcal{R}_x \\ \mathcal{R}_y \\ \mathcal{R}_\psi \end{bmatrix} = \underbrace{\begin{bmatrix} mgf_r \\ 0 \\ 0 \end{bmatrix}}_{\mathcal{R}_1} + \frac{1}{2}\rho \begin{bmatrix} A_x C_x(\beta)|v_x|v_x \\ A_y C_y(\beta)|v_y|v_y \\ 0 \end{bmatrix} \tag{7.84}$$

where f_r is the rolling resistance coefficient, ρ represents the air density, A_j the vehicle area in the direction $j \in \{x, y\}$, and C_j the drag coefficient, which may be dependent on the vehicle side-slip angle $\beta = \text{atan}(v_x/v_y)$ [132].

In view of the relation (7.4), the resistance force $\mathcal{R}$ can also be rewritten as a function of the vehicle position $\mathbf{p}$ and vehicle speed $\dot{\mathbf{p}}$ (expressed in the XY components). To show this fact, recall that

$$v_x = \mathbf{e}_1^T \mathbf{T}^{-1}(\mathbf{p})\dot{\mathbf{p}} \tag{7.85}$$
$$v_y = \mathbf{e}_2^T \mathbf{T}^{-1}(\mathbf{p})\dot{\mathbf{p}} \tag{7.86}$$

where $\mathbf{e}_1 = [1 \quad 0 \quad 0]^T$, $\mathbf{e}_2 = [0 \quad 1 \quad 0]^T$. Inserting these relations in the second component of (7.84), one has:

$$\frac{1}{2}\rho \begin{bmatrix} A_x C_x(\beta)|v_x|v_x \\ A_y C_y(\beta)|v_y|v_y \\ 0 \end{bmatrix} = \underbrace{\frac{1}{2}\rho \begin{bmatrix} A_x C_x(\text{atan}(\frac{\mathbf{e}_1^T\mathbf{T}^{-1}(\mathbf{p})\dot{\mathbf{p}}}{\mathbf{e}_2^T\mathbf{T}^{-1}(\mathbf{p})\dot{\mathbf{p}}}))|\mathbf{e}_1^T\mathbf{T}^{-1}(\mathbf{p})\dot{\mathbf{p}}|\mathbf{e}_1^T\mathbf{T}^{-1}(\mathbf{p}) \\ A_y C_y(\text{atan}(\frac{\mathbf{e}_1^T\mathbf{T}^{-1}(\mathbf{p})\dot{\mathbf{p}}}{\mathbf{e}_2^T\mathbf{T}^{-1}(\mathbf{p})\dot{\mathbf{p}}}))|\mathbf{e}_2^T\mathbf{T}^{-1}(\mathbf{p})\dot{\mathbf{p}}|\mathbf{e}_2^T\mathbf{T}^{-1}(\mathbf{p}) \\ \mathbf{0} \end{bmatrix}}_{\mathcal{R}_2(\mathbf{p},\dot{\mathbf{p}})} \dot{\mathbf{p}} \tag{7.87}$$

which leads us to the following compact representation of the resistance forces:

$$\mathcal{R}(\mathbf{p}, \dot{\mathbf{p}}) = \mathcal{R}_1 + \mathcal{R}_2(\mathbf{p}, \dot{\mathbf{p}})\dot{\mathbf{p}} \tag{7.88}$$

7.9 Appendix: Proof of Proposition 7.1

To avoid overloading the notation (particularly the sub-indices), and since the sliding control law with conditional integrator is employed in more than one control loop, the demonstration of Proposition 7.1 is carried out with the help of a generalized symbology. In particular, the single-input single-output dynamic model (7.52) is redefined as

$$\dot{e}_v = w + \mathcal{D} \tag{7.89}$$

where $|\mathcal{D}| \leq \overline{\mathcal{D}}$ is a bounded disturbance, $w = \Delta a$ the control input, defined as:

$$w = -k_a \,\text{sat}(\frac{\sigma}{\varepsilon}) \tag{7.90}$$

$$\sigma = e_v + k_\eta \eta \tag{7.91}$$

$$\dot{\eta} = -k_\eta \eta + \varepsilon \,\text{sat}(\frac{\sigma}{\varepsilon}) \tag{7.92}$$

It can be readily verified that by a suitable introduction of sub-indices, e_v can take any of the speed errors $e_{vj}, \quad j \in \mathfrak{J}$, the control law, $w = \Delta a$ one of the control inputs Δa_j, $j \in \mathfrak{J}$, etc. (The same idea applies to the remaining variables $\sigma, \eta, \varepsilon, k_\eta, k_a, \mathcal{D}, \overline{\mathcal{D}}, ...$). Based on this model, we will now demonstrate the three main points of Proposition 7.1.

7.9.1 Part 1

This result was established by [165] and presented here for completeness of the proposition's proof. Consider the following Lyapunov candidate function: $V(\eta) = 0.5\eta^2$. By calculating its time-derivative:

$$\dot{V} = \eta\dot{\eta} = \eta\left(-k_\eta\eta + \varepsilon \,\text{sat}(\frac{\sigma}{\varepsilon})\right) \tag{7.93}$$

$$= -k_\eta\eta^2 + \varepsilon \,\text{sat}(\frac{\sigma}{\varepsilon})\eta \tag{7.94}$$

$$= -k_\eta\eta^2 + \varepsilon|\eta| \tag{7.95}$$

$$= -k_\eta|\eta|\left(|\eta| - \frac{\varepsilon}{k_\eta}\right) \tag{7.96}$$

one can find that $\dot{V} < 0$ for $|\eta| > \varepsilon/k_\eta$; thus, the system will be attracted to the set $\Omega_\eta = \{|\eta| \leq \varepsilon/k_\eta\}$. Further, if the initial value of η lies in the Ω_η, i.e., $\eta(0) \in \Omega_\eta$, the above result also implies that $\eta(t) \in \Omega_\eta, \quad \forall t \geq 0$, which shows the first point of the proposition.

7.9.2 Part 2

To show the attractiveness to Ξ, we can start by considering the candidate Lyapunov function $V(\sigma) = 0.5\sigma^2$. Expanding the time-derivative of V:

$$\begin{aligned}
\dot{V} &= \sigma\dot{\sigma} = \sigma\left(\dot{e}_v + k_\eta\dot{\eta}\right) \\
&= \sigma\left(w + \mathcal{D} + k_\eta\left(-k_\eta\eta + \varepsilon\,\mathrm{sat}(\frac{\sigma}{\varepsilon})\right)\right) \\
&= \sigma\left(w + \mathcal{D} - k_\eta^2\eta + k_\eta\varepsilon\,\mathrm{sat}(\frac{\sigma}{\varepsilon})\right) \\
&= \sigma\left(-k_a\,\mathrm{sat}(\frac{\sigma}{\varepsilon}) + \mathcal{D} - k_\eta^2\eta + k_\eta\varepsilon\,\mathrm{sat}(\frac{\sigma}{\varepsilon})\right) \\
&= -k_a\,\mathrm{sat}(\frac{\sigma}{\varepsilon})\sigma + \mathcal{D}\sigma - k_\eta^2\eta\sigma + k_\eta\varepsilon\,\mathrm{sat}(\frac{\sigma}{\varepsilon})\sigma
\end{aligned}$$

and limiting our attention to the set $\Omega_\sigma = \{|\sigma| \geq \varepsilon\}$, it can be concluded that $\mathrm{sat}(\frac{\sigma}{\varepsilon})\sigma = |\sigma|, \forall\sigma \in \Omega_\sigma$. Thus,

$$\begin{aligned}
\dot{V} &= -k_a|\sigma| + \mathcal{D}\sigma - k_\eta^2\eta\sigma + k_\eta\varepsilon|\sigma|, \quad \forall\sigma \in \Omega_\sigma \\
&\leq -k_a|\sigma| + |\mathcal{D}||\sigma| + k_\eta^2|\eta||\sigma| + k_\eta\varepsilon|\sigma|, \quad \forall\sigma \in \Omega_\sigma
\end{aligned} \tag{7.97}$$

Further, taking into account the boundedness of $|\mathcal{D}| \leq \overline{\mathcal{D}}$ and invariance of the set Ω_η, i.e., $|\eta| \leq \varepsilon/k_\eta$, the above inequality can be rewritten as:

$$\dot{V} \leq -|\sigma|\left(k_a - \overline{\mathcal{D}} - 2k_\eta\varepsilon\right), \quad \forall\sigma \in \Omega_\sigma$$

Consequently, by imposing $k_a \geq \overline{\mathcal{D}} + 2k_\eta\varepsilon + c_0$ (which comes from (7.54)) and a positive value for c_0 (selected by the designer), we obtain

$$\dot{V} \leq -c_0|\sigma|, \quad \forall\sigma \in \Omega_\sigma \tag{7.98}$$

which shows that the system state will be attracted, in finite time, to the inside of $\{|\sigma| \leq \varepsilon\}$. Next, expanding the definition of σ

$$\begin{aligned}
|\sigma| \leq \varepsilon \Leftrightarrow, \qquad & -\varepsilon \leq e_v + k_\eta\eta \leq \varepsilon \Leftrightarrow \\
& -\varepsilon - k_\eta|\eta| \leq -\varepsilon - k_\eta\eta \leq e_v \leq \varepsilon - k_\eta\eta \leq \varepsilon + k_\eta|\eta| \\
& -\varepsilon - k_\eta|\eta| \leq e_v \leq \varepsilon + k_\eta|\eta|
\end{aligned}$$

and exploring the invariance of Ω_η, i.e., $|\eta| \leq \varepsilon/k_\eta$, we obtain

$$-2\varepsilon \leq e_v \leq 2\varepsilon \Leftrightarrow \{|e_v| \leq 2\varepsilon\}$$

which reveals that the attractiveness to $\{|\sigma| \leq \varepsilon\}$ also implies the attractiveness to $\{|e_v| \leq 2\varepsilon\}$. This fact, together with the invariance of Ω_η, demonstrates the second point of the Proposition.

7.9.3 Part 3

Inside the set $\{|\sigma| \leq \varepsilon\}$, the closed loop model is described by:

$$\dot{e}_v = -k_a \frac{\sigma}{\varepsilon} + \mathcal{D}(e_v) \tag{7.99}$$

$$\sigma = e_v + k_\eta \eta \tag{7.100}$$

$$\dot{\eta} = e_v, \tag{7.101}$$

and has the following equilibrium points:

$$e_v^{eq} = 0, \qquad \eta^{eq} = \frac{\varepsilon}{k_a k_\eta}\mathcal{D}(0), \qquad \sigma^{eq} = \frac{\varepsilon}{k_a}\mathcal{D}(0) \tag{7.102}$$

Notice that, in this formulation, we are assuming that the disturbance is (possibly) dependent on the tracking error. Since our goal is to show that the system converges to this equilibrium point (with zero tracking error), it is convenient to consider the following change of variable:

$$\tilde{\sigma} = \sigma - \sigma^{eq}, \qquad \tilde{\eta} = \eta - \eta^{eq} \tag{7.103}$$

as well as its dynamics:

$$\frac{d}{dt}\begin{bmatrix}\tilde{\sigma}\\ \tilde{\eta}\end{bmatrix} = \begin{bmatrix}-\frac{k_a}{\varepsilon} & 0\\ 1 & -k_\eta\end{bmatrix}\begin{bmatrix}\tilde{\sigma}\\ \tilde{\eta}\end{bmatrix} + \begin{bmatrix}1\\ 0\end{bmatrix}\left(\mathcal{D}(\tilde{\sigma} - k_\eta\tilde{\eta}) - \mathcal{D}(0)\right)$$

To show that $(\tilde{\sigma}, \tilde{\eta}) \to (0, 0)$, consider the following Lyapunov candidate function

$$V(\tilde{\sigma}, \tilde{\eta}) = \frac{1}{2}\tilde{\sigma}^2 + \frac{1}{2}\tilde{\eta}^2 \tag{7.104}$$

as well as its time-derivative

$$\begin{aligned}\dot{V} &= \tilde{\sigma}\dot{\tilde{\sigma}} + \tilde{\eta}\dot{\tilde{\eta}}\\ &= \tilde{\sigma}\left(-\frac{k_a}{\varepsilon}\tilde{\sigma} + (\mathcal{D}(\tilde{\sigma} - k_\eta\tilde{\eta}) - \mathcal{D}(0))\right) + \tilde{\eta}\,(\tilde{\sigma} - k_\eta\tilde{\eta})\\ &= -\frac{k_a}{\varepsilon}\tilde{\sigma}^2 - k_\eta\tilde{\eta}^2 + \tilde{\eta}\tilde{\sigma} + \tilde{\sigma}\,(\mathcal{D}(\tilde{\sigma} - k_\eta\tilde{\eta}) - \mathcal{D}(0))\end{aligned} \tag{7.105}$$

By upper-bounding the last term,

$$\tilde{\sigma}\,(\mathcal{D}(\tilde{\sigma} - k_\eta\tilde{\eta}) - \mathcal{D}(0)) \leq |\tilde{\sigma}|\,|\,(\mathcal{D}(\tilde{\sigma} - k_\eta\tilde{\eta}) - \mathcal{D}(0))\,|$$

and noticing that the disturbance $\mathcal{D}$ is assumed to be Lipchitz (with constant L) in the domain under consideration, we have:

$$\begin{aligned}|\tilde{\sigma}|\,|\,(\mathcal{D}(\tilde{\sigma} - k_\eta\tilde{\eta}) - \mathcal{D}(0))\,| &\leq |\tilde{\sigma}|L|\tilde{\sigma} - k_\eta\tilde{\eta}|\\ &\leq |\tilde{\sigma}|L(|\tilde{\sigma}| + k_\eta|\tilde{\eta}|)\\ &\leq L\tilde{\sigma}^2 + Lk_\eta|\tilde{\eta}||\tilde{\sigma}|\end{aligned}$$

Inserting this relation in (7.105), the time-derivative of the Lyapunov function can be upper bounded by

$$\begin{aligned}\dot{V} &\leq -k_\eta\tilde{\eta}^2 - \left(\frac{k_a}{\varepsilon} - L\right)\tilde{\sigma}^2 + \tilde{\eta}\tilde{\sigma} + Lk_\eta|\tilde{\eta}||\tilde{\sigma}| \\ &\leq -k_\eta\tilde{\eta}^2 - \left(\frac{k_a}{\varepsilon} - L\right)\tilde{\sigma}^2 + (1 + Lk_\eta)|\tilde{\eta}||\tilde{\sigma}| \\ &= -\begin{bmatrix}|\tilde{\eta}| & |\tilde{\sigma}|\end{bmatrix}\underbrace{\begin{bmatrix} k_\eta & -\frac{1+Lk_\eta}{2} \\ -\frac{1+Lk_\eta}{2} & \left(\frac{k_a}{\varepsilon} - L\right)\end{bmatrix}}_{\mathbf{P}}\begin{bmatrix}|\tilde{\eta}| \\ |\tilde{\sigma}|\end{bmatrix}\end{aligned} \tag{7.106}$$

which is negative definite if all the leading principal minors of P are positive, that is:

- $k_\eta > 0$
- $k_\eta\left(\frac{k_a}{\varepsilon} - L\right) > \left(\frac{1+Lk_\eta}{2}\right)^2$

The second condition is also equivalent to $\varepsilon < 4k_ak_\eta/\left(4Lk_\eta + (LK_\eta + 1)^2\right)$. Consequently, as long as the controller's parameters fulfil these conditions, the system will converge to $(\tilde{\sigma}, \tilde{\eta}) \to (0, 0)$. Due to the definition of $\tilde{\sigma}$ and $\tilde{\eta}$, one can straightforwardly verify that the converge of $\tilde{\sigma}, \tilde{\eta}$ to zero also implies that $e_v^{eq} = 0$. This concludes the demonstration of the Proposition.

7.10 Appendix: Inversion of the Tyre's Force Model

The goal of this section is to derive an inverse relation for the tyre's friction model, presented in Section 7.2.3. More precisely, the problem we aim to solve is described as: given a reference force (F_x^*, F_y^*), determine the value of torque T and steer δ that will produce the desired reference force. This problem will be tackled with a three-step approach: *i*) we will start by calculating the total slip of the tyre (σ); *ii*) next, the inverse formula for the longitudinal and lateral theoretical slips will be derived; *iii*) based on this information, the torque and steer ultimately will be determined. For reasons that will be clear later on, it is also helpful to define the modulus of the requested force (F^*), as well as its angle ($\angle F^*$):

$$F^* = \|[F_x^* \quad F_y^*]^T\|, \qquad \angle F^* = \operatorname{atan}\left(\frac{F_y^*}{F_x^*}\right) \tag{7.107}$$

Similarly to the previous Appendix, and to keep the notation simple, the variable's sub-indices associated with the individual tyres will be omitted, e.g., T_i, δ_i, with $i \in \mathfrak{T}$, will be referred to only as T and δ.

7.10.1 Determination of total slip

To start with, let us consider the modulus of the friction force generated by the tyre

$$F(\sigma, F_z) = \mu_{max}F_z g(\sigma) \tag{7.108}$$

where $g(\sigma) = \sin(C\operatorname{atan}(B\sigma))$ was extracted from (7.12) (notice that the inverse model presented in this section can be straightforwardly extended to other parameterizations).

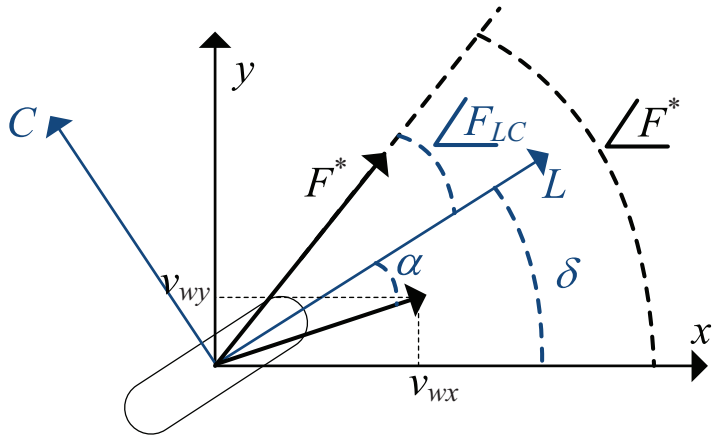

Figure 7.23: Variables employed in the inversion of the tyre model.

By inverting this model, it can be concluded that the total slip of the tyre must lie in the set

$$\Lambda = \left\{ \sigma \ : \ \sigma = g^{-1} \left(\frac{\| [F_x^* \quad F_y^*]^T \|}{\mu_{max} F_z} \right) \right\} \tag{7.109}$$

Remark 7.6. in general, Λ can have no solution ($\Lambda = \emptyset$), one solution or more than one solution. The first case is generally associated with unfeasible force requests, and is the one that deserves some care. To avoid situations where the model inverse does not have a solution, the designer must always ensure that the reference force is feasible (e.g., by imposing appropriate physical constraints in F_x^*, F_y^*).

7.10.2 Determination of lateral and longitudinal theoretical slips

After establishing the possible values for the total slip, it is necessary to split it between longitudinal (σ_L) and lateral (σ_C) "theoretical" slips . According to the model discussed in Section 7.2.3, this split must satisfy two constraints. The first is a quadratic:

$$\sigma_L^2 + \sigma_C^2 = \sigma^2, \qquad \sigma \in \Lambda \tag{7.110}$$

and the second is associated with the relation between $\angle F^*$ (specified in the xy axis) and the tyre's force angle in the LC axis (where the tyre's force model is described), that is

$$\angle F^* = \angle F_{LC} + \delta = \text{atan}(\frac{F_C}{F_L}) + \delta \tag{7.111}$$

where $\angle F_{LC}$ is the angle of the tyre's force vector with regard to the L axis (see Figure 7.23). By noticing that

$$\delta - \alpha = \text{atan}(\frac{v_{wy}}{v_{wx}}) \tag{7.112}$$

where v_{wx}, v_{wy} are the wheel's velocities in the x and y directions (assumed to be known), we may rewrite (7.111) as:

$$\begin{aligned}\angle F^* &= \operatorname{atan}(\frac{F_C}{F_L}) + \alpha + \operatorname{atan}(\frac{v_{wy}}{v_{wx}}) \\ &= \operatorname{atan}\left(\frac{\frac{\sigma_C}{\sigma}F(.)}{\frac{\sigma_L}{\sigma}F()}\right) + \alpha + \operatorname{atan}(\frac{v_{wy}}{v_{wx}}) \\ &= \operatorname{atan}\left(\frac{\sigma_C}{\sigma_L}\right) + \alpha + \operatorname{atan}(\frac{v_{wy}}{v_{wx}})\end{aligned} \tag{7.113}$$

which can be further expanded with the relation $\tan(\alpha) = \sigma_C(1+\kappa) = \frac{\sigma_C}{1-\sigma_L}$, that is

$$\angle F^* = \operatorname{atan}\left(\frac{\sigma_C}{\sigma_L}\right) + \operatorname{atan}\left(\frac{\sigma_C}{1-\sigma_L}\right) + \operatorname{atan}(\frac{v_{wy}}{v_{wx}}) \tag{7.114}$$

Rearranging the previous equation:

$$\operatorname{atan}\left(\frac{\sigma_C}{\sigma_L}\right) + \operatorname{atan}\left(\frac{\sigma_C}{1-\sigma_L}\right) = \angle F^* - \operatorname{atan}(\frac{v_{wy}}{v_{wx}}) \tag{7.115}$$

and applying to the left side the following trigonometric relation [299]:

$$\operatorname{atan}(z_1) + \operatorname{atan}(z_2) = \operatorname{atan}\left(\frac{z_1+z_2}{1-z_1 z_2}\right) \tag{7.116}$$

we obtain

$$\frac{\sigma_C}{\sigma_L - \sigma^2} = \tan\left(\angle F^* - \operatorname{atan}(\frac{v_{wy}}{v_{wx}})\right) \tag{7.117}$$

As a result, the theoretical slips of the tyre model can be obtained by solving the following set of equalities

$$\begin{cases}\sigma_L^2 + \sigma_C^2 = \sigma^2, & \sigma \in \Lambda \\ \sigma_C = \left(\sigma_L - \sigma^2\right)\tan\left(\angle F^* - \operatorname{atan}(\frac{v_{wy}}{v_{wx}})\right)\end{cases} \tag{7.118}$$

It is worth pointing out that, in the above equations, there are only two unknowns: σ_L, σ_C. This means that (7.118) can be geometrically interpreted as an intersection of a straight line with a circle. Further, an analytical solution for this problem can also be straightforwardly derived (omitted here for the sake of brevity).

7.10.3 Determination of Wheel Torque and Steer

After determining σ_L and σ_C, the values of the tyre longitudinal (κ) and lateral slip (α) can be extracted using the relations:

$$\kappa = \frac{\sigma_L}{1-\sigma_L}, \qquad \alpha = \operatorname{atan}\frac{\sigma_C}{1-\sigma_L} \tag{7.119}$$

Based on this information, and in (7.112), the steer angle is given by:

$$\delta = \alpha + \operatorname{atan}(\frac{v_{wy}}{v_{wx}}) = \operatorname{atan}\frac{\sigma_C}{1-\sigma_L} + \operatorname{atan}(\frac{v_{wy}}{v_{wx}}) \tag{7.120}$$

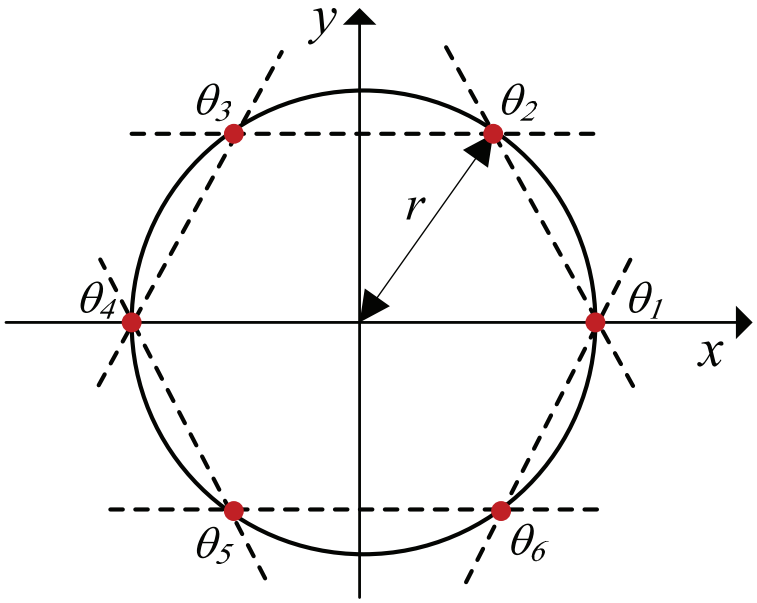

Figure 7.24: Example of approximating a circle constraint with a polytope ($N = 6$).

With regard to the wheel torque, we consider again a steady state approximation for the wheel dynamics (see (7.22)), which enables us to obtain the wheel torque as follows:

$$T \approx rF_L = r\frac{\sigma_L}{\sigma}F^* \tag{7.121}$$

7.11 Appendix: Linear Approximation of the friction circle constraint

Consider the following ball, centred at the origin and with radius r:

$$B(r) = \{(x, y) \in \mathbb{R}^2 \ : \ x^2 + y^2 \leq r^2\} \tag{7.122}$$

Our goal is to approximate this set with the following polytope

$$\hat{B}(r) = \{(x, y) \in \mathbb{R}^2 \ : \mathbf{C}\begin{bmatrix} x \\ y \end{bmatrix} \leq \mathbf{D}r\} \tag{7.123}$$

where $\mathbf{C} \in \mathbb{R}^{N\times 2}$, $\mathbf{D} \in \mathbb{R}^{N\times 1}$ are matrices to be defined, and N the number of half-spaces that characterise the polytope.

To solve this approximation problem, let us consider N points evenly spread along the border of the (2-dimensional) ball $B(r)$. Mathematically, these points can be described as (see also Figure 7.24):

$$(r\cos(\theta_i), r\sin(\theta_i)), \quad i \in 1, \ldots, N \tag{7.124}$$

$$\theta_i = \frac{2\pi}{N}(i-1) \tag{7.125}$$

Further, the straight line that connects the point i and $i+1$ is defined as

$$y = m_{i+1}x + rb_{i+1}, \qquad i \in 1, \ldots, N-1 \tag{7.126}$$

where the slope m_{i+1} and offset b_{i+1} are given by:

$$m_{i+1} = \frac{\sin\theta_i - \sin\theta_{i+1}}{\cos\theta_i - \cos\theta_{i+1}}, \quad b_{i+1} = \sin\theta_i - m_{i+1}\cos\theta_i$$

Based on this setting, our idea is to approximate the ball $B(r)$ with the intersection of the half-spaces associated with the equality (7.126). Toward that goal, it is convenient to first consider the points lying in the region $[0, \pi]$, which can be identified with the following set of indices: $I^+ = \{\, i \in [1, N] \;:\; \theta_{i+1} \in [0, \pi] \,\}$. In this region, the approximation polytope should be below the straight line (7.126), that is

$$y \leq m_{i+1}x + rb_{i+1}, \quad i \in I^+ \tag{7.127}$$

which can also be rewritten in the following matrix notation:

$$\underbrace{\begin{bmatrix} -m_2 & 1 \\ \vdots & \vdots \\ -m_{1+N^+} & 1 \end{bmatrix}}_{\mathbf{C}^+} \begin{bmatrix} x \\ y \end{bmatrix} \leq r \underbrace{\begin{bmatrix} b_2 \\ \vdots \\ b_{1+N^+} \end{bmatrix}}_{\mathbf{D}^+} \tag{7.128}$$

where $N^+ = \#I^+$ (i.e., number of element in the set I^+).

A similar idea applies to the remaining points, i.e., $I^- = \{\, i \in [1, N] \;:\; \theta_{i+1} \in (\pi, 2\pi] \,\}$, but with one important modification: the approximation polytope should lie above the straight line (7.126), that is:

$$y \geq m_{i+1}x + rb_{i+1}, \quad i \in I^- \tag{7.129}$$

which can also be rewritten in the following matrix notation:

$$\underbrace{\begin{bmatrix} m_{2+N^+} & -1 \\ \vdots & \vdots \\ m_N & -1 \end{bmatrix}}_{\mathbf{C}^-} \begin{bmatrix} x \\ y \end{bmatrix} \leq r \underbrace{\begin{bmatrix} -b_{2+N^+} \\ \vdots \\ -b_N \end{bmatrix}}_{\mathbf{D}^-} \tag{7.130}$$

By combining (7.128) and (7.130), the final approximation polytope is described by

$$\mathbf{C} \begin{bmatrix} x \\ y \end{bmatrix} \leq r\mathbf{D} \tag{7.131}$$

where

$$\mathbf{C} = \begin{bmatrix} \mathbf{C}^- \\ \mathbf{C}^+ \end{bmatrix}, \qquad \mathbf{D} = \begin{bmatrix} \mathbf{D}^- \\ \mathbf{D}^+ \end{bmatrix} \tag{7.132}$$

Notice that, by replacing x with F_{xi}, y with F_{yi} and r with $\mu_{max}F_{zi}$, the methodology described above can be directly applied to the friction circle constraint, described in Section 7.5.3.

Table 7.1: Parameters of the vehicle and controller

Variable	Symbol	**Value**
vehicle mass	m	1100 kg
yaw inertia	I_z	996 kg m^2
distance between front axle and COG	l_1	1.2 m
distance between rear axle and COG	l_2	1.3m
COG height	h	0.37 m
trackwidth	c	1.5 m
rolling resistance	f_r	.004
Aero. drag coefficient (frontal)	C_x	0.35
Aero. drag coefficient (lateral)	C_y	0.7
Frontal Area	A_x	1.6 m
Lateral Area	A_y	1.6 m
air density	ρ	1.206 kg/m^3
wheel radius	r	0.3 [m]
MTF parameter	B	7
MTF parameter	C	1.6
MTF parameter	D	1
Maximum power/IWM	$\overline{P}$	36 kW
Maximum torque/IWM	$\overline{T}$	777 Nm
Position and Speed Controllers		
$[k_{ax}, k_{ay}, k_{a\psi}]$	$[2.9, 2.9, 0.6]$	
$[k_{\eta x}, k_{\eta y}, k_{\eta\psi}]$	$[2.2, 0.7, 2.2]$	
$[\varepsilon_x, \varepsilon_y, \varepsilon_\psi]$	$[1.7, 1.1, 0.1]$	
$[k_{vX}, k_{vY}, k_{v\psi}]$	$[0.2, 0.2, 0.2]$	
$[k_{\eta X}, k_{\eta Y}, k_{\eta\psi}]$	$[2.8, 2.8, 0.2]$	
$[\varepsilon_X, \varepsilon_Y, \varepsilon_\psi]$	$[2.0, 2.0, 0.1]$	
Control Allocation		
$\mathbf{Q}$	$\mathrm{diag}([1, 1, 5])$	

7.12 Parameters of the Model and Controller

See Table 7.1.

Part II

Hybridization of the EV Energy Sources

Chapter 8

Combined Sizing and Energy Management in EVs with Batteries and SCs

Abstract: *This chapter is concerned with the study of combined sizing and energy management algorithms for electric vehicles (EVs) endowed with batteries and supercapacitors (SCs). The main goal is to find the number of cells of each source that minimizes the installation and running costs of the EV, taking into account the performance requirements specified for the vehicle and the technical constraints of the energy sources. To tackle this problem, two methodologies will be investigated. The first considers a filter-based approach to perform the power split among the sources; it will be shown that, under some practical assumptions, the resultant sizing problem can be posed as a linear programming problem and solved using efficient numerical techniques. The second methodology employs an optimal non-causal energy management, which, when integrated with the sizing problem, yields a nonlinear optimization problem. These two methodologies will then be applied to size the storage unit of a small EV. The results indicate that the filter-based approach, although simple and numerically efficient, generally requires an oversized storage unit. Furthermore, it was also concluded that, if the range requirements of the EV are not very high (below* $50km$*), the use of SCs enables energy savings of up to* 7.8%*.*

8.1 Introduction

This chapter marks the beginning of the second main theme of the document: hybridization of the energy storage systems (ESS). Due to well-known constraints in the ESS's technologies, discussed in Section 1.1.2, there has been a growing interest in developing hybridization strategies, employing, for that purpose, various combinations of fuel-cells, batteries and supercapacitors (SCs) [58, 59, 60, 61, 62]. Among the many possible combinations, our interest here lies in the battery and SCs hybridization, with an active parallel arrangement, i.e., the sources are connected to the DC bus through two bidirectional DC/DC converters. To control and manage this hybrid ESS, we advocate a two-layer separation, illustrated in Figure 8.1: *i*) on the top layer, the Vehicle Energy Management (VEM) task is responsible for defining the power-sharing (or current) strategy between

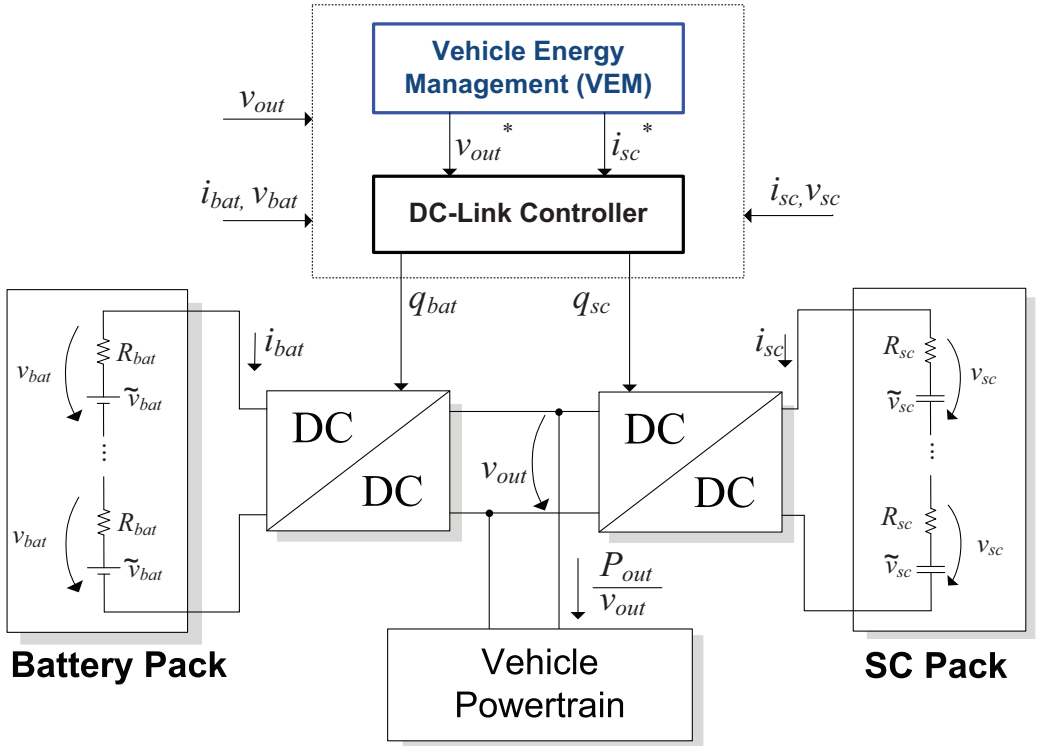

Figure 8.1: Block diagram of the hybrid ESS considered in this work.

the battery and SCs; *ii*) on the lower layer, a DC-Link controller manipulates the duty cycles of the DC/DC converters in order to enforce the set-points required by the VEM. The main goal of this chapter is to investigate the interdependence between the VEM layer and the sizing of the storage system, whereas the design of the DC-Link controller will be tackled in the next chapter.

When sizing the ESS of a vehicle, the selected storage unit must be capable of providing enough power and energy to fulfil the vehicle's specifications, like the range, maximum speed and acceleration, climbing capabilities, etc. For ESS composed by a single source, it is, in general, not too difficult to size the storage unit capable of fulfilling these fundamental requirements. For instance, in battery-powered EVs, we can easily pick a minimum battery pack that is able to provide the necessary energy and peak power required by the vehicle. However, for ESS composed by more than one source, the selection process is not that straightforward because the operating points of each source are dependent on how the power is split among them. In other words, there is interdependence between the energy management algorithm and the sizing task. This matter is further complicated by the different costs, energy efficiencies, degradation properties, and lifetime that each source presents. Notice that, while the energy management for the batteries-SCs hybridization has been widely investigated in the last few years (see, e.g., [73, 74, 300]), the sizing task for this particular ESS configuration has received less attention in the literature. References [301, 302, 303] present preliminary studies on the battery-SC sizing task, but fail to provide an accurate account of the energy losses in the powertrain components and/or ignore the important coupling between the sizing and energy management. With regard to this last factor, recent studies on the design of FC-batteries [304, 305], hybrid [306], and plug-in [307] EVs have shown that, to maximize the benefits of hybridization, it is

imperative to take into account the coupling between the sizing and the energy management. Accordingly, the present work extends these previous studies by contemplating the combined sizing/energy management problem for the batteries-SCs hybridization. To gain some insight on this issue, we will start by designing the ESS with the assumption that the power allocation between the sources is performed with a frequency-based strategy, i.e., employ the SCs to handle the high-frequency power peaks, while the batteries provide the low-frequency demands. Despite being simple and numerically efficient, the frequency-based sizing only provides rough estimates. This factor prompted us to develop a second methodology, relying purely on an optimization framework (both for sizing and energy management), which, as will be shown in the latter part of the chapter, outperforms the frequency-based approach.

The remainder of this chapter is organized as follows: Section 8.2 introduces the mathematical model of the energy sources and the losses model in the powertrain's components, and also defines the power and energy requirements for the sizing problem. The filter-based sizing is given in Section 8.3, which is then followed in Section 8.4 by the optimal-based sizing. These two approaches are then applied in Section 8.5 to size the hybrid ESS of a small EV, while the final conclusions are presented in Section 8.6.

8.2 ESS Model and Requirements

8.2.1 Simplified Model for the Cells

As depicted in Figure 8.1, this work considers that each energy source in the EV is composed by a string of identical n_j cells, $j \in \{bat, sc\}$. For each cell, a simplified voltage-resistor model is employed [56]:

$$\frac{dQ_j(t)}{dt} = -i_j(t), \qquad q_j(t) = \frac{Q_j(t)}{\overline{Q}_j} \tag{8.1a}$$

$$\tilde{v}_j(q_j(t)) = a_j + b_j q_j(t) \tag{8.1b}$$

$$v_j(t) = \tilde{v}_j(t) - R_j i_j(t) \tag{8.1c}$$

where Q_j represents the cell's charge, $\overline{Q}_j$ the maximal charge, and q_j the state of charge (SOC). The internal voltage $\tilde{v}_j$ is considered as an affine map, with the SOC as input, offset a_j, and gain b_j; the cell's output voltage v_j is obtained by subtracting the voltage drop in R_j (the equivalent internal resistance of the cell). The power delivered by the hybrid ESS can be expressed as

$$P_{in}(t) = P_{bat}(t) + P_{sc}(t) = \sum_{j \in \{bat, sc\}} n_j \tilde{v}_j(t) i_j(t), \tag{8.2}$$

Integrating this relation we can determine the energy consumption of the vehicle ($E_{in} = \int_0^T P_{in}(t)dt$). Although more precise models for the SCs [308] and batteries [309] are available, the simplified representation considered in this work is a sufficient means to analyse the main energy phenomena, enabling us to gain some insight regarding the optimum sizing and energy management, without introducing unnecessary complexity into the mathematical structure of the problem. In fact, this approach is widely used in the literature related to the energy management of hybrid sources [304, 306, 307, 310].

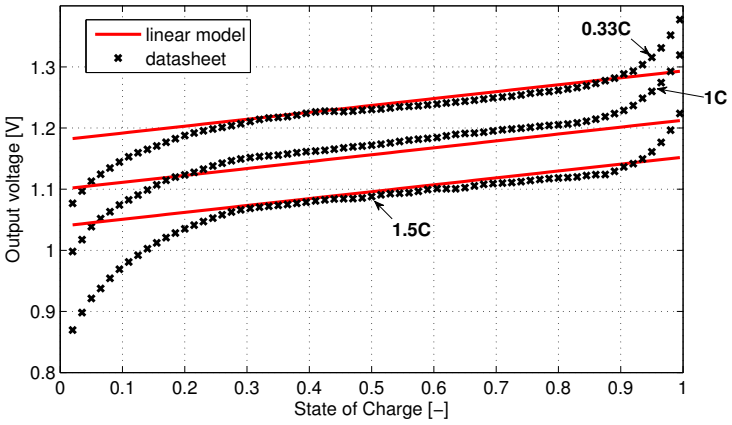

Figure 8.2: Discharge curves of the battery cell with nominal temperature and different rates.

Extraction of the Cell's Parameters

The battery and SCs under consideration here were selected having in mind the hybridization of the energy source of the uCar EV (see Appendix A). The selection process of the cells was constrained by a reduced budget and a very limited set of supplier options. These constraints ended up confining our choice to NiMH batteries, based on the cells of the module NHE 10-100 [311](nominal voltage of 1.2V, 100Ah), and the SCs BCAP1500 [312] (1500F@2.7V).

The identification of the battery parameters $\hat{\theta}_{bat} = \begin{bmatrix} a_{bat} & b_{bat} & R_{bat} \end{bmatrix}$ was carried out with the help of a weighted least squares method, which seeks to approximate the cell's discharge curve with the linear model (8.1). This fitting problem can be defined as:

$$\min_{\hat{\theta}_{bat}} \sum_{k=1}^{N_I} \varrho_k \left(v_{bat}(t_k) - \begin{bmatrix} 1 & q_{bat}(t_k) & -i_{bat}(t_k) \end{bmatrix} \hat{\theta}_{bat} \right)^2 \tag{8.3}$$

where $v_{bat}(t_k)$, $q_{bat}(t_k)$ and $i_{bat}(t_k)$ are the battery voltage, SOC and current measures acquired during the discharge test of the cell, and N_I is the number of samples. The weight ϱ_k was included in the fitting problem in order to decrease the contribution of the samples where the nonlinearity effects are more pronounced, i.e., when q_{bat} reaches the operation extremes. Given that the battery under consideration presents an almost linear behaviour for $q_{bat} \in [0.2, 0.8]$ (see Figure 8.2), the weight ϱ_k was selected as:

$$\varrho_k = \begin{cases} 1, & \text{if } 0.2 \leq q_{bat}(t_k) \leq 0.8 \\ 0, & \text{otherwise} \end{cases} \tag{8.4}$$

As illustrated in Figure 8.2, the identified model obtained with (8.3) renders a very reasonable approximation for the linear region of the discharge curve, showing a maximum fitting error of only 0.02V for $q_{bat} \in [0.2, 0.9]$. Notice that, in order to prevent the early degradation of the cells, it is a common practice to avoid the battery use when q_{bat} is too low/high; so, this means that, the linear range mentioned above ends up representing the bulk of the cell's working range.

Regarding parameters of the SCs, $\hat{\theta}_{sc} = \begin{bmatrix} a_{sc} & b_{sc} & R_{sc} \end{bmatrix}$, we recall the fundamental relation between the SCs internal voltage, capacitance (C) and charge:

$$\tilde{v}_{sc}(t) = \frac{1}{C} Q_{sc}(t) = \frac{\overline{Q}_{sc}}{C} q_{sc}(t) = \overline{v}_{sc} q_{sc}(t) \tag{8.5}$$

where $\overline{v}_{sc}$ is the SC voltage when fully charged. Equating the previous relation with (8.1b), we have $a_{sc} = 0$, $b_{sc} = \overline{v}_{sc}$; since the nominal SC voltage $\overline{v}_{sc}$ and internal resistance R_{sc} are generally given in the datasheet, the parameters $\hat{\theta}_{sc}$ can be straightforwardly determined using the information provided by the SC's manufacturer. The values of $\hat{\theta}_{bat}$, $\hat{\theta}_{sc}$, together with the cost (c_j) and mass (m_j) per cell are defined in Appendix 8.7.

8.2.2 Nominal Driving Cycling, Power and Energy Demand

In terms of vehicle performance specification, the hybrid ESS should be designed in order to satisfy the power and energy demands of a given nominal driving cycle, with speed profile $V(t)$, road angle $\alpha(t)$, $t \in [0, T_{dc}]$, and duration T_{dc}. There are two main approaches to characterize the driving cycle's variables. The first approach follows a stochastic setting and considers that the variables $V(t), \alpha(t), T_{dc}$ have a non-negligible degree of uncertainty, which can be characterized by probabilistic models, such as the Markov chains [313, 314]. This approach is particularly useful for general-purpose vehicles, where the exact mission profile is not known in advance and is affected by difficult-to-model factors, such as road type, traffic conditions, etc. On the other hand, the second approach regards the driving cycle's variables $V(t), \alpha(t), T_{dc}$ as deterministic, i.e., without uncertainty, and is suitable for vehicles in which the mission has a well-defined pattern. Collection trucks [315], buses [307], mail delivery, and similar vehicles, represent a class of vehicles in which the deterministic approach is acceptable. In this work, we will assume that the uCar vehicle operates with a well-defined driving cycle, and the hybrid ESS will be sized within a deterministic setting. It is also worth pointing out that the typical performance metrics employed at the vehicle design stage, such as top speed, minimum acceleration times, maximum gradability, and vehicle range, can be easily incorporated in the $V(t)$ and $\alpha(t)$ profiles.

Using the nominal driving cycle information, together with the application of Newton's law, the power requested to the hybrid ESS can be defined as (see [9] for additional details):

$$P_{out}(t) = \underbrace{V(t)\left(\frac{1}{2}\rho_a C_d A_f V(t)^2\right)}_{P_a(t)} + M \underbrace{\left(g f_r \cos(\alpha(t)) + g \sin(\alpha(t)) + \frac{dV(t)}{dt}\right) V(t)}_{\Delta_P(t)}$$

where M is the vehicle total mass, g the acceleration due to gravity, P_a is the power due to aerodynamic drag, and $M\Delta_P$ the power due to inertial, grading and rolling resistance forces (The definition and value of the remaining parameters are presented in Appendix 8.7).

Since M is also affected by the ESS mass, i.e., $M = m + n_{bat} m_{bat} + n_{sc} m_{sc}$, where m is the vehicle mass without the ESS, P_{out} can be further decomposed into two components:

$$\begin{aligned} P_{out}(t) &= \underbrace{P_a(t) + \Delta_P(t) m}_{P_0(t)} + \Delta_P(t)\left(n_{bat} m_{bat} + n_{sc} m_{sc}\right) \\ &= P_0(t) + \Delta_P(t)\left(n_{bat} m_{bat} + n_{sc} m_{sc}\right) \end{aligned} \tag{8.6}$$

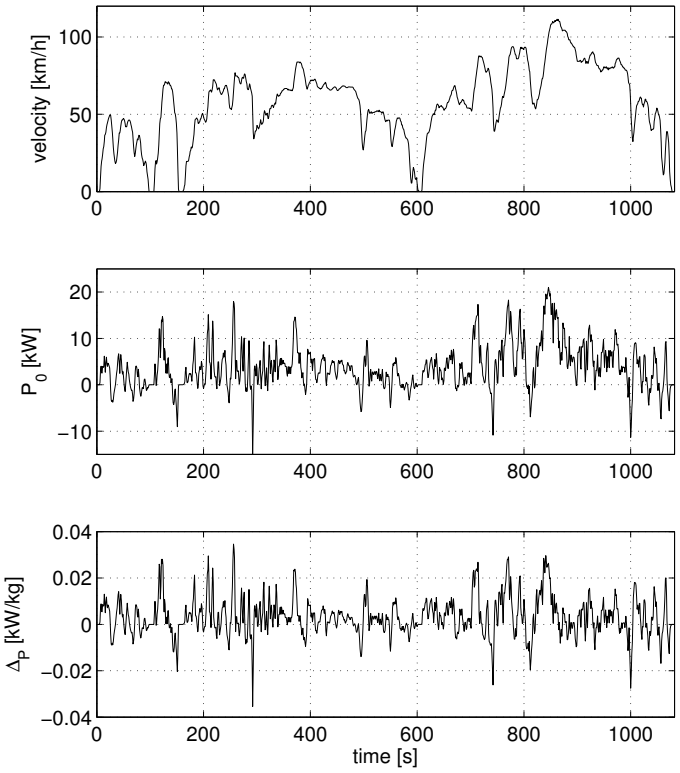

Figure 8.3: Velocity and power request associated with the ARTEMIS road cycle (considering $\alpha(t) = 0$), which is regarded as the nominal driving cycle throughout this chapter.

where $P_0(t)$ [W] is the nominal power, and $\Delta_P(t)$ [W/kg] the power increase due to the ESS mass. This power decomposition is illustrated in Figure 8.3 for the ARTEMIS road cycle, which is regarded as the nominal driving cycle throughout this chapter.

The energy requested to the ESS can be obtained by direct integration of $P_{out}(t)$:

$$\begin{aligned} E_{out}(t) &= \underbrace{\int_0^t P_0(s)ds}_{E_0(t)} + (n_{bat}m_{bat} + n_{sc}m_{sc}) \underbrace{\int_0^t \Delta_P(s)ds}_{\Delta_E(t)} \\ &= E_0(t) + \Delta_E(t)\,(n_{bat}m_{bat} + n_{sc}m_{sc}) \end{aligned} \tag{8.7}$$

where E_0 [Ws] is the nominal energy, and Δ_E [Ws/kg] the energy increase due to the ESS mass. Although one may question the need to contemplate the influence of the ESS mass in the power/energy required by the driving cycle, it is important to have in mind that this parameter is unknown at the start of the sizing phase. Furthermore, for light EVs, which is the type of vehicle under consideration here, the ESS represents an important portion of the global vehicle's mass, and, as will be shown later on, has a non-negligible impact on the energy consumption of the EV.

8.2.3 Power Losses

The power delivered by the hybrid ESS must take into account not only the power required by the driving cycle (P_{out}), but also the power losses in the powertrain components, such as the transmission ($P_{l,TR}$), electric motor ($P_{l,EM}$), DC/DC converters ($P_{l,DCDC}$), and

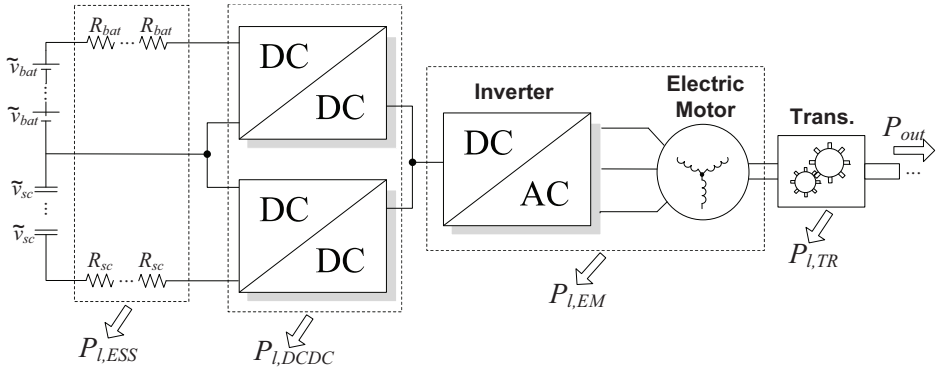

Figure 8.4: Summary of the energy losses in the ESS and powertrain components.

ESS ($P_{l,ESS}$). As a result, the following power balance constraint must be respected:

$$P_{in} = P_{out} + P_l, \quad P_l = P_{l,ESS} + P_{l,DCDC} + P_{l,EM} + P_{l,TR} \tag{8.8}$$

This section presents a brief review of practical losses model for the powertrain components, targeting its final incorporation in the sizing problem.

Under the assumption that the ESS response can be approximated by the voltage-resistor model presented in (8.1), the energy losses in this component are given by:

$$P_{l,ESS}(t) \;=\; n_{bat}R_{bat}i_{bat}(t)^2 + n_{sc}R_{sc}i_{sc}(t)^2 \tag{8.9}$$

Both batteries and SCs are connected to the DC bus via two bidirectional boost converters (see Figure 8.1), with identical characteristics. According to [316, 317, 318], the energy losses in the DC/DC converters are due to: *i*) conduction losses in the semiconductors; *ii*) switching losses; and *iii*) losses in the passive elements (inductor and capacitor). These three types of losses can be compactly expressed as:

$$\begin{aligned} P_{l,DCDC}(t) \;&=\; \sum_{j\in\{bat,sc\}} C_0 + \left(C_1 + C_2\tilde{d}(v_j(t), i_j(t))\right)|i_j(t)| + \left(C_3 + C_4\tilde{d}(v_j(t), i_j(t))\right) i_j(t)^2 \\ \tilde{d}(v_j, i_j) \;&=\; \begin{cases} 1 - \frac{v_j}{v_{out}}, & \text{if } i_j \geq 0 \\ \frac{v_j}{v_{out}}, & \text{otherwise} \end{cases} \end{aligned} \tag{8.10}$$

where v_{out} is the converter output voltage, C_m, $m = 0, \ldots, 4$, the parameters of the loss model, which are dependent on the converter's components, e.g., equivalent series resistance of the inductor, IGBT and diode, energy dissipated in the turn on and off of the semiconductors, etc. For a detailed account of the model derivation and its physical interpretation, the interested reader is referred to the literature [316]. Figure 8.5 shows the power losses of the DC/DC converter under consideration for the uCar vehicle, which is based on the SKM 600GB066D power semiconductor and an inductor with approximately 25mOhm of equivalent series resistance. From these results, it is interesting to point out that, while the efficiency of the converter is dependent on the input voltage, the absolute value of the power losses appears to be little affected by the input voltage. Furthermore, one can also verify that, for this particular converter, the power losses seem to be dominated by the quadratic term of (8.10). Motivated by these observations, and to facilitate the incorporation of the converter losses in the (optimal) sizing problem, the $P_{l,DCDC}(t)$

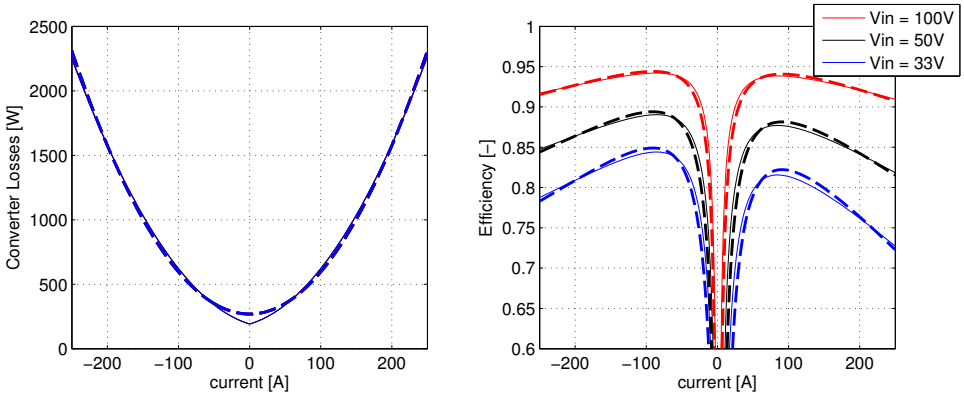

Figure 8.5: Power losses and efficiency of the DC/DC converter ($C_0 = 191.9, C_1 = 1.69, C_2 = -0.1, C_3 = 0.026, C_4 = 0.001, v_{out} = 200V$). The dashed line represents the quadratic approximation of the losses, obtained with (8.11).

will be approximated with the following quadratic model:

$$P_{l,DCDC}(t) \approx \sum_{j \in \{bat,sc\}} D_0 + D_1 i_j^2(t) \tag{8.11}$$

As can be seen in Figure 8.5 (dashed lines), the errors introduced by this approximation are negligible.

After increasing the source's voltage to the levels required by the DC bus, the next stage is to generate the torque/force necessary for the EV motion. As illustrated in Figure 8.4, this torque is produced through the electrical motor and its value adjusted by the DC/AC power converter (also known as the inverter). Although the energy losses of these components can be analytically determined (see, e.g., [319] and [320]), this study follows a more pragmatic approach, based on efficiency maps. Accordingly, we will fit the efficiency map of the motor+inverter, provided by the manufacturer or extracted from experimental tests, using the following approximation function:

$$P_{l,EM}(t) = \mathbf{M}^T \varphi(T(t), \omega(t)) \tag{8.12}$$

$$\varphi(T, \omega) = \begin{bmatrix} 1 & |\omega| & |T| & |T\omega| & T^2 & \omega^2 \end{bmatrix} \tag{8.13}$$

$$\omega(t) = \frac{G}{r} V(t), \quad T(t) = \frac{P_{out}(t) + P_{l,TR}(t)}{\omega(t)} \tag{8.14}$$

where T is the motor torque, ω the motor speed, G the reduction ratio between the motor and the wheel, r the wheel radius, and $\mathbf{M} \in \mathbb{R}^6$ the parameters of the loss model. Similar to the DC/DC converter, the majority of the parameters in $\mathbf{M}$ have physical meaning, e.g., M_5 is associated with the copper losses, M_2 can be related with hysteresis losses, and M_6 with Eddy current losses [319]. Figure 8.6 depicts the efficiency map and power losses for the motor+inverter considered for the vehicle, as well as the power losses resulting from the approximation (8.12). Despite the existence of some fitting errors, these are relatively low, and still acceptable for sizing purposes.

The final element in the vehicle powertrain is the transmission, which, from a practical perspective, can be modelled as a constant efficiency component [9]:

$$P_{l,TR}(t) \approx |P_{out}(t)|(1 - \eta_{TR}) \tag{8.15}$$

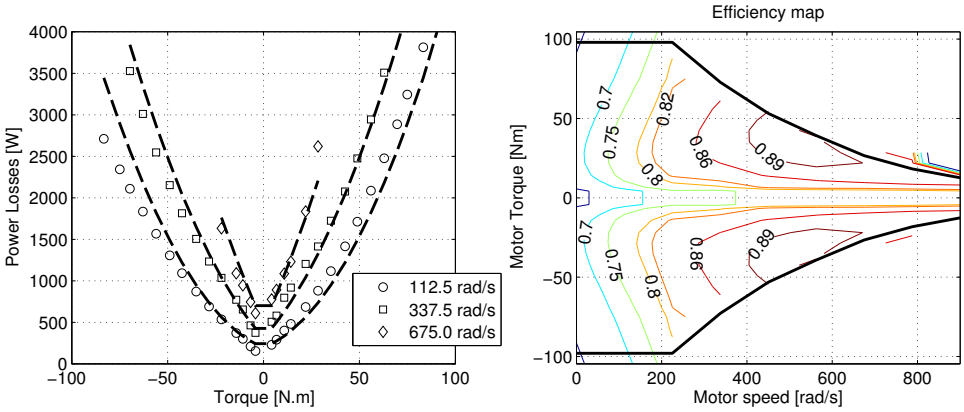

Figure 8.6: Power losses and efficiency of the electric motor + inverter, which is based on a 25kW PM motor retrieved from the QSS library [321]. The dashed line in the left plot represents the losses approximation obtained with (8.12).

where η_{TR} is the transmission efficiency.

8.3 Filter-based Sizing

After establishing the simplified source's models, the first methodology for the hybrid ESS sizing will now be described. As mentioned in Section 8.1, the sizing process is dependent on the energy management strategy employed to split the power among the sources. There are many possibilities to perform this division, ranging from optimal approaches [300, 322], machine learning [73] and simple heuristics, like the filter-based allocation [74, 323, 324]. In this section, the sizing of the hybrid ESS will be performed supposing that the power blending among the sources is based on low/high pass filters. The filter-based allocation policy is normally motivated by the complementary features presented by each source, i.e., SCs generally have high peak power capability and low energy, while batteries display opposite features (higher energy storage capability and moderate peak power). These intrinsic features cause the SCs to be regarded as an auxiliary source that should provide the power peaks during the acceleration/braking transients (which can be seen as the high-frequency content of P_{out}), while the batteries are responsible for ensuring the steady-state power delivery, associated with the low-frequency content of P_{out}. It is based on this line of reasoning that the frequency-based power allocation emerges as one of the most simple and appealing strategies for the real-time managing of hybrid ESS's [74, 323, 324], and which motivated us to use it in the first sizing approach. Based on this allocation policy, our goal here is to find the number of batteries (n_{bat}) and SCs (n_{sc}) that minimize the cells' acquisition costs, satisfying both the power and energy required by the nominal driving cycle.

8.3.1 Problem Formulation

As a starting point, consider the decomposition of the power requested to the hybrid ESS as a sum of low-frequency and high-frequency signals:

$$P_{out}(t) = \mathcal{L}_\tau\{P_{out}(t)\} + \mathcal{H}_\tau\{P_{out}(t)\} \tag{8.16}$$

where $\mathcal{L}_\tau, \mathcal{H}_\tau$ are first-order low-pass and high-pass operators, respectively, with time constant equal to τ [s], and defined as:

$$\mathcal{L}_\tau\big\{x(t)\big\} = \{y(t) \mid \quad \tau\dot{y}(t) + y(t) = x(t)\}, \quad \mathcal{H}_\tau\big\{x(t)\big\} = x(t) - \mathcal{L}_\tau\big\{x(t)\big\} \tag{8.17}$$

By exploring the linear property of these operators, and taking into account (8.6), the power decomposition can be further expanded as

$$\begin{aligned} \mathcal{L}_\tau\{P_{out}\} &= \mathcal{L}_\tau\left\{P_0(t)\right\} + \mathcal{L}_\tau\left\{\Delta_P(t)\right\}\left(n_{bat}m_{bat} + n_{sc}m_{sc}\right) \\ &= P_0^{\mathcal{L}}(t) + \Delta_P^{\mathcal{L}}(t)\left(n_{bat}m_{bat} + n_{sc}m_{sc}\right) \end{aligned}$$

where $P_0^{\mathcal{L}}$, and $\Delta_P^{\mathcal{L}}$ are the low-pass components of P_0 and Δ_P. Likewise, $\mathcal{H}_\tau\big\{P_{out}(t)\big\}$ can be represented using the "high-pass" components $P_0^{\mathcal{H}}$, and $\Delta_P^{\mathcal{H}}$, omitted here for the sake of brevity. Regarding the energy of the driving cycle, a similar decomposition can be established:

$$\begin{aligned} E_{out}(t) &= \int_0^t \left(P_0^{\mathcal{L}}(s) + \Delta_P^{\mathcal{L}}(s)\left(n_{bat}m_{bat} + n_{sc}m_{sc}\right)\right) ds + \\ &\quad \int_0^t \left(P_0^{\mathcal{H}}(s) + \Delta_P^{\mathcal{H}}(s)\left(n_{bat}m_{bat} + n_{sc}m_{sc}\right)\right) ds \\ &= E_0^{\mathcal{L}}(t) + E_0^{\mathcal{H}}(t) + \quad \left(\Delta_E^{\mathcal{L}}(t) + \Delta_E^{\mathcal{H}}(t)\right)\left(n_{bat}m_{bat} + n_{sc}m_{sc}\right) \end{aligned}$$

where $E_0^{\mathcal{L}}, E_0^{\mathcal{H}}, \Delta_E^{\mathcal{L}}, \Delta_E^{\mathcal{H}}$ are the low-pass and high-pass components of the driving cycle's energy (E_0) and energy increments (Δ_E).

Now, suppose that:

- the maximum energy provided by each cell, e_j [Ws/cell], as well as its peak power capability, p_j [W/cell], are known;
- the energy losses of the powertrain components, presented in Section 8.2.3, can be lumped together, and approximated as a single equivalent component with constant efficiency $\hat{\eta}_{PT}$.

Although it is difficult to determine the exact value of these metrics, which may even vary in time (e.g., the power capability of the SCs is strongly dependent on its SOC), our interest here is just to gain some insight about the fundamental issues and trade-offs related to the hybrid ESS sizing.

Spurred by the frequency-based power allocation, we will constrain the admissible number of batteries and SCs cells to the set:

$$\begin{aligned} \Omega(\tau) = \Bigg\{ (n_{bat}, n_{sc}) : \\ p_{bat}n_{bat}\hat{\eta}_{PT} &\geq P_0^{\mathcal{L}}[k] + \Delta_P^{\mathcal{L}}[k]\left(n_{bat}m_{bat} + n_{sc}m_{sc}\right) \\ p_{sc}n_{sc}\hat{\eta}_{PT} &\geq P_0^{\mathcal{H}}[k] + \Delta_P^{\mathcal{H}}[k]\left(n_{bat}m_{bat} + n_{sc}m_{sc}\right) \\ e_{bat}n_{bat}\hat{\eta}_{PT} &\geq E_0^{\mathcal{L}}[k] + \Delta_E^{\mathcal{L}}[k]\left(n_{bat}m_{bat} + n_{sc}m_{sc}\right) \\ e_{sc}n_{sc}\hat{\eta}_{PT} &\geq E_0^{\mathcal{H}}[k] + \Delta_E^{\mathcal{H}}[k]\left(n_{bat}m_{bat} + n_{sc}m_{sc}\right) \\ & \quad k = 0, \ldots, N, \quad 0 \leq n_{bat} \leq \overline{n}_{bat}, \quad 0 \leq n_{sc} \leq \overline{n}_{sc} \Bigg\} \end{aligned} \tag{8.18}$$

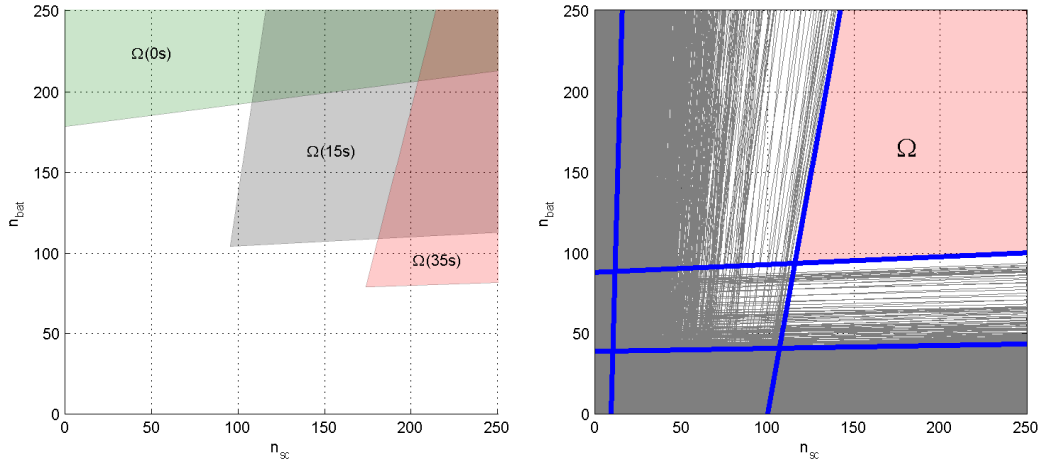

(a) (b)

Figure 8.7: a) Typical example of the domain $\Omega(\tau)$; b) inequality constraints employed in the construction of $\Omega(\tau)$ set during the ARTEMIS road driving cycle. (Grey lines represent the power and energy inequalities for all the points in the driving cycle; the dominant inequalities are shown in blue.)

where $\bullet[k] = \bullet(kT_s)$, T_s is the sampling time, N is the number of points employed in the driving cycle discretization, and $\overline{n}_{bat}, \overline{n}_{sc}$ is the maximum number of cells. Inspecting the formulation of this set, one can find that the first two linear inequalities specifies that the battery (SC) should provide the low (high) frequency content of the driving cycle, whereas the third and fourth inequalities are concerned with similar arguments, but applied to the energy requirements. The time constant τ employed in the frequency splitting also plays an important role in the construction of the $\Omega(\tau)$, and, to some extent, it can be seen as a parameter that controls the degree of hybridization in the ESS (see Figure 8.7(a)). In fact, it is interesting to note that, as limit cases, we have ESS's where only batteries ($\tau = 0$) or SCs ($\tau = \infty$) are employed. Furthermore, the power and energy constraints of Ω should be, in theory, evaluated for all the time instants of the driving cycle. However, from a practical point of view, it is expected that the set Ω will be dominated by the power and/or energy peaks required by the EV. Consequently, in order to quickly approximate Ω, we can replace $P_0^{\mathcal{L}}[k], \Delta_P^{\mathcal{L}}[k], P_0^{\mathcal{H}}[k], \Delta_P^{\mathcal{H}}[k], E_0^{\mathcal{L}}[k], \Delta_E^{\mathcal{L}}[k], E_0^{\mathcal{H}}[k], \Delta_E^{\mathcal{H}}[k]$ by their upper bounds (e.g., $\overline{P_0^{\mathcal{L}}} = \max_k P_0^{\mathcal{L}}[k]$), which enables us to reduce the number of inequalities to only four (4). In the majority of the times, we found that this simplification generally introduces negligible errors (see, e.g., the blue constraints in Figure 8.7(b)).

Based on this setting, it is our intention to find the triplet $(n_{bat}, n_{sc}, \tau) \in \Omega(\tau) \times [\underline{\tau}, \overline{\tau}]$ that minimizes the cells' cost, which can be posed as:

$$\begin{aligned} &\min_{n_{bat}, n_{sc}, \tau} \; c_{bat} n_{bat} + c_{sc} n_{sc} \\ &s.t. \qquad \boldsymbol{A}(\tau) \begin{bmatrix} n_{bat} \\ n_{sc} \end{bmatrix} \leq \boldsymbol{B}(\tau) \\ &\qquad\quad \underline{\tau} \leq \tau \leq \overline{\tau} \end{aligned} \tag{8.19}$$

where $\boldsymbol{A} \in \mathbb{R}^{p \times 2}$ and $\boldsymbol{B} \in \mathbb{R}^{p \times 1}$ represent the matrix notation of the p inequalities that can be extracted from (8.18). This problem depends on τ in a non-linear way, which may pose some challenges to the numerical solver. In order to attenuate this issue, we will

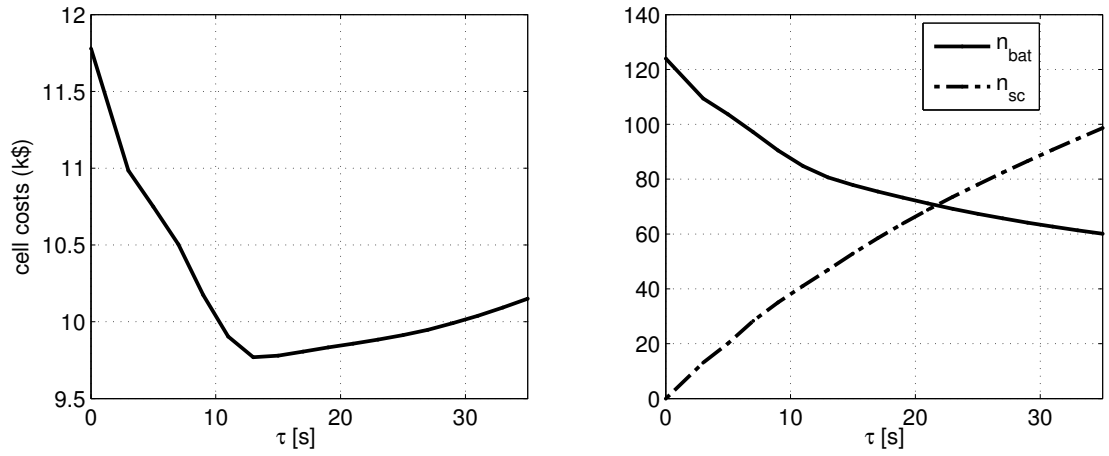

Figure 8.8: $J_A(\tau), n_{bat}(\tau), n_{sc}(\tau)$ when sizing the hybrid ESS to satisfy the ARTEMIS road cycle.

solve the optimization problem in a two-step process. Firstly, notice that, for a fixed τ, both the constraints and cost function are linear in (n_{bat}, n_{sc}); so (8.19), as long as τ is constant, can be treated as a linear programming problem. Based on this observation, we can straightforwardly evaluate (8.19) for a possible list of admissible time constants $[\tau_1, \ldots, \tau_M]$, generating a family of sizing results and cost function, parameterized in τ, i.e., $J_A(\tau), n_{bat}(\tau), n_{sc}(\tau)$. The optimal solution can then be readily extracted by selecting the $J_A(\tau)$ with minimum cost, which represents the second and last step in the solving process. In the numerical optimization literature, this approach is also known as the "optimizing over some variables" technique [112, Chap. 4].

8.3.2 Sizing Example and Discussion

With the purpose of preliminarily evaluating the filter-based sizing, we will now apply this methodology to build a battery-SC ESS capable of meeting the requirements of the ARTEMIS road cycle (the parametric details of the EV and energy sources are described in Appendix 8.7 and in Section 8.5). Figure 8.8 illustrates the intermediate results associated with the first step in the resolution of (8.19), i.e., $J_A(\tau), n_{bat}(\tau), n_{sc}(\tau)$. These results confirm that the parameter τ indirectly controls the degree of hybridization of the ESS: *i*) for $\tau \approx 0$, we have the case where only batteries are employed, showing a relatively high installation cost (11.8k$); *ii*) as we increase τ, it is apparent that the cost decreases, reaching a minimum at $\tau = 13$s (9.8k$); *iii*) ultimately, for $\tau > 13$s the SCs usage becomes more relevant, which again raises the costs. A second sizing example is shown in Figure 8.9, for the case where the driving cycle's range increases progressively up to 138km. Looking at the J_A evolution, it is worth noting that for EV ranges between 17 and 69kms, the degree of hybridization remains almost constant, having minimum cost for $\tau = 13$s. On the other hand, when the range requirements exceeds 69km, the SCs' use becomes less beneficial (from an installation cost point of view), and the degree of hybridization, as well as the number of SCs, is reduced. This behaviour suggests that there is a range threshold where the hybridization of battery-SCs provides the maximum gains (in this example, the threshold is 69 km).

In conclusion, the filter-based sizing presented in this section is a simple, numerically efficient tool, offering a rapid way to determine an order of magnitude estimate for (n_{bat}, n_{sc}). Further, by playing with the τ parameter, we can also gain valuable insight

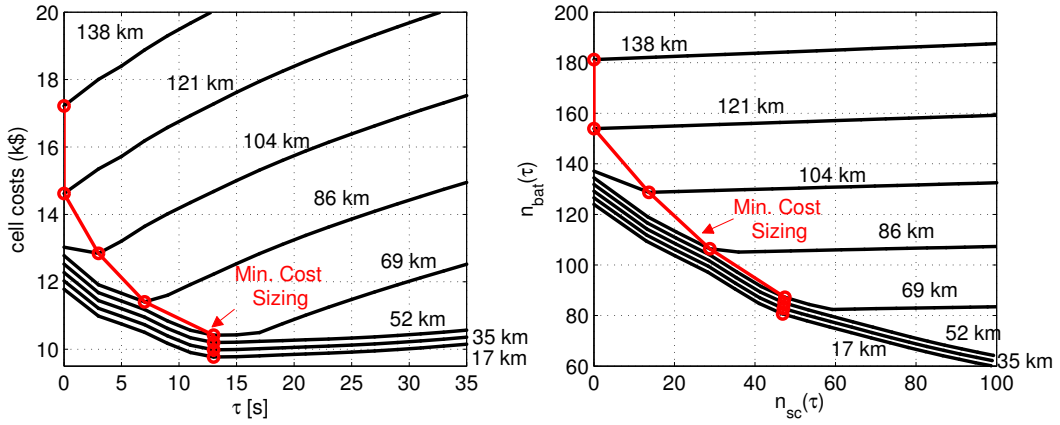

Figure 8.9: Evaluation of $J_A(\tau), n_{bat}(\tau), n_{sc}(\tau)$ for the ARTEMIS road driving cycle (repeated several times to increase the range requirements).

on the trade-offs associated with the SCs' inclusion in the hybrid ESS. However, due to some simplifications, this approach only provides a rough approximation of the ideal sizing. Perhaps the most notorious drawback is the assumption of constant peak power and energy per cell metrics (e_j and p_j). In practice, it is well known that these metrics are hardly constant and depend on the source's SOC and the load power being requested. Given that these factors were, so far, neglected, conservative estimates of e_j, p_j have to be applied, which, as we will see in a later section, generally limit the performance of the filter-based sizing.

8.4 Optimal Sizing

In order to overcome the limitations of the filter-based sizing, a second sizing methodology, based entirely on an optimization framework, will now be developed. As already discussed, the sizing process is intrinsically connected to the strategy employed in the energy management of the sources. From a theoretical standpoint, the energy management is, in its essence, an optimal control problem, i.e., the goal is to find a power division between the sources that minimize a given performance criterion (e.g., energy losses [322] or the battery stress [300]). Similarly, the sizing process also can be posed as an optimization problem, targeting, for example, the minimization of the source's installation costs. Consequently, since both the sizing and the energy management are naturally formulated within an optimization setting, it is natural to consider both tasks simultaneously. In other words, the main idea here is to combine the hybrid ESS sizing with the (optimal) energy management algorithm.

8.4.1 Problem Formulation

As a performance index, our goal is to minimize a weighted version of the total cost of ownership of the EV, including the cells' acquisition costs ($c_{bat}n_{bat} + c_{sc}n_{sc}$), as well as

the charging cost of the EV during its expected lifetime. This latter cost is defined as:

$$\begin{aligned} J_R &= \gamma \int_0^{T_{dc}} \left(P_{out}(t) + P_l(t)\right) dt \\ &\approx \gamma T_s \sum_{k=0}^{N-1} \left(P_{out}[k] + P_l[k]\right) \end{aligned} \tag{8.20}$$

with γ [\$/Ws] a constant parameter that translates the vehicle's energy consumption to an economic cost. One possible way to define γ is to consider

$$\gamma = \sum_{y=1}^{N_y} l_y \alpha_y \tag{8.21}$$

where N_y is the estimated lifetime of the hybrid ESS (in years), l_y is the number of journeys that the vehicle is expected to perform in the year $y \in [1, 2, \ldots, N_y]$, and α_y is the cost (\$/Ws) of the electricity in the year y. Naturally, l_y and N_y should be selected having in mind the limitation of charge/discharge cycles of the ESS.

The combined sizing/energy management problem is defined as

$$\begin{aligned} \min_{n_j, q_j, \tilde{v}_j, i_j, P_{out}, P_l, T} \quad & \left(w \sum_{j \in \{bat, sc\}} c_j n_j \right) + \gamma T_s \sum_{k=0}^{N-1} \left(P_{out}[k] + P_l[k]\right) \\ s.t. \quad & q_j[k+1] = q_j[k] - i_j[k] \frac{T_s}{\overline{Q_j}}, \quad q_j[0] = q_{j,0} \\ & \tilde{v}_j[k] = a_j + b_j q_j[k] \\ & \sum_{j \in \{bat, sc\}} n_j \tilde{v}_j[k] i_j[k] = P_{out}[k] + P_l[k] \\ & P_0[k] + \Delta_P[k] \sum_{j \in \{bat, sc\}} n_j m_j = P_{out}[k] \\ & \mathbf{M}^T \varphi(T[k], \omega[k]) + |P_{out}[k]|(1 - \eta_{TR}) + \\ & \qquad \sum_{j \in \{bat, sc\}} D_0 + (D_1 + n_j R_j) \left(i_j[k]\right)^2 = P_l[k] \\ & T[k] = \frac{P_{out}[k] + |P_{out}[k]|(1 - \eta_{TR})}{\omega[k]} \\ & \underline{q_j} \leq q_j[k] \leq \overline{q_j}, \quad 0 \leq n_j \leq \overline{n}_j \\ & \underline{i_j} \leq i_j[k] \leq \overline{i_j}, \quad \frac{1}{N+1} \sum_{k=0}^{N} i_j[k]^2 \leq \chi_j^2 \overline{I}_{rms,j}^2 \\ & k \in \{0, \ldots N\}, \quad j \in \{bat, sc\} \end{aligned} \tag{8.22}$$

where $q_{j,0}$ is the initial SOC, $\underline{q_j}/\overline{q_j}$ the minimum/maximum allowable SOC, $\underline{i_j}/\overline{i_j}$ the minimum/maximum peak currents of each source, and $\overline{I}_{rms,j}$ the maximum RMS current. Examining the problem constraints, one can readily verify that the first two are the result of the discretization (with the Euler method) of the battery/SC cells' model, defined in (8.1), whereas the third, fourth and fifth impose the balance between the power delivered by

the ESS, the powertrain losses, and the vehicle load. The sixth establishes the operating point of the electric motor, which is important to calculate its losses, while the last set of constraints are related to the SOC and current limits. The problem also contains a parameter $\chi_j \in [0, 1]$ that can be explored by the designer to reduce the RMS current in the cells; this is particularly useful to limit the stress in the battery pack. As for the cost function, it is worth highlighting the presence of the trade-off factor $w \in [0, 1]$, which enables the designer to pursue different goals, for example:

- $w = 1$, aims to minimize the total cost of the vehicle (cells' + running costs);
- $w = 0$, focuses only on the minimization of the vehicle's running costs ($=\gamma E_{in}$), which are directly related to the vehicle's energy consumption (E_{in});
- $w \in (0, 1)$ constitutes a trade-off between the cells' cost and the energy consumption of the EV.

To a certain extent, it is expected that the two goals in consideration, cells' cost and energy efficiency, will be conflicting with each other. For example, if the aim is to build an EV with low energy consumption ($w = 0$), then it is predictable that the number of SCs (the most energy efficient and lighter source) will be higher, which may lead to a significant increase in the cells' cost. Conversely, if the total cost of the hybrid ESS is the main concern ($w = 1$), it is expected that the number of batteries and SCs will be reduced, which, in principle, will increase the energy losses, particularly Joule losses. In this context, it is the designer's responsibility to decide, through the parameter w, an appropriate trade-off between cost and energy efficiency that best suits the requirements for the hybrid ESS.

Remark 8.1. Fixing, à priori, the number of cells n_{bat}, n_{sc} in (8.22), produces the typical "benchmark" problem for the optimal power allocation between multiple sources.

8.4.2 Solving Methodology

To handle the optimization problem (8.22) we start by translating it to the AMPL (A Mathematical Programming Language) language [325], an environment dedicated to modelling large-scale optimization problems. The main advantages in using this environment are: *i*) the formulation is carried out in an almost natural language, making it very easy to specify and modify the decision variables, constraints and all the other elements in the problem; *ii*) it allows the user to interface with different types of numerical solvers (linear, nonlinear, open-source, commercial, etc.); *iii*) it automatically generates the gradients information for the problem, based on automatic differentiation strategies[326], which is critical for the convergence of the numerical optimization methods. After the problem's translation we employed the IPOPT solver, and open-source nonlinear programming solver, to numerically extract the solution for the problem (see [327] for a detailed account of the inner details of the algorithm). It is also noteworthy that the IPOPT, together with the AMPL, can be used free of charge through the NEOS server[328].

Besides the numerical solver and the gradient information, the initial guess for the decision variables represent another key aspect of the algorithm performance. In order to cope with this challenge, we start by determining an initial estimative for the number of cells $(\hat{n}_{bat}, \hat{n}_{sc})$, using the output of the filter-based sizing, discussed in the previous section. The value of the remaining decision variables are then estimated by solving the "benchmark" power allocation, mentioned in Remark 8.1, i.e. (8.22) is relaxed by fixing

the number of cells ($\hat{n}_{bat}, \hat{n}_{sc}$). As will be shown later in the chapter, we found this initialization procedure to be very effective, and able to successfully handle longer driving cycles ($N > 8000$).

At this stage, it is worth discussing some of the shortcomings of the optimization-based sizing adopted in this chapter. First, notice that, while the cost function and the majority of the constraints are linear, the power balance constraints have equalities involving the product of decision variables (e.g., $n_j \tilde{v}_j[k] i_j[k]$), as well as quadratic terms in the current, which makes the problem non-convex (recall that a convex problem only accepts affine equalities [112]). Thus, the resulting optimization problem is nonlinear and non-convex, which poses some numerical challenges to obtain global optimal solutions. Nevertheless, we will show in the next section that these (locally optimal) solutions still perform better than the ones obtained with the simplified filter-based sizing.

Secondly, the sizing process is performed under the assumption of an ideal energy management, with advance access to the driving cycle profile. Since this information will hardly be available during the real-time operation, the sizing solutions may be slightly optimistic. In any case, the optimal sizing is still of practical interest, as it allows us to obtain a benchmark solution, establishing the maximum gains that can be achieved with the ESS hybridization.

In third place, the problem formulation also assumes that the numbers of cells, n_{bat}, n_{sc}, are real numbers, while in practice it must belong to an integer range. This approximation brings important advantages to the numerical solution of the problem, since it allows us to avoid the use of more complicated mixed-integer nonlinear programming solvers. In addition, as the hybrid ESS is normally composed of a large number of batteries and SCs, it is expected that the rounding errors in n_{bat}, n_{sc} will have a minor impact in the final solution [307].

8.5 Case Study Example

The two sizing methodologies described above will be applied in this section to design the hybrid ESS of a future version of the uCar vehicle (see Appendix 8.7 for the parametric details). The ARTEMIS road cycle [329] will be used as the basic speed profile that the EV should meet, which means a top speed of 111 km/h, maximum accelerations up to 8.5 km/h/s^2 and a minimum range of 17.23km, as illustrated in Figure 8.3. In order to investigate different demands in terms of the EV autonomy, the ARTEMIS road cycle was repeated several times (up to 8). For comparison purposes, we also evaluated the case where the battery is used as the single source of the EV (i.e., fixing $n_{sc} = 0$ in (8.22)), which is named as the "battery only" solution hereafter.

8.5.1 Minimization of Vehicle's Total Costs

Filter-based Sizing vs Optimal Sizing

Figure 8.10 and 8.11 depict the sizing results for the situations with: *i*) battery only; *ii*) filter-based sizing; and *iii*) optimal sizing, targeting the minimization of the vehicle's total cost ($w = 1.0$). Broadly speaking, the filter-based solution displays a similar trend to that of the optimal sizing, i.e., as the range increases, the number of SCs is reduced and the batteries increase. However, due to the conservative estimates of e_j, p_j, discussed in Section 8.3.2, the filter-based solution normally requires a greater number of cells and installation cost. Regarding the energy losses depicted in Figure 8.11(b), it is interesting

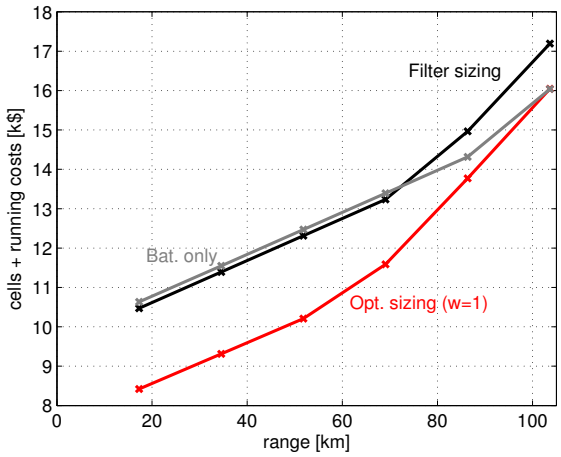

Figure 8.10: Combined costs (cells + energy charge of the EV) for different ESS's: *i*) battery only, *ii*) hybrid ESS, sized with the filter; *iii*) hybrid ESS, sized with the optimal approach ($w = 1$). The ARTEMIS road was used as the nominal driving cycle.

to note that, in comparison with the "battery only" solution, the hybrid ESS, sized with the optimal approach, shows a slight increase in the powertrain losses (E_l). At first glance, one might expect that the "battery only" solution would be a less efficient storage system, given that no auxiliary aid is provided by the SCs. Nonetheless, the fact remains that, as this ESS configuration entails a larger number of battery cells ($105 - 120$, depending on the range), the Joule losses tend to be reduced. This larger number of battery cells also raises the input voltage of the DC/DC converter, which contributes to higher operation efficiency for this component (see Figure 8.5). Notice that, at this stage, our goal is centred on the minimization of the cells and running costs of the EV ($w = 1.0$), and not on the vehicle's energy efficiency (which will be discussed later on).

Finally, these results also reveal that the filter-based sizing is the solution with minimum energy consumption and losses (as a result of being oversized).

Detailed Analysis of the Optimal Sizing ($w = 1.0$)

Since the optimal sizing provides the better overall performance (see Figure 8.10), we will now discuss in more detail the results obtained with this method. Referring again to Figure 8.11(a), it can be verified that, if the desired range per charge of the EV is below 50 km, the inclusion of the SC in the ESS (sized with the optimal approach) contributes to a significant downsize of the battery pack (from ˜105 cells to only ˜63 cells). This downsize has positive and negative consequences. On the plus side, we can see that the cost of the cells is significantly reduced: using a single battery pack to meet the 50km range needs an investment of ˜10.3k$, while the hybrid ESS only requires ˜8.0k$; this represents a 22.2% reduction in the cells' costs. Another advantage of the battery downsize is the decrease of the ESS storage mass (see Figure 8.11(c)), which then contributes to a reduction of 3% in the energy required by the driving cycle (E_{in}), as illustrated in Figure 8.11(b). The main inconvenience associated with the battery downsize is the increase of the energy losses E_l, the causes of which were already discussed. Nonetheless, these higher energy losses are compensated by the energy savings resulting from the lighter ESS, and, in the end, the overall energy consumption of the vehicle E_{in} is little affected; as shown in Figure 8.11(b),

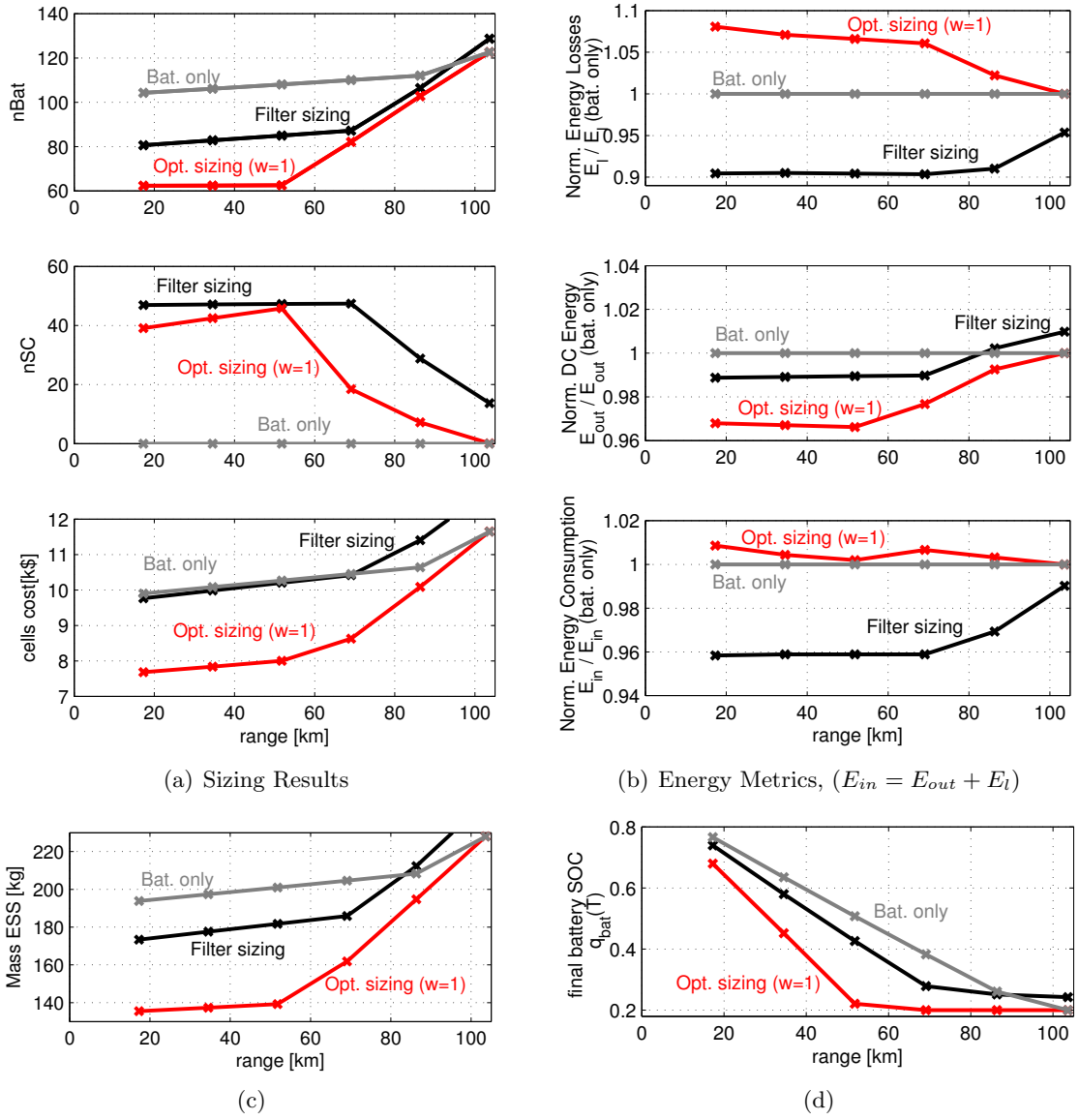

(a) Sizing Results

(b) Energy Metrics, ($E_{in} = E_{out} + E_l$)

(c)

(d)

Figure 8.11: Performance comparison between different ESS: *i*) battery only, *ii*) hybrid ESS, sized with the filter; *iii*) hybrid ESS, sized with the optimal approach ($w = 1.0$). The ARTEMIS road was used as the nominal driving cycle.

for the hybrid ESS sized with the optimal approach, E_{in} exhibits a small increase of 0.2% to 0.9%.

On the other hand, when the EV range requirements increases above 50km, there is a decline in the number of SC cells, and the hybrid ESS sizing ends up converging to the situation where only batteries are employed. To explain this trend, it is helpful to look at the final SOC value of the battery ($q_{bat}(T_{dc})$), depicted in Figure 8.11(d). From these results it can be concluded that, for driving ranges inferior to 50km, the battery is not completely discharged at the end of the driving cycle, which suggests that the (peak) power constraint is the dominant factor in the ESS sizing. Thus, given the high power capability of the SCs, there is more freedom to reduce the battery power stress, which results in its downsize. However, as the EV autonomy increases above 50km, the energy

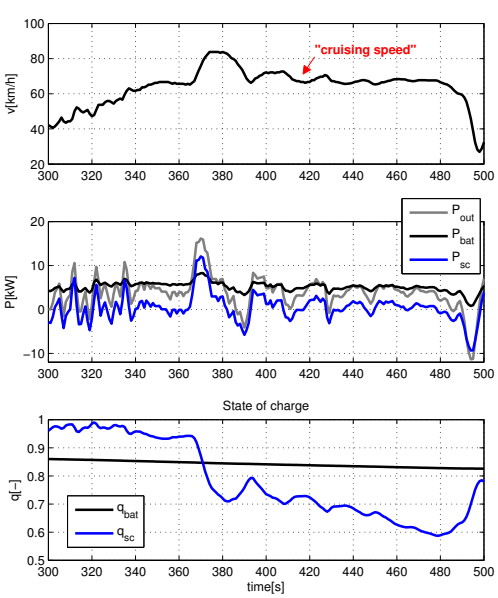

(a) "cruising speed"

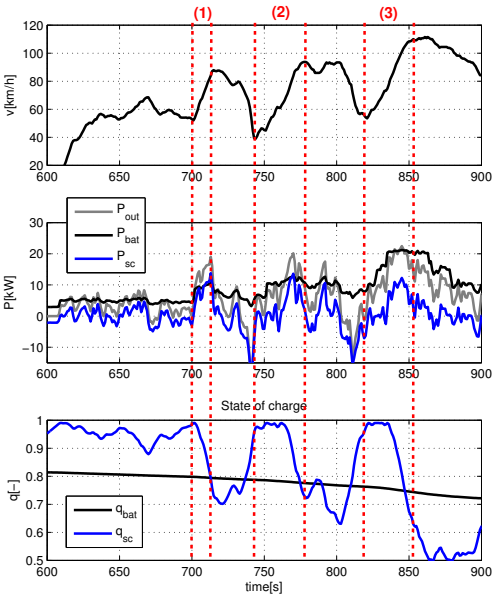

(b) strong acceleration periods

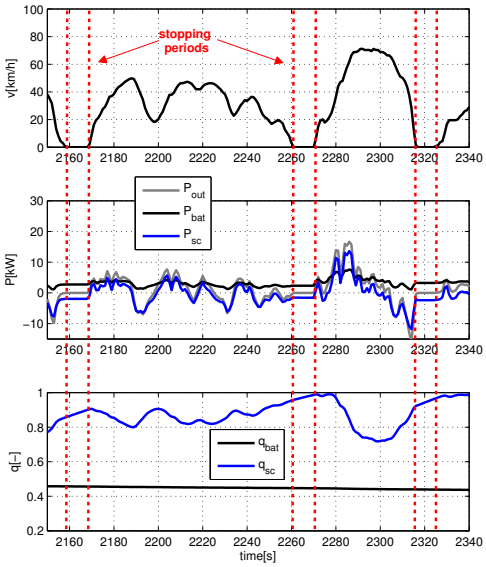

(c) stopping periods

Figure 8.12: Energy management results for the optimal approach ($w = 1.0$); the range requirement for this simulation was set at 52km, and the ARTEMIS road was used as the nominal driving cycle.

constraint becomes more relevant (notice that $q_{bat}(T_{dc})$ is close to the minimum limit), and the sizing is dominated by the energy demand. Since the SCs have very low energy densities, the benefit of this source, from an installation cost perspective, diminishes as the range demand increases. As a side note, it is worth mentioning that this trend was also predicted by the filter-based sizing, exemplified in Figure 8.9.

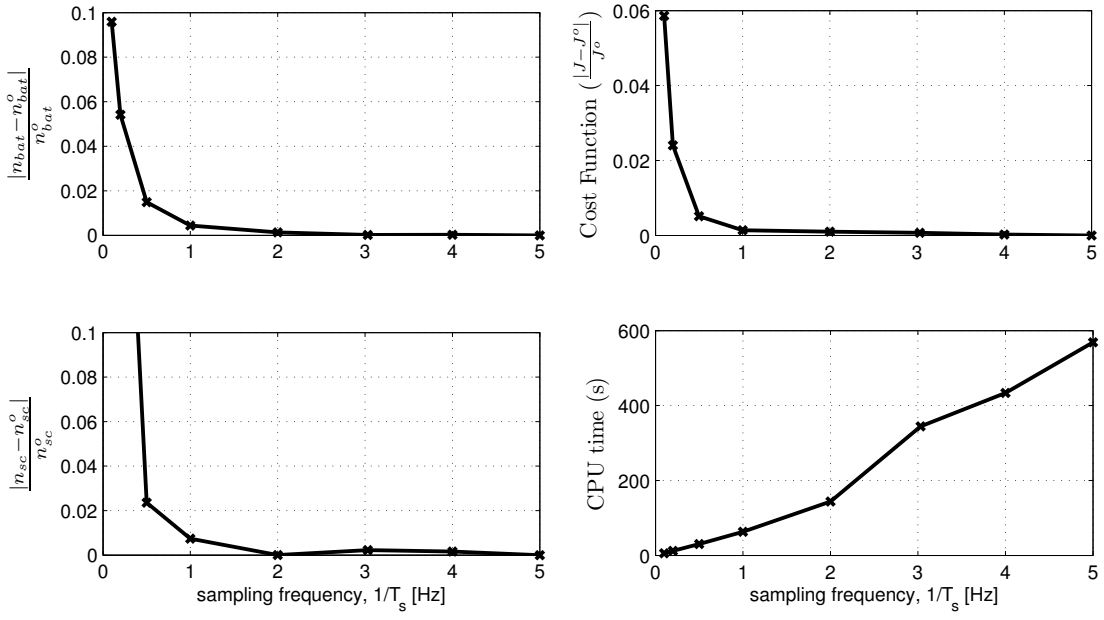

Figure 8.13: Influence of the sampling time employed in the optimization problem (8.22). The ARTEMIS road (50km) was used as the nominal driving cycle, with $w = 1$. The terms n^o_{bat}, n^o_{sc}, J^o refer to the best solution that was found among all the sampling times evaluated.

Energy Management with Nominal Driving Cycle

Besides the sizing task, the optimal approach also enables us to determine the ideal power split between the batteries and SCs. For example, Figure 8.12 illustrates the power sharing between the sources, obtained when using (8.22) to size the storage unit for a range of 50km ($n_{bat} = 63$, $n_{sc} = 46$). Analysing these results one can find that, when the vehicle is travelling at "cruising" speed, the battery should provide (roughly) the low frequency content of the driving cycle power, while the SCs should respond to the high frequencies [see Figure 8.12(a)]. This remark turns out to be very important for the development of causal allocation strategies: since the low/high frequency decomposition can be easily emulated through low/high pass filters, the use of power allocation based on filters has become one of the most popular methods for the real-time managing of hybrid ESS [74, 323, 324].

Inspecting Figure 8.12(b) reveals that, during acceleration and braking transients, the SC provides important assistance to the batteries. From a practical perspective, the main challenge in managing these transients is to decide when to deploy the limited charge of the SCs. For example, for transients with short duration, the SCs should be used as soon as the vehicle is accelerated (see, e.g., zone 1, highlighted in Figure 8.12(b)). On the other hand, for longer acceleration periods (see, e.g., zones 2 and 3 highlighted in Figure 8.12(b)) the SC deployment should be reserved to the later part of the transient, where its usage is more helpful to limit the peak power requested to the battery, as well as its losses. Predicting the duration of these acceleration transients, while easy for the non-causal setting proposed in (8.22), is extremely difficult for causal control systems, and remains one of the ultimate challenges in the real-time energy management of hybrid ESS. Finally, one can also find that it is advantageous to keep charging the SCs during the period of time when the vehicle is stationary [see Figure 8.12(c)].

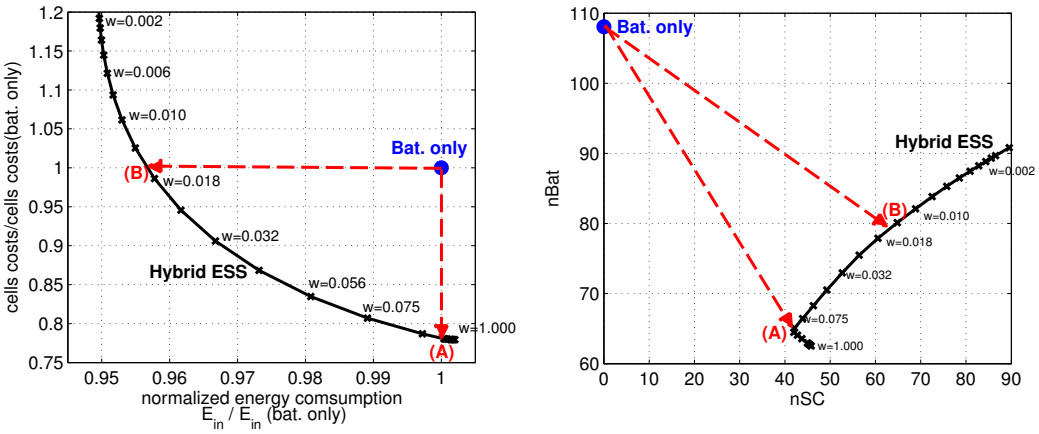

Figure 8.14: Trade-off between cells' cost and energy efficiency, when sizing the hybrid ESS with the optimal approach. The ARTEMIS road (50km) was used as the nominal driving cycle.

Influence of the Sampling Time

The sampling time (T_s) is an important parameter for solving (8.22) due to its influence in the solution accuracy and problem size (recall that the dimension of some of the decision variables is given by $N = T_{dc}/T_s$). To investigate the effect of this parameter in the solving process, we conducted a set of simulations with different $T_s \in [0.2, 10]$s, as illustrated in Figure 8.13. From these plots, it can be concluded that using sampling times lower than 1s does not significantly increase the accuracy of the solution; in fact, the computational time increases, without any apparent benefit. The use of T_s higher than 1s is not advisable either, as the solution accuracy degrades considerably, particularly in n_{sc}. These results suggests that $T_s = 1$s is a good compromise value between solution accuracy and CPU time, and, for this reason, was the sampling time adopted throughout this chapter.

8.5.2 Trade-off between Installation Cost and Energy Consumption

Up to now, the sizing of the hybrid ESS privileged the economic factor by targeting the minimization of the total costs of ownership of the EV. However, the optimal sizing formulation contains a tuning parameter (w) that allows the designer to explore trade-offs between cells' cost and energy efficiency. To illustrate how this trade-off can be realised in practice, Figure 8.14 shows the influence of w when sizing a hybrid ESS for a range of 50 km. Qualitatively, these plots show that, if we pretend to decrease the EV's energy consumption, then the number of cells (particularly the SCs), and the corresponding costs, must be raised, which are in accordance with our engineer intuition. Additionally, in comparison with the "battery only" solution, the trade-off curve of the hybrid ESS shows that:

- using the same investment in cells as the "battery only" solution, the hybrid ESS reduces the energy consumption by 4% (see point B in Figure 8.14);
- with the same energy consumption as the "battery only", the hybrid ESS can decrease the cells' costs by 22% (see point A in Figure 8.14);

In conclusion, these results demonstrate that with the optimal-based sizing, the designer has the option to select a trade-off point that best suits the system requirements and the available budget for the EV construction.

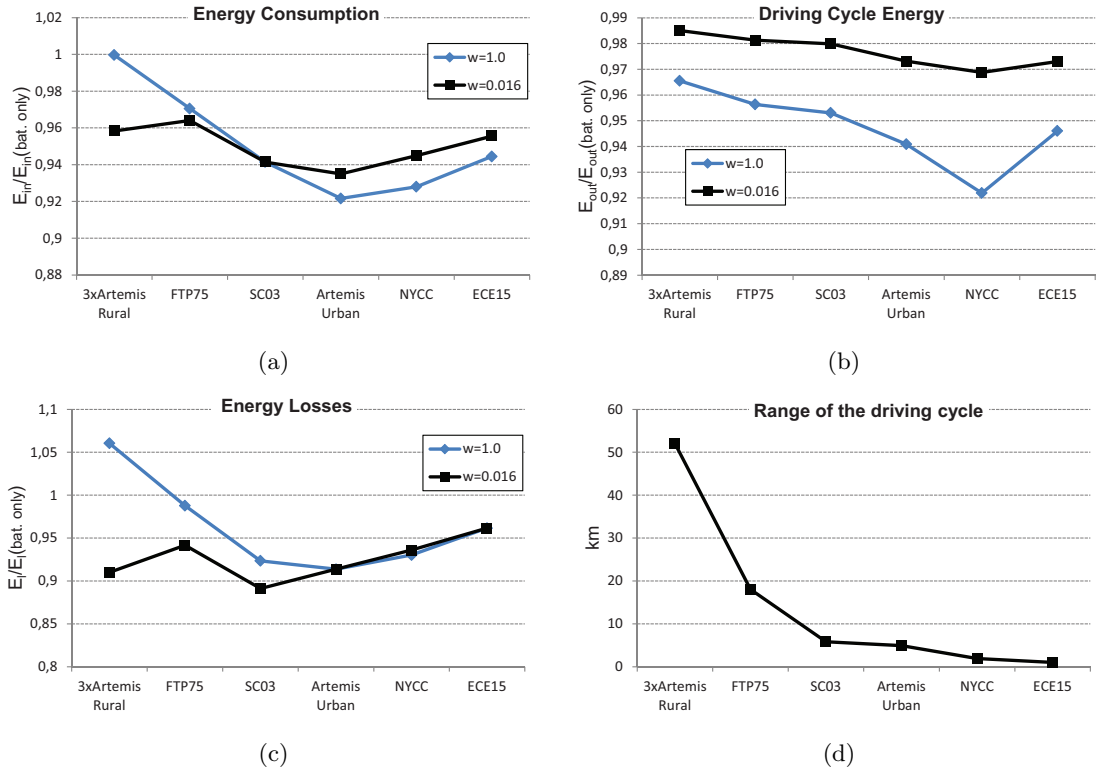

Figure 8.15: Normalized energy consumptions of the hybrid ESS, when subject to nominal (ARTEMIS Rural, 50km) and non-nominal driving cycles.

Energy Management with non-Nominal Driving Cycles

Although the sizing task was carried out under the assumption of a nominal driving cycle, it is also worth investigating how the resulting hybrid ESS performs when the driving conditions deviate from nominal ones. With this goal in mind, several numerical simulations were carried out for some typical driving cycles, such as the ECE15, ARTEMIS Urban, NYCC, FTP75, and SFTP S03 [329]. For each driving cycle, three types of ESS were considered: *i*) battery only ($n_{bat} = 109$, $n_{sc} = 0$); *ii*) hybrid ESS ($n_{bat} = 63$, $n_{sc} = 46$), targeting the minimization of the vehicle's costs, $w = 1.0$; and *ii*) hybrid ESS ($n_{bat} = 78$, $n_{sc} = 61$), targeting a trade-off between cost and energy efficiency, $w = 0.016$, which corresponds to point B in Figure 8.14. In all the cases, the ESS was sized using (8.22) for a range of 50km.

Figure 8.15 shows the overall results of the various configurations under study. It can be seen that, in all the non-nominal driving cycles, the inclusion of the SCs reduces the energy consumption (E_{in}) between 3% and 7.8%, being higher in the urban driving cycles (NYCC and ARTEMIS urban). To some extent these results were expected since, in urban scenarios, with short distances and where the start/stop patterns are frequent, it is reasonable to expect that the aid provided by the SC will be more beneficial to the energy consumption of the EV.

Another factor that deserves to be highlighted is the influence of the parameter w. It was already verified that, when sizing the hybrid ESS with minimum cost ($w = 1.0$), the energy savings in E_{in} throughout the nominal driving cycle are almost null. However, this property cannot be generalized to non-nominal driving cycles, as shown in Figure 8.15.

By the same token, the hybrid ESS sized with $w = 0.016$, although providing 4% energy savings in the nominal driving cycle, evidences higher energy consumptions (in comparison with $w = 1.0$) for the urban driving cycles. The reason for this apparent contradiction is related to the interplay that exists between energy losses (E_l), the driving cycle's energy (E_{out}) and the duration of the driving cycle, which is illustrated in Figure 8.15. In particular, the lighter hybrid ESS ($w = 1.0$) seems to pay off in urban scenarios (despite the higher energy losses), while the more energy-efficient[1] hybrid ESS ($w = 0.016$) is penalized by the heavier cells' mass; the opposite behaviour is verified when the cycle's range increases (see, e.g., the consumption for the FPT75 case).

8.6 Conclusion

In this chapter, two methodologies for sizing hybrid ESSs composed of batteries and SCs, were developed. The first, named filter-based sizing, employs a simple frequency power decomposition to manage the hybrid ESS, and assumes that the peak power and energy capabilities of each source are known. This approach is very helpful to understand the basic mechanisms and the trade-offs associated with battery-SCs hybridization, but, due to the approximations and simplifications, is only able to provide a rough estimate of the ideal sizing. In order to increase the accuracy of the sizing process, an optimization-based approach was then proposed. The main novelty of this latter methodology is the combination of the sizing task with the (optimal) energy management algorithm of the sources. For the particular parametric configuration under study, and assuming daily ranges inferior to 50km, it was concluded that, by adding SCs to the ESS, the overall costs (installation + charging) of the EV can be reduced by almost 20%. In addition, depending on the type of driving cycle, the hybrid ESS showed energy savings of up to 7.8%, representing an important contribution toward the increase of the vehicle's range. As future work, it is our intention to incorporate additional performance metrics in the sizing problem, such as the battery stress and degradation, and tackle the real-time energy management problem.

8.7 Appendix: ESS and Vehicle parameters

The parameters of the vehicle and energy sources are present in Table 8.1.

[1] in the sense that the energy losses are minimial

Table 8.1: Vehicle and powertrain parameters

Variable	**Value**
Vehicle mass [without sources] (m)	500 kg
Rolling resistor coefficient (f_r)	0.013
aerodynamic drag coefficient (C_d)	0.35
vehicle frontal area (A_f)	1.8 m^2
sample time T_s	1[s]
cost factor γ	0.11[$/Ws]
average cost of a cell, c_{bat}/c_{sc}	95/45 [$]
average mass of a cell, m_{bat}/m_{sc}	1.86/0.5 [kg]
resistance of a cell, R_{bat}/R_{sc}	1.2/0.47 [mOhm]
voltage offset, a_{bat}/a_{sc}	1.22/0 [V]
voltage gain, b_{bat}/b_{sc}	0.11/2.70 [V/-]
cell charge, $\overline{Q}_{bat}/\overline{Q}_{sc}$	360/4.0 [kAs]
cell min. SOC, $\underline{q}_{bat}/\underline{q}_{sc}$	0.2/0.5 [-]
cell max. SOC, $\overline{q}_{bat}/\overline{q}_{sc}$	0.90/0.99 [-]
initial SOC, $q_{bat,0}/\ q_{sc,0}$	0.90/0.99 [-]
maximum current, $\bar{i}_{bat}/\bar{i}_{sc}$	300/400 [A]
minimum current, $\underline{i}_{bat}/\underline{i}_{sc}$	-300/-400 [A]
max. RMS current, $\overline{I}_{rms,bat}/\overline{I}_{rms,sc}$	100/140 [Arms]
derrating factor, $\overline{\chi}_{bat}/\overline{\chi}_{sc}$	0.9/1 [-]
usable energy of a cell, e_{bat}/e_{sc}	81.5/1.1[Wh]
peak power of a cell, p_{bat}/p_{sc}	273/1080 [W]
DC/DC efficiency parameter, D_0	270[W]
DC/DC efficiency parameter, D_1	32[mOhm]
transmission efficiency, η_{TR}	0.98
Motor losses parameters, $\mathbf{M}^T$	$\left[144, 0.5, 0, 0.07, 0.36, 0\right]$

Chapter 9

Robust DC-Link Control in EVs with Multiple Energy Sources

Abstract: *Following the hybrid ESS topology introduced in the previous chapter, we will now investigate the design of the DC-Link controller in order to regulate the DC-bus voltage and track the SC current. For this purpose, we start by showing that the converters uncertainty, e.g., the powertrain load, can be modelled as a convex polytope. The DC-Link controller is then posed as a robust Linear-quadratic Regulator (LQR) problem and, by exploring the convex polytope, converted in a Linear Matrix Inequalities (LMI) framework, which can be efficiently solved by numerical means. Finally, the operation envelope of the controller is extended by scheduling the gains according to energy sources voltages, an important feature to cope with the voltage variations in the SCs. To analyse the performance of the control architecture, a reduced-scale prototype was built. The experimental results show that, compared with the non-robust and non-gain-scheduled controllers, the proposed DC-Link controller offers a better transient response and robustness to disturbances. Further, the global performance of the controller is also evaluated during some driving cycles.*

9.1 Introduction

After introducing in Chapter 8 the (off-line) Vehicle Energy Management (VEM) layer, as well as the sizing task for the storage unit, this section will address the design of the DC-Link controller. Recall that the DC-Link controller has the responsibility to manipulate the converters duty cycles so that the DC-bus voltage and the current (or power) of the auxiliary source, the SC, follow the setpoints requested by the VEM (see Figure 9.1). Assuming that the control of the DC-bus voltage and SC current are independent of each other, the control problem can be simplified by using linear control techniques. For example, [63] and [68] report a design where linear Proportional+Integral (PIs) are employed to build a DC-Link controller based on two parallel loops: *i*) a current loop to regulate the auxiliary current (SCs in our work), and *ii*) a voltage-current (cascade) loop to, through the main source, keep a constant output voltage. The main drawback of this approach is

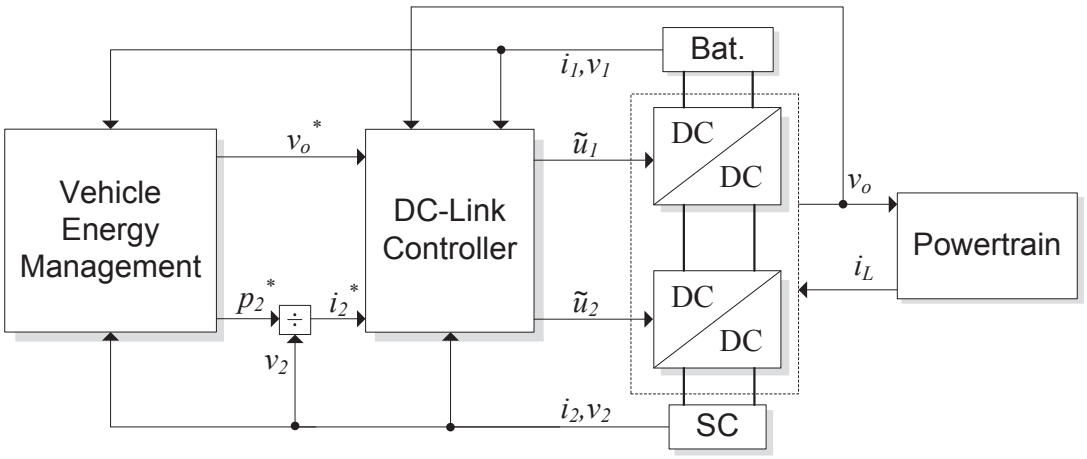

Figure 9.1: Generic architecture of the hybrid ESS with batteries and SCs. Notice that, compared with the previous chapter, there is a small change in the indexes notation: variables with sub-script 1 refer to the primary source, batteries, while the sub-script 2 is employed in the secondary source, the SCs.

the fact that the voltage-current loop is not completely independent of the auxiliary current (e.g., a change in the current of the auxiliary source (SCs) affects the DC-bus voltage), which can lead to undesirable interaction between the loops. To attenuate this issue, [330] proposed a simple decoupling concept that compensates the voltage-current controller for setpoint modifications in the auxiliary source. However, this decoupling relies on a power balance principle that is only valid in steady state conditions. Another popular approach in the power electronics community is to linearise the (nonlinear) DC-DC converter model around an operating point and then design the feedback controller to locally stabilize the system [331]. For the hybrid ESS case, the main challenge is to ensure stability and good transient performance, in spite of disturbances, like the powertrain loads (e.g., accelerating and regenerative braking present very different operation modes) and input voltages (e.g., typically, throughout the EV operation, the SC voltage displays variations of up to 50% of its nominal value). Consequently, to cope with all this uncertainty it is necessary to endow the feedback controller with robust control techniques.

The main goal of the present chapter is to develop and evaluate a robust DC-Link controller for hybrid ESS composed by batteries and SCs, connected through the parallel of two step-up converters (see Figure 9.1). In the power electronics literature, the robust control of DC-DC converters with SISO - Single Input Single Output - structure has been extensively studied in recent years, especially the boost and buck-boost topologies (see, e.g., [332, 333, 334, 335]). Spurred by the DC-link control problem, these previous studies are extended here for the MIMO - Multiple Input Multiple Output - structure, with particular emphasis on the configuration where two boost converters must operate in parallel and satisfy several control objectives (e.g., regulate the converter's output voltage and SCs' current). Toward that end, a robust Linear-quadratic Regulator (LQR) is proposed and then numerically solved within a Linear Matrix Inequalities (LMIs) framework. Besides the robustness property, the controller also features an extended operation envelope thanks to the gain-scheduling of the energy source voltages, which is particularly helpful in coping with voltage variations in the SCs. Experimental validation of the control architecture is carried out in a reduced-scale hybrid ESS and its advantages, against non-robust

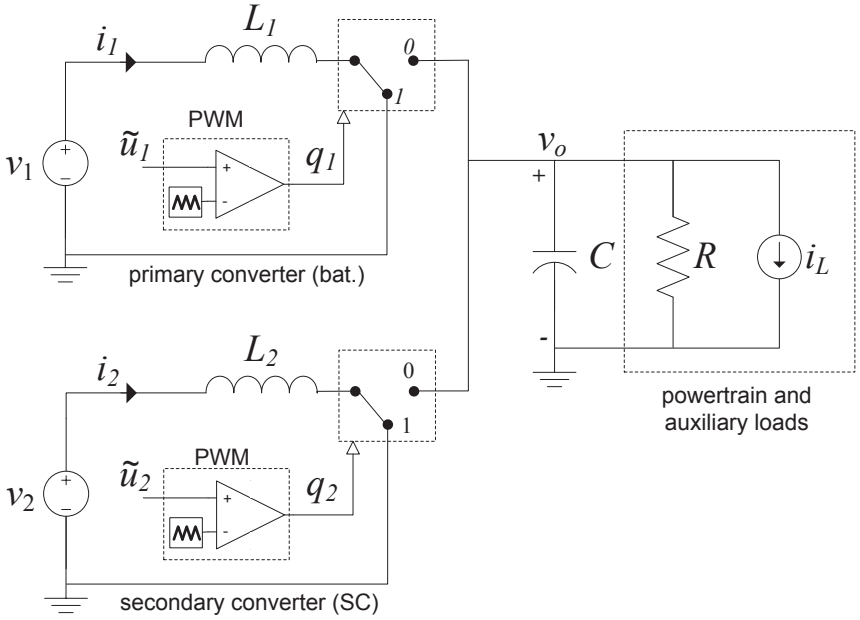

Figure 9.2: Equivalent circuit of the DC-DC power converters employed in the hybrid ESS.

and non-gain-scheduled controllers, investigated.

The remainder of this chapter is organized as follows: Section 9.2 presents the power converter model and a convenient state space normalization. The robust DC-Link controller is then discussed in Section 9.3 and experimentally validated, through a reduced scale test bench, in Section 9.4. Finally, Section 9.5 provides the concluding remarks.

9.2 Model of the Power Converters

As depicted in Figure 9.2, the topology used for the hybrid ESS is composed of two bidirectional boost DC-DC converters connected in parallel. These converters are supplied by two sources, a primary (the battery) and a secondary (the SCs), and have the responsibility to step-up the input voltages to the DC-Link levels, providing, simultaneously, an adequate bidirectional energy flow between the sources and the loads. As a starting point for the analysis of this system, the average model of the power converters [331, 336] is outlined:

$$L_1 \frac{di_1}{dt} = v_1 - v_o(1 - \tilde{u}_1) \tag{9.1a}$$

$$L_2 \frac{di_2}{dt} = v_2 - v_o(1 - \tilde{u}_2) \tag{9.1b}$$

$$C \frac{dv_o}{dt} = i_1(1 - \tilde{u}_1) + i_2(1 - \tilde{u}_2) - \frac{v_o}{R} - i_L \tag{9.1c}$$

where i_1, i_2 are the inductors (average) currents and v_o the output (average) DC-Link voltage. The two control inputs are the converters' duty cycles $(\tilde{u}_1, \tilde{u}_2) \in [0,1] \times [0,1]$; the model parameters are as follows: L_1, L_2 represent the converter inductances, C the output capacitance and R the nominal resistance associated to the vehicle auxiliary loads. Finally, the exogenous inputs are represented by the battery (v_1) and SC (v_2) voltage and by the bounded load current $i_L \in [\underline{i_L}, \overline{i_L}]$ that models the vehicle power requests,

which is positive during accelerations and negative when regenerative braking is applied; for mathematical convenience, i_L may also incorporate variations in the load of the auxiliary systems. Regarding the notation employed in the above model: the variables with subscript 1 are related to the primary source (the batteries), while subscript 2 refers to the secondary energy source (the SCs). Furthermore, throughout this work, and unless otherwise stated, we will refer to the minimum/maximum values that a given variable can take with an underline/overline notation (e.g., $\underline{i_L}, \overline{i_L}$).

In practice, the duty cycles $(\tilde{u}_1, \tilde{u}_2)$ are used by the pulse-width-modulator (PWM) block to generate the discrete gating signals $(q_1, q_2) \in \{0,1\} \times \{0,1\}$ and switch the power semiconductors, as illustrated in Figure 9.2. With the aim of simplifying the analysis, the above model assumes ideal switches, neglects parasite elements in the inductances and capacitors, and, in general, is able to capture the converters' dynamics up to one-tenth the switching frequency [336], which is enough for the controller design.

9.2.1 Normalized average model

In order to facilitate the controller design, consider the following state normalization and time-scale transformation:

$$\begin{bmatrix} x_1 \\ x_2 \\ x_3 \end{bmatrix} = \begin{bmatrix} \frac{1}{v_1}\sqrt{\frac{L_1}{C}} & 0 & 0 \\ 0 & \frac{1}{v_2}\sqrt{\frac{L_1}{C}} & 0 \\ 0 & 0 & \frac{1}{v_1} \end{bmatrix} \begin{bmatrix} i_1 \\ i_2 \\ v_o \end{bmatrix}, \quad \tau = \frac{t}{\sqrt{L_1 C}} \tag{9.2}$$

where x_1, x_2 are the normalized input currents, x_3 the normalized output voltage and τ the normalized time. Applying these relations to (9.1) yields:

$$\frac{dx_1}{d\tau} = 1 - x_3 u_1 \tag{9.3a}$$

$$\theta_1 \frac{dx_2}{d\tau} = 1 - x_3 u_2 w_1 \tag{9.3b}$$

$$\frac{dx_3}{d\tau} = x_1 u_1 + \frac{x_2}{w_1} u_2 - \frac{x_3}{\theta_2} - \Delta_1 \tag{9.3c}$$

where,

$$\theta_1 = \frac{L_2}{L_1}, \quad \theta_2 = R\sqrt{\frac{C}{L_1}}, \quad w_1 = \frac{v_1}{v_2}, \quad \Delta_1 = \frac{1}{v_1}\sqrt{\frac{L_1}{C}} i_L \tag{9.4}$$

and with the duty cycle logic complemented:

$$u_1 = 1 - \tilde{u}_1, \quad u_2 = 1 - \tilde{u}_2 \tag{9.5}$$

It is important to note that the change of variable (9.2) has been adopted in previous studies (see, e.g., [337, 338, 339, 340]), and is exploited here to represent the boost converters of the sources in a dimensionless form. Compared with the original model, this dimensionless representation features the following main advantages: *i*) the number of parameters is reduced from four (L_1, L_2, R, C) to only two (θ_1, θ_2), and *ii*) the number of exogenous inputs is decreased from three (v_1, v_2, i_L) to two (w_1, the ratio of input voltages, and Δ_1, the normalized load current). Hence, in the new coordinate system, the

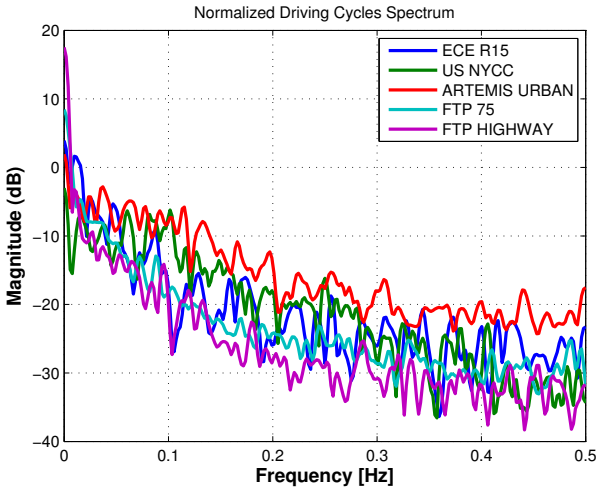

Figure 9.3: Spectral density for some typical driving cycles.

mathematical description of the converter is simplified, which, as we will see in the next section, facilitates the model analysis and controller design.

In the sequel, we will work with the normalized model and assume that all the state variables are available to the controller, as well as the exogenous signals v_1 and v_2. Even though this requirement implies the need for several sensors, in practice the majority of these variables are available in the ESS since, for the sake of state-of-charge (SOC) calculation, the power flow in the energy sources, i.e., (v_1, i_1) and (v_2, i_2), must be accurately monitored.

9.3 DC-Link Controller

In this section, we present the DC-Link control layer for the hybrid ESS structure illustrated in Figure 9.1. It is assumed that the desired DC-bus voltage v_o^* and the SC current setpoint i_2^* $(= p_2^*/v_2)$, are specified by the VEM layer, e.g., using one of the methods mentioned in the Introduction, and are available to the lower control layers.

9.3.1 Control Problem

Given that the controller formulation will be based on the normalized model (9.3), it is appropriate to start the design by also normalizing the setpoints provided by the VEM layer. Accordingly, by applying the change of variable (9.2) to $(v_o^*\ ,\ i_2^*)$, we obtain the normalized references (x_2^*, x_3^*). After this preliminary step, the control objectives can be established as follows: find a control law for (u_1, u_2) so that the converter outputs $\boldsymbol{y}$ follow the normalized setpoints:

$$\boldsymbol{y}(\tau) = \begin{bmatrix} x_2(\tau) \\ x_3(\tau) \end{bmatrix} \rightarrow \begin{bmatrix} x_2^* \\ x_3^* \end{bmatrix} \tag{9.6}$$

as quickly as possible, and being robust to uncertainties in the system (e.g., the powertrain load current).

It is noteworthy that, in practice, (x_2^*, x_3^*) vary over time, depending on the vehicle state, driving cycle and VEM algorithm. Consequently, from a theoretical perspective, the

regulation problem stated above should be posed as an output-tracking problem. However, by following the tracking setting, it becomes necessary to find a stable inversion of the system [341], which is hampered by the nonlinearities and non-minimum phase nature of the boost converter. As a matter of fact, the stable inverse of the boost model requires the inversion of the internal dynamics - in our case the battery current - producing an Abel differential equation, difficult to solve analytically (see [340] and references therein). To overcome these hurdles, and under the assumption of slowly time-varying references (x_2^*, x_3^*), we will simplify the control problem, replacing the output-tracking setting by a regulation one. The above assumption, perfectly reasonable for x_3^* given that, in the majority of the time, we aim to keep a constant DC bus voltage, is more arguable in the case of the SC current setpoint x_2^*. Nevertheless, if we take into account the spectral distribution of the typical driving cycles to which the EV is subject, depicted in Figure 9.3, and even if x_2^* (or equivalently i_2^*) has to provide the high frequency components, one can easily verify that the SC current/power will hardly contain a significant spectral content above 0.5Hz. (This argument can also be extended to the disturbance Δ_1.) As a result, given the expected fast bandwidth of the DC-Link controller, we can take (x_2^*, x_3^*) as slowly time-varying parameters, enabling the indirect solution of the tracking problem through a regulation setting.

In terms of nomenclature, and for reasons that will be clear later, we will consider that the desired normalized output voltage $x_3^* = \theta_3$ is constant, while the variation of the SC current reference is bounded: $x_2^* = \Delta_2 \in [\underline{\Delta_2}, \overline{\Delta_2}] \subset \mathbb{R}$. Moreover, to cope with the inevitable parametric mismatch and non-modelled factors, the controller will also incorporate integral action. Augmenting the normalized model (9.3) with integral error, the converter can be represented by the following MIMO model:

$$\frac{d\boldsymbol{x}}{d\tau} = f(\boldsymbol{x}, \boldsymbol{u}, \boldsymbol{\theta}, w_1, \boldsymbol{\Delta}) = \begin{bmatrix} 1 - x_3 u_1 \\ (1 - x_3 u_2 w_1)/\theta_1 \\ x_1 u_1 + \frac{x_2}{w_1} u_2 - \frac{x_3}{\theta_2} - \Delta_1 \end{bmatrix} \tag{9.7a}$$

$$\frac{d\boldsymbol{\sigma}}{d\tau} = g(\boldsymbol{x}, \boldsymbol{\theta}, \boldsymbol{\Delta}) = \begin{bmatrix} x_2 - \Delta_2 \\ x_3 - \theta_3 \end{bmatrix} \tag{9.7b}$$

$$\boldsymbol{y} = \begin{bmatrix} x_2 & x_3 \end{bmatrix}^T \tag{9.7c}$$

where $\boldsymbol{x} = \begin{bmatrix} x_1 & x_2 & x_3 \end{bmatrix}^T$ and $\boldsymbol{\sigma} = \begin{bmatrix} \sigma_1 & \sigma_2 \end{bmatrix}^T$ are the states, $\boldsymbol{u} = \begin{bmatrix} u_1 & u_2 \end{bmatrix}^T \in [0,1] \times [0,1]$ is the control signal and $\boldsymbol{\theta} = \begin{bmatrix} \theta_1 & \theta_2 & \theta_3 \end{bmatrix}^T$ the model's constant parameters. The exogenous signal $w_1 \in \mathcal{D}_w \subset \mathbb{R}$ is known and belongs to the bounded set $\mathcal{D}_w$, which can be calculated considering the expected voltage variation in the energy sources, e.g., $\mathcal{D}_w = [\underline{v_1}/\overline{v_2},\ \overline{v_1}/\underline{v_2}]$. The bounded disturbance is described by $\boldsymbol{\Delta} = \begin{bmatrix} \Delta_1 & \Delta_2 \end{bmatrix}^T \in [\underline{\Delta_1}, \overline{\Delta_1}] \times [\underline{\Delta_2}, \overline{\Delta_2}] = \mathcal{D}_\Delta \subset \mathbb{R}^2$. Besides the already-mentioned considerations about the setpoints (x_2^*, x_3^*), the controller will further assume that the model parameters $\boldsymbol{\theta}$ are known and $\boldsymbol{x}, \boldsymbol{\sigma}$ are available for feedback.

Our approach to the DC-Link controller design will be based on a robust, state feedback, control law. The first step of the design is to determine the equilibrium points of the nonlinear system (9.7) and perform the linearization around these points. Then, it will be shown that the resulting uncertain linear model lies in a convex polytope. This convex property will be further explored to, starting from a robust LQR setting, formulate an optimization problem with LMIs and extract the feedback gains. Finally, the operation range of the DC-Link controller will be extended by gain-scheduling the control gains

with the exogenous signal w_1. Notice that w_1, although unknown at the design stage, can be monitored during the system operation and, due to its slow variation, is a natural candidate for gain-scheduling.

9.3.2 Control Law, Equilibrium Points and Linearization

As a starting point for the DC-Link controller design, suppose that the gain-scheduled variable $w_1 = \beta \in \mathcal{D}_w$ is constant (later we shall consider the time-varying case). With the aim of stabilize (9.7), we propose a state feedback controller, expressed as:

$$\boldsymbol{u} = \boldsymbol{K}_x(\beta)\boldsymbol{x} + \boldsymbol{K}_\sigma(\beta)\boldsymbol{\sigma} \tag{9.8}$$

where $\boldsymbol{K}_x(\beta) \in \mathbb{R}^{2\times 3}$ and $\boldsymbol{K}_\sigma(\beta) \in \mathbb{R}^{2\times 2}$ are the feedback gains. Under the reasonable assumption of non-singular $\boldsymbol{K}_\sigma(\beta)$, the family of equilibrium points of the MIMO system can be defined as:

$$\begin{gathered}\boldsymbol{x}_{ss} = \left[\left(\tfrac{\theta_3^2}{\theta_2} + \theta_3\Delta_1 - \tfrac{\Delta_2}{\beta^2}\right) \quad \Delta_2 \quad \theta_3)\right]^T,\ \boldsymbol{u}_{ss} = \left[\tfrac{1}{\theta_3} \quad \tfrac{1}{\theta_3\beta}\right]^T \\ \boldsymbol{\sigma}_{ss} = \left(\boldsymbol{K}_\sigma(\beta)\right)^{-1}\left(\boldsymbol{u}_{ss} - \boldsymbol{K}_x(\beta)\boldsymbol{x}_{ss}\right)\end{gathered} \tag{9.9}$$

Next, to investigate the local stability properties, the system (9.7),(9.8) is linearized around the equilibrium point, resulting in the following state space representation:

$$\frac{d\boldsymbol{x}_\delta}{d\tau} = \boldsymbol{A}\boldsymbol{x}_\delta + \boldsymbol{B}(\boldsymbol{\Delta})\left(\boldsymbol{K}_x\boldsymbol{x}_\delta + \boldsymbol{K}_\sigma\boldsymbol{\sigma}_\delta\right) \tag{9.10}$$

$$\frac{d\boldsymbol{\sigma}_\delta}{d\tau} = \boldsymbol{C}\boldsymbol{x}_\delta \tag{9.11}$$

where $\boldsymbol{x}_\delta = \boldsymbol{x} - \boldsymbol{x}_{ss}$, $\boldsymbol{\sigma}_\delta = \boldsymbol{\sigma} - \boldsymbol{\sigma}_{ss}$, $\boldsymbol{u}_\delta = \boldsymbol{u} - \boldsymbol{u}_{ss}$, and the matrices $\boldsymbol{A} = \frac{\partial f}{\partial \boldsymbol{x}}$, $\boldsymbol{B}(\boldsymbol{\Delta}) = \frac{\partial f}{\partial \boldsymbol{u}}$ and $\boldsymbol{C} = \frac{\partial g}{\partial \boldsymbol{x}}$ are the Jacobians of the vector field, evaluated at the equilibrium point, and given by:

$$\boldsymbol{A} = \frac{1}{\theta_3}\begin{bmatrix}0 & 0 & -1\\ 0 & 0 & -\frac{1}{\theta_1}\\ 1 & \frac{1}{\beta^2} & -\frac{\theta_3}{\theta_2}\end{bmatrix}, \qquad \boldsymbol{B}(\boldsymbol{\Delta}) = \begin{bmatrix}-\theta_3 & 0\\ 0 & -\frac{\theta_3}{\theta_1}\beta\\ x_{1ss}(\boldsymbol{\Delta}) & \frac{\Delta_2}{\beta}\end{bmatrix}, \quad \boldsymbol{C} = \begin{bmatrix}0 & 1 & 0\\ 0 & 0 & 1\end{bmatrix} \tag{9.12}$$

For ease of notation, the dependence of β in the feedback gains was dropped.

9.3.3 Polytopic Uncertainty

In the previous linear model, only the matrix $\boldsymbol{B}$ is affected by the disturbance $\boldsymbol{\Delta}$, which, for convenience, can be re-written as:

$$\boldsymbol{B}(\boldsymbol{\Delta}) = \underbrace{\begin{bmatrix}-\theta_3 & 0\\ 0 & -\frac{\theta_3}{\theta_1}\beta\\ 0 & 0\end{bmatrix}}_{\boldsymbol{B}_0} + \underbrace{\begin{bmatrix}0 & 0\\ 0 & 0\\ 1 & 0\end{bmatrix}}_{\boldsymbol{B}_a} x_{1ss}(\boldsymbol{\Delta}) + \underbrace{\begin{bmatrix}0 & 0\\ 0 & 0\\ 0 & \frac{1}{\beta}\end{bmatrix}}_{\boldsymbol{B}_b}\Delta_2 \tag{9.13}$$

where $x_{1ss}(\boldsymbol{\Delta})$ represents the battery current at the equilibrium (first element of $\boldsymbol{x}_{ss}$). Notice that this relation displays an affine form in the variables x_{1ss} and Δ_2. This fact,

together with the bounds

$$x_{1ss}(\boldsymbol{\Delta}) \in [\underline{x}_1, \overline{x}_1] \qquad \Delta_2 \in [\underline{\Delta}_2, \overline{\Delta}_2] \tag{9.14}$$

where $\underline{x}_1, \overline{x}_1$ can be easily extracted from $\mathcal{D}_\Delta, \mathcal{D}_w$, enable us to represent the uncertainty of the linear model in a convex polytope, composed by four vertices:

$$\begin{aligned}[\boldsymbol{A} \quad \boldsymbol{B}(\boldsymbol{\Delta})] \in \text{co}\{&[\boldsymbol{A} \quad (\boldsymbol{B}_0 + \boldsymbol{B}_a\underline{x}_1 + \boldsymbol{B}_b\underline{\Delta}_2)],\\ &[\boldsymbol{A} \quad (\boldsymbol{B}_0 + \boldsymbol{B}_a\underline{x}_1 + \boldsymbol{B}_b\overline{\Delta}_2)],\\ &[\boldsymbol{A} \quad (\boldsymbol{B}_0 + \boldsymbol{B}_a\overline{x}_1 + \boldsymbol{B}_b\underline{\Delta}_2)],\\ &[\boldsymbol{A} \quad (\boldsymbol{B}_0 + \boldsymbol{B}_a\overline{x}_1 + \boldsymbol{B}_b\overline{\Delta}_2)]\}\end{aligned} \tag{9.15}$$

The well-known convex-hull operator [342], co{.}, introduced above, is given by

$$[\boldsymbol{A} \quad \boldsymbol{B}(\boldsymbol{\Delta})] \in \left\{ \sum_{i=1}^{L} \lambda_i [\boldsymbol{A}_i \quad \boldsymbol{B}_i] \;:\; \lambda_i \geq 0,\; \sum_{i=1}^{L} \lambda_i = 1 \right\} \tag{9.16}$$

where $[\boldsymbol{A}_i \quad \boldsymbol{B}_i]$ represents vertices of the polytope, defined in (9.15), and $L = 4$.

9.3.4 Control Synthesis

After the derivation of the linearized uncertain model, in this section we will explain how the state feedback matrices $(\boldsymbol{K}_x, \boldsymbol{K}_\sigma)$ can be selected, in order to obtain a stable and robust controller. With this goal in mind, let's consider the augmented state $\boldsymbol{\xi}_\delta = \begin{bmatrix}\boldsymbol{x}_\delta & \boldsymbol{\sigma}_\delta\end{bmatrix}^T$ and its dynamics:

$$\frac{d\boldsymbol{\xi}_\delta}{d\tau} = \underbrace{\begin{bmatrix}\boldsymbol{A} & 0\\ \boldsymbol{C} & 0\end{bmatrix}}_{\mathcal{A}} \boldsymbol{\xi}_\delta + \underbrace{\begin{bmatrix}\boldsymbol{B}(\boldsymbol{\Delta})\\ 0\end{bmatrix}}_{\mathcal{B}(\boldsymbol{\Delta})} \underbrace{\begin{bmatrix}\boldsymbol{K}_x & \boldsymbol{K}_\sigma\end{bmatrix}}_{\mathcal{K}} \boldsymbol{\xi}_\delta \tag{9.17a}$$

$$= (\mathcal{A} + \mathcal{B}(\boldsymbol{\Delta})\mathcal{K})\,\boldsymbol{\xi}_\delta \tag{9.17b}$$

Following the discussion carried out in the previous section, the augmented state and input matrix $(\mathcal{A}, \mathcal{B}(\boldsymbol{\Delta}))$, assumed to form a controllable pair in $\boldsymbol{\Delta} \in \mathcal{D}_\Delta$, are contained in the following convex polytope:

$$[\mathcal{A} \quad \mathcal{B}(\boldsymbol{\Delta})] \in \text{co}\{[\mathcal{A}_1 \quad \mathcal{B}_1], [\mathcal{A}_2 \quad \mathcal{B}_2], [\mathcal{A}_3 \quad \mathcal{B}_3], [\mathcal{A}_4 \quad \mathcal{B}_4]\} \tag{9.18}$$

where $\mathcal{A}_i, \mathcal{B}_i, i = 1, \ldots, L$, follows from (9.15) and (9.17).

In simple terms, the first robust stability problem that we need to solve can be stated as: find the state feedback gains $\mathcal{K}$ such that $(\mathcal{A} + \mathcal{B}(\boldsymbol{\Delta})\mathcal{K})$ is Hurwitz for any $\boldsymbol{\Delta} \in \mathcal{D}_\Delta$. To address this problem we can apply the Lyapunov method and pose a LMI problem, solvable by numerical means (see [342, Chapter 7]). However, this formulation neglects a very important aspect: the transient response of the closed-loop system is not taken into account in the control synthesis. Thus, to ensure a satisfactory transient performance, in addition to robustness, we will seek the minimization of the following quadratic cost function

$$J = \int_0^\infty \boldsymbol{\xi}_\delta(s)^T \left(\boldsymbol{Q} + \mathcal{K}^T \boldsymbol{R} \mathcal{K}\right) \boldsymbol{\xi}_\delta(s) ds \tag{9.19}$$

where $\boldsymbol{Q} = \boldsymbol{Q}^T > 0$, $\boldsymbol{R} = \boldsymbol{R}^T > 0$ are positive-definite, symmetric, matrices defined by the designer, and which characterize, indirectly, the closed-loop transient response. Toward the robust minimization of J (which can also be seen as a robust LQR problem), consider a quadratic Lyapunov candidate function, $V = \boldsymbol{\xi}_\delta^T \boldsymbol{P} \boldsymbol{\xi}_\delta$, with $\boldsymbol{P} = \boldsymbol{P}^T > 0$, as well as its time derivative:

$$\dot{V} = \boldsymbol{\xi}_\delta^T \left((\mathcal{A} + \mathcal{B}(\boldsymbol{\Delta})\mathcal{K})^T \boldsymbol{P} + \boldsymbol{P} (\mathcal{A} + \mathcal{B}(\boldsymbol{\Delta})\mathcal{K}) \right) \boldsymbol{\xi}_\delta \tag{9.20}$$

Spurred by the guaranteed-cost control concept [343], suppose that a pair $(\mathcal{K}, \boldsymbol{P})$ can be chosen such that the following inequality is satisfied:

$$\dot{V} = \boldsymbol{\xi}_\delta^T \left((\mathcal{A} + \mathcal{B}(\boldsymbol{\Delta})\mathcal{K})^T \boldsymbol{P} + \boldsymbol{P} (\mathcal{A} + \mathcal{B}(\boldsymbol{\Delta})\mathcal{K}) \right) \boldsymbol{\xi}_\delta < -\boldsymbol{\xi}_\delta^T \left(\boldsymbol{Q} + \mathcal{K}^T \boldsymbol{R} \mathcal{K} \right) \boldsymbol{\xi}_\delta \tag{9.21}$$

for any $\boldsymbol{\Delta} \in \mathcal{D}_\Delta$. Since $\boldsymbol{Q}, \boldsymbol{R} > 0$, it follows that $\boldsymbol{Q} + \mathcal{K}^T \boldsymbol{R} \mathcal{K} > 0$, $\dot{V} < 0 \; \forall \boldsymbol{\xi}_\delta \neq 0$ and asymptotic stability is obtained [96]. Next, integrating the previous relation

$$\int_0^\infty \dot{V}(s) ds = V(\infty) - V(0) < -\int_0^\infty \boldsymbol{\xi}_\delta^T \left(\boldsymbol{Q} + \mathcal{K}^T \boldsymbol{R} \mathcal{K} \right) \boldsymbol{\xi}_\delta ds \tag{9.22}$$

and using the asymptotic stability property, i.e., $V(\infty) \to 0$, we have:

$$J < V(0) = \boldsymbol{\xi}_\delta(0)^T \boldsymbol{P} \boldsymbol{\xi}_\delta(0) \tag{9.23}$$

Hence, the cost J can be bounded by the initial value of the Lyapunov function, which also depends on the initial state $\boldsymbol{\xi}_\delta(0)$. In order to eliminate this dependence, we can consider a stochastic interpretation of (9.23), suggested in [344],[345], and take $\boldsymbol{\xi}_\delta(0)$ as a random vector with zero mean and covariance equal to the identity matrix; applying the expected value operator to the resulting random variable, $\mathbb{E}\{\boldsymbol{\xi}_\delta(0)^T \boldsymbol{P} \boldsymbol{\xi}_\delta(0)\}$, a new upper bound, independent of $\boldsymbol{\xi}_\delta(0)$, is obtained [344]:

$$J < \text{trace}(\boldsymbol{P}) \tag{9.24}$$

Returning to the inequality (9.21), it can be shown that, by exploring the convexity property of the uncertain polytope, (9.21) holds if the following matrix inequalities are true:

$$(\mathcal{A}_i + \mathcal{B}_i \mathcal{K})^T \boldsymbol{P} + \boldsymbol{P} (\mathcal{A}_i + \mathcal{B}_i \mathcal{K}) + \boldsymbol{Q} + \mathcal{K}^T \boldsymbol{R} \mathcal{K} < 0 \tag{9.25}$$

for $i = 1, \ldots, L$. This result, together with (9.24), enables us to recast the robust optimization problem as:

$$\begin{aligned} &\min_{\mathcal{K}, \boldsymbol{P}} \quad \text{trace}\,(\boldsymbol{P}) \\ &s.t. \quad \boldsymbol{P} > 0, \quad (9.25), \quad i = 1, \ldots, L, \end{aligned} \tag{9.26}$$

At this stage, it is worth mention that the formulation (9.26) intends to minimize the upper bound on the cost function J. This approach is known in the literature as the guaranteed-cost control [343, 344], and ensures that the resulting controller will be able to provide an adequate level of performance, in spite of uncertainties in the model. The main obstacles to the numerical resolution of (9.26) are the non-convex constraints; to

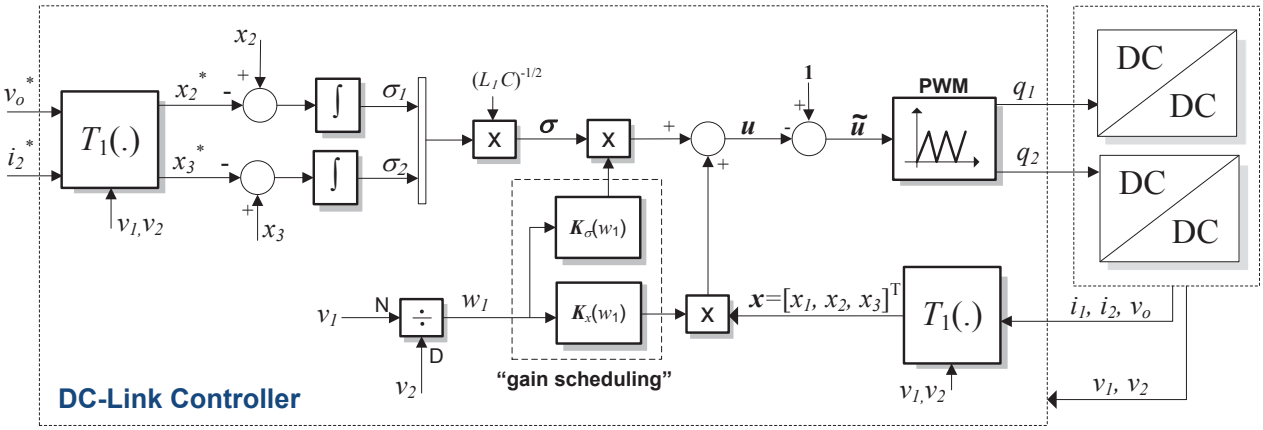

Figure 9.4: Block diagram of the proposed DC-Link controller; notice that the change of variable $T_1(.)$ is described by (9.2).

overcome this difficulty, we apply the following change of variable (suggested in [342]):

$$\boldsymbol{Y} = \boldsymbol{P}^{-1} \qquad \boldsymbol{L} = \mathcal{K}\boldsymbol{Y} \tag{9.27}$$

which, after some algebraic manipulation, allow us to reformulate the robust stabilization problem in a more practical setting:

Proposition 9.1. *Consider the model* (9.17)*, under polytopic uncertainty* (9.18)*. The guaranteed-cost control problem defined in* (9.26) *is equivalent to:*

$$\begin{aligned} \min_{\boldsymbol{L},\boldsymbol{Y}} \quad & -\operatorname{trace}(\boldsymbol{Y}) \\ s.t. \quad & \begin{bmatrix} -\boldsymbol{Y}\mathcal{A}_i^T - \mathcal{A}_i\boldsymbol{Y} - \mathcal{B}_i\boldsymbol{L} - \boldsymbol{L}^T\mathcal{B}_i^T & \boldsymbol{Y} & \boldsymbol{L}^T \\ \boldsymbol{Y} & \boldsymbol{Q}^{-1} & 0 \\ \boldsymbol{L} & 0 & \boldsymbol{R}^{-1} \end{bmatrix} > 0 \\ & \boldsymbol{Y} > 0, i = 1, \ldots, L \end{aligned} \tag{9.28}$$

where $\mathcal{K} = \begin{bmatrix} \boldsymbol{K}_x & \boldsymbol{K}_\sigma \end{bmatrix} = \boldsymbol{L}\boldsymbol{Y}^{-1}$.

Notice that, in this last formulation, the constraints are placed as LMIs, which are convex and easier to treat numerically. Actually, the YALMIP [346] and SeDuMi solver [347] were employed to numerically extract the optimal solution of the above problem.

9.3.5 Gain-scheduling

So far, we have assumed that the exogenous input $w_1 = v_1/v_2$ is constant, but, in practice, this variable depends on the voltage of the energy sources, which varies over the EV operation. In order to deal with this variation, and extend the operation range of the DC-Link controller, the feedback gains $\boldsymbol{K}_x, \boldsymbol{K}_\sigma$ will be modified (scheduled) according to the value of w_1 (the scheduled variable). Toward that aim, we start by discretizing the exogenous input w_1 over its domain ($\mathcal{D}_w$):

$$[\beta_1, \beta_2, \ldots, \beta_N] \in (\mathcal{D}_w)^N \subset \mathbb{R}^N \tag{9.29}$$

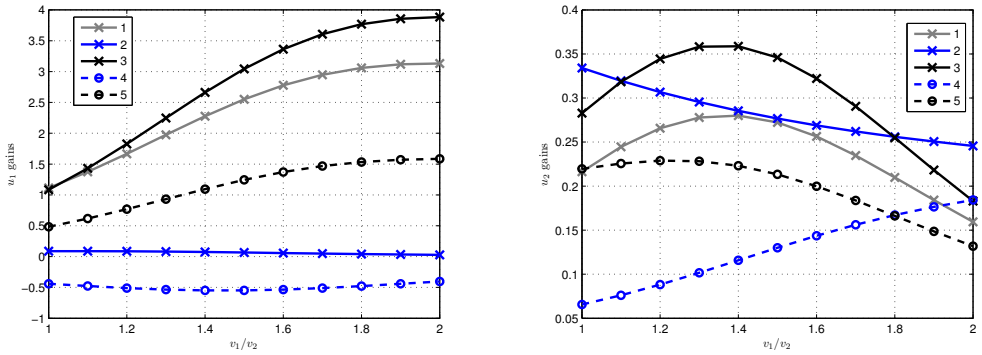

(a) u_1 gains (b) u_2 gains

Figure 9.5: Feedback gains of the gain-scheduled DC-Link controller (9.31) employed in the experimental validation; the u_1 gains, represent the first row of the matrix $[\boldsymbol{K}_x(w_1)\ \boldsymbol{K}_\sigma(w_1)]$, while the u_2 gains are the second row.

Next, for each one of these discrete values, we apply (9.28) to calculate (off-line) the corresponding set of control gains:

$$\big(\boldsymbol{K}_x(\beta_1), \boldsymbol{K}_\sigma(\beta_1)\big), \ldots, \big(\boldsymbol{K}_x(\beta_N), \boldsymbol{K}_\sigma(\beta_N)\big) \tag{9.30}$$

The gain-scheduled controller is then obtained by replacing β (constant) with w_1 (slowly time varying) in (9.8) and interpolating the controller gains at intermediate points, producing the final control law:

$$\boldsymbol{u} = \boldsymbol{K}_x(w_1)\boldsymbol{x} + \boldsymbol{K}_\sigma(w_1)\boldsymbol{\sigma} \tag{9.31}$$

which is illustrated in Figure 9.4. To qualitatively analyze the influence of scheduled variable w_1 in the feedback gains, Figure 9.5 represents the (linear) interpolation results of the $\boldsymbol{K}_x(w_1)$ and $\boldsymbol{K}_\sigma(w_1)$ used in the experimental validation (whose details will be discussed in the next section). From these results, it is interesting to note that some feedback gains are almost insensitive to w_1 variations, e.g., the x_2 feedback gain in the u_1 channel, while others shows the opposite behaviour (e.g., the x_3 feedback gain in the u_1 channel depicts a variation of more than 300% throughout the w_1 operation range). Furthermore, it is also worth mentioning that the dimensionless model (9.3) adopted in the DC-Link controller design brings important advantages to the gain-scheduling implementation; to be more precise, instead of using two scheduled variables (v_1 and v_2), as would be the case if the original model (9.1) was employed in the controller design, the approach proposed in this chapter only needs a single variable, i.e., the voltage ratio w_1.

Remark 9.1. In order to ensure that the gain-scheduling controller (9.31) maintains the stability and transient response performance, it is necessary that the exogenous input vary slowly in time [348]. To show that this requirement holds in our design, recall the definition $w_1 = v_1/v_2$ and notice that the time variation of the battery voltage v_1, when compared with the high excursion that is usually observed in v_2, can be safely neglected. In other words, v_2 is definitely the variable that contributes most to the variation of w_1.

Hence, using the SC ideal model, the evolution of v_2 can be described by

$$v_2(t) = v_2(0) + \frac{1}{C_{SC}} \int_0^t i_2(s)ds \tag{9.32}$$

where C_{SC} is the equivalent capacitance of the SCs. As C_{SC} is normally chosen with a relatively high value, the integral relation (9.32) provides a slow variation in v_2. Consequently, taking into consideration the time-scale that the DC-Link controller operates (some milliseconds), it is perfectly reasonably to admit w_1 as slowly varying exogenous input.

Remark 9.2. In this chapter, it was considered that the DC-Link voltage must remain constant throughout the EV operation, which may be conservative for some designs. For instance, the DC-bus voltage increase can be helpful when the load power is high [349] or during the field-weakening operation of the electric motor [350]. Nonetheless, the design described here can be easily extended to deal with variable x_3^*, e.g., by adding a second gain-scheduling variable (x_3^*) to the controller.

From a practical point of view, implementing the control law (9.31), in particular the integral action, requires certain care on a number of details. First, it should be noted that the controller was formulated in normalized time (τ), while its implementation will be done in normal time (t); therefore, it is imperative to introduce a correction factor when integrating the regulation error:

$$\frac{d\boldsymbol{\sigma}}{dt} = \frac{1}{\sqrt{L_1 C}} \frac{d\boldsymbol{\sigma}}{d\tau} \tag{9.33}$$

Second, to avoid unwanted transients upon the controller activation, the initial value of the integrator, $\boldsymbol{\sigma}(0)$, should be selected, taking into account the initial conditions (i.e., $\boldsymbol{x}(0)$, $w_1(0)$) and the intended initial duty cycles $\boldsymbol{u}(0)$. Based on this information, we can invert (9.31) and extract an adequate value for $\boldsymbol{\sigma}(0)$. Finally, as the control signals are physically limited, it is essential to incorporate anti-windup mechanisms into the integrators to ensure a proper operation when $\boldsymbol{u}$ saturates. With this concern in mind, we employed the technique of conditional integrator [351].

9.4 Experimental Validation

9.4.1 Overview of the Experimental Setup

The experimental validation of the DC-Link controller was carried out in a small laboratory test bench, built with the intention of studying, in a reduced power scale, the hybrid ESS of the uCar. This reduced-scale setup (DC Link with 500W, 100V), illustrated in Figure 9.6, is endowed with two types of energy sources: a battery pack and an SCs bank. The former is composed of four NiMH SAFT modules (12 V, 13.5 Ah) [352] in series, while the latter is obtained by two branches of SCs in parallel of a series of 18 cells (100 F, 2.7 V, 21.4 A), manufactured by NESSCAP [353]. Each energy source is connected to the DC Link through a bidirectional boost converter, whose power electronics were accomplished by two (of the three) arms of the SEMIKRON - SKS 11F B6CI (600V/18A) module, switched at 10kHz. The remaining arm of the power module is used to build a third bidirecional boost converter with the objective of emulating the (reduced) powertrain load that is requested

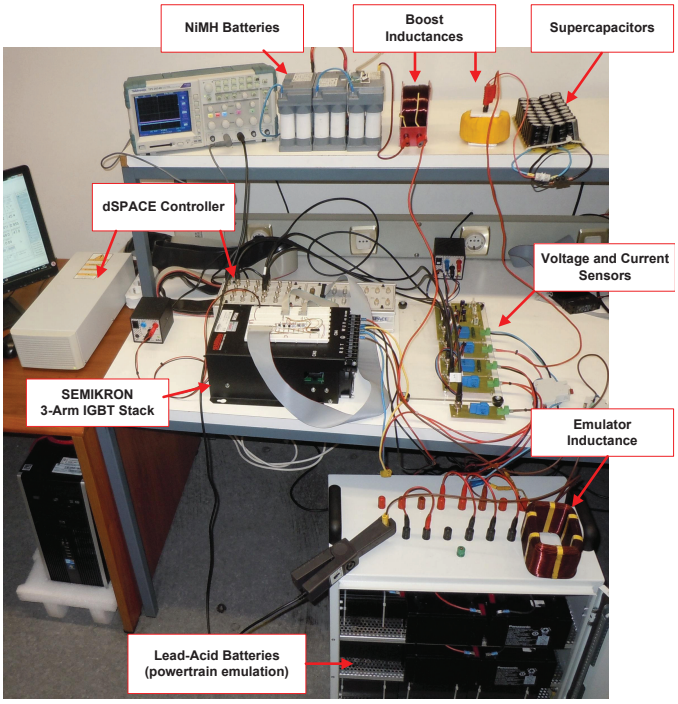

Figure 9.6: Experimental test bench employed in the DC-Link controller validation.

to the DC Link . Table 9.1 describes the parametric values employed in the experimental setup.

Concerning the DC-Link controller implementation, a dSPACE DS1103 realtime card was employed and programmed with the help of the Matlab-Simulink-RTW environment. The voltage and current measurements, accomplished through Hall effect transducers, LEM: LV25-P and HY15-P, respectively, are acquired by the analog-to-digital converters of the dSPACE board, in synchrony with the PWM signals.

Before the final implementation, the performance, robustness and gain-scheduling parameters of the DC-Link controller must be chosen. The performance parameters were taken as:

$$\boldsymbol{R} = \text{diag}\left([1\ 1]\right), \quad \boldsymbol{Q} = 1.10^{-2}\,\text{diag}\left([1\ 1\ 1\ 5\ 5]\right) \tag{9.34}$$

where diag(.) is the diagonal matrix. Regarding the robustness parameters, associated with the uncertainty bounds, they were defined as $x_{1ss}(\boldsymbol{\Delta}) \in [-0.7, 0.7]$, $\Delta_2 \in [-0.5, 0.5]$, which is equivalent to a variation of $\pm$11A in the battery current, $\pm$8A in the SCs and enough to cover the power range of the experimental tests. Further, taking into account the expected range for v_1 and v_2 voltages, defined in Table 9.1, it was assumed that the gain-scheduled variable $w_1 = v_1/v_2$ belongs to the set $[1, 2]$. Then, w_1 was discretized with a fixed-step size of 0.1, generating a grid with $N = 11$ points $(\beta_1, \beta_2, \ldots, \beta_N)$, and, for each one of these, (9.28) was solved with the YALMIP+SeDuMi solver, producing a family of controllers described in (9.30). The final implementation of the LQR-Robust-Gain-Scheduling (LQR-R-GS) controller in the dSPACE was carried out with the help of lookup tables, used to store the family of feedback gains (9.30), and by interpolating them for intermediate results (see Figure 9.5). Albeit the lookup tables must store 110 points and perform 10 interpolations in each sampling time, the complexity of this operation is moderately low because all the tables share the same input, which enables the application

Table 9.1: Parameters of the experimental test bench

Parameter	Value
L_1	10 mH
L_2	5 mH
C	1 mF
R	250Ω
v_1	$[47\ 52]V$
v_2	$[26\ 48]V$

of efficient pre-lookup techniques [354].

As control objectives, it is required that the LQR-R-GS keeps the output voltage constant at $v_o^* = 100$V and ensures that the SC current tracks a given time-varying reference i_2^*.

9.4.2 Evaluation of the Robust Formulation

The first batch of experimental tests intends to assess the benefits of designing the DC-Link controller within a robust framework. To that purpose, the LQR-R-GS was compared against a nominal LQR controller, named LQR-N, which does not take into consideration any kind of uncertainty in the model and assumes constant exogenous inputs. In other words, the LQR-N has fixed Δ_1, Δ_2 and w_1. Given that the EV operating conditions change significantly through time, a difficulty that emerges when implementing the nominal controller is the selection of the operating point. To address this problem, we employed the average operating point of the system, which, for our purposes here, was taken as $(x_{1ss}, x_{2ss}, w_1) = (0.4, 0.2, 1.042)$, or, in non-normalized variables $(i_{1ss}, i_{2ss}, v_1/v_2) =$ (6.32A, 3.16A, 50V/48V). Moreover, the LQR-N gains were obtained by solving (9.19) with the MATLAB *lqr* command, and, to make a fair comparison, both controllers share the same performance weights, defined in (9.34). The resulting nominal controller is defined as:

$$\begin{aligned} \boldsymbol{K}_{LQR-N} &= \begin{bmatrix} \boldsymbol{K}_{x,N} & \boldsymbol{K}_{\sigma,N} \end{bmatrix} \\ &= \begin{bmatrix} -0.457 & -0.031 & -0.268 & 0.125 & -0.185 \\ -0.036 & -0.331 & -0.005 & -0.185 & -0.126 \end{bmatrix} \end{aligned} \tag{9.35}$$

As far as i_2^* is concerned, during the first experimental test a small pulse (100ms and 8A of peak) is applied to the SC reference, maintaining the others exogenous inputs/disturbances (w_1, i_L) constant. Analyzing the experimental results depicted in Figure 9.7, one can find that the LQR-R-GS offers a superior transient performance in regulating the output voltage, reducing the peak voltage errors from 6% (LQR-N) to less than 2%, while a small improvement is obtained in the i_2^* tracking. Some of these differences can be explained by looking more closely at the control signals evolution, i.e., the duty cycles $(\tilde{u}_1, \tilde{u}_2)$. For instance, the results show that the nominal controller is much faster to modify the duty cycle of the SCs, u_2, than u_1. As a consequence, during the initial positive step ($t \in [0.01,\ 0.11]$s), the batteries are slower coming out of service (and the SCs too quick supplying the power), which lead to excess energy being injected in the

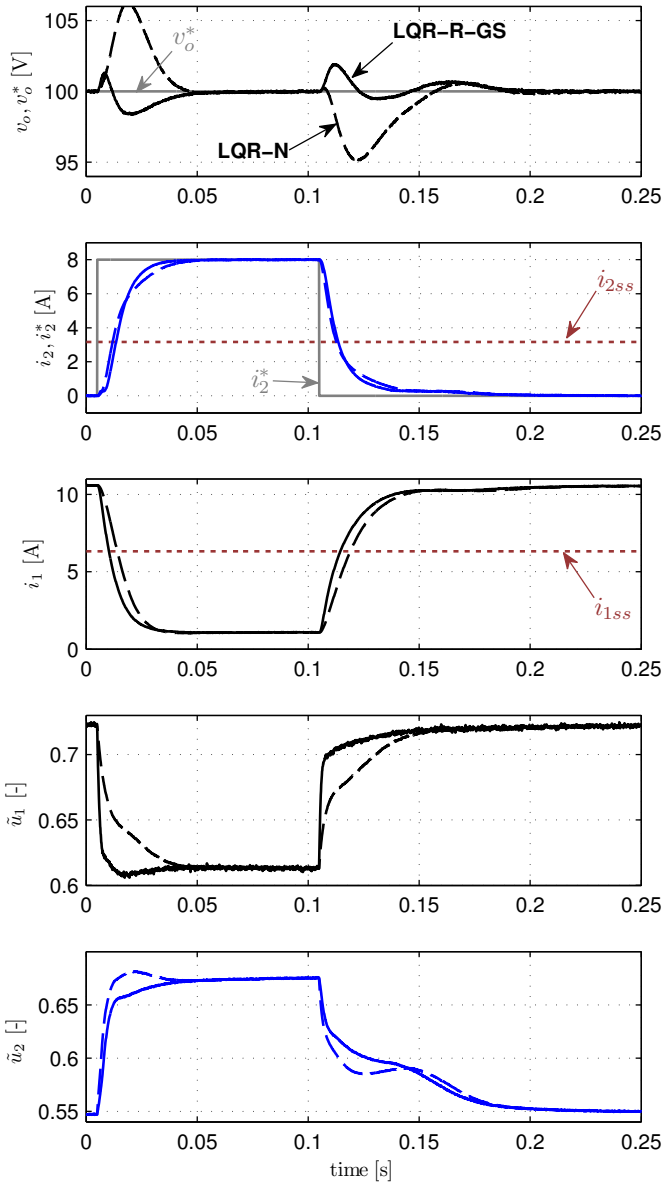

Figure 9.7: Experimental results of the LQR-R-GS (full line) and nominal LQR (dashed line) controllers when excited with a step in i_2^*. The nominal point employed in the nominal LQR tuning is $(i_{1ss}, i_{2ss}) = (6.32\text{A}\ , 3.16\text{A})$ (dotted line) and the remaining exogenous inputs/disturbances are kept constant ($i_L = 4.0\text{A}$, $w_1 = 50\text{V}/48\text{V}$).

DC-Bus. This energy, in turn, is absorbed by the DC-Link capacitor, producing a considerable voltage overshoot that is present with the LQR-N controller (a dual case occurs at $t \in [0.11,\ 0.25]$s, where the battery re-entry in service is also slow, leading to the voltage undershoot). From a theoretical point of view, the transient performance deterioration seen in the LQR-N was, to some extent, expected, since the controller is moving around the nominal point employed in its tuning (see i_{1ss} and i_{2ss} plotted in Figure 9.7). On the other hand, the LQR-R-GS design takes into account the uncertainty in the operating conditions and provides a better coordination among the sources. It is also worth mentioning that, thanks to the integral action, no differences are found between controllers in steady state.

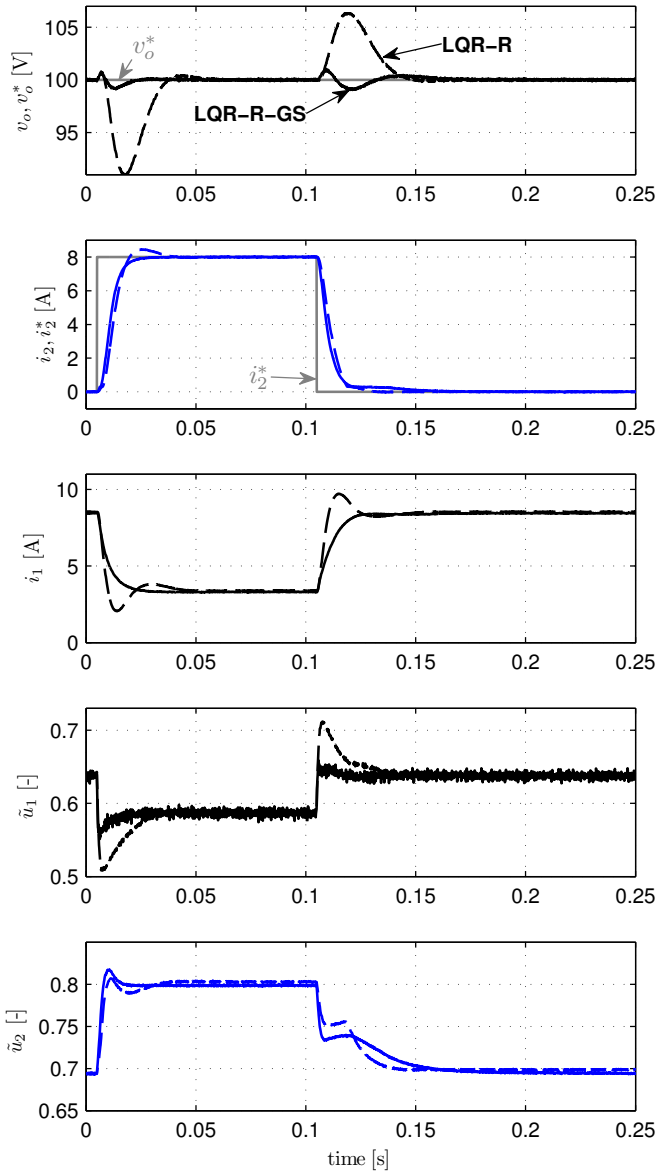

Figure 9.8: Experimental results of the LQR-R-GS (full line) and robust LQR without gain-scheduling (dashed line) controllers when excited with a step in i_2^*. The SC voltage is approaching the full discharge ($w_1 = 50\text{V}/32\text{V}$), but remains approximately constant throughout the test, as well as the load current $i_L = 3.5\text{A}$; the LQR-R (without gain-scheduling) was configured assuming a fully charged SCs.

9.4.3 Evaluation of the Gain-Scheduling

After establishing the benefits of the robust formulation, we will now assess the impact of gain-scheduling the DC-Link controller with the input voltages ratio ($w_1 = v_1/v_2$). To investigate this issue, the LQR-R-GS will be compared with the robust LQR without gain-scheduling, i.e., assuming a constant exogenous input $w_1 = \beta_e$. This latter controller, referred to as LQR-R, is characterized by a state feedback with the structure $\boldsymbol{K}_{LQR-R} = \begin{bmatrix}\boldsymbol{K}_{x,R} & \boldsymbol{K}_{\sigma,R}\end{bmatrix}$, where the fixed gains are extracted from Figure 9.5, i.e., $\boldsymbol{K}_{x,R} = \boldsymbol{K}_x(\beta_e)$, $\boldsymbol{K}_{\sigma,R} = \boldsymbol{K}_\sigma(\beta_e)$. Concerning the experiments conducted in this section, the LQR-R was configured assuming a fully charged SC ($\beta_e = 50\text{V}/48\text{V}$), and evaluated for the case where

the SC is close to the discharge point ($v_1/v_2 = 50\text{V}/32\text{V}$). The remaining conditions are similar to the ones used in the previous test.

The experimental results, present in Figure 9.8, demonstrate a superior transient performance of LQR-R-GS against the LQR-R: the voltage regulation error for the gain-scheduling controller is less than 2%, contrasting with the 8% peak error for the LQR-R, while minor differences are observed in SC current tracking. Further insight can be gain by analyzing these results from a power flow perspective. The non-scheduled controller is configured under the assumption that the SCs are fully charged with 48V; thus, when the 8A step is applied to i_2^*, the LQR-R takes for granted that the SC will supply $48 \times 8 = 384\text{W}$ (the model did not consider losses) and, as result, reduces the battery power in the same proportion. However, in practice, the SC has a lower voltage, 32V, resulting in power deliver of only $32 \times 8 = 256\text{W}$, i.e., much less than was expected. Meanwhile, the power reduction conducted in the battery is still done under the assumption of fully charged SCs, which generates a power shortage in the DC-Link, driving to the voltage undershoot that occurs with the LQR-R controller around $t \in [0.01\ \ 0.05]$s (a dual situation happens at $t \in [0.11\ \ 0.15]$s, but with an inverse consequence: excessive power in the DC-Link). Actually, in order to recover the voltage stability, the LQR-R must rely on integral action to eliminate the parametric mismatch, leading to the observed transient degradation. On the other hand, the scheduled controller benefits greatly from adapting the gains accordingly to the exogenous input, producing a much better power shift among the energy sources and reducing the power imbalances during transients.

9.4.4 Evaluation with Driving Cycles

Up until now, the experimental tests focused primarily on assessing the local transient performance of the LQR-R-GS for a limited set of operating points. In this section, we will move on to a global evaluation, covering a wider range of operating conditions and concentrating on a more realistic setting, based on driving cycles. Toward that aim, the load emulator was configured to take, from the DC-Link, a given amount of power, in accordance with some pre-defined cycles. Of the various driving cycles experimentally evaluated, two of them were selected and shown here. Firstly, a manual cycle, composed of 8 s acceleration, 25s of cruising at constant speed and 8s of deceleration (plus 8s of standstill), was built and applied to the experimental setup (see Figure 9.9(a)). Secondly, a re-scaled FTP75 cycle was tested, of which the results for the period between 136s and 341s are presented in Figure 9.9(b).

A second important modification carried out in these latter tests concerns the generation of the SCs' current/power setpoints, which is the responsibility of the VEM layer (see Figure 9.1). Accordingly, the SCs' current reference was generated using a frequency-based power allocation, mathematically defined as a high pass filter:

$$i_2^* = \frac{\tau_f s}{\tau_f s + 1} \frac{p_L}{v_2} \tag{9.36}$$

where s is the Laplace operator, τ_f is the time constant of the filter, and p_L the power requested by the vehicle. This filter-based power split, previously discussed in the literature [59, 74, 355], is motivated by the idea of using the SCs to satisfy the high frequency content of the DC-Link power p_L, while the average power is provided by the batteries. Even if the development of a real-time VEM algorithm is not the main subject of the current work, (9.36) represents a simple and practical way to generate the SC setpoint i_2^*, and also enable us to validate the LQR-R-GS controller in a more realistic setting.

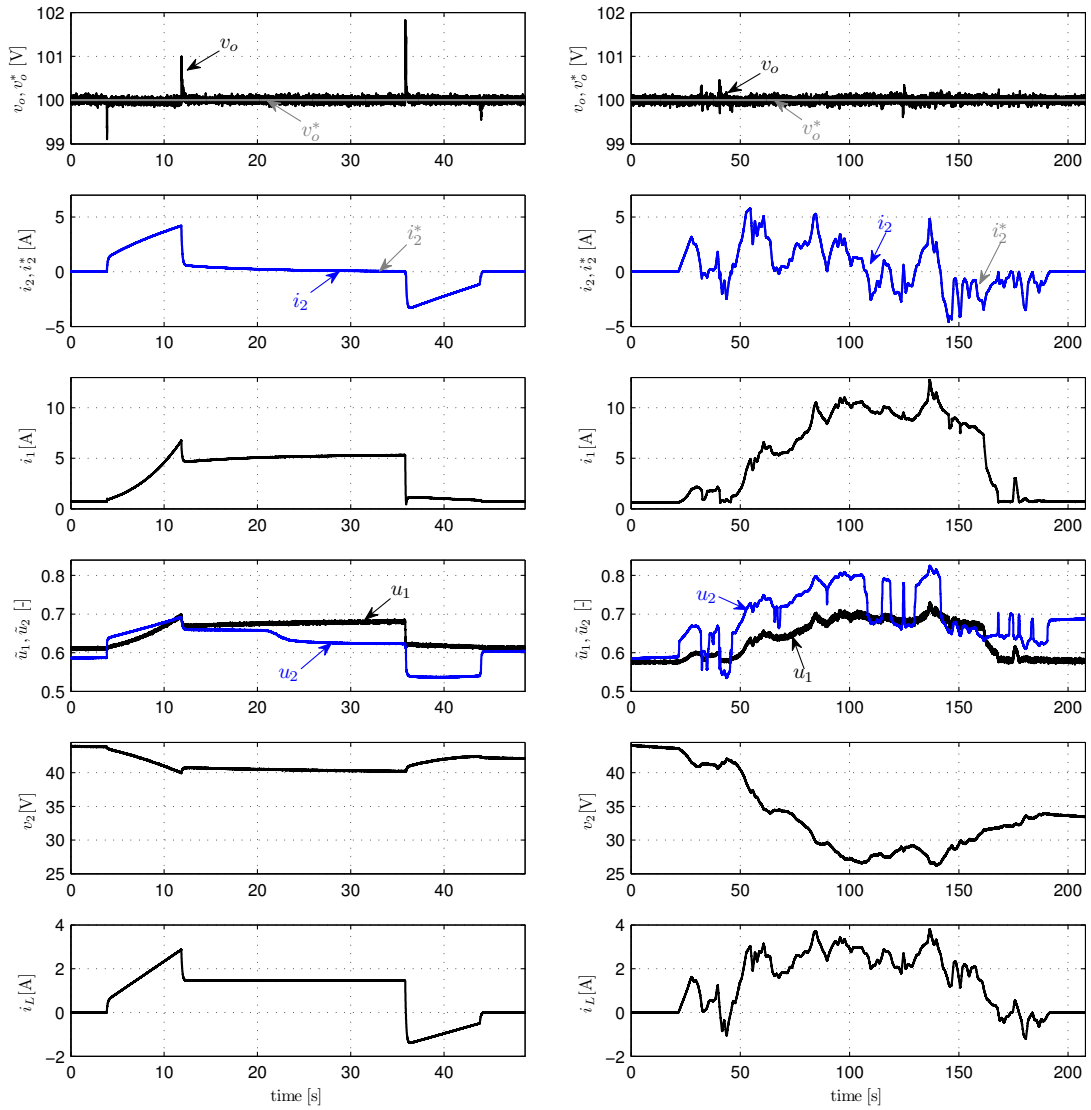

(a) manual cycle, comprising standstill, accelerating, cruising and decelerating operation modes

(b) FTP75 driving cycle (136 to 351s)

Figure 9.9: Experimental results for some selected driving cycles. The high pass filter (9.36), responsible for generating i_2^*, was configured with $\tau_f = 8s$ (manual cycle) and $\tau_f = 15s$ (FTP75 cycle).

Figure 9.9(a) and 9.9(b) depicts the final experimental results for the driving cycles mentioned above. In both cases, the DC Link output voltage v_o is accurately regulated, presenting maximum voltage errors below 2%, in the manual cycle, and 0.5% in the FTP75. Similarly, the tracking of the SC current displays negligible errors and, for time scales under consideration, i_2^* is almost overlapped with the measured current i_2. The FTP75 test also enables us to investigate the LQR-R-GS performance when subject to a considerable excursions in the SC voltage, which greatly affects the gain-scheduling variable $w_1 = v_1/v_2$. Despite facing a 50% variation in v_2 throughout the FTP75 test, the LQR-R-GS controller schedules its gains according to these variations and is able to keep a uniform performance in the DC-Link control task, independent of the SC state of charge. Finally, Figure 9.10

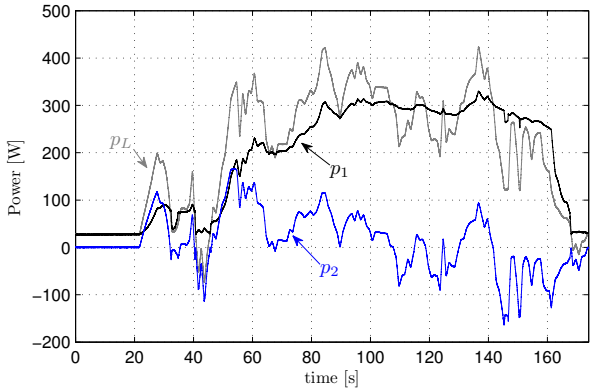

(a) FTP75 driving cycle (136 to 351s)

Figure 9.10: Experimental results of power provided by the battery ($p_1 = v_1 i_1$), SC ($p_2 = v_2 i_2$), and requested by the load ($p_L = (i_L + \frac{v_o}{R})v_o$) during the tests depicted in Figure 9.9.

depicts the power sharing between the sources throughout the FTP75 cycle. Analyzing these results, one can find that the batteries supplies the average power requested by the EV load (p_L), while the SCs covers the acceleration transients and high frequency content, which are in accordance with the expected behaviour for the frequency-based power splitting employed in the VEM layer.

9.5 Conclusion

In this chapter, a robust DC-Link controller for the hybridization of batteries and SCs, through an active parallel topology composed of two bidirectional boost DC-DC converters, was presented. The proposed approach relies on a LQR framework and is able to control, simultaneously and in a coordinated manner, the DC bus voltage and the SC current. This LQR setting was then extended to deal with two important issues in the DC-Link layer: model uncertainty and exogenous disturbances. Regarding the former issue, we notice that a convex uncertain model can be built for the power converters, enabling us to translate the robust LQR into a LMI-based optimization problem, easily solvable by numerical means. To handle the latter issue, the controller was gain-scheduled with the energy sources voltages, which, in view of the SCs' voltage variations, proved to be very effective. The implementation of the gain-scheduling technique also benefited greatly from the dimensionless representation of the DC-DC converters, which enabled us to handle the effect of the two energy sources voltages in the DC-Link controller using only a single scheduled variable, i.e., the ratio $w_1 = v_1/v_2$. Experimental validation, carried out in a reduced scale test bench, demonstrated the effectiveness of the proposed DC-Link controller. In particular, it was shown that, in comparison with two other methods (a nominal LQR and a robust LQR without gain-scheduling), the proposed controller offers a better transient response, especially in the DC-bus regulation task. Additional experimental evaluation with realistic driving cycles (FTP75) was also provided, confirming a satisfactory performance of the DC-link controller when subject to a wider range of operation conditions.

Chapter 10

Conclusion and Future Work

This work investigated control allocation (CA) techniques as an enabling tool for exploring the potential offered by redundant vehicle configurations. As a first application, the CA concept was employed in the design of a torque blending strategy for the EV braking system. This allocation strategy is based on an optimization framework and enables us to determine the optimal split between electric and friction brake torque, taking into account energy performance metrics, actuator constraints and different actuators' bandwidths. Besides the torque splitting strategy, the proposed design is also endowed with a wheel slip controller. This controller relies on an adaptive mechanism to deal with the parametric uncertainty in the tyre-road friction model, whereas the non-parametric uncertainty is tackled through the dead-zone modification. The effectiveness of the torque blending and the (adaptive) wheel slip controller were demonstrated through several CarSim simulations. From these results, it is worth mentioning that: *i*) despite the reduced control authority of the IWM, its high bandwidth was shown to be useful in the improvement of the transient response of the wheel slip controller; *ii*) we found that the IWM acceleration mode, an unusual operation mode during braking manoeuvres, can also be very helpful for stabilizing the tyre slip, e.g., by quickly decreasing the wheel moment in cases of sudden drops in the tyre-road friction; *iii*) similar to the previous point, for the cases when the EV energy storage is fully charged (thus no electric braking is possible) the acceleration torque is again helpful in maintaining the slip regulation with uniform performance, i.e., independent of the state of charge of the energy storage; and *iv*) the proposed torque blending, based on the CA technique, revealed tolerance to some types of IWM failures.

As discussed in Chapter 7, the CA methodology was also applied in the development of a motion controller for highly redundant EVs, composed of four IWMs and four-wheel steer. Since this configuration enables the individual control of the lateral and longitudinal force generated by each tyre, the CA is well-placed to take advantage of vehicle's redundancy, e.g., to minimise the friction use of the tyres. With these ideas in mind, two CA algorithms for the assignment of the tyres' forces were explored. The first method is, in its essence, an extension of the cascading generalized inverse; it builds on the idea that the angles of the tyres' forces can be fixed with the pseudo-inverse solution of the CA problem, while the force's magnitude can be obtained with the help of fast QP solvers. It was shown that this approach generates allocation results very quickly (less than 400 us on average); but, in general, does not cope well with unfeasible forces requests. To overcome this issue, an alternative approach, based on the linearization of the friction circle, was then developed. Despite requiring more computational effort, this second CA approach better

handles the unfeasible forces and still presents computational times suitable for real-time purposes (less than 1 ms on average). On top of the CA layer, we have also developed a motion controller for the path following problem of highly redundant EVs. This controller relies on a combination of robust feedback techniques with optimal (feedforward) control methods. The optimal feedforward term generates, through a convex optimal problem, the speed and force (ideal) setpoints that allow the vehicle to follow a given path in: *i*) minimum time, *ii*) minimum energy; or *iii*) a trade-off between the previous two. To cope with model uncertainties and disturbances, a robust feedback structure, based on a cascade of position-speed loops and tuned with the help of sliding modes techniques, was incorporated into the motion controller. Several simulations carried out in the high-fidelity CarSim simulator have demonstrated the effectiveness of the motion controller and the CA methods.

Chapter 4 revisited the wheel slip control problem within a pure robust setting. To this end, a sliding mode controller was proposed, which is capable of simultaneously handling parametric and non-parametric uncertainties, and features a chattering-free operation, thanks to the conditional integrator technique. One of the main issues with slip regulation (either robust or adaptive) consists of identifying the (slip) set-point that maximizes the tyre longitudinal friction force. Motivated by this issue, a practical linear parameterization (LP) was derived to approximate the nonlinear Burckhardt friction model, featuring good fitting capabilities and reduced complexity. The real-time identification of the LP was then performed with the help of a constrained version of the RLS method, which, due to the inclusion of prior knowledge on the model parameters, reduces the estimator variance. CarSim simulations and experimental tests, carried out in the uCar prototype, showed good slip regulation and robustness to disturbances of the sliding mode control, while the peak friction observer provided accurate estimates.

The present study also developed control strategies for the vehicles' actuators, with particular focus on the brake-by-wire (BBW) sub-system. More specifically, we have proposed a reduced model, based on an uncertain second-order system, for capturing the fundamental dynamics of the BBW actuator. Despite the approximation errors, this reduced model was proved to be a very useful representation for control design purposes. Another contribution of this study was the development of a new LP for the friction model, which is able to tolerate significant uncertainty in all friction parameters, most notably the Stribeck speed. Based on this LP and on the reduced-actuator model, we then designed an adaptive-robust controller to regulate the braking pressure of the BBW actuator. The advantages of this control law against other control approaches were investigated through a series of experimental tests, carried out in a test bench. It was concluded that in comparison with dither-based friction compensation, our controller can reduce the energy consumption of the BBW actuator by more than 40%, an important feature for sensitive energy applications, as is the case with the EVs. Further, we also verified that, in comparison with the nominal friction compensation technique, the proposed adaptive-robust controller copes better with parametric uncertainty in the friction model.

The second part of the present research investigated the energy management and control of EVs powered by batteries and SCs. This research was initiated by addressing the sizing problem of the hybrid storage system; that is, finding the number of battery and SCs cells capable of fulfilling the power and energy requirements specified for the vehicle. Toward that goal, a combined sizing and energy management optimisation problem was formulated and then solved with the help of a nonlinear numerical solver. The main conclusion was that, if the daily ranges of the EV are not very high (that is, inferior to 50

km in our study), then the SCs can be exploited to downsize the battery pack and reduce by 20% the overall installation costs of the storage unit. Alternatively, and depending on the trade-off preferences specified by the designer (i.e., cost vs energy efficiency), the hybrid storage unit can also be sized to decrease the energy losses by up to 7.8%. These results put in evidence the fact that the SC usage is very attractive for EVs where the range requirements are not very strict, such as neighborhood EVs or individual mobility solutions for city environments. Conversely, for general-purpose EVs, which are normally associated with higher autonomies, the use of a hybrid storage unit will, inevitably, lead to higher installations costs.

With regard to the control of the hybrid storage unit, our attention was concentrated on the DC-Link controller problem. The main contribution for this area was the development of a robust, gain-scheduled, LQR controller that is able to stabilise the DC-link output voltage and regulate the power flow among the energy sources, in spite of model uncertainties (e.g., load current) and exogenous disturbances, such as the variation in the SC voltage. Experimental results carried out in a reduced test bench demonstrated that, in comparison with two other controllers (non-robust and non-gain-scheduled versions), the proposed method significantly improves the transient response of the power converter, particularly the regulation task of the output voltage.

10.1 Outlook for Future Work

As far as the EV safety is concerned, it would be interesting, in future works, to pursue the following ideas:

- Despite the extensive experimental tests carried out in this work, it was not possible validate the torque blending strategy, discussed in Chapter 3, in a real EV. This validation should be tackled in future studies. Similarly, the experimental comparison between the wheel-slip controller based on sliding modes (Chapter 4) against the adaptive solution proposed in Chapter 3 represents another valuable task to be addressed in forthcoming studies.

- Another avenue that can be explored is an extension of the optimal LP, proposed in Chapter 5, to address lateral friction forces and, possibly, combined forces, i.e., with simultaneous longitudinal and lateral tyre slip. In particular, it would be interesting to explore this LP to identify, in real-time, the lateral friction coefficient and, perhaps, investigate its usefulness in estimating other difficult-to-measure variables, like the vehicle side-slip.

- Regarding the path following algorithm, Chapter 7 assumed that the desired path for the vehicle is known in advance, and the convex minimum-time problem can be solved "off-line". Future research should address the application/development of numerical solvers that can treat this convex problem in real-time and investigate more deeply the interaction between the (proposed) path following algorithm and the path planning layer. In addition, experimental validation of the path following algorithm in a real car would also be a valuable (and very challenging) task.

- The fail-safe operation of redundant EVs is another major research topic that deserves further attention. We believe that the CA-based framework, developed in this work (both for the torque blending as well as for the motion controller), is well

placed to cope with this problem; nonetheless, further research should be carried out to evaluate the CA performance under failure scenarios.

With regard to the second theme of the work, energy management in EVs with multiple sources, it would be interesting to pursue, in future work, the following research lines:

- Due to the non-convex constraints, the methodology employed in Chapter 8 to solve the combined sizing/energy management problem does not ensure global optimal solutions. One possibility to overcome this limitation is to use solvers based on the dynamic programming method; however, the high number of decision variables, together with the well-known high computational times, may hinder the use of such a tool for the sizing problem, particularly for longer driving cycles. Another promising alternative, worth investigating in the future, is the adoption of convexification techniques, which are becoming increasingly popular in the literature [112].

- It would also be pertinent to: *i*) incorporate in the sizing problem models for the battery stress, degradation, dynamics and thermal evolution; *ii*) investigate the effect of different battery technologies in the sizing results (i.e., NiMH+SC, Li-ion+SC, etc.); *iii*) perform further sensitive studies, e.g., how the sizing evolves for differing cell costs, charging costs, vehicle mass, etc; and *iv*) complement the batteries and SCs with a third energy source, such as fuel cells.

- The energy-management problem was developed, together with the sizing task, within a non-causal setting, i.e., it requires advance knowledge of the vehicle driving cycle to extract the optimal power allocation. Despite being useful for determining a benchmark solution, its applicability for the real-time energy management is limited. Consequently, in future works the on-line energy-management problem should also be addressed. For that purpose, preliminary work has been conducted already, formulated within the control allocation framework and fuzzy logic (see [322] for additional details). In the near future, we plan to extend this research into other directions, such as identifying the vehicle running conditions (e.g., urban driving, highway driving, etc.) and adapting the allocator priorities according to the identified running conditions.

- Finally, for the DC-Link control layer, it would be interesting to extend the robust control approach developed in Chapter 9 to a more efficient power-conversion structure, such as the interleaved configuration for DC/DC converters [317, 318].

Appendix A

Description of the uCar Prototype

This section presents the uCar Electric Vehicle prototype, initially developed by the We-MoveU project [356] and employed in this work to validate the wheel slip control and μ estimator algorithms. The main features of the uCar consist of the distributed powertrain architecture, composed of two electric motors coupled to the front wheels of the vehicle, and its control systems based on Field Programmable Gate Array (FPGA) technology. As illustrated in Figure A.1, this control chip builds around a reusable intellectual property core, named Propulsion Control Unit (PCU), containing motor control functions, algorithms for energy loss minimization and wheel-slip controls. The main motivations for developing the FPGA centric architecture have been cost and performance issues. These issues have led, in the last decade, to an increased penetration of the FPGAs in industry applications with multi-motor configurations, such as a multi-axis robotic manipulator arm [357], process control [358] and other power-electronics applications [359]. The main driving forces behind this paradigm shift are the parallel features and high calculation capacity offered by the FPGAs, which allow pure modularity, i.e., the control modules share the same physical unit, but run in a truly concurrent mode. In contrast, traditional software-based solutions, like Digital Signal Processors (DSPs), have some difficulties with implementing high bandwidth control for more than two motors simultaneously, a consequence of its sequential processing. Consequently, in EVs with multi-motor configurations, the concentration of all powertrain functionalities in a single FPGA-based module can improve system performance, since faster control loops are achieved and several DSPs' control units can be replaced by a single FPGA. The interested reader is referred to [360] for additional details regarding the FPGAs' advantages in EVs with distributed propulsion.

A.1 Propulsion Control Unit (PCU)

For each driving wheel of the uCar EV, an individual PCU module is associated, which independently regulates the motor torque and flux. To reach this aim, the PCU is composed by 3 sub-modules: *i*) motor-control; *ii*) loss minimization; *iii*) traction control and μ estimator. The PCU used in this work targets the control of induction motors (IM), since they offer low cost, high reliability and simple manufacture. Moreover, it is worth mentioning that the FPGA implementation can be easily reconfigured to handle diverse types of EVs configurations (with 1, 2 or 4 electric motors), by changing the number of PCU instantiations. To complement the PCU, a processor is also embedded in the FPGA to handle the communications and datalogging tasks, perform the system managing, i.e.,

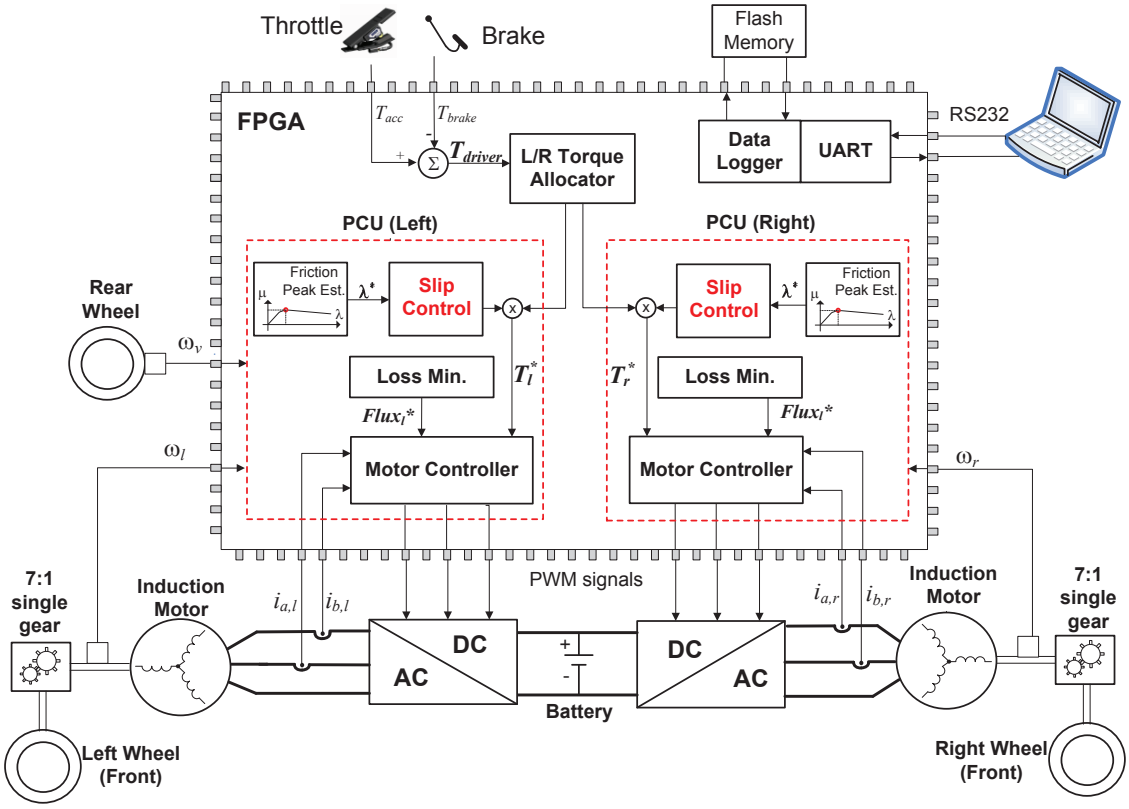

Figure A.1: Block diagram of the powertrain controller employed in the experimental EV prototype; the Propulsion Control Unit (PCU), a reusable module, addresses the main control requirements (torque and flux control, energy loss minimization and wheel slip control) of each electric motor in the powertrain.

a state machine to handle the various operation modes in the vehicle (idle, run, stop, fail, charging, etc...), and execute slow control loops.

A brief overview of each one of the PCU sub-modules will be described in the next sections.

A.1.1 Motor Control

The classic indirect Field Oriented Control (iFOC) theory, with the current controllers formulated in the synchronous frame (dq coordinates) [361, 362], was the strategy elected to design the motor control (MC) sub-module. As can be seen in Figure A.2, the MC starts by translating the stator current i_a and i_b to a coordinate system synchronous with the rotor flux vector, using, for this purpose, the well-known Clarke and Park transformations. These currents are then regulated independently by two linear Proportional + Integral controllers: the first indirectly controls the motor torque (i_q), while the second affects the motor flux (i_d). The outputs of the current controllers, specifying the desired motor voltage in Cartesian coordinates (m_q, m_d), are then converted to the polar representation ($|m|$, θ_{dq}) using the CORDIC (COordinate Rotation DIgital Computer [363]) algorithm. The final step is to transform the reference voltage to the stationary reference frame ($|m|$, θ) and apply it to the Space Vector Pulse-Width Modulator [364], generating the duty

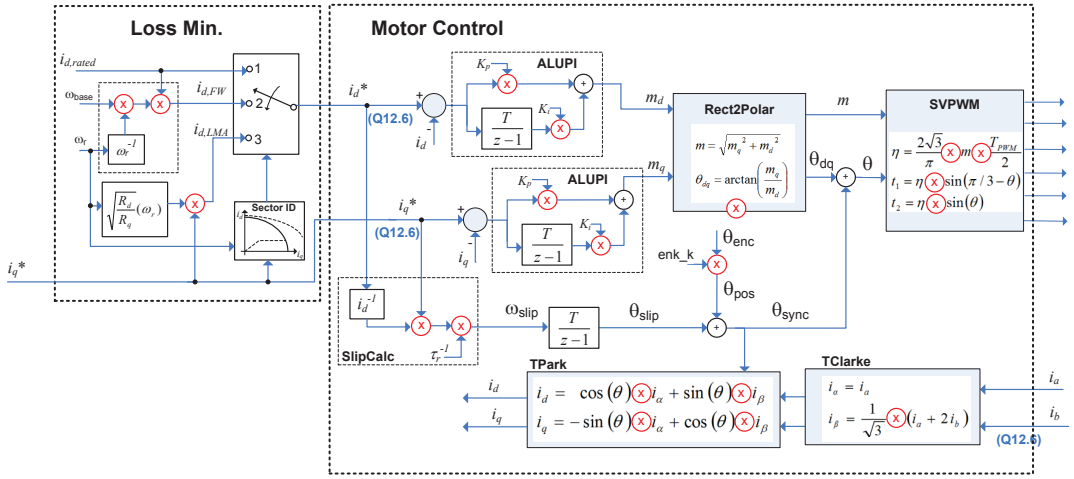

Figure A.2: Illustration of the main mathematical operations carried out by Motor Control and the Loss Minimization Algorithm (LMA) inside the PCU (Propulsion Control Unit).

cycles for the DC/AC inverter. Additional modules for motor slip calculation and encoder angle normalization are also included in the MC.

Within the PCU, the MC is the most computational intensive block, demanding considerable computational resources, proportional to the number of motors in the powertrain, and reduced execution times (tens of microseconds). Among these resources, the multiplier is one of the most requested operators and it is, simultaneously, a scarce asset in the FPGA. For instance, considering an EV topology with 2 electric motors, which is the configuration used in our prototype, each MC would need 17 multipliers (see Figure A.2), or 34 multipliers for the 2 MC. For such reason, to avoid the use of costly FPGAs, special care must be taken when implementing the motor control block. As a result, in order to minimize the number of resources in the FPGA, and also the overall cost, an efficient computational block was employed, which permits time-sharing of the available multipliers without compromising the controller bandwidth (see [365, 366] for further details). It is also interesting to note that, the MC blocks (i.e., PI controllers, coordinates transformations, SVPWMs) can be easily reconfigured to control other types of motors frequently employed in the EV applications, such as permanent magnet and brushless DC motors, a feature explored in [356].

A.1.2 Motor Efficiency

For battery based EVs, the powertrain energy efficiency, and in particular the motor efficiency, is a critical factor for maximizing the "range per charge" performance metric. It is a well-known fact that the IMs have lower power density and, more important, are less efficient that the PM based motors [13]. On the other hand, they also offer low cost and high reliability, which lead us to design our powertrains around this type of motor. To partially attenuate the energy efficiency drawback, the traditional IM constant flux + field weakening method was replaced with a Loss Minimization Algorithm (LMA), proposed in [319]. The LMA belongs to the class of real-time model-base loss minimization algorithm [368], and uses the solution of a parameterized IM loss model to select the most efficient flux set-point for each motor operating point (speed and torque). Albeit the LMA is sensitive to parameter uncertainty, its implementation is relatively simple and suitable

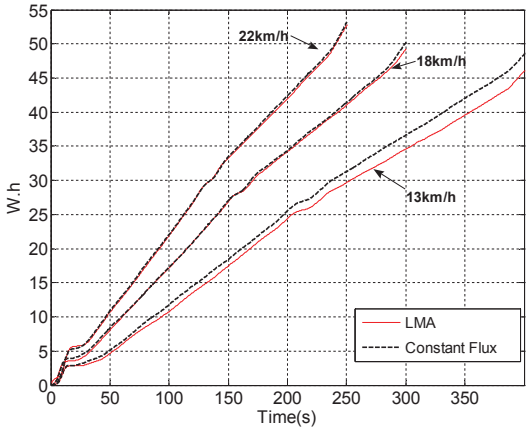

Figure A.3: Energy consumption of the EV with LMA algorithm against the traditional constant flux. The vehicle is running in a plain road, with constant speed and the IM is operating in the constant torque region (additional details can be found on [367]).

for real-time operation, offers a good transient behaviour and the experiments carried out in our prototypes show that considerable energy saving are possible. To illustrate this last point, consider the energy consumption of the EV prototype, depicted in Figure A.3, obtained in a plain road with constant-speed. It is clear that the most favourable operating point for the LMA is at low speeds with low torque requests, where energy saving up to 15% is achieved (see [365, 367] for additional details). On the contrary, for higher speeds, the LMA is less effective because the load torque increase, mainly due to the aerodynamic drag, which obliges the application a flux closer to the rated value, thus less flexibility is available for optimal flux selection. Even if the LMA will never elevate the IM energy efficiency to the PM levels, we believe that the LMA (or other flux adaption method) is a must-have for any energy efficient IM based EV, and have a beneficial effect in urban driving, where the speeds and loads are lower and more freedom for the optimal flux adaption is available.

A.1.3 Safety Systems

Active safety systems are of paramount importance in modern transportation applications and represent an unavoidable functionality to reduce and prevent road accidents [40]. Therefore, the powertrain control of EVs must address this concern by offering driving aid mechanisms to mitigate the effects of a loss of the vehicle longitudinal and/or lateral controllability. In order to improve the EV safety, the PCU includes a wheel sip controller and an estimator for the tyre-road peak friction (μ), whose details were already discussed in Chapter 4 and 5.

A.2 The uCar Prototype

As proof of concept for the PCU, a multi-motor EV prototype was built (see Figure A.4), featuring two, low voltage, 2.2 kW three-phase cage induction motors (26V, Δ , 63Arms and 1410 rpm), coupled to the front wheels through a single-gear transmission (fixed ratio

(a) Vehicle

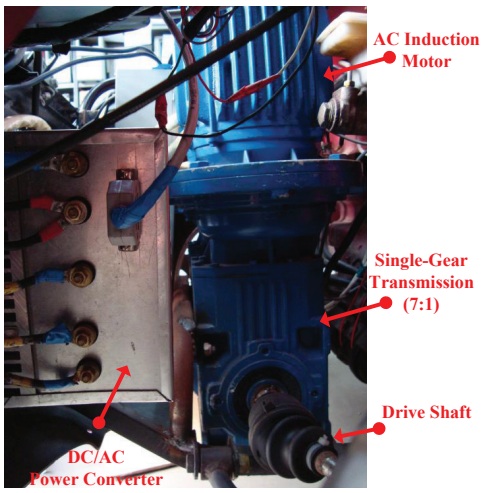

(b) Powertrain for each front wheel

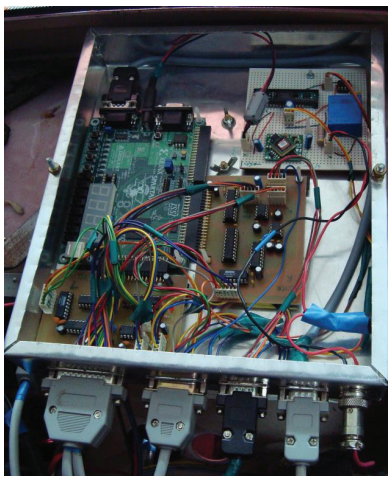

(c) FPGA control system

Figure A.4: The uCar Electric Vehicle prototype, featuring two low voltage induction motors coupled to the front wheels and a single FPGA control system.

of $7:1$). Without passengers, the vehicle weighs 600kg (45% front, 55% rear and wheelbase of 1.73m), and is powered by lead-acid batteries ($48V$, 5.28kWh). As shown in Figure A.1, all the EV control functionalities are implemented in a low cost FPGA XC3S1000 [369], including two PCU's for each motor in the powertrain.

References

[1] European Environment Agency, "Passenger car ownership in the EEA," *http://www.eea.europa.eu/data-and-maps/figures/passenger-car-ownership-in-the-eea*, 2009.

[2] G. Genta and L. Morello, *The Automotive Chassis, Volume 1: Components Design.* Springer, 2009.

[3] ——, *The Automotive Chassis, Volume 2: System Design.* Springer, 2009.

[4] Eurostat, *Energy, Transport and Environment Indicators.* European Union, 2012.

[5] BP, "BP statistical review of world energy," 2011.

[6] European Environment Agency, "Monitoring the co2 emissions from new passenger cars in the eu: summary of data for 2011," 2012.

[7] K. B. Wipke, M. R. Cuddy, and S. D. Burch, "Advisor 2.1: a user-friendly advanced powertrain simulation using a combined backward/forward approach," *IEEE Transactions on Vehicular Technology*, vol. 48, no. 6, pp. 1751–1761, 1999.

[8] C. C. Chan, A. Bouscayrol, and K. Chen, "Electric, hybrid, and fuel-cell vehicles: Architectures and modeling," *IEEE Transactions on Vehicular Technology*, vol. 59, no. 2, pp. 589–598, 2010.

[9] M. Ehsani, Y. Gao, S. E. Gay, and A. Emadi, *Modern electric, hybrid electric, and fuel cell vehicles: fundamentals, theory, and design*, 2nd ed. CRC Press, 2010.

[10] C. C. Chan, "The state of the art of electric and hybrid vehicles," *Proceedings of the IEEE*, vol. 90, no. 2, pp. 247–275, 2002.

[11] J. A. P. Lopes, F. J. Soares, and P. M. R. Almeida, "Integration of electric vehicles in the electric power system," *Proceedings of the IEEE*, vol. 99, no. 1, pp. 168–183, 2011.

[12] G. Yimin, C. Liang, and M. Ehsani, "Design and control principles of hybrid braking system for ev, hev and fcv," in *IEEE Vehicle Power and Propulsion Conference (VPPC)*, 2007.

[13] Z. Q. Zhu and D. Howe, "Electrical machines and drives for electric, hybrid, and fuel cell vehicles," *Proceedings of the IEEE*, vol. 95, no. 4, pp. 746–765, 2007.

[14] S. Murata, "Innovation by in-wheel-motor drive unit," in *10th International Symposium on Advanced Vehicle Control (AVEC)*, 2010.

[15] Y. Hori, "Future vehicle driven by electricity and control - research on four-wheel-motored uot electric march ii," *IEEE Transactions on Industrial Electronics*, vol. 51, no. 5, pp. 954–962, 2004.

[16] D. J. Yin, S. Oh, and Y. Hori, "A novel traction control for ev based on maximum transmissible torque estimation," *IEEE Transactions on Industrial Electronics*, vol. 56, no. 6, pp. 2086–2094, 2009.

[17] R. de Castro, R. E. Araujo, and D. Freitas, "A single motion chip for multi-motor ev control," in *10th International Symposium on Advanced Vehicle Control (AVEC)*, 2010.

[18] L. Pinto, S. Aldworth, M. Watkinson, P. Jeary, and M. Franco-Jorge, "Advanced yaw motion control of a hybrid vehicle using twin rear electric motors," in *10th International Symposium on Advanced Vehicle Control (AVEC)*, 2010.

[19] K. Jeongmin, P. Chiman, H. Sungho, Y. Hori, and K. Hyunsoo, "Control algorithm for an independent motor-drive vehicle," *IEEE Transactions on Vehicular Technology*, vol. 59, no. 7, pp. 3213–3222, 2010.

[20] "Electric raceabout," *http://www.raceabout.fi/*, 2011.

[21] R. Wang, Y. Chen, D. Feng, X. Huang, and J. Wang, "Development and performance characterization of an electric ground vehicle with independently actuated in-wheel motors," *Journal of Power Sources*, vol. 196, no. 8, pp. 3962–3971, 2011.

[22] K. Kiyomoto, T. Hidetoshi, S. Hiroshi, and Y. Hiroichi, "Advancd redundancy technology for a drive system using in-wheel motors," *World Electric Vehicle Journal*, vol. 1, 2007.

[23] H. Fujimoto and Y. Yamauchi, "Advanced motion control of electric vehicle based on lateral force observer with active steering," in *IEEE International Symposium on Industrial Electronics*, 2010.

[24] J. Brembeck, L. M. Ho, A. Schaub, C. Satzger, J. Tobolar, J. Bals, and G. Hirzinger, "Romo - the robotic electric vehicle," in *22nd International Symposium on Dynamics of Vehicles on Roads and Tracks*, 2011.

[25] P. He, Y. Hori, M. Kamachi, K. Walters, and H. Yoshida, "Future motion control to be realized by in-wheel motored electric vehicle," in *31st Annual Conference of IEEE Industrial Electronics Society*, 2005.

[26] J. Voelcker, "Top 10 tech cars [hybrid electric vehicles]," *IEEE Spectrum*, vol. 42, no. 3, pp. 22–30, 2005.

[27] P. E. Ross and D. Schneider, "Top ten tech cars - 2010," *IEEE Spectrum*, vol. 47, no. 4, pp. 28–58, 2010.

[28] J. Rauh and D. Ammon, "System dynamics of electrified vehicles: some facts, thoughts, and challenges," *Vehicle System Dynamics*, vol. 49, no. 7, pp. 1005–1020, 2011.

[29] "Venturi volage," *http://www.venturi.fr/en/Range/Volage/Technical-specifications*, 2011.

[30] J. Deur, D. Pavković, G. Burgio, and D. Hrovat, "A model-based traction control strategy non-reliant on wheel slip information," *Vehicle System Dynamics*, vol. 49, no. 8, pp. 1245–1265, 2011.

[31] T. Weiskircher, J. E. Diang, and S. Muller, "Control performance and energy consumption of an electric vehicle with single-wheel drives and steer-by-wire," in *22nd International Symposium on Dynamics of Vehicles on Roads and Tracks*, 2011.

[32] R. Sampaio, A. Hernandes, V. Fernandes, M. Becker, and A. Siqueira, "A new control architecture for robust controllers in rear electric traction passenger hevs," *IEEE Transactions on Vehicular Technology*, vol. 61, no. 8, pp. 3441–3453, 2012.

[33] N. Mutoh, Y. Hayano, H. Yahagi, and K. Takita, "Electric braking control methods for electric vehicles with independently driven front and rear wheels," *IEEE Transactions on Industrial Electronics*, vol. 54, no. 2, pp. 1168–1176, 2007.

[34] N. Mutoh, T. Kazama, and K. Takita, "Driving characteristics of an electric vehicle system with independently driven front and rear wheels," *IEEE Transactions on Industrial Electronics*, vol. 53, no. 3, pp. 803–813, 2006.

[35] C. Geng, L. Mostefai, M. Denai, and Y. Hori, "Direct yaw-moment control of an in-wheel-motored electric vehicle based on body slip angle fuzzy observer," *IEEE Transactions on Industrial Electronics*, vol. 56, no. 5, pp. 1411–1419, 2009.

[36] H. Shimizu, J. Harada, C. Bland, K. Kawakami, and L. Chan, "Advanced concepts in electric vehicle design," *IEEE Transactions on Industrial Electronics*, vol. 44, no. 1, pp. 14–18, 1997.

[37] J. S. Martinez, D. Hissel, M. C. Pera, and M. Amiet, "Practical control structure and energy management of a testbed hybrid electric vehicle," *IEEE Transactions on Vehicular Technology*, vol. 60, no. 9, pp. 4139–4152, 2011.

[38] R. Wang and J. Wang, "Fault-tolerant control with active fault diagnosis for four-wheel independently driven electric ground vehicles," *IEEE Transactions on Vehicular Technology*, vol. 60, no. 9, pp. 4276–4287, 2011.

[39] M. Anderson and D. Harty, "Unsprung mass with in-wheel motors - myths and realities," in *10th International Symposium on Advanced Vehicle Control (AVEC)*, 2010.

[40] A. T. van Zanten, "Evolution of electronic control systems for improving the vehicle dynamic behavior," in *Proceedings of the International Symposium on Advanced Vehicle Control (AVEC)*, 2002, pp. 7–15.

[41] S. A. Ferguson, "The effectiveness of electronic stability control in reducing real-world crashes: A literature review," *Traffic Injury Prevention*, vol. 8, no. 4, pp. 329–338, 2007.

[42] D. A. Crolla and D. Cao, "The impact of electric and hybrid powertrains on vehicle dynamics and control systems," in *22nd International Symposium on Dynamics of Vehicles on Roads and Tracks*, 2011.

[43] F. Wang and B. Zhuo, "Regenerative braking strategy for hybrid electric vehicles based on regenerative torque optimization control," *Proceedings of the Institution of Mechanical Engineers, Part D: Journal of Automobile Engineering*, vol. 222, no. 4, pp. 499–513, 2008.

[44] S. Horiuchi, "Evaluation of chassis control method through optimization based controllability region computation," in *22nd International Symposium on Dynamics of Vehicles on Roads and Tracks*, 2011.

[45] R. Isermann, R. Schwarz, and S. Stolzl, "Fault-tolerant drive-by-wire systems," *IEEE Control Systems Magazine*, vol. 22, no. 5, pp. 64–81, 2002.

[46] Siemens VDO, "Making a case for in-wheel systems: the ecorner project," in *Green Car Congress*, 2006.

[47] R. Gashi and D. Laurent, "Vehicle ground connection comprising a wheel and a suspension"," in *Patent US2008/0100020*, 2008.

[48] S.-K. Chen, N. Moshchuk, F. Nardi, and J. Ryu, "Vehicle rollover avoidance," *IEEE Control Systems Magazine*, vol. 30, no. 4, pp. 70–85, 2010.

[49] S. Sato and H. Fujimoto, "Proposal of pitching control method based on slip-ratio control for electric vehicle," in *34th Annual Conference of IEEE Industrial Electronics*, 2008, pp. 2823–2828.

[50] C. Poussot-Vassal, O. Sename, L. Dugard, P. Gáspár, Z. Szabó, and J. Bokor, "Attitude and handling improvements through gain-scheduled suspensions and brakes control," *Control Engineering Practice*, vol. 19, no. 3, pp. 252–263, 2011.

[51] J. Andreasson and T. Bünte, "Global chassis control based on inverse vehicle dynamics models," *Vehicle System Dynamics: International Journal of Vehicle Mechanics and Mobility*, vol. 44, no. 1 supp 1, pp. 321 – 328, 2006.

[52] M. Jonasson, J. Andreasson, B. Jacobson, and A. S. Trigell, "Global force potential of over-actuated vehicles," *Vehicle System Dynamics: International Journal of Vehicle Mechanics and Mobility*, vol. 48, no. 9, pp. 983 – 998, 2010.

[53] J. Tjonnas and T. A. Johansen, "Stabilization of automotive vehicles using active steering and adaptive brake control allocation," *IEEE Transactions on Control Systems Technology*, vol. 18, no. 3, pp. 545 – 558, 2010.

[54] R. Rajamani, N. Piyabongkarn, J. Lew, K. Yi, and G. Phanomchoeng, "Tire-road friction-coefficient estimation," *IEEE Control Systems Magazine*, vol. 30, no. 4, pp. 54–69, 2010.

[55] V. Srinivasan, "Batteries for vehicular applications," *Lawrence Berkeley National Lab*, 2008.

[56] L. Guzzella and A. Sciarretta, *Vehicle Propulsion Systems: Introduction to Modeling and Optimization.* Springer Verlag, 2007.

[57] S. Vazquez, S. M. Lukic, E. Galvan, L. G. Franquelo, and J. M. Carrasco, "Energy storage systems for transport and grid applications," *IEEE Transactions on Industrial Electronics*, vol. 57, no. 12, pp. 3881–3895, 2010.

[58] A. Khaligh and Z. Li, "Battery, ultracapacitor, fuel cell, and hybrid energy storage systems for electric, hybrid electric, fuel cell, and plug-in hybrid electric vehicles: State of the art," *IEEE Transactions on Vehicular Technology*, vol. 59, no. 6, pp. 2806–2814, 2010.

[59] T. Azib, O. Bethoux, G. Remy, C. Marchand, and E. Berthelot, "An innovative control strategy of a single converter for hybrid fuel cell/supercapacitor power source," *IEEE Transactions on Industrial Electronics*, vol. 57, no. 12, pp. 4024–4031, 2010.

[60] J. Dixon, I. Nakashima, E. F. Arcos, and M. Ortuzar, "Electric vehicle using a combination of ultracapacitors and zebra battery," *IEEE Transactions on Industrial Electronics*, vol. 57, no. 3, pp. 943–949, 2010.

[61] M. B. Camara, H. Gualous, F. Gustin, and A. Berthon, "Design and new control of DC/DC converters to share energy between supercapacitors and batteries in hybrid vehicles," *IEEE Transactions on Vehicular Technology*, vol. 57, no. 5, pp. 2721–2735, 2008.

[62] M. B. Camara, H. Gualous, F. Gustin, A. Berthon, and B. Dakyo, "Dc/dc converter design for supercapacitor and battery power management in hybrid vehicle applications-polynomial control strategy," *IEEE Transactions on Industrial Electronics*, vol. 57, no. 2, pp. 587–597, 2010.

[63] P. Thounthong, V. Chunkag, P. Sethakul, B. Davat, and M. Hinaje, "Comparative study of fuel-cell vehicle hybridization with battery or supercapacitor storage device," *IEEE Transactions on Vehicular Technology*, vol. 58, no. 8, pp. 3892–3904, 2009.

[64] N. Woonki, P. Taesik, K. Taehyung, and K. Sangshin, "Light fuel-cell hybrid electric vehicles based on predictive controllers," *IEEE Transactions on Vehicular Technology*, vol. 60, no. 1, pp. 89–97, 2011.

[65] A. Kuperman and I. Aharon, "Battery–ultracapacitor hybrids for pulsed current loads: A review," *Renewable and Sustainable Energy Reviews*, vol. 15, no. 2, pp. 981–992, 2011.

[66] M. Ortuzar, J. Moreno, and J. Dixon, "Ultracapacitor-based auxiliary energy system for an electric vehicle: Implementation and evaluation," *IEEE Transactions on Industrial Electronics*, vol. 54, no. 4, pp. 2147–2156, 2007.

[67] Z. Li, O. Onar, A. Khaligh, and E. Schaltz, "Design, control, and power management of a battery/ultra-capacitor hybrid system for small electric vehicles," in *Proc. SAE World Congr. Exh.*, 2009.

[68] L. Solero, A. Lidozzi, and J. A. Pomilio, "Design of multiple-input power converter for hybrid vehicles," *IEEE Transactions on Power Electronics*, vol. 20, no. 5, pp. 1007–1016, 2005.

[69] A. A. Ferreira, J. A. Pomilio, G. Spiazzi, and L. de Araujo Silva, "Energy management fuzzy logic supervisory for electric vehicle power supplies system," *IEEE Transactions on Power Electronics*, vol. 23, no. 1, pp. 107–115, 2008.

[70] S. M. Lukic, C. Jian, R. C. Bansal, F. Rodriguez, and A. Emadi, "Energy storage systems for automotive applications," *IEEE Transactions on Industrial Electronics*, vol. 55, no. 6, pp. 2258–2267, 2008.

[71] O. Sundstrom, D. Ambuhl, and L. Guzzella, "On implementation of dynamic programming for optimal control problems with final state constraints," *Oil Gas Sci. Technol. – Rev. IFP*, vol. 65, no. 1, pp. 91–102, 2010.

[72] C. Romaus, K. Gathmann, and J. Böcker, "Optimal energy management for a hybrid energy storage system for evs based on stochastic dynamic programming," *IEEE Vehicle Power and Propulsion Conference*, 2010.

[73] J. Moreno, M. E. Ortuzar, and J. W. Dixon, "Energy-management system for a hybrid electric vehicle, using ultracapacitors and neural networks," *IEEE Transactions on Industrial Electronics*, vol. 53, no. 2, pp. 614–623, 2006.

[74] A. L. Allegre, A. Bouscayrol, and R. Trigui, "Influence of control strategies on battery/supercapacitor hybrid energy storage systems for traction applications," in *IEEE Vehicle Power and Propulsion Conference (VPPC)*, 2009, pp. 213–220.

[75] J. M. Wang and R. G. Longoria, "Coordinated and reconfigurable vehicle dynamics control," *IEEE Transactions on Control Systems Technology*, vol. 17, no. 3, pp. 723–732, 2009.

[76] H. Chou and B. D'andréa-Novel, "Global vehicle control using differential braking torques and active suspension forces," *Vehicle System Dynamics: International Journal of Vehicle Mechanics and Mobility*, vol. 43, no. 4, pp. 261 – 284, 2005.

[77] M. Montazeri-Gh and M. Soleymani, "Investigation of the energy regeneration of active suspension system in hybrid electric vehicles," *IEEE Transactions on Industrial Electronics*, vol. 57, no. 3, pp. 918–925, 2010.

[78] B. Schofield, "Model-based vehicle dynamics control for active safety," PhD Thesis, Department of Automatic Control, Lund University, Sweden, 2008.

[79] Y. Shibahata, "Progress and future direction of chassis control technology," *Annual Reviews in Control*, vol. 29, no. 1, pp. 151–158, 2005.

[80] J. Tjønnås, "Nonlinear and adaptive dynamic control allocation," PhD Thesis, Norwegian University of Science and Technology, 2008.

[81] W. C. Durham, "Constrained control allocation," *Journal of Guidance Control and Dynamics*, vol. 16, no. 4, pp. 717–725, 1993.

[82] M. Bodson, "Evaluation of optimization methods for control allocation," *Journal of Guidance, Control, and Dynamics*, vol. 25, no. 4, pp. 703–711, 2002.

[83] D. Enns, "Control allocation approaches," in *AIAA Guidance, Navigation, and Control Conference and Exhibit*, 1998, pp. 98–108.

[84] M. W. Oppenheimer, D. B. Doman, and M. A. Bolender, "Control allocation for over-actuated systems," in *14th Mediterranean Conference on Control and Automation*, 2006, pp. 1–6.

[85] T. I. Fossen, T. A. Johansen, and T. Perez, *A Survey of Control Allocation Methods for Underwater Vehicles*. Vienna: I-Tech Education and Publishing, 2009, ch. 7.

[86] J. H. Plumlee, D. M. Bevly, and A. S. Hodel, "Control allocation in ground vehicles," *International Journal of Vehicle Design*, vol. 42, no. 3-4, pp. 215–243, 2006.

[87] A. Ben-Israel and T. Greville, *Generalized inverses: Theory and applications*. Springer Verlag, 2003.

[88] J. A. M. Petersen and M. Bodson, "Constrained quadratic programming techniques for control allocation," *IEEE Transactions on Control Systems Technology*, vol. 14, no. 1, pp. 91–98, 2006.

[89] T. A. Johansen, T. I. Fossen, and P. Tondel, "Efficient optimal constrained control allocation via multiparametric programming," *Journal of Guidance Control and Dynamics*, vol. 28, no. 3, pp. 506–515, 2005.

[90] E. Ruth, O. N. Smogeli, T. Perez, and A. J. Sorensen, "Antispin thrust allocation for marine vessels," *IEEE Transactions on Control Systems Technology*, vol. 17, no. 6, pp. 1257–1269, 2009.

[91] O. Harkegard, "Backstepping and control allocation with applications to flight control," PhD Thesis, Linkoping University, 2003.

[92] I. Hwang, S. Kim, Y. Kim, and C. E. Seah, "A survey of fault detection, isolation, and reconfiguration methods," *IEEE Transactions on Control Systems Technology*, vol. 18, no. 3, pp. 636–653, 2010.

[93] J. M. Buffington and D. F. Enns, "Lyapunov stability analysis of daisy chain control allocation," *Journal of Guidance Control and Dynamics*, vol. 19, no. 6, pp. 1226–1230, 1996.

[94] O. Harkegard, "Dynamic control allocation using constrained quadratic programming," *Journal of Guidance, Control and Dynamics*, vol. 27, no. 6, pp. 1028–1034, 2004.

[95] M. W. Oppenheimer and D. B. Doman, "Methods for compensating for control allocator and actuator interactions," *Journal of Guidance Control and Dynamics*, vol. 27, no. 5, pp. 922–927, 2004.

[96] H. Khalil, *Nonlinear Systems*, 3rd ed. Prentice Hall, 2002.

[97] J. M. Buffington, D. F. Enns, and A. R. Teel, "Control allocation and zero dynamics," *Journal of Guidance Control and Dynamics*, vol. 21, no. 3, pp. 458–464, 1998.

[98] K. A. Bordignon, "Constrained control allocation for systems with redundant control effectors," PhD Thesis, Virginia Polytechnic Institute and State University, 1996.

[99] T. A. Johansen, "Optimizing nonlinear control allocation," in *43rd IEEE Conference on Decision and Control*, vol. 4, 2004, pp. 3435–3440 Vol.4.

[100] K. A. Bordignon and W. C. Durham, "Closed-form solutions to constrained control allocation problem," *Journal of Guidance Control and Dynamics*, vol. 18, no. 5, pp. 1000–1007, 1995.

[101] D. G. Luenberger, *Optimization by vector space methods.* Wiley-IEEE, 1969.

[102] D. G. Luenberger and Y. Ye, *Linear and nonlinear programming, 3rd Ed.* Springer, 2008.

[103] S. A. Snell, D. F. Enns, and W. L. Garrard, "Nonlinear inversion flight control for a supermaneuverable aircraft," *Journal of Guidance Control and Dynamics*, vol. 15, no. 4, pp. 976–984, 1992.

[104] O. Mokhiamar and M. Abe, "How the four wheels should share forces in an optimum cooperative chassis control," *Control Engineering Practice*, vol. 14, no. 3, pp. 295–304, 2006.

[105] H. Alwi, C. Edwards, O. Stroosma, and J. A. Mulder, "Fault tolerant sliding mode control design with piloted simulator evaluation," *Journal of Guidance Control and Dynamics*, vol. 31, no. 5, pp. 1186–1201, 2008.

[106] J. C. Virnig and D. S. Bodden, "Multivariable control allocation and control law conditioning when control efectors limit," *AIAA Guidance, Navigation, and Control Conference and Exhibit, Scottsdale*, 1994.

[107] K. Bordignon and J. Bessolo, "Control allocation for the x-35b," in *AIAA Guidance, Navigation, and Control Conference and Exhibit*, 2002.

[108] J. Y. Jin, "Modified pseudoinverse redistribution methods for redundant controls allocation," *Journal of Guidance, Control and Dynamics*, vol. 28, no. 5, pp. 1076–1079, 2005.

[109] W. C. Durham, "Constrained control allocation - 3-moment problem," *Journal of Guidance Control and Dynamics*, vol. 17, no. 2, pp. 330–336, 1994.

[110] Y. Ikeda and M. Hood, "An application of l1 optimization to control allocation," *AIAA Guidance, Navigation, and Control Conference and Exhibit*, 2000.

[111] J. F. Buffington, "Modular control law design for the innovative control effectors (ice) tailless fighter aircraft configuration," in *U.S. Air Force Research Lab. Rept.*, 1999.

[112] S. Boyd and L. Vandenberghe, *Convex Optimization.* Cambridge University Press, 2004.

[113] A. Bjorck, *Numerical methods for least squares problems.* SIAM, 1996.

[114] T. A. Johansen, T. I. Fossen, and S. P. Berge, "Constrained nonlinear control allocation with singularity avoidance using sequential quadratic programming," *IEEE Transactions on Control Systems Technology*, vol. 12, no. 1, pp. 211–216, 2004.

[115] T. A. Johansen, T. P. Fuglseth, P. Tøndel, and T. I. Fossen, "Optimal constrained control allocation in marine surface vessels with rudders," *Control Engineering Practice*, vol. 16, no. 4, pp. 457–464, 2008.

[116] W. C. Durham, "Attainable moments for the constrained control allocation problem," *Journal of Guidance Control and Dynamics*, vol. 17, no. 6, pp. 1371–1373, 1994.

[117] J. J. Burken, P. Lu, Z. L. Wu, and C. Bahm, "Two reconfigurable flight-control design methods: Robust servomechanism and control allocation," *Journal of Guidance Control and Dynamics*, vol. 24, no. 3, pp. 482–493, 2001.

[118] O. Harkegard, "Efficient active set algorithms for solving constrained least squares problems in aircraft control allocation," in *Proceedings of the 41st IEEE Conference on Decision and Control*, 2002.

[119] P. Lu, "Constrained tracking control of nonlinear systems," *Systems and Control Letters*, vol. 27, no. 5, pp. 305–314, 1996.

[120] J. Wang, "Coordinated and reconfigurable vehicle dynamics control," PhD Thesis, The University of Texas at Austin, 2007.

[121] A. Bemporad, M. Morari, V. Dua, and E. N. Pistikopoulos, "The explicit linear quadratic regulator for constrained systems," *Automatica*, vol. 38, no. 1, pp. 3–20, 2002.

[122] P. Tøndel, T. A. Johansen, and A. Bemporad, "An algorithm for multi-parametric quadratic programming and explicit mpc solutions," *Automatica*, vol. 39, no. 3, pp. 489–497, 2003.

[123] M. Kvasnica, P. Grieder, and M. Baotic, "Multi parametric toolbox, mpt," 2006.

[124] P. Tøndel, T. A. Johansen, and A. Bemporad, "Evaluation of piecewise affine control via binary search tree," *Automatica*, vol. 39, no. 5, pp. 945–950, 2003.

[125] J. Tjønnås and T. A. Johansen, "Adaptive control allocation," *Automatica*, vol. 44, no. 11, pp. 2754–2765, 2008.

[126] J. Tjonnas and T. A. Johansen, "Optimizing adaptive control allocation with actuator dynamics," in *46th IEEE Conference on Decision and Control*, 2007, pp. 3780–3785.

[127] S. Savaresi and M. Tanelli, *Active braking control systems design for vehicles.* Springer-Verlag, 2010.

[128] M. Klomp, "Longitudinal force distribution using quadratically constrained linear programming," *Vehicle System Dynamics*, vol. 49, no. 12, pp. 1823–1836, 2011.

[129] E. Ono, Y. Hattori, Y. Muragishi, and K. Koibuchi, "Vehicle dynamics integrated control for four-wheel-distributed steering and four-wheel-distributed traction/braking systems," *Vehicle System Dynamics*, vol. 44, no. 2, pp. 139–151, 2006.

[130] S. I. Sakai, H. Sado, and Y. Hori, "Anti-skid control with motor in electric vehicle," in *6th International Workshop on Advanced Motion Control*, 2000.

[131] T. A. Johansen, I. Petersen, J. Kalkkuhl, and J. Ludemann, "Gain-scheduled wheel slip control in automotive brake systems," *IEEE Transactions on Control Systems Technology*, vol. 11, no. 6, pp. 799–811, 2003.

[132] T. D. Gillespie, *Fundamentals of Vehicle Dynamics.* Society of Automotive Engineers, Inc., 1992.

[133] U. Kiencke and L. Nielsen, *Automotive Control Systems For Engine, Driveline, and Vehicle*. Springer-Verlag, 2005.

[134] J. T. Spooner, M. Maggiore, R. Ordonez, and K. M. Passino, *Stable Adaptive Control and Estimation for Nonlinear Systems: Neural and Fuzzy Approximator Techniques*. John Wiley and Sons, Inc., 2002.

[135] R. de Castro, R. E. Araujo, and D. Freitas, "Optimal linear parameterization for on-line estimation of tire-road friction," in *18th World Congress of the International Federation of Automatic Control (IFAC)*, 2011.

[136] M. Tanelli, L. Piroddi, and S. M. Savaresi, "Real-time identification of tire-road friction conditions," *IET Control Theory and Applications*, vol. 3, no. 7, pp. 891–906, 2009.

[137] H. F. Grip, L. Imsland, T. A. Johansen, J. C. Kalkkuhl, and A. Suissa, "Vehicle sideslip estimation," *IEEE Control Systems Magazine*, vol. 29, no. 5, pp. 36–52, 2009.

[138] L. H. Zhao, Z. Y. Liu, and H. Chen, "Design of a nonlinear observer for vehicle velocity estimation and experiments," *IEEE Transactions on Control Systems Technology*, vol. 19, no. 3, pp. 664–672, 2011.

[139] S. Solyom, A. Rantzer, and J. Ludemann, "Synthesis of a model-based tire slip controller," *Vehicle System Dynamics*, vol. 41, no. 6, pp. 475–499, 2004.

[140] E. de Vries, A. Fehn, and D. Rixen, "Flatness-based model inverse for feed-forward braking control," *Vehicle System Dynamics*, vol. 48, no. sup1, pp. 353–372, 2010.

[141] S. C. Baslamisli, I. E. Kose, and G. Anlas, "Robust control of anti-lock brake system," *Vehicle System Dynamics*, vol. 45, no. 3, pp. 217–232, 2007.

[142] J. I. Miller and D. Cebon, "A high performance pneumatic braking system for heavy vehicles," *Vehicle System Dynamics*, vol. 48, no. sup1, pp. 373–392, 2010.

[143] M. Tanelli, C. Vecchio, M. Corno, A. Ferrara, and S. M. Savaresi, "Traction control for ride-by-wire sport motorcycles: A second-order sliding mode approach," *IEEE Transactions on Industrial Electronics*, vol. 56, no. 9, pp. 3347–3356, 2009.

[144] B. D. O. Anderson and A. Dehghani, "Challenges of adaptive control-past, permanent and future," *Annual Reviews in Control*, vol. 32, no. 2, pp. 123–135, 2008.

[145] J.-J. E. Slotine and W. Li, *Applied nonlinear control*. Prentice Hall, 1991.

[146] "Carsim 8.0 user manual," 2009.

[147] H. B. Pacejka, *Tyre and vehicle dynamics*. Butterworth-Heinemann, 2002.

[148] M. Tanelli, G. Osorio, M. di Bernardo, S. M. Savaresi, and A. Astolfi, "Existence, stability and robustness analysis of limit cycles in hybrid anti-lock braking systems," *International Journal of Control*, vol. 82, no. 4, pp. 659–678, 2009.

[149] F. Borrelli, A. Bemporad, M. Fodor, and D. Hrovat, "An MPC/hybrid system approach to traction control," *IEEE Transactions on Control Systems Technology*, vol. 14, no. 3, pp. 541–552, 2006.

[150] S. M. Savaresi, M. Tanelli, and C. Cantoni, "Mixed slip-deceleration control in automotive braking systems," *Journal of Dynamic Systems, Measurement, and Control*, vol. 129, no. 1, pp. 20–31, 2007.

[151] Y. Hori, "Application of electric motor, supercapacitor, and wireless power transfer to enhance operation of future vehicles," in *IEEE International Symposium on Industrial Electronics*, 2010.

[152] C. Canudas-de Wit, P. Tsiotras, E. Velenis, M. Basset, and G. Gissinger, "Dynamic friction models for road/tire longitudinal interaction," *Vehicle System Dynamics*, vol. 39, no. 3, pp. 189–226, 2003.

[153] M. Tanelli, A. Astolfi, and S. M. Savaresi, "Robust nonlinear output feedback control for brake by wire control systems," *Automatica*, vol. 44, no. 4, pp. 1078–1087, 2008.

[154] L. Imsland, T. A. Johansen, T. I. Fossen, H. Grip, J. C. Kalkkuhl, and A. Suissa, "Vehicle velocity estimation using nonlinear observers," *Automatica*, vol. 42, no. 12, pp. 2091–2103, 2006.

[155] Y. Hori, Y. Toyoda, and Y. Tsuruoka, "Traction control of electric vehicle: Basic experimental results using the test EV "UOT Electric March"," *IEEE Transactions on Industry Applications*, vol. 34, no. 5, pp. 1131–1138, 1998.

[156] C. Unsal and P. Kachroo, "Sliding mode measurement feedback control for antilock braking systems," *IEEE Transactions on Control Systems Technology*, vol. 7, no. 2, pp. 271–281, 1999.

[157] M. Amodeo, A. Ferrara, R. Terzaghi, and C. Vecchio, "Wheel slip control via second-order sliding-mode generation," *IEEE Transactions on Intelligent Transportation Systems*, vol. 11, no. 1, pp. 122–131, 2010.

[158] E. Kayacan, Y. Oniz, and O. Kaynak, "A grey system modeling approach for sliding-mode control of antilock braking system," *IEEE Transactions on Industrial Electronics*, vol. 56, no. 8, pp. 3244–3252, 2009.

[159] L. Chih-Min and C. F. Hsu, "Neural-network hybrid control for antilock braking systems," *IEEE Transactions on Neural Networks*, vol. 14, no. 2, pp. 351–359, 2003.

[160] ——, "Self-learning fuzzy sliding-mode control for antilock braking systems," *IEEE Transactions on Control Systems Technology*, vol. 11, no. 2, pp. 273–278, 2003.

[161] S. Taehyun, C. Sehyun, and L. Seok, "Investigation of sliding-surface design on the performance of sliding mode controller in antilock braking systems," *IEEE Transactions on Vehicular Technology*, vol. 57, no. 2, pp. 747–759, 2008.

[162] L. Hyeongcheol and M. Tomizuka, "Adaptive vehicle traction force control for intelligent vehicle highway systems (IVHSs)," *IEEE Transactions on Industrial Electronics*, vol. 50, no. 1, pp. 37–47, 2003.

[163] N. Patel, C. Edwards, and S. K. Spurgeon, "Optimal braking and estimation of tyre friction in automotive vehicles using sliding modes," *International Journal of Systems Science*, vol. 38, no. 11, pp. 901 – 912, 2007.

[164] Y. Xinghuo and O. Kaynak, "Sliding-mode control with soft computing: A survey," *IEEE Transactions on Industrial Electronics*, vol. 56, no. 9, pp. 3275–3285, 2009.

[165] S. Seshagiri and H. K. Khalil, "Robust output feedback regulation of minimum-phase nonlinear systems using conditional integrators," *Automatica*, vol. 41, no. 1, pp. 43–54, 2005.

[166] A. van Zanten, R. Erhardt, and A. Lutz, "Measurement and simulation of transients in longitudinal and lateral tire forces," *SAE Trans.*, vol. 99, no. 6, pp. 300–318, 1990.

[167] M. Schinkel and K. Hunt, "Anti-lock braking control using a sliding mode like approach," in *Proceedings of the American Control Conference*, vol. 3, 2002, pp. 2386–2391.

[168] S. Seshagiri, "Position control of permanent magnet stepper motors using conditional servocompensators," *IET Control Theory and Applications*, vol. 3, no. 9, pp. 1196–1208, 2009.

[169] M. Burger, A. Pavlov, and K. Pettersen, "Conditional integrators for path following and formation control of marine vessels under constant disturbances," in *Proceedings of the 8th IFAC International Conference on Manoeuvring and Control of Marine Craft*, 2009.

[170] E. Promtun and S. Seshagiri, "Sliding mode control of pitch-rate of an f-16 aircraft," in *Proceedings of the 17th IFAC World Congress*, 2008.

[171] S. Seshagiri and H. K. Khalil, "Universal integral controllers with anti-reset windup for minimum phase nonlinear systems," in *Proceedings of the 40th IEEE Conference on Decision and Control*, 2001.

[172] R. de Castro, R. E. Araujo, and D. Freitas, "Hybrid ABS with electric motor and friction brakes," in *22nd International Symposium on Dynamics of Vehicles on Roads and Tracks*, 2011.

[173] F. Gustafsson, "Slip-based tire road friction estimation," *Automatica*, vol. 33, no. 6, pp. 1087–1099, 1997.

[174] E. Ono, K. Asano, M. Sugai, S. Ito, M. Yamamoto, M. Sawada, and Y. Yasui, "Estimation of automotive tire force characteristics using wheel velocity," *Control Engineering Practice*, vol. 11, no. 12, pp. 1361–1370, 2003.

[175] S. Muller, M. Uchanski, and K. Hedrick, "Estimation of the maximum tire-road friction coefficient," *Journal of Dynamic Systems, Measurement, and Control*, vol. 125, no. 4, pp. 607–617, 2003.

[176] J. M. Wang, L. Alexander, and R. Rajamani, "Friction estimation on highway vehicles using longitudinal measurements," *Journal of Dynamic Systems Measurement and Control-Transactions of the ASME*, vol. 126, no. 2, pp. 265–275, 2004.

[177] A. Andrieux, P. O. Vandanjon, R. Lengelle, and C. Chabanon, "New results on the relation between tyre-road longitudinal stiffness and maximum available grip for motor car," *Vehicle System Dynamics*, vol. 48, no. 12, pp. 1511–1533, 2010.

[178] C. R. Carlson and J. C. Gerdes, "Consistent nonlinear estimation of longitudinal tire stiffness and effective radius," *IEEE Transactions on Control Systems Technology*, vol. 13, no. 6, pp. 1010–1020, 2005.

[179] U. Kiencke, "Realtime estimation of adhesion characteristic between tyres and road," in *Proc. of the IFAC 12th Triennial World Congress*, vol. 1, 1993, pp. 15–22.

[180] S. Germann, M. Wurtenberger, and A. Daiss, "Monitoring of the friction coefficient between tyre and road surface," in *Proceedings of the 3rd IEEE Conference on Control Applications*, vol. 1, 1994, pp. 613–618.

[181] J. Yi, L. Alvarez, and R. Horowitz, "Adaptive emergency braking control with underestimation of friction coefficient," *IEEE Transactions on Control Systems Technology*, vol. 10, no. 3, pp. 381–392, 2002.

[182] W. Pasillas-Lepine, "Hybrid modeling and limit cycle analysis for a class of five-phase anti-lock brake algorithms," *Vehicle System Dynamics*, vol. 44, no. 2, pp. 173–188, 2006.

[183] R. de Castro, R. E. Araujo, J. S. Cardoso, and D. Freitas, "A new linear parametrization for peak friction coefficient estimation in real time," in *IEEE Vehicle Power and Propulsion Conference (VPPC)*, 2010.

[184] L. Alvarez and Y. Jingang, "Adaptive emergency braking control in automated highway systems," in *Proceedings of the 38th IEEE Conference on Decision and Control*, vol. 4, 1999, pp. 3740–3745.

[185] T. L. Chia, P. C. Chow, and H. J. Chizeck, "Recursive parameter identification of constrained systems: an application to electrically stimulated muscle," *IEEE Transactions on Biomedical Engineering*, vol. 38, no. 5, pp. 429–442, 1991.

[186] L. S. Resende, J. M. T. Romano, and M. G. Bellanger, "A fast least-squares algorithm for linearly constrained adaptive filtering," *IEEE Transactions on Signal Processing*, vol. 44, no. 5, pp. 1168–1174, 1996.

[187] L. Li and F.-Y. Wang, *Advanced motion control and sensing for intelligent vehicles.* Springer Verlag, 2007.

[188] M. Corno, M. Gerard, M. Verhaegen, and E. Holweg, "Hybrid ABS control using force measurement," *IEEE Transactions on Control Systems Technology*, vol. 20, no. 5, pp. 1223 – 1235, 2012.

[189] B. v. Leeuwen and J. Zuurbier, "Vehicle state estimation based on load sensing," in *Vehicle Dynamics Expo*, 2007.

[190] S. M. Savaresi, M. Tanelli, P. Langthaler, and L. Del Re, "New regressors for the direct identification of tire deformation in road vehicles via in-tire accelerometers," *IEEE Transactions on Control Systems Technology*, vol. 16, no. 4, pp. 769–780, 2008.

[191] G. Baffet, A. Charara, and G. Dherbomez, "An observer of tire-road forces and friction for active security vehicle systems," *IEEE/ASME Transactions on Mechatronics*, vol. 12, no. 6, pp. 651–661, 2007.

[192] L. R. Ray, "Nonlinear tire force estimation and road friction identification: Simulation and experiments," *Automatica*, vol. 33, no. 10, pp. 1819–1833, 1997.

[193] I. Ziena Optimization, "Knitro 6.0 user manual," 2009.

[194] TMPT, "Tyre model performance test," 2003, http://tmpt.tuwien.ac.at/.

[195] L. Ljung, *System Identification: Theory for the User*. Prentice Hall, 1999.

[196] C. Rao, H. Toutenburg, Shalabh, and C. Heumann, *Linear models and generalizations: least squares and alternatives*, 3rd ed. Springer Verlag, 2008.

[197] R. Isermann and M. Munchhof, *Identification of Dynamic Systems: An Introduction with Applications*. Springer-Verlag, 2011.

[198] A. Alenany, H. Shang, M. Soliman, and I. Ziedan, "Improved subspace identification with prior information using constrained least squares," *IET Control Theory and Applications*, vol. 5, no. 13, pp. 1568–1576, 2011.

[199] L. A. Aguirre, M. F. S. Barroso, R. R. Saldanha, and E. M. A. M. Mendes, "Imposing steady-state performance on identified nonlinear polynomial models by means of constrained parameter estimation," *IEE Proceedings - Control Theory and Applications,*, vol. 151, no. 2, pp. 174–179, 2004.

[200] A. Stotsky and I. Kolmanovsky, "Application of input estimation techniques to charge estimation and control in automotive engines," *Control Engineering Practice*, vol. 10, no. 12, pp. 1371–1383, 2002.

[201] M. Yamakado, J. Takahashi, S. Saito, A. Yokoyama, and M. Abe, "Improvement in vehicle agility and stability by g-vectoring control," *Vehicle System Dynamics*, vol. 48, no. sup1, pp. 231–254, 2010.

[202] D. F. Reuter, E. W. Lloyd, J. W. Z. II, and J. A. Elliott, "Hydraulic design considerations for EHB systems," in *SAE World Congress*, 2003.

[203] N. D'alfio, A. Morgando, and A. Sorniotti, "Electro-hydraulic brake systems: design and test through hardware-in-the-loop simulation," *Vehicle System Dynamics: International Journal of Vehicle Mechanics and Mobility*, vol. 44, no. 1 supp 1, pp. 378–392, 2006.

[204] J. Kwak, B. Yao, and A. Bajaj, "Analytical model development and model reduction for electromechanical brake system," *International Mechanical Engineering Congress and Exposition*, 2004.

[205] C. Line, "Modelling and control of an automotive electromechanical brake," PhD Thesis, University of Melbourne, 2007.

[206] A. Sorniotti and G. Repici, "Hardware in the loop with electro-hydraulic brake systems," in *9th WSEAS International Conference on Systems*, 2005.

[207] I. Petersen, "Wheel slip control in abs brakes using gain scheduled optimal control with constraints," PhD Thesis, Norwegian University of Science and Technology, 2003.

[208] A. Dardanelli, G. Alli, and S. Savaresi, "Modeling and control of an electromechanical brake-by-wire actuator for a sport motorbike," in *5th IFAC Symposium on Mechatronic Systems*, 2010.

[209] G. Panzani, M. Corno, F. Todeschini, S. Fiorenti, and S. M. Savaresi, "Analysis and control of a brake by wire actuator for sport motorcycles," in *The 13th Mechatronics Forum International Conference*, 2012.

[210] J. Chihoon, H. Sungho, and K. Hyunsoo, "Clamping-force control for electromechanical brake," *IEEE Transactions on Vehicular Technology*, vol. 59, no. 7, pp. 3205–3212, 2010.

[211] C. Line, C. Manzie, and M. C. Good, "Electromechanical brake modeling and control: From PI to MPC," *IEEE Transactions on Control Systems Technology*, vol. 16, no. 3, pp. 446–457, 2008.

[212] C. F. Lee and C. Manzie, "Near-time-optimal tracking controller design for an automotive electromechanical brake," *Proceedings of the Institution of Mechanical Engineers, Part I: Journal of Systems and Control Engineering*, vol. 226, no. 4, pp. 537–549, 2012.

[213] B. Armstrong and C. Canudas de Wit, *Friction Modeling and Compensation.* CRC, 1996.

[214] G. Liu, "Decomposition-based friction compensation of mechanical systems," *Mechatronics*, vol. 12, no. 5, pp. 755–769, 2002.

[215] P. Bigras, "Reduced nonlinear observer for bounded estimation of the static friction model with the Stribeck effect," *Systems and Control Letters*, vol. 58, no. 2, pp. 119–123, 2009.

[216] F. Jatta, G. Legnani, and A. Visioli, "Friction compensation in hybrid force/velocity control of industrial manipulators," *IEEE Transactions on Industrial Electronics*, vol. 53, no. 2, pp. 604–613, 2006.

[217] B. Bona, M. Indri, and N. Smaldone, "Rapid prototyping of a model-based control with friction compensation for a direct-drive robot," *IEEE/ASME Transactions on Mechatronics*, vol. 11, no. 5, pp. 576–584, 2006.

[218] D. P. Hess and A. Soom, "Friction at a lubricated line contact operating at oscillating sliding velocities," *Journal of Tribology*, vol. 112, no. 1, pp. 147–152, 1990.

[219] L. Marton and B. Lantos, "Control of robotic systems with unknown friction and payload," *IEEE Transactions on Control Systems Technology*, vol. 19, no. 6, pp. 1534–1539, 2011.

[220] L. Marton, S. Fodor, and N. Sepehri, "A practical method for friction identification in hydraulic actuators," *Mechatronics*, vol. 21, no. 1, pp. 350–356, 2011.

[221] L. Marton and B. Lantos, "Modeling, identification, and compensation of stick-slip friction," *IEEE Transactions on Industrial Electronics*, vol. 54, no. 1, pp. 511–521, 2007.

[222] A. Acquistapace and S. Mazzoleni, "Modellistica e controllo di un impianto frenante brake-by-wire per motocicli ad alte prestazioni," Master Thesis, Politecnico di Milano, 2012.

[223] H. Merritt, *Hydraulic Control Systems.* Wiley, 1967.

[224] G. Bitz, "Braking system with EBS and prefill function and electronic braking control method," *U.S. Patent 7806486*, 2010.

[225] Freescale, "56f8300 hybrid controller used in control of electro-mechanical brake," *Application Note Num. 1999*, 2004.

[226] J.-C. Mare, "Friction modelling and simulation at system level: a practical view for the designer," *Proceedings of the Institution of Mechanical Engineers, Part I: Journal of Systems and Control Engineering*, vol. 226, no. 6, pp. 728–741, 2012.

[227] C. Canudas de Wit, H. Olsson, K. J. Astrom, and P. Lischinsky, "A new model for control of systems with friction," *IEEE Transactions on Automatic Control*, vol. 40, no. 3, pp. 419–425, 1995.

[228] B. Armstrong, P. Dupont, and C. Canudas de Wit, "A survey of models, analysis tools and compensation methods for the control of machines with friction," *Automatica*, vol. 30, no. 7, pp. 1083–1138, 1994.

[229] J. Astrom and C. Canudas-de Wit, "Revisiting the LuGre friction model," *IEEE Control Systems Magazine*, vol. 28, no. 6, pp. 101–114, 2008.

[230] Y. Bin and J. Chang, "Advanced motion control: From classical PID to nonlinear adaptive robust control," in *11th IEEE International Workshop on Advanced Motion Control*, 2010, pp. 815–829.

[231] P. Ioannou and J. Sun, *Robust adaptive control.* Prentice Hall, 1996.

[232] J. Farrell and M. Polycarpou, *Adaptive approximation based control: Unifying neural, fuzzy and traditional adaptive approximation approaches.* John Wiley and Sons, 2006.

[233] S. Diop, J. W. Grizzle, P. E. Moraal, and A. Stefanopoulou, "Interpolation and numerical differentiation for observer design," in *American Control Conference*, vol. 2, 1994, pp. 1329–1333.

[234] M. Vakil, R. Fotouhi, and P. N. Nikiforuk, "Energy-based approach for friction identification of robotic joints," *Mechatronics*, vol. 21, no. 3, pp. 614–624, 2011.

[235] W. Shang, S. Cong, and F. Kong, "Identification of dynamic and friction parameters of a parallel manipulator with actuation redundancy," *Mechatronics*, vol. 20, no. 2, pp. 192–200, 2010.

[236] H. Wei-Sheng, L. Chun-Wei, H. Pau-Lo, and Y. Syh-Shiuh, "Precision control and compensation of servomotors and machine tools via the disturbance observer," *IEEE Transactions on Industrial Electronics*, vol. 57, no. 1, pp. 420–429, 2010.

[237] M. R. Kermani, R. V. Patel, and M. Moallem, "Friction identification and compensation in robotic manipulators," *IEEE Transactions on Instrumentation and Measurement*, vol. 56, no. 6, pp. 2346–2353, 2007.

[238] W. Shang, S. Cong, and Y. Zhang, "Nonlinear friction compensation of a 2-DOF planar parallel manipulator," *Mechatronics*, vol. 18, no. 7, pp. 340–346, 2008.

[239] D. Bi, Y. F. Li, S. K. Tso, and G. L. Wang, "Friction modeling and compensation for haptic display based on support vector machine," *IEEE Transactions on Industrial Electronics*, vol. 51, no. 2, pp. 491–500, 2004.

[240] R. Kelly, J. Llamas, and R. Campa, "A measurement procedure for viscous and coulomb friction," *IEEE Transactions on Instrumentation and Measurement*, vol. 49, no. 4, pp. 857–861, 2000.

[241] R. Hensen, G. Angelis, M. Molengraft, A. Jager de, and J. Kok, "Grey-box modeling of friction: An experimental case-study," *European Journal of Control*, vol. 6, no. 3, pp. 258–267, 2000.

[242] B. Friedland and Y. J. Park, "On adaptive friction compensation," *IEEE Transactions on Automatic Control*, vol. 37, no. 10, pp. 1609–1612, 1992.

[243] L. Teh-Lu and I. C. Tsun, "An exponentially stable adaptive friction compensator," *IEEE Transactions on Automatic Control*, vol. 45, no. 5, pp. 977–980, 2000.

[244] H. Abdellatif and B. Heimann, "New experimental results on the compensation of static friction in passive joints of robotic manipulators," *IEEE Transactions on Control Systems Technology*, vol. 18, no. 5, pp. 1005–1010, 2010.

[245] V. Lampaert, J. Swevers, and F. Al-Bender, "Modification of the Leuven integrated friction model structure," *IEEE Transactions on Automatic Control*, vol. 47, no. 4, pp. 683–687, 2002.

[246] F. Al-Bender and J. Swevers, "Characterization of friction force dynamics," *IEEE Control Systems Magazine*, vol. 28, no. 6, pp. 64–81, 2008.

[247] L. Tong Heng, T. Kok Kiong, and H. Sunan, "Adaptive friction compensation with a dynamical friction model," *IEEE/ASME Transactions on Mechatronics*, vol. 16, no. 1, pp. 133–140, 2011.

[248] C. Canudas-de Wit, "Workshop on systems with friction - identification and compensation," in *IEEE Conference on Decision and Control*, 1998.

[249] L. Lu, B. Yao, Q. Wang, and Z. Chen, "Adaptive robust control of linear motors with dynamic friction compensation using modified LuGre model," *Automatica*, vol. 45, no. 12, pp. 2890–2896, 2009.

[250] C. Canudas de Wit and P. Lischinsky, "Adaptive friction compensation with partially known dynamic friction model," *International Journal of Adaptive Control and Signal Processing*, vol. 11, no. 1, pp. 65–80, 1997.

[251] L. Freidovich, A. Robertsson, A. Shiriaev, and R. Johansson, "Lugre-model-based friction compensation," *IEEE Transactions on Control Systems Technology*, vol. 18, no. 1, pp. 194–200, 2010.

[252] B. Bona and M. Indri, "Friction compensation in robotics: an overview," in *44th IEEE Conference on Decision and Control and European Control Conference*, 2005, pp. 4360–4367.

[253] D. Naso, F. Cupertino, and B. Turchiano, "Precise position control of tubular linear motors with neural networks and composite learning," *Control Engineering Practice*, vol. 18, no. 5, pp. 515–522, 2010.

[254] M. Feemster, P. Vedagarbha, D. M. Dawson, and D. Haste, "Adaptive control techniques for friction compensation," *Mechatronics*, vol. 9, no. 2, pp. 125–145, 1999.

[255] D. Naso, F. Cupertino, and B. Turchiano, "NPID and adaptive approximation control of motion systems with friction," *IEEE Transactions on Control Systems Technology*, vol. 20, no. 1, pp. 214 – 222, 2012.

[256] S. N. Huang, K. K. Tan, and T. H. Lee, "Adaptive motion control using neural network approximations," *Automatica*, vol. 38, no. 2, pp. 227–233, 2002.

[257] S. S. Ge, T. H. Lee, and S. X. Ren, "Adaptive friction compensation of servo mechanisms," *International Journal of Systems Science*, vol. 32, no. 4, pp. 523 – 532, 2001.

[258] R. R. Selmic and F. L. Lewis, "Neural-network approximation of piecewise continuous functions: application to friction compensation," *IEEE Transactions on Neural Networks*, vol. 13, no. 3, pp. 745–751, 2002.

[259] L. Marton and B. Lantos, "Control of mechanical systems with Stribeck friction and backlash," *Systems and Control Letters*, vol. 58, no. 2, pp. 141–147, 2009.

[260] L. Marton, "On analysis of limit cycles in positioning systems near Striebeck velocities," *Mechatronics*, vol. 18, no. 1, pp. 46–52, 2008.

[261] A. Hac, D. Doman, and M. Oppemheimer, "Unified control of brake- and steer-by-wire systems using optimal control allocation methods," *SAE paper*, 2006.

[262] E. Coelingh and S. Solyom, "All aboard the robotic road train," *IEEE Spectrum*, vol. 49, no. 11, pp. 34–39, 2012.

[263] E. Coelingh, "Active safety technologies at volvo car corporation," in *10th International Symposium on Advanced Vehicle Control (AVEC)*, 2010.

[264] C. Urmson, "Realizing self-driving vehicles," in *IEEE Intelligent Vehicles Symposium*, 2012.

[265] A. Broggi, P. Medici, P. Zani, A. Coati, and M. Panciroli, "Autonomous vehicles control in the vislab intercontinental autonomous challenge," *Annual Reviews in Control*, vol. 36, no. 1, pp. 161–171, 2012.

[266] P. Morin and C. Samson, *Motion Control of Wheeled Mobile Robots.* Springer Berlin Heidelberg, 2008, pp. 799–826.

[267] A. D. Luca, G. Oriolo, and C. Samson, *Feedback Control of a Nonholonomic Car-like Robot*, 1998, vol. 229, pp. 171–253.

[268] O. Amidi, "Integrated mobile robot control," Carnegie Mellon University, Tech. Rep., 1990.

[269] S. Thrun, M. Montemerlo, H. Dahlkamp, *et al.*, *Stanley: The Robot That Won the DARPA Grand Challenge.* Springer Berlin Heidelberg, 2007, ch. 1, pp. 1–43.

[270] J. M. Snider, "Automatic steering methods for autonomous automobile path tracking," Carnegie Mellon University, Tech. Rep., 2009.

[271] M. Werling, L. Groll, and G. Bretthauer, "Invariant trajectory tracking with a full-size autonomous road vehicle," *IEEE Transactions on Robotics*, vol. 26, no. 4, pp. 758–765, 2010.

[272] A. Ferrara and C. Vecchio, "Second order sliding mode control of vehicles with distributed collision avoidance capabilities," *Mechatronics*, vol. 19, no. 4, pp. 471–477, 2009.

[273] S. Suryanarayanan, M. Tomizuka, and T. Suzuki, "Design of simultaneously stabilizing controllers and its application to fault-tolerant lane-keeping controller design for automated vehicles," *IEEE Transactions on Control Systems Technology*, vol. 12, no. 3, pp. 329–339, 2004.

[274] S. Yong-Duan, C. He-Nan, and L. Dan-Yong, "Virtual-point-based fault-tolerant lateral and longitudinal control of 4W-steering vehicles," *IEEE Transactions on Intelligent Transportation Systems*, vol. 12, no. 4, pp. 1343–1351, 2011.

[275] K. Kritayakirana and J. C. Gerdes, "Using the centre of percussion to design a steering controller for an autonomous race car," *Vehicle System Dynamics*, vol. 50, no. sup1, pp. 33–51, 2012.

[276] R. Marino, S. Scalzi, and M. Netto, "Nested PID steering control for lane keeping in autonomous vehicles," *Control Engineering Practice*, vol. 19, no. 12, pp. 1459–1467, 2011.

[277] K. L. R. Talvala, K. Kritayakirana, and J. C. Gerdes, "Pushing the limits: From lanekeeping to autonomous racing," *Annual Reviews in Control*, vol. 35, no. 1, pp. 137–148, 2011.

[278] K. Kritayakirana and J. C. Gerdes, "Autonomous cornering at the limits: Maximizing a "g–g" diagram by using feedforward trail-braking and throttle on-exit," in *IFAC Symposium on Advances in Automotive Control*, 2010.

[279] K. Kritayakirana and C. Gerdes, "Autonomous cornering at the limits: Designing a longitudinal feedback controller using a tire slip circle," in *10th International Symposium on Advanced Vehicle Control*, 2010.

[280] M. Jonasson and J. Andreasson, "Exploiting autonomous corner modules to resolve force constraints in the tyre contact patch," *Vehicle System Dynamics*, vol. 46, no. 7, pp. 553 – 573, 2008.

[281] W. Danwei and Q. Feng, "Trajectory planning for a four-wheel-steering vehicle," in *Proceedings 2001 ICRA. IEEE International Conference on Robotics and Automation*, vol. 4, 2001, pp. 3320–3325.

[282] D. Verscheure, B. Demeulenaere, J. Swevers, J. De Schutter, and M. Diehl, "Time-optimal path tracking for robots: A convex optimization approach," *IEEE Transactions on Automatic Control*, vol. 54, no. 10, pp. 2318–2327, 2009.

[283] F. Pfeiffer and R. Johanni, "A concept for manipulator trajectory planning," *IEEE Journal of Robotics and Automation*, vol. 3, no. 2, pp. 115–123, 1987.

[284] J. Betts, *Practical methods for optimal control and estimation using nonlinear programming*. Society for Industrial and Applied Mathematics, 2010.

[285] M. Canale, L. Fagiano, M. Milanese, and P. Borodani, "Robust vehicle yaw control using an active differential and IMC techniques," *Control Engineering Practice*, vol. 15, no. 8, pp. 923–941, 2007.

[286] M. Abe and W. Manning, *Vehicle handling dynamics: theory and application*. Butterworth-Heinemann/Elsevier, 2009.

[287] J. Ackermann and W. Sienel, "Robust yaw damping of cars with front and rear wheel steering," *IEEE Transactions on Control Systems Technology*, vol. 1, no. 1, pp. 15–20, 1993.

[288] R. Marino and F. Cinili, "Input-output decoupling control by measurement feedback in four-wheel-steering vehicles," *IEEE Transactions on Control Systems Technology*, vol. 17, no. 5, pp. 1163–1172, 2009.

[289] Oxford Technical Solutions, "RT inertial and GPS measurement systems (RT4003 user manual)," 2013.

[290] R. de Castro, R. E. Araujo, and D. Freitas, "Real-time estimation of tyre-road friction peak with optimal linear parameterisation," *IET Control Theory and Applications*, vol. 6, no. 14, pp. 2257–2268, 2012.

[291] A. V. Rao, "A survey of numerical methods for optimal control," in *AAS/AIAA Astrodynamics Specialist Conference*, 2009.

[292] M. Grant, S. Boyd, and Y. Ye, *Disciplined Convex Programming*, ser. Nonconvex Optimization and Its Applications. Springer US, 2006, vol. 84, ch. 7, pp. 155–210.

[293] CVX Research, Inc., "CVX: Matlab software for disciplined convex programming, version 2.0 beta," 2012.

[294] R. H. Tütüncü, K. C. Toh, and M. J. Todd, "Solving semidefinite-quadratic-linear programs using SDPT3," *Mathematical Programming*, vol. 95, no. 2, pp. 189–217, 2003.

[295] K. Bayar, J. Wang, and G. Rizzoni, "Development of a vehicle stability control strategy for a hybrid electric vehicle equipped with axle motors," *Proceedings of the Institution of Mechanical Engineers, Journal of Automobile Engineering,Part D*, 2012.

[296] T. Weiskircher and S. Müller, "Control performance of a road vehicle with four independent single-wheel electric motors and steer-by-wire system," *Vehicle System Dynamics*, vol. 50, no. sup1, pp. 53–69, 2012.

[297] M. Jonasson, J. Andreasson, S. Solyom, B. Jacobson, and A. S. Trigell, "Utilization of actuators to improve vehicle stability at the limit: From hydraulic brakes toward electric propulsion," *Journal of Dynamic Systems, Measurement, and Control*, vol. 133, no. 5, p. 051003, 2011.

[298] J. Mattingley and S. Boyd, "CVXGEN: a code generator for embedded convex optimization," *Optimization and Engineering*, vol. 13, no. 1, pp. 1–27, 2012.

[299] I. Stegun, *Handbook of Mathematical Functions: With Formulas, Graphs, and Mathematical Tables*. Dover Publ., 1964.

[300] E. Vinot, R. Trigui, and B. Jeanneret, "Optimal management of electric vehicles with a hybrid storage system," in *IEEE Vehicle Power and Propulsion Conference*, 2010.

[301] G. Yimin and M. Ehsani, "Parametric design of the traction motor and energy storage for series hybrid off-road and military vehicles," *IEEE Transactions on Power Electronics*, vol. 21, no. 3, pp. 749–755, 2006.

[302] H. Douglas and P. Pillay, "Sizing ultracapacitors for hybrid electric vehicles," in *31st Annual Conference of IEEE Industrial Electronics Society*, 2005.

[303] R. Sadoun, N. Rizoug, P. Bartholomeus, B. Barbedette, and P. Le Moigne, "Optimal sizing of hybrid supply for electric vehicle using li-ion battery and supercapacitor," in *IEEE Vehicle Power and Propulsion Conference (VPPC)*, 2011.

[304] M.-J. Kim and H. Peng, "Power management and design optimization of fuel cell/battery hybrid vehicles," *Journal of Power Sources*, vol. 165, no. 2, pp. 819–832, 2007.

[305] A. Ravey, R. Roche, B. Blunier, and A. Miraoui, "Combined optimal sizing and energy management of hybrid electric vehicles," in *IEEE Transportation Electrification Conference and Expo (ITEC)*, 2012.

[306] O. Sundstrom, L. Guzzella, and P. Soltic, "Torque-assist hybrid electric powertrain sizing: From optimal control towards a sizing law," *IEEE Transactions on Control Systems Technology*, vol. 18, no. 4, pp. 837–849, 2010.

[307] N. Murgovski, L. Johannesson, J. Sjöberg, and B. Egardt, "Component sizing of a plug-in hybrid electric powertrain via convex optimization," *Mechatronics*, vol. 22, no. 1, pp. 106–120, 2012.

[308] N. Rizoug, P. Bartholomeus, and P. Le Moigne, "Modeling and characterizing supercapacitors using an online method," *IEEE Transactions on Industrial Electronics*, vol. 57, no. 12, pp. 3980–3990, 2010.

[309] S. Pelissier, "Batteries for electric and hybrid vehicles: State of the art, modeling, testing and aging," in *Vehicle Power and Propulsion Conference*, 2010.

[310] C. Mid-Eum, K. Seong-Woo, and S. Seung-Woo, "Energy management optimization in a battery/supercapacitor hybrid energy storage system," *IEEE Transactions on Smart Grid*, vol. 3, no. 1, pp. 463–472, 2012.

[311] Saft, "NHE 10-100 Ni-MH datasheet," 2011.

[312] Maxwell, "K2 series ultracapacitors datasheet," 2012.

[313] G. Souffran, L. Miegeville, and P. Guerin, "Simulation of real-world vehicle missions using a stochastic markov model for optimal powertrain sizing," *IEEE Transactions on Vehicular Technology*, vol. 61, no. 8, pp. 3454–3465, 2012.

[314] L. Tae-Kyung, B. Adornato, and Z. S. Filipi, "Synthesis of real-world driving cycles and their use for estimating PHEV energy consumption and charging opportunities: Case study for midwest/U.S," *IEEE Transactions on Vehicular Technology*, vol. 60, no. 9, pp. 4153–4163, 2011.

[315] A. Ravey, N. Watrin, B. Blunier, D. Bouquain, and A. Miraoui, "Energy-source-sizing methodology for hybrid fuel cell vehicles based on statistical description of driving cycles," *IEEE Transactions on Vehicular Technology*, vol. 60, no. 9, pp. 4164–4174, 2011.

[316] D. Graovac, M. Prschel, and A. Kniep, "MOSFET power losses calculation using the datasheet parameters," 2006, Infineon Technologies AG.

[317] M. Kabalo, D. Paire, B. Blunier, D. Bouquain, M. Godoy Simoes, and A. Miraoui, "Experimental validation of a high-voltage-ratio low input current ripple converters for hybrid fuel cell supercapacitors systems," *IEEE Transactions on Vehicular Technology*, vol. 61, no. 8, pp. 3430–3440, 2012.

[318] O. Hegazy, J. Van Mierlo, and P. Lataire, "Analysis, modeling, and implementation of a multidevice interleaved DC/DC converter for fuel cell hybrid electric vehicles," *IEEE Transactions on Power Electronics*, vol. 27, no. 11, pp. 4445–4458, 2012.

[319] S. Lim and K. Nam, "Loss-minimising control scheme for induction motors," *IEE Proceedings - Electric Power Applications*, vol. 151, no. 4, pp. 385–397, 2004.

[320] F. Casanellas, "Losses in PWM inverters using IGBTs," *IEE Proceedings -Electric Power Applications*, vol. 141, no. 5, pp. 235–239, 1994.

[321] L. Guzzella and A. Amstutz, "The QSS toolbox manual," 2005, http://www.idsc.ethz.ch/Downloads/qss.

[322] R. de Castro, P. Melo, P. Pacheco, R. E. Araujo, and D. Freitas, "A control allocation approach to manage multiple energy sources in EVs," in *IEEE Vehicle Power and Propulsion Conference (VPPC)*, 2011.

[323] C. R. Akli, X. Roboam, B. Sareni, and A. Jeunesse, "Energy management and sizing of a hybrid locomotive," in *European Conference on Power Electronics and Applications*, 2007.

[324] J. Curti, X.Huang, R. Minaki, and Y. Hori, "A simplified power management strategy for a supercapacitor/battery hybrid energy storage system using the half-controlled converter," in *38th Annual Conference of the IEEE Industrial Electronics Society*, 2012.

[325] R. Fourer, D. Gay, and B. Kernighan, *AMPL: a modeling language for mathematical programming.* Thomson/Brooks/Cole, 2003.

[326] D. M. Gay, *Automatic Differentiation of Nonlinear AMPL Models.* SIAM, 1991.

[327] A. Wachter and L. T. Biegler, "On the implementation of a primal-dual interior point filter line search algorithm for large-scale nonlinear programming," *Mathematical Programming*, vol. 106, no. 1, pp. 25–57, 2006.

[328] J. Czyzyk, M. P. Mesnier, and J. J. More, "The NEOS server," *IEEE Computational Science and Engineering*, vol. 5, no. 3, pp. 68–75, 1998.

[329] T. J. Barlow, S. Latham, I. S. McCrae, and P. G. Boulter, "A reference book of vehicle driving cycles for use in the measurments of road vehicles emissions," TRL Limited, Tech. Rep., 2009.

[330] R. de Castro, J. P. Trovao, P. Pacheco, P. Melo, P. G. Pereirinha, and R. E. Araujo, "DC link control for multiple energy sources in electric vehicles," in *IEEE Vehicle Power and Propulsion Conference (VPPC)*, 2011.

[331] R. Erickson and D. Maksimović, *Fundamentals of power electronics*, 2nd ed. Kluwer Academic Publishers, 2001.

[332] C. Olalla, R. Leyva, A. El Aroudi, and I. Queinnec, "Robust LQR control for PWM converters: An LMI approach," *IEEE Transactions on Industrial Electronics*, vol. 56, no. 7, pp. 2548–2558, 2009.

[333] C. Olalla, R. Leyva, A. El Aroudi, P. Garces, and I. Queinnec, "LMI robust control design for boost PWM converters," *IET Power Electronics*, vol. 3, no. 1, pp. 75–85, 2010.

[334] C. Olalla Martinez, I. Queinnec, R. Leyva, and A. El Aroudi, "Optimal state-feedback control of bilinear DC-DC converters with guaranteed regions of stability," *IEEE Transactions on Industrial Electronics*, vol. 59, no. 10, pp. 3868–3880, 2012.

[335] C. Olalla, I. Queinnec, R. Leyva, and A. El Aroudi, "Robust optimal control of bilinear DC-DC converters," *Control Engineering Practice*, vol. 19, no. 7, pp. 688–699, 2011.

[336] D. Maksimovic, A. M. Stankovic, V. J. Thottuvelil, and G. C. Verghese, "Modeling and simulation of power electronic converters," *Proceedings of the IEEE*, vol. 89, no. 6, pp. 898–912, 2001.

[337] H. Sira-Ramírez, "On the generalized PI sliding mode control of DC-to-DC power converters: A tutorial," *International Journal of Control*, vol. 76, no. 9, pp. 1018 – 1033, 2003.

[338] H. Sira-Ramírez, R. Silva-Ortigoza, and E. Corporation, *Control design techniques in power electronics devices*. Springer-Verlag, 2006.

[339] C. Albea, F. Gordillo, and C. Canudas-de Wit, "Adaptive control design for a boost inverter," *Control Engineering Practice*, vol. 19, no. 1, pp. 32–44, 2011.

[340] J. M. Olm, X. Ros-Oton, and Y. B. Shtessel, "Stable inversion of abel equations: Application to tracking control in DC-DC nonminimum phase boost converters," *Automatica*, vol. 47, no. 1, pp. 221–226, 2011.

[341] S. Devasia, C. Degang, and B. Paden, "Nonlinear inversion-based output tracking," *IEEE Transactions on Automatic Control*, vol. 41, no. 7, pp. 930–942, 1996.

[342] S. Boyd, L. El Ghaoui, E. Feron, and V. Balakrishnan, *Linear matrix inequalities in system and control theory*. Society for Industrial Mathematics, 1994.

[343] S. Chang and T. Peng, "Adaptive guaranteed cost control of systems with uncertain parameters," *IEEE Transactions on Automatic Control*, vol. 17, no. 4, pp. 474–483, 1972.

[344] I. R. Petersen and D. C. McFarlane, "Optimal guaranteed cost control and filtering for uncertain linear systems," *IEEE Transactions on Automatic Control*, vol. 39, no. 9, pp. 1971–1977, 1994.

[345] S. Tarbouriech, G. Garcia, J. da Silva, and I. Queinnec, *Stability and stabilization of linear systems with saturating actuators*. Springer, 2011.

[346] J. Lofberg, "Modeling and solving uncertain optimization problems in YALMIP," in *Proceedings of the 17th IFAC World Congress*, 2008.

[347] J. F. Sturm, "Using SeDuMi 1.02, a matlab toolbox for optimization over symmetric cones," *Optimization Methods and Software*, vol. 11, no. 1-4, pp. 625–653, 1999.

[348] W. J. Rugh and J. S. Shamma, "Research on gain scheduling," *Automatica*, vol. 36, no. 10, pp. 1401–1425, 2000.

[349] E. Rask, M. Duoba, and H. Lohse-Busch, "Recent hybrid electric vehicle trends and technologies," in *IEEE Vehicle Power and Propulsion Conference (VPPC11)*, 2011.

[350] K. Yamamoto, K. Shinohara, and T. Nagahama, "Characteristics of permanent-magnet synchronous motor driven by PWM inverter with voltage booster," *IEEE Transactions on Industry Applications*, vol. 40, no. 4, pp. 1145–1152, 2004.

[351] A. Visioli, *Practical PID control*. Springer Verlag, 2006.

[352] Saft, "Smart VH module datasheet," doc. 11088-2-0604.

[353] NESSCAP, "Nesscap ultracapacitor datasheet (eshsr-0100c0–002r7)," 2003.

[354] Mathworks, "Prelookup block module documentation," in *http://www.mathworks.com/help/toolbox/simulink/slref/prelookup.html*, 2011.

[355] T. Azib, O. Bethoux, G. Remy, and C. Marchand, "Saturation management of a controlled fuel-cell/ultracapacitor hybrid vehicle," *IEEE Transactions on Vehicular Technology*, vol. 60, no. 9, pp. 4127–4138, 2011.

[356] R. E. Araujo, H. S. Oliveira, J. R. Soares, N. M. Cerqueira, and R. de Castro, "Diferencial electronico," 2009, patent PT103817.

[357] C. Jung Uk, L. Quy Ngoc, and J. Jae Wook, "An FPGA-based multiple-axis motion control chip," *IEEE Transactions on Industrial Electronics*, vol. 56, no. 3, pp. 856–870, 2009.

[358] K. Tazi, E. Monmasson, and J. P. Louis, "Description of an entirely reconfigurable architecture dedicated to the current vector control of a set of ac machines," in *The 25th Annual Conference of the IEEE Industrial Electronics Society*, 1999.

[359] E. Monmasson and M. N. Cirstea, "FPGA design methodology for industrial control systems - a review," *IEEE Transactions on Industrial Electronics*, vol. 54, no. 4, pp. 1824–1842, 2007.

[360] R. de Castro, R. E. Araujo, and D. Freitas, *FPGA Based Powertrain Control for Electric Vehicles*. InTech, 2011.

[361] D. Novotny and T. Lipo, *Vector control and dynamics of AC drives*. Oxford University Press, 1996.

[362] R. E. Araujo, "Control system of three-phase induction motor based on the principle of field orientation," Master Thesis, Faculdade de Engenharia da Universidade do Porto, 1991.

[363] R. Andraka, "A survey of cordic algorithms for FPGAs," in *ACM/SIGDA 6th International Symposium on Field Programmable Gate Arrays*, 1998.

[364] R. de Castro, R. E. Araujo, and H. Oliveira, "Design, development and characterisation of a FPGA platform for multi-motor electric vehicle control," in *The 5th IEEE Vehicle Power and Propulsion Conference*, 2009.

[365] R. de Castro, R. E. Araujo, and D. Freitas, "Reusable ip cores library for ev propulsion systems." in *IEEE International Symposium on Industrial Electronics*, 2010.

[366] R. de Castro, R. E. Araujo, and H. Oliveira, "Control in multi-motor electric vehicle with a FPGA platform," in *IEEE International Symposium on Industrial Embedded Systems*, 2009, pp. 219–227.

[367] R. E. Araujo, G. Ribeiro, R. P. de Castro, and H. S. Oliveira, "Experimental evaluation of a loss-minimization control of induction motors used in EV," in *34th Annual Conference of IEEE Industrial Electronics*, 2008, pp. 1194–1199.

[368] A. M. Bazzi and P. T. Krein, "Review of methods for real-time loss minimization in induction machines," *IEEE Transactions on Industry Applications*, vol. 46, no. 6, pp. 2319–2328, 2010.

[369] Xilinx, "Spartan 3 FPGA family-complete datasheet," 2008.